THE UNIVERSITY OF CHICAGO

LEVERAGING ELECTRON- AND PROTON-STORING LIGANDS FOR SELECTIVE NI- AND CU-CATALYZED REDOX TRANSFORMATIONS

A DISSERTATION SUBMITTED TO

THE FACULTY OF THE DIVISION OF THE PHYSICAL SCIENCES

IN CANDIDACY FOR THE DEGREE OF

DOCTOR OF PHILOSOPHY

DEPARTMENT OF CHEMISTRY

BY

MAIA ELIZABETH CZAIKOWSKI

CHICAGO, ILLINOIS

AUGUST 2025

Abstract

Modern civilization depends on catalytic processes for essential products – from fertilizers that sustain global food production, to pharmaceuticals, to industrial materials. The critical advantage of catalysis lies in its resource and energy efficiency, and the study of catalytic processes connects fundamental science with practical advances. There are myriad approaches to catalyst design: heterogeneous inorganic materials, homogeneous metal-ligand complexes, and metal-free organocatalysts have all proven successful in different cases. Of course, nature also provides elegant examples of catalytic engines with impressive rates of reactivity and exquisite selectivity. Equally impressive is that these enzymes mainly utilize first-row transition metals which are earth-abundant and largely non-toxic. The organization of the active site secondary sphere in these enzymatic active sites serves a host of functions including enforcing substrate coordination through hydrogen bonding and controlling the flow of protons and electrons in a reaction. Bio-inspired approaches in ligand design allow chemists to borrow these successful strategies from nature without having to extract or synthesize bio-catalysts.

Metal-ligand cooperativity, or the active participation of both the metal and ligand in chemical transformations, is one powerful strategy from biology that can be mimicked in synthetic chemistry. For example, redox-active ligands allow for multi-electron reactions using metals that typically engage in single-electron processes. What's more, proton-shuttling moieties on the ligand scaffold can enable fine-tuned control over the transfer of proton, H-atom, or hydride equivalents in addition to providing hydrogen bonding interactions to position a substrate or stabilize an intermediate. Combining multiple metal-ligand cooperative strategies in a single ligand has been shown to be an effective approach in widely utilized reactions such as the hydrogenation of unsaturated groups. Within this field, a 2,5-dihydrazonopyrrole (DHP) scaffold has been

demonstrated to store and transfer a full equivalent of H_2 from the ligand backbone. This thesis focuses on DHP complexes of Ni and Cu and the development of catalytic redox methods utilizing the cooperative properties of these complexes.

In Chapter I, I discuss the synthesis of a DHP complex with Cu and its reactivity with O_2. This Cu-O_2 complex engages in a range of aerobic catalytic oxidations with substrates including alcohols and aldehydes. While several examples of bio-inspired Cu(II) superoxo model complexes have been reported, they are not typically competent aerobic catalysts, which positions this system uniquely to provide mechanistic insight into the role of these intermediates in catalytic aerobic oxidative transformations.

In Chapter II, I introduce an electrochemical method for the selective semi-hydrogenation of terminal alkynes using a DHP complex of Ni. Mechanistic studies show that the transformation is inner-sphere, with *Z*-selectivity for selected cases of internal alkyne semi-hydrogenation. Calculations support a ligand-based hydrogen-atom transfer pathway rather than a hydride mechanism, which is commonly invoked for transition metal hydrogenation catalysts. The efficient flow of H-atom equivalents toward substrate reduction over hydrogen evolution provides a blueprint for applying similar strategies toward a range of electroreductive transformations.

In Chapter III, I build off of the electrosynthetic platform discussed in the previous chapter to develop a method for the selective hydroalkylation of terminal alkynes to generate a variety of 1,1-disubstituted olefins. This approach avoids the use of harsh reductants and employs a weak acid, making it tolerant of amine and ketone functional groups. Mechanistic studies demonstrate the essential role of the ligand steric environment in dictating product regioselectivity. Calculations support an outer sphere alkyl radical addition instead of a Ni-mediated inner-sphere insertion mechanism which is commonly invoked for transition metal hydroalkylation catalysts. The scope

of the reaction includes primary and secondary alkyl iodide electrophiles along with unactivated alkyne substrates. These findings underscore how metal-ligand cooperativity, particularly with ligand-based storage of protons and electrons, supports catalytic platforms which can be tuned for varied electrosynthetic applications beyond hydrogenation.

Please note, all chapters have an independent compound and figure numbering system. Supplementary data and information are provided in the corresponding appendix for each chapter.

Contents

List of Figures

List of Tables

Appendix I

Appendix II

Acknowledgments

I want to thank my advisor, John Anderson, for providing the opportunity to do research in his lab and for being a wonderful mentor. Seeing the passion, hard work, and rigor that John brings to scientific discussion and research inspired and motivated me throughout my degree. John is also dedicated to his students and prioritizes their progress as a scientist and an individual. My understanding always deepened as a result of the time John was willing to spend talking through results and complex questions. I am tremendously grateful for the flexibility John showed as I navigated my career development, his support gave me the opportunity and confidence to pursue my goals to the fullest.

I would also like to thank Professors Anna Wuttig and Mark Levin for serving on my thesis committee and for generously lending their time over the years to discuss my research. Their perspectives brought up new questions and ideas that improved my work, and I enjoyed their thoughtful discussions.

I had the pleasure of working with many fantastic scientists and supportive colleagues in the Anderson Lab during my time here. My first research mentor in the group, Kate Jesse, was incredibly knowledgeable and patient with me as a new member of the lab. I have so much appreciation for the work it took to train me even as she prepared for her own graduation. I also benefited from working with my sub-group partner, Sophie Anferov. I learned from Sophie to explore projects with curiosity and follow interesting leads in new directions. She was also an exceptional writing partner for two review articles we authored together. I would also like to acknowledge Andrew McNeece, who began exploring the (DHP)Cu complex and provided the groundwork for my first project in the group.

I am very thankful to Ningxin Jiang, who ventured with me into the world of electrochemistry. His positivity and creative thinking always made him a joy to work with. Joseph Schneider was also a vital resource as I learned how to run DFT calculations and try more complicated computational investigations. I am very appreciative of the alacrity with which he answered my questions and the many template files he shared with me. I would also like to recognize Patrick Crossland for devoting so much time to teaching me XAS data processing and EXAFS fitting. His guidance and sense of humor made the process highly interesting and even a bit fun. I admire all of the graduate students and post-docs who helped to shape my early development in the group: Maggie Kelty, McKenna Goetz, Norman Zhao, Jorge Martinez, Jiaze Xie, Andrew Ritchhart, and Lei Wang.

The brilliant and kind people I get to work with consistently brighten my day and make the lab a positive place. I've enjoyed sharing a desk area with Joe Scott, Alexandra Krupinski, and Lauren McNamara. Joe is routinely and unintentionally hilarious, and he is also extremely thoughtful about his science and the processes of the lab. Alex has been a wonderful addition to the bifunctional sub-group. I am so excited by the directions her research is going, and she is a kind and friendly presence in lab. It is very special to have entered the program with Lauren and grown together as scientists over the years. I especially cherish our shared enthusiasm for lab décor and the many lab outings and trips we've shared. Thank you also to Alex Tascher, who worked with me as an undergraduate and made important contributions to the semi-hydrogenation project. I wish her the best in her bright future. I would also like to acknowledge Chen-Yu Lien, Shilin Zeng, and Nate Lopez for being wonderful lab-mates.

Additionally, I was fortunate to carry out research at GSK during my PhD, and I am so appreciative of the mentors and friends I met during my time there. Working there opened new

scientific opportunities for me in medicinal chemistry, and I benefited greatly from being in proximity to so many talented and supportive chemists.

My friends in Chicago have kept me grounded and brought so much fun into my time living in the city. First and foremost, meeting Olivia Laxton has been the best part of grad school, and I am so thankful that we got to live together for four years. Liv is hilarious, driven, and has the confidence and ability to advocate for herself and others, which I always admire. Thank you also to all the Dolphins (both official and unofficial) who welcomed me when I first moved to Chicago and have become my close friends.

Sam, my incredible partner, has shown both steadfast support and genuine interest in my work throughout my degree. I deeply cherish that I had the chance to live in his hometown and experience it through his perspective while creating our own memories together. I value how we encourage each other to take on challenges and pursue ambitious goals. At the same time, sharing his company in both quiet moments and celebrations brings me tremendous comfort and rejuvenation.

I want to thank my parents, Mary and Neil, for giving me every opportunity to explore my interests and express myself growing up. I never doubted that I could be whatever I wanted thanks to their love and the values they instilled. Our phone calls and visits always invigorate me, and their advice and encouragement over the course of my degree was invaluable. I also want to thank my brother, Matthew, for never failing to bring laughter to my life. We make a great team, and I am so proud of him. My extended family has also championed me from afar, and every time we get together my heart is beaming. To my Chicago family: Ann, John, and Ella, thank you for graciously welcoming me and supporting me with lovely meals and excellent company. My circle of supporters, advisors, and friends fills me with gratitude and confidence. Thank you all.

Introduction

Utilizing Metal-Ligand Cooperativity for Catalyst Design

Catalytic transformations frequently involve multiple electron transfer processes. While second- and third-row transition metals naturally facilitate two-electron transfer mechanisms, making them effective catalysts for numerous industrial applications, their scarcity, high cost, and toxicity present significant drawbacks (Figure 1A and B). [1,2]

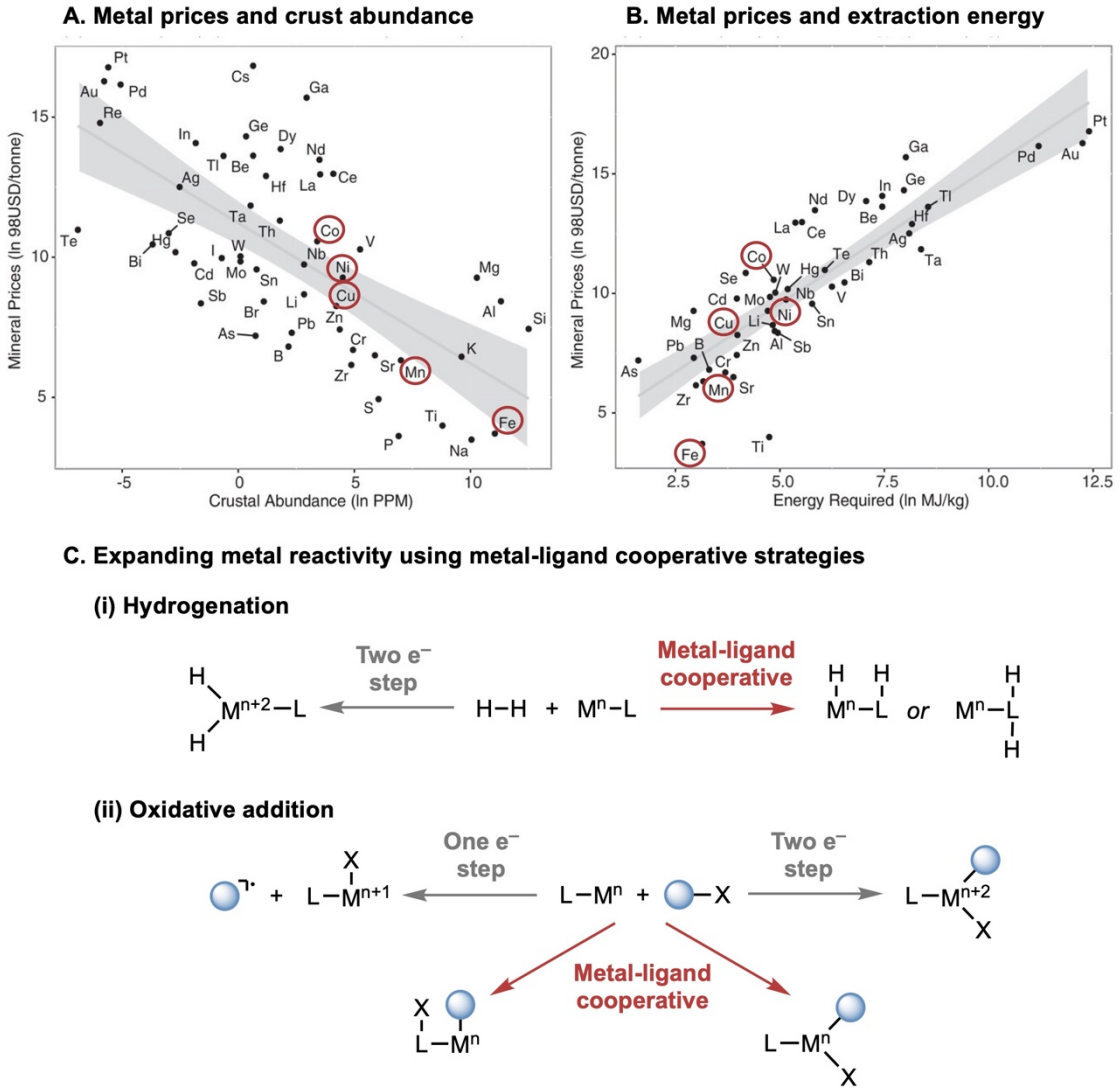

Figure 1. A. Log-linear relationships between metal prices, abundance, and **B.** extraction energy.[1] **C.** Examples of metal-ligand cooperativity in bond activation steps. Graphs A and B adapted with permission from John Wiley & Sons, Copyright 2025.

To develop more sustainable catalytic systems, it is advantageous to turn toward more abundant and economical first-row transition metals such as Mn, Fe, Co, Ni, Cu, and Zn. However, these non-precious metals routinely engage in single-electron transfer reactions, which introduces challenges in controlling reactivity and selectivity. Metal-ligand cooperation offers a promising approach to address these limitations (**Figure 1C**).

In conventional catalytic systems, bond formation and cleavage primarily occur at the metal center while the coordinating ligand remains ancillary. The ligand's role is typically limited to providing coordination, modifying the metal's electronic properties through electron-donating or withdrawing effects, or exerting steric influence through bulky functional groups. However, significantly enhanced catalytic efficiency can be achieved when the metal-bound organic scaffold actively participates in the elementary steps of catalytic reactions.[3]

Over recent decades, various ligands have been developed with distinct properties to enable metal-ligand cooperative catalysis. These include ligands capable of forming hydrogen bonds with substrates to achieve supramolecular control,[4-8] proton-responsive ligands that undergo property changes upon protonation/deprotonation,[9-14] ligands featuring molecular recognition centers for selective functional group interactions,[15-19] photo-active ligands that respond to light irradiation,[20-23] and redox-active ligands that accept and donate electrons during catalysis.[24-29] Many of these properties feature frequently in metalloenzymes found in nature and aid in enabling exquisite selectivity and activity in enzymatic processes.[30,31]

Among varied cooperative ligands, redox-active ligands offer particular advantages due to their capacity to undergo multiple redox processes (**Figure 2**). By functioning as "electron reservoirs," these ligands can store and release electrons as required during catalytic cycles, allowing base metals to effectively catalyze reactions that would otherwise require second- or

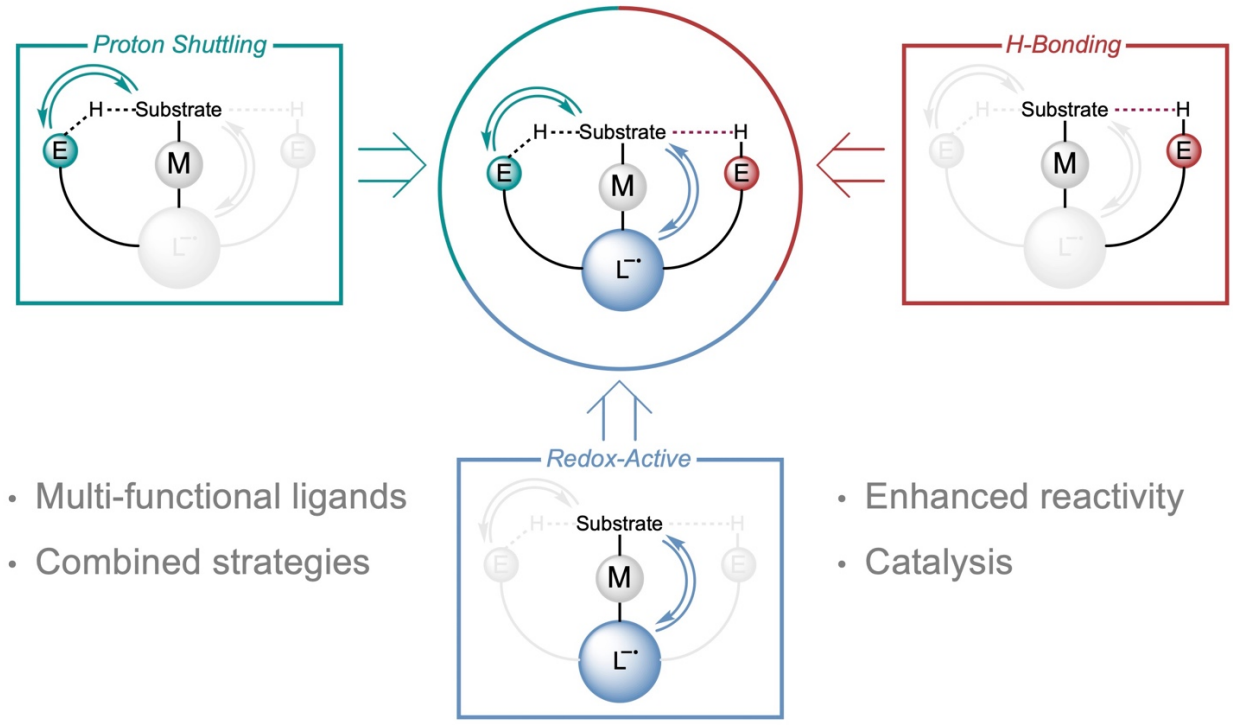

Figure 2. Individual strategies for metal-ligand cooperative scaffolds and how they can combine to produce multi-functional ligands.

third-row transition metals. Electron transfer can occur at either the metal center or the ligand with varying degrees of electron delocalization depending on the electronic structure of the scaffold. While the formal oxidation state on the separate metal and ligand fragments may be ambiguous due to extensive electron delocalization and metal ion characteristics, these systems have attracted interest due to their applicability in catalysis as well as their similarities to metalloenzyme mechanisms.[32]

Combining multiple features of metal-ligand cooperative design has many compelling benefits (**Figure 2**). For instance, the reversible storage of protons *and* electrons can assist in the mediation of proton-coupled-electron-transfer (PCET) instead of solely proton-transfer (PT) or electron-transfer (ET) Systems designed with both electron storage capabilities and proton-accepting sites can facilitate these complex transfers. Recent advances include ligands capable of

storing complete hydrogen atom equivalents or even molecular hydrogen (H_2), either across extended conjugated frameworks or localized double bonds. The design criteria for effective cooperative ligands are demanding, as they must incorporate sites for electron and proton storage while maintaining traditional ligand functions like stabilizing a metal center. Despite these challenges, the field continues to develop sophisticated ligand frameworks with diverse structural motifs that can support multiple proton and electron transfers.

H-Atom and H_2 Storing Ligand Scaffolds for PCET Reactivity

Adapted from: Czaikowski, M.E.*; Anferov, S.W.*; Anderson, J.S. *Trends in Chemistry*, **2021**, *3* (12), 993.

Most of the ligands that engage in PCET reactivity rely upon conjugated systems that have previously been shown to exhibit redox-active behavior.[24-29] The main design principle to enable PCET reactivity is the inclusion of a basic moiety where a proton can be stored. Such sites also have the added advantage of providing hydrogen bonding motifs which can interact with a substrate or stabilize the ligand through non-covalent interactions (**Figure 2**).

One successful application of this strategy comes from the Heyduk group, where O-N-O pincer ligands perform PT, PTET, and PTETET reactivity depending on the substrate utilized (**Figure 3A, i**).[33] Prototypical redox-active pyridinediimine scaffolds also feature prominently in this area. Gilbertson and coworkers also invoke PTETET with an iron pyridinediimine complex featuring an appended base that serves as a proton shuttle in enhancing rates of catalytic nitrite reduction (**Figure 3A, ii**).[34] The Berben group has used aluminum complexes for stoichiometric ligand-promoted activation of water and amines which was later was expanded to include catalytic oxidative couplings of benzylic amines (**Figure 3A, iii**).[35]

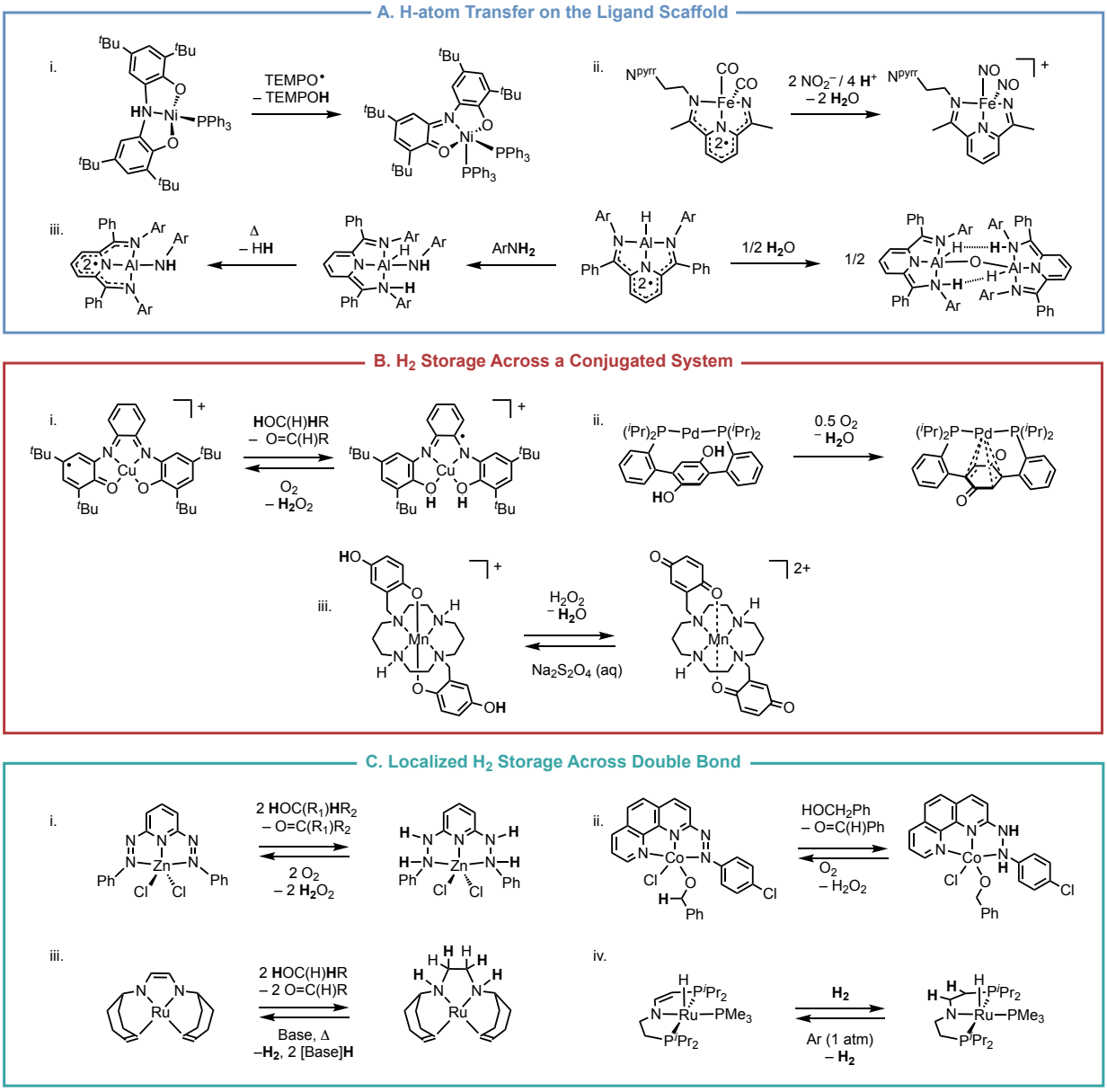

Figure 3. Selected examples of ligands capable of storing **A.** H-atoms, **B.** H_2 across an extended conjugated system, and **C.** H_2 across a double bond. H-atoms being transferred between ligand and substrate and bolded.

The storage and transfer of a full equivalent or more of H_2 on the ligand scaffold enables more diverse reactivity. Furthermore, this strategy also mimics systems in enzyme active sites. While successful implementations of this strategy are still limited, two general approaches have emerged: storing H_2 across an extended conjugated framework (**Figure 3B**) or across a localized

double bond (**Figure 3C**). Both of these tactics have different benefits. Extended π-systems have the advantage of accessible redox chemistry, as well as more flexible arrangement of the H-substituents. Conversely, localized double bonds can be more easily appended onto ligand scaffolds, and multiple localized double bonds make storing multiple equivalents of H_2 more facile.

An early example of ligand-based proton and electron storage comes from a galactose oxidase model complex with a salen-like diaminobenzene ligand (**Figure 3B, i**).[36] The Agapie group also used a bis-phosphine ligand with a strategically positioned hydroquinone moiety to transfer H_2 in the reduction of dioxygen to water (**Figure 3B, ii**).[37] Ligand-based H_2 transfer is enforced by the coordination of the quinoid moiety to the metal center which inhibits oxygen binding. Goldsmith and coworkers have also incorporated hydroquinone- based motifs into ligands for novel applications in H_2O_2 dismutation or sensing in MRI contrast agents (**Figure 3B, iii**).[38] Goswami and coworkers utilized a related hydrazine-based pincer ligand, but in this case H_2 storage occurs at localized N=N bonds. In this example, two successive alcohol dehydrogenations lead to storage of $4(H^+, e^-)$ on the ligand with a redox-inactive Zn metal center (**Figure 3C, i**).[39] These hydrogenated complexes can subsequently reduce dioxygen to hydrogen peroxide to enable aerobic catalysis. Related N=N motifs have also been employed in the catalytic generation of quinazolin-4(3H)-ones from amides and alcohols (**Figure 3C, ii**).[40] DFT calculations on this Co(II)-arylazo system from the Paul group support that ligand-based redox circumvents more energetically taxing metal-centered multi-electron redox steps.

The Grützmacher group has reported an example where H_2 incorporation occurs across a supporting ligand C=C double bond. This system incorporates $H_2 + 2(H^+)$ on the diazadiene ligand

moiety (**Figure 3C, iii**).[41] The ligand functions cooperatively with a Ru metal-center to activate C– H bonds in alcohols and transfer an H-atom equivalent to the unsaturated C=C groups on the ligand backbone. Mechanistic investigations indicate that this process occurs in a successive manner, and the catalytic cycle is closed when the fully reduced metal-ligand complex releases H_2 under basic conditions. Reversible hydrogenation of a C=C bond has also been observed in a PNP-type ligand scaffold reported by Schneider and coworkers. Here, the authors noted that H_2 storage and release can also serve to tune metal-centered reactivity (**Figure 3C, iv**).[42] The hydrogenated ligand backbone exhibits stronger π-donation and alters primary coordination sphere interactions.

While leveraging ligand-based storage of protons and electrons is still a nascent area, the above examples demonstrate that this strategy enables the transfer of multiple proton and electron equivalents in stoichiometric and catalytic systems. The future of this field lies in moving beyond proof-of-concept by tuning and controlling these intricate systems. As the next section will discuss, it is also beneficial to merge metal-ligand cooperative complexes with enabling technologies to develop modern catalytic platforms.

Metal-Ligand Cooperativity in Reductive Chemical Electrosynthesis

Adapted from: Czaikowski, M.E.*; Anferov, S.W.*; Anderson, J.S. *Chem Catalysis*, **2024**, *4* (1), 100922.

Electrochemistry has been an increasingly useful tool for organic synthesis as it can selectively generate reactive intermediates under mild conditions using an applied potential. Concurrently, synergistic activity of a metal and ligand has been used in thermal catalysis and electrocatalytic renewable fuel generation for substrate selectivity and improved catalyst activity. Combining these synthetic strategies is an attractive approach for mild, selective, and sustainable electrosynthesis.

One of the appealing design principles of electrosynthetic approaches is the modularity and tunability of the overall reaction set up. Features such as electrochemical potential and current can be tuned separately from experimental factors such as electrode material, solvent, or even concentrations of other chemical reagents. Even more complex variables can be modulated when considering designed solid-state electrodes[43-45] and/or the electrochemical interface between the electrode and solution.[46] The inherent synthetic tunability of molecular catalysts, as amply illustrated in thermal catalysis and electrocatalytic renewable fuel generation, also provides a powerful approach to tune electrosynthetic transformations. Use of these strategies in electrosynthetic transformations, both reductive and oxidative, is still nascent, despite the ubiquity of metal-ligand cooperativity in the previously mentioned applications. [47-51,52-63] This motivates further application of synergistic design principles in electrosynthetic transformations across many scales.

Selected examples illustrating the utility of metal-ligand cooperativity in reductive organic electrosynthesis are summarized in **Figure 4** and **5**. These complexes have been applied for C–C bond formation, difunctionalization, ketone reduction, and olefin hydrogenation/dehydrogenation processes. Key advantages that emerge from these electrochemical set-ups include mild reaction conditions that can tolerate otherwise sensitive functional groups as well as tuneability afforded by separately controlling acid species and applied potential. This allows modulation of both the thermodynamics and the kinetics of a given reaction. For the examples discussed below, many perform electrolysis at constant potential. The ability to choose a specific potential for these reactions provides a precise control over driving force to a degree that is not feasible with chemical reductants. Alternatively, some examples also employ constant current electrolysis, favored by many for synthetic applications due to operational simplicity. Stoichiometric acid is also needed

for hydrogenative transformations, but there is no requirement for stoichiometric reducing agents or hydride donors as in comparable thermal systems. Besides an electrolyte, many systems have minimal additives and operate at room temperature.

There are several approaches to metal-ligand cooperativity in electroreductive processes which mirror analogous thermal systems. Pendant or backbone amine groups can serve as proton/H-atom shuttles likely because they can be weakly basic and have relatively weak BDEs when coupled with a redox-active moiety. Furthermore, extensive π-conjugation using bipyridine and terpyridine ligands, among other scaffolds, stabilizes ligand-based radicals for metal-ligand cooperative redox transformations of a substrate.

As many electro-reductive transformations with added proton sources must compete with hydrogen evolution reactivity, achieving good Faradaic efficiencies for the targeted organic transformations requires minimization of this parasitic reaction. Several strategies using ligand design, choice of metal, acid pK_a, solvent, electrode material, and applied potential can be effective.[64,65]

Applications of H-Storing Ligands in Reductive Electrosynthesis

Transformations such as ketone reduction to alcohols and alkene hydrogenation have been demonstrated to proceed electrochemically using catalysts that can store an H-atom ($H^+ + e$).[66,67,68] Installing pendant amine arms in the secondary coordination sphere of an *o*-substituted bipyridine ligand facilitates proton transfer from the ligand to a Mn center upon one-electron reduction to yield a Mn–H complex (**Figure 4, i**).[66] Here, it is likely that the well-precedented redox non-innocence of the bipyridine scaffold plays an important role. Electrochemical evidence for this

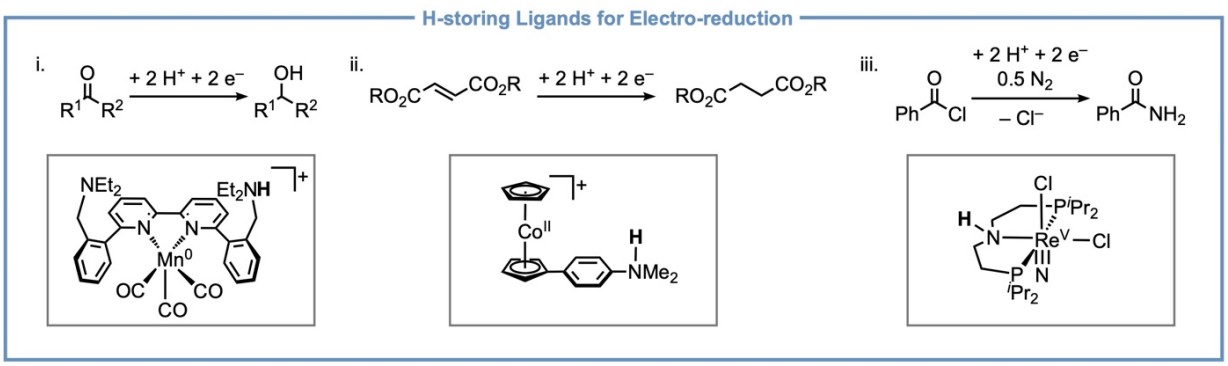

Figure 4. Reductive electrocatalytic transformations using catalysts with ligand-based H-storage. Intermediate structures from the proposed catalytic cycles are depicted to highlight the properties of each ligand.

ligand-assisted proton transfer comes in the form of an irreversible pre-wave before the catalytic reductive feature in the CV. This feature is proposed to correspond to the formation of a Mn-H intermediate from a reduced, arm-protonated Mn complex. The Mn–H species cannot form in the presence of H_2 alone, which highlights the unique thermodynamic advantage of having separate $H^+ + e^-$ sources in an electrochemical set-up. The authors were able to favor ketone hydrogenation over H_2 evolution by using a weaker acid (TFE) and achieved an FE of 80% for *iso*-propanol formation from acetone.

Ligand design can also be employed to minimize undesired HER. In the case of a cobaltocenium-dimethylaniline complex, the phenyl ring spacer decouples the redox and proton transfer sites on the mediator, inhibiting HER while still enabling reactivity with a substrate (**Figure 4, ii**).[67] No substrate binding is observed experimentally or computationally to the Co center. However, DFT calculations predict that ligand templating with the electron-withdrawing groups on the olefin substrate is critical for selectivity. The ester substituents are predicted to π-stack with the cyclopentadienyl ligand to stabilize the anionic intermediate and prevent dimerization. The ease of H-atom transfer from the mediator to a substrate is also enabled by the weak bond dissociation free energy (BDFE) of 39 kcal/mol for the N–H bond.

In addition to multiple thermal examples of metal-ligand cooperativity using unsaturated PNP pincer ligands, this ligand scaffold also enables electrocatalysis. A rhenium PNP complex was shown to both activate N_2 and facilitate a reductive N transfer (**Figure 4, iii**).[68] A benzoyl chloride substrate was converted to benzamide, and equal yields of benzonitrile and benzoic acid. Combining an applied potential along with 2,6-dichlorophenol enables ligand reduction to turn over the catalytic cycle. This example highlights how the adoption of electrochemistry in a multi-step cycle or synthesis can provide a selective and efficient means to achieve a reductive transformation.

Applications of Electron Storing and Transferring Ligands in Reductive Electrosynthesis

While H-storing ligands are appealing for reductive transformations, redox-active ligands also enable reductive transformations where protons are not required or are transferred in outer-sphere processes. In an example of ligand-redox electrocatalysis, *o*-diiminoquinones have been utilized to generate 4-coordinate Co complexes, and under reducing potentials these complexes form a dianionic intermediate capable of activating benzyl bromide to form bibenzyl (**Figure 4, i**).[69]

Upon screening conditions for the redox-neutral ring-opening functionalization of cyclopropyl ketones, the Weix group discovered that applying a reducing potential improved yields compared to standard conditions (**Figure 4, ii**).[70] The role of the reducing equivalents in this system is to rescue off-cycle oxidized catalysts formed by comproportionation and regenerate the active reduced form of the catalyst. The catalyst itself, a Ni terpyridine complex, possesses a redox-active ligand radical which operates in tandem with the Ni(I/II) couple.

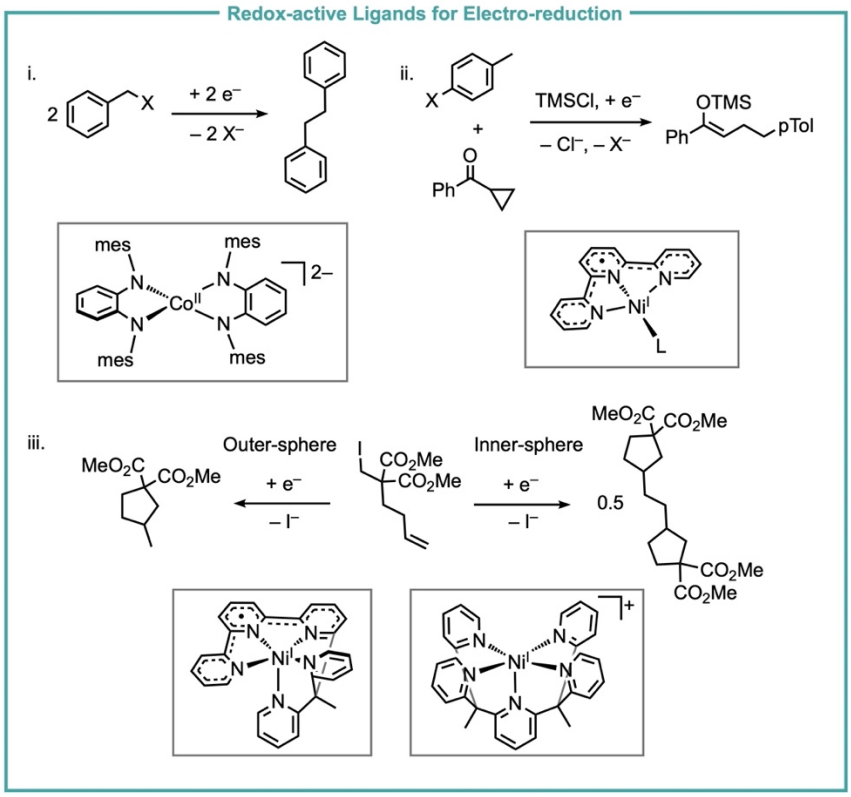

Figure 5. Reductive electrocatalytic transformations using catalysts with redox-active ligands. Intermediate structures from the proposed catalytic cycles are depicted to highlight the properties of each ligand.

Electro-reduction of a substrate using a redox-active ligand can enable reactivity differences compared to metal-centered redox catalysis. Detailed studies on a square pyramidal Ni complex bearing either a redox-active terpyridine moiety or a redox-innocent penta-pyridyl ligand revealed altered reactivity with an alkyl iodide substrate depending on the chosen ligand scaffold (**Figure 4, iii**).[71] The cyclized monomeric product was favored for outer-sphere electron transfer in the case of the redox-active ligand complex, and the coupled dimer product was generated in the case of inner-sphere electron transfer with the solely Ni-based redox catalyst. The ability of the ligand-based radical species to engage in outer-sphere electron transfer followed by trapping of the radical substrate by the Ni center is thought to lead to the observed selectivity for cyclized

over dimerized products. These examples illustrate the breadth of approaches utilizing metal-ligand cooperativity in electrocatalysis, and particularly how the ability to tune both acid source and applied potential proves advantageous for reductive transformations.

The modularity of both ligand design as well as electrocatalysis allows for a broad array of tuning, including synthetic changes to the ligand and the use of different reagents (i.e. acids/bases) or electrocatalytic conditions (electrode, electrolyte, current, potential). This modularity, as well as exciting initial proofs-of-concept in applying metal-ligand cooperativity, suggest that leveraging this strategy in electrosynthesis will be a powerful and general approach over the coming years.

Dihydrazonopyrrole Ligands: Development and Reactivity

Previous work in the Anderson group synthesizing proton-storing and redox active ligands has focused on a dihydrazonopyrrole (DHP) scaffold. The ligand has three possible redox states, which, when combined with a redox active metal center, result in rich electronic properties for the resultant complexes (**Figure 6**). The DHP ligand also has two sites of protonation at the β-hydrazone position of the ligand arms. Altogether, the ligand backbone can store a full equivalent of H_2, which in turn can be transferred to a substrate without invoking an oxidation state change

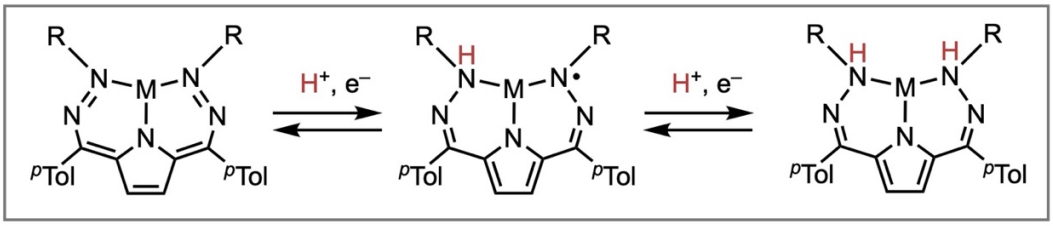

Figure 6. Dihydrazonopyrrole (DHP) scaffold with generic R-group substituents and metal center. Reversible redox activity and proton storage is depicted.

at the metal center. The β-hydrazone R-substituent can be modified in a relatively facile manner via the condensation reaction of a chosen hydrazine with a 2,5-ditolylacylpyrrole precursor.

Since developing the synthetic protocol for these DHP ligands, several studies have established the bifunctional properties of these complexes when ligated to first-row transition metals. Using the phenyl derivative of this ligand (R = phenyl, ^{Ph}DHP), the three redox states of the ligand could be characterized in addition to the deprotonated and singly protonated states.[72] Furthermore, the T-shaped geometry adopted by the ligand could also be characterized crystallographically, and different capping ligands including phosphines, pyridine, and acetonitrile were employed to stabilize the Ni complex. Subsequently, a synthetic method to remove the capping ligand and reveal the three-coordinate T-shaped complex was developed.[73] This expanded the reactivity of the (^{Ph}DHP)Ni complex due to enhanced substrate binding at the fourth coordination site of the Ni center. In the ligand radical state, the (^{Ph}DHP)Ni complex homolytically activates H_2O to form a dimer with a bridging hydroxide.[73] This non-symmetric dimer contained one oxidized ligand and one reduced and protonated ligand. Reacting the dimer with triphenylphosphine resulted in O-atom transfer to form triphenylphosphine-oxide as well as competitive C–H activation and oxidation of the ligand arm. Due to the formation of a kinetically persistent dimeric product consisting of two mono-protonated (^{Ph}DHP)Ni complexes, catalytic turnover and further oxidative reactivity was deactivated.

A key synthetic development which has expanded the reactivity of DHP-metal complexes was replacement of the phenyl R-groups with *tert*-butyl groups ($^{t\text{Bu}}$DHP). A T-shaped ($^{t\text{Bu}}$DHP)Ni complex with a ligand-based radical could be synthesized from metalation directly without the need for additional stabilizing ligands.[74] Furthermore, the bulkier *tert*-butyl groups prevent the formation of dimers, which was a pitfall for reactivity with the phenyl derivative. The ($^{t\text{Bu}}$DHP)Ni

complex activates O_2 via ligand-based electron transfer to generate a Ni(II) superoxo complex.[74] This superoxo complex performs stoichiometric oxidations of benzyl alcohol and toluene to generate benzaldehyde. An Fe complex of $^{t\text{Bu}}$DHP also engages in O_2 activation and subsequent reactivity.[75] Notably, an H-atom from the ligand can transfer to a proposed Fe-superoxo species to generate an Fe-hydroperoxo, which can participate in O-atom transfer reactivity with triphenylphosphine. The yield of triphenylphosphine oxide was stoichiometric with respect to Fe, indicating that only one O-atom from the hydroperoxo moiety was transferred to a substrate. Additionally, hydrogen peroxide was detected in solution, presumably from transfer of the ligand's second H-atom donor site to the Fe-hydroperoxo intermediate to generate free hydrogen peroxide and the dehydrogenated ligand complex. Hydrogen peroxide was also the major product formed from electrocatalytic and stoichiometric water oxidation utilizing a ($^{t\text{Bu}}$DHP)Co[Cl] complex.[76] Unlike the Fe system, computational evidence suggests that the ligand does not store H-atom equivalents over the course of the reaction, but the electron-storing properties of the $^{t\text{Bu}}$DHP ligand are still invoked in the proposed mechanism. Testing Cu-ligated $^{t\text{Bu}}$DHP complexes for oxidative reactivity was a logical next step due to the prominence of Cu in aerobic oxidative catalysis in both biology and synthetic chemistry. The synthesis of a ($^{t\text{Bu}}$DHP)Cu complex and its reactivity with O_2 will be discussed in **Chapter 1** along with the first example of oxidative catalysis with a DHP-ligated complex.

The storage and catalytic transfer of H_2 on DHP ligand scaffolds was demonstrated initially with the oxidized ($^{t\text{Bu}}$DHP)Ni[OTf] complex.[77] The mechanism of hydrogenation catalysis, including substrate coordination by the Ni center and H-atom transfer from the ligand-stored reducing equivalents, is reminiscent of enzymatic active sites where H_2 transfer can be mediated by the secondary coordination sphere. By metalating with Co instead of Ni, dramatically improved

catalytic efficiency could be achieved for thermal hydrogenations using H_2 as a stoichiometric reductant.[78] Building from this demonstrated hydrogenation reactivity, we wondered if a DHP ligated metal complex could engage in similar hydrogen storage and transfer under electrochemical conditions. Electrosynthesis offers benefits in terms of sustainability and efficiency, but it can also enable enhanced chemoselectivity and tunable reactivity. Specific to the ($^{t\text{Bu}}$DHP)Ni system, the reduction of the ligand by H_2 was sluggish, which presented an opportunity to improve the catalytic performance of this complex by shifting to an electrochemical platform. Instead of chemical reductants, the addition of protons and electrons are controlled separately through the addition of acid and an applied electric potential, respectively. The development of this electrocatalytic system for alkyne semi-hydrogenation and its adaptation for hydroalkylation reactivity will be discussed in **Chapters 2** and **3**. This strategy provides a blueprint for harnessing metal-ligand cooperativity in reductive chemistry and using electrochemical platforms as a tool for enabling selective and efficient catalysis.

References

1. Watson, B. J.; Eggert, R. G., Understanding relative metal prices and availability: Combining physical and economic perspectives. *J. Ind. Ecol.* **2021,** *25* (4), 890-899.
2. Egorova, K. S.; Ananikov, V. P., Which Metals are Green for Catalysis? Comparison of the Toxicities of Ni, Cu, Fe, Pd, Pt, Rh, and Au Salts. *Angew. Chem. Int. Ed.* **2016,** *55* (40), 12150-12162.
3. Anferov, S. W.; Czaikowski, M. E.; Anderson, J. S., Metal–ligand cooperative transfer of protons and electrons. *Trends Chem.* **2021,** *3* (12), 993-996.
4. Perdriau, S.; Zijlstra, D. S.; Heeres, H. J.; de Vries, J. G.; Otten, E., A Metal–Ligand Cooperative Pathway for Intermolecular Oxa-Michael Additions to Unsaturated Nitriles. *Angew. Chem. Int. Ed.* **2015,** *54* (14), 4236-4240.
5. Reek, J. N. H.; de Bruin, B.; Pullen, S.; Mooibroek, T. J.; Kluwer, A. M.; Caumes, X., Transition Metal Catalysis Controlled by Hydrogen Bonding in the Second Coordination Sphere. *Chem. Rev.* **2022,** *122* (14), 12308-12369.
6. Hoveyda, A. H.; Lombardi, P. J.; O'Brien, R. V.; Zhugralin, A. R., H-Bonding as a Control Element in Stereoselective Ru-Catalyzed Olefin Metathesis. *J. Am. Chem. Soc.* **2009,** *131* (24), 8378-8379.
7. Olivos Suarez, A. I.; Jiang, H.; Zhang, X. P.; de Bruin, B., The radical mechanism of cobalt(ii) porphyrin-catalyzed olefin aziridination and the importance of cooperative H-bonding. *Dalton Trans.* **2011,** *40* (21), 5697-5705.
8. Marelius, D. C.; Darrow, E. H.; Moore, C. E.; Golen, J. A.; Rheingold, A. L.; Grotjahn, D. B., Hydrogen-Bonding Pincer Complexes with Two Protic N-Heterocyclic Carbenes from Direct Metalation of a 1,8-Bis(imidazol-1-yl)carbazole by Platinum, Palladium, and Nickel. *Chem. Eur. J.* **2015,** *21* (31), 10988-10992.
9. Periana, R. A.; Taube, D. J.; Gamble, S.; Taube, H.; Satoh, T.; Fujii, H., Platinum Catalysts for the High-Yield Oxidation of Methane to a Methanol Derivative. *Science* **1998,** *280* (5363), 560-564.
10. Hashiguchi, B. G.; Young, K. J. H.; Yousufuddin, M.; Goddard, W. A., III; Periana, R. A., Acceleration of Nucleophilic CH Activation by Strongly Basic Solvents. *J. Am. Chem. Soc.* **2010,** *132* (36), 12542-12545.
11. Himeda, Y.; Onozawa-Komatsuzaki, N.; Sugihara, H.; Kasuga, K., Simultaneous Tuning of Activity and Water Solubility of Complex Catalysts by Acid−Base Equilibrium of Ligands for Conversion of Carbon Dioxide. *Organometallics* **2007,** *26* (3), 702-712.
12. Noyori, R.; Hashiguchi, S., Asymmetric Transfer Hydrogenation Catalyzed by Chiral Ruthenium Complexes. *Acc. Chem. Res.* **1997,** *30* (2), 97-102.
13. Gunanathan, C.; Ben-David, Y.; Milstein, D., Direct Synthesis of Amides from Alcohols and Amines with Liberation of H_2. *Science* **2007,** *317* (5839), 790-792.
14. Henry, R. M.; Shoemaker, R. K.; DuBois, D. L.; DuBois, M. R., Pendant Bases as Proton Relays in Iron Hydride and Dihydrogen Complexes. *J. Am. Chem. Soc.* **2006,** *128* (9), 3002-3010.
15. Noyori, R., Asymmetric Catalysis: Science and Opportunities (Nobel Lecture). *Angew. Chem. Int. Ed.* **2002,** *41* (12), 2008-2022.
16. Breslow, R.; Huang, Y.; Zhang, X.; Yang, J., An artificial cytochrome P450 that hydroxylates unactivated carbons with regio- and stereoselectivity and useful catalytic turnovers. *Proc. Natl. Acad. Sci.* **1997,** *94* (21), 11156-11158.
17. Das, S.; Incarvito, C. D.; Crabtree, R. H.; Brudvig, G. W., Molecular Recognition in the Selective Oxygenation of Saturated C-H Bonds by a Dimanganese Catalyst. *Science* **2006,** *312* (5782), 1941-1943.
18. Wilson, M. E.; Whitesides, G. M., Conversion of a protein to a homogeneous asymmetric hydrogenation catalyst by site-specific modification with a diphosphinerhodium(I) moiety. *J. Am. Chem. Soc.* **1978,** *100* (1), 306-307.
19. Šmejkal, T.; Breit, B., A Supramolecular Catalyst for the Decarboxylative Hydroformylation of α,β-Unsaturated Carboxylic Acids. *Angew. Chem. Int. Ed.* **2008,** *47* (21), 3946-3949.
20. Segarra-Maset, M. D.; van Leeuwen, P. W. N. M.; Freixa, Z., Light Switches the Ligand! Photochromic Azobenzene–Phosphanes. *Eur. J. Inorg. Chem.* **2010,** *2010* (14), 2075-2078.
21. Sud, D.; Norsten, T. B.; Branda, N. R., Photoswitching of Stereoselectivity in Catalysis Using a Copper Dithienylethene Complex. *Angew. Chem. Int. Ed.* **2005,** *44* (13), 2019-2021.
22. Rölz, M.; Butschke, B.; Breit, B., Azobenzene-Integrated NHC Ligands: A Versatile Platform for Visible-Light-Switchable Metal Catalysis. *J. Am. Chem. Soc.* **2024,** *146* (19), 13210-13225.
23. Sherstiuk, A.; Lledós, A.; Lönnecke, P.; Hernando, J.; Sebastián, R. M.; Hey-Hawkins, E., Dithienylethene-Based Photoswitchable Phosphines for the Palladium-Catalyzed Stille Coupling Reaction. *Inorg. Chem.* **2024,** *63* (17), 7652-7664.

24. Chirik, P. J.; Wieghardt, K., Radical Ligands Confer Nobility on Base-Metal Catalysts. *Science* **2010,** *327* (5967), 794-795.
25. Mondal, R.; Guin, A. K.; Chakraborty, G.; Paul, N. D., Metal–ligand cooperative approaches in homogeneous catalysis using transition metal complex catalysts of redox noninnocent ligands. *Org. & Biomol. Chem.* **2022,** *20* (2), 296-328.
26. Kaim, W., The Shrinking World of Innocent Ligands: Conventional and Non-Conventional Redox-Active Ligands. *Eur. J. Inorg. Chem.* **2012,** *2012* (3), 343-348.
27. Blanchard, S.; Derat, E.; Desage-El Murr, M.; Fensterbank, L.; Malacria, M.; Mouriès-Mansuy, V., Non-Innocent Ligands: New Opportunities in Iron Catalysis. *Eur. J. Inorg. Chem.* **2012,** *2012* (3), 376-389.
28. Schauer, P. A.; Low, P. J., Ligand Redox Non-Innocence in Transition-Metal σ-Alkynyl and Related Complexes. *Eur. J. Inorg. Chem.* **2012,** *2012* (3), 390-411.
29. Bart, S. C.; Chłopek, K.; Bill, E.; Bouwkamp, M. W.; Lobkovsky, E.; Neese, F.; Wieghardt, K.; Chirik, P. J., Electronic Structure of Bis(imino)pyridine Iron Dichloride, Monochloride, and Neutral Ligand Complexes: A Combined Structural, Spectroscopic, and Computational Study. *J. Am. Chem. Soc.* **2006,** *128* (42), 13901-13912.
30. Wodrich, M. D.; Hu, X., Natural inspirations for metal–ligand cooperative catalysis. *Nat. Rev. Chem.* **2017,** *2* (1), 0099.
31. Chu, K.-T.; Liu, Y.-C.; Huang, Y.-L.; Hsu, C.-H.; Lee, G.-H.; Chiang, M.-H., A Reversible Proton Relay Process Mediated by Hydrogen-Bonding Interactions in [FeFe]Hydrogenase Modeling. *Chem. Eur. J.* **2015,** *21* (31), 10978-10982.
32. Chaudhuri, P.; Verani, C. N.; Bill, E.; Bothe, E.; Weyhermüller, T.; Wieghardt, K., Electronic Structure of Bis(o-iminobenzosemiquinonato)metal Complexes (Cu, Ni, Pd). The Art of Establishing Physical Oxidation States in Transition-Metal Complexes Containing Radical Ligands. *J. Am. Chem. Soc.* **2001,** *123* (10), 2213-2223.
33. Charette, B. J.; Ziller, J. W.; Heyduk, A. F., Exploring Ligand-Centered Hydride and H-Atom Transfer. *Inorg. Chem.* **2021,** *60* (7), 5367-5375.
34. Cheung, P. M.; Burns, K. T.; Kwon, Y. M.; Deshaye, M. Y.; Aguayo, K. J.; Oswald, V. F.; Seda, T.; Zakharov, L. N.; Kowalczyk, T.; Gilbertson, J. D., Hemilabile Proton Relays and Redox Activity Lead to {FeNO}x and Significant Rate Enhancements in NO2– Reduction. *J. Am. Chem. Soc.* **2018,** *140* (49), 17040-17050.
35. Myers, T. W.; Berben, L. A., Aluminum–Ligand Cooperative N–H Bond Activation and an Example of Dehydrogenative Coupling. *J. Am. Chem. Soc.* **2013,** *135* (27), 9988-9990.
36. Chaudhuri, P.; Hess, M.; Müller, J.; Hildenbrand, K.; Bill, E.; Weyhermüller, T.; Wieghardt, K., Aerobic Oxidation of Primary Alcohols (Including Methanol) by Copper(II)− and Zinc(II)−Phenoxyl Radical Catalysts. *J. Am. Chem. Soc.* **1999,** *121* (41), 9599-9610.
37. Horak, K. T.; Agapie, T., Dioxygen Reduction by a Pd(0)–Hydroquinone Diphosphine Complex. *J. Am. Chem. Soc.* **2016,** *138* (10), 3443-3452.
38. Karbalaei, S.; Knecht, E.; Franke, A.; Zahl, A.; Saunders, A. C.; Pokkuluri, P. R.; Beyers, R. J.; Ivanović-Burmazović, I.; Goldsmith, C. R., A Macrocyclic Ligand Framework That Improves Both the Stability and T1-Weighted MRI Response of Quinol-Containing H2O2 Sensors. *Inorg. Chem.* **2021,** *60* (12), 8368-8379.
39. Pramanick, R.; Bhattacharjee, R.; Sengupta, D.; Datta, A.; Goswami, S., An Azoaromatic Ligand as Four Electron Four Proton Reservoir: Catalytic Dehydrogenation of Alcohols by Its Zinc(II) Complex. *Inorg. Chem.* **2018,** *57* (12), 6816-6824.
40. Sinha, S.; Das, S.; Mondal, R.; Mandal, S.; Paul, N. D., Cobalt complexes of redox noninnocent azo-aromatic pincers. Isolation, characterization, and application as catalysts for the synthesis of quinazolin-4(3H)-ones. *Dalton Trans.* **2020,** *49* (25), 8448-8459.
41. Rodríguez-Lugo, R. E.; Trincado, M.; Vogt, M.; Tewes, F.; Santiso-Quinones, G.; Grützmacher, H., A homogeneous transition metal complex for clean hydrogen production from methanol-water mixtures. *Nature Chem.* **2013,** *5* (4), 342-7.
42. Käß, M.; Friedrich, A.; Drees, M.; Schneider, S., Ruthenium Complexes with Cooperative PNP Ligands: Bifunctional Catalysts for the Dehydrogenation of Ammonia–Borane. *Angew. Chem. Int. Ed.* **2009,** *48* (5), 905-907.
43. Jackson, M. N.; Oh, S.; Kaminsky, C. J.; Chu, S. B.; Zhang, G.; Miller, J. T.; Surendranath, Y., Strong Electronic Coupling of Molecular Sites to Graphitic Electrodes via Pyrazine Conjugation. *J. Am. Chem. Soc.* **2018,** *140* (3), 1004-1010.

44. Kaminsky, C.J., Weng, S., Wright, J. *et al.* Adsorbed cobalt porphyrins act like metal surfaces in electrocatalysis. *Nat. Catal.* **2022**, 5, 430–442.
45. Lin, Z.; Han, C.; O'Connell, G. E. P.; Lu, X., Recent Progress on Electrode Design for Efficient Electrochemical Valorisation of CO_2, O_2, and N_2. *Angew. Chem. Int. Ed.* **2023,** *62* (38), e202301435.
46. Badgurjar, D.; Huynh, M.; Masters, B.; Wuttig, A., Non-Covalent Interactions Mimic the Covalent: An Electrode-Orthogonal Self-Assembled Layer. *J. Am. Chem. Soc.* **2023,** *145* (32), 17734-17745.
47. Guan, W.; Chang, Y.; Lin, S., Electrochemically Driven Deoxygenative Borylation of Alcohols and Carbonyl Compounds. *J. Am. Chem. Soc.* **2023,** *145* (31), 16966-16972.
48. Cherney, A. H.; Reisman, S. E., Nickel-Catalyzed Asymmetric Reductive Cross-Coupling Between Vinyl and Benzyl Electrophiles. *J. Am. Chem. Soc.* **2014,** *136* (41), 14365-14368.
49. Sigeru, T.; Ping, L.; Hideo, T., Electrochemical Os-Catalyzed Asymmetric Dihydroxylation of Olefins with Sharpless' Ligand. *Chem. Lett.* **1995,** *24* (4), 319-320.
50. Fu, N.; Song, L.; Liu, J.; Shen, Y.; Siu, J. C.; Lin, S., New Bisoxazoline Ligands Enable Enantioselective Electrocatalytic Cyanofunctionalization of Vinylarenes. *J. Am. Chem. Soc.* **2019,** *141* (37), 14480-14485.
51. Gnaim, S.; Bauer, A.; Zhang, H.-J.; Chen, L.; Gannett, C.; Malapit, C. A.; Hill, D. E.; Vogt, D.; Tang, T.; Daley, R. A.; Hao, W.; Zeng, R.; Quertenmont, M.; Beck, W. D.; Kandahari, E.; Vantourout, J. C.; Echeverria, P.-G.; Abruna, H. D.; Blackmond, D. G.; Minteer, S. D.; Reisman, S. E.; Sigman, M. S.; Baran, P. S., Cobalt-electrocatalytic HAT for functionalization of unsaturated C–C bonds. *Nature* **2022,** *605* (7911), 687-695.
52. Malapit, C. A.; Prater, M. B.; Cabrera-Pardo, J. R.; Li, M.; Pham, T. D.; McFadden, T. P.; Blank, S.; Minteer, S. D., Advances on the Merger of Electrochemistry and Transition Metal Catalysis for Organic Synthesis. *Chem. Rev.* **2022,** *122* (3), 3180-3218.
53. Li, C.; Kawamata, Y.; Nakamura, H.; Vantourout, J. C.; Liu, Z.; Hou, Q.; Bao, D.; Starr, J. T.; Chen, J.; Yan, M.; Baran, P. S., Electrochemically Enabled, Nickel-Catalyzed Amination. *Angew. Chem. Int. Ed.* **2017,** *56* (42), 13088-13093.
54. Kawamata, Y.; Vantourout, J. C.; Hickey, D. P.; Bai, P.; Chen, L.; Hou, Q.; Qiao, W.; Barman, K.; Edwards, M. A.; Garrido-Castro, A. F.; deGruyter, J. N.; Nakamura, H.; Knouse, K.; Qin, C.; Clay, K. J.; Bao, D.; Li, C.; Starr, J. T.; Garcia-Irizarry, C.; Sach, N.; White, H. S.; Neurock, M.; Minteer, S. D.; Baran, P. S., Electrochemically Driven, Ni-Catalyzed Aryl Amination: Scope, Mechanism, and Applications. *J. Am. Chem. Soc.* **2019,** *141* (15), 6392-6402.
55. Barman, K.; Edwards, M. A.; Hickey, D. P.; Sandford, C.; Qiu, Y.; Gao, R.; Minteer, S. D.; White, H. S. Electrochemical reduction of $[Ni(Mebpy)_3]^{2+}$: elucidation of the redox mechanism by cyclic voltammetry and steady-state voltammetry in low ionic strength solutions. *Chem. ElectroChem* **2020**, *7*, 1473– 1479.
56. Ibrahim, M. Y. S.; Cumming, G. R.; Gonzalez de Vega, R.; Garcia-Losada, P.; de Frutos, O.; Kappe, C. O.; Cantillo, D., Electrochemical Nickel-Catalyzed C(sp3)–C(sp3) Cross-Coupling of Alkyl Halides with Alkyl Tosylates. *J. Am. Chem. Soc.* **2023,** *145* (31), 17023-17028.
57. Lin, Y.; von Münchow, T.; Ackermann, L., Cobaltaelectro-Catalyzed C–H Annulation with Allenes for Atropochiral and P-Stereogenic Compounds: Late-Stage Diversification and Continuous Flow Scale-Up. *ACS Catal.* **2023,** *13* (14), 9713-9723.
58. Fu, X.; Ran, T.; Zhou, Y.; Liu, J., Electroreductive Nickel-Catalyzed Allylation of Aryl Chlorides. *J. Org. Chem.* **2023,** *88* (9), 6132-6139.
59. Kerackian, T.; Bouyssi, D.; Pilet, G.; Médebielle, M.; Monteiro, N.; Vantourout, J. C.; Amgoune, A., Nickel-Catalyzed Electro-Reductive Cross-Coupling of Aliphatic N-Acyl Imides with Alkyl Halides as a Strategy for Dialkyl Ketone Synthesis: Scope and Mechanistic Investigations. *ACS Catal.* **2022,** *12* (19), 12315-12325.
60. Cai, C.-Y.; Zheng, Y.-T.; Li, J.-F.; Xu, H.-C., Cu-Electrocatalytic Diazidation of Alkenes at ppm Catalyst Loading. *J. Am. Chem. Soc.* **2022,** *144* (27), 11980-11985.
61. Chen, W.; Ni, S.; Wang, Y.; Pan, Y., Electrochemical-Promoted Nickel-Catalyzed Reductive Allylation of Aryl Halides. *Org. Lett.* **2022,** *24* (20), 3647-3651.
62. Xiong, P.; Hemming, M.; Ivlev, S. I.; Meggers, E., Electrochemical Enantioselective Nucleophilic α-C(sp3)–H Alkenylation of 2-Acyl Imidazoles. *J. Am. Chem. Soc.* **2022,** *144* (15), 6964-6971.
63. Rowbotham, J. S.; Reeve, H.A.; Vincent, K.A. Hybrid Chemo-, Bio-, and Electrocatalysis for Atom-Efficient Deuteration of Cofactors in Heavy Water, *ACS Catal.*, **2021***, 11*, 2596-2604

64. Rountree, E. S.; McCarthy, B. D.; Eisenhart, T. T.; Dempsey, J. L., Evaluation of Homogeneous Electrocatalysts by Cyclic Voltammetry. *Inorg. Chem.* **2014,** *53* (19), 9983-10002.
65. Suryanarayanan, V.; Noel, M., A comparative evaluation on the voltammetric behavior of boron-doped diamond (BDD) and glassy carbon (GC) electrodes in different electrolyte media. *J. Electroanal. Chemistry* **2010,** *642* (1), 69-74.
66. Fokin, I.; Kuessner, K.-T.; Siewert, I., Electroreduction of Carbonyl Compounds Catalyzed by a Manganese Complex. *ACS Catal.* **2022,** *12* (14), 8632-8640.
67. Derosa, J.; Garrido-Barros, P.; Peters, J. C., Electrocatalytic Reduction of C–C π-Bonds via a Cobaltocene-Derived Concerted Proton–Electron Transfer Mediator: Fumarate Hydrogenation as a Model Study. *J. Am. Chem. Soc.* **2021,** *143* (25), 9303-9307.
68. Schendzielorz, F.; Finger, M.; Abbenseth, J.; Würtele, C.; Krewald, V.; Schneider, S., Metal-Ligand Cooperative Synthesis of Benzonitrile by Electrochemical Reduction and Photolytic Splitting of Dinitrogen. *Angew. Chem. Int. Ed.* **2019,** *58* (3), 830-834.
69. van der Meer, M.; Rechkemmer, Y.; Peremykin, I.; Hohloch, S.; van Slageren, J.; Sarkar, B., (Electro)catalytic C–C bond formation reaction with a redox-active cobalt complex. *Chem. Commun.* **2014,** *50* (76), 11104-11106.
70. Gilbert, M. M.; Trenerry, M. J.; Longley, V. R.; Castro, A. J.; Berry, J. F.; Weix, D. J., Ligand–Metal Cooperation Enables Net Ring-Opening C–C Activation/Difunctionalization of Cyclopropyl Ketones. *ACS Catal.* **2023,** *13* (17), 11277-11290.
72. Chang, M.-C.; McNeece, A. J.; Hill, E. A.; Filatov, A. S.; Anderson, J. S., Ligand-Based Storage of Protons and Electrons in Dihydrazonopyrrole Complexes of Nickel. *Chem. Eur. J.* **2018,** *24* (31), 8001-8008.
73. Chang, M.-C.; Jesse, K. A.; Filatov, A. S.; Anderson, J. S., Reversible homolytic activation of water via metal–ligand cooperativity in a T-shaped Ni(ii) complex. *Chem. Sci.* **2019,** *10* (5), 1360-1367.
74. McNeece, A. J.; Jesse, K. A.; Xie, J.; Filatov, A. S.; Anderson, J. S., Generation and Oxidative Reactivity of a Ni(II) Superoxo Complex via Ligand-Based Redox Non-Innocence. *J. Am. Chem. Soc.* **2020,** *142* (24), 10824-10832.
75. Jesse, K. A.; Anferov, S. W.; Collins, K. A.; Valdez-Moreira, J. A.; Czaikowski, M. E.; Filatov, A. S.; Anderson, J. S., Direct Aerobic Generation of a Ferric Hydroperoxo Intermediate Via a Preorganized Secondary Coordination Sphere. *J. Am. Chem. Soc.* **2021,** *143* (43), 18121-18130.
76. Anferov, S. W.; Boyn, J.-N.; Mazziotti, D. A.; Anderson, J. S., Selective Cobalt-Mediated Formation of Hydrogen Peroxide from Water under Mild Conditions via Ligand Redox Non-Innocence. *J. Am. Chem. Soc.* **2024,** *146* (9), 5855-5863.
77. McNeece, A. J.; Jesse, K. A.; Filatov, A. S.; Schneider, J. E.; Anderson, J. S., Catalytic hydrogenation enabled by ligand-based storage of hydrogen. *Chem. Commun.* **2021,** *57* (32), 3869-3872.
78. Anferov, S. W.; Filatov, A. S.; Anderson, J. S., Cobalt-Catalyzed Hydrogenation Reactions Enabled by Ligand-Based Storage of Dihydrogen. *ACS Catal.* **2022,** *12* (16), 9933-9943.

Chapter 1: Generation and Aerobic Oxidative Catalysis of a Cu(II) Superoxo Complex Supported by a Redox-Active Ligand

This chapter has been adapted from the following: Czaikowski, M.E.; McNeece, A.J.; Boyn, J.N.; Jesse, K.A.; Anferov, S.W.; Filatov, A.S.; Mazziotti, D.A.; Anderson, J.S. *J. Am. Chem. Soc.* **2022**, *144*, 34, 15569-15580.

Introduction

Dioxygen is an abundant, inexpensive, atom-economical, and environmentally benign oxidant compared to widely used stoichiometric reagents such as chromium and manganese oxides, peracids, and hypervalent iodine species.[1-11] Nevertheless, implementing O_2 in a catalytic regime requires mechanistic control over its kinetically unfavorable activation and overoxidation of substrates. Copper-based systems, particularly those coupled with redox-active additives such as aminoxyl radicals, have emerged as effective catalysts for aerobic oxidations (**Figure 1A**).[12-26] Enabled by copper's accessible redox chemistry, facile ligand exchange, and broad functional group compatibility, synthetic C–H functionalization methods have been developed to access two-electron processes, especially when combined with co-catalysts.[27-31]

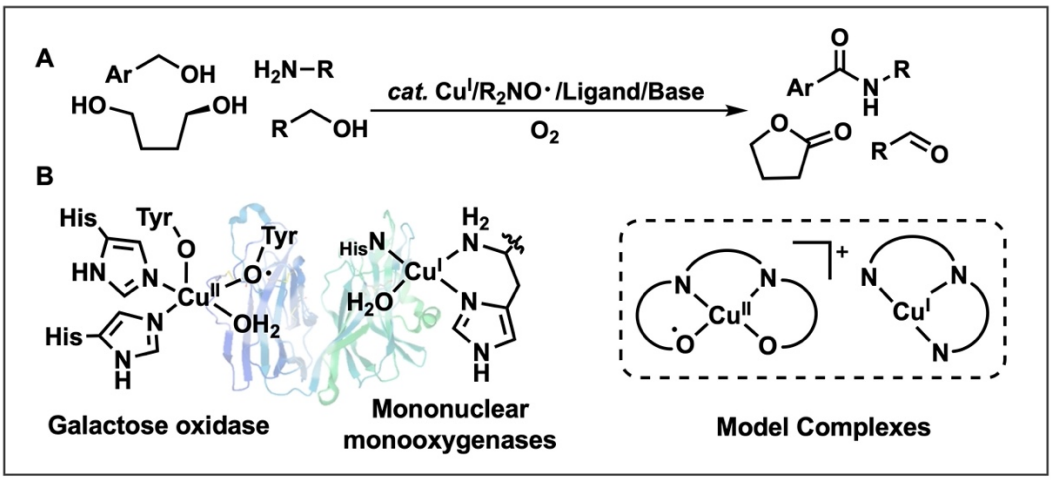

Figure 1. Overview of representative **A.** Cu(I) + aminoxyl catalysts for aerobic oxidations and **B.** general model compound structures inspired by Cu monooxygenase and oxidase active sites.

The efficacy of Cu in aerobic oxidation chemistry is in large part motivated by its prevalence in biological oxidations.[32] This prevalence has spurred efforts to synthesize compounds that model the active sites of Cu-containing monooxygenase and oxidase (**Figure 1B**). Efforts over many years have successfully isolated examples of several oxygenated Cu intermediates such as mononuclear Cu-superoxo species.[20,22-24,33-42] While synthetic Cu(II)-superoxo complexes have been characterized,[35-37,40,41] well-characterized end-on examples in a monooxygenase-like N3 T-shaped ligand geometry are comparatively rare.[24,38,43] These bioinspired Cu systems have also been applied to alcohol oxidation and hydroxylation reactivity, but in these cases thorough observation or characterization of discrete intermediates, such as Cu-superoxo complexes, is often not possible; detailed characterization on unifying intermediates such as Cu-superoxo complexes is lacking generally for catalytic systems.[17,18,24,44] Thus, while enzyme model complexes enable the isolation of putative catalytic intermediates, these model systems are typically not competent catalysts. In support of this scarcity, there has been only one example of a catalytic transformation mediated by a well-characterized Cu-superoxo complex, and this example is a redox-neutral aldol coupling.[43] Conversely, thoroughly characterized superoxo intermediates in aerobic catalysis have been observed in Mn, Fe, and Co-based systems which makes the rarity of similarly observable species in the ubiquitous aerobic catalysis of Cu even more notable.[45-48]

Previous investigations of biomimetic reactivity with dihydrazonopyrrole (DHP) ligand scaffolds explored H^+, e^-, H-atom, or H_2 transfer similar to biological cofactors or active sites. This strategy has enabled the generation of superoxo and hydroperoxo intermediates with Ni and Fe respectively,[49,50] but no aerobic catalysis was observed in these systems. We rationalized that the noted aerobic chemistry of Cu might enable oxidative catalysis, and that the established redox-activity of the DHP ligand might facilitate the observation and characterization of catalytic

intermediates such as superoxo complexes. Described below is the success of this strategy with thorough characterization of a Cu-superoxo intermediate which notably engages in aerobic catalysis at room temperature with a variety of substrates. These results further underscore how biomimetic approaches can facilitate aerobic catalysis and provide insights into the possible agency of oxygenated Cu intermediates such as superoxo and hydroperoxo species as active oxidants.

Results and Discussion

Synthesis and Electronic Structure of 1 and 2

Deprotonation of the dihydrazonopyrrole proligand $^{t\text{Bu,Tol}}$DHP·2 HCl with 4 eq of *n*-BuLi and 0.5 eq 1-hexene followed by addition to $CuCl_2$ yields [$^{t\text{Bu,Tol}}$DHP$^{2-\bullet}$]Cu (**1**) as a deep blue complex in 37% yield (**Figure 2**).[50] Single crystal X-ray diffraction (SXRD) reveals a T-shaped

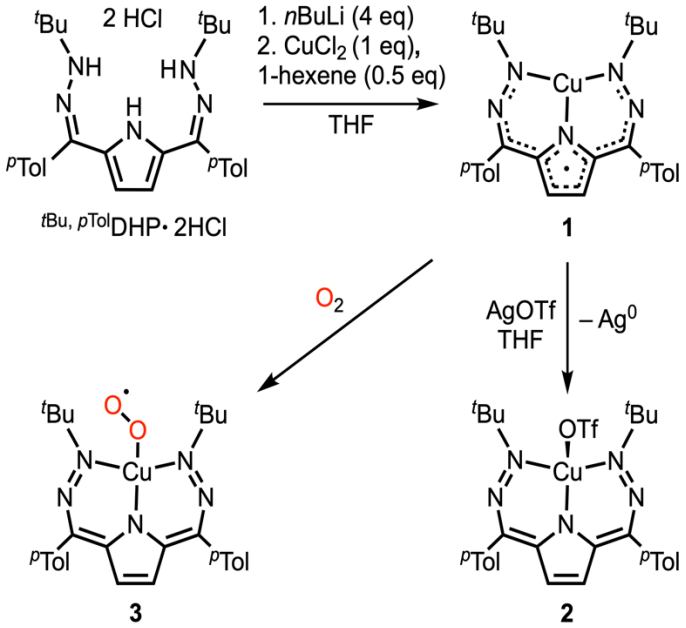

Figure 2. Synthesis of **1**, **2**, and **3**.

complex with Cu–N1/N5 bond lengths of 1.895(3) and 1.890(3) Å and N3–Cu–N5/N1 bond angles of 93.83(1)º and 93.66(1)º (**Figure 3A**). Complex **1** is diamagnetic (Appendix I: **Figure S1**), but ligand-based redox events previously characterized for [$^{t\text{Bu,Tol}}$DHP$^{2-\bullet}$]Ni raise the possibility of an antiferromagnetically coupled (DHP$^{2-\bullet}$)Cu(II) electronic description for **1** rather than a d^{10} (DHP^{-})Cu(I) complex.[47,50,51] The cyclic voltammogram (CV) of **1** shows three reversible redox features: an oxidation at −0.05 and reductions at −1.45, and −2.03 V vs Fc/Fc^{+} (**Figure 3B**, black). Based on the observed features for [$^{t\text{Bu,Tol}}$DHP$^{2-\bullet}$]Ni (**Figure 3B**, gray) and a putative Cu(II)/DHP$^{2-\bullet}$ electronic structure for **1** (see below), these three features can be tentatively assigned as the (DHP^{-})Cu(II)/(DHP$^{2-\bullet}$)Cu(II), (DHP$^{2-\bullet}$)Cu(II)/(DHP^{3-})(Cu(II), and (DHP^{3-})Cu(II)/(DHP^{3-})Cu(I) couples respectively. The oxidative feature is shifted 250 mV more positive compared to [$^{t\text{Bu,Tol}}$DHP$^{2-\bullet}$]Ni, which demonstrates that the Cu system is more oxidizing.

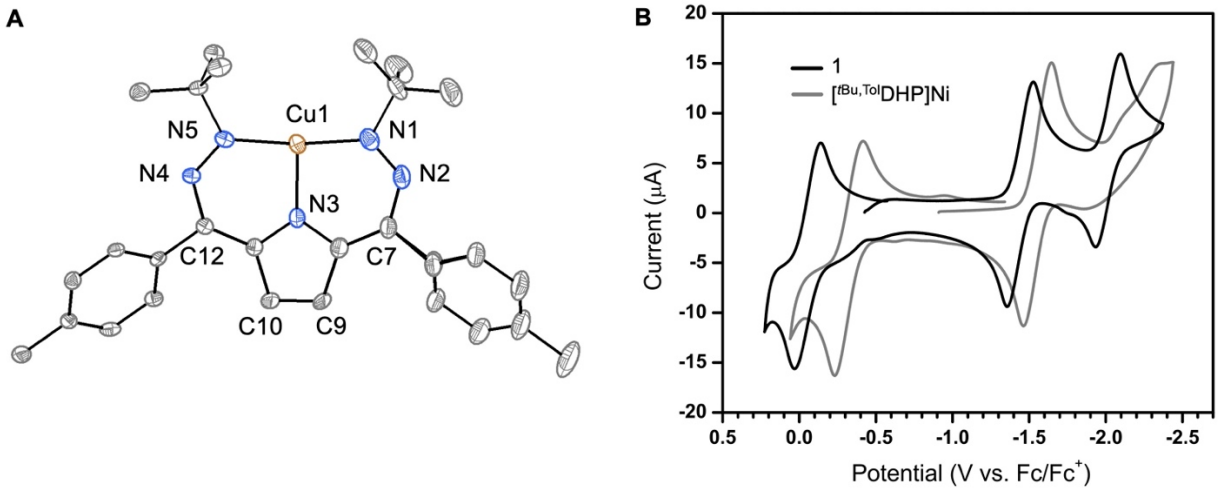

Figure 3. A. SXRD of **1**. Ellipsoids are set to 50% probability and hydrogen atoms have been omitted for clarity. Selected bond lengths and angles: Cu1–N1 1.895(3) Å, Cu1–N3 1.952(3) Å, Cu1–N5 1.890(3) Å, N1–N2 1.289(3) Å, N5–N4 1.293(4) Å, C9–C10 1.347(5) Å, N1–Cu1–N3 93.66(1)º, N5–Cu1–N3 93.83(1)º. **B.** Cyclic voltammogram of **1** (black line) and [$^{t\text{Bu,Tol}}$DHP•]Ni (gray line) in THF (1 mM [Cu] or [Ni], 0.1 M NBu_4PF_6, scan rate 100 mV s^{-1}). The small shoulder at –0.3 V for **1** arises from a small impurity in the electrolyte (Appendix I: **Figure S29**).

Based on this electrochemical data, we chemically oxidized **1** with 1.1 equiv of AgOTf, resulting in an immediate color change from blue to green and formation of [$^{t\text{Bu,Tol}}$DHP^{-}]CuOTf (**2**) (**Figure 2**). The SXRD structure for **2** shows a Cu–OTf bond length of 2.076(2) Å and a distorted tetrahedral geometry with τ_4 and τ_4' values of 0.49 and 0.50, respectively (Appendix I: **Figure S43**). Complex **2** has broad ^{1}H NMR resonances typical of a paramagnetic Cu(II) center. Evans method analysis provides a μ_{eff} of 1.72 μ_B which is consistent with an $S = ½$ spin state (spin only value: 1.73 μ_B) (Appendix I: **Figure S3**). The X-band EPR spectrum of **2** in 1:1 toluene:methylene chloride is consistent with this assignment, with a near-axial signal at $g = 2.063$, 2.064, and 2.083 (Appendix I: **Figure S19**). The ^{19}F NMR signal for **2** is broadened and shifted compared to free triflate consistent with some solution state anion binding (Appendix I: **Figure S4**). Changes to the DHP bond lengths upon oxidation of **1** to **2** support that ligand-based oxidation may be occurring. Notably, the shortening of the N1-N2/N5-N4 hydrazone arms and C9-C10 pyrrole backbone bond lengths matches a simplistic resonance description of the expected bond contractions upon oxidation of the radical dianion ligand to the monoanion (Appendix I: **Table S19**). Nevertheless, we wanted to obtain additional support for this formal (DHP$^{2-\bullet}$)Cu(II) electronic structure assignment.

We acquired Cu K-edge X-ray absorption spectroscopy (XAS) spectra of **1** and **2** to further probe the geometry and proposed electronic structures using **2** as a bona-fide Cu(II) reference complex (**Figure 4A**). Complex **1** has an intense rising-edge feature at 8982.5 eV which we assign as a shakedown 1s $\rightarrow$ 4p transition with a simultaneous ligand-to-metal charge transfer excitation by analogy to the same feature observed in the isostructural complex [$^{t\text{Bu,Tol}}$DHP$^{2-\bullet}$]Ni.[50] Similar rising edge shakedown features are observed for Cu(II) complexes which supports our assignment

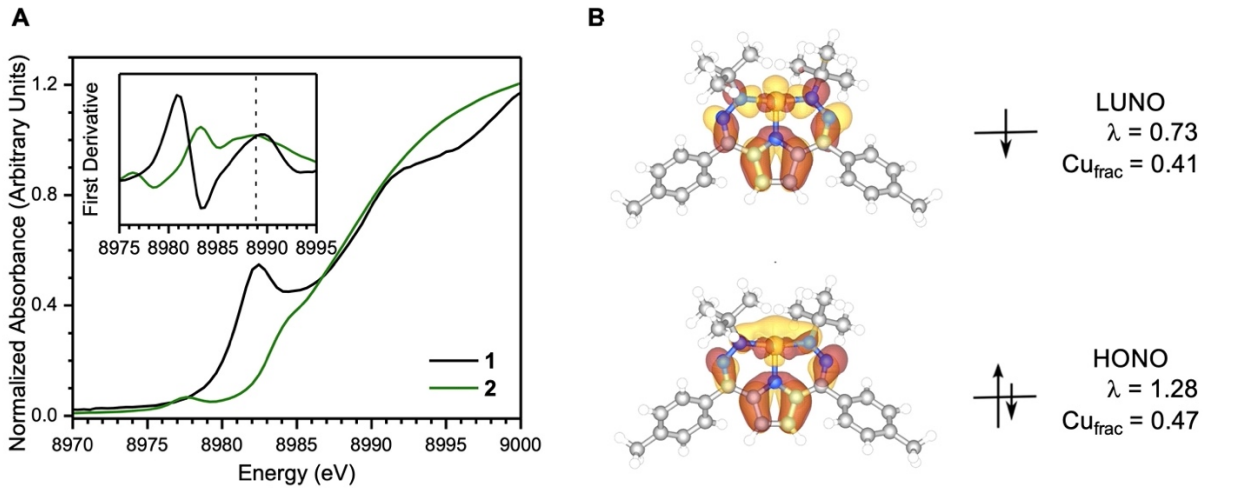

Figure 4. A. Cu K-edge X-ray absorption data for **1** (black) and **2** (green) with the smoothed first derivative of normalized absorbance (inset). Dashed line indicates the energy at half-maximum normalized absorbance. **B.** Frontier natural orbitals and their natural occupation numbers (λ) for **1** along with fractional atomic orbital contributions to the natural orbitals for Cu (Cu_{frac}). Data obtained via [14,14] V2RDM CASSCF calculations with the 6-31G* basis set.

of a ($DHP^{2-\bullet}$)Cu(II) electronic structure, however we note that rising edge features are also observed for Cu(I) complexes which convolutes this assignment.[52-55]

The energy of the 1s → 4p transition for **1** is lower than that for square planar Cu(II) complexes, which may reflect that the open coordination site trans to the pyrrole for this T-shaped complex stabilizes the $4p_x$ orbital and shifts the transition to lower energy.[56-60] Related rising edge features have also been associated with some T-shaped Cu(I) complexes, where the electric dipole-allowed 1s → 4p transition corresponds to a sharp rising edge peak, although such peaks are typically of a larger normalized intensity than what is observed for **1**.[61,62] In addition to the rising-edge feature, there is a notable absence of a pre-edge feature which might be expected for a Cu(II) center. However, we note that the intensity of the rising edge feature might obscure any pre-edge peak. Further insight into the electronic structure of **1** can be obtained by comparing its K-edge position to that of **2**. Visual inspection of the edge energies at half-maximum for **1** and **2** reveal nearly superimposable edges suggesting very similar Cu(II) oxidation states.[47,50] Inspection of the

first derivative of the edge (**Figure 4A** inset) reveals a slight shift to lower energy for **2** (~1 eV), but edge-shifts between Cu(I) and Cu(II) complexes are typically larger, on the order of 2 eV.[63,64] Finally, we note that the intense shakedown peak in **1** is significantly attenuated and shifted to higher energy in **2**, changes which are consistent with a higher coordination number in **2** versus **1**.[64] In short, the XANES spectra of **1** and **2** are slightly more suggestive of a ($DHP^{2-\bullet}$)Cu(II) electronic structure in **1**, but convolutions prevent a definitive assignment.

To gain more insight on the electronic structure of **1**, particularly regarding the oxidation state at Cu, we undertook computational investigations. Geometries of the singlet and triplet states of the LCu complex were optimized using Density Functional Theory (DFT) at the B3LYP/6-31G* level of theory, revealing a singlet ground state with an adiabatic triplet-singlet gap of $\Delta H(T - S)$ = 3.94 kcal/mol (Appendix I: **Figures S40** and **S41**). To resolve the effects of multi-reference correlation in a possible ($DHP^{2-\bullet}$)Cu(II) open shell singlet, further calculations were then carried out using the variational two-electron reduced-density-matrix (V2RDM) complete active space self-consistent field (CASSCF) method. Utilizing the singlet ground state DFT geometry in combination with an active space of 14 electrons distributed in 14 spatial orbitals, [14,14], and a 6-31G* basis set, the V2RDM calculations also predict a strongly correlated singlet ground state and a vertical triplet-singlet gap of 1.51 kcal/mol.

The singlet ground state displays significant biradical character with frontier natural occupation numbers (NON) of 1.28 and 0.73 for the highest occupied natural orbital (HONO) and the lowest unoccupied natural orbital (LUNO), respectively. A molecular orbital diagram of the frontier natural orbitals shows the unpaired electron density to be delocalized across both the Cu center as well as the π system of the ligand (**Figure 4B**). To further analyze the delocalization of the unpaired electron density, the fraction of Cu atomic orbital contributions to the frontier NOs

was calculated, revealing the HONO and LUNO to be localized to 47% and 41% on the Cu center, respectively (Appendix I: **Table S18**). Thus, while the bonding in **1** appears to be highly covalent, with contributions from both Cu(I) and Cu(II) limiting resonance structures, the sum of the experimental and theoretical studies suggest that a Cu(II) oxidation state is most appropriate.

Reactivity with O_2

With the assignment of a DHP ligand radical for **1**, we then wanted to determine if this ligand-stored electron could activate O_2 in analogy with proposals for galactose oxidase (GO) and previously observed reactivity with DHP complexes of Ni.[49,50] Addition of an excess of dry O_2 to complex **1** elicits a color change from blue to green and a broadened ^{1}H NMR spectrum indicative of the formation of a paramagnetic product (**Figure 2**, Appendix I: **Figure S5**). This product has been assigned as an end-on κ1 Cu-superoxo complex [$^{t\text{Bu,Tol}}$DHP$^-$]CuO_2 (**3**) based on various spectroscopic methods. The conversion of **1** to **3** was monitored by UV-visible spectroscopy revealing an isosbestic transition (**Figure 5A**). The intense absorbance of **1** at 618 nm, assigned as a $\pi \rightarrow \pi^*$ transition on the DHP ligand, diminishes as new features centered at 420 and 670 nm arise. The growth of a feature at 420 nm is consistent with an O $\rightarrow$ Cu charge transfer absorption frequently observed for Cu-superoxo complexes.[39] The extinction coefficient of the shoulder at 420 nm (13,600 $M^{-1}cm^{-1}$) is higher than would be expected for an end-on superoxo complex (4,000-5,000 $M^{-1}cm^{-1}$), but we note overlapping higher energy absorbances which likely increase the overall absorbance in this region.[65] The isosbestic transformation occurs at room temperature as well as at −80 °C with no other noticeable intermediates. The rate of the disappearance of the

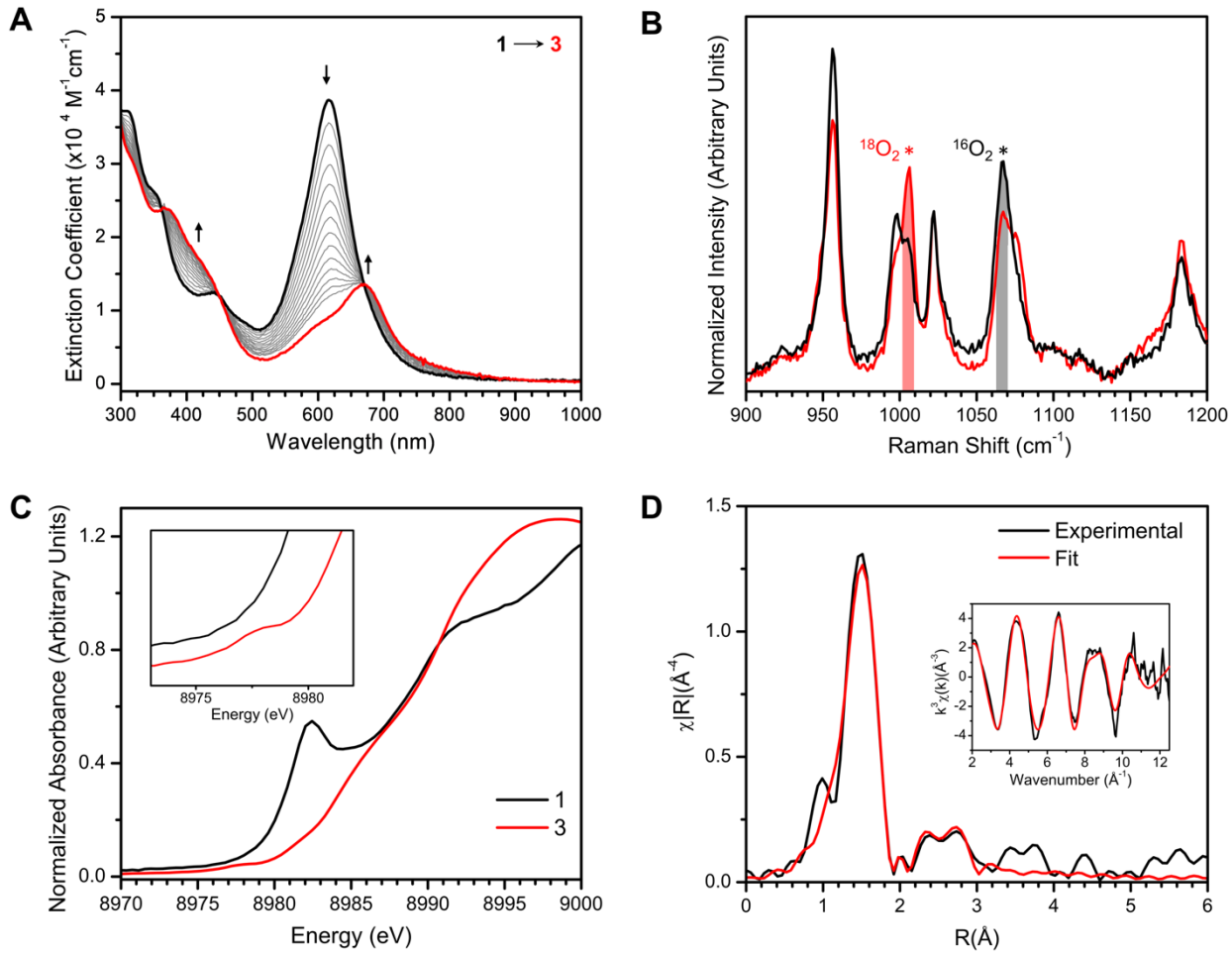

Figure 5. A. UV-visible spectroscopy of 0.015 mM **1** in DCM at 25 ºC upon addition of 2 mL of O_2 where **1** is black and **3** is red. Formation of **3** with scans every 2 minutes starting 4 minutes after O_2 addition. Extinction coefficient is based on initial concentration of **1**, assuming complete conversion to **3**. **B.** Variable isotope Raman spectra of the reaction of **1** with O_2 at room temperature to form **3**. The reactions with $^{16}O_2$ vs. $^{18}O_2$ are shown in the superoxo stretching region. **C.** Cu K-edge X-ray absorption data for **1** (black) and **3** (red) with an expanded pre-edge region (inset). **D.** R-space EXAFS fitting for **3**, with k-space shown in the inset (data, black; fits, red)

major absorbance of **1** in the presence of excess O_2 can be well-fit to a pseudo first-order decay (Appendix I: **Figure S23**).

Raman vibrational spectra were collected on thin films of **3** to confirm the presence of a Cu-superoxo moiety (**Figure 5B**). Laser excitation at 633 nm gave a band at 1067 cm^{-1} that shifts upon $^{18}O_2$ labeling to 1006 cm^{-1}, consistent with the simple harmonic oscillator predicted shift for

an O–O stretch of 60 cm^{-1} and also in good agreement with previous reports of end-on superoxo complexes.[38-40] In contrast, bridging and mononuclear peroxo complexes typically have stretches in the 750-950 cm^{-1} region.[66] We have not identified isotopically sensitive peaks in the Cu–O stretching region, however these low energy features are not as easily interpretable, putatively due to coupling to other vibrational modes as suggested by frequency calculations. This data supports the presence of a superoxo ligand in **3**, but we wanted to acquire further data to determine whether the superoxo binding mode was end-on or side-on.

We therefore acquired XAS data on **3** both to understand the electron transfer to form the superoxo as well as to obtain structural characterization on this complex. The XANES region of **3** shows clear changes compared to **1** including a low intensity pre-edge feature at 8975.5 eV assigned as a 1s $\rightarrow$ 3d transition (**Figure 5C**). The intensity of the pre-edge feature depends on the degree of p–d mixing, with DFT calculations predicting the p-orbital contribution to the highest lying d-orbital to be 1.1% (Appendix I: **Table S8**). The K-edge energies at half maximum intensity for **1** and **3** are nearly superimposable, consistent with a ligand to O_2 electron transfer event as would be expected from the ($DHP^{2-\bullet}$)Cu(II) electronic structure of **1**.[47,50] The extended X-ray absorption fine structure (EXAFS) region was also fit for the first three shells surrounding Cu with a k-space window from 2 to 12.5 Å–1 (**Figure 5D**). The fit confirms the assignment of an end-on Cu-superoxo complex, with a primary coordination shell (R = 1.94(2) Å) consisting of 4 N/O scatterers (Appendix I: **Table S3**). The terminal Cu···O scattering path was also fit in the second shell with a distance of R = 2.89(2) Å. This length is in remarkably good agreement with the DFT computed structure of **3** (see below, Appendix I: **Table S4**). We note that the inclusion of the superoxo ligand is essential to achieve good fits; removing either the β Cu···O scatterer or the superoxo entirely resulted in worse σ^2 values and larger errors (Appendix I: **Table S5**).

DFT computations also support the assignment of **3** as an end-on Cu-superoxo complex. The optimized open-shell triplet electronic configuration of **3** is predicted to be 4.6 kcal/mol more stable than the optimized open-shell singlet. Evan's method measurements support the assignment of a triplet ground state with μ_{eff} = 3.1 μ_B (spin only: 2.83 μ_B), although some degradation of the sample convolutes interpretation of this data (Apendix I: **Figure S6**). The predicted triplet ground state for **3** is unsurprising as there is precedent for triplet states in Cu-superoxo complexes that arise from O–O π^* character mixing with the Cu dz^2 orbital.[67] The optimized geometry of **3** has a Cu–O–O angle of 113° and a distance between Cu and the distal O-atom of 2.84 Å which again matches very well with the parameters obtained from EXAFS fitting (Appendix I: **Figure S34**).

Oxidative Catalysis and Mechanism

After rigorously characterizing **3** as an open-shell triplet Cu-superoxo complex, we monitored its oxidative reactivity with diphenylhydrazine (DPH) by UV-visible spectroscopy (Appendix I: **Figure S24**). After monitoring the conversion from **1** to **3** under O_2, the cuvette was purged with N_2 before injecting 10 equiv of DPH. Within 20 seconds the main superoxo absorbance at 670 nm was quenched, and the characteristic absorbance of **1** at 618 nm along with features from 300 to 450 nm corresponding to azobenzene were observed. This observation supports that **3** is a competent oxidizing species and prompted us to determine whether catalytic oxidations mediated by **3** might be possible (**Figure 6**).

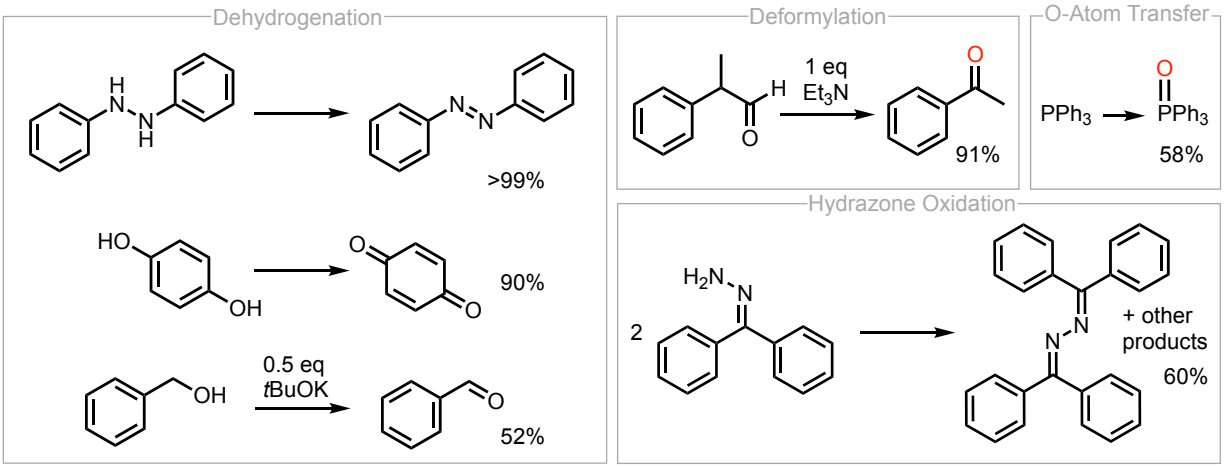

Figure 6. Catalytic oxidative reactivity of **3.** All reactions were carried out with 10 mol% **1** under 1 atm O_2 for 18 h in DCM, with the exception of benzyl alcohol which was in THF to better tolerate *t*BuOK. Yield determined by ^{1}H NMR spectroscopy (^{31}P NMR for PPh_3) and is based on integration compared to an internal standard (mesitylene) or the ratio of product/(product + starting material) for PPh_3.

Addition of 1 atm of O_2 to either DPH or 1,4-hydroquinone in the presence of 10 mol % of **1** results in the formation of azobenzene and paraquinone respectively, both in >90% yield (Appendix I: **Figures S7** and **S10**). Catalytic O-atom transfer with triphenylphosphine proceeds similarly with nearly 6 turnovers (Appendix I: **Figure S8**). This catalytic system is also competent for substrates with homolytically stronger E–H bonds if strong bases are used. Benzyl alcohol conversion to benzaldehyde occurs catalytically if 0.5 equiv of KO*t*Bu are added to the catalytic mixture (Appendix I: **Figure S9**). We hypothesize that deprotonation to generate benzyloxide may facilitate alkoxide binding or other subsequent mechanistic steps. We note related deprotonations in the mechanisms of both GO and Cu aminoxyl catalysis, so the need for base in our system is not unexpected. The muted reactivity of **1** with other stronger C–H bonds such as dihydroanthracene suggests a weak O–H BDE for the putative Cu-hydroperoxo product. Indeed, DFT calculations predict an O–H BDE of 70 $kcal^{-1}mol^{-1}$ for this species, supporting this hypothesis (Appendix I: **Table S7**).

Complex **1** also serves as a competent catalyst for oxidative reactivity beyond H-atom abstraction or phosphine oxidation. Catalytic deformylation of 2-phenylpropionaldehyde proceeds with 1 equiv of Et_3N to afford acetophenone in 91% yield (Appendix I: **Figure S11**). The proposed mechanism for aerobic deformylation involves initial nucleophilic attack by the superoxo moiety, likely aided in this system by the donating nature of the $^{t\text{Bu,Tol}}$DHP ligand's electron-rich *t*Bu groups.[68] Previously reported examples of aerobic aldehyde deformylation catalysts employ Fe and Co, but this reactivity profile is rare for Cu-superoxo species.[45-47]

Inspired by studies of hydrazone oxidation to form diazo compounds by synthetic Cu systems,[69] we also examined the reaction of 10 mol % **1** and benzophenone hydrazone under O_2. This reaction yields a 1:2 mixture of benzophenone and coupled azine with no detectable diazo product (Appendix I: **Figure S14**). This product mixture has been reported as the result of downstream reactivity of diazo complexes via hydrolysis.[70] While the coupled azine may formally be the product of self-condensation, we note it is not observed in significant quantities from self-decay of the starting hydrazone or in the presence of simple Cu salts as possible Lewis acids (Appendix I: **Table S1**). This instead suggests an oxidative process, similar to previously reported transformations.[70] Control reactions for all tested catalytic transformations support the importance of the (DHP)Cu complexes in supporting oxidative catalysis. While some examples exhibit background reactivity with simple Cu salts, the (DHP)Cu system shows uniformly higher reactivity (Appendix I: **Table S1**).

With the catalytic activity of **1** established, we then wanted to understand the mechanism of oxidative catalysis more thoroughly. We first investigated whether O_2 was being reduced directly to water, or if H_2O_2 was generated as a byproduct of catalysis. A test for H_2O_2 formation was carried out for the reaction with DPH by the addition of the H_2O_2 selective chemical test agent

1,3-diphenylisobenzofuran (DPBF).[71] Mass spectrometric analysis of the reaction mixture reproducibly showed the formation of the product 9-hydroxyanthracen-10(9H)-one which is diagnostic for the presence of H_2O_2 (Appendix I: **Figure S15**). Quantification of H_2O_2 via iodometric titration from reactions with hydroquinone show that the yield of H_2O_2 is small, but reproducible (Appendix I: **Table S2**, **Figure S18**). The formation of H_2O_2 is reasonable for a reaction mechanism where two H-atom equivalents from DPH or hydroquinone are transferred to a superoxo moiety resulting in the azobenzene product and H_2O_2 as a byproduct. The low observed yield of H_2O_2 is consistent with its ability to also serve as an oxidant for either substrate or in-situ formed Cu complexes (Appendix I: **Figure S27**).

The thermodynamic barriers of such a pathway along with putative transition states and intermediates were then investigated using DFT calculations for **3** (**Figure 7**). Hydrazine was used

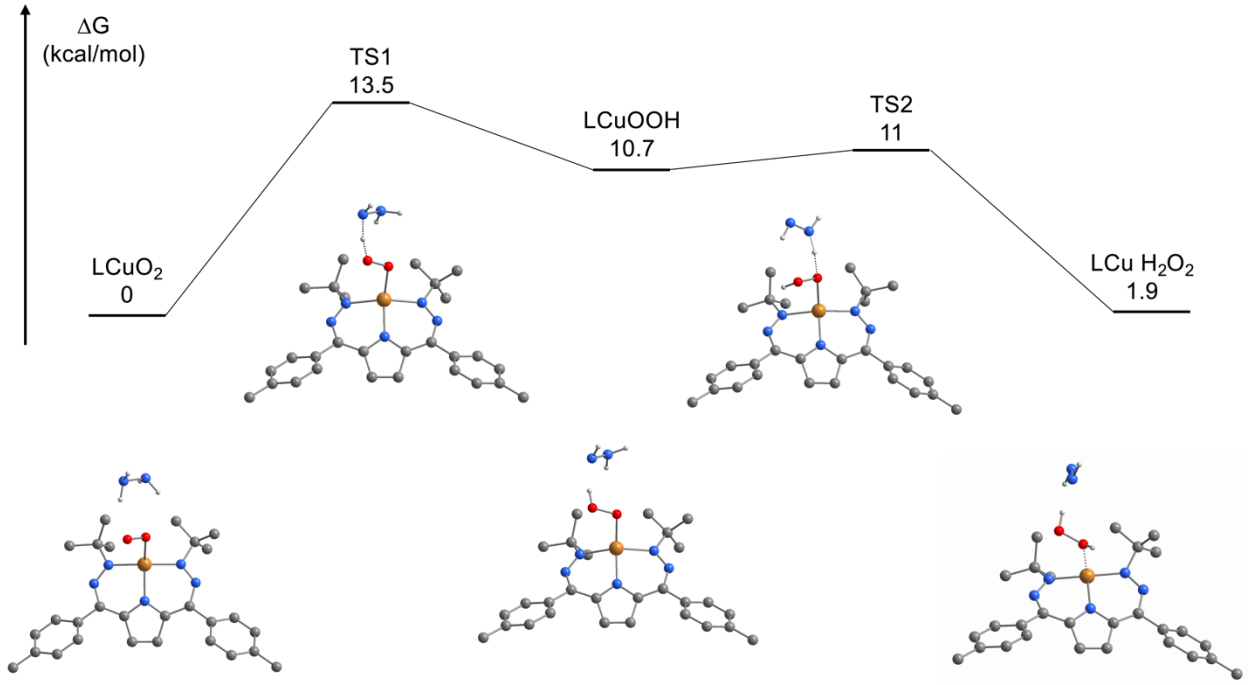

Figure 7. DFT computed geometries and energies of hydrazine dehydrogenation by **3**. Calculations were carried out with the M06L functional and a def2-TZVP basis set, with a def2-TZVPP basis set for Cu. Cu is shown in orange, C in gray, N in blue, O in red, and H in white. Only H-atoms involved in substrate dehydrogenation are shown.

as a substrate for computational efficiency, assuming that the transition state barriers should either be similar to or higher than DPH. Calculations comparing the thermodynamic favorability of DPH and hydrazine dehydrogenation predict that the former reaction is approximately 9 $kcal^{-1}$ mol^{-1} more downhill in energy, supporting that the use of hydrazine instead of DPH is a conservative model (Appendix I: **Table S14**). The first optimized transition state to form a Cu-hydroperoxo intermediate has a barrier of 13.2 $kcal^{-1}$ mol^{-1}, followed by a nearly barrierless (0.3 $kcal^{-1}$ mol^{-1}) second H-atom abstraction. Inspection of the Mulliken charges along the reaction coordinate suggest that each transition state is best described as an H-atom ($H^+ + e^-$) transfer rather than a heterolytic proton and hydride transfer (Appendix I: **Table S15**). The calculated transition state barriers are reasonable for a room temperature reaction and show that the Cu-superoxo species is a feasible active oxidant in the dehydrogenation of DPH. These calculations support the hypothesis that **3** is an active oxidant in catalysis. Indeed, we observe substantially enhanced rates of decay of independently generated **3** under N_2 in the presence of substrates (Appendix I: **Figure S26**).

The muted aerobic catalysis of **1** with alcohol and hydrocarbon substrates prompts questions about the identity of the active oxidant more broadly in aerobic Cu catalysis (**Figure 8**). In many Cu/aminoxyl catalytic cycles, the oxidizing species for C–H activation is proposed to be a free or complexed aminoxyl radical.[72,73] In these cases, the primary role of O_2 is proposed to be re-oxidation of the metal center and regeneration of aminoxyl species from hydroxylamines. Parallel trends can be drawn in biological systems. For instance, proposed GO enzymatic cycles involve a H-atom transfer to a coordinating modified tyrosyl radical residue along with electron transfer to the Cu center as the active alcohol oxidizing steps, with O_2 serving to regenerate the oxidized active site.[74] Conversely, studies of lytic polysaccharide monooxygenase (LPMO) active sites implicate a more direct substrate oxidizing role for O_2 derived species such as Cu-oxyl or Cu-

hydroxo species.[75,76] While several Cu-superoxo complexes have been shown to initiate the oxidation of moderately strong C–H and O–H bonds (BDE's of ~70-83 $kcal^{-1}mol^{-1}$), most model systems have not been able to mimic the reactivity of monooxygenase enzymes which commonly activate C–H bonds with strengths of up to 87 $kcal^{-1}mol^{-1}$.[77-80]

We observe no hydroxylation reactivity with aliphatic C–H substrates in the present system. This observation supports the proposed mechanistic paradigms of synthetic Cu systems and GO where oxygenated Cu species are primarily invoked as intermediates en-route to the active oxidizing species as opposed to directly oxidizing substrates. In this way, the importance of metal-ligand cooperativity in these systems is further underscored in that the supporting ligand (or co-catalyst in the case of aminoxyl systems) must be suitably oxidizing to directly react with

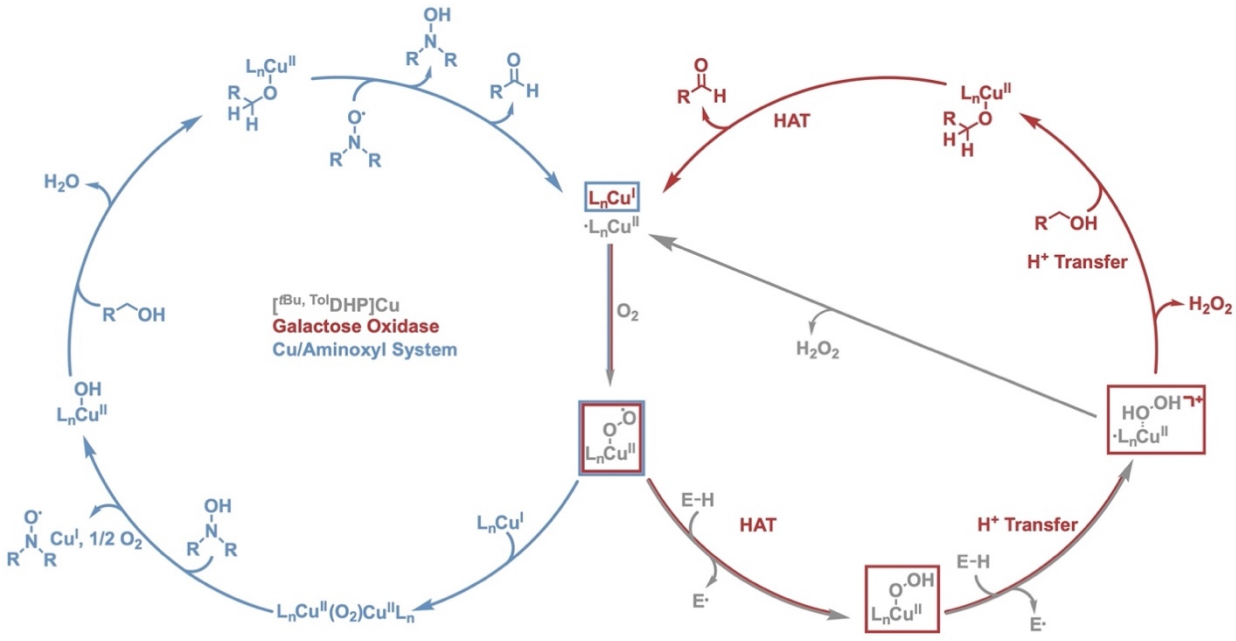

Figure 8. Mechanistic comparison of synthetic and biological Cu aerobic oxidative catalysts. The colored arrows and structures refer to mechanistic steps and intermediates for the [$^{tBu, Tol}$DHP]Cu (gray), GO (red), and Cu/aminoxyl (blue) catalytic systems, with overlayed multi-color arrows and boxes notating steps or intermediates that are shared by the indicated systems. Note that the two rightmost steps for GO are intramolecular proton transfers mediated by an active site phenol/phenolate which is not shown.

substrates in order to be regenerated by, or otherwise react with, O_2. Indeed, while we observe that DPH is readily converted to azobenzene by the oxidized (DHP^{-}) complex **2**, this complex shows no reactivity with other substrates such as alcohols or hydrocarbons under N_2 (Appendix I: **Table S1**). Conversely, the oxidative deformylation and phosphine oxidation reactivity must stem from an oxygenated Cu compound, i.e. **3**. Thus, our studies suggest that while Cu-superoxo complexes are important catalytic species in aerobic oxidative reactivity, for instance in reactions with net O-atom transfer or in the activation of weak E–H bonds, in more demanding dehydrogenation cycles they may be more commonly involved in regenerating the active species as opposed to directly oxidizing substrates themselves.

Conclusion

This chapter has described the synthesis and characterization of a mononuclear Cu complex with a T-shaped geometry. Detailed spectroscopic and computational investigations support a ligand-radical Cu(II) electronic structure for this complex. Addition of O_2 at room temperature results in the formation of a superoxo complex which has been thoroughly characterized by several spectroscopic methods. This complex is a catalyst at room temperature for the aerobic oxidation of hydrazine, alcohol, phosphine, aldehyde, and hydrazone substrates.

This work represents an unusual example of a thoroughly characterized Cu-superoxo complex which also mediates aerobic oxidation. The predicted weak BDE of a putative Cu-hydroperoxo intermediate and the observed sluggish reactivity of this system towards alcohols and hydrocarbons suggests that superoxo intermediates may commonly feature in the regeneration of active substrate oxidants in aerobic catalysis as opposed to featuring as active oxidants themselves.

This proposal underscores the importance of metal-ligand cooperativity in aerobic catalysis in the design of synthetic systems.

Experimental

General Considerations. All reagents were purchased from commercial suppliers and used without further purification unless otherwise specified. All manipulations were carried out under an atmosphere of N_2 using standard Schlenk and glovebox techniques. Glassware was dried at 180 °C for a minimum of 2 h and cooled under vacuum prior to use. Solvents were dried on a solvent purification system from Pure Process Technology, passed over a column of activated alumina, and stored over 4 Å molecular sieves under N_2. Tetrahydrofuran was stirred over NaK alloy and run through an additional activated alumina column prior to use to ensure dryness. C_6D_6, CD_2Cl_2, and d_8-THF were stored over 4 Å molecular sieves under N_2. Solvents were tested for H_2O and O_2 using a standard solution of sodium-benzophenone ketyl radical anion. O_2 was passed through packed Drierite (calcium sulfate, anhydrous) drying agent before addition to the reaction vessel. ^1H, $^{31}P\{1H\}$, and $^{19}F\{1H\}$ NMR spectra were recorded on a Bruker DRX 400 or 500 MHz spectrometer. Chemical shifts are reported in ppm units referenced to residual solvent resonances for ^1H spectra, UV-visible spectra were recorded on a Thermo Evolution 300 spectrometer, and the addition of gases were performed by injecting via syringe into a cuvette sealed with a septum. UV-visible spectra at low temperature were done using a Unisoku cryostat. Raman spectra were recorded using a Horiba LabRAM HR Evolution system. EPR spectra were recorded on an Elexsys E500 spectrometer with an Oxford ESR 900 X-band cryostat and a Bruker Cold-Edge Stinger and were simulated using the Easyspin suite in Matlab software.[81] GC/MS was collected on an Agilent

SQ GCMS with 5977A single quad MS and 7890B GC. Elemental analysis was performed by Midwest Microlabs. Electrochemical measurements were performed using a BAS Epsilon potentiostat and analyzed using BAS Epsilon software version 1.40.67NT. Cyclic voltammetry measurements were made using a glassy carbon working electrode, platinum wire counter electrode, and silver wire pseudoreference electrode and were referenced to internal Fc/Fc+.

X-ray Structure Determination. The diffraction data were measured at 100 K on a Bruker D8 VENTURE with PHOTON 100 CMOS detector system equipped with a Mo-target microfocus X-ray tube (λ = 0.71073 Å). Data reduction and integration were performed with the Bruker APEX3 software package (Bruker AXS, version 2015.5-2, 2015). Data were scaled and corrected for absorption effects using the multiscan procedure implemented in SADABS (Bruker AXS, version 2014/5, 2015, part of the Bruker APEX3 software package and APEX4 software package). The structure was solved by the dual method implemented in SHELXT and refined by a full-matrix least-squares procedure using the OLEX2 software package (XL refinement program version 2014/7). Suitable crystals were mounted on a cryo-loop and transferred into the cold nitrogen stream of the Bruker D8 Venture diffractometer. Most of the hydrogen atoms were generated by geometrical considerations and constrained to idealized geometries and allowed to ride on their carrier atoms with an isotropic displacement parameter related to the equivalent displacement parameter of their carrier atoms. Compound **1** was modeled for three-component disorder of one of the *p*-Tol rings. For compound **2**, a solvent mask as implemented in OLEX2 was used as the exact solvent composition could not be identified. A mixture of solvents was used for crystallization and the presence of multiple solvents was identified by NMR.

X-ray Absorption Measurements. Frozen solution samples were prepared by making a 0.02 M solution of **1** in THF of the starting material for **1** and **2**, and for **3** the solution was removed from the glovebox and reacted with O_2 by syringing the gas into the sample and bubbling through. For sample solutions of **1**, **2**, and **3**, the solution was transferred with a syringe to a Teflon window lined with Kapton tape. The solution was frozen using liquid nitrogen, then stored in liquid nitrogen until collection. Data were acquired at the Advanced Photon Source at Argonne National Laboratory with a bending magnet source with ring energy at 7.00 GeV. Cu K-edge data were acquired at the MRCAT 10-BM beam line. The incident, transmitted, and reference X-ray intensities were monitored using gas ionization chambers. A metallic Cu foil standard was used as a reference for energy calibration and was measured simultaneously with experimental samples. X-ray absorption spectra were collected at room temperature. The first inflection point of the foil spectrum was assigned to 8978.9 eV. Normalization and background subtraction of the data were performed using Athena from the Demeter software suite. The EXAFS curve-fitting analysis program OPT in EXAFSPAK (George, G.N. Stanford Synchrotron Radiation Laboratory: Stanford, CA, 2000) was used to fit the EXAFS data. The theoretical paths were generated using FEFF (version 7.0). The starting structural model for **3** was obtained from the DFT optimized structure. During the fitting process, the bond distance (R) and the mean-square thermal and static deviation in R (σ^2), were allowed to vary. The threshold energy (E_0), was allowed to vary but was constrained as a common value for all components in a given fit. The amplitude reduction factor (S_0^2) was fixed at 0.9 and the coordination numbers (N) were systematically varied to achieve the best fit.

Synthesis of [$^{t\text{Bu,Tol}}$DHP•]Cu (1). To a stirring THF (10 mL) solution of $^{t\text{Bu,Tol}}$DHP 2HCl (100 mg, 0.19 mmol) was added 2.5 M *n*BuLi in hexanes (0.31 mL, 4 eq), which turned the solution from yellow to red. The red mixture was stirred for 5 min and before adding 1-hexene (12 μL, 0.5 eq) and the resulting mixture was added to a stirring slurry of $CuCl_2$ in THF (27 mg, 0.19 mmol, 1 eq), turning deep blue. 1-hexene is thought to serve as an H-atom acceptor and improves the yield of the metalation moderately. After stirring for 2 h, the solution was filtered and all volatiles were removed under vacuum, resulting in a dark blue residue. The residue was taken up in benzene, passed through a silica plug, and then evaporated under vacuum to give **1** as a blue powder. Yield: 47 mg, 0.09 mmol, 37%. Single crystals suitable for X-ray diffraction were obtained by crystallization from concentrated petroleum ether at −35 °C. ^{1}H NMR (400 MHz, C_6D_6, 25 °C): δ 7.87 (d, 4H), 7.67 (s, 2H), 7.19 (d, 4H), 2.24 (s, 6H), 1.69 (s, 18H). ^{13}C{^{1}H} NMR (125 MHz, C_6D_6, 25 °C) δ 142.02, 138.75, 137.02, 135.59, 134.03, 131.38, 129.39, 69.62, 30.81, 21.22. UV-visible spectrum (DCM solution): 440 nm (ε_0 12,400 $M^{-1}cm^{-1}$), 616 nm (ε_0 38,700 $M^{-1}cm^{-1}$).IR (nujol mull, cm^{-1}): 2720 (m), 2672 (m), 1510 (s, C=N), 1297 (s), 1254 (m), 1171 (s), 1091 (m), 1016 (m), 823 (s), 785 (m), 720 (s). Anal. Calc. C, 66.7; H, 6.8; N, 13.9; Found: C, 66.9; H, 7.1; N, 13.0. HRA-MS (*m/z*) [M]+ $C_{28}H_{34}CuN_5$: 503.211 Found: 503.211. Bulk purity also determined to be 99.5% by ^{1}H NMR referenced to a mesitylene internal standard (Figure S12).

Synthesis of [$^{t\text{Bu,Tol}}$DHP]CuOTf (2). To a stirring solution of **1** in THF (0.020 g, 0.04 mmol, 5 mL) was added a THF (2 mL) solution of AgOTf (0.01 g, 2 mL, 1 equiv), resulting in color change from blue to deep green. The reaction was stirred for 30 min, then filtered and evaporated under vacuum. Single crystals suitable for X-Ray diffraction were obtained from a concentrated

petroleum ether solution at −35 °C. ^{1}H NMR (400 MHz, C_6D_6, 25 °C): 7.54, 5.93, 3.86, 2.04, 1.34. $^{19}F\{^{1}H\}$ NMR (125 MHz, C_6D_6, 25 °C) δ −74.08. Evans method (C_6D_6, 25 °C, μ_B) μ_{eff} = 1.72. UV-visible spectrum (DCM solution): 448 nm (ε_0 11,200 $M^{-1}cm^{-1}$), 638 nm (ε_0 11,300 $M^{-1}cm^{-1}$), 704 nm (shoulder). IR (nujol mull, cm^{-1}): 2720 (m), 2667 (m), 1306 (m), 1267 (m), 1167 (s), 1101 (m), 1006 (s), 960 (m), 887 (m), 843 (m). Anal. Calc. C, 53.3; H, 5.3; N, 10.7; Found: C, 53.2; H, 5.0; N, 10.5. HRA-MS (*m/z*) [M]+ $C_{29}H_{34}CuF_3N_5O_3S$: 652.163 Found: 652.173.

Synthesis of [$^{t\text{Bu,Tol}}$DHP]CuO_2 (3). A solution of **1** in DCM (or THF) was removed from the glovebox, and an excess of dry O_2 was bubbled through the solution using a 500 μL gas syringe, resulting in a color change from blue to green. The completeness of the reaction was tracked by taking aliquots for UV-visible spectroscopy. UV-visible spectrum (DCM solution): 420 nm (ε_0 16,900 $M^{-1}cm^{-1}$) 670 nm (ε_0 13,600 $M^{-1}cm^{-1}$).

Raman Sample Preparation of 3. A concentrated solution of **1** in DCM was removed from the glovebox in a sealed vial with a septum. O_2 was syringed into the vial (3 mL) and the reaction was allowed to stir as the solution turned green, indicating formation of **3**. The reaction progress could be tracked by diluting aliquots and taking a UV-vis spectrum. When the conversion to **3** was complete, the concentrated solution was drop-cast onto a glass microscope slide under a positive flow of N_2 that rapidly evaporated the solvent. The sample was then covered with a microscope cover glass, and an adhesive spacer sealed the sample between the microscope slide and cover glass to prevent contact with air during data collection. The Raman spectrum was collected with

633 nm laser on 1% power, 30 s acquisition times, 12 acquisitions, and 50X LWD microscope objective.

Oxidative Reactivity. In a nitrogen glovebox, to a solution of **1** in CD_2Cl_2 (1 mg, 0.002 mmol) was added diphenylhydrazine (4 mg, 0.02 mmol, 10 equiv) and mesitylene (2.8 μL). This was added to a 50 mL Schlenk tube with a stir bar and removed from the box. After one freeze pump thaw cycle, the tube was charged with 1 atm of dry O_2 and stirred overnight. The solution was then transferred to an NMR tube for product characterization. For benzyl alcohol, *t*BuOK (1 mg, 0.01 mmol, 5 equiv) was added along with the substrate. For 2-phenylpropionaldehyde, Et_3N (2.8 μL, 0.02 mmol, 10 equiv) was added with the substrate. ^1H NMR yields were determined by integration against the internal mesitylene standard. $^{31}P\{^1H\}$ NMR yields for the oxidation of PPh_3 were determined from the ratio of product/(product + starting material) integrations. Yields for benzophenone hydrazone oxidation were determined by gas chromatography (versus a mesitylene internal standard) due to overlapping NMR signals for the different product species and the starting material.

Reactivity with Diphenylisobenzofuran (DPBF). In a 100 mL Schlenk tube, **1** (1 mg, 0.002 mmol), diphenylhydrazine (DPH) (4 mg, 0.02 mmol), and DPBF (5 mg, 0.02 mmol) were dissolved in DCM (0.5 mL). After 1 freeze pump thaw cycle, the tube was charged with 1 atm O_2 and allowed to react for 1 h (this completion time with DPH previously determined by ^1H NMR). The product mixture was then diluted with DCM to 1.5 mL, filtered, and analyzed by GC-MS.

Computational Methodology. For V2RDM CASSCF, geometry optimizations were carried out with DFT, utilizing the B3LYP functional[82] in combination with the 6-31G∗ basis set,[83] as implemented in Gaussian 16 Rev. A.03.[84] Multireference correlation was resolved with variational 2-electron reduced density matrix (V2RDM) complete active space self-consistent field (CASSCF)[85,86] calculations as implemented in the Maple Quantum Chemistry Package.[87,88] V2RDM calculations utilized an active space of 14 electrons distributed in 14 spatial orbitals, [14,14], and a 6-31G∗ basis set. Structures of **3** as well as the intermediates and transition states for the reaction coordinate with hydrazine were optimized in ORCA[89] using the M06L functional and def2-TZVPP basis set on Cu, def2-TZVP basis set on all other atoms. Frequency calculations were performed to confirm the structures are at local minima on the potential energy surface.

References

1. Arends, I. W. C. E.; Sheldon, R. A., Bäckvall, J. E. Modern Oxidation of Alcohols, *Modern Oxidation Methods*, Wiley-VCH, 2010.
2. Caron, S.; Dugger, R. W.; Ruggeri, S. G.; Ragan, J. A.; Ripin, D. H. B., Large-Scale Oxidations in the Pharmaceutical Industry. *Chem. Rev.* **2006,** *106*, 2943-2989.
3. Piancatelli, G.; Scettri, A.; D'auria, M., Pyridinium chlorochromate: a versatile oxidant in organic synthesis. *Synthesis* **1982,** *1982* (04), 245-258.
4. Corey, E. J.; Suggs, J. W., Pyridinium chlorochromate. An efficient reagent for oxidation of primary and secondary alcohols to carbonyl compounds. *Tetrahedron Lett.* **1975,** *16* (31), 2647-2650.
5. Taylor, R. J. K.; Reid, M.; Foot, J.; Raw, S. A., Tandem Oxidation Processes Using Manganese Dioxide: Discovery, Applications, and Current Studies. *Acc. Chem. Res.* **2005,** *38* (11), 851-869.
6. Chandra, P.; Ghosh, T.; Choudhary, N.; Mohammad, A.; Mobin, S. M., Recent advancement in oxidation or acceptorless dehydrogenation of alcohols to valorised products using manganese based catalysts. *Coord. Chem. Rev.* **2020,** *411*, 213241.
7. Cella, J. A.; Kelley, J. A.; Kenehan, E. F., Nitroxide-catalyzed oxidation of alcohols using m-chloroperbenzoic acid. New method. *J. Org. Chem.* **1975,** *40* (12), 1860-1862.
8. Kim, H. R.; Jung, J. H.; Kim, J. N.; Ryu, E. K., Oxidation of Benzylic and Secondary Alcohols Using m-Chloroperbenzoic Acid/Hydrogen Chloride/N,N-Dimethylformamide System. *Synth. Commun.* **1990,** *20* (5), 637-640.
9. De Mico, A.; Margarita, R.; Parlanti, L.; Vescovi, A.; Piancatelli, G., A Versatile and Highly Selective Hypervalent Iodine (III)/2,2,6,6-Tetramethyl-1-piperidinyloxyl-Mediated Oxidation of Alcohols to Carbonyl Compounds. *J. Org. Chem.* **1997,** *62* (20), 6974-6977.
10. Yoshimura, A.; Zhdankin, V. V., Advances in Synthetic Applications of Hypervalent Iodine Compounds. *Chem. Rev.* **2016,** *116* (5), 3328-3435.
11. Maity, A.; Hyun, S.-M.; Powers, D. C., Oxidase catalysis via aerobically generated hypervalent iodine intermediates. *Nat. Chem.* **2018,** *10* (2), 200-204.
12. Semmelhack, M. F.; Schmid, C. R.; Cortes, D. A.; Chou, C. S., Oxidation of alcohols to aldehydes with oxygen and cupric ion, mediated by nitrosonium ion. *J. Am. Chem. Soc.* **1984,** *106* (11), 3374-3376.
13. Hoover, J. M.; Stahl, S. S., Highly Practical Copper(I)/TEMPO Catalyst System for Chemoselective Aerobic Oxidation of Primary Alcohols. *J. Am. Chem. Soc.* **2011,** *133* (42), 16901-16910.
14. Markó, I. E.; Giles, P. R.; Tsukazaki, M.; Chellé-Regnaut, I.; Gautier, A.; Brown, S. M.; Urch, C. J., Efficient, Ecologically Benign, Aerobic Oxidation of Alcohols. *J. Org. Chem.* **1999,** *64* (7), 2433-2439.
15. Dijksman, A.; Arends, I. W. C. E.; Sheldon, R. A., Cu(ii)-nitroxyl radicals as catalytic galactose oxidase mimics. *Org. Biomol. Chem.* **2003,** *1* (18), 3232-3237.
16. Asami, K.; Takashina, A.; Kobayashi, M.; Iwatsuki, S.; Yajima, T.; Kochem, A.; van Gastel, M.; Tani, F.; Kohzuma, T.; Thomas, F.; Shimazaki, Y., Characterization of one-electron oxidized copper(ii)-salophen-type complexes; effects of electronic and geometrical structures on reactivities. *Dalton Trans.* **2014,** *43* (5), 2283-2293.
17. Chaudhuri, P.; Hess, M.; Weyhermüller, T.; Wieghardt, K., Aerobic Oxidation of Primary Alcohols by a New Mononuclear CuII-Radical Catalyst. *Angew. Chem. Int. Ed.* **1999,** *38* (8), 1095-1098.
18. Chaudhuri, P.; Hess, M.; Müller, J.; Hildenbrand, K.; Bill, E.; Weyhermüller, T.; Wieghardt, K., Aerobic Oxidation of Primary Alcohols (Including Methanol) by Copper(II)− and Zinc(II)−Phenoxyl Radical Catalysts. *J. Am. Chem. Soc.* **1999,** *121* (41), 9599-9610.
19. Rajabimoghadam, K.; Darwish, Y.; Bashir, U.; Pitman, D.; Eichelberger, S.; Siegler, M. A.; Swart, M.; Garcia-Bosch, I., Catalytic Aerobic Oxidation of Alcohols by Copper Complexes Bearing Redox-Active Ligands with Tunable H-Bonding Groups. *J. Am. Chem. Soc.* **2018,** *140* (48), 16625-16634.
20. Iovan, D. A.; Wrobel, A. T.; McClelland, A. A.; Scharf, A. B.; Edouard, G. A.; Betley, T. A., Reactivity of a stable copper–dioxygen complex. *Chem. Comm.* **2017,** *53* (74), 10306-10309.
21. Neira, A. C.; Martínez-Alanis, P. R.; Aullón, G.; Flores-Alamo, M.; Zerón, P.; Company, A.; Chen, J.; Kasper, J. B.; Browne, W. R.; Nordlander, E.; Castillo, I., Oxidative Cleavage of Cellobiose by Lytic Polysaccharide Monooxygenase (LPMO)-Inspired Copper Complexes. *ACS Omega* **2019,** *4* (6), 10729-10740.

22. Bhadra, M.; Transue, W. J.; Lim, H.; Cowley, R. E.; Lee, J. Y. C.; Siegler, M. A.; Josephs, P.; Henkel, G.; Lerch, M.; Schindler, S.; Neuba, A.; Hodgson, K. O.; Hedman, B.; Solomon, E. I.; Karlin, K. D., A Thioether-Ligated Cupric Superoxide Model with Hydrogen Atom Abstraction Reactivity. *J. Am. Chem. Soc.* **2021,** *143* (10), 3707-3713.
23. Sánchez-Eguía, B. N.; Flores-Alamo, M.; Orio, M.; Castillo, I., Side-on cupric–superoxo triplet complexes as competent agents for H-abstraction relevant to the active site of PHM. *Chem. Comm.* **2015,** *51* (55), 11134-11137.
24. Kunishita, A.; Kubo, M.; Sugimoto, H.; Ogura, T.; Sato, K.; Takui, T.; Itoh, S., Mononuclear Copper(II)−Superoxo Complexes that Mimic the Structure and Reactivity of the Active Centers of PHM and DβM. *J. Am. Chem. Soc.* **2009,** *131* (8), 2788-2789.
25. Ahmad Bhat, I.; Avinash, I.; Kumar Sachan, S.; Singh, S.; Anantharaman, G., Efficient Synthesis of Cu(II)-N-Heterocyclic Carbene Complexes in Water and Their Activity Towards Aerobic Alcohol Oxidation. *Eur. J. Inorg. Chem.* **2021,** *2021* (44), 4560-4565.
26. Betzemeier, B.; Cavazzini, M.; Quici, S.; Knochel, P., Copper-catalyzed aerobic oxidation of alcohols under fluorous biphasic conditions. *Tetrahedron Lett.* **2000,** *41* (22), 4343-4346.
27. Kirillova, M. V.; Fernandes, T. A.; André, V.; Kirillov, A. M., Mild C–H functionalization of alkanes catalyzed by bioinspired copper(ii) cores. *Org. Biomol. Chem.* **2019,** *17* (33), 7706-7714.
28. Boldron, C.; Özalp-Yaman, Ş.; Gamez, P.; Tooke, D. M.; Spek, A. L.; Reedijk, J., Selective copper(ii)-mediated oxidative coupling of a nucleophilic reagent to the para-methyl group of 2,4,6-trimethylphenol. *Dalton Trans.* **2005,** (21), 3535-3541.
29. Bolm, C.; Schlingloff, G.; Bienewald, F., Copper- and vanadium-catalyzed asymmetric oxidations. *J. Mol. Catal. A: Chem.* **1997,** *117* (1), 347-350.
30. Zultanski, S. L.; Zhao, J.; Stahl, S. S., Practical Synthesis of Amides via Copper/ABNO-Catalyzed Aerobic Oxidative Coupling of Alcohols and Amines. *J. Am. Chem. Soc.* **2016,** *138* (20), 6416-6419.
31. Bower, J. K.; Cypcar, A. D.; Henriquez, B.; Stieber, S. C. E.; Zhang, S., C(sp3)–H Fluorination with a Copper(II)/(III) Redox Couple. *J. Am. Chem. Soc.* **2020,** *142* (18), 8514-8521.
32. Que, L. and Tolman, W. B. Biologically inspired oxidation catalysis. *Nature* **2008**, 455, 333–34.
33. Walton, P. H.; Davies, G. J., On the catalytic mechanisms of lytic polysaccharide monooxygenases. *Curr. Opin. Chem. Biol.* **2016,** *31*, 195-207.
34. Kjaergaard, C. H.; Qayyum, M. F.; Wong, S. D.; Xu, F.; Hemsworth, G. R.; Walton, D. J.; Young, N. A.; Davies, G. J.; Walton, P. H.; Johansen, K. S.; Hodgson, K. O.; Hedman, B.; Solomon, E. I., Spectroscopic and computational insight into the activation of O_2 by the mononuclear Cu center in polysaccharide monooxygenases. *Proc. Natl. Acad. Sci.* **2014,** *111* (24), 8797-8802.
35. Lee, J. Y.; Peterson, R. L.; Ohkubo, K.; Garcia-Bosch, I.; Himes, R. A.; Woertink, J.; Moore, C. D.; Solomon, E. I.; Fukuzumi, S.; Karlin, K. D., Mechanistic Insights into the Oxidation of Substituted Phenols via Hydrogen Atom Abstraction by a Cupric–Superoxo Complex. *J. Am. Chem. Soc.* **2014,** *136* (28), 9925-9937.
36. Würtele, C.; Gaoutchenova, E.; Harms, K.; Holthausen, M. C.; Sundermeyer, J.; Schindler, S., Crystallographic Characterization of a Synthetic 1:1 End-On Copper Dioxygen Adduct Complex. *Angew. Chem. Int. Ed.* **2006,** *45* (23), 3867-3869.
37. Komiyama, K.; Furutachi, H.; Nagatomo, S.; Hashimoto, A.; Hayashi, H.; Fujinami, S.; Suzuki, M.; Kitagawa, T., Dioxygen Reactivity of Copper(I) Complexes with Tetradentate Tripodal Ligands Having Aliphatic Nitrogen Donors: Synthesis, Structures, and Properties of Peroxo and Superoxo Complexes. *Bull.Chem. Soc. Jap.* **2004,** *77* (1), 59-72.
38. Donoghue, P. J.; Gupta, A. K.; Boyce, D. W.; Cramer, C. J.; Tolman, W. B., An Anionic, Tetragonal Copper(II) Superoxide Complex. *J. Am. Chem. Soc.* **2010,** *132* (45), 15869-15871.
39. Weitzer, M.; Schindler, S.; Brehm, G.; Schneider, S.; Hörmann, E.; Jung, B.; Kaderli, S.; Zuberbühler, A. D., Reversible Binding of Dioxygen by the Copper(I) Complex with Tris(2-dimethylaminoethyl)amine (Me6tren) Ligand. *Inorg. Chem.* **2003,** *42* (6), 1800-1806.
40. Maiti, D.; Fry, H. C.; Woertink, J. S.; Vance, M. A.; Solomon, E. I.; Karlin, K. D., A 1:1 Copper−Dioxygen Adduct is an End-on Bound Superoxo Copper(II) Complex which Undergoes Oxygenation Reactions with Phenols. *J. Am. Chem. Soc.* **2007,** *129* (2), 264-265.
41. Bhadra, M.; Lee, J. Y. C.; Cowley, R. E.; Kim, S.; Siegler, M. A.; Solomon, E. I.; Karlin, K. D., Intramolecular Hydrogen Bonding Enhances Stability and Reactivity of Mononuclear Cupric Superoxide Complexes. *J. Am. Chem. Soc.* **2018,** *140* (29), 9042-9045.

42. Woertink, J. S.; Tian, L.; Maiti, D.; Lucas, H. R.; Himes, R. A.; Karlin, K. D.; Neese, F.; Würtele, C.; Holthausen, M. C.; Bill, E.; Sundermeyer, J.; Schindler, S.; Solomon, E. I., Spectroscopic and Computational Studies of an End-on Bound Superoxo-Cu(II) Complex: Geometric and Electronic Factors That Determine the Ground State. *Inorg. Chem.* **2010,** *49* (20), 9450-9459.
43. Abe, T.; Hori, Y.; Shiota, Y.; Ohta, T.; Morimoto, Y.; Sugimoto, H.; Ogura, T.; Yoshizawa, K.; Itoh, S., Cupric-superoxide complex that induces a catalytic aldol reaction-type C–C bond formation. *Commun.Chem.* **2019,** *2* (1), 12.
44. Concia, A. L.; Beccia, M. R.; Orio, M.; Ferre, F. T.; Scarpellini, M.; Biaso, F.; Guigliarelli, B.; Réglier, M.; Simaan, A. J., Copper Complexes as Bioinspired Models for Lytic Polysaccharide Monooxygenases. *Inorg. Chem.* **2017,** *56* (3), 1023-1026.
45. Winslow, C.; Lee, H. B.; Field, M. J.; Teat, S. J.; Rittle, J., Structure and Reactivity of a High-Spin, Nonheme Iron(III)- Superoxo Complex Supported by Phosphinimide Ligands. *J. Am. Chem. Soc.* **2021,** *143* (34), 13686-13693.
46. Annaraj, J.; Suh, Y.; Seo, M. S.; Kim, S. O.; Nam, W., Mononuclear nonheme ferric-peroxo complex in aldehyde deformylation. *Chem. Comm.* **2005,** (36), 4529-4531.
47. Corcos, A. R.; Villanueva, O.; Walroth, R. C.; Sharma, S. K.; Bacsa, J.; Lancaster, K. M.; MacBeth, C. E.; Berry, J. F., Oxygen Activation by Co(II) and a Redox Non-Innocent Ligand: Spectroscopic Characterization of a Radical–Co(II)–Superoxide Complex with Divergent Catalytic Reactivity. *J. Am. Chem. Soc.* **2016,** *138* (6), 1796-1799.
48. Liu, L.-L.; Li, H.-X.; Wan, L.-M.; Ren, Z.-G.; Wang, H.-F.; Lang, J.-P., A Mn(iii)–superoxo complex of a zwitterionic calix[4]arene with an unprecedented linear end-on Mn(iii)–O2 arrangement and good catalytic performance for alkene epoxidation. *Chem. Comm.* **2011,** *47* (39), 11146-11148.
49. Jesse, K. A.; Anferov, S. W.; Collins, K. A.; Valdez-Moreira, J. A.; Czaikowski, M. E.; Filatov, A. S.; Anderson, J. S., Direct Aerobic Generation of a Ferric Hydroperoxo Intermediate Via a Preorganized Secondary Coordination Sphere. *J. Am. Chem. Soc.* **2021,** *143* (43), 18121-18130.
50. McNeece, A. J.; Jesse, K. A.; Xie, J.; Filatov, A. S.; Anderson, J. S., Generation and Oxidative Reactivity of a Ni(II) Superoxo Complex via Ligand-Based Redox Non-Innocence. *J. Am. Chem. Soc.* **2020,** *142* (24), 10824-10832.
51. McNeece, A. J.; Jesse, K. A.; Filatov, A. S.; Schneider, J. E.; Anderson, J. S., Catalytic hydrogenation enabled by ligand-based storage of hydrogen. *Chem. Comm.* **2021,** *57* (32), 3869-3872.
52. Rudolph, J.; Jacob, C. R., Revisiting the Dependence of Cu K-Edge X-ray Absorption Spectra on Oxidation State and Coordination Environment. *Inorg. Chem.* **2018,** *57* (17), 10591-10607.
53. Bair, R. A.; Goddard, W. A., Ab initio studies of the x-ray absorption edge in copper complexes. I. Atomic Cu^{2+} and $Cu(II)Cl_2$. *Phys. Rev. B* **1980,** *22* (6), 2767-2776.
54. Tomson, N. C.; Williams, K. D.; Dai, X.; Sproules, S.; DeBeer, S.; Warren, T. H.; Wieghardt, K., Re-evaluating the Cu K pre-edge XAS transition in complexes with covalent metal–ligand interactions. *Chem. Sci.* **2015,** *6* (4), 2474-2487.
55. Walroth, R. C.; Uebler, J. W. H.; Lancaster, K. M., Probing CuI in homogeneous catalysis using high-energy-resolution fluorescence-detected X-ray absorption spectroscopy. *Chem. Comm.* **2015,** *51* (48), 9864-9867.
56. Sarangi, R., X-ray absorption near-edge spectroscopy in bioinorganic chemistry: Application to M-O(2) systems. *Coord. Chem. Rev.* **2013**, *257* (2), 459-472.
57. Donoghue, P. J.; Tehranchi, J.; Cramer, C. J.; Sarangi, R.; Solomon, E. I.; Tolman, W. B., Rapid C–H Bond Activation by a Monocopper(III)–Hydroxide Complex. *J. Am. Chem. Soc.* **2011,** *133* (44), 17602-17605.
58. Sarangi, R.; Aboelella, N.; Fujisawa, K.; Tolman, W. B.; Hedman, B.; Hodgson, K. O.; Solomon, E. I., X-ray Absorption Edge Spectroscopy and Computational Studies on LCuO2 Species: Superoxide−CuII versus Peroxide−CuIII Bonding. *J. Am. Chem. Soc.* **2006,** *128* (25), 8286-8296.
59. Lim, H.; Thomas, K. E.; Hedman, B.; Hodgson, K. O.; Ghosh, A.; Solomon, E. I., X-ray Absorption Spectroscopy as a Probe of Ligand Noninnocence in Metallocorroles: The Case of Copper Corroles. *Inorg. Chem.* **2019,** *58* (10), 6722-6730.
60. DuBois, J. L.; Mukherjee, P.; Stack, T. D. P.; Hedman, B.; Solomon, E. I.; Hodgson, K. O., A Systematic K-edge X-ray Absorption Spectroscopic Study of Cu(III) Sites. *J. Am. Chem. Soc.* **2000,** *122* (24), 5775-5787.
61. Meyet, J.; Ashuiev, A.; Noh, G.; Newton, M. A.; Klose, D.; Searles, K.; van Bavel, A. P.; Horton, A. D.; Jeschke, G.; van Bokhoven, J. A.; Copéret, C., Methane-to-Methanol on Mononuclear Copper(II) Sites Supported on Al2O3: Structure of Active Sites from Electron Paramagnetic Resonance. *Angew. Chem. Int. Ed.* **2021,** *60* (29), 16200-16207.

62. Zsombor-Pindera, J.; Effaty, F.; Escomel, L.; Patrick, B.; Kennepohl, P.; Ottenwaelder, X., Five Nitrogen Oxidation States from Nitro to Amine: Stabilization and Reactivity of a Metastable Arylhydroxylamine Complex. *J. Am. Chem. Soc.* **2020**, *142* (45), 19023-19028.
63. Liu, Y.; Resch, S. G.; Klawitter, I.; Cutsail III, G. E.; Demeshko, S.; Dechert, S.; Kühn, F. E.; DeBeer, S.; Meyer, F., An Adaptable N-Heterocyclic Carbene Macrocycle Hosting Copper in Three Oxidation States. *Angew. Chem. Int. Ed.* **2020,** *59* (14), 5696-5705.
64. Kau, L. S.; Spira-Solomon, D. J.; Penner-Hahn, J. E.; Hodgson, K. O.; Solomon, E. I., X-ray absorption edge determination of the oxidation state and coordination number of copper. Application to the type 3 site in Rhus vernicifera laccase and its reaction with oxygen. *J. Am. Chem. Soc.* **1987**, *109* (21), 6433-6442.
65. Mirica, L. M.; Ottenwaelder, X.; Stack, T. D. P., Structure and Spectroscopy of Copper−Dioxygen Complexes. *Chem. Rev.* **2004**, *104* (2), 1013-1046.
66. Nakamoto, K., Infrared and Raman spectra of inorganic and coordination compounds, part B: applications in coordination, organometallic, and bioinorganic chemistry. John Wiley & Sons: 2009.
67. Ginsbach, J. W.; Peterson, R. L.; Cowley, R. E.; Karlin, K. D.; Solomon, E. I., Correlation of the Electronic and Geometric Structures in Mononuclear Copper(II) Superoxide Complexes. *Inorg. Chem.* **2013**, *52* (22), 12872-12874.
68. Pirovano, P.; Magherusan, A. M.; McGlynn, C.; Ure, A.; Lynes, A.; McDonald, A. R., Nucleophilic Reactivity of a Copper(II)–Superoxide Complex. *Angew. Chem. Int. Ed.* **2014**, *53* (23), 5946-5950.
69. Liu, W.; Twilton, J.; Wei, B.; Lee, M.; Hopkins, M. N.; Bacsa, J.; Stahl, S. S.; Davies, H. M. L., Copper-Catalyzed Oxidation of Hydrazones to Diazo Compounds Using Oxygen as the Terminal Oxidant. *ACS Catal.* **2021**, *11* (5), 2676-2683.
70. Ibata, T.; Singh, G. S., Formation of diazoketones and azines by improved oxidation of ketohydrazones using Cu(acac)2 as a catalyst. *Tetrahedron Lett.* **1994**, *35* (16), 2581-2584.
71. Żamojć, K.; Zdrowowicz, M.; Rudnicki-Velasquez, P. B.; Krzymiński, K.; Zaborowski, B.; Niedziałkowski, P.; Jacewicz, D.; Chmurzyński, L., The development of 1,3-diphenylisobenzofuran as a highly selective probe for the detection and quantitative determination of hydrogen peroxide. *Free Radic. Res.* **2017**, *51* (1), 38-46.
72. Iron, M. A.; Szpilman, A. M., Mechanism of the Copper/TEMPO-Catalyzed Aerobic Oxidation of Alcohols. *Chem. Eur. J.* **2017**, *23* (6), 1368-1378.
73. Ryland, B. L.; McCann, S. D.; Brunold, T. C.; Stahl, S. S., Mechanism of Alcohol Oxidation Mediated by Copper(II) and Nitroxyl Radicals. *J. Am. Chem. Soc.* **2014**, *136* (34), 12166-12173.
74. Himo, F.; Eriksson, L. A.; Maseras, F.; Siegbahn, P. E. M., Catalytic Mechanism of Galactose Oxidase: A Theoretical Study. *J. Am. Chem. Soc.* **2000**, *122* (33), 8031-8036.
75. Liu, J. J.; Diaz, D. E.; Quist, D. A.; Karlin, K. D., Copper(I)-Dioxygen Adducts and Copper Enzyme Mechanisms. *Isr. J. Chem.* **2016**, *56* (9-10), 738-755.
76. Wang, B.; Walton, P. H.; Rovira, C., Molecular Mechanisms of Oxygen Activation and Hydrogen Peroxide Formation in Lytic Polysaccharide Monooxygenases. *ACS Catal.* **2019**, *9* (6), 4958-4969.
77. Quek, S. Y.; Debnath, S.; Laxmi, S.; van Gastel, M.; Krämer, T.; England, J., Sterically Stabilized End-On Superoxocopper(II) Complexes and Mechanistic Insights into Their Reactivity with O–H, N–H, and C–H Substrates. *J. Am. Chem. Soc.* **2021,** *143* (47), 19731-19747.
78. Peterson, R. L.; Himes, R. A.; Kotani, H.; Suenobu, T.; Tian, L.; Siegler, M. A.; Solomon, E. I.; Fukuzumi, S.; Karlin, K. D., Cupric Superoxo-Mediated Intermolecular C−H Activation Chemistry. *J. Am. Chem. Soc.* **2011**, *133* (6), 1702-1705.
79. Kim, S.; Lee, J. Y.; Cowley, R. E.; Ginsbach, J. W.; Siegler, M. A.; Solomon, E. I.; Karlin, K. D., A N3S(thioether)-Ligated CuII-Superoxo with Enhanced Reactivity. *J. Am. Chem. Soc.* **2015,** *137* (8), 2796-2799.
80. Klinman, J. P., The Copper-Enzyme Family of Dopamine β-Monooxygenase and Peptidylglycine α-Hydroxylating Monooxygenase: Resolving the Chemical Pathway for Substrate Hydroxylation. *J. Biol. Chem.* **2006,** *281* (6), 3013-3016.
81. Stoll, S.; Schweiger, A. EasySpin, a comprehensive software package for spectral simulation and analysis in EPR. *J. Magn. Reson*. **2006**, *178* (1), 42−55.
82 Becke, A. D. Density-functional thermochemistry. III. The role of exact exchange. *J. Chem. Phys.* **1993**, *98*, 5648–5652.

83. Francl, M. M.; Pietro, W. J.; Hehre, W. J.; Binkley, J. S.; Gordon, M. S.; DeFrees, D. J.; Pople, J. A. Self-consistent molecular orbital methods. XXIII. A polarization-type basis set for second-row elements. *J. Chem. Phys.* **1982**, *77*, 3654–3665.
84. Frisch, M. J. et al. Gaussian 16 Revision A.03. 2016; Gaussian Inc. Wallingford CT.
85. Gidofalvi, G.; Mazziotti, D. A. Active-space two-electron reduced-density-matrix method: Complete active-space calculations without diagonalization of the N-electron Hamiltonian. *J. Chem. Phys.* **2008**, *129*, 134108.
86. Mazziotti, D. A. Large-Scale Semidefinite Programming for Many-Electron Quantum Mechanics. *Phys. Rev. Lett.* **2011**, *106*, 083001.
87. Maplesoft, Maple. https://www.maplesoft.com, 2021; Accessed: 2022-04-01.
88. Maplesoft, Quantum Chemistry Toolbox in Maple. https: //www.maplesoft.com, 2022.
89. Neese, F., The ORCA program system. WIREs Computational Molecular Science **2012**, *2* (1), 73-78.

Chapter II: Electrocatalytic Semi-Hydrogenation of Terminal Alkynes using Ligand-Based Transfer of Protons and Electrons

This chapter has been adapted from the following: Czaikowski, M.E.; Anferov, S.W.; Tascher, A.P.; Anderson, J.S. *J. Am. Chem. Soc.* **2024**, *146*, 1, 476-486.

Introduction

The semi-hydrogenation of alkynes is an important transformation in many pharmaceutical, agrochemical, and materials applications.[1-3] This importance has spurred a great deal of research into methodologies for the selective semi-hydrogenation of alkynes, with primary goals being the prevention of overreduction to alkanes as well as controlling *E*/*Z* selectivity (**Figure 1**). Lindlar's catalyst is a classic heterogeneous example which mediates the semi-hydrogenation of internal alkynes with *Z*-selectivity. There have also been impressive advances with homogeneous catalysts for both *E*- and *Z*-selective semi-hydrogenations, as well as recent advances in using more abundant first-row transition metal catalysts.[4-10]

Despite these advances, there are several drawbacks to currently employed semi-hydrogenation technologies. Most methodologies typically operate under an H_2 atmosphere which

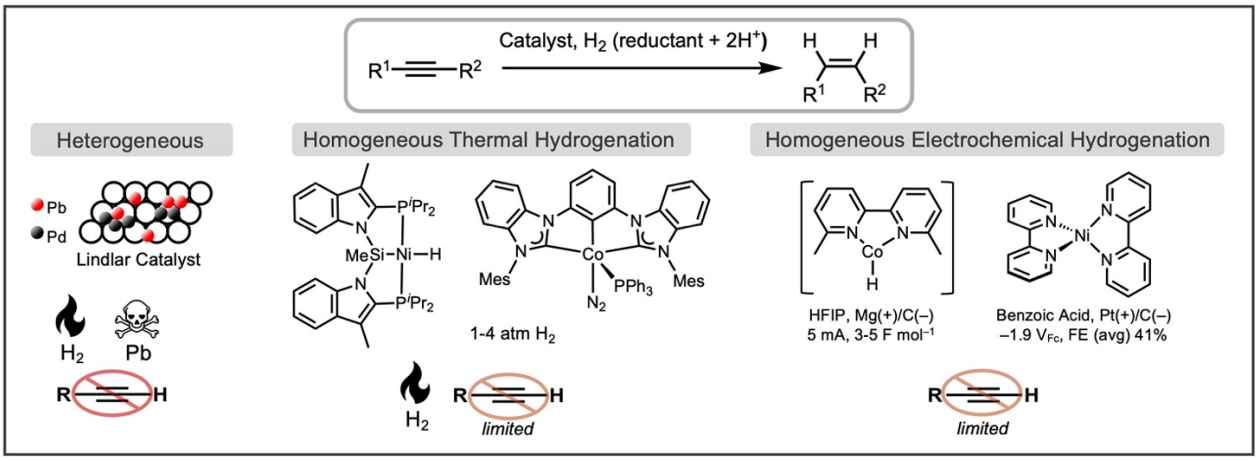

Figure 1. Overview of hydrogenation strategies including heterogeneous, homogeneous, and electrochemical systems.

poses flammability and pressure hazards (**Figure 1**). Furthermore, selectivity against overreduction to alkanes is typically dependent on steric changes upon conversion from an alkyne to an alkene. This manifests in a dearth of catalysts that are selective for the semi-hydrogenation of unprotected terminal alkynes without deleterious alkyne dimerization, overreduction, or catalyst decomposition.[11,12] These challenges motivate the discovery of new alkyne semi-hydrogenation processes.

In thinking of alternative semi-hydrogenation protocols, and particularly in strategies that avoid the use of gaseous H_2, electrochemical transformations have many innate benefits. Electrocatalysis allows for precisely controlled redox transformations without the addition of stoichiometric chemical reductants or oxidants.[13-16] The direct synthetic use of electricity can also provide a sustainable methodology when sourced renewably. These factors, coupled with the decreasing cost of renewable electricity, motivates investigations into converting classic thermal industrial and fine chemical transformations into electrocatalytic processes.[17] These attractive features have made electrocatalytic reductive transformations a burgeoning area, but homogeneous electrocatalysts are comparatively under-explored for these useful reactions.[18-28]

For alkyne semi-hydrogenation in particular, two electrocatalytic Ni and Co bipyridine complexes have shown good efficiency with internal alkynes with good to excellent Z selectivity.[29,30] However, both of these systems suffer from poor tolerance of terminal alkyne substrates attributed to the propensity for dimerization and overreduction. Recent mechanistic investigations of the Ni bipyridine electrocatalytic system suggest a hydride-free mechanism for this transformation, which is in contrast to the prevailing mechanism for most homogeneous semi-hydrogenation catalysts involving the formation of a metal hydride which engages in alkyne

reduction.[31] In either mechanistic scenario, the controlled flow of H-atom equivalents is critical to turnover and selectivity.

Utilizing ligand-based storage of H_2, or equivalently H^+ and e^- equivalents, to mediate both reductive and oxidative transformations is a powerful strategy in catalysis. This approach relies on storage and transfer of H-atom equivalents from the ligand, akin to enzymatic systems, thus enabling new ways to achieve challenging and novel transformations.[32-42] While several systems have demonstrated H-atom storage, examples of the ligand-based storage of a full equivalent of H_2 are more uncommon.[43-57] Previous work in this area has highlighted a dihydrazonopyrrole (DHP) ligand scaffold that can store a full equivalent of H_2 and engages in catalytic thermal hydrogenations of alkenes and quinones.[32,58] Given this reactivity, we questioned whether H_2 could be replaced by acid and an electrode and also whether the metal-ligand cooperative hydrogenation reactivity and selectivity of this system would be altered under this electrochemical regime.

Indeed, detailed below are results supporting that (DHP)Ni complexes are excellent electrocatalysts for the selective semi-hydrogenation of alkynes. Specifically, we see good selectivity and conversion with a broad scope of alkynes, particularly terminal alkynes, without evidence for overreduction or oligomerization. Mechanistic investigations underscore the importance of DHP ligand stored reducing equivalents, in parallel to recent observations of hydride free mechanisms.[31] Finally, this system displays good efficacy and scope for a variety of substrates including drug molecules and diynes. These results add to the growing body of literature demonstrating the utility of reductive electrocatalysis in providing alternative strategies to classic transformations and also demonstrate how metal-ligand cooperative strategies for H_2 or H-atom storage can enable new catalysis.

Results and Discussion

Electrochemical Characterization

The previously reported complex ($^{t\text{Bu,Tol}}$DHP)Ni(II) (**1**) was initially targeted as a pre-catalyst.[59] The cyclic voltammogram (CV) of **1** in acetonitrile shows two reversible redox events at peak potentials ($E_{1/2}$) of –0.1 and –1.1 V vs $Fc^{0/+}$. We assign these features to a ligand-based oxidation and reduction of the starting complex to form $\mathbf{1}^+$ and $\mathbf{1}^-$, respectively (**Figure 2A**). Additionally, the CV of **1** in THF possesses a quasi-reversible reduction at –2.6 V vs $Fc^{0/+}$ which we assign to a putative Ni(II)/(I) couple (Appendix II: **Figure S13**). To test the possibility of electrochemical hydrogenation with **1**, we initially investigated how these CV features were affected by added acid. These experiments are particularly important as parasitic H_2 evolution is likely to be competitive with any desired hydrogenation reactivity.

The first reduction feature of **1** shifts 300 mV anodically and becomes irreversible upon the addition of 10 equivalents of benzoic acid, likely due to protonation of the ligand altering the

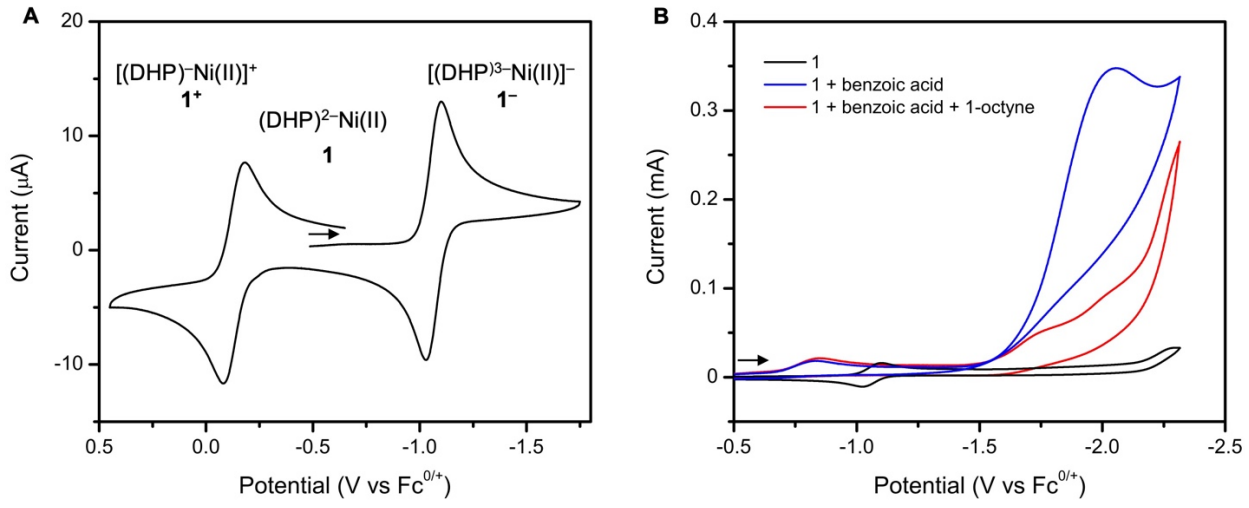

Figure 2. A. CV of **1** (1 mM) in MeCN. 0.1 M $TBAPF_6$, 100 mV s^{-1}, scanning reductively. **B.** CV of **1** alone, with 10 eq benzoic acid, and with 10 eq benzoic acid and 10 eq 1-octyne. 1 mM **1**, 0.1 M $TBAPF_6$ in MeCN, 100 mV s^{-1}, scanning reductively.

reversibility of this reduction (**Figure 2B**). Complex **1** also displays an electrocatalytic onset at –1.5 V vs $Fc^{0/+}$ in the presence of benzoic acid. This onset is 500 mV less negative than the onset potential of benzoic acid on the carbon electrode surface alone. This catalytic response is due to H_2 evolution and we note that many Ni catalysts are known to be active electrocatalysts for this reaction (Appendix II: **Figure S60**).[60-71]

Despite the potential for H_2 evolution side reactivity, we still wanted to test whether the net H^+ and e^- equivalents delivered electrochemically could be harnessed for hydrogenation reactivity. Indeed, upon addition of 1-octyne, the catalytic feature at –1.5 V vs $Fc^{0/+}$ is suppressed and adopts a new waveform consistent with a change in reactivity in the presence of an alkyne substrate (**Figure 2B**). This suggests that the catalytically active form of **1** may selectively react with an alkyne substrate despite competing hydrogen evolution reactivity (HER). These promising initial results from CV prompted us to perform bulk electrolyses to determine the major product of alkyne reactivity and whether this catalytic system diverts H-atom equivalents from HER efficiently.

Semi-Hydrogenation Reactivity and Scope

Bulk electrolysis was carried out under constant current in a divided cell. Under standard conditions ([Ni] = 1 mM; [alkyne] = 10 mM; [BA] = 100 mM; i = 4 mA, t = 55 min) terminal alkyne substrates were successfully semi-hydrogenated and overreduced or oligomerized byproducts were not detected by GC/MS analysis. The semi-hydrogenated product of 1-octyne is produced in 71% chemical yield and 33% Faradaic efficiency (FE). The conversion of phenylacetylene to styrene proceeds in 96% chemical yield with a 45% FE. While the yield and FE for aliphatic terminal alkynes are somewhat lower than for phenylacetylenes, the observed

conversion and yields here are among the best reported across both aryl and alkyl terminal alkynes in any homogeneous catalytic system. Control electrolyses excluding **1** or benzoic acid showed no conversion of the 1-octyne starting material. Substituting **1** with a generic Ni salt, $Ni(MeCN)_3OTf_2$, resulted in a mixture of 1-octene and oligomeric products in 11% and 14% yield, respectively (Appendix II: **Figure S62**). This loss of selectivity and conversion for semi-hydrogenation with a generic Ni salt is reminiscent of the lower yields and conversion for many other catalysts for the reduction of terminal alkyne substrates, indicating an essential role for the dihydrazonopyrrole ligand in the high selectivity we observe. As a final control, post-electrolysis electrodes are inactive in fresh electrolyte without **1**. Together, these tests strongly support that the active catalyst species involves a well-defined molecular ($^{t\text{Bu,Tol}}$DHP)Ni complex.

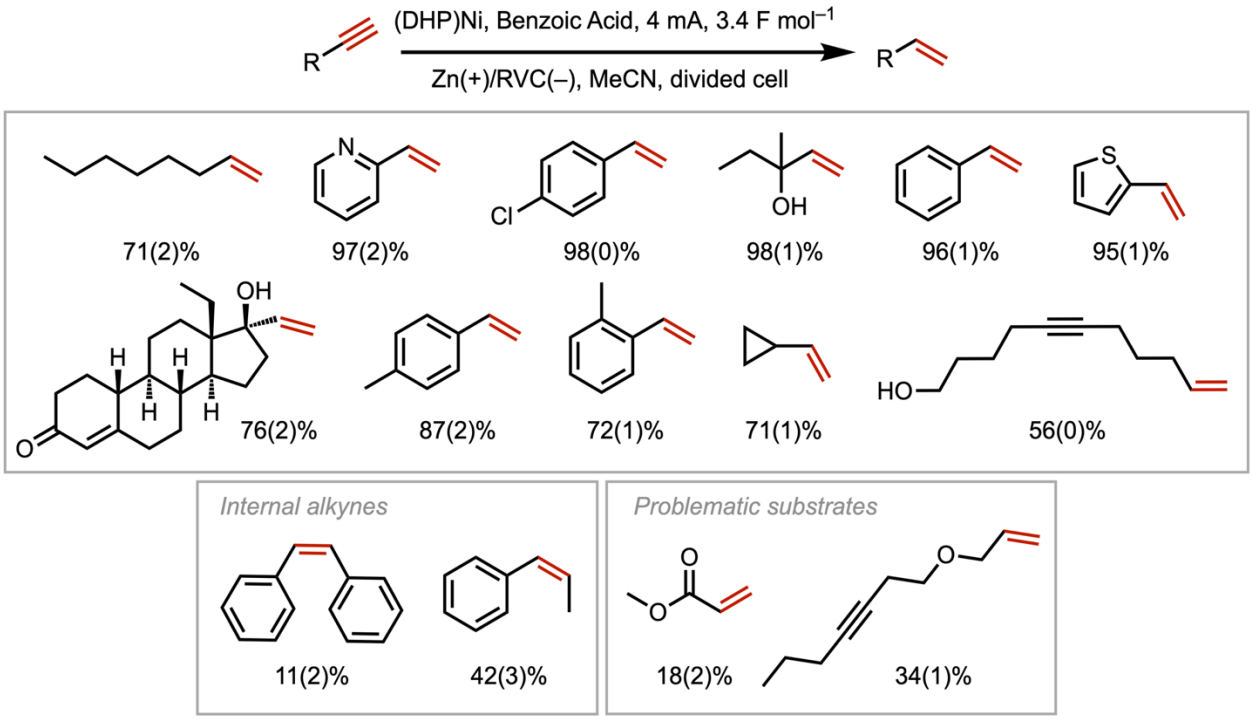

Figure 3. Substrate scope for alkyne semi-hydrogenation using 1 mM **1**, 10 mM substrate, and 100 mM benzoic acid in MeCN. 0.1 M $TBAPF_6$, constant current electrolysis, t = 55 min. In-situ chemical yields given as a percentage with standard deviation in parentheses. F mol^{-1} calculated based on alkene under galvanostatic conditions at 4 mA.

Various parameters were tuned to optimize the conditions for bulk electrolysis and maximize the yield of semi-hydrogenated products. Modifying the current showed that 4 mA produced an optimal yield while maintaining a surprisingly good FE of 40-50% for most substrates (Appendix II: **Table S1**). Using hexafluoroisopropanol as a proton source resulted in poor yields, as did switching to THF solvent. Maximum yield and FE were achieved at 55 minutes of constant current with plateauing yields with further time (Appendix II: **Figure S19**). An RVC electrode was selected to disfavor HER, and yields improved by 10-20% compared to a graphite rod electrode.[72] Optimized electrolyses were performed in a divided cell. While conversion also proceeds in good yield with an undivided cell, Zn^0 plating from the sacrificial Zn anode onto the RVC cathode was avoided in a divided cell.

A variety of substrates were then tested with these optimized conditions to determine the reaction scope. A broad set of functional groups were tolerated including pyridines, thiophenes, aryl chlorides, cyclopropyl, and hydroxyl groups (**Figure 3**). Good yields of the corresponding terminal alkene were also observed for the common drug compound levonorgestrel, which possesses a tertiary alcohol group as well as an α,β-unsaturated carbonyl. This result supports the ability of **1** to perform late-stage semi-hydrogenations of terminal alkynes in complicated molecules. Furthermore, 3.4 F mol^{-1} is passed in all cases, consistent with near-50% FE for semi-hydrogenation over hydrogen evolution for most substrates. The functional group tolerance of **1** is improved in comparison to recent Ni electrocatalysts[30] and is similar to recent Co systems,[29] with the notable exception of ester groups which are not well-tolerated in our case. We note that the activity of **1** for unprotected terminal alkynes is unusual for homogeneous electrocatalytic systems, with only limited activity or selectivity in previous reports.

We can also compare the activity of **1** to the limited examples of terminal alkyne thermal semi-hydrogenations using H_2. Complex **1** has an improved scope and yield over a previously reported Mn bis(di-*iso*-propylphosphino)ethane catalyst,[5] and comparable tolerance of chlorides, thiophenes, and methyl-substituted phenylacetylenes to an Fe N-methyl PNP pincer catalyst.[7] We note the observation that improving the bulkiness of the PNP pincer ligand for the aforementioned Fe catalyst improved selectivity for the semi-hydrogenated terminal alkene product rather than dimerized or overreduced byproducts.[7] Likewise, in our system we hypothesize that the bulkiness of the *t*Bu groups around the Ni center introduces steric hindrance that selects for terminal alkyne substrates over alkenes or bulkier internal alkynes. This is exemplified by the 11% yield of stilbene obtained from diphenylacetylene with **1** under the standard electrolysis conditions with the remainder of the carbon balance corresponding to unreacted starting material.

Catalytic Mechanism

The high activity and selectivity of **1** motivated us to investigate its mechanism. An important mechanistic question is whether **1** directly reduces alkynes, or whether in-situ generated H_2 enables thermal hydrogenation catalysis. However, electrolysis of **1** and 1-octyne with an atmosphere of H_2 results in <5% yield of 1-octene (Appendix II: **Table S1**). This demonstrates that any H_2 generated during electrocatalysis contributes only minimally to product formation. This finding is consistent with previous studies which showed this system is capable of activating H_2 for quinone hydrogenation, but not for alkenes.[58]

The order in benzoic acid for semi-hydrogenation cannot be concretely determined by analyzing the CV due to overlapping HER (**Figure 2**). However, we note that the initial feature of the catalytic wave only appears when substrate is present along with acid, and that increasing

benzoic acid concentration does not increase the current of this feature (Appendix II: **Figure S17**). These observations suggest that catalytic turnover is zero order in acid, which is supported by the DFT calculated rate-determining step of intramolecular HAT (*vide infra*). The addition of 1-octyne suppresses the HER wave of **1** but increasing the 1-octyne concentration beyond an equimolar amount with benzoic acid does not provide any further change in the catalytic wave (Appendix II: **Figure S15**).

We then analyzed the speciation of **1** with added acid or substrate by CV. The addition of 1-octyne to **1** without any added acid shows no change in the reversible redox features, suggesting that **1** does not bind 1-octyne in its neutral or $\mathbf{1}^{-}$ reduced oxidation state (Appendix II: **Figure S14**). The addition of sub-stoichiometric benzoic acid to **1** without added 1-octyne induces a color change from deep purple to maroon and improved solubility in MeCN compared to the starting complex. The CV of this mixture shows a gradual diminishment of the reversible redox feature at

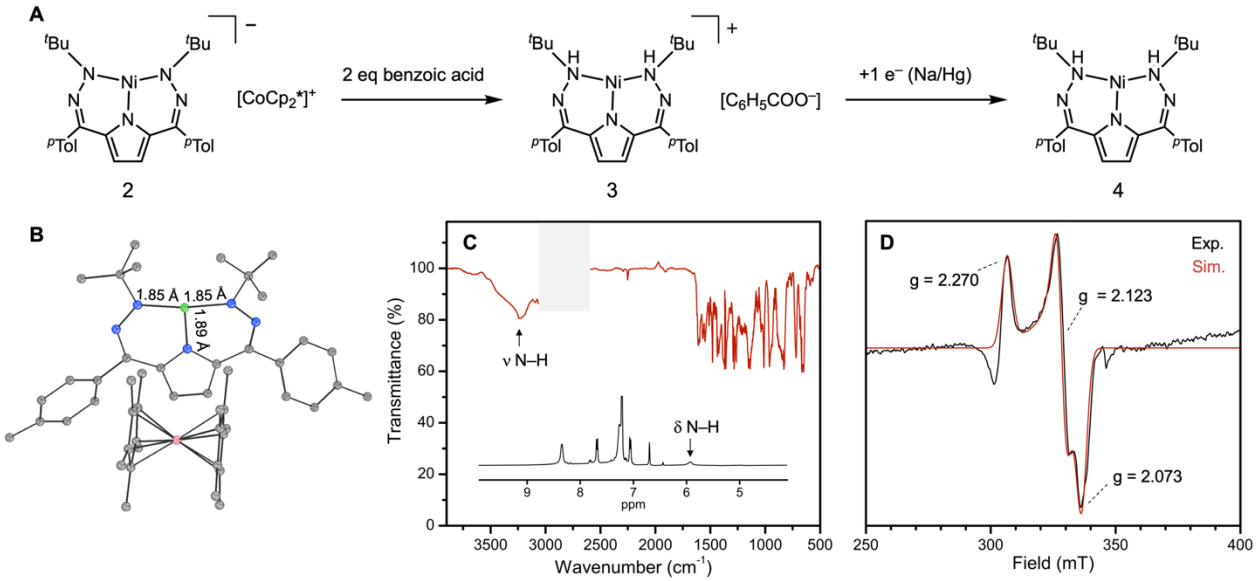

Figure 4. A. Synthesis of in-situ ($^{t\text{Bu,Tol}}$DHP)Ni intermediates **B.** SXRD structure of **2**. Ellipsoids are set to 50% probability. Hydrogen atoms have been omitted for clarity. **C.** IR in THF and NMR (inset, in C_6D_6/d_8-THF) spectra of **3** in showing the N–H stretching feature and chemical shift, respectively. Imperfect solvent subtraction is removed from the IR spectrum for clarity. **D.** X-band EPR spectrum of **4** in MeCN at 15 K. We note the small paramagnetic impurities at 300 and 345 mT, see Appendix II, Figure S23 for full spectrum.

–1.1 V vs $Fc^{0/+}$ as two new irreversible features arise at –0.6 and –0.9 V vs $Fc^{0/+}$ (Appendix II: **Figure S16**). Eventually, the dominant feature is a broad irreversible reduction at –0.9 V vs $Fc^{0/+}$ after >2 equivalents of benzoic acid have been added (Appendix II: **Figure S17**). We postulate that the speciation at low concentrations of acid arises from an equilibrium between mono- and di-protonated analogues of **1**. The single irreversible feature with additional acid possibly corresponds to the reduction of a di-protonated ligand-metal complex. However, more detailed assignment of differentially protonated congeners of **1** is challenging due to the paramagnetic nature of these species.

While the product(s) of **1** and benzoic acid are paramagnetic and difficult to characterize, initial reduction of **1** with 1 eq of $CoCp_2^*$ provides $[(^{t\text{Bu,Tol}}\text{DHP})\text{Ni}]^-[CoCp_2^*]^+$ (**2**) which is diamagnetic (**Figure 4B**). This enables protonation studies with NMR spectroscopy, and the addition of 2 equivalents of benzoic acid to **2** results in a color change from indigo to light yellow. We tentatively assign this new product as $[(^{t\text{Bu,Tol}}\text{DHPH}_2)\text{Ni}]^+[\text{BzO}]^-$ (**3**) where the β-Ns of both hydrazone arms have been protonated. Evidence of these protonated ligand arms is provided by ^{1}H NMR (β-NHs: 5.92 ppm) and IR (N–H: 3250 cm^{-1}) spectroscopies which show diagnostic resonances and stretches, respectively (Figure 4C). Furthermore, the ^{1}H NMR of **3** is in agreement with the previously reported and characterized complex $(^{t\text{Bu,Tol}}\text{DHPH}_2)\text{NiOTf}$.[58]

Interestingly, no hydrogenated products are observed when **3** is stirred with excess 1-octyne. This indicates that **3** is not the active hydrogenating intermediate. The catalytic CVs for **1** support this hypothesis. The onset potential for catalysis begins nearly 0.7 V negative of the first irreversible reduction of the Ni complex in the presence of benzoic acid. We hypothesized that an additional reduction event corresponding to a formal Ni(II)/Ni(I) couple might be necessary for catalysis. Indeed, isolated $(^{t\text{Bu,Tol}}\text{DHPH}_2)\text{NiOTf}$ has an irreversible reduction feature at –1.6 V vs

$Fc^{0/+}$, which is nearly superimposable with the catalytic onset of **1** in the presence of benzoic acid (Appendix II: **Figure S21**). As this complex has a reduced DHP ligand, this feature is most reasonably assigned as a Ni(II)/Ni(I) couple. The irreversibility of this feature is likely induced by a chemical change such as proton loss upon reduction. While **3** is not reactive with 1-octyne, the addition of Na amalgam as a reductant with **3** leads to the production of 1-octene in 27% yield (Appendix II: **Figure S6**). We attribute this comparatively low yield to some decomposition of complex **3** owing to the strongly reducing conditions. Stirring 1-octyne and benzoic acid with Na/Hg in the absence of **3** recovers only 1-octyne starting material. To further corroborate the presence of a Ni(I) species, compound **3** was stirred with Na/Hg followed by rapid freezing at –78 °C. The X-band EPR spectrum is consistent with a Ni(I) species, with a broad rhombic signal and features at g = 2.073, 2.123, and 2.270 (**Figure 4D**). The EPR spectrum is distinct from that of complex **1** which is formally Ni(II) with a ligand radical.[59] These combined data, and particularly the need to add an additional reductant to **3** to react with alkynes, supports that a reduction to a Ni(I) species (**4**) is critical to initiating catalysis.

With evidence supporting the necessity of the two-electron reduction of **1** in the presence of acid before the system is catalytically active, we then investigated the chronoamperometry of bulk electrolyses to gain additional mechanistic insights. Specifically, we had noted a distinctive initiation period which we thought might correspond to an initial reduction of the Ni species in solution (Appendix II: **Figure S19**). Calculating the moles of electrons passed during this period corresponds with a two-electron reduction of the added catalyst (see Appendix II). Use of ($^{t\text{Bu,Tol}}$DHPH$_2$)NiOTf instead of **1** should in principle reduce this induction period as the catalyst is already reduced. Satisfyingly, this substitution indeed shortens the initiation period and reaches

a similar potential and overall yield as the standard conditions which supports the hypothesis that a Ni(I) species needs to be generated (Appendix II: **Figure S20**).

We also wanted to obtain more insight on the net H-atom transfer steps of catalysis and so we analyzed the products of the low-yielding internal alkyne substrates diphenylacetylene and 1-phenyl-1-propyne. We found that both of these substrates gave the *Z*-isomer of the stilbene and β-methyl-styrene products, respectively (Appendix II: **Figures S49** and **S50**). While no *E* products were detected for these internal alkyne substrates, deuterium labelling studies with d_1-benzoic acid and phenylacetylene revealed a 1:0.6 *Z*:*E* ratio for terminal alkyne semi-hydrogenation (**Figure 5C**). These observations suggest that the semi-hydrogenation proceeds in a *cis*-selective manner with some possible competition or isomerization for terminal alkyne substrates. It is possible that the smaller steric profile of terminal alkene products might favor coordination to Ni and subsequent isomerization.

As a last mechanistic test, we also investigated the possible involvement of radical intermediates such as free alkenyl radicals. We note that previous thermal hydrogenations with DHP complexes of Co do show evidence for radical intermediates.[32] To test this possibility we employed a radical cyclization probe, allyl-2-ethynylbenzene, which might be expected to undergo a cyclization to a five-membered ring from a putative radical intermediate (**Figure 5B**). While this compound is unstable and undergoes some degree of polymerization in MeCN, we detected no cyclized products and solely the expected 1,2-divinylbenzene product which should arise from hydrogenation (Appendix II: **Figure S10**). The rate constant for cyclization for similar vinyl radical species is on the order of 10^8 s^{-1}, supporting that semi hydrogenation proceeds through a concerted mechanism without long-lived radical intermediates.[73]

We then employed density functional theory (DFT) computations to gain additional mechanistic insight and to fill in a complete mechanistic cycle (**Figure 5A**). Beginning from the fully reduced Ni(I) complex **4**, coordination to 1-butyne gives calculated bond distances of 1.969 and 2.008 Å, showing a nearly symmetrically bound alkyne. The first net H-atom transfer (HAT) has an estimated upper limit transition state barrier of 28.5 kcal/mol (TS1, see below and Appendix II for further discussion, Appendix II: **Figure S66**, **S75**) and is overall exergonic by 11.7 kcal/mol.

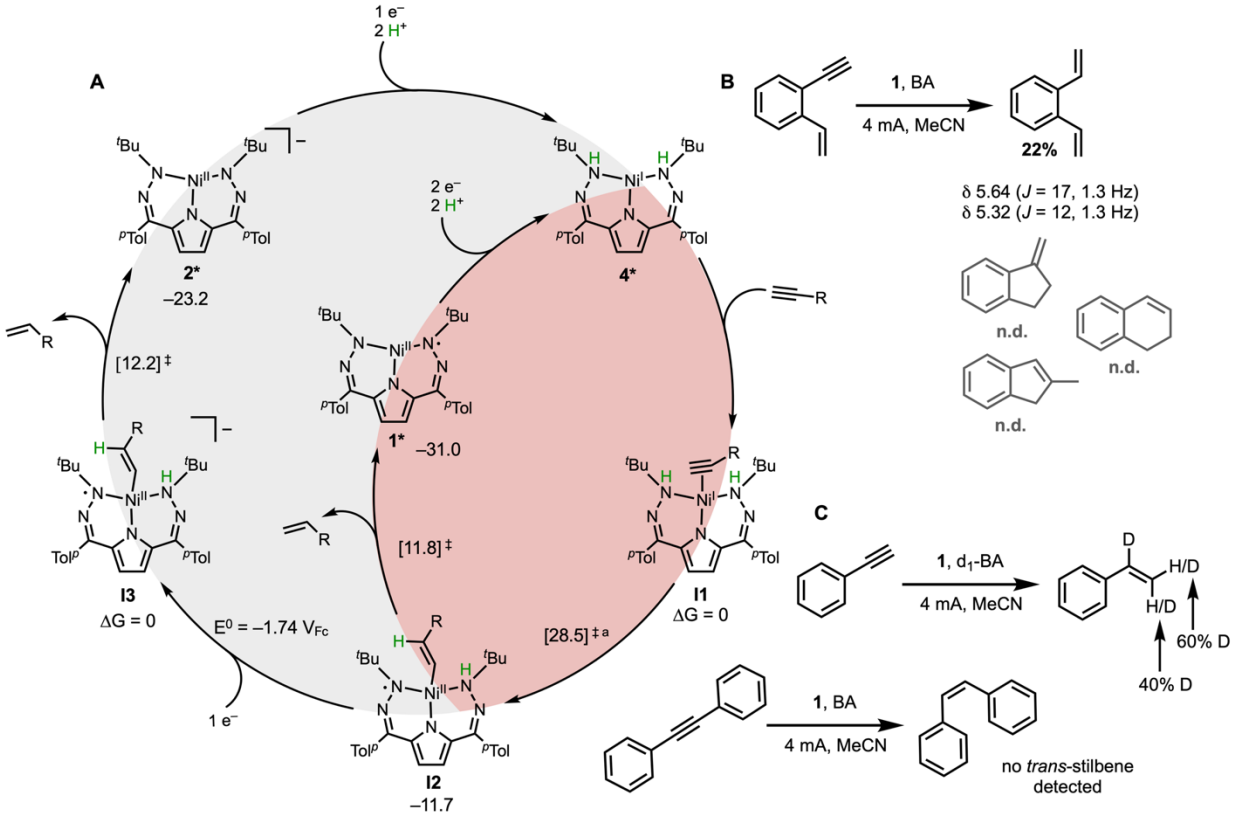

Figure 5. Mechanistic studies. **A.** Proposed catalytic cycle with neutral and anionic pathways shown. [a]This TS1 energy is an upper-limit from the most reasonable TS1 geometry obtained but is not fully optimized (See Appendix II, **Figures S66**, **S75**). DFT computed energies (kcal/mol) were carried out with the M06L functional, def2-TZVPP basis set for Ni, and def2-TZVP for all other atoms. Asterisks indicate experimentally characterized intermediates. **B.** Radical probe experiment using allyl-2-ethynylbenzene and **C.** deuterium incorporation experiment using d_1-benzoic acid with phenylacetylene, and semi-hydrogenation of diphenylacetylene to give 11% chemical yield of *cis*-stilbene with no *trans* product detected. Standard electrolysis conditions: [Ni] = 1 mM; [alkyne] = 10 mM; [BA] = 100 mM; [$TBAPF_6$] = 0.1 M; i = 4 mA, t = 55 min, MeCN, RVC/Zn.

After this initial step to form **I2**, we envisioned two plausible pathways by which the cycle could proceed. A second HAT could release the alkene product and give **1**. This path proceeds via a ~23 kcal/mol transition state barrier (TS2, Appendix II: **Figure S71**) for an overall 19 kcal/mol downhill process. If instead the alkenyl adduct is first reduced by one electron to generate **I3**, the subsequent transition state barrier for HAT is 12.2 kcal/mol (TS2–, Appendix II: **Figure S69**) for an overall 23.2 exergonic process. Both pathways regenerate the starting species **4** by subsequent reduction and protonation. DFT calculations predict that TS1 represents the rate determining step, however, we have had difficulties obtaining a reliable geometry and energy for this TS (see experimental and Appendix II: **Figure S66**, **S75**). Furthermore, the comparable energy between TS1 (28.5 kcal/mol) and TS2 (23.5 kcal/mol) makes drawing concrete conclusions about the rate determining step difficult. The low transition state barrier for the second HAT step, along with the accessible calculated reduction potential of –1.74 V vs $Fc^{0/+}$ in MeCN, supports that reduction to an anionic alkenyl intermediate **I3** is at least a plausible cycle.

One interesting feature of this proposed cycle is the lack of any metal-hydride intermediates. To further test this observation, we computationally explored the feasibility of a Ni hydride species via reduction and migration of one proton from the ligand. The formation of a (DHP)Ni–H species is calculated to be slightly endergonic, and the resultant coordinatively saturated hydride species is not computed to have favorable alkyne binding (Appendix II: **Tables S16**, **S17**). We also note that we have seen no evidence by either ^{1}H NMR or IR spectroscopy that would indicate the presence of a hydride species, but we do observe ligand-based proton storage for **3** which is the pre-cursor to the proposed catalytically active complex **4** (Appendix II: **Figures S3** and **S24**). These data suggest that ligand-based reactivity is the most viable pathway. This hydride-free pathway echoes recent mechanistic proposals from Leitner and co-workers where an

ECEC semi-hydrogenation pathway with a nickelacyclopropene adduct resting state was invoked.[31] This system uses a bipyridine ligand and relied on direct outer sphere protonation to a reduced metallacyclopropene intermediate followed by rapid electron transfer. In contrast, both experimental and computational evidence supports a more concerted H-atom transfer in the present system. The DFT-calculated BDE for the DHP N–H bond of 56 kcal/mol is comparatively small and thus energetically accessible for an HAT pathway (Appendix II: **Table S14**). Inspection of the Mulliken charges along the reaction coordinate also suggests that each transition state is best described as an H-atom ($H^+ + e^-$) transfer rather than a heterolytic proton and hydride transfer (Appendix II: **Table S15**). Thus, while both of these Ni based electrocatalysts rely on hydride free mechanisms, the present DHP system leverages ligand-based interactions to specifically shuttle H-atom equivalents to the bound alkyne substrate as opposed to more purely outer-sphere steps in the bipyridine system.

Conclusion

Described above is a homogeneous electrocatalytic system for the semi-hydrogenation of terminal alkynes and corresponding mechanistic investigations which support a ligand-assisted mechanism and Z-selective hydrogenation. The ($^{t\text{Bu,Tol}}$DHP)Ni complex catalyzes selective semi-hydrogenation of a variety of alkyne substrates including those with alcohol, thiophene, pyridine, cyclopropyl, and chloride functional groups. The selective semi-hydrogenation of terminal alkynes without significant oligomerization or overreduction is unusual generally, and particularly so for an electrochemical system.

Mechanistic investigations support the importance of HAT from ligand-stored H-atom equivalents to Ni coordinated alkyne substrates. In the proposed catalytic pathway, the ligand and metal center work in tandem to selectively shuttle protons and electrons in a coordinated manner. While most examples of hydrogenation catalysts employ a metal hydride mechanism, this DHP system is unique in its involvement of ligand-based H-atom storage, drawing inspiration from enzymatic processes. This catalytic design strategy, particularly as employed in reductive electrocatalysis here, opens new possibilities for selective and efficient transformations. Specifically, the use of electrochemical hydrogenation schemes enables fine tuning of parameters including applied current, potential, and acid pK_a, offering possibly more delicate control compared to chemical redox conditions. The utility of the DHP scaffold in avoiding competitive HER offers promise for general application in various reductive processes that more typically rely upon H_2.

Experimental

General Considerations. All reagents were purchased from commercial suppliers and used without further purification unless otherwise specified. Complex **1** was synthesized following a previously reported procedure.[59] All manipulations were carried out under an atmosphere of N_2 using standard Schlenk and glovebox techniques. Glassware was dried at 180 °C for a minimum of 2 h and cooled under vacuum prior to use. Solvents were dried on a solvent purification system from Pure Process Technology, passed over a column of activated alumina, and stored over 4 Å molecular sieves under N_2. Tetrahydrofuran was stirred over NaK alloy and run through an additional activated alumina column prior to use to ensure dryness. C_6D_6 and CD_3CN were stored

over 4 Å molecular sieves under N_2. Solvents were tested for H_2O and O_2 using a standard solution of sodium-benzophenone ketyl radical anion. Tetrabutylammonium hexafluorophosphate and benzoic acid were dried under vacuum at 100°C over 8 hours.

^1H and ^{13}C NMR spectra were recorded on a Bruker DRX 400 MHz spectrometer. Chemical shifts are reported in ppm units referenced to residual solvent resonances for ^1H spectra. Infrared spectra were recorded using a Bruker Tensor II spectrometer with OPUS software suite. IR samples were prepared using a solution cell with KBr windows. EPR spectra were recorded on an Elexsys E500 spectrometer with an Oxford ESR 900 X-band cryostat and a Bruker Cold-Edge Stinger and were simulated using the Easyspin suite in Matlab software.[74] GC/MS data was collected on an Agilent SQ GCMS with 5977A single quad MS and 7890B GC. Elemental analysis was performed by Midwest Microlabs. Electrochemical measurements were performed using a BAS Epsilon potentiostat and analyzed using BAS Epsilon software version 1.40.67NT.

Electrochemical experiments. Experiments were performed inside the glovebox with a MeCN/0.1 M nBu$_4$NPF$_6$ electrolyte solution at room temperature. Cyclic voltammetry measurements were made with a [Ni] = 1 mM using a glassy carbon working electrode, platinum wire counter electrode, and silver wire pseudoreference electrode and were referenced to internal Fc/Fc^+ by adding ferrocene at the end of measurements. A one-compartment glass cell was filled with 4 mL of electrolyte solution. The working electrode was polished over a microcloth pad (Buehler) using an alumina slurry (0.05mm EMS), followed by rinsing with deionized water and isopropyl alcohol. Reference and counter electrodes were rinsed with acetone. CVs were recorded at a scan rate of 100 mV/s scanning reductively.

Electrolyses were performed in a H-type glass cell with anode and cathode chambers separated by a glass frit. An RVC (reticulated vitreous carbon, ERG Duocel, 2 cm x 0.5 cm x 0.5 cm) electrode, Zn rod (National Bureau of Standards, 3 cm x 0.5 cm x 0.5 cm), and a $AgBF_4$/Ag electrode (BASi, 0.05 mm, 10 mM $AgBF_4$ solution in MeCN 0.1 M nBu$_4$NPF$_6$) were used as working, counter, and reference electrodes, respectively. To each chamber of the H-cell was added 4 mL of electrolyte solution and stir bars. Typically, 2 mg of (DHP)Ni (final concentration 1 mM), 100 mL of a mesitylene (internal standard) solution in MeCN (final concentration of 10 mM), 100 mL of a substrate solution in MeCN (final concentration of 10 mM), and benzoic acid (final concentration 1 M) were added to the cathodic chamber. Electrolyses were performed under galvanostatic conditions and aliquots were taken and diluted in MeCN before analysis by gas chromatography (GC). For determining final in-situ yield, the electrolyte solution was passed through an alumina pad and 200 mL of CD_3CN was added to 200 mL of electrolyte solution and analyzed by ^{1}H NMR using a mesitylene internal standard (10 mM, δ 6.77 ppm, 3H) and a solvent suppression pulse sequence. All electrolyses were performed in triplicate. For substrates with < 95% yield of the semi-hydrogenated product, GC-MS chromatograms and mass spectra are provided to check for the presence of alkene or dimerized products (See SI). Cyclopropylacetylene and methyl propiolate were too low-boiling to detect over trace solvents by GC-MS on our instrument. Potentials reported for chronopotentiometry electrolysis experiments are referenced to Fc/Fc^+ by external measurement in an independent cell versus the $AgBF_4$/Ag electrode of $E_{1/2}(Fc/Fc^+) = 0.48$ V vs $AgBF_4$/Ag. For electrolysis under an H_2 atmosphere, the cathodic chamber was prepared in an N_2 glovebox, removed from the glovebox, and sparged with H_2 for 10 min before starting electrolysis, and then constantly during electrolysis.

X-ray structure determination. The diffraction data for **2** were measured at 100 K on a Bruker D8 fixed-chi with PILATUS1M (CdTe) pixel array detector (synchrotron radiation, λ = 0.41328 Å (30 keV)) at the Chem-MatCARS 15-ID-B beamline at the Advanced Photon Source (Argonne National Laboratory). Data reduction and integration were performed with the Bruker APEX3 software package (Bruker AXS, version 2017.3-0, 2018). Data were scaled and corrected for absorption effects using the multiscan procedure as implemented in SADABS (Bruker AXS, version 2014/5).[75] The structures were solved by SHELXT (Version 2014/5)[76] and refined by a full-matrix least-squares procedure using OLEX2 (XL refinement program version 2018/1).[77,78] Structure solutions were performed with the use of standard restraints and constraints as implemented in ShelXL. We note the structure of **2** has A level CheckCIF alerts arising from the fact that this data set was collected on a synchrotron, resulting in somewhat limited data completeness. Additional crystallographic and refinement data can be found in Appendix II.

Synthesis of ($^{t\text{Bu,Tol}}$DHPl)Ni[CoCp2*] (2). A solution of decamethyl-cobaltocene ($CoCp_2^*$, 20 mg, 0.06 mmol) in THF (1 mL) was added all at once to a stirring solution of **1** (30 mg, 0.06 mmol) in THF (2 mL). After stirring at room temperature for 2 hours, the color of the reaction mixture changed from deep violet to deep indigo. The solution was filtered, and the solvent was removed under vacuum resulting in a deep indigo solid. The product was purified by recrystallization (concentrated THF, –35 °C). Yield: 44 mg, 0.053 mmol, 88%. ^{1}H NMR (400 MHz, C_6D_6): δ = 7.5 (d, 4H, *J* = 7.4 Hz), 7.08 (d, 4H, *J* = 7.0 Hz), 5.86 (s, 2H), 2.33 (s, 6H), 1.25 (s, 18H), 1.7 (s, 30H). ^{13}C{^{1}H} NMR (125 MHz, C_6D_6): δ 141.7, 142.3, 138.1, 136.0, 129.3, 128.4, 111.5, 94.9, 52.7, 29.3, 20.9, 7.5. IR (ATR, cm^{-1}): 2954 (m), 2911 (m), 1511 (m, C=N), 1371 (m), 1341 (s), 1197 (m), 1103 (m), 1013 (s), 882 (w), 823 (s, C=C of $CoCp_2^*$) , 681 (m), 589 (m), 442 (m). Anal. Calc.:

C, 69.57; H, 7.78; N, 8.45; Found: C, 69.13; H, 7.57; N, 8.25. HRA-MS (*m/z*) $[M]^+$ $C_{48}H_{64}N_5CoNi$: 827.385 Found: 827.383.

Synthesis of (^{tBu,Tol}DHPH$_2$)Ni(C6H5COO–) (3). To a stirring solution of **2** (10 mg, 0.012 mmol) at room temperature in a glovebox under N_2 atmosphere in THF (300 mL) was added benzoic acid (2.9 mg, 0.024 mmol) dissolved in THF (300 mL). After stirring for 15 minutes, the solution was filtered, and the solvent was removed under vacuum. ^{1}H NMR (400 MHz, C_6D_6 with a few drops of d_8-THF for solubility): δ = 7.61 (d, 4H, *J* = 7.3 Hz), 7.03 (d, 4H, *J* = 7.1 Hz), 6.66 (s, 2H), 5.92 (bs, 2H), 2.12 (s, 6H), 1.18 (s, 18H). IR (solution cell, THF, cm^{-1}): 3250 (b, N–H).

Chemical reduction of 1-octyne with 3 and Na/Hg. To a stirring solution of **3** (7.5 mg, 0.012 mmol) at room temperature in a glovebox under N_2 atmosphere in CD_3CN (600 mL) was added 1-octyne (17 μL, 0.12 mmol) and Na amalgam (5% Na, 10 mg). After stirring for 30 minutes, the solution was filtered to remove the amalgam and transferred to an NMR tube to look for the presence of 1-octene by ^{1}H NMR. Mesitylene was used as an internal standard (1.7 μL, 0.012 mmol). The control reaction was performed under the same conditions except for the absence of **3** in solution. See Appendix II.

Synthesis of d_1-benzoic acid. Benzoic acid anhydride (Sigma Aldrich, 1.0 g, 4.4 mmol) was stirred in D_2O (Cambridge Isotope, 99.9%, 10 mL) and refluxed under N_2 for 48 hr. Upon cooling to room temperature, the product began to crystallize and could be collected by filtration as a white solid. The solid was further dried and purified by sublimation at 100 °C under reduced pressure

before use. The ^{1}H NMR spectrum is consistent with benzoic acid with the absence of a broad OH peak usually found at 11.5 ppm. Comparison with the ^{1}H NMR spectrum of benzoic acid anhydride shows that no starting material remains. See Appendix II, Figure S8 for overlayed spectra.

Synthesis of 1-(prop-2-yn-1-yloxy)hept-3-yne. To a stirred solution of 3-heptyn-1-ol (1.5 g, 13.4 mmol) in DMF (60 mL) K_2CO_3 (7.40 g, 53.6 mmol) was added in one portion. The resulting mixture was heated at 70 °C for 0.5 h, then 3-bromo-1-propyne (1.9 g, 16.1 mmol) dissolved in DMF (40 mL) was added slowly over 5 min. The mixture was heated at 70 °C for another 48 h. After this time, 15 mL of water was added to the reaction. The mixture was extracted with Et_2O (3 x 100 mL). The combined organic layers were washed with water (4 x 100 mL) and brine (100 mL). After removal of the solvent under reduced pressure, the resulting yellow oil was purified by flash chromatography on silica gel (Hexanes/EtOAc 95:5). Yield 96 mg (0.64 mmol, 5%). ^{1}H NMR (400 MHz, $CDCl_3$, RT): δ = 4.73 (d, 2H, *J* = 2.4 Hz), 4.23 (t, 2H, *J* = 7.1 Hz), 2.55 (tt, 2H, *J* = 2.4 Hz), 2.52 (t, 1H, *J* = 2.4 Hz), 2.11 (tt, 2H, *J* = 2.4 Hz), 1.50 (m, 2H, *J* = 7.2 Hz), 0.96 (t, 3H, *J* = 7.4 Hz). ^{13}C {^{1}H} NMR (125 MHz, $CDCl_3$, RT): δ = 154.4, 82.4, 75.7, 74.8, 66.7, 55.3, 22.2, 20.7, 19.3, 13.4.

Computational Methodology. Intermediates and transition states for the reaction coordinate with 1-butyne were optimized in ORCA[79] using the M06L functional and def2-TZVPP basis set on Ni, def2-TZVP basis set on all other atoms. Frequency calculations were performed to confirm the structures are at local minima on the potential energy surface. The calculated BDE for the ligand NH's was determined using free energies from frequency calculations with the M06L functional and def2-TZVPP basis set for Ni, def2-TZVP for all other atoms. A simplified ligand with *i*Pr

groups in the place of the *p*-tol substituents were utilized as well as a 1-butyne substrate to reduce the number of atoms per calculation. We were unable to optimize a geometry for TS1 as all TS calculations resulted in either falling off of the TS geometry to reactants or products or a lack of convergence. The proposed geometry for TS1 was obtained from a relaxed surface scan. (Appendix II, Figure S66) Frequency calculations on this geometry show two imaginary modes. The first corresponds to an N–H stretch for the productive reaction, and the second is a low magnitude (30 cm^{-1}) spurious ligand arm rotation. Thus, this geometry should be a reasonable estimate of the true TS geometry. This geometry for TS1 was further analyzed with an intrinsic reaction coordinate calculation (IRC) to verify it as a reasonable geometry (Appendix II, Figure S75). The IRC calculation was performed by using geometries along the optimized transition state imaginary vibrational mode and calculating the forward and backward segments separately. The IRC calculations support the obtained geometry for TS1. The same functional and basis sets were used for all calculations.

References

1. Swamy, K. C. K.; Reddy, A. S.; Sandeep, K.; Kalyani, A., Advances in chemoselective and/or stereoselective semihydrogenation of alkynes. *Tet. Lett.* **2018,** *59*, 419-429. DOI: 10.1016/j.tetlet.2017.12.057
2. Decker, D.; Drexler, H.-J.; Heller, D.; Beweries, T., Homogeneous catalytic transfer semihydrogenation of alkynes – an overview of hydrogen sources, catalysts and reaction mechanisms. *Catal. Sci. & Tech.* **2020,** *10*, 6449-6463. DOI: 10.1039/D0CY01276A
3. Li, X.-T.; Chen, L.; Shang, C.; Liu, Z.-P., Selectivity control in alkyne semihydrogenation: Recent experimental and theoretical progress. *Chinese J. Catal.* **2022,** *43*, 1991-2000. DOI: 10.1016/S1872-2067(21)64036-6
4. Lindlar, H., Ein neuer Katalysator für selektive Hydrierungen. *Helv. Chim. Acta* **1952,** *35*, 446-450. DOI: 10.1002/hlca.19520350205
5. Farrar-Tobar, R. A.; Weber, S.; Csendes, Z.; Ammaturo, A.; Fleissner, S.; Hoffmann, H.; Veiros, L. F.; Kirchner, K., E-Selective Manganese-Catalyzed Semihydrogenation of Alkynes with H2 Directly Employed or In Situ-Generated. *ACS Catal.* **2022,** *12*, 2253-2260. DOI: 10.1021/acscatal.1c06022
6. Tokmic, K.; Fout, A. R., Alkyne Semihydrogenation with a Well-Defined Nonclassical Co–H2 Catalyst: A H2 Spin on Isomerization and E-Selectivity. *J. Am. Chem. Soc.* **2016,** *138*, 13700-13705. DOI: 10.1021/jacs.6b08128
7. Gorgas, N.; Brünig, J.; Stöger, B.; Vanicek, S.; Tilset, M.; Veiros, L. F.; Kirchner, K., Efficient Z-Selective Semihydrogenation of Internal Alkynes Catalyzed by Cationic Iron(II) Hydride Complexes. *J. Am. Chem. Soc.* **2019,** *141*, 17452-17458. DOI: 10.1021/jacs.9b09907
8. Hale, D. J.; Ferguson, M. J.; Turculet, L., (PSiP)Ni-Catalyzed (E)-Selective Semihydrogenation of Alkynes with Molecular Hydrogen. *ACS Catal.* **2022,** *12*, 146-155. DOI: 10.1021/acscatal.1c04537
9. Kaicharla, T.; Zimmermann, B. M.; Oestreich, M.;Teichert, J. F., Using alcohols as simple H2-equivalents for copper-catalysed transfer semihydrogenations of alkynes. *Chem. Comm.* **2019,** *55*, 13410-13413. DOI: 10.1039/C9CC06637C
10. Sansores-Paredes, M. L. G.; Lutz, M.; Moret, M.-E., Cooperative H2 activation at a nickel(0)–olefin centre. Nat. Chem. 2023. DOI: https://doi.org/10.1038/s41557-023-01380-1
11. Wang, S.; Uwakwe, K.; Yu, L.; Ye, J.; Zhu, Y.; Hu, J.; Chen, R.; Zhang, Z.; Zhou, Z.; Li, J.; Xie, Z.; Deng, D., Highly efficient ethylene production via electrocatalytic hydrogenation of acetylene under mild conditions. *Nature Commun.* **2021,** *12*, 7072. DOI: 10.1038/s41467-021-27372-8
12. Li, H.; Gao, Y.; Wu, Y.; Liu, C.; Cheng, C.; Chen, F.; Shi, Y.; Zhang, B., σ-Alkynyl Adsorption Enables Electrocatalytic Semihydrogenation of Terminal Alkynes with Easy-Reducible/Passivated Groups over Amorphous PdSx Nanocapsules. *J. Am. Chem. Soc.* **2022,** *144*, 19456-19465. DOI: 10.1021/jacs.2c07742
13. Yan, M.; Kawamata, Y.; Baran, P. S., Synthetic Organic Electrochemical Methods Since 2000: On the Verge of a Renaissance. *Chem. Rev.* **2017,** *117*, 13230-13319.
14. Wiebe, A.; Gieshoff, T.; Möhle, S.; Rodrigo, E.; Zirbes, M.; Waldvogel, S. R., Electrifying Organic Synthesis. *Angew. Chem. Int. Ed.* **2018,** *57*, 5594-5619.
15. Jutand, A., Contribution of Electrochemistry to Organometallic Catalysis. *Chem. Rev.* **2008,** *108*, 2300-2347.
16. Francke, R.; Little, R. D., Redox catalysis in organic electrosynthesis: basic principles and recent developments. *Chem. Soc. Rev.* **2014,** *43*, 2492-2521.
17. IRENA (2021), Renewable Power Generation Costs in 2020, International Renewable Energy Agency, Abu Dhabi.
18. Zhang, S.; Findlater, M., Electrochemically Driven Hydrogen Atom Transfer Catalysis: A Tool for C(sp3)/Si–H Functionalization and Hydrofunctionalization of Alkenes. *ACS Catal.* **2023,** *13*, 8731-8751. DOI: 10.1021/acscatal.3c01221
19. Kaeffer, N.; Leitner, W., Electrocatalysis with Molecular Transition-Metal Complexes for Reductive Organic Synthesis. *JACS Au* **2022,** *2*, 1266-1289.
20. Du, P.; Mubarak, M. S.; Karty, J. A.; Peters, D. G., Electrosynthesis of 4-Methylcoumarin via Cobalt(I)-Catalyzed Reduction of 2-Acetylphenyl 2-Chloroacetate or 2-Acetylphenyl 2,2-Dichloroacetate. *J. Electrochem. Soc.* **2007,** *154*, F231.

21. Raess, P. W.; Mubarak, M. S.; Ischay, M. A.; Foley, M. P.; Jennermann, T. B.; Raghavachari, K.; Peters, D. G., Catalytic reduction of 1-iodooctane by nickel(I) salen electrogenerated at carbon cathodes in dimethylformamide: Effects of added proton donors and a mechanism involving both metal- and ligand-centered one-electron reduction of nickel(II) salen. *J. Electroanal. Chem.* **2007,** *603*, 124-134.
22. Mubarak, M. S.; Jennermann, T. B.; Ischay, M. A.; Peters, D. G., Catalytic Reduction of Phenyl-Conjugated Acetylenic Halides by Nickel(I) Salen: Cyclization versus Coupling. *Eur. J. Org. Chem.* **2007,** *2007* , 5346-5352.
23. Miranda, J. A.; Wade, C. J.; Little, R. D., Indirect Electroreductive Cyclization and Electrohydrocyclization Using Catalytic Reduced Nickel(II) Salen. *J. Org. Chem.* **2005,** *70*, 8017-8026.
24. Fokin, I.; Kuessner, K.-T.; Siewert, I., Electroreduction of Carbonyl Compounds Catalyzed by a Manganese Complex. *ACS Catal.* **2022,** *12*, 8632-8640.
25. Derosa, J.; Garrido-Barros, P.; Peters, J. C., Electrocatalytic Reduction of C–C π-Bonds via a Cobaltocene-Derived Concerted Proton–Electron Transfer Mediator: Fumarate Hydrogenation as a Model Study. *J. Am. Chem. Soc.* **2021,** *143*, 9303-9307.
26. Schendzielorz, F.; Finger, M.; Abbenseth, J.; Würtele, C.; Krewald, V.; Schneider, S., Metal-Ligand Cooperative Synthesis of Benzonitrile by Electrochemical Reduction and Photolytic Splitting of Dinitrogen. *Angew. Chem. Int. Ed.* **2019,** *58*, 830-834.
27. van der Meer, M.; Rechkemmer, Y.; Peremykin, I.; Hohloch, S.; van Slageren, J.; Sarkar, B., (Electro)catalytic C–C bond formation reaction with a redox-active cobalt complex. *Chem. Commun.* **2014,** *50*, 11104-11106.
28. Wuttig, A.; Derrick, J. S.; Loipersberger, M.; Snider, A.; Head-Gordon, M.; Chang, C. J.; Toste, F. D., Controlled Single-Electron Transfer via Metal–Ligand Cooperativity Drives Divergent Nickel-Electrocatalyzed Radical Pathways. *J. Am. Chem. Soc.* **2021,** *143*, 6990-7001.
29. Gnaim, S.; Bauer, A.; Zhang, H.-J.; Chen, L.; Gannett, C.; Malapit, C. A.; Hill, D. E.; Vogt, D.; Tang, T.; Daley, R. A.; Hao, W.; Zeng, R.; Quertenmont, M.; Beck, W. D.; Kandahari, E.; Vantourout, J. C.; Echeverria, P.-G.; Abruna, H. D.; Blackmond, D. G.; Minteer, S. D.; Reisman, S. E.; Sigman, M. S.; Baran, P. S., Cobalt-electrocatalytic HAT for functionalization of unsaturated C–C bonds. *Nature* **2022,** *605*, 687-695. DOI: 10.1038/s41586-022-04595-3
30. Lee, M.-Y.; Kahl, C.; Kaeffer, N.; Leitner, W., Electrocatalytic Semihydrogenation of Alkynes with [Ni(bpy)3]2+. *JACS Au* **2022,** *2*, 573-578. DOI: 10.1021/jacsau.1c00574
31. Durin, G.; Lee, M.-Y.; Pogany, M. A.; Weyhermüller, T.; Kaeffer, N.; Leitner, W., Hydride-Free Hydrogenation: Unraveling the Mechanism of Electrocatalytic Alkyne Semihydrogenation by Nickel–Bipyridine Complexes. *J. Am. Chem. Soc.* **2023**, *145*, 17103-17111.
32. Anferov, S. W.; Filatov, A. S.; Anderson, J. S., Cobalt-Catalyzed Hydrogenation Reactions Enabled by Ligand-Based Storage of Dihydrogen. *ACS Catal.* **2022,** *12*, 9933-9943.
33. Käß, M.; Friedrich, A.; Drees, M.; Schneider, S. Ruthenium Complexes with Cooperative PNP Ligands: Bifunctional Catalysts for the Dehydrogenation of Ammonia–Borane. *Angew. Chem., Int. Ed.* **2009**, *48*, 905– 907, DOI: 10.1002/anie.200805108
34. Khaskin, E.; Iron, M. A.; Shimon, L. J. W.; Zhang, J.; Milstein, D. N– H activation of amines and ammonia by Ru via metal– ligand cooperation. *J. Am. Chem. Soc.* **2010**, *132*, 8542, DOI: 10.1021/ja103130u
35. Feller, M.; Diskin-Posner, Y.; Shimon, L. J. W.; Ben-Ari, E.; Milstein, D. N–H Activation by Rh (I) via Metal–Ligand Cooperation. *Organometallics* **2012**, *31*, 4083, DOI: 10.1021/om300248r
36. He, L. P.; Chen, T.; Gong, D.; Lai, Z.; Huang, K. W. Enhanced reactivities toward amines by introducing an imine arm to the pincer ligand: direct coupling of two amines to form an imine without oxidant. *Organometallics* **2012**, *31*, 5208, DOI: 10.1021/om300422v
37. Rodríguez-Lugo, R. E.; Trincado, M.; Vogt, M.; Tewes, F.; Santiso-Quinones, G.; Grützmacher, H. A homogeneous transition metal complex for clean hydrogen production from methanol–water mixtures. *Nat. Chem.* **2013**, *5*, 342– 347, DOI: 10.1038/nchem.1595
38. Myers, T. W.; Berben, L. A. Aluminum–ligand cooperative N–H bond activation and an example of dehydrogenative coupling. *J. Am. Chem. Soc.* **2013**, *135*, 9988– 9990, DOI: 10.1021/ja4032874
39. Xu, R.; Chakraborty, S.; Bellows, S. M.; Yuan, H.; Cundari, T. R.; Jones, W. D. Iron-Catalyzed Homogeneous Hydrogenation of Alkenes under Mild Conditions by a Stepwise, Bifunctional Mechanism. *ACS Catal.* **2016**, *6*, 2127– 2135, DOI: 10.1021/acscatal.5b02674

40. Sherbow, T. J.; Fettinger, J. C.; Berben, L. A. Control of Ligand pKa Values Tunes the Electrocatalytic Dihydrogen Evolution Mechanism in a Redox-Active Aluminum(III) Complex. *Inorg. Chem.* **2017,** *56*, 8651– 8660, DOI: 10.1021/acs.inorgchem.7b00230
41. Rajabimoghadam, K.; Darwish, Y.; Bashir, Y.; Pirman, D.; Eichelberger, S.; Sieler, M. A.; Swart, M.; Garcia-Bosch, I. Catalytic aerobic oxidation of alcohols by copper complexes bearing redox-active ligands with tunable H-bonding groups. *J. Am. Chem. Soc.* **2018**, *140*, 16625– 16634, DOI: 10.1021/jacs.8b08748
42. Sinha, S.; Das, S.; Mondal, R.; Mandal, S.; Paul, N. D. Cobalt complexes of redox noninnocent azo-aromatic pincers. Isolation, characterization, and application as catalysts for the synthesis of quinazolin-4 (3 H)-ones. *Dalton Trans.* **2020**, *49*, 8448– 8459, DOI: 10.1039/D0DT00394H
43. Thompson, E. J.; Berben, L. A. Electrocatalytic Hydrogen Production by an Aluminum (III) Complex: Ligand-Based Proton and Electron Transfer. *Angew. Chem., Int. Ed.* **2015**, *54*, 11642– 11646, DOI: 10.1002/anie.201503935
44. Margulieux, G. W.; Bezdek, M. J.; Turner, Z. R.; Chirik, P. J. Ammonia Activation, H2 Evolution and Nitride Formation from a Molybdenum Complex with a Chemically and Redox Noninnocent Ligand. *J. Am. Chem. Soc.* **2017**, *139*, 6110– 6113, DOI: 10.1021/jacs.7b03070
45. Dauth, A.; Gellrich, U.; Diskin-Posner, Y.; Ben-David, Y.; Milstein, D. The ferraquinone–ferrahydroquinone couple: combining quinonic and metal-based reactivity. *J. Am. Chem. Soc.* **2017**, *139*, 2799– 2807, DOI: 10.1021/jacs.6b13050
46. Rosenkoetter, K. E.; Wojnar, M. K.; Charette, B. J.; Ziller, J. W.; Heyduk, A. F. Hydrogen-atom noninnocence of a tridentate [SNS] pincer ligand. *Inorg. Chem.* **2018**, *57*, 9728– 9737, DOI: 10.1021/acs.inorgchem.8b00618
47. Ward, M. B.; Scheitler, A.; Yu, M.; Senft, L.; Zillmann, A. S.; Gorden, J. D.; Schwartz, D. D.; Ivanović-Burmazović, D. D.; Goldsmith, C. R. Superoxide dismutase activity enabled by a redox-active ligand rather than metal. *Nat. Chem.* **2018**, *10*, 1207– 1212, DOI: 10.1038/s41557-018-0137-1
48. Drummond, M. J.; Ford, C. L.; Gray, D. L.; Popescu, C. V.; Fout, A. R. Radical Rebound Hydroxylation Versus H-Atom Transfer in Non-Heme Iron(III)-Hydroxo Complexes: Reactivity and Structural Differentiation. *J. Am. Chem. Soc.* **2019**, *141*, 6639– 6650, DOI: 10.1021/jacs.9b01516
49. Purse, B. W.; Tran, L.-H.; Piera, J.; Åkermark, B.; Bäckvall, J.-E. Bäckvall, Synthesis of New Hybrid Hydroquinone/Cobalt Schiff Base Catalysts: Efficient Electron-Transfer Mediators in Aerobic Oxidation. *Chem. – Eur. J.* **2008**, *14*, 7500– 7503, DOI: 10.1002/chem.200800657
50. Myers, T. W.; Berben, L. A. Aluminium–ligand cooperation promotes selective dehydrogenation of formic acid to H2 and CO2. *Chem. Sci.* **2014**, *5*, 2771– 2777, DOI: 10.1039/C4SC01035C
51. Henthorn, J. T.; Lin, S.; Agapie, T. Combination of Redox-Active Ligand and Lewis Acid for Dioxygen Reduction with π-Bound Molybdenum– Quinonoid Complexes. *J. Am. Chem. Soc.* **2015**, *137*, 1458– 1464, DOI: 10.1021/ja5100405
52. Lagaditis, P. O.; Schluschaß, B.; Demeshko, S.; Würtele, C.; Schneider, S. Square-Planar Cobalt (III) Pincer Complex. *Inorg. Chem.* **2016**, *55*, 4529– 4536, DOI: 10.1021/acs.inorgchem.6b00369
53. Schneck, F.; Finger, M.; Tromp, M.; Schneider, S. Chemical Non-Innocence of an Aliphatic PNP Pincer Ligand. *Chem. – Eur. J.* **2017**, *23*, 33– 37, DOI: 10.1002/chem.201604407
54. Lindley, B. M.; Bruch, Q. J.; White, P. S.; Hasanayn, F.; Miller, A. J. M. Ammonia Synthesis from a Pincer Ruthenium Nitride via Metal–Ligand Cooperative Proton-Coupled Electron Transfer. *J. Am. Chem. Soc.* **2017**, *139*, 5305– 5308, DOI: 10.1021/jacs.7b01323
55. Pramanick, R.; Bhattacharjee, R.; Sengupta, D.; Datta, A.; Goswami, S. An azoaromatic ligand as four electron four proton reservoir: catalytic dehydrogenation of alcohols by its zinc (II) complex. *Inorg. Chem.* **2018**, *57*, 6816– 6824, DOI: 10.1021/acs.inorgchem.8b00034
56. Jain, R.; Mamun, A. A.; Buchanan, R. M.; Kozlowski, P. M.; Grapperhaus, C. A. Ligand-assisted metal-centered electrocatalytic hydrogen evolution upon reduction of a bis (thiosemicarbazonato) Ni (II) complex. *Inorg. Chem.* **2018**, *57*, 13486– 13493, DOI: 10.1021/acs.inorgchem.8b02110
57. Sherbow, T. J.; Thompson, E. J.; Arnold, A.; Sayler, R. I.; Britt, R. D.; Berben, L. A. Electrochemical Reduction of N2 to NH3 at Low Potential by a Molecular Aluminum Complex. *Chem. – Eur. J* **2019**, *25*, 454– 458, DOI: 10.1002/chem.201804454
58. McNeece, A. J.; Jesse, K. A.; Filatov, A. S.; Schneider, J. E.; Anderson, J. S., Catalytic hydrogenation enabled by ligand-based storage of hydrogen. *Chem. Comm.* **2021,** *57*, 3869-3872.

59. McNeece, A. J.; Jesse, K. A.; Xie, J.; Filatov, A. S.; Anderson, J. S., Generation and Oxidative Reactivity of a Ni(II) Superoxo Complex via Ligand-Based Redox Non-Innocence. *J. Am. Chem. Soc.* **2020,** *142*, 10824-10832.
60. Beyene, B. B.; Hung, C.-H., Recent progress on metalloporphyrin-based hydrogen evolution catalysis. *Coord. Chem. Rev.* **2020,** *410*, 213234.
61. Canaguier, S.; Artero, V.; Fontecave, M., Modelling NiFe hydrogenases: nickel-based electrocatalysts for hydrogen production. *Dalton Trans.* **2008**, 315-325.
62. Dressel, J.M.; Cook, E.N.; Hooe, S.L.; Moreno, J. J.; Dickie, D.A.; Machan, C.W., Electrocatalytic hydrogen evolution reaction by a Ni(N2O2) complex based on 2,2'-bipyridine. *Inorg. Chem. Front.* **2023,** *10*, 972-978.
63. Fang, M.; Engelhard, M. H.; Zhu, Z.; Helm, M. L.; Roberts, J.A.S., Electrodeposition from acidic solutions of Nickel bis(benzenedithiolate) produces a hydrogen evolving Ni-S film on glassy carbon. *ACS Catal.* **2014,** *4*, 90-98.
64. Han, Z.; Shen, L.; Brennessel, W. W.; Holland, P. L.; Eisenberg, R., Nickel Pyridinethiolate Complexes as Catalysts for the Light-Driven Production of Hydrogen from Aqueous Solutions in Noble-Metal-Free Systems. *J. Am. Chem. Soc.* **2013,** *135*, 14659-14669.
65. Helm, M. L.; Stewart, M. P.; Bullock, R. M.; DuBois, M. R.; DuBois, D. L., A Synthetic Nickel Electrocatalyst with a Turnover Frequency Above 100,000 s-1 for H2 Production. *Science* **2011,** *333*, 863-866.
66. Jacques, P.; Artero, V.; Pecaut, J.; Fontecave, M., Cobalt and nickel diimine-dioxime complexes as molecular electrocatalysts for hydrogen evolution with low overvoltages. *Proc. Natl. Acad. Sci.* **2009,** *106*, 20627-20632.
67. Khrizanforova, V. V.; Fayzullin, R. R.; Musina, E. I.; Karasik, A. A.; Budnikova, Y. H., Electrochemical and catalytic properties of nickel(II) complexes with bis(imino)acenaphthene and diazadiphosphacyclooctane ligands. *Mendeleev Commun.* **2020,** *30*, 302-304.
68. Martin, D. J.; McCarthy, B. D.; Donley, C. L.; Dempsey, J. L., Electrochemical hydrogenation of a homogeneous nickel complex to form a surface adsorbed hydrogen-evolving species. *Chem. Comm.* **2015,** *51*, 5290-5293.
69. Pantani, O.; Anxolabéhère-Mallart, E.; Aukauloo, A.; Millet, P., Electroactivity of cobalt and nickel glyoximes with regard to the electro-reduction of protons into molecular hydrogen in acidic media. *Electrochem. Commun.* **2007,** *9*, 54-58.
70. Rao, H.; Yu, W.-Q.; Zheng, H.-Q.; Bonin, J.; Fan, Y.-T.; Hou, H.-W., Highly efficient photocatalytic hydrogen evolution from nickel quinolinethiolate complexes under visible light irradiation. *J. Power Sources* **2016,** *324*, 253-260.
71. Shotonwa, I. O.; Ejeromedoghene, O.; Adesoji, A. O.; Adewuyi, S., Electrochemistry and electrocatalysis of H2 generation using hexacoordinated nickel—based complexes. *Catal. Comm.* **2023,** *179*, 106680.
72. Rountree, E. S.; McCarthy, B. D.; Eisenhart, T. T.; Dempsey, J. L., Evaluation of Homogeneous Electrocatalysts by Cyclic Voltammetry. Inorg. Chem. 2014, 53, 9983-10002.
73. Newcomb, M., Radical Kinetics and Clocks. In *Encyclopedia of Radicals in Chemistry, Biology and Materials*, John Wiley & Sons, 2012.
74. Stoll, S.; Schweiger, A. EasySpin, a comprehensive software package for spectral simulation and analysis in EPR. *J. Magn. Reson*. **2006**, *178*, 42−55.
75. Krause, L.; Herbst-Irmer, R.; Sheldrick, G. M.; Stalke, D. Comparison of Silver and Molybdenum Microfocus X-Ray Sources for Single-Crystal Structure Determination. J. Appl. Crystallogr. **2015**, *48*, 3–10.
76. Sheldrick, G. M. SHELXT - Integrated Space-Group and Crystal-Structure Determination. Acta Crystallogr., Sect. A: Found. Adv. **2015**, *71*, 3– 8.
77. Dolomanov, O. V.; Bourhis, L. J.; Gildea, R. J.; Howard, J. A. K.; Puschmann, H. OLEX2: A Complete Structure Solution, Refinement and Analysis Program. J. Appl. Crystallogr. **2009**, *42*, 339– 341.
78. Sheldrick, G. M. Crystal Structure Refinement with SHELXL. Acta Crystallogr., Sect. C: Struct. Chem. **2015**, *71*, 3– 8.
79. Neese, F. The ORCA program system. *WIREs Comput. Mol. Sci.* **2012**, *2*, 73-78.

Chapter III: Markovnikov-Selective Electrocatalytic Hydroalkylation Enabled by Metal-Ligand Cooperative Storage of H-Atom Equivalents

This chapter has been adapted from the following: Czaikowski, M.E.; Boyn, J.N.; Anderson, J.S. *ACS Catal.*, **2025**, *15*, 10694-10701.

Introduction

Olefins are important functional groups that are present in various natural products, drug molecules, and synthetic intermediates. Multiple synthetic methods exist for olefin installation, including elimination reactions, reduction of alkynes, and condensation reactions.[1] The Wittig reaction is a particularly significant method for olefin synthesis in modern organic chemistry, particularly as a route to 1,1-disubstituted olefins from ketone synthons.[2] However, functional group tolerance can be limiting due to the reactive phosphonium ylide reagent required for this reaction (**Figure 1A**). Furthermore, while Heck and related cross coupling methods typically provide 1,2-disubsituted regioisomers, there has been significant progress in discovering catalysts which are selective for 1,1-disubstituted products, frequently with benzyl halide coupling partners.[3,4] Still,

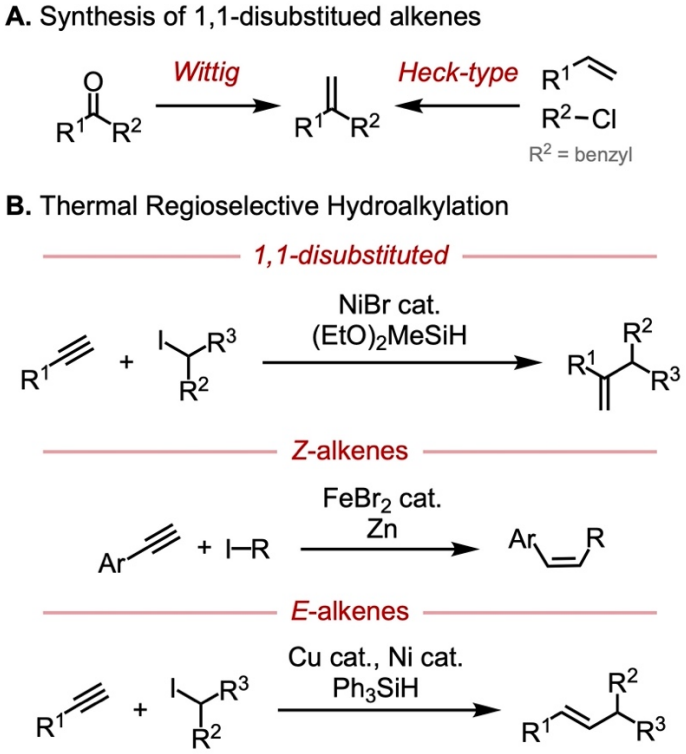

Figure 1. A. Overview of strategies for the synthesis of 1,1-disubstitued alkenes by classic thermal reactions using non-alkyne synthons, and **B.** thermal hydroalkylation targeting (*Z*), (E), and 1,1-disubstituted alkenes

achieving selectivity for disubstituted terminal olefins over internal *E*- or *Z*-alkene products remains challenging.

Intermolecular hydrofunctionalization of alkynes with electrophilic alkyl reagents has emerged as an attractive approach to access *Z*-, *E*-, and 1,1-disubstituted alkenes (**Figure 1B**).[5] Under thermal conditions, transition metal catalysts employed with alkyl electrophiles and a chemical reductant can produce the desired alkene regioisomer from accessible and inexpensive alkyne precursors.[6-14] Selectivity for the thermodynamically less favorable alkene product can be realized by leveraging the steric environment enforced by particular ligands, often via careful control of M–H insertion into the alkyne. However, limitations with some substrates such as those containing carbonyls or protic moieties remain. Expanding on the development of these thermal transformations, we were interested in harnessing electricity to avoid the use of chemical redox agents, enable milder reaction conditions, and potentially expand functional group compatibility. While electrosynthetic methods are being developed for many reductive transformations including alkene and alkyne hydrofunctionalization,[15-24] electrochemical hydroalkylation of alkynes remains underexplored.

The utility of ligand-based storage of protons and electrons to mediate the semihydrogenation of terminal alkynes has been previously demonstrated under electrochemical conditions (See **Chapter II**).[25] Mechanistic investigations of this system support the agency of ligand-stored reducing equivalents rather than a metal hydride intermediate. We hypothesized that this DHP (DHP = 2,5-bis((2-*t*-butylhydrazono)(*p*-tolyl)methyl)-pyrrole) ligand scaffold could also be applied in other reductive processes that typically rely on chemical hydride sources, namely hydroalkylation. In particular, we reasoned that the addition of alkyl electrophiles could intercept partially reduced or activated alkyne intermediates prior to semihydrogenation. Careful tuning of

electrochemical conditions switches the reactivity of the previously discussed (DHP)Ni complex from alkyne semihydrogenation to alkyne hydrofunctionalization with the addition of an acid and alkyl halide. This catalytic system exhibits good selectivity for 1,1-disubstituted alkenes and functional group tolerance for sensitive carbonyls and amines. This method represents an electrosynthetic alkyne hydroalkylation with unusual selectivity catalyzed by a homogeneous transition metal catalyst, as well as a unique method for non-Wittig olefin synthesis.

Results and Discussion

Reaction Optimization

We have previously reported that DHP ligands exhibit both redox activity and protonation sites (**Figure 2**).[26] This uniquely flexible ancillary ligand also enables highly selective and efficient electrochemical alkyne semihydrogenation.[25] A key intermediate in the catalytic cycle was a transient Ni alkyne adduct, and we postulated that this intermediate could be intercepted by an in-situ generated alkyl radical for hydroalkylation reactivity. We therefore explored the addition of alkyl electrophiles in the presence of acid for reductive electrolyses. Phenylacetylene and octyl halide/pseudohalide reagents were used as trial coupling partners. Initial screens under the previously employed semihydrogenation conditions with alkyl iodides immediately resulted in the formation of hydroalkylated products. Analyzing the product mixtures further by NMR revealed regioselectivity for 1,1-disubstituted terminal olefins (Appendix III: **Figure S4**). Acid screening was then performed to improve the ratio of hydroalkylated products to semi-hydrogenated byproducts (Appendix III: **Table S1**). In contrast to benzoic acid, which was optimal for semihydrogenation reactivity, substitution with more weakly acidic phenol, along with a reduction

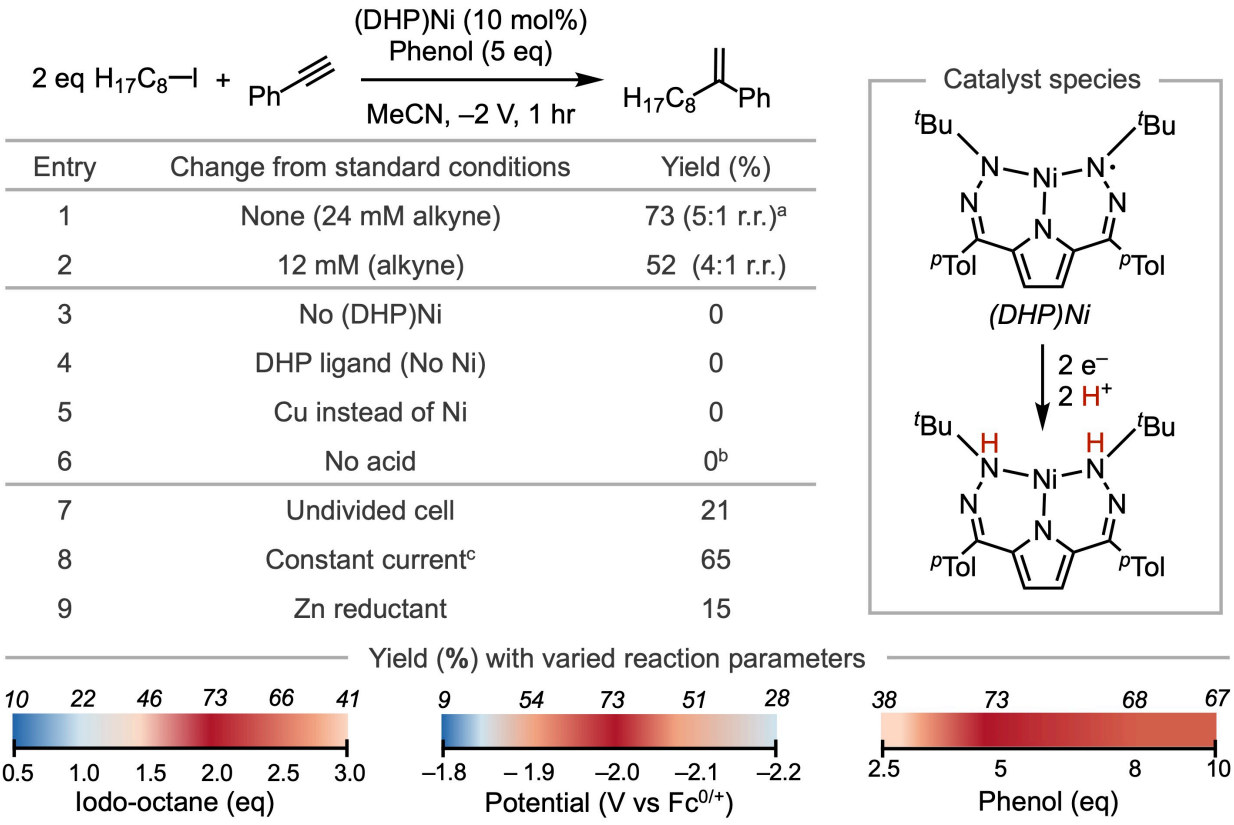

Entry	Change from standard conditions	Yield (%)
1	None (24 mM alkyne)	73 (5:1 r.r.)[a]
2	12 mM (alkyne)	52 (4:1 r.r.)
3	No (DHP)Ni	0
4	DHP ligand (No Ni)	0
5	Cu instead of Ni	0
6	No acid	0[b]
7	Undivided cell	21
8	Constant current[c]	65
9	Zn reductant	15

Figure 2. Optimization of terminal alkyne hydroalkylation reaction. Isolated yields for entries 1-2. Yields determined by GC-MS for entries 3-8. Standard conditions: 0.1 M $TBAPF_6$ electrolyte, 24 mM alkyne, divided cell, RVC(–)/Zn(+), V vs $Fc^{0/+}$. [a]Other side products: 36% $C_{16}H_{34}$, 5% styrene semi-hydrogenation product (yields determined by GC-MS). [b]Other products: $C_{16}H_{34}$ 42%, coupled product dec-1-ynylbenzene putatively formed from addition of the alkyl radical followed by elimination. This product is not observed under acidic conditions. [c]5 mA constant current for 1 hr, 18 C passed.

in added acid equivalents, was found to disfavor semihydrogenation and provide higher yields of the hydroalkylated product.

A variety of electrophiles were also tested under reductive electrochemical conditions, with a particular focus on their ability to generate alkyl radicals (Appendix III: **Table S2**). Selecting a species with a reduction potential that aligned with the catalytic onset for Ni in the presence of acid and alkyne substrate proved to be crucial for accessing the desired hydroalkylated product in good yield. Radical-generating species with comparatively more positive reduction potentials such

as redox-active esters (E_{red} = –1.3 V vs $Fc^{0/+}$) performed poorly, putatively due to kinetically competitive reduction and protonation of the reagent. In contrast, alkyl bromides have a more negative reduction potential compared to (DHP)Ni and were also not suitable coupling partners. Alkyl iodides have reduction potentials close to that of the catalytic onset and are stable in the presence of phenol, and thus these substrates prove optimal. An excess of iodo-octane was found to improve the yield of 1,1-disubsituted alkene product due to competitive background homo-coupling of octyl radical species (**Figure 2**, bottom).

During the reaction optimization it was discovered that increasing the concentration for all reaction components improved the yield and slightly improved the regioselectivity for the 1,1-disubstituted product (**Figure 2**, Entries 1 and 2). We hypothesize that increasing the concentration of the homogeneous catalyst at the electrode surface along with increasing the rate of encounter between electro-generated Ni-alkyne species and organic radicals underpins this overall improvement in product yield.

Controls support that (DHP)Ni complexes are requisite catalysts for this transformation. The DHP ligand alone is not catalytically active (**Figure 2**, Entry 4). A different DHP metal complex is also not suitable for catalysis, with (DHP)Cu failing to yield any of the desired product (**Figure 2**, Entry 5). The reaction proceeds in slightly lower yield under constant current conditions rather than constant potential, and the yield of hydroalkylated product is significantly reduced in an undivided electrochemical cell (**Figure 2**, Entries 7 and 8). Efforts to replicate reactivity with a Zn reductant instead of applied potential provided significantly lower yields of the hydroalkylated product (**Figure 2**, Entry 9). All of these trials support the unique viability of electrocatalysis with (DHP)Ni for this selective hydroalkylation, and thus we turned to examine the scope of this interesting transformation.

Hydroalkylation Substrate Scope

With optimized conditions in hand, the reaction scope was tested with several alkyne substrates as well as both primary and secondary alkyl iodides (**Figure 3**). Phenylacetylene derivatives as well as long-chain terminal alkynes were well-tolerated in the system. Alkynyl ethers are also viable substrates with moderate yield (**Figure 3**, **11**). Piperidine moieties are also compatible with the system (**Figure 3**, **5**). Additionally, aryl chlorides and trifluoromethyl substitutions were well-tolerated (**Figure 3**, **3** and **4**). Primary alkyl iodides generally give higher yields than secondary alkyl iodides (**Figure 3**, **3** and **9**), and no reactivity was observed with *t*Bu-iodide as a test for tertiary alkyl iodide compatibility. The less sterically hindered attack of a primary alkyl radical species on a putative Ni-alkyne intermediate likely explains this trend in

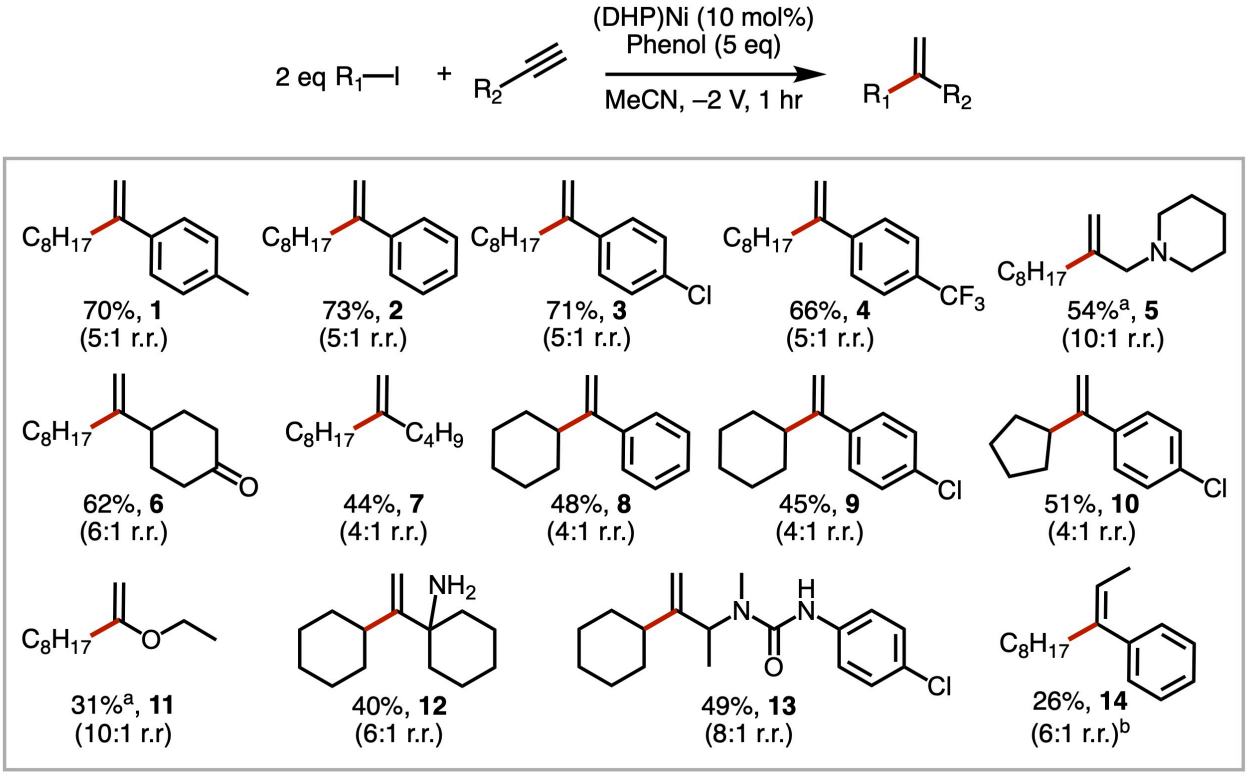

Figure 3. Yields and regioisomeric ratios for 1,1-disubstituted products. Reported values are isolated yields as an average of triplicate runs unless otherwise noted. Standard conditions: 0.1 M $TBAPF_6$ electrolyte, 24 mM alkyne, divided cell, RVC(–)/Zn(+), V vs $Fc^{0/+}$. [a] Yield determined by GC-MS using mesitylene as an internal standard and is an average of triplicate runs. [b] 100% (Z)-isomer for major product, 6:1 r.r. for the site of alkyl substitution.

reactivity despite the comparative stability of secondary and tertiary radicals. Supporting this hypothesis, improved yields are observed when slightly smaller cyclopentyl iodide is used instead of cyclohexyl iodide.

Steric restrictions are also present for the alkyne substrate scope, with the internal alkyne 1-phenyl-1-propyne furnishing the hydroalkylated product **14** in lower yield. However, we note that the regioisomeric selectivity is comparable to terminal alkyne substrates, and the major product is formed exclusively as the (*Z*)-isomer (**Figure S27**).

In contrast to Wittig conditions, ketones and amines are well-tolerated in the system (**Figure 3**, **6** and **12**). The herbicide compound Buturon, which contains a phenylurea moiety, can be successfully alkylated to form the corresponding branched alkene product in good yield (**Figure 3**, **13**). However, we do note that alcohol substrates are not well-tolerated under these electrolysis conditions (Appendix III: **Figure S1**). This demonstrates a useful application for catalytic hydroalkylation in the targeted synthesis of 1,1-disubstituted alkenes without requiring the protection or late installation of sensitive functional groups.

Catalytic Mechanism

We were interested in investigating the mechanism of this hydroalkylation platform by performing both experimental and computational studies to understand the observed regioselectivity. Cyclic voltammogram data shows a characteristic catalytic wave when (DHP)Ni is in the presence of both phenol and an alkyne substrate, likely due to semihydrogenation reactivity (**Figure 4A**, left, purple trace). In the absence of phenol, no catalytic onset is observed. The addition of iodo-octane (I-oct in **Figure 4A**) does not change the voltage position or wave shape of the catalytic feature, although an increased current response at more cathodic potential is

observed due to the reduction of iodo-octane at the electrode (**Figure 4A**, left, blue trace). With only (DHP)Ni and iodo-octane present, a broad current increase is observed from –1.4 V to –1.8 V along with an irreversible feature at –1.85 V, indicating some reactivity between (DHP)Ni and iodo-octane (**Figure 4A**, left, green trace). However, once acid and alkyne substrate are added to solution, the electrochemical signatures associated with (DHP)Ni and iodo-octane reactivity are diminished or completely obscured by new features (**Figure 4A**, left, blue trace).

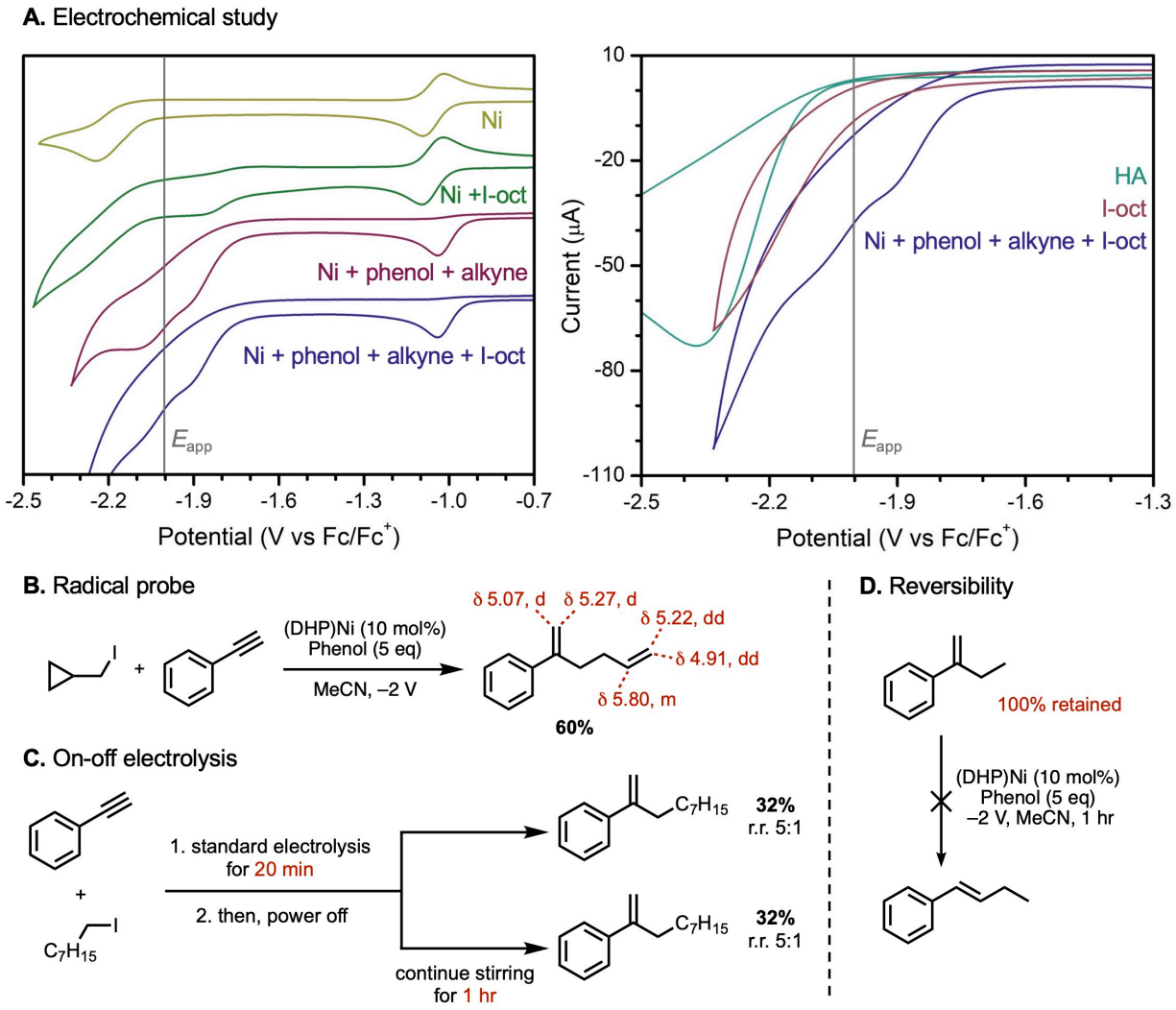

Figure 4. Mechanistic studies: **A.** electrochemical studies tracking changes in CV traces with the catalyst and reaction components (left) as well as the reduction potentials of phenol and I-octane (I-oct) in comparison to the applied potential during bulk electrolysis (right), Alkyne (1 eq), I-oct (2 eq), phenol (5 eq), (DHP)Ni (0.1 eq). **B.** cyclopropyl methyl iodide radical probe substrate, **C.** on-off electrolysis experiment, and **D.** reversibility experiments subjecting the 1,1-disubstituted alkene product to standard electrolysis conditions.

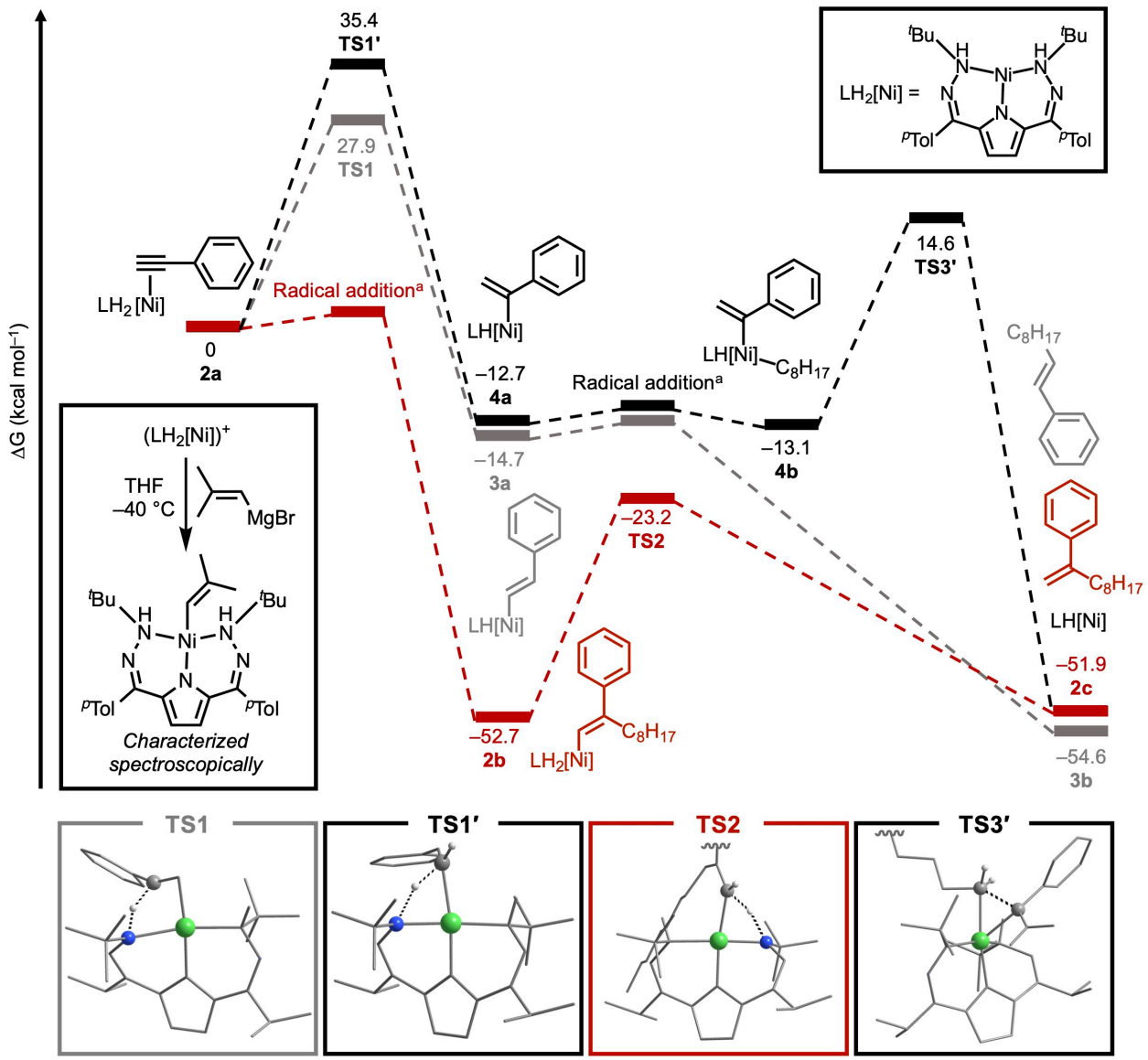

Figure 5. DFT calculated reaction pathway showing different proposed mechanisms for 1,1-disubsituted or E-alkene products. **Red:** initial *gem*-selective radical addition, **Black:** initial *gem*-selective H-transfer, and **Gray:** initial *E*-selective H-transfer pathways shown. All energies are relative to 0 kcal/mol. TS optimized structures are simplified for clarity. Full optimized TS structures are available in the Supporting Information. The experimental synthesis of an isolated Ni-alkenyl complex to utilize as a model for intermediate **2b** is shown in the inset. [a]Outer sphere radical addition was determined to be barrierless in continuum solvent conditions (DFT Calculations in Appendix III). DFT computed energies (kcal/mol) were carried out with the M06L functional, def2-TZVPP basis set for Ni, and def2-TZVP for all other atoms.

Comparison of the reduction potentials of iodo-octane and phenol individually show that the applied potential during electrolysis (E_{app}) does not meet the threshold for direct phenol reduction, but it is reducing enough to generate alkyl radical species from iodo-octane in solution (**Figure 4A**, right). Indeed, chemical tests support the presence of alkyl radical species. When cyclopropylmethyl iodide is used with phenylacetylene, the ring-opened diene product is observed (**Figure 4B**, S24). On-off electrolyses show no background reactivity that would suggest a radical chain process to generate the hydroalkylated product (**Figure 4C**). This is consistent with applied potential-driven turnover. Subjecting a 1,1-disubstituted alkene substrate to electrolysis conditions shows complete retention of the starting material regioisomer, consistent with irreversible C–C bond formation in the reaction mechanism (**Figure 4D**).

Density functional theory (DFT) calculations were used to test proposed intermediates and transition states invoked in both 1,1-disubstituted product formation (**Figure 5**, Red and Black) and *E*-alkene formation (**Figure 5**, Gray). Beginning from a Ni-alkyne adduct (**2a**), the order of ligand-based H-transfer and outer sphere alkyl radical addition determines the geometry of the resulting Ni-alkenyl intermediates (**2b**, **3a**, and **4a**)) and thus the resultant product isomer. Consistent with our observed selectivity, the **TS1** and **TS1′** barriers for H-transfer to the terminal and internal alkyne position form **3a** and **4a** are greater than the outer sphere alkyl radical addition to form **2b**, which is effectively barrierless (Appendix III: **Figure S51**). 1,2-addition across the alkyne bond to form an end-on bound Ni-alkenyl intermediate **3a** is thermodynamically favorable, as previously established in semihydrogenation reactivity,[25] but the transition state for this process is still quite high. The essentially barrierless addition of the alkyl radical species along with the thermodynamic stability of the resulting intermediate **2b** dictates selectivity for the 1,1-

disubstituted regioisomer despite the *E*-alkene product **3b** being more thermodynamically favorable.

A 1,1-disubsituted Ni-alkenyl intermediate, similar to the proposed intermediate **2b**, was synthesized to determine the feasibility of such a species during catalysis (Error! Reference source not found., inset). The (DHP·H_2)Ni[OTf] complex, which can be synthesized from direct metalation,[26] was reacted with isobutenyl Grignard at –40 °C, and the direct formation of a Ni-isobutenyl adduct was observed by ^{1}H and ^{13}C NMR, including the diagnostic resonance of the alkenyl C–H (**Figures S30**-**S34**). This Ni-isobutenyl species was quasi-stable at room temperature and in the presence of excess phenol (**Figure S35**), but ill-defined decomposition products were observed with the addition of exogenous reductant in the form of Na amalgam. The relative stability of this Ni-isobutenyl species is consistent with the high computed barrier to HAT and loss of alkene product. However, this stability is also apparently inconsistent with the rates of product formation observed in catalysis. This may likely suggest that additional reduction may occur before alkene release under electrolysis conditions, and we have proposed a similar mechanistic paradigm with this system in semihydrogenation electrocatalysis.[25] Alternatively, we also note that this isobutenyl substrate has a smaller steric profile than many of the substrates tested electrochemically. This smaller profile may make this intermediate more stable than catalytically competent ones. Indeed, we note that small alkyl-iodides (i.e. MeI) are not competent coupling partners, potentially supporting this hypothesis. Regardless, the isolation of a Ni-alkenyl species analogous to intermediate **2b** supports the feasibility of generating such a species in this reactivity.

Another possible mechanistic proposal involves alkyl radical capture at the open coordination site of the Ni catalyst without an alkyne substrate bound.[27] Reversible Ni-alkyl bond homolysis could function as a reservoir for alkyl radical species. The bond dissociation energy

(BDE) of 32 kcal/mol for a Ni–octyl adduct supports that radical capture and bond homolysis are energetically accessible under the reaction conditions (Appendix III: **Table S5**). Despite the possible role for (DHP)Ni as an off-cycle alkyl radical reservoir, the coordination of both an alkyne substrate and octyl radical fragment to give a five-coordinate Ni center (**Figure 5**, **4b**) is 42 kcal/mol uphill compared to intermediate **2b**. Furthermore, coordination of an alkyne substrate to a Ni-octyl intermediate is predicted to be highly unfavorable (Appendix III: **Figure S53**). This reinforces the proposed outer-sphere pathway for alkyl radical addition and contrasts with existing hydrofunctionalization mechanistic pathways which proceed through radical capture to a metal center followed by reductive elimination to furnish the 1,1-disubstituted alkene product.[7,8,10,12]

Conclusion

We have reported the discovery of an electrocatalytic terminal alkyne hydroalkylation platform employing a redox-active and proton-storing ligand coordinated to a Ni center. The reaction leverages ligand geometry and steric pressure to selectively generate 1,1-disubsituted alkene products over the more thermodynamically favorable *E*-alkenes. Notably, the reaction conditions tolerate ketone and amine functional groups which can be sensitive to Wittig olefination conditions. Mechanistic investigations confirm the presence of radical intermediates as well as steric factors which dictate the observed regioselectivity. Overall, this hydroalkylation system exemplifies the broad utility of electrocatalysts which leverage metal-ligand cooperativity. Additionally, simple modulation of reaction parameters enables adaptation of this flexible catalyst platform for multiple types of reductive transformations.

Experimental

General Considerations

Reagents were purchased from commercial suppliers and used directly, unless otherwise indicated. (DHP)Ni was synthesized according to the previously reported procedure.[28] Reactions were performed under an atmosphere of N_2 using Schlenk techniques or in a glovebox (MBraun UniLab Pro SP). Glassware was dried at 180 °C for at least 2 h and cooled under vacuum or N_2 before use. Solvents were dried using a solvent purification system (Pure Process Technology), passed over a column of activated alumina, and stored over 4 Å molecular sieves in an N_2 atmosphere. Deuterated solvents were stored over 4 Å molecular sieves. Tetrabutylammonium hexafluorophosphate was dried under vacuum at 100 °C for 8 h, and crystalline phenol was dried under vacuum at 22 °C. Preparative TLC was carried out using Merck silica gel 60 F_{254} glass plates.

^1H, ^{13}C, an ^{19}F NMR spectra were collected on a Bruker DRX 400 MHz or 600 MHz spectrometer. For ^1H spectra, chemical shifts are reported in parts per million units referenced to residual solvent resonances. ^{13}C NMR chemical shifts are reported in parts per million referenced to the carbon resonance of the solvent. GC/MS data was collected on an Agilent Tech HP-5 Å MS (electron ionization, 30 m x 0.25 mm x 0.25 mM column) with an Agilent 5975 Series MSD, Hewlett Packard 7683 Series injector and Agilent 6890 series GC instrument. High resolution Mass spectra were collected on an Agilent 6224 TOF-MS spectrometer. Electrochemical measurements were recorded using a BASi Epsilon potentiostat with software version 1.40.67NT.

Electrochemical experiments were carried out inside an N_2 atmosphere glovebox using an MeCN and 0.1 M $TBAPF_6$ electrolyte solution at 22 °C. Cyclic voltammetry was measured with

a 1 mM solution of (DHP)Ni using a glassy carbon working electrode, platinum wire counter electrode, and silver wire pseudoreference electrode. Cyclic voltammogram data were referenced to $Fc^{0/+}$ by adding ferrocene to the solution at the end of measurements. For taking cyclic voltammogram data, a one-compartment glass cell was filled with 4 mL of electrolyte solution. The glassy carbon working electrode was polished before each experiment using an alumina slurry (0.05 mM) on a microcloth pad followed by rinsing with deionized water and acetone. Reference and counter electrodes were rinsed with acetone. Cyclic voltammograms were recorded at a 100 mV/s scan rate, scanning reductively.

Bulk electrolyses were performed in an H-type glass cell (James Glass Inc.) with an ultra-fine glass frit separating anode and cathode chambers. A reticulated vitreous carbon (RVC) working electrode (ERG Duocel, 2 cm x 0.5 cm x 0.5 cm), Zn rod counter electrode (National Bureau of Standards, 3 cm x 0.5 cm diameter), and an $AgBF_4$/Ag non-aqueous reference electrode (BASi, 0.05 mm, 10 mM $AgBF_4$ in MeCN/0.1 M $TBAPF_6$) were used. The Zn rod and Ag wire electrodes were polished with P600 sandpaper and sonicated for 5 min in isopropyl alcohol before being rinsed with acetone. Freshly prepared RVC electrodes (dried in a 180°C oven) were used for each electrolysis. To each chamber of the H-cell was added 3.5 mL of electrolyte solution and a stir bar. Standard electrolysis conditions contain (DHP)Ni (4 mg, 2.3 mM), alkyne (23 mM), mesitylene internal standard (23 mM), alkyl iodide (46 mM), and phenol (37 mg, 114 mM) in $TBAPF_6$/MeCN electrolyte solution (0.1 M, 3.5 mL). Electrolyses were performed under potentiostatic conditions unless otherwise noted, and reaction aliquots were filtered through activated alumina to remove metal species and diluted with MeCN before analysis by GC/MS. To determine weighted isolated yields, the organic products were extracted with diethyl ether (three times), filtered, and separated by preparative TLC on silica gel.

Computational Methodology

Intermediates and transition states for the reaction coordinate were optimized in ORCA 5.0[29] using the M06L functional and def2-TZVPP basis set on Ni, def2-TZVP basis set on all other atoms. Acetonitrile solvation effects were modeled implicitly utilizing the PCM model. Frequency calculations were performed to confirm the structures are at local minima on the potential energy surface. Transition states were confirmed to have only one imaginary mode in frequency calculations. The calculated BDE for the Ni-octyl species was determined using free energies from frequency calculations with the M06L functional and def2-TZVPP basis set for Ni, def2-TZVP for all other atoms. A simplified ligand with *i*Pr groups in the place of the *p*-tol substituents were utilized to reduce the number of atoms per calculation. Constrained reaction coordinate scans for radical addition steps were performed over the forming C-C bond utilizing broken-symmetry, unrestricted KS-DFT at the PBE0-D3BJ/def2-SVP level of theory as implemented in Gaussian 16 Rev.A.03.[30] Acetonitrile solvation effects were modeled implicitly utilizing the SMD model.

Synthesis of (DHPH2)Ni-isobutene

To a solution of ($DHPH_2$)Ni[OTf] (4.2 mg, 6.4 mmol) in d_8-THF (0.5 mL) at –40 °C under N_2 was added 15 mL of isobutenylmagnesium bromide solution (0.5 M in THF) and stirred for 5 min (300 rpm). The solution was transferred to a J. Young NMR tube at ambient temperature, and the product was analyzed without further purification. ^{1}H NMR (600 MHz, d_8-THF, 23 °C): d = 7.68 (d, 4H, *J* = 8.0 Hz), 7.26 (d, 4H, *J* = 8.0 Hz), 6.35 (s, 2H, ^{pyrrole}C-*H*), 6.20 (s, 2H, N-*H*), 5.96 (s, 1H, C*H*=C(CH_3)$_2$), 2.42 (s, 6H), 1.70 (s, 6H, CH=C(CH_3)$_2$), 1.29 (s, 18H). ^{13}C{^{1}H} NMR (101

MHz, d_8-THF, 23 °C): d = 165.8, 140.4, 134.0, 129.5, 128.5, 121.5, 118.8, 63.8, 28.3, 23.2, 20.4.

$^{19}F\{^1H\}$ NMR (125 MHz, d_8-THF, 23 °C): d = –79.

References

1. Zweifel, G.S.; Nantz, M.H. Formation of Carbon-Carbon p-bonds. In *Modern Organic Synthesis: An Introduction*; W.H. Freeman and Company, 2007; pp 359-395.
2. Maercker, A. The Wittig Reaction. In *Organic Reactions*, 2011; pp 270-490. https://doi.org/10.1002/0471264180.or014.03
3. Matsubara, R.; Gutierrez, A. C.; Jamison, T. F., Nickel-Catalyzed Heck-Type Reactions of Benzyl Chlorides and Simple Olefins. *J. Am. Chem. Soc.* **2011,** *133*, 19020-19023.
4. Sabarre, A.; Love, J., Synthesis of 1,1-Disubstituted Olefins via Catalytic Alkyne Hydrothiolation/Kumada Cross-Coupling. *Organic Letters* **2008,** *10*, 3941-3944. https://doi.org/10.1021/ol8012843
5. Chen, J.; Wei, W.-T.; Li, Z.; Lu, Z., Metal-catalyzed Markovnikov-type selective hydrofunctionalization of terminal alkynes. *Chem. Soc. Rev.* **2024,** *53*, 7566-7589. https://doi.org/10.1039/D4CS00167B
6. Lu, X.-Y.; Liu, J.-H.; Lu, X.; Zhang, Z.-Q.; Gong, T.-J.; Xiao, B.; Fu, Y., 1,1-Disubstituted olefin synthesis via Ni-catalyzed Markovnikov hydroalkylation of alkynes with alkyl halides. *Chem. Commun.* **2016,** *52*, 5324-5327. https://doi.org/10.1039/C6CC00176A
7. Li, Y.; Liu, D.; Wan, L.; Zhang, J.-Y.; Lu, X.; Fu, Y., Ligand-Controlled Cobalt-Catalyzed Regiodivergent Alkyne Hydroalkylation. *J. Am. Chem. Soc.* **2022,** *144*, 13961-13972. https://doi.org/10.1021/jacs.2c06279
8. Pan, S.; Chen, F.; Zhang, Y.; Shao, L.; Chu, L., Nickel-Catalyzed Markovnikov-Selective Hydrodifluoromethylation of Alkynes Using BrCF2H. *Angew. Chem. Int. Ed.* **2023,** *62*, e202305426. https://doi.org/10.1002/anie.202305426
9. Zhao, X.; Zhu, S.; Qing, F.-L.; Chu, L., Reductive hydrobenzylation of terminal alkynes via photoredox and nickel dual catalysis. *Chem. Commun.* **2021,** *57*, 9414-9417. https://doi.org/10.1039/D1CC03668H
10. Zhang, Y.; Tanabe, Y.; Kuriyama, S.; Nishibayashi, Y., Photoredox- and Nickel-Catalyzed Hydroalkylation of Alkynes with 4-Alkyl-1,4-dihydropyridines: Ligand-Controlled Regioselectivity. *Chem. Eur. J.* **2022,** *28*, e202200727. https://doi.org/10.1002/chem.202200727
11. Yadav, J. S.; Reddy, B. V. S.; Reddy, P. M. K.; Gupta, M. K., Zn/[bmim]PF6-mediated Markovnikov allylation of unactivated terminal alkynes. *Tet. Lett.* **2005,** *46*, 8411-8413. https://doi.org/10.1002/chin.200611067
12. Till, N. A.; Smith, R. T.; MacMillan, D. W. C., Decarboxylative Hydroalkylation of Alkynes. *J. Am. Chem. Soc.* **2018,** *140*, 5701-5705. https://doi.org/10.1021/jacs.8b02834
13. Chen, J.; Ying, J.; Lu, Z., Cobalt-catalyzed branched selective hydroallylation of terminal alkynes. *Nature Commun.* **2022,** *13*, 4518. https://doi.org/10.1038/s41467-022-32291-3
14. V. Fiandanese, G. Marchese, F. Naso, L. Ronzini, Synthesis of 1,1-Disubstituted Ethenes by Means of Sequential Cross-Coupling Reactions**,** *Synthesis* **1987**, 1034–1036. https://doi.org/10.1055/S-1987-28164
15. Lu, L.; Siu, J. C.; Lai, Y.; Lin, S., An Electroreductive Approach to Radical Silylation via the Activation of Strong Si–Cl Bond. *J. Am. Chem. Soc.* **2020,** *142*, 21272-21278. https://doi.org/10.1021/jacs.0c10899
16. Biremond, T.; Jubault, P.; Poisson, T., Electrochemical Hydrosilylation of Alkynes. *ACS Org. & Inorg. Au* **2022,** *2*, 148-152. https://doi.org/10.1021/acsorginorgau.1c00035
17. Song, L.; Fu, N.; Ernst, B. G.; Lee, W. H.; Frederick, M. O.; DiStasio, R. A.; Lin, S., Dual electrocatalysis enables enantioselective hydrocyanation of conjugated alkenes. *Nat. Chem.* **2020**, *12*, 747–754. https://doi.org/10.1038/s41557-020-0469-5
18. Sun, X.; Zheng, K. Electrochemical halogen-atom transfer alkylation via α-aminoalkyl radical activation of alkyl iodides. *Nat Commun.* **2023**, *14*, 6825. https://doi.org/10.1038/s41467-023-42566-y
19. Li, P.; Kou, G.; Feng, T.; Wang, M.; Qiu, Y., Electrochemical NiH-Catalyzed C(sp3)−C(sp3) Coupling of Alkyl Halides and Alkyl Alkenes. *Angew. Chem. Int. Ed.* **2023,** *62*, e202311941. https://doi.org/10.1002/anie.202311941
20. Zhang, W.; Lin, S., Electroreductive Carbofunctionalization of Alkenes with Alkyl Bromides via a Radical-Polar Crossover Mechanism. *J. Am. Chem. Soc.* **2020,** *142*, 20661-20670. https://doi.org/10.1021/jacs.0c08532
21. Zhang, H.; Guo, L.; Yang, C.; Xia, W., Highly stereoselective synthesis of trans-alkenes via electrochemical Ni-catalyzed hydroarylation of alkynes with aryl iodides. *Org. & Biomol. Chem.* **2023,** *21*, 5189-5193. https://doi.org/10.1039/D3OB00705G
22. Gnaim, S.; Bauer, A.; Zhang, H.-J.; Chen, L.; Gannett, C.; Malapit, C. A.; Hill, D. E.; Vogt, D.; Tang, T.; Daley, R. A.; Hao, W.; Zeng, R.; Quertenmont, M.; Beck, W. D.; Kandahari, E.; Vantourout, J. C.; Echeverria,

P.-G.; Abruna, H. D.; Blackmond, D. G.; Minteer, S. D.; Reisman, S. E.; Sigman, M. S.; Baran, P. S., Cobalt-electrocatalytic HAT for functionalization of unsaturated C–C bonds. *Nature* **2022,** *605*, 687-695. https://doi.org/10.1038/s41586-022-04595-3
23. Zhang, S.; Findlater, M., Electrochemically Driven Hydrogen Atom Transfer Catalysis: A Tool for C(sp3)/Si–H Functionalization and Hydrofunctionalization of Alkenes. *ACS Catal.* **2023**, 8731-8751. https://doi.org/10.1021/acscatal.3c01221
24. Zhang, W.; Guan, W.; Martinez Alvarado, J. I.; Novaes, L. F. T.; Lin, S., Deep Electroreductive Chemistry: Harnessing Carbon- and Silicon-Based Reactive Intermediates in Organic Synthesis. *ACS Catal.* **2023,** *13*, 8038-8048. https://doi.org/10.1021/acscatal.3c01174
25. Czaikowski, M. E.; Anferov, S. W.; Tascher, A. P.; Anderson, J. S., Electrocatalytic Semihydrogenation of Terminal Alkynes Using Ligand-Based Transfer of Protons and Electrons. *J. Am. Chem. Soc.* **2024,** *146*, 476-486. https://doi.org/10.1021/jacs.3c09885
26. McNeece, A. J.; Jesse, K. A.; Filatov, A. S.; Schneider, J. E.; Anderson, J. S. Catalytic hydrogenation enabled by ligand-based storage of hydrogen. *Chem. Commun.* **2021**, *57*, 3869– 3872. https://doi.org/10.1039/D0CC08236H
27. Lin, Q.; Spielvogel, E. H.; Diao, T., Carbon-centered radical capture at nickel(II) complexes: Spectroscopic evidence, rates, and selectivity. *Chem* **2023,** *9*, 1295-1308. https://doi.org/10.1016/j.chempr.2023.02.010
28. McNeece, A. J.; Jesse, K. A.; Xie, J.; Filatov, A. S.; Anderson, J. S. Generation and Oxidative Reactivity of a Ni(II) Superoxo Complex via Ligand-Based Redox Non-Innocence, J. Am. Chem. Soc. 2020, 142, 10824– 10832, https://doi.org/10.1021/jacs.0c03244
29. Neese, F. The ORCA program system. *WIREs Comput. Mol. Sci.* **2012**, *2*, 73-78.
30. Gaussian 16, Revision A.03, Frisch, M. J.; Trucks, G. W.; Schlegel, H. B.; Scuseria, G. E.; Robb, M. A.; Cheeseman, J. R.; Scalmani, G.; Barone, V.; Petersson, G. A.; Nakatsuji, H.; Li, X.; Caricato, M.; Marenich, A. V.; Bloino, J.; Janesko, B. G.; Gomperts, R.; Mennucci, B.; Hratchian, H. P.; Ortiz, J. V.; Izmaylov, A. F.; Sonnenberg, J. L.; Williams-Young, D.; Ding, F.; Lipparini, F.; Egidi, F.; Goings, J.; Peng, B.; Petrone, A.; Henderson, T.; Ranasinghe, D.; Zakrzewski, V. G.; Gao, J.; Rega, N.; Zheng, G.; Liang, W.; Hada, M.; Ehara, M.; Toyota, K.; Fukuda, R.; Hasegawa, J.; Ishida, M.; Nakajima, T.; Honda, Y.; Kitao, O.; Nakai, H.; Vreven, T.; Throssell, K.; Montgomery, J. A., Jr.; Peralta, J. E.; Ogliaro, F.; Bearpark, M. J.; Heyd, J. J.; Brothers, E. N.; Kudin, K. N.; Staroverov, V. N.; Keith, T. A.; Kobayashi, R.; Normand, J.; Raghavachari, K.; Rendell, A. P.; Burant, J. C.; Iyengar, S. S.; Tomasi, J.; Cossi, M.; Millam, J. M.; Klene, M.; Adamo, C.; Cammi, R.; Ochterski, J. W.; Martin, R. L.; Morokuma, K.; Farkas, O.; Foresman, J. B.; Fox, D. J. Gaussian, Inc., Wallingford CT, 2016.

Appendix I: Chapter I Supplementary Information

NMR Spectra

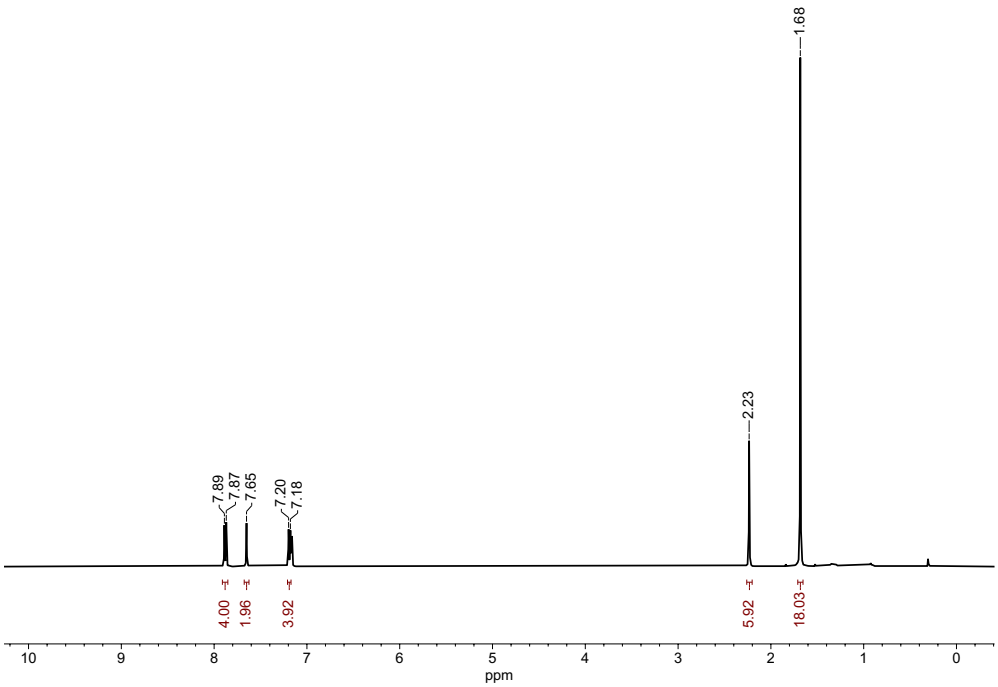

Figure S1. ^{1}H NMR of **1** in C_6D_6.

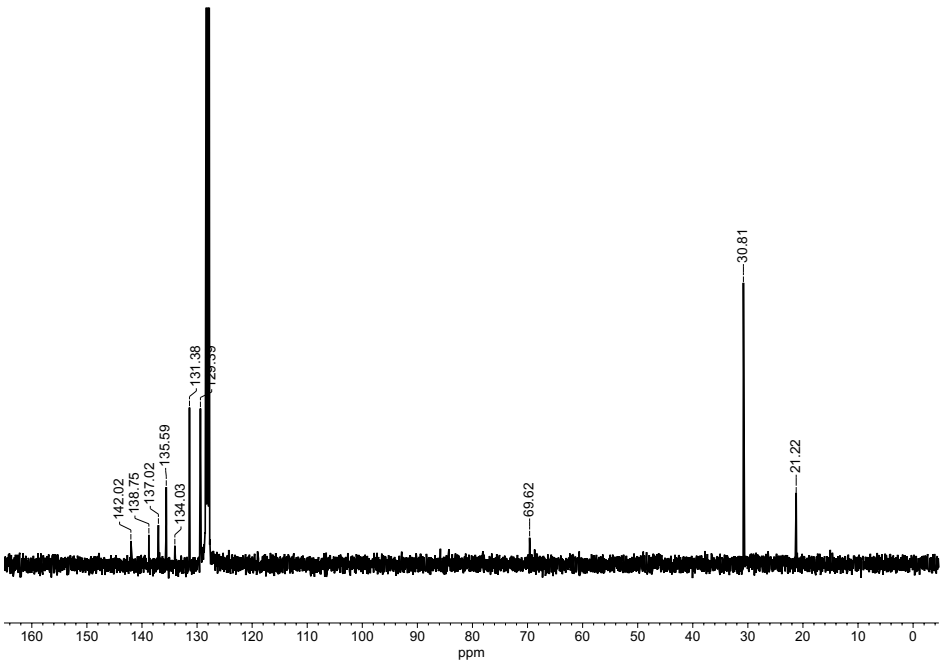

Figure S2. $^{13}C\{^{1}H\}$ NMR of **1** C_6D_6.

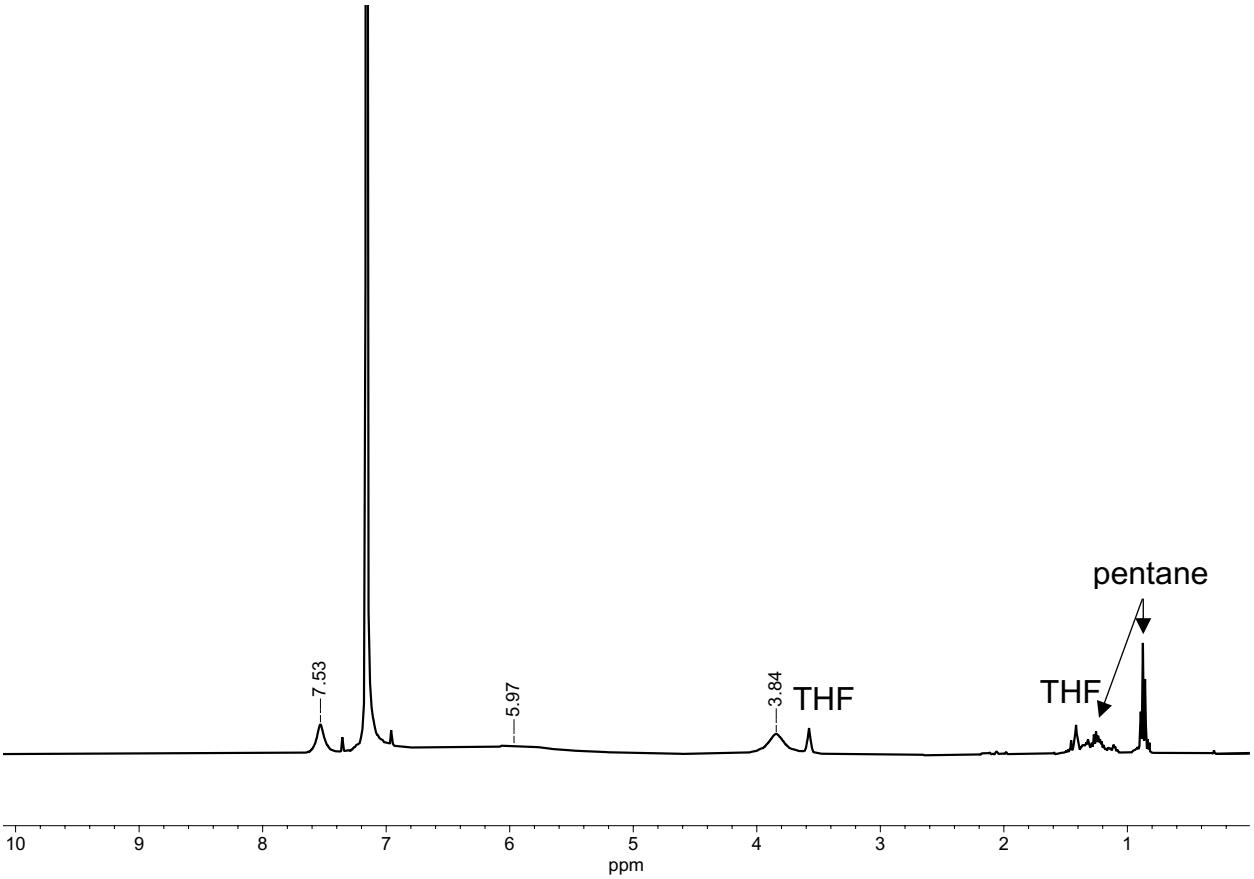

Figure S3. ^{1}H NMR of **2** in C_6D_6.

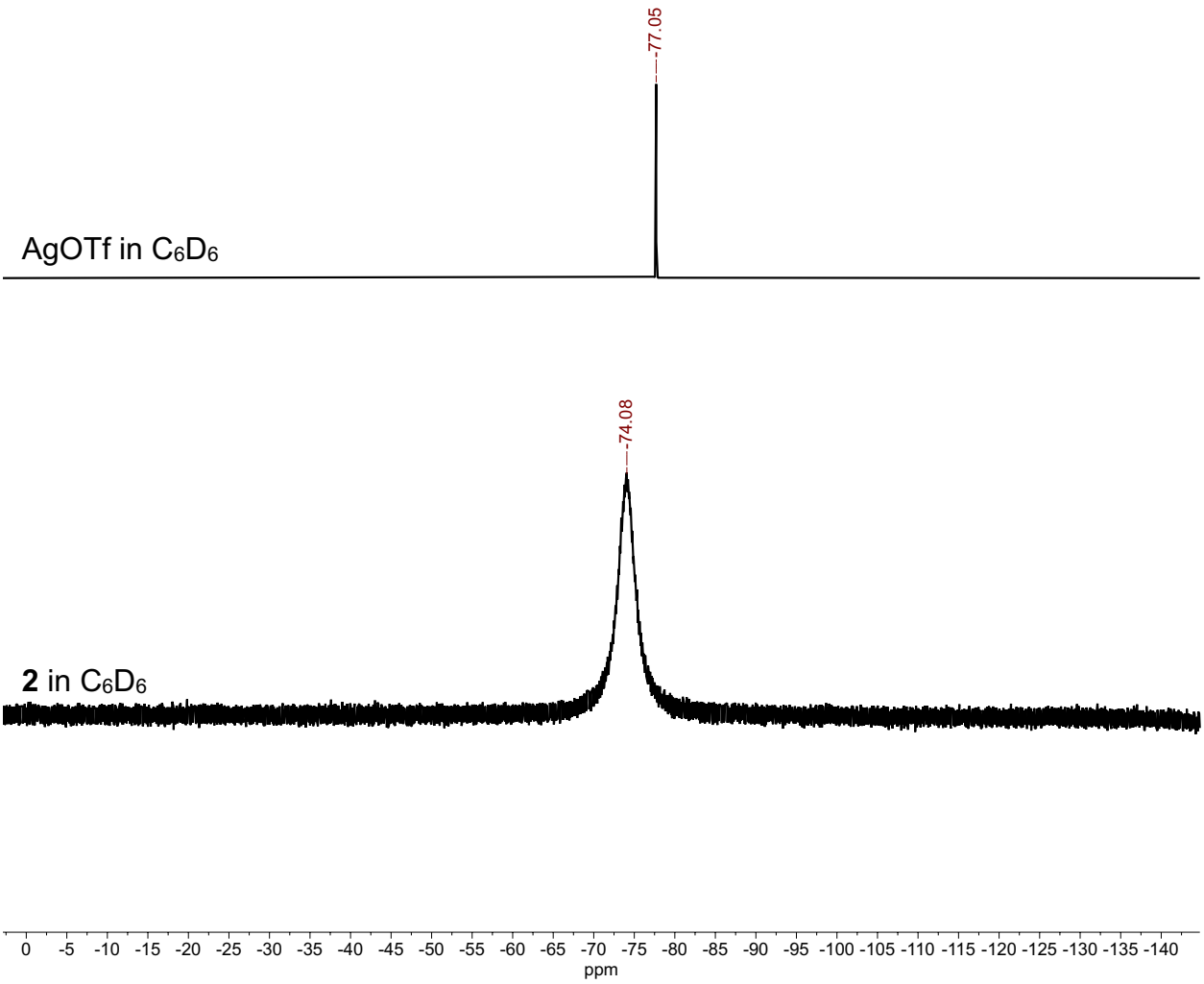

Figure S4. ^{19}F NMR of **2** in C_6D_6 with comparison to free triflate in solution.

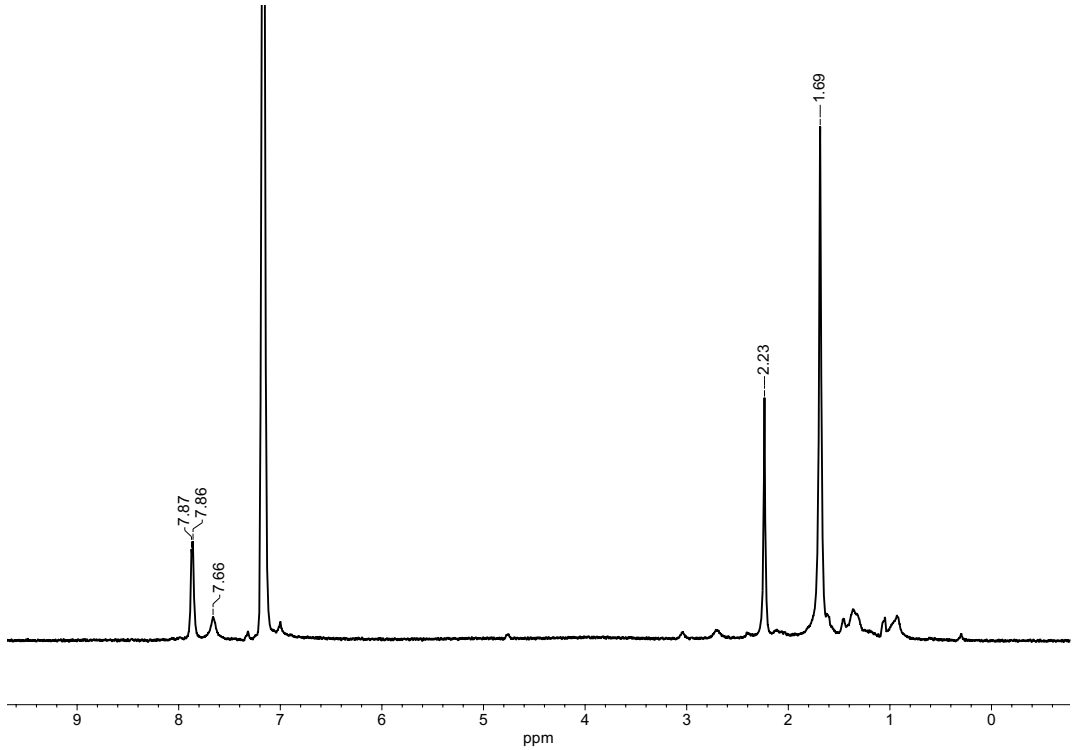

Figure S5. ^{1}H NMR of **3** in C_6D_6 generated from a concentrated solution of **1** under 1 atm O_2.

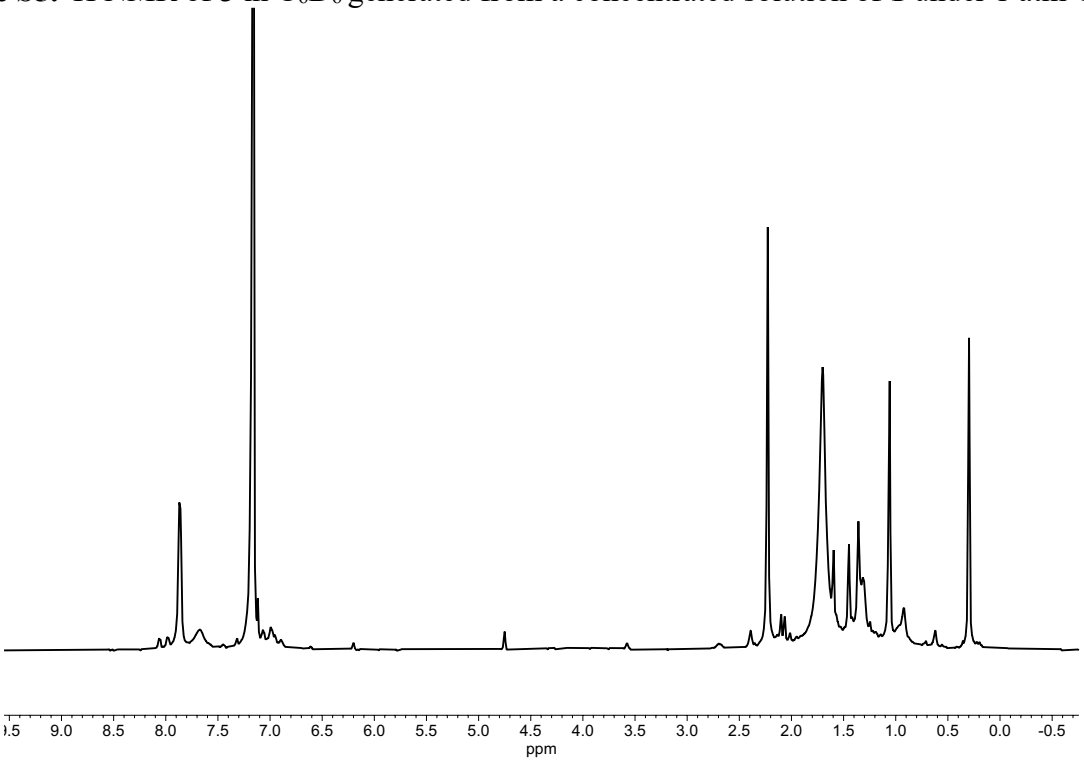

Figure S6. ^{1}H NMR Evans method of **3** in C_6D_6. Internal solvent standard peak shift of −485 Hz (to 6.19 ppm) corresponds to a magnetic moment of 3.12 μ_B.

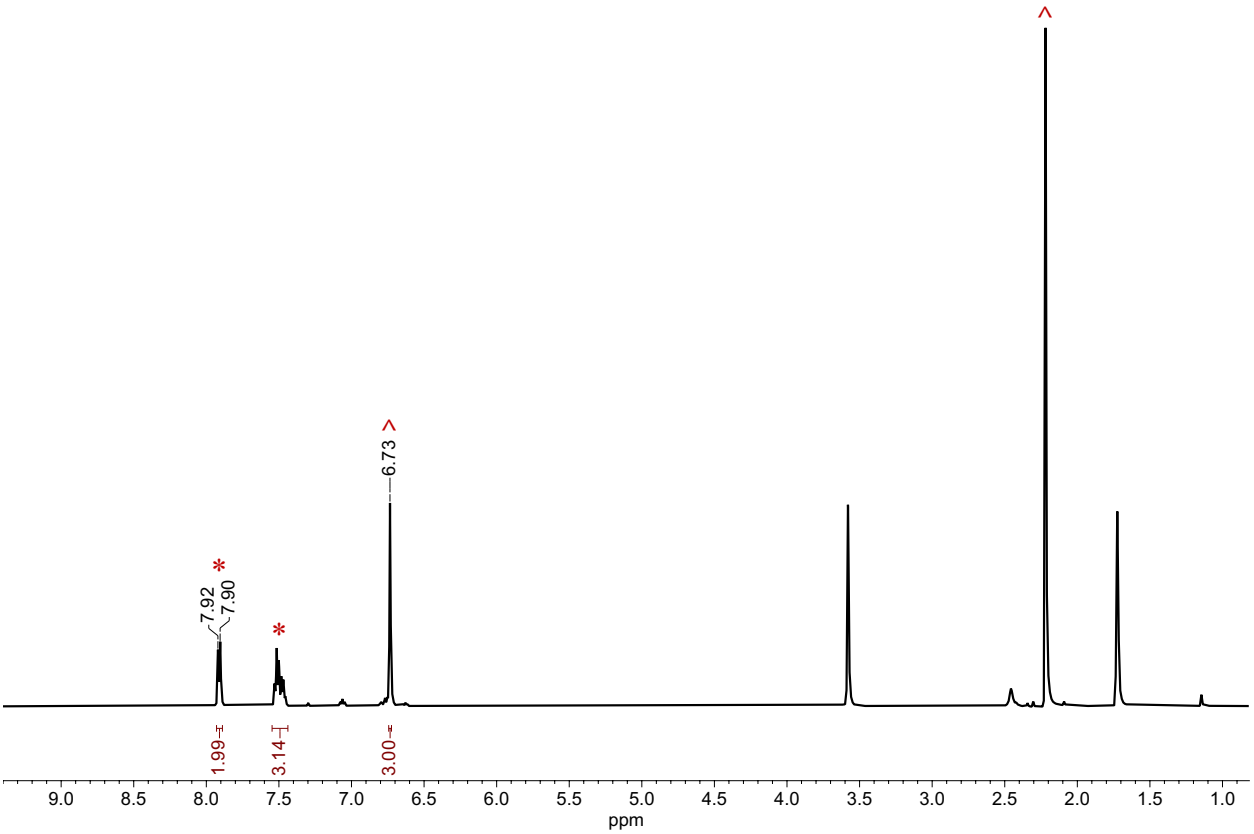

Figure S7. ^{1}H NMR in C_6D_6 of the reaction of **1** with DPH and O_2 and 2 eq mesitylene relative to DPH. *Azobenzene ^Mesitylene

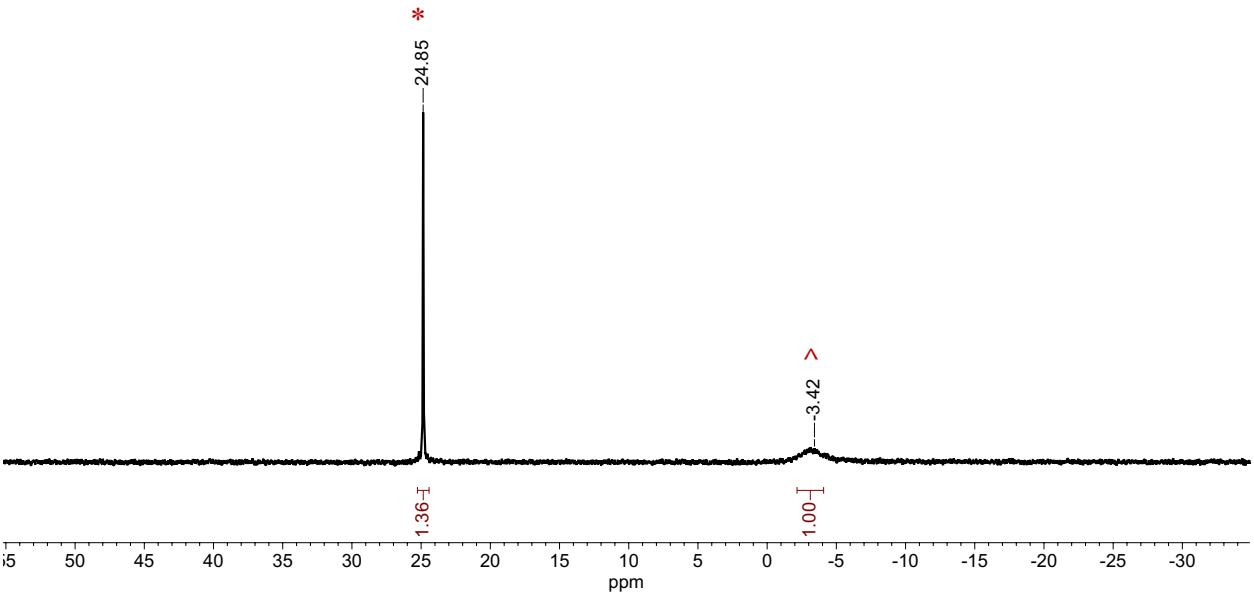

Figure S8. ^{31}P NMR of the reaction of **1** with PPh_3 in the presence of O_2 showing conversion to PPh_3O. PPh_3O was quantified by percent conversion based on integration of the PPh_3 (^) and PPh_3O (*) peaks.

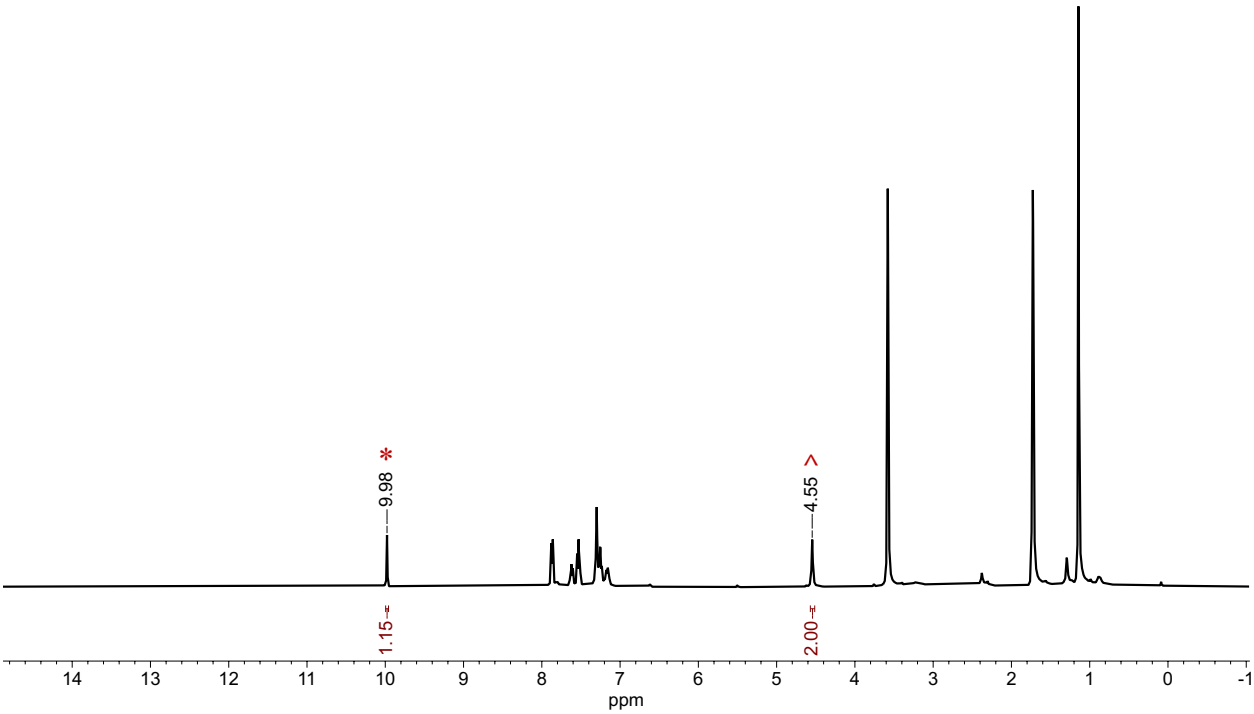

Figure S9. ^{1}H NMR in C_6D_6 of the reaction of **1** with benzyl alcohol in the presence of O_2. *Benzaldehyde (1H), ^ benzyl alcohol (2H)

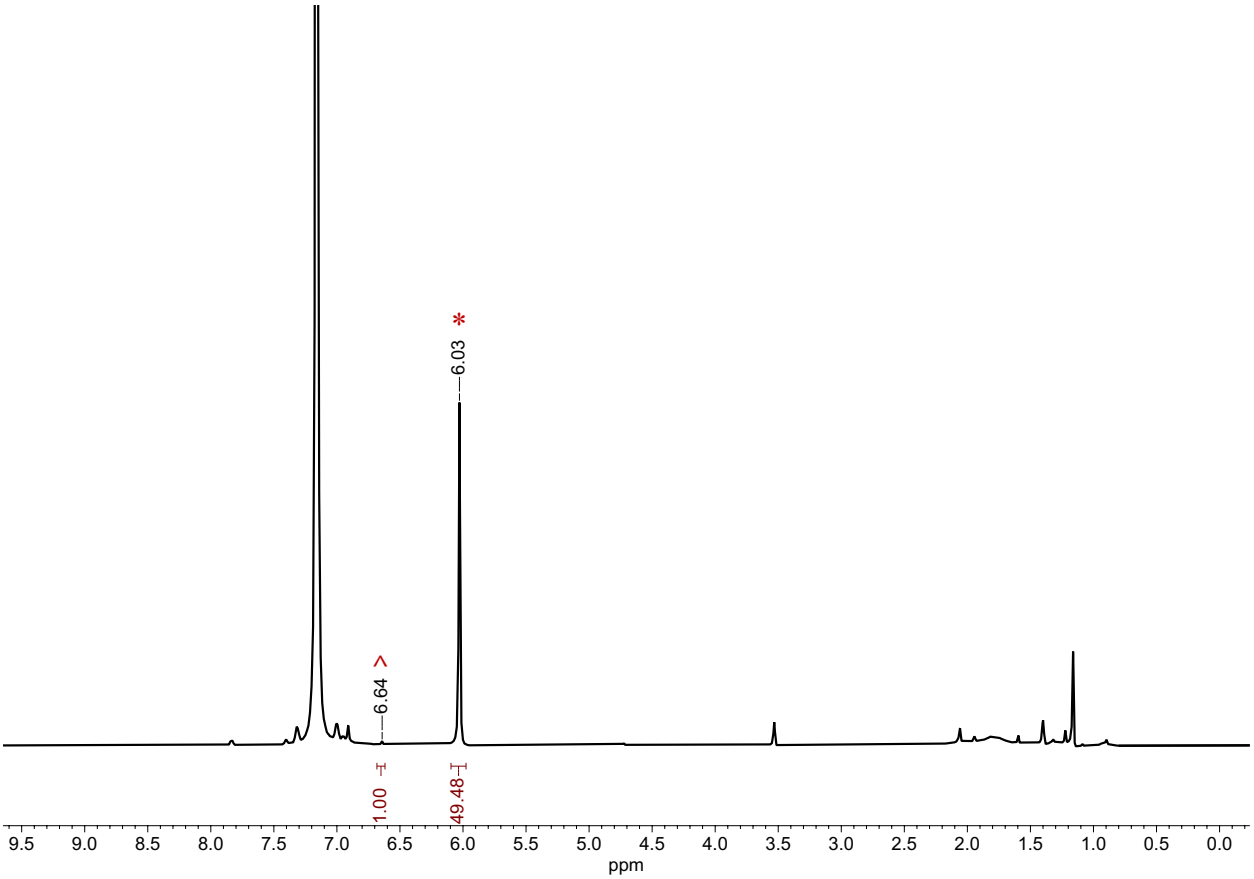

Figure S10. ^{1}H NMR in C_6D_6 of the reaction of **1** with 1,4-hydroquinone in the presence of O_2. ^Hydroquinone, *Benzoquinone

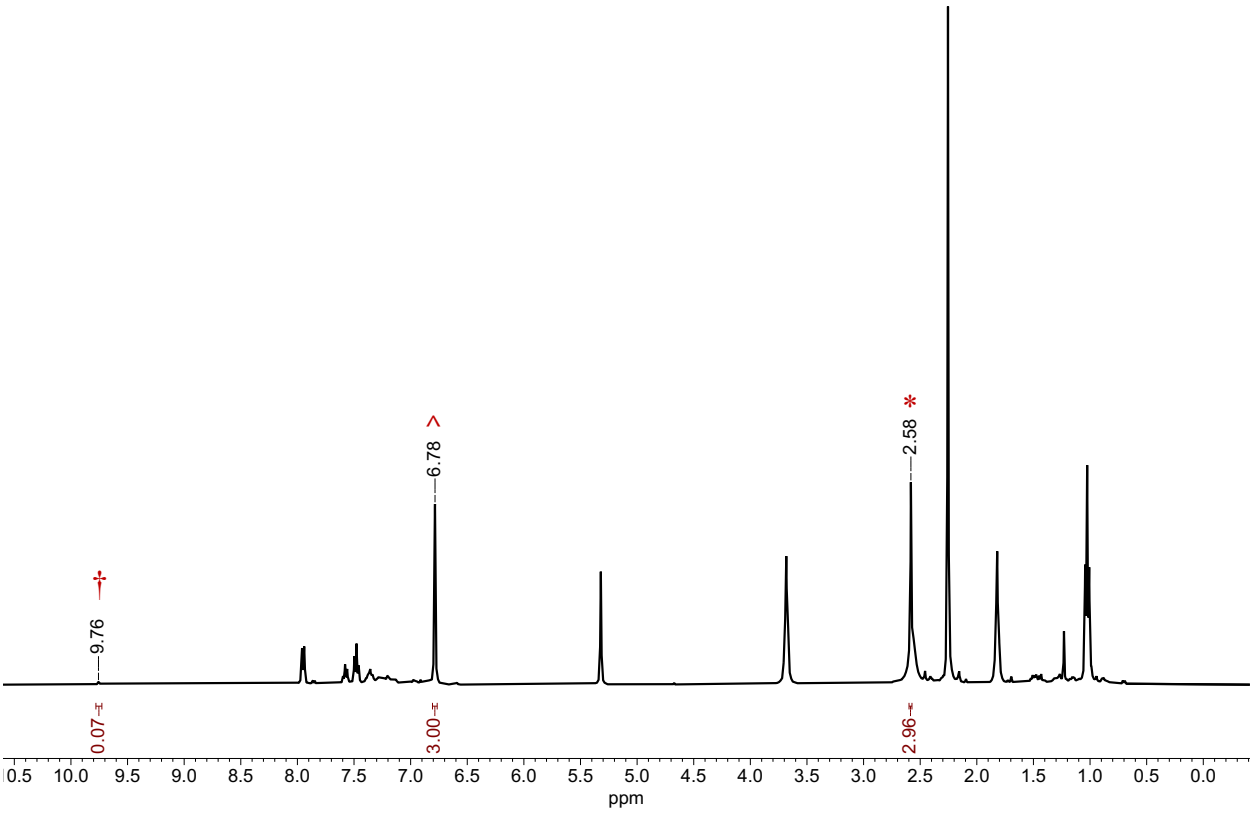

Figure S11. ^{1}H NMR in CD_2Cl_2 of the reaction of **1** with 2-phenylpropionaldehyde (2-PPA) to acetophenone in the presence of O_2. ^ Mesitylene (3H); †2-PPA (1H); *Acetophenone (3H). We note that controls were performed to ensure the absence of water in this reaction including performing the reaction over molecular sieves (no change in yield of acetophenone compared to the reaction without sieves).

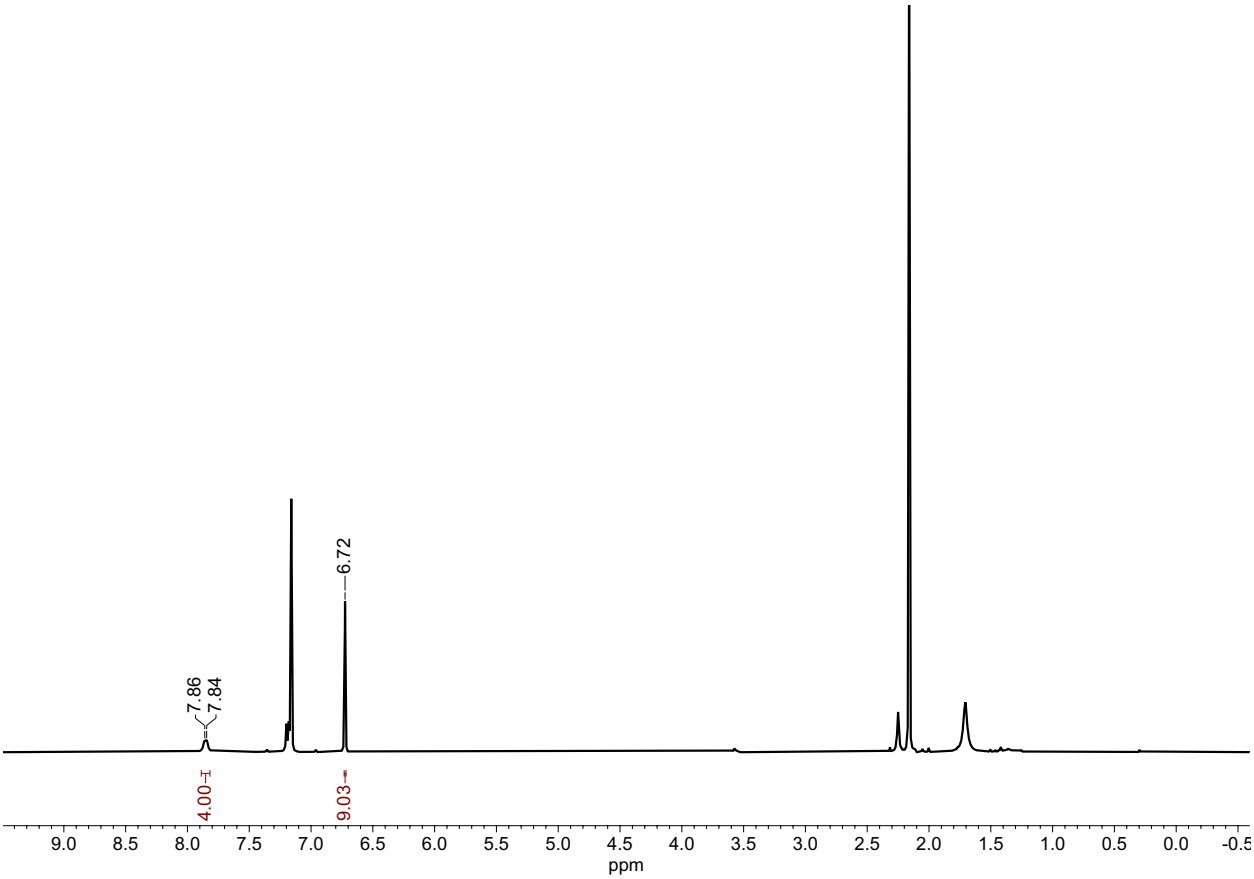

Figure S12. ^{1}H NMR in C_6D_6 of **1** (7.86, 4H) with 3 eq mesitylene (6.72, 3H) relative to Cu indicating 99.7% bulk purity. Integration widths from the peak center are $\pm 1.5 \times$ HWHM (half-width at half-max).

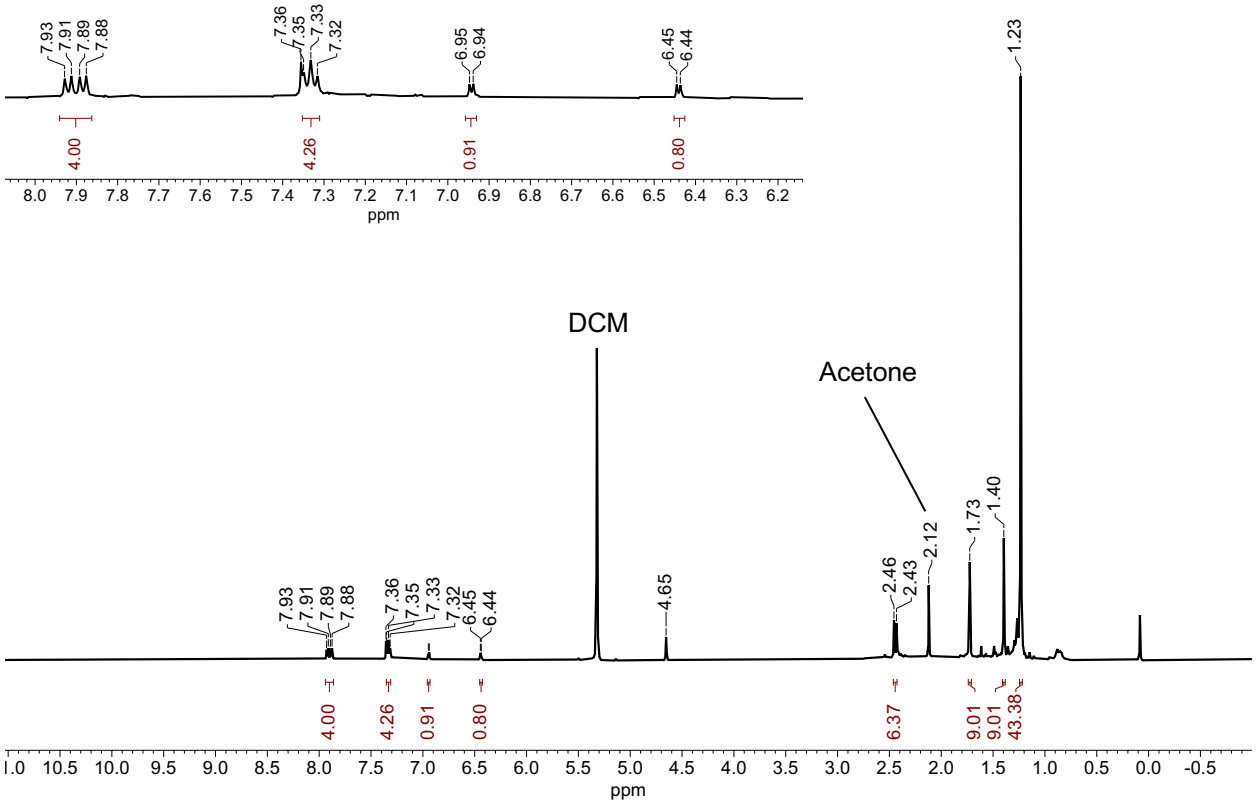

Figure S13. ^{1}H NMR in CD_2Cl_2 of the major decomposition product from the reaction with **1** and O_2.

Mass Spectra

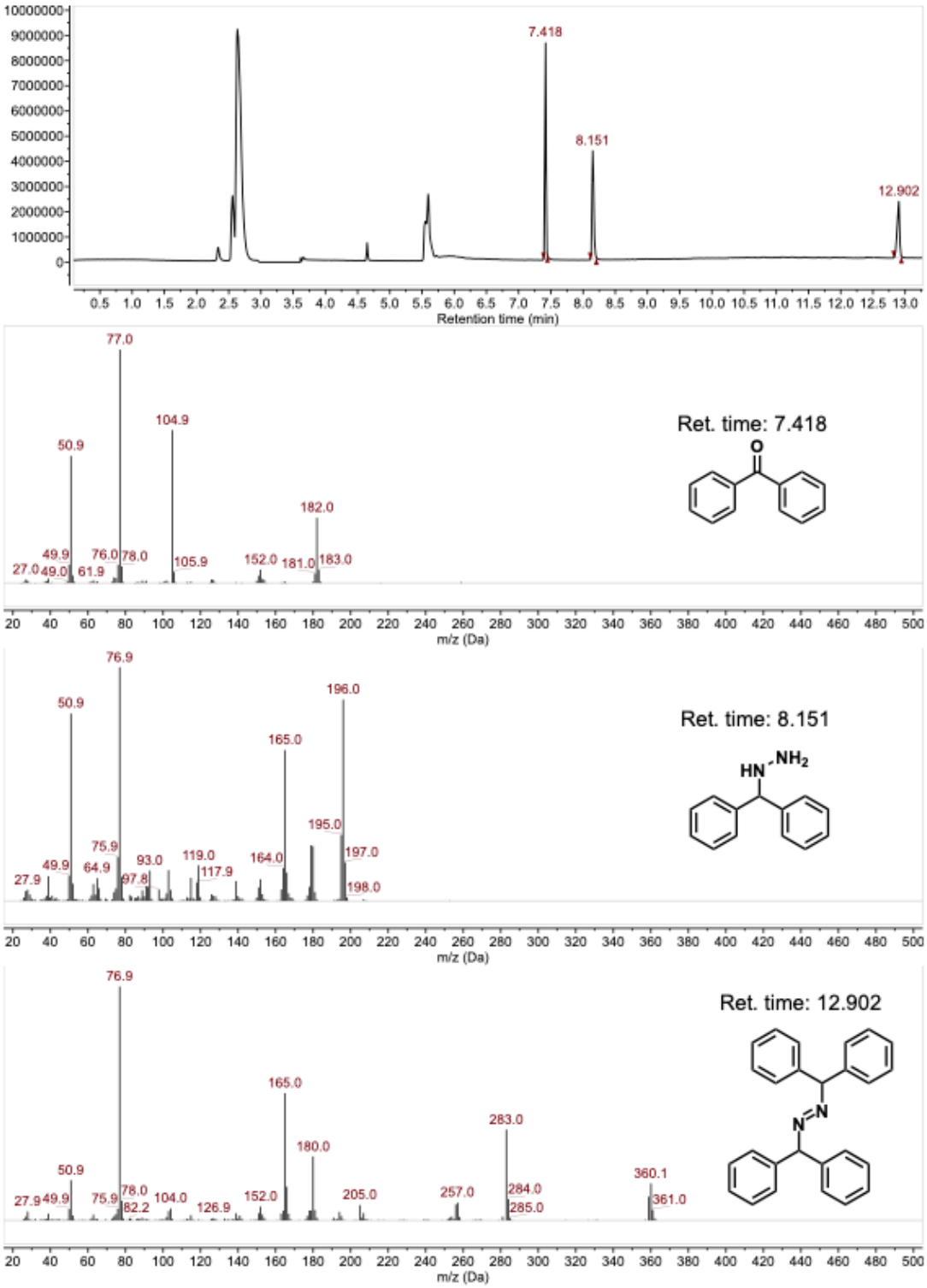

Figure S14. GC-MS of the resulting product mixture of the reaction of **1** with excess O_2 and 10 equivalents of benzophenone hydrazone in DCM.

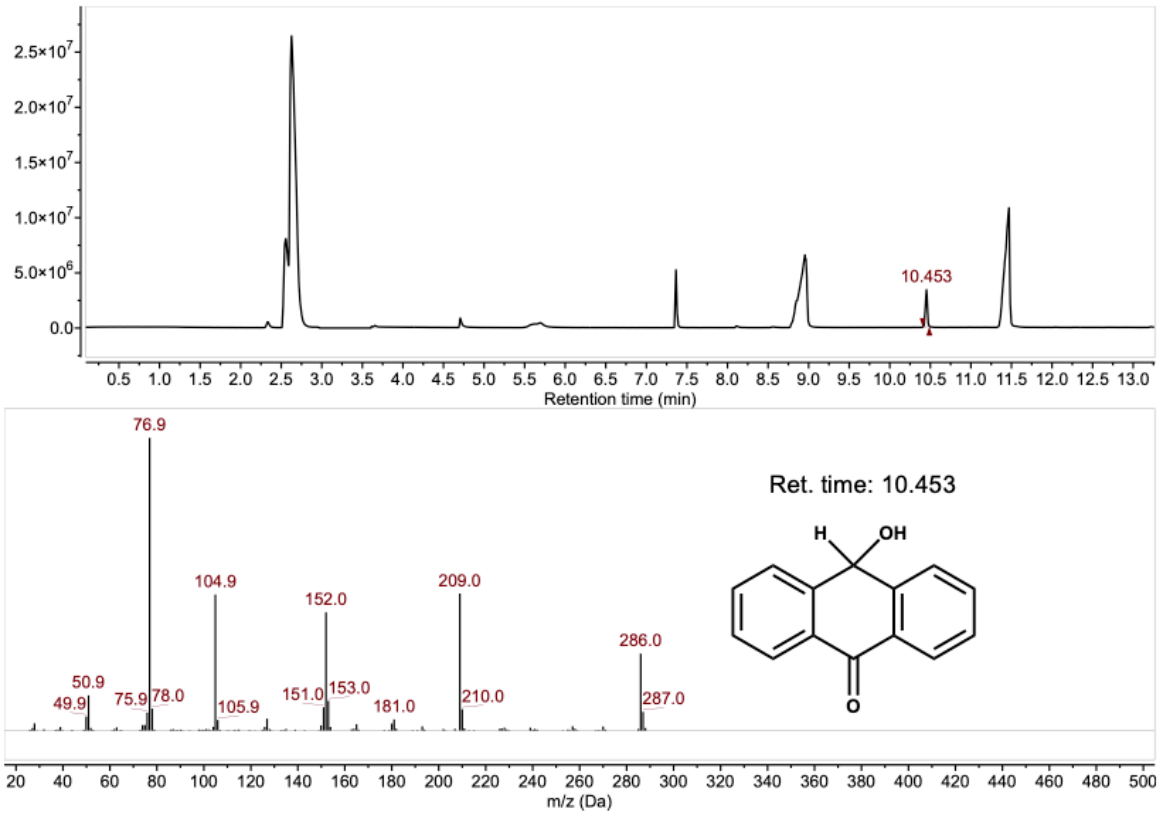

Figure S15. GC-MS of the reaction of **1** with O_2 and DPH with DPBF added to form 9-hydroxyanthracen-10(9H)-one.

```
mple Name: MEC072022_LC_decomp_dcm
```

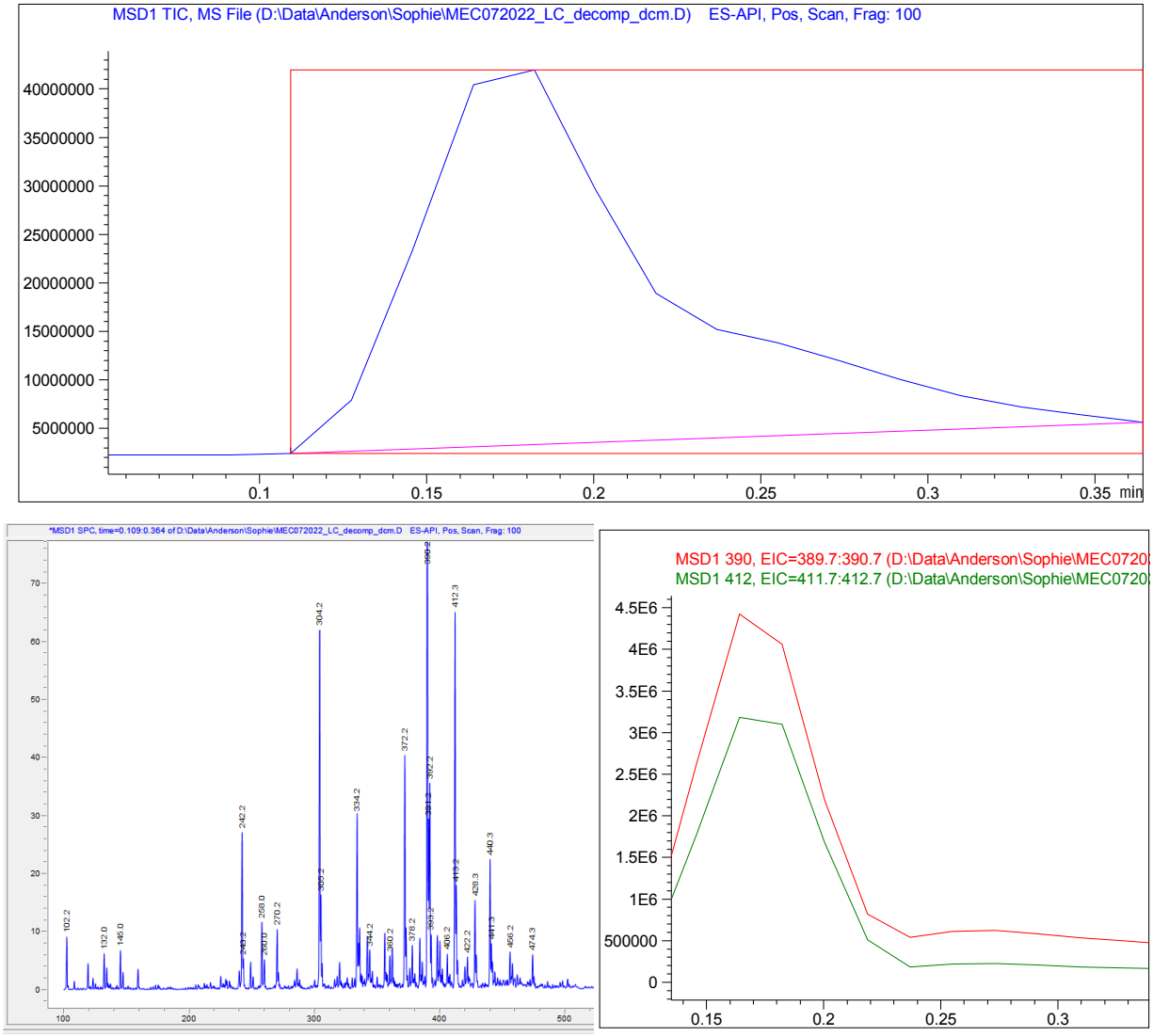


```
Peak #1 at  0.175 min ( 0.109 to  0.364 min)
-> The analysis found only one component, indicating a pure peak. <-
```

Figure S16. ESI(+) LC-MS report for the decomposition product of **1** and O_2. DHP ligand m/z 440.

ıple Name: blank_DCM_07202022

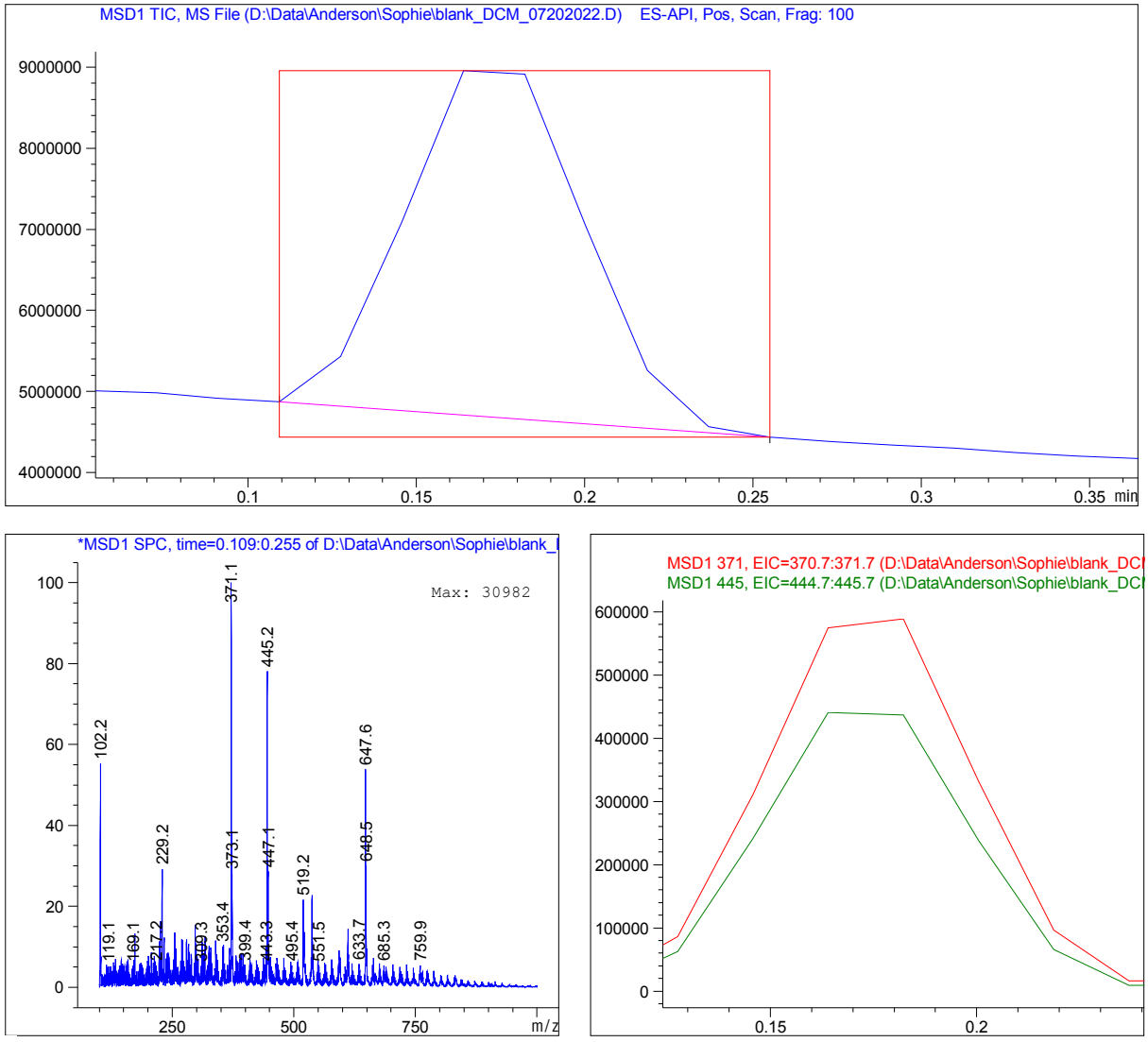

Peak #1 at 0.173 min (0.109 to 0.255 min)
-> The analysis found only one component, indicating a pure peak. <-

Figure S17. ESI(+) LC-MS report of DCM solvent blank.

Control Reactions

Table S1. Control oxidation reactions. [a]All reactions were run in DCM for 18 h with the exception of benzyl alcohol which was in THF to better tolerate the addition of a strong base. Abbreviations: Diphenylhydrazine (DPH), 2-phenylpropionaldehyde (2-PPA), benzophenone hydrazone (BPH)

Substrate	**Conditions** [a]	**% conv. (oxidized product)**
DPH	1 atm O_2	5
DPH	10 mol% 1, N_2	0
DPH	10 mol% (DHP)$Cu^{II}OTf$, N_2	45
DPH	10 mol% (DHP)$Cu^{II}OTf$, O_2	71
DPH	1 eq Ligand, 1 atm O_2	38
DPH	10 mol% CuCl, 1 atm O_2	82
DPH	10 mol% $Cu(MeCN)_4PF_6$, 1 atm O_2	Quant.
DPH	20 mol% 1, N_2 (2 hr)	0
PPh_3	1 atm O_2	0
PPh_3	1 eq Ligand, 1 atm O_2	0
PPh_3	10 mol% (DHP)$Cu^{II}OTf$, O_2	1
PPh_3	10 mol% CuCl, 1 atm O_2	0
PPh_3	10 mol% $Cu(MeCN)_4PF_6$, 1 atm O_2	0
Hydroquinone	1 atm O_2	0
Hydroquinone	10 mol% (DHP)$Cu^{II}OTf$, N_2	5
Hydroquinone	10 mol% (DHP)$Cu^{II}OTf$, O_2	1
Hydroquinone	1 eq Ligand, 1 atm O_2	0

Hydroquinone	10 mol% CuCl, 1 atm O_2	7
Hydroquinone	10 mol% $Cu(MeCN)_4PF_6$, 1 atm O_2	0
Benzyl Alcohol	0.5 eq *t*BuOK, 1 atm O_2	24
Benzyl Alcohol	0.5 eq *t*BuOK, 1 eq Ligand, 1 atm O_2	18
Benzyl Alcohol	10 mol% (DHP)$Cu^{II}OTf$, N_2	0
Benzyl Alcohol	0.5 eq *t*BuOK, 10 mol% (DHP)$Cu^{II}OTf$, O_2	8
Benzyl Alcohol	0.5 eq *t*BuOK, 10 mol% CuCl, 1 atm O_2	40
Benzyl Alcohol	0.5 eq *t*BuOK, 10 mol% $Cu(MeCN)_4PF_6$, 1 atm O_2	9
2-PPA	1 eq Et_3N, 1 atm O_2	0
2-PPA	1 eq Et_3N, 1 eq Ligand, 1 atm O_2	31
2-PPA	1 eq Et_3N, 10 mol% (DHP)$Cu^{II}OTf$, O_2	75
2-PPA	1 eq Et_3N, 10 mol% CuCl, 1 atm O_2	44
2-PPA	1 eq Et_3N, 10 mol% $Cu(MeCN)_4PF_6$, 1 atm O_2	54
BPH	1 atm O_2	2
BPH	1 eq Ligand, 1 atm O_2	12
BPH	10 mol% (DHP)$Cu^{II}OTf$, O_2	4
BPH	10 mol% CuCl, 1 atm O_2	5
BPH	10 mol% $Cu(MeCN)_4PF_6$, 1 atm O_2	28

Table S2. Iodometric titration of the reaction with **1** and hydroquinone (HQ) in the presence of O_2. Background tests were performed on DI water and the concentration of H_2O_2 was determined using $n(H_2O_2) = \frac{1}{2}n(Na_2S_2O_3)$. Iodometric titration was performed according to literature procedure.[1]

Experiment	$Na_2S_2O_3$ (0.01 M) added	Background subtracted	$[H_2O_2]$
1 + HQ + O_2	0.30(1) mL	0.25 mL	64(3) μM
Background	0.04(1) mL	–	10(1) μM

Iodometric quantification using NaI: In the glovebox, a DCM solution of **1** (1 mg, 0.002 mmol, 10 mol%) and 1,4-hydroquinone (2 mg, 0.02 mmol, 1 eq) was prepared in a vial with a septum screw top with a stir bar. After the addition of O_2 and subsequent reaction to form benzoquinone, the vial was purged with N_2 to remove excess oxygen. The solution in the vial was then transferred to the glovebox where it was washed with hexanes, filtered, and a 100 μL aliquot of the filtrate was transferred to a quartz cuvette containing an acetonitrile solution of NaI (0.02 g). The solution was diluted to 2 mL with acetonitrile and transferred for UV-vis absorbance measurement (Blue trace). For the control with **1** (Red trace), a 100 μL aliquot of the same filtrate described above was added to a cuvette and diluted to 2 mL with acetonitrile, but no NaI was added. For the NaI control (Black trace), the experiment for H_2O_2 detection was replicated as described above except that **1** and hydroquinone were omitted from the reaction mixture.

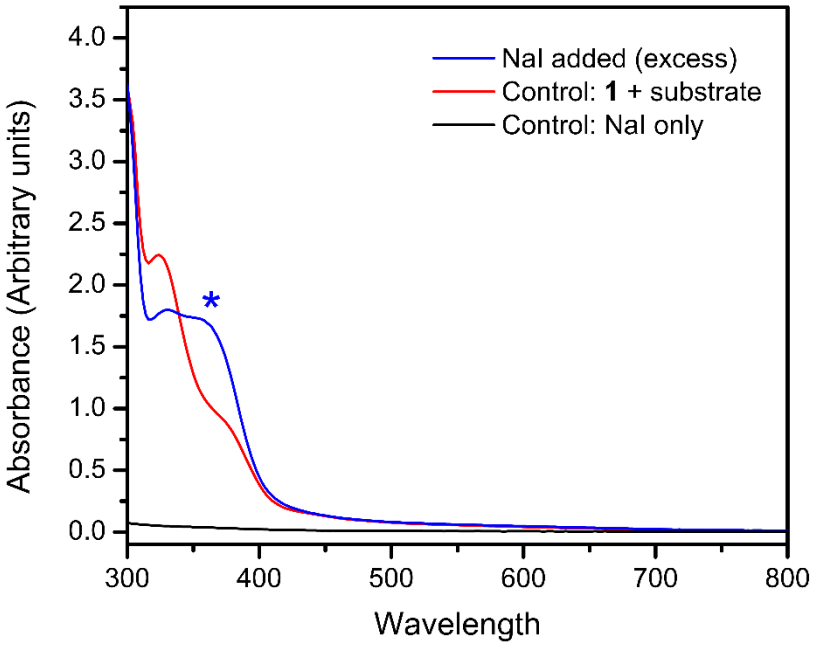

Figure S18. UV-vis spectrum of the addition of excess NaI after the reaction of **1** and 1,4-hydroquinone (blue) along with the control with no NaI added (red) and NaI only (black). I_3^- absorbance corresponds to trace H_2O_2 (8 mol% benzoquinone product).

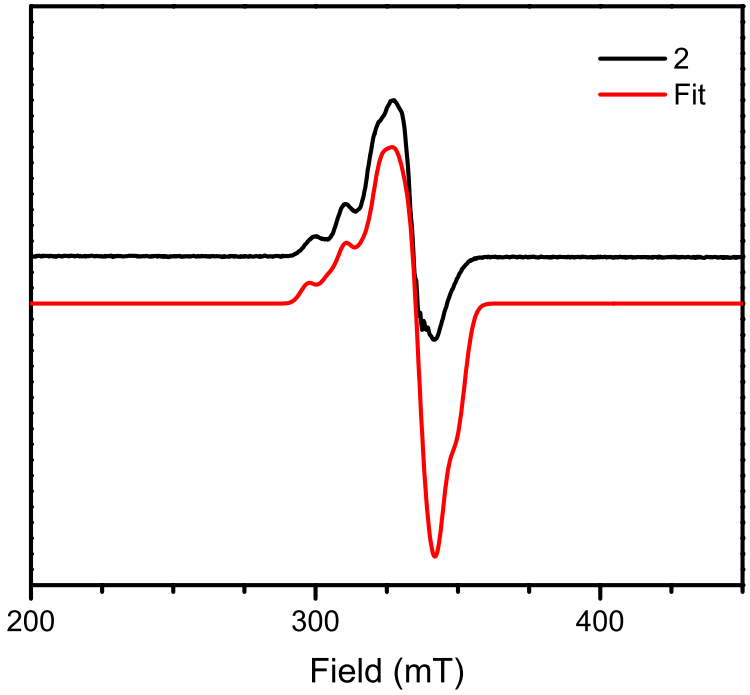

Figure S19. X-band perpendicular mode EPR spectrum of a 15 mM solution of **2** in 1:1 DCM/Toluene at 15 K. Conditions: MW frequency, 9.63 GHz; MW power, 0.6 mW. Fitting parameters: g = 2.064, 2.065, 2.083; Nuclei = Cu, N; A = [21, 5, 81; 10, 23, 47].

UV-visible Spectroscopy

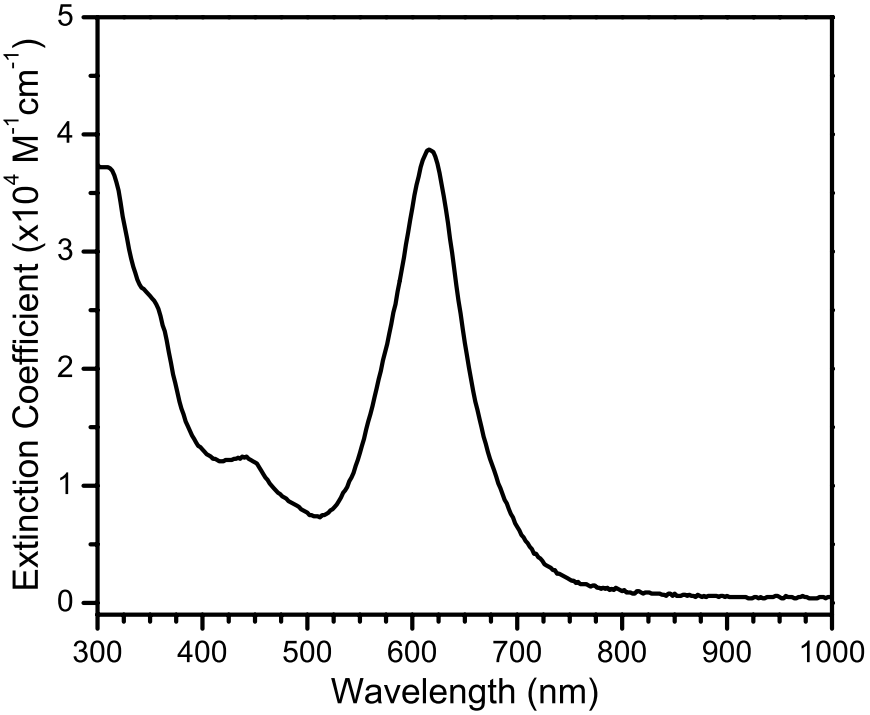

Figure S20. UV-visible spectrum of 0.01 mM **1** in DCM at room temperature.

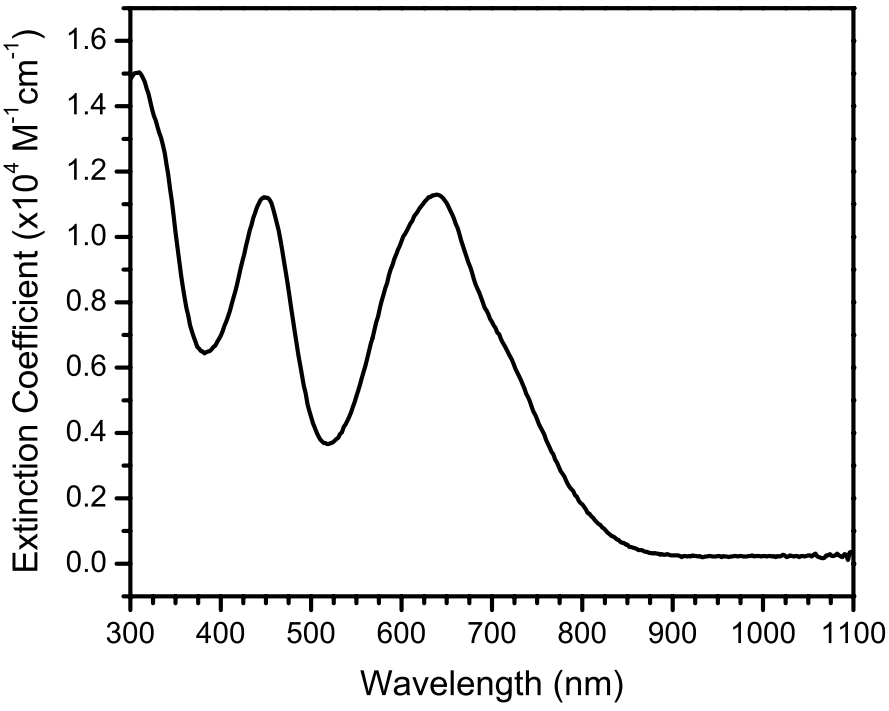

Figure S21. UV-visible spectrum of 0.06 mM **2** in DCM at room temperature.

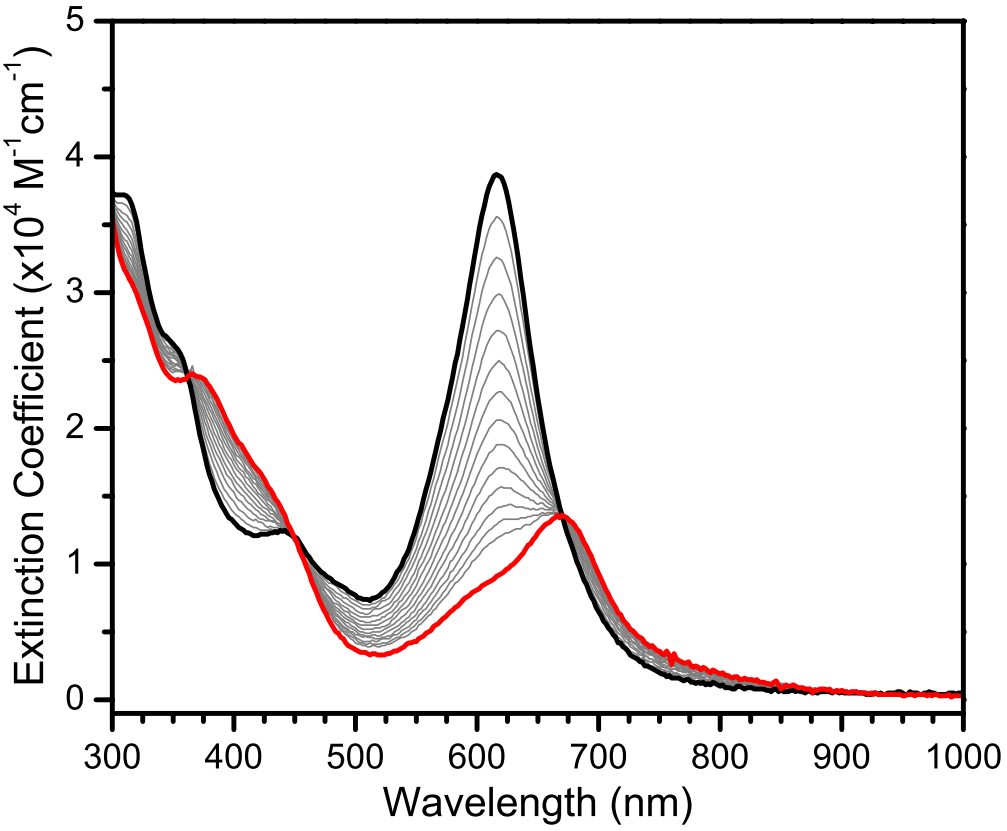

Figure S22. UV-visible spectra of the conversion of a stirring 0.01 mM solution of **1** (black) to **3** (red) in DCM at room temperature after injection of an excess of O_2 with scans every 2 min. Extinction coefficient was calculated based on initial concentration of **1**.

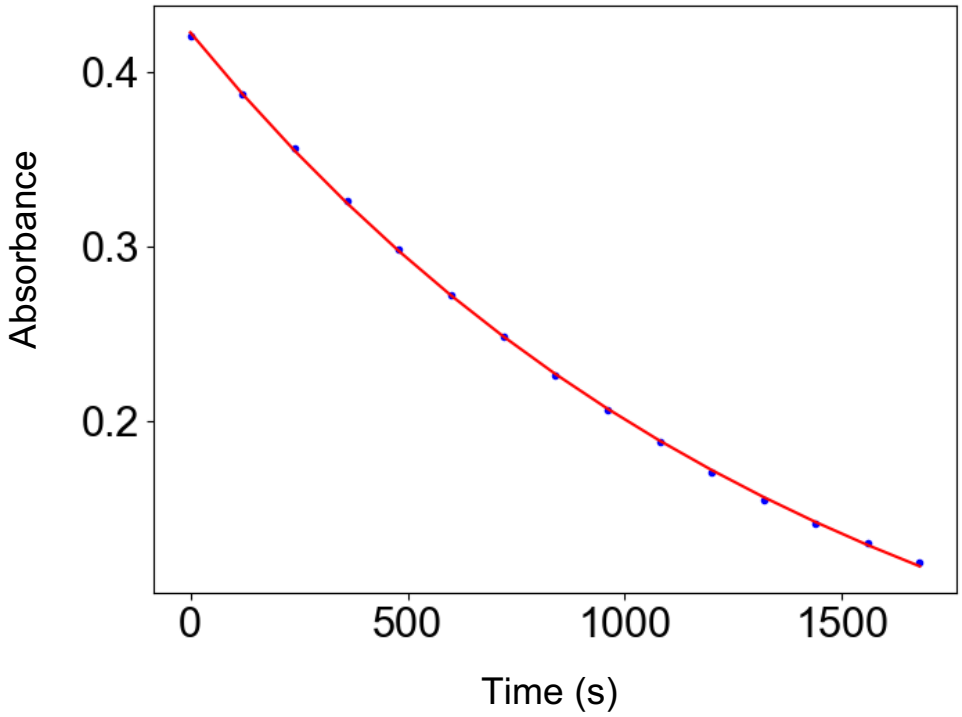

Figure S23. Exponential fit for the UV-visible absorbance at 616 for 0.01 mM solution of **1** in DCM over time after addition of excess O_2. k_{eff} = 6.82× 10^{-4} R^2 = 0.9998, Standard error = 1.660 × 10^{-5}.

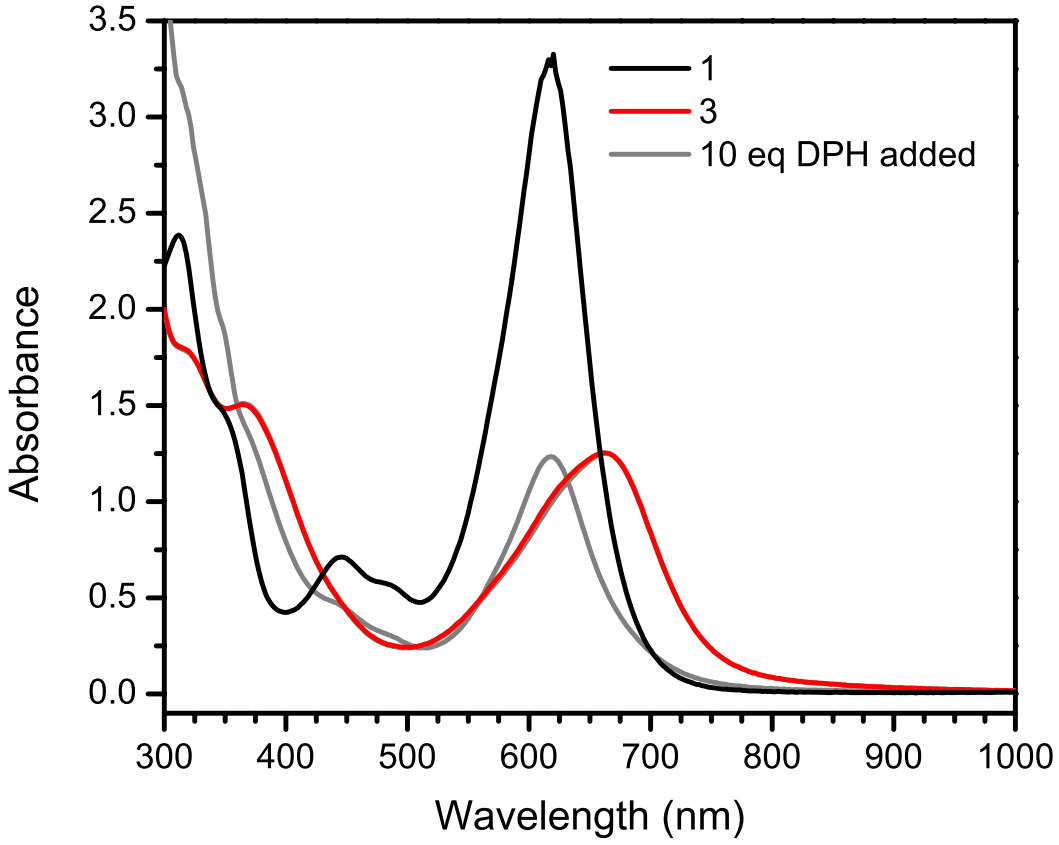

Figure S24. UV-visible spectra of **1** (black), after conversion to **3** (red), and after purging with N_2 and adding 10 eq of diphenylhydrazine (DPH) relative to Cu. DCM, room temperature.

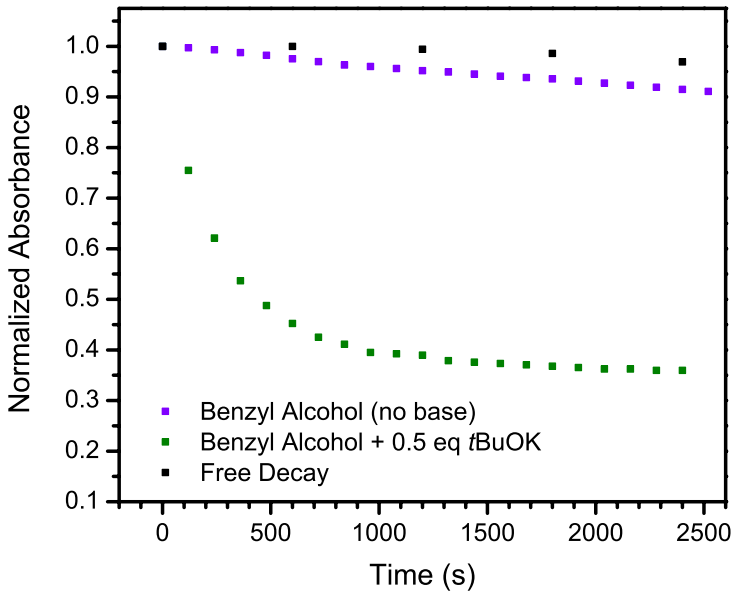

Figure S25. Absorbance at 670 nm as a function of time for the reaction of **3** with benzyl alcohol (1 eq relative to Cu) with or without *t*BuOK at room temperature in THF. Compound **3** was generated from **1** + O_2 (excess) and purged with N_2 to remove O_2 before substrate addition.

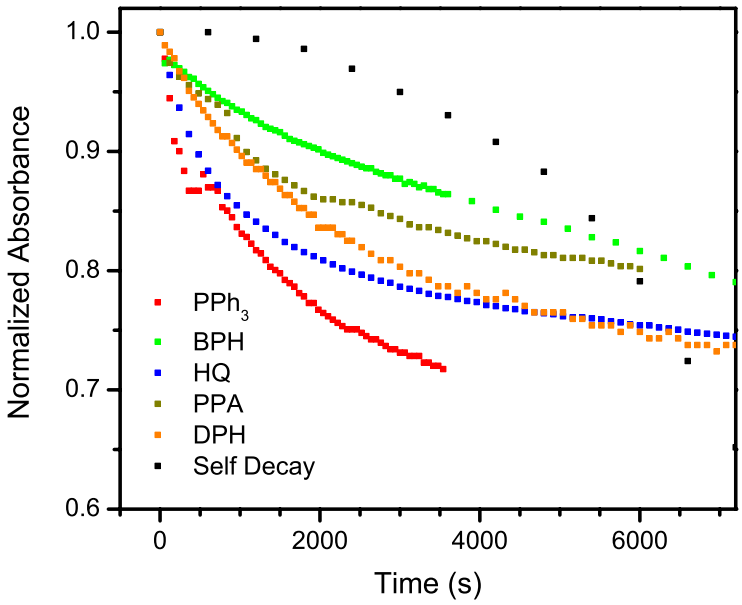

Figure S26. Absorbance at 670 nm as a function of time for the reaction of **3** with triphenylphosphine (PPh_3), benzophenone hydrazone (BPH), 1,4-hydroquinone (HQ), 2-phenylpropionaldehyde (PPA), and diphenylhydrazine (DPH) in DCM at room temperature. PPA was pre-mixed with 1 eq Et_3N for consistency with the catalytic reaction conditions. Compound **3** was generated from **1** + O_2 (excess) and purged with N_2 to remove O_2 before substrate addition.

The self decay of **3** was monitored after purging with N_2 and allowing **3** to decay in the absence of any added substrate.

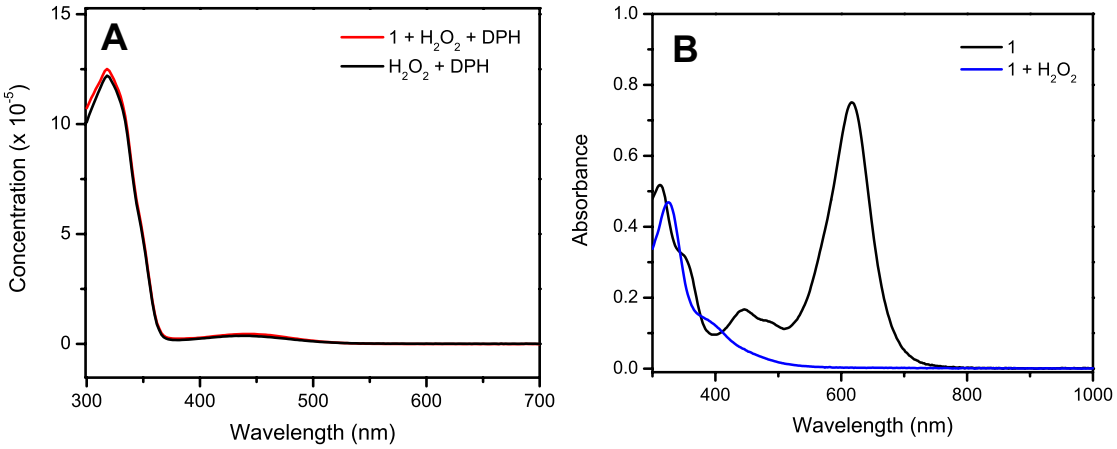

Figure S27. (A) UV-visible spectra showing azobenzene formation (band at 320 nm) after reacting DPH (3.7 mg, 0.02 mmol) with 1 equiv H_2O_2 (as H_2O_2 ($O{=}PPh_3$)$_2$) under control conditions (black) and in the presence of 10 mol% **1** (red). DCM, room temperature, N_2 atmosphere. (B) UV-visible spectrum of **1** after stirring with 1 equiv H_2O_2 (as H_2O_2 ($O{=}PPh_3$)$_2$) in DCM at room temperature for 2 hr (blue) along with the initial UV-visible spectrum of **1** (black).

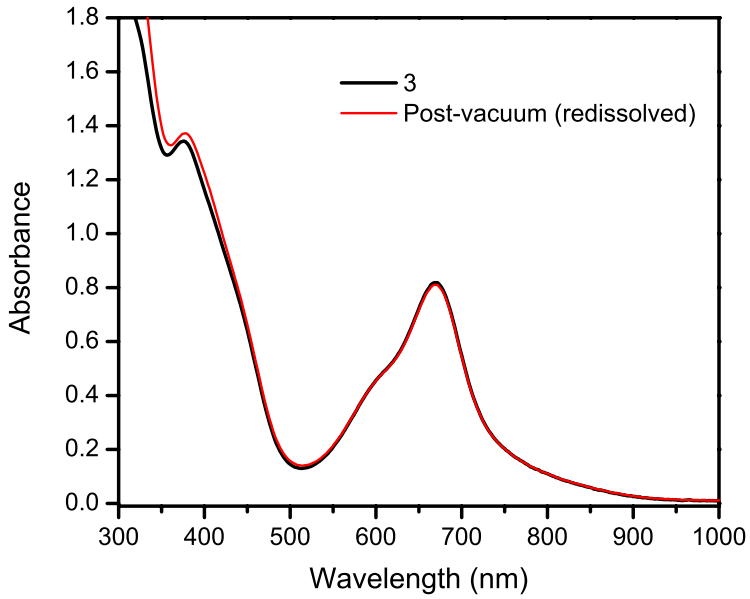

Figure S28. UV-visible spectrum of **3** (black) and after drying under vacuum and re-dissolving in DCM (red) (0.06 mM **3**, DCM, room temperature).

Cyclic Voltammogram

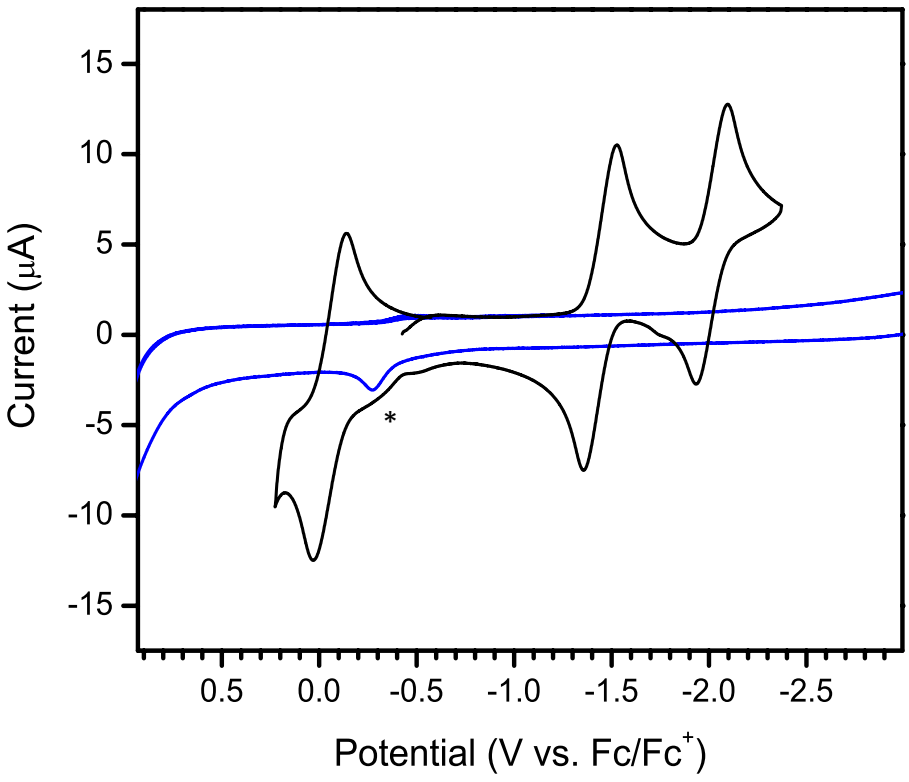

Figure S29. Cyclic voltammogram of **1** (black, 1 mM [Cu]) and blank electrolyte solution (blue line) in THF (0.1 M NBu_4PF_6, scan rate 100 mV s^{-1}). *Minor contamination from electrolyte solution.

XAS and EXAFS Fitting

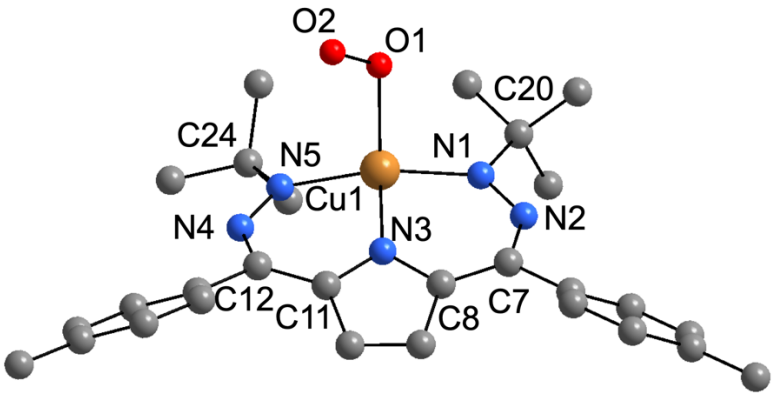

Table S3. Best Fits for the Cu K-edge EXAFS Data of **3**

Complex	N/Path	R (Å)	σ^2 (Å^2)	ΔE_0	Error *F*
[**3**] (DHP)CuO_2	4 Cu-N/O	1.94	690	5.26	0.32
	3 Cu-N/O	2.89	301		
	4 Cu-C/N	3.08	371		
	2 Cu-C/N	3.28	169		

The estimated standard deviations in R are $\pm$0.02 Å. The σ^2 values are multiplied by 10^5. s_0^2 = 0.9. Fitting range: k: 2-12.5 Å^{-1}. N, Coordination numbers; R, interatomic distances; σ^2, Debye-Waller factors (the mean square deviations in interatomic distance). Error *F* is $[\sum k^6(\chi_{exptl} - \chi_{calcd})^2 / \sum k^6(\chi_{exptl}{}^2]^{1/2}$. Errors in the identity of the scatterer Z are $\pm$1.

Table S4. Comparison of EXAFS and DFT calculated bond lengths of **3**. The EXAFS fit determines one radius (R) for each shell (resolution for k range from 2-12.5 $Å^{-1}$ is 0.148 Å). See Figure S31 for the DFT calculated structure of **3**.

Complex **3**	N	DFT model	XAFS R (Å)
Cu–N1	4	1.977	1.94
Cu–N5		1.993	
Cu–N3		1.961	
Cu–O1		2.097	
Cu–O2	3	2.839	2.89
Cu–N2		2.919	
Cu–N4		2.918	
Cu–C20	4	2.933	3.08
Cu–C24		2.934	
Cu–C8		3.156	
Cu–C11		3.158	
Cu–C7	2	3.287	3.28
Cu–C12		3.286	

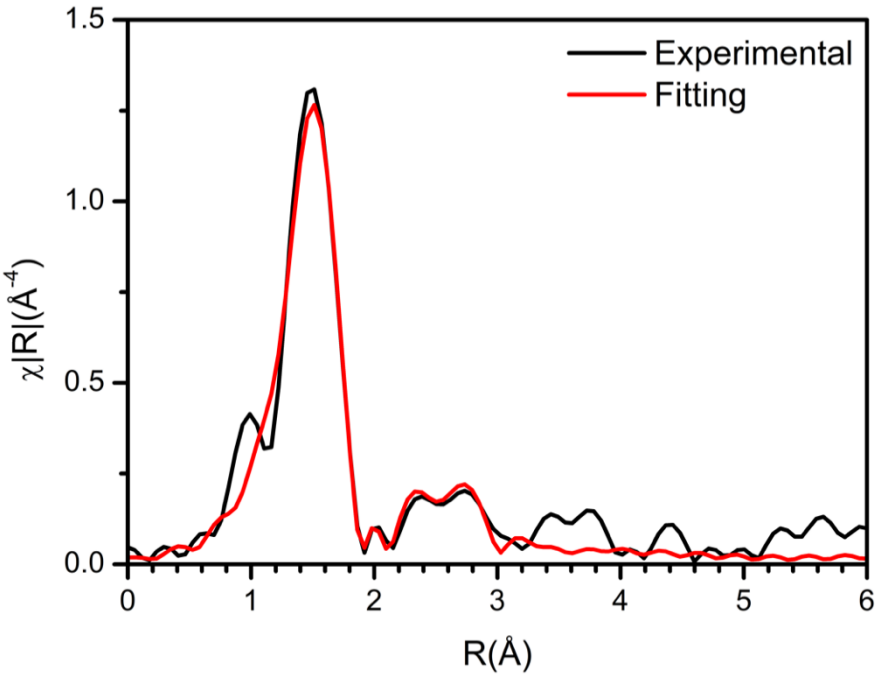

Figure S30. EXAFS (black) and fit (red) in R-space at the Cu K-edge absorption of **3**.

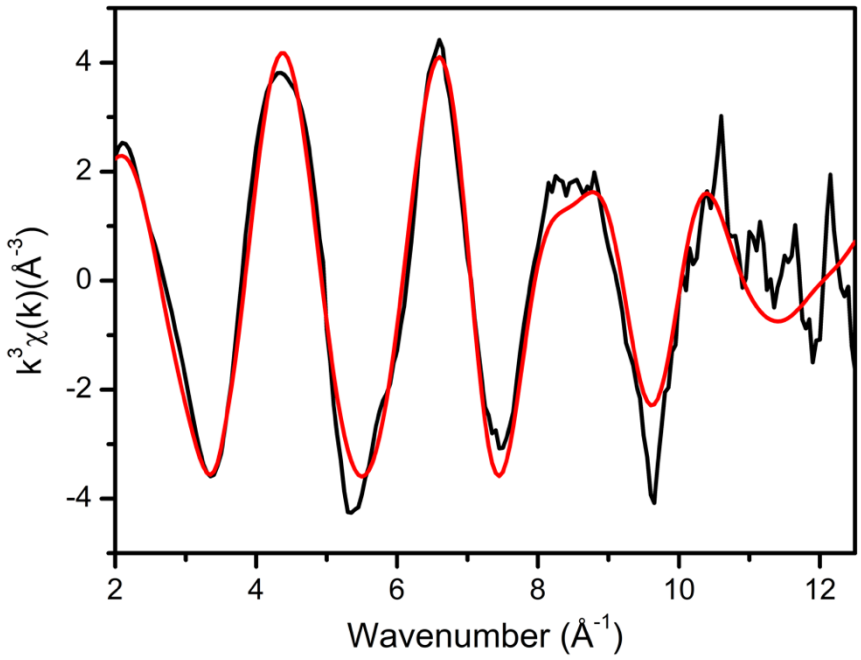

Figure S31. EXAFS (black) and fit (red) in k-space at the Cu K-edge absorption of **3**.

Table S5. EXAFS fitting results for **3** with altered or removed superoxo contributions.

Complex	N/Path	R (Å)	σ^2 (Å^2)	ΔE_0	Error *F*
[**3**] Best Fit	4 Cu-N/O	1.94	690	5.26	0.32
	3 Cu-N/O	2.89	301		
	4 Cu-C/N	3.08	371		
	2 Cu-C/N	3.28	169		
O1 shell*	3 Cu-N/O	1.98	352	5.95	0.29
	1 Cu-N/O	*1.86*	*-130*		
	3 Cu-N/O	2.87	324		
	4 Cu-C/N	3.06	410		
	2 Cu-C/N	3.26	88		
O2 shell*	4 Cu-N/O	1.94	687	5.22	0.31
	1 Cu-N/O	*2.85*	*-430*		
	2 Cu-N/O	2.99	*-30*		
	4 Cu-C/N	3.23	274		
	2 Cu-C/N	3.47	267		
no O2	4 Cu-N/O	1.94	694	5.35	0.33
	2 Cu-N/O	2.86	528		
	4 Cu-C/N	3.21	918		
	2 Cu-C/N	3.49	1959		
no superoxo	3 Cu-N/O	1.95	548	6.57	0.36
	2 Cu-N/O	2.86	509		
	4 Cu-C/N	3.23	1019		
	2 Cu-C/N	3.59	1828		

*Without changing the total number of scatterers, attempts to fit O1 or O2 in separate shells results in negative Debye-Waller factors (italicized), indicating that these scatterers are within resolution of N-atoms at similar distance (R). This is supported by the calculated resolution of 0.15 Å and DFT-predicted bond lengths.

The estimated standard deviations in R are $\pm$0.02 Å. The σ^2 values are multiplied by 10^5. s_0^2 = 0.9. Fitting range: k: 2-12.5 $Å^{-1}$. N, Coordination numbers; R, interatomic distances; $\sigma^{2,}$ Debye-Waller factors (the mean square deviations in interatomic distance). Error F is $[\sum k^6(\chi_{exptl} - \chi_{calcd})^2 / \sum k^6(\chi_{exptl}{}^2]^{1/2}$. Errors in the identity of the scatterer Z are $\pm$1.

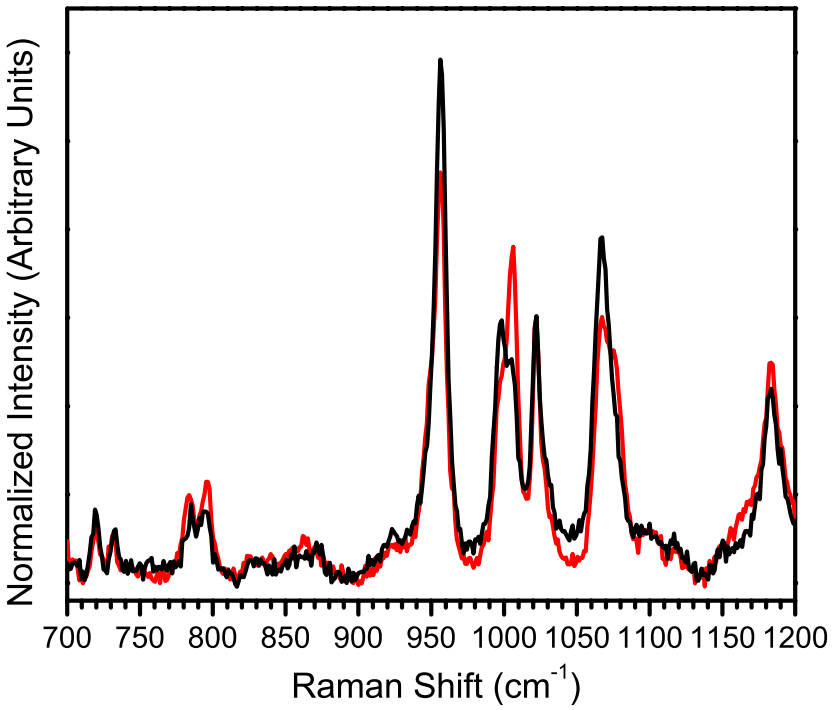

Figure S32. Expanded Raman spectrum of **3** generated at room temperature with $^{16}O_2$ (black) and $^{18}O_2$ (red).

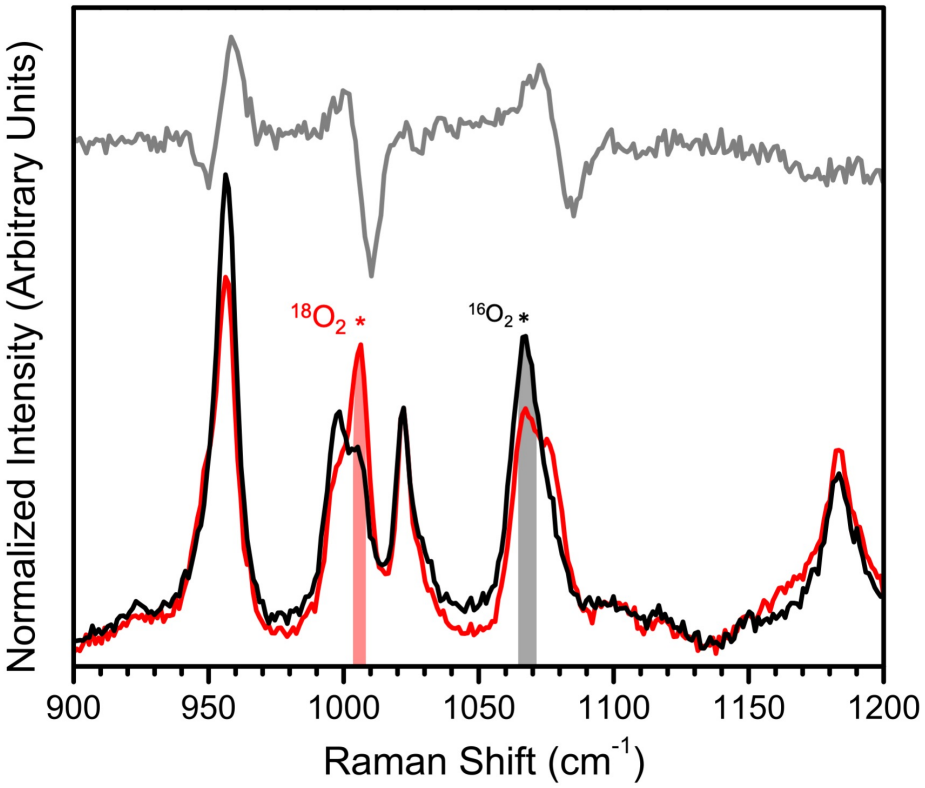

Figure S33. Raman spectrum of **3** showing the superoxo stretching region with a superimposed $^{16}O_2 - {}^{18}O_2$ difference spectrum (gray).

DFT Computations

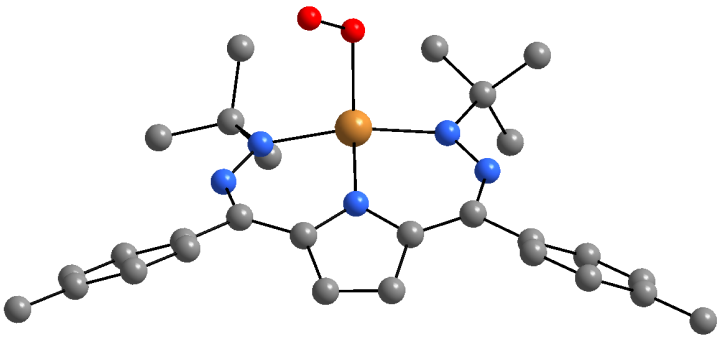

Figure S34. Calculated structure of **3**.

Table S6. Coordinates of calculated structure of **3**.

Cu	31.17529	4.8888	6.91961
N	29.58277	3.77729	6.47256
N	29.14702	2.80476	7.17626
N	31.76253	3.57285	8.24953
N	34.03981	5.22812	7.35891
N	33.01564	5.55897	6.65206
C	26.01684	-1.02433	11.40065
H	26.56306	-1.70509	12.07294
H	25.38462	-1.63306	10.73953
H	25.35404	-0.40973	12.03117
C	26.96515	-0.16258	10.60853
C	27.90026	0.66416	11.25217
H	27.93201	0.69043	12.34528
C	28.77329	1.47184	10.52722
H	29.4593	2.13454	11.05794
C	28.7537	1.47919	9.11764
C	27.80833	0.66016	8.47172
H	27.77229	0.65563	7.38186
C	29.6666	2.35266	8.35421
C	31.0014	2.56766	8.76401
C	31.8232	1.76097	9.65478
C	33.06744	2.32703	9.66398
C	33.01369	3.48407	8.77907
C	34.05434	4.36765	8.4139
C	28.92701	3.85462	5.10646
C	27.70672	2.93845	4.9869
H	27.9795	1.87969	5.08471
H	27.24747	3.08988	3.99805
H	26.96068	3.17205	5.75864
C	30.00202	3.4348	4.08791
H	30.90658	4.05067	4.19566
H	29.61728	3.5575	3.06431

H	30.28469	2.38165	4.23248
C	28.51009	5.31495	4.88814
H	27.73809	5.61137	5.61209
H	28.10279	5.43493	3.87336
H	29.36208	5.99747	5.00356
C	33.44253	6.50246	5.53327
C	32.20488	6.9145	4.73851
H	31.69508	6.0384	4.31298
H	32.50574	7.56416	3.90374
H	31.49013	7.46919	5.36111
C	34.4308	5.75923	4.62094
H	35.31518	5.44126	5.18877
H	34.75758	6.4186	3.80292
H	33.96171	4.86752	4.17818
C	34.10003	7.74586	6.15441
H	33.39831	8.25776	6.82979
H	34.38811	8.44807	5.35793
H	34.99474	7.46627	6.72551
C	35.36273	4.29868	10.56448
C	36.57175	4.32626	11.26164
C	37.797	4.44392	10.59249
C	37.76596	4.54182	9.19019
C	36.56529	4.51673	8.4886
H	36.56471	4.59488	7.40054
C	39.10361	4.47522	11.34181
C	35.33453	4.38123	9.16086
C	26.93837	-0.1432	9.20537
H	26.2223	-0.7771	8.67538
H	34.4241	4.24558	11.11884
H	36.55995	4.2712	12.35381
H	38.70543	4.63594	8.63858
H	38.94334	4.40028	12.42646
H	39.65658	5.40785	11.14341
H	39.75714	3.64127	11.03768
O	30.31058	6.76208	7.2962
O	29.3221	6.69079	8.0937
H	31.5241	0.9234	10.17826
H	33.88826	1.99796	10.19595

Table S7. Tabulated energies for calculation of O–H BDE. Phenol BDE determined from experimental published value (*J. Org. Chem.* ***1996,*** *61* (26), 9259-9263.)

	CuLOO$^{\bullet}$ (**3**)	Phenol	→	CuLOOH	PhO$^{\bullet}$	Reaction Energy	O–H BDE = Reaction energy – 88 kcal/mol (Phenol BDE)
Energy (kcal/mol)	-1978018.05	-192949.98		-1978407.10	-192548.38	-17.88	70

Table S8. Kohn-Sham orbital contributions in **3**.

Complex MO	**3** alpha 141
3dz2	0.022626
3dxz	0.004238
3dyz	0.057808
3dx2y2	0.241331
3dxy	0.425581
4pz	-0.001283
4px	-0.006088
4py	-0.004104
% p character	-0.011475
% d character	0.751584

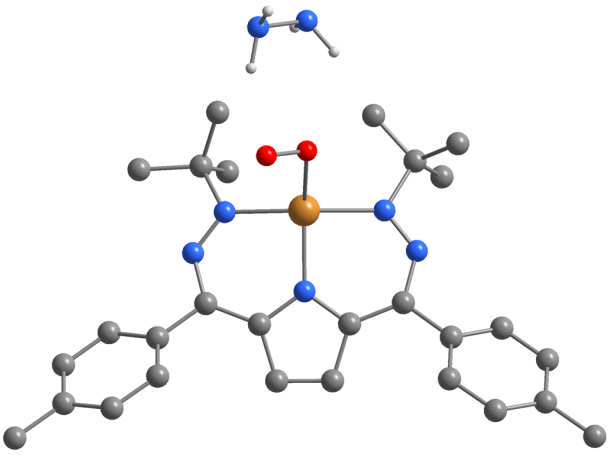

Figure S35. Calculated structure of **3** and hydrazine intermediate.

Table S9. Coordinates for the structure of **3** and hydrazine intermediate.

Cu	31.1520961	4.96742611	7.09701793
N	29.5084229	3.8813358	6.68779944
N	29.1124132	2.8606059	7.3202899
N	31.784827	3.5422425	8.31199369
N	34.0522267	5.19957277	7.46960959
N	33.0338486	5.55543415	6.79749953
C	26.2171294	-1.3622029	11.288185
H	26.7983196	-2.0418541	11.9367966
H	25.6064511	-1.9783707	10.6083817
H	25.5250088	-0.8150836	11.9545172

C	27.1104947	-0.421836	10.5425768
C	28.0537588	0.3624592	11.2242758
H	28.1261911	0.2870239	12.3165244
C	28.8851395	1.24623867	10.5467349
H	29.5851539	1.86939029	11.1158526
C	28.8155348	1.3802341	9.14694875
C	27.8587767	0.60784568	8.46428141
H	27.7850948	0.68942545	7.37480749
C	29.6870619	2.32476252	8.43049646
C	31.0315217	2.51945645	8.79760305
C	31.860734	1.66959357	9.62502126
C	33.105575	2.22771445	9.63752075
C	33.0376924	3.42225477	8.82075146
C	34.0762753	4.32182157	8.50185278
C	28.80283	4.04799722	5.35952899
C	27.465712	3.32570811	5.32745958
H	27.5798921	2.23206218	5.3862737
H	26.9469164	3.56519786	4.38303899
H	26.8216777	3.64379425	6.1651498
C	29.7492224	3.46553225	4.31149833
H	30.7364537	3.96097982	4.34061371
H	29.3265728	3.60184923	3.30024942
H	29.9049477	2.38532927	4.47907257
C	28.6008012	5.53839151	5.13747539
H	27.9242504	5.96877289	5.89584209
H	28.1562577	5.71264771	4.14221502
H	29.5565493	6.08736641	5.17725383
C	33.449883	6.45880982	5.64785938
C	32.2141229	6.76803044	4.82527021
H	31.756215	5.84246354	4.43395715
H	32.4826496	7.39623441	3.9584581
H	31.4566396	7.31217348	5.41151355
C	34.4755901	5.72688049	4.79087458
H	35.3827681	5.48418181	5.36899903
H	34.7717675	6.3559446	3.93310327
H	34.0601921	4.78405252	4.39128644
C	34.0390007	7.73595073	6.23460716
H	33.3020465	8.26294522	6.866598
H	34.3441368	8.41907341	5.4225266
H	34.9272995	7.50875818	6.84858871
C	35.4268223	4.05705354	10.6090844
C	36.6440235	4.076924	11.2860065
C	37.8440242	4.3664662	10.6235227
C	37.7720278	4.64595981	9.24882164
C	36.5627281	4.62563738	8.56709733
H	36.5395585	4.8402064	7.49337349
C	39.1561895	4.37167483	11.3417775
C	35.3583483	4.31699197	9.22949098
C	27.0317053	-0.2758602	9.14992467
H	26.3061488	-0.8771212	8.58814563
H	34.5049208	3.8651409	11.1703452
H	36.6593782	3.87870932	12.3649665
H	38.6917236	4.88429472	8.69958775
H	39.0249133	4.36914123	12.4362359

H	39.7668511	5.25082312	11.0705777
H	39.7602362	3.48162686	11.0827875
O	30.4179798	6.84379385	7.42206331
O	29.3702669	6.79038707	8.1500197
H	31.5485239	0.73755855	10.0996106
H	34.0020871	1.82874829	10.1148124
H	28.2627587	8.39719662	7.16415936
H	30.1659717	9.0835066	6.29381847
N	28.1348265	9.12355487	6.44214967
N	29.352214	9.28294835	5.69427798
H	29.3524785	8.53528813	4.99447145
H	28.0134507	9.99479081	6.96736963

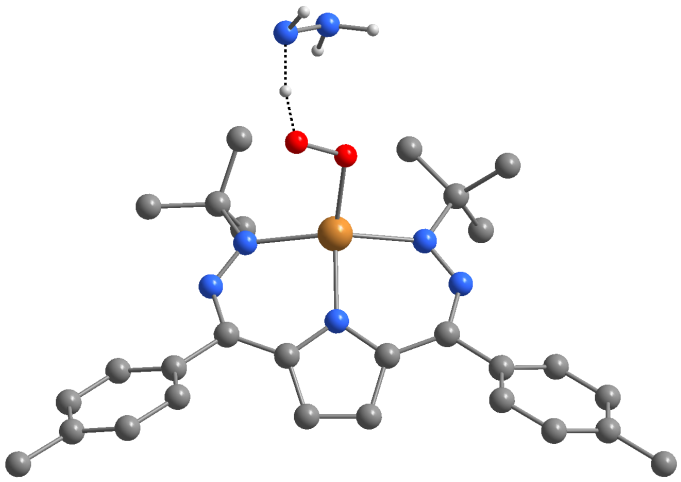

Figure S36. Calculated structure of TS1.

Table S10. Coordinates for TS1.

Cu	31.0973716	5.06947331	7.17229012
N	29.4775306	3.93515599	6.70626956
N	29.0914737	2.8988614	7.31494724
N	31.7665704	3.57934546	8.28546838
N	34.0578773	5.19988199	7.42840761
N	33.0403114	5.58714623	6.78106673
C	26.19616	-1.3454756	11.2591182
H	26.7292826	-1.883259	12.0622944
H	25.7488658	-2.0912953	10.5815018
H	25.3612311	-0.8073422	11.7467306
C	27.0993715	-0.4044932	10.5261875
C	28.0456843	0.37288901	11.2102031
H	28.1262734	0.28521236	12.3009789
C	28.8731577	1.26486235	10.5366056
H	29.5765023	1.88180389	11.1083024
C	28.7975581	1.41193749	9.13897305
C	27.8382221	0.64412254	8.4535247
H	27.7610522	0.73397498	7.36493692

C	29.6639106	2.36254764	8.42440984
C	31.0109562	2.55977045	8.77913559
C	31.8403564	1.70659495	9.60125388
C	33.0875735	2.25844454	9.60712993
C	33.021844	3.45325762	8.79262474
C	34.0695442	4.34148582	8.47762083
C	28.8046487	4.09831618	5.3610729
C	27.4499912	3.41063571	5.31335176
H	27.5340522	2.31673319	5.40798496
H	26.9637906	3.6323784	4.34732147
H	26.7896151	3.77216277	6.12024293
C	29.7568241	3.4758613	4.3421767
H	30.7599089	3.93598261	4.39791703
H	29.3671206	3.61853307	3.31872262
H	29.8702809	2.39211954	4.52134314
C	28.6502981	5.58982868	5.11893796
H	27.9550026	6.04125976	5.84717383
H	28.2615362	5.77375698	4.10242048
H	29.6243659	6.09915329	5.21454066
C	33.4632799	6.44974171	5.60402928
C	32.2230138	6.77814395	4.79769959
H	31.7452978	5.85966665	4.4137109
H	32.4894871	7.40338068	3.92785184
H	31.4860737	7.32746303	5.4072205
C	34.4609963	5.68168822	4.74690523
H	35.370506	5.42849979	5.3169306
H	34.7594328	6.29133579	3.87580055
H	34.020495	4.74219497	4.36660317
C	34.0896021	7.72358341	6.16103851
H	33.3741981	8.27417665	6.79778537
H	34.3939876	8.3889557	5.33386655
H	34.9837461	7.48799679	6.76363001
C	35.4014907	4.08934334	10.5961098
C	36.6120989	4.11422958	11.2846607
C	37.8181578	4.39872717	10.631078
C	37.7591783	4.66684175	9.25346099
C	36.5567282	4.64110993	8.5597995
H	36.5442111	4.8464112	7.48407661
C	39.1243518	4.40999435	11.3605752
C	35.3458232	4.33831175	9.21350846
C	27.0153271	-0.2458346	9.13458584
H	26.2897891	-0.8445475	8.56988028
H	34.4733982	3.90174331	11.1487189
H	36.6177441	3.92424178	12.3652077
H	38.6850647	4.89907135	8.71194979
H	38.9841911	4.40535339	12.4538912
H	39.7324493	5.29279316	11.0951966
H	39.7352726	3.52391927	11.1041014
O	30.4866668	6.90432559	7.47394991
O	29.2518303	6.94131757	8.07424289
H	31.5248237	0.77541306	10.0752457
H	33.9858067	1.85720067	10.0795284
H	28.6523308	7.73101301	7.45042182
H	30.072444	9.38174437	6.10959454

N	28.2299481	8.7406008	6.71802236
N	29.1828056	8.98874293	5.77576809
H	29.3414415	8.17144815	5.1846851
H	28.2647038	9.54005302	7.36661022

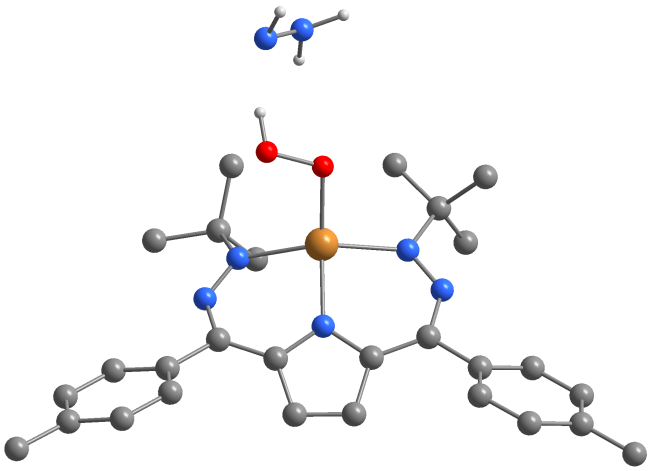

Figure S37. Calculated structure of LCuOOH and hydrazine radical intermediate.

Table S11. Coordinates for LCuOOH and hydrazine radical intermediate.

Cu	31.0688361	5.08406071	7.35414231
N	29.4946053	3.89089277	6.77224089
N	29.1183248	2.84062676	7.35046879
N	31.7659128	3.53000316	8.32608357
N	34.0279826	5.21776052	7.51847589
N	32.9896759	5.6435104	6.92882924
C	26.1086889	-1.2419289	11.3970145
H	26.6657473	-1.9138453	12.073274
H	25.4892771	-1.8621453	10.7285941
H	25.4202841	-0.6584566	12.0368083
C	27.0302995	-0.3432755	10.6346202
C	28.0634057	0.34686037	11.2879857
H	28.1947612	0.21895564	12.3697418
C	28.9121661	1.20293624	10.5968748
H	29.6845692	1.75436046	11.1454757
C	28.7750659	1.39795075	9.20891114
C	27.729897	0.71812709	8.55459052
H	27.5984261	0.85153819	7.47563701
C	29.6579834	2.31889055	8.4831974
C	31.0137134	2.50294198	8.81563188
C	31.8581006	1.62734204	9.59369153
C	33.1090732	2.17318033	9.58300823

C	33.0312868	3.3898673	8.80543581
C	34.0728985	4.29246183	8.50572539
C	28.9785197	4.00852973	5.35615335
C	27.7440898	3.15514414	5.12135438
H	27.9561727	2.07886282	5.22045013
H	27.3696632	3.33652175	4.09879118
H	26.938414	3.40967165	5.83098082
C	30.1337478	3.52819587	4.47751187
H	31.0622164	4.08621031	4.69723661
H	29.8894665	3.67072705	3.41002057
H	30.3370184	2.45654906	4.65007522
C	28.6721328	5.47593864	5.10773873
H	27.7943048	5.80029496	5.69197133
H	28.4592614	5.64460382	4.03730812
H	29.5277287	6.10977079	5.39835051
C	33.3767351	6.58709698	5.79925351
C	32.1244353	6.95844245	5.02805412
H	31.651195	6.06917602	4.57747917
H	32.3843833	7.64535932	4.20361128
H	31.3814732	7.45432229	5.67419628
C	34.3676533	5.88229774	4.88140625
H	35.296751	5.62224709	5.41521831
H	34.6322914	6.53586044	4.03155365
H	33.9353706	4.95153239	4.47116542
C	33.9973626	7.83103147	6.42559136
H	33.2832159	8.33008985	7.10457344
H	34.2816784	8.55079548	5.63777121
H	34.9018836	7.57237531	7.00270996
C	35.4854	3.93512351	10.5608608
C	36.7231729	3.92345603	11.1999459
C	37.9049651	4.22376349	10.5101922
C	37.7931775	4.54393294	9.14708195
C	36.5631976	4.55635358	8.50323203
H	36.5090255	4.80437495	7.43776994
C	39.2383291	4.20123431	11.188629
C	35.3762675	4.24097955	9.1931961
C	26.8834114	-0.1341905	9.25529727
H	26.0853414	-0.6610171	8.7170385
H	34.5796149	3.72999304	11.1435026
H	36.7690584	3.69246532	12.2715737
H	38.6982107	4.7905779	8.57721313
H	39.1392002	4.18648823	12.2864835
H	39.8520118	5.07629676	10.911249
H	39.8242385	3.30728109	10.9026851
O	30.3349	6.83778927	7.59151876
O	28.9683583	6.73905378	8.00883567
H	31.5488265	0.68574633	10.0508496
H	34.0163521	1.75524114	10.0225059
H	29.5834966	9.83894386	5.41872129
N	28.058092	8.83323113	6.34921328
N	28.8577776	9.124283	5.31697389
H	29.1378717	8.31775064	4.76012846
H	28.04885	9.67291852	6.94729587
H	28.5249761	7.39204629	7.38960094

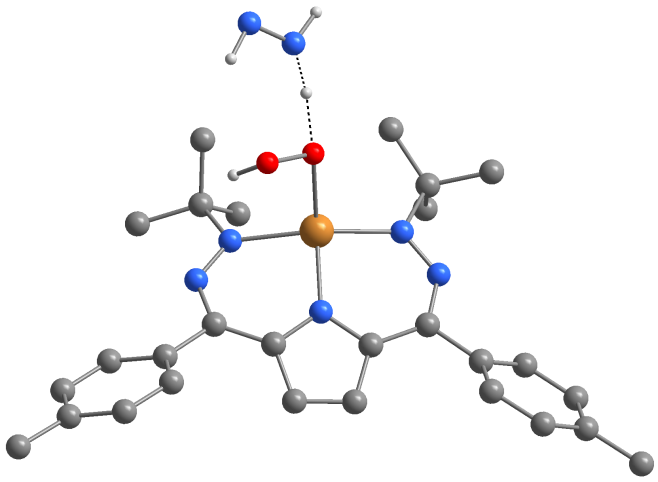

Figure S38. Calculated structure of TS2.

Table S12. Coordinates for TS2.

Cu	31.1972084	5.02761204	7.05631882
N	29.6404532	3.87137151	6.57178719
N	29.1366206	2.93354982	7.28744032
N	31.7672907	3.71148537	8.36718956
N	34.0808425	5.33310118	7.54436804
N	33.0462626	5.72650155	6.89096651
C	26.0027888	-1.058035	11.2904756
H	25.8641928	-2.0202278	10.7679618
H	24.9990459	-0.5993994	11.3742301
H	26.3413754	-1.2720021	12.3178613
C	26.9570223	-0.1614034	10.5657491
C	27.8491687	0.66860668	11.2572718
H	27.856153	0.6535581	12.3544304
C	28.7192488	1.52253176	10.5833816
H	29.381099	2.17725158	11.1622719
C	28.7405692	1.57916852	9.17923461
C	27.8377902	0.75122063	8.48425104
H	27.8359828	0.76974385	7.38900277
C	29.6399713	2.49536853	8.45270295
C	30.9661759	2.74462877	8.90274121
C	31.7353509	1.98368499	9.84333349
C	33.0026039	2.51808127	9.85350525
C	33.0039371	3.61586009	8.93102876
C	34.0889964	4.45351011	8.55423475
C	29.0602071	3.95461496	5.18048487
C	28.0196294	2.87605052	4.92590331
H	28.4431129	1.86561576	5.04778871
H	27.6454055	2.97198427	3.89141953
H	27.1614032	2.96331844	5.61155922

C	30.2345244	3.77853618	4.2213268
H	31.0134965	4.54687031	4.3877441
H	29.8949918	3.86990959	3.17411377
H	30.7045431	2.78715589	4.34725219
C	28.4404804	5.33592565	5.00699038
H	27.6190357	5.49590978	5.7299099
H	28.0193501	5.44644948	3.99205385
H	29.1917856	6.13182156	5.14753496
C	33.4362644	6.61431499	5.73581772
C	32.1931422	7.35263366	5.26947017
H	31.3699397	6.65868444	5.01377024
H	32.4203625	7.94232374	4.36464398
H	31.8299223	8.04602954	6.0468422
C	33.9810263	5.72209659	4.62428932
H	34.8624756	5.15572532	4.97376866
H	34.2877638	6.32937152	3.75328778
H	33.2228777	4.9965756	4.27866821
C	34.4945361	7.62384891	6.16697456
H	34.1658079	8.19325331	7.05422825
H	34.6770026	8.3443191	5.35002505
H	35.4498729	7.13232376	6.41142812
C	35.5176349	4.23873541	10.6248634
C	36.7674619	4.18055003	11.2402265
C	37.9521019	4.23731982	10.4957599
C	37.834113	4.36456021	9.10160527
C	36.5916148	4.4280338	8.48353857
H	36.5273387	4.5220195	7.3930375
C	39.2962908	4.17466556	11.1516918
C	35.400421	4.35756882	9.23080813
C	26.9731301	-0.0987802	9.16292207
H	26.295553	-0.7428361	8.58762305
H	34.6137014	4.22658967	11.2449827
H	36.8237144	4.10214052	12.3333845
H	38.7431764	4.40415559	8.48763911
H	39.2134992	4.15473292	12.2507923
H	39.9231225	5.04227269	10.8767342
H	39.8617991	3.2751851	10.8456178
O	30.1855749	6.78518471	7.35339764
O	29.0565924	6.44774356	8.23089492
H	31.3855821	1.11385596	10.4023158
H	33.8604047	2.16357139	10.4273466
H	29.5775169	7.83789013	6.6941779
N	27.6801671	8.79279195	6.50512509
N	28.9043011	8.66829876	6.24619519
H	29.2553287	9.32830292	5.53624849
H	27.4616122	8.07173607	7.22384595
H	28.6313567	5.71065978	7.73878091

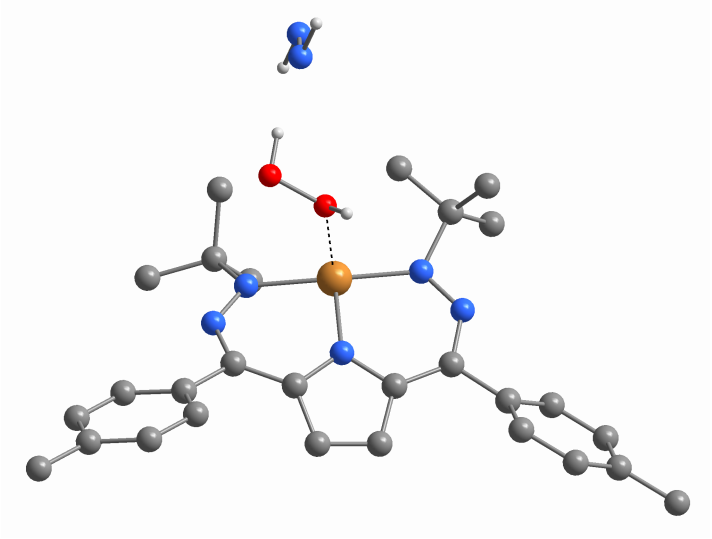

Figure S39. Calculated structure of LCu + H_2O_2 + diazene intermediate.

Table S13. Coordinates for intermediate LCu + H_2O_2 + diazene intermediate.

Cu	31.3491524	4.64476802	6.78850511
N	29.7223199	3.65350169	6.44541926
N	29.2059082	2.78094001	7.22166134
N	31.8094224	3.53448996	8.31835699
N	34.0685062	5.26970299	7.51185267
N	33.0540576	5.53455717	6.75199853
C	25.8700485	-0.7157625	11.546617
H	26.3792952	-1.3883625	12.2596703
H	25.2169787	-1.332219	10.9070861
H	25.217484	-0.0606938	12.1535812
C	26.8499799	0.0767907	10.7394807
C	27.8794744	0.80059017	11.3598671
H	27.9616393	0.7871479	12.4541985
C	28.7883104	1.54789075	10.6186149
H	29.5596034	2.12674617	11.1400063
C	28.7191468	1.59663272	9.21282598
C	27.6786397	0.87981549	8.59171685
H	27.6011377	0.89605575	7.49939718
C	29.6716652	2.39858507	8.42892475
C	31.0204969	2.57793341	8.85539186
C	31.8128523	1.78130385	9.75898636
C	33.0768993	2.31851583	9.75752992
C	33.0633309	3.42506853	8.83095677
C	34.1281698	4.26636351	8.41496592
C	29.2093206	3.59701074	5.02923302
C	28.0957781	2.5835637	4.83981323
H	28.4202897	1.56179844	5.09672896
H	27.7739192	2.58688146	3.78319628
H	27.2199562	2.82462213	5.46521389
C	30.4142818	3.24324382	4.16080861
H	31.2363048	3.97241065	4.30709781

H	30.1388911	3.26005842	3.09146801
H	30.7990933	2.23775857	4.40538673
C	28.7213853	5.00362468	4.69987803
H	27.8483363	5.28059589	5.31799427
H	28.4282875	5.0732723	3.63694415
H	29.5219305	5.74456494	4.88635045
C	33.2580985	6.85487251	6.04691954
C	32.0093737	7.11594519	5.22199301
H	31.8595488	6.33059292	4.45839815
H	32.0889508	8.08524561	4.69845001
H	31.1092595	7.15054788	5.86316547
C	34.4777434	6.74530938	5.13965362
H	35.3852402	6.51263108	5.72215159
H	34.6441846	7.69820893	4.60616293
H	34.3395089	5.95144371	4.38350529
C	33.4431751	7.95761363	7.0837868
H	32.5643384	8.015367	7.75201908
H	33.566408	8.94025288	6.59479534
H	34.3352798	7.76569569	7.7034341
C	35.6299597	3.99151483	10.4307468
C	36.900852	3.91761599	10.9989734
C	38.05741	4.00022647	10.2136759
C	37.8902482	4.17266263	8.83005177
C	36.6250502	4.25253258	8.2597916
H	36.5213995	4.38558079	7.17632065
C	39.4244018	3.91821903	10.8188836
C	35.4628897	4.15368027	9.04664478
C	26.7705127	0.13902444	9.34021589
H	25.9768635	-0.4164265	8.82418966
H	34.7479088	3.96284	11.0806565
H	36.9972533	3.80688527	12.0864798
H	38.7773908	4.23629079	8.1868546
H	39.3822095	3.8844268	11.9198882
H	40.0487737	4.78329465	10.5313759
H	39.9685031	3.01721105	10.4806231
O	30.060129	6.37417235	8.06834714
O	28.6180726	6.53343601	8.10276233
H	31.4739333	0.91731484	10.3345018
H	33.9519576	1.92616579	10.2790888
N	28.5158976	8.86556472	6.46798835
N	28.6071551	9.03792373	5.25132185
H	28.7497947	8.09838731	4.81500956
H	28.3718083	9.79751631	6.91677373
H	28.524846	7.32509261	7.49447635
H	30.3100563	6.61715302	8.98434798

Table S14. Tabulated Gibbs free energies for the oxidation of diphenylhydrazine (DPH) and hydrazine from frequency calculations using M06L functional and def2-TZVP basis set.

Reaction and Gibbs Free Energy Value (Eh)					($G_{prod.} - G_{reac.}$)	
DPH	½ O_2	→	Azobenzene	H_2O	Hartrees	kcal/mol

-573.27	-75.10		-572.10	-76.34	0.0625	-39.19
Hydrazine	½ O_2	→	Diazene	H_2O		
-111.72	-75.10		-110.53	-76.34	0.0488	-30.64

Table S15. Mulliken charges for H's involved in the dehydrogenation of hydrazine by **3** for the first H-atom transfer event (H75) and the second H-atom transfer event (H70).

	Mulliken Charge	
Complex	H75	H70
$LCuO_2$	0.272046	0.276732
TS1	0.278173	0.285222
LCuOOH	0.359653	0.296413
TS2	0.38196	0.333127
LCu H_2O_2	0.39112	0.372452

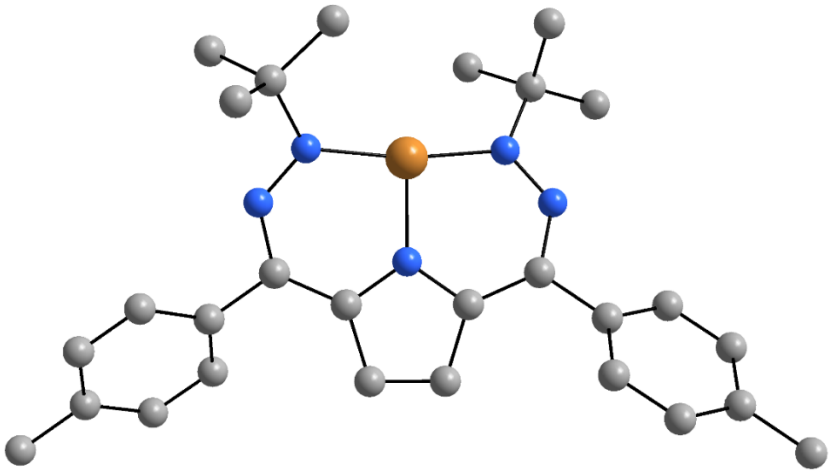

Figure S40. Calculated structure for **1** in the singlet ground state.

Table S16. Coordinates for **1** in the singlet ground state.

Cu	31.439971	4.4792189	6.61802845
N	29.5658134	4.12471322	6.68095553
N	29.0147111	3.20428877	7.40771924
N	31.8134277	3.47431152	8.20280796
N	34.1965491	4.84365836	7.21822534

N	33.257519	4.96909908	6.32702964
C	26.3743178	-2.0871464	10.1048753
H	25.9630801	-1.8886384	11.1079973
H	26.9534525	-3.019249	10.1582243
H	25.5181219	-2.2543997	9.43308152
C	27.2257325	-0.9387732	9.62814883
C	26.6610782	0.32595985	9.38485968
H	25.5899376	0.47472809	9.54846006
C	27.4371203	1.39576091	8.95112353
H	26.9793226	2.3691037	8.7713482
C	28.8237597	1.24931217	8.74820177
C	29.387787	-0.0184535	8.97748375
H	30.4495845	-0.1766119	8.77906047
C	29.6544867	2.37672808	8.26916906
C	30.9588712	2.59790013	8.79332603
C	31.6128512	2.05354985	9.96839324
H	31.1946368	1.32218902	10.6538891
C	32.8733546	2.60349017	10.0164637
H	33.6374729	2.41906694	10.766817
C	32.9777344	3.5219971	8.8985544
C	34.0639009	4.33387985	8.46160907
C	28.5574952	5.05911801	6.04774374
C	27.1744808	4.97786688	6.69877694
H	26.7145046	3.99094622	6.55761106
H	26.520488	5.73769867	6.24477399
H	27.2355368	5.1757444	7.77841106
C	28.4731613	4.67033359	4.5614006
H	29.4590043	4.74786422	4.07976865
H	27.7735861	5.33600493	4.03355458
H	28.1165777	3.63532745	4.45546298
C	29.1236408	6.47731485	6.19567398
H	29.1222053	6.79707989	7.24824969
H	28.5235566	7.19056714	5.61192599
H	30.1623893	6.51914329	5.82566371
C	33.8500466	5.2440818	4.95914287
C	32.6905711	5.39481542	3.97536527
H	32.0534446	4.49511234	3.97541259
H	33.0778698	5.53644947	2.95560826
H	32.0649118	6.26386039	4.22809577
C	34.7416901	4.06220055	4.54611322
H	35.5543758	3.92554989	5.27210231
H	35.1836132	4.24444906	3.55501549
H	34.1579493	3.13032641	4.49861233
C	34.6648463	6.54531206	5.0225209
H	34.0338977	7.38100991	5.36047628
H	35.0596211	6.79070391	4.02547726
H	35.5037848	6.43898358	5.72228839
C	35.0646956	4.85215238	10.7082119
C	36.1646118	5.10831525	11.52911
C	37.4704107	5.10022011	11.022076
C	37.6352742	4.83012803	9.65219947
C	36.5441496	4.5775516	8.82747381
H	36.6937787	4.3658587	7.76818388
C	38.6588706	5.3771213	11.905714

C	35.2321883	4.5749213	9.34041506
C	28.6017648	-1.087266	9.4114036
H	29.0684182	-2.0630989	9.57020397
H	34.0582834	4.89878158	11.1287766
H	36.000641	5.33552535	12.5858385
H	38.6421214	4.81155559	9.22526523
H	38.349403	5.57883837	12.9404432
H	39.2294478	6.24887892	11.5464903
H	39.352957	4.52064842	11.9203142

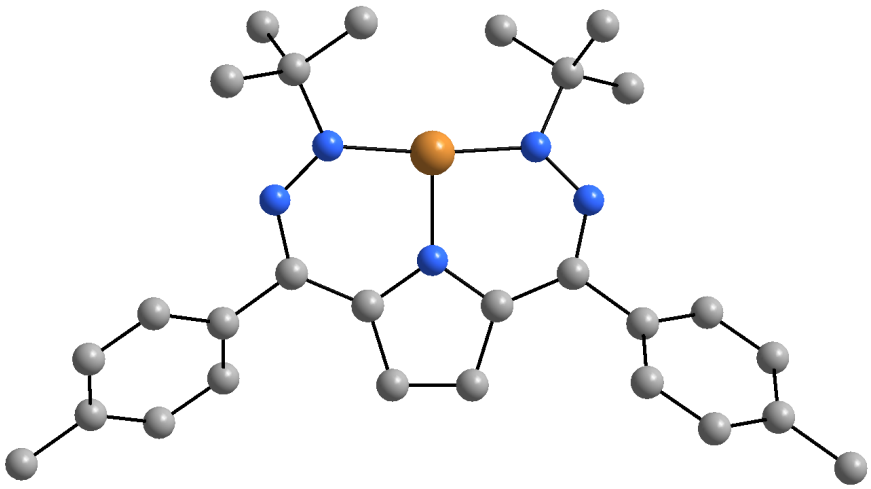

Figure S41. Calculated structure for **1** in the triplet ground state.

Table S17. Coordinates for **1** in the triplet ground state.

Cu	-0.000034	1.565217	0.000004
N	1.798652	1.679066	-0.535294
N	2.712883	0.751178	-0.356048
N	0	-0.290053	0.000047
N	-2.712919	0.751181	0.356028
N	-1.798718	1.679117	0.53526
C	7.163196	-3.843139	0.766084
H	7.216284	-4.638342	0.010112
H	7.156418	-4.326986	1.74834
H	8.087489	-3.259834	0.683274
C	5.941521	-2.976929	0.568406
C	5.912475	-1.984343	-0.422875
H	6.79049	-1.827222	-1.046442
C	4.782315	-1.20076	-0.628616
H	4.780121	-0.439908	-1.40218
C	3.626063	-1.378453	0.151059
C	3.659213	-2.360945	1.153336
H	2.797682	-2.494953	1.800555
C	2.432345	-0.517419	-0.057187

C	1.117826	-1.075919	0.00797
C	0.689815	-2.443259	0.006631
H	1.342562	-3.304236	-0.006633
C	-0.689799	-2.443264	-0.006306
H	-1.342537	-3.304246	0.007036
C	-1.117819	-1.075929	-0.007787
C	-2.432348	-0.517423	0.057259
C	2.368269	2.975194	-1.014651
C	3.467208	2.743533	-2.06493
H	4.327694	2.233613	-1.628137
H	3.798485	3.706247	-2.471178
H	3.089342	2.132325	-2.891849
C	2.939835	3.751567	0.186866
H	2.162815	3.957302	0.932922
H	3.367412	4.709567	-0.131677
H	3.725911	3.162009	0.668809
C	1.211531	3.745671	-1.669932
H	0.828803	3.205417	-2.542976
H	1.542639	4.736524	-1.998153
H	0.375683	3.905639	-0.976242
C	-2.368362	2.97523	1.014604
C	-1.211763	3.745472	1.67043
H	-0.829572	3.20514	2.543666
H	-1.542794	4.736411	1.998463
H	-0.375511	3.905197	0.977158
C	-3.467721	2.743598	2.064444
H	-4.328217	2.234036	1.627252
H	-3.798852	3.706305	2.470828
H	-3.090307	2.132075	2.891335
C	-2.939376	3.751858	-0.18702
H	-2.162042	3.957641	-0.932732
H	-3.366988	4.709844	0.13151
H	-3.725324	3.162463	-0.669374
C	-3.659083	-2.361066	-1.153248
C	-4.795614	-3.144372	-1.353685
C	-5.941445	-2.977013	-0.568495
C	-5.91252	-1.984345	0.422674
C	-4.782367	-1.200733	0.628489
H	-4.780286	-0.439796	1.401971
C	-7.162933	-3.843492	-0.766137
C	-3.626041	-1.378488	-0.151023
C	4.795787	-3.144245	1.353704
H	4.794344	-3.890718	2.145223
H	-2.797488	-2.495092	-1.800378
H	-4.794093	-3.890874	-2.14518
H	-6.790617	-1.827156	1.046102
H	-7.158967	-4.322791	-1.75065
H	-8.087489	-3.261506	-0.677491
H	-7.212657	-4.642326	-0.013756

Table S18. Tabulated NO fractional occupation on Cu for the V2RDM calculated HONO and LUNO states determined by the quotient of the sum of squared atomic orbital coefficients (AO) for Cu divided by the sum of squared atomic orbital coefficients for the complex.

	$\sum AO_{Cu}^2$	$\sum AO_{Tot}^2$	Cu Fractional Contribution
HONO	0.384802	0.814228	0.472642
LUNO	0.371591	0.908608	0.409318

X-ray Crystallography

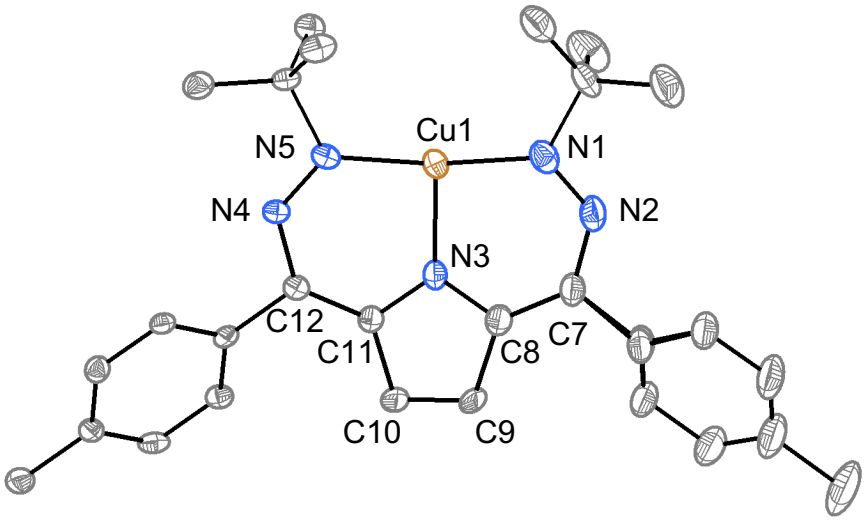

Figure S42. SXRD of **1**. Ellipsoids are set to 50% probability.

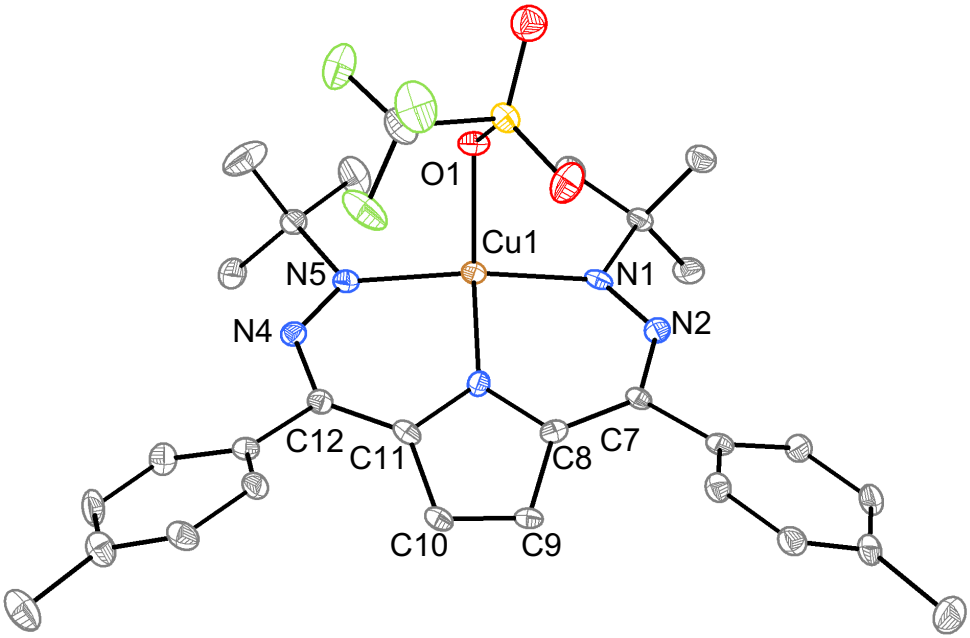

Figure S43. SXRD of **2**. Ellipsoids are set to 50% probability. τ_4 and τ_4' values of 0.49 and 0.50, respectively

Table S19. Comparison of bond lengths for **1** and **2**.

Bond	(1) Å	(2) Å	Δ Å
Cu-N1/ Cu-N5	1.895(3) 1.890(5)	1.976(3) 1.968(3)	0.081 0.078
Cu-N3	1.952(3)	1.891(3)	-0.061
N1-N2/ N5-N4	1.289(3) 1.293(4)	1.285(4) 1.282(4)	-0.006 -0.011
N2-C7/ N4-C12	1.384(4) 1.369(5)	1.364(4) 1.372(4)	-0.020 0.003
C7-C8/ C12-C11	1.398(4) 1.393(4)	1.385(5) 1.382(4)	-0.013 -0.011

C8-C9/ C11-C10	1.453(5) 1.459(5)	1.446(5) 1.455(5)	-0.007 -0.006
C9-C10	1.347(5)	1.336(5)	-0.011
Cu-O1	-	2.076(2)	

Table S20. Crystal data and structure refinement for **1** and **2**.

Identification code	(1)	(2)
Empirical formula	$C_{28}H_{34}CuN_5$	$C_{29}H_{34}CuF_3N_5O_3S$
Formula weight	504.14	653.22
Temperature/K	100(2)	100(2)
Crystal system	monoclinic	triclinic
Space group	C2/c	P-1
a/Å	51.589(3)	13.5820(11)
b/Å	5.7227(4)	16.2112(13)
c/Å	17.4463(11)	16.8010(14)
α/°	90	118.365(2)
β/°	92.884(3)	91.035(3)
γ/°	90	103.702(3)
Volume/Å3	5144.1(6)	3125.4(4)
Z	8	4
ρcalcg/cm3	1.302	1.430
μ/mm-1	0.874	0.824
F(000)	2128.0	1398.0
Crystal size/mm3	0.32 × 0.24 × 0.18	0.165× 0.065 × 0.045
Radiation	MoKα (λ = 0.71073)	MoKα (λ = 0.71073)
2Θ range for data collection/°	4.676 to 48.376	4.494 to 51.458
Index ranges	-58 ≤ h ≤ 58, -6 ≤ k ≤ 6, -20 ≤ l ≤ 19	-15 ≤ h ≤ 16, -19 ≤ k ≤ 19, -20 ≤ l ≤ 20
Reflections collected	13160	39814
Independent reflections	4010 [R_{int} = 0.0524, R_{sigma} = 0.0539]	11867 [R_{int} = 0.0991, R_{sigma} = 0.1037]
Data/restraints/parameters	4010/367/389	11867/34/915
Goodness-of-fit on F2	1.041	1.005
Final R indexes [I>=2σ (I)]	R_1 = 0.0448, wR_2 = 0.0910	R_1 = 0.0511, wR_2 = 0.0871
Final R indexes [all data]	R_1 = 0.0669, wR_2 = 0.0994	R_1 = 0.1033, wR_2 = 0.1009
Largest diff. peak/hole / e Å-3	0.51/-0.33	0.46/-0.43

Appendix II: Chapter II Supplementary Information

NMR spectra

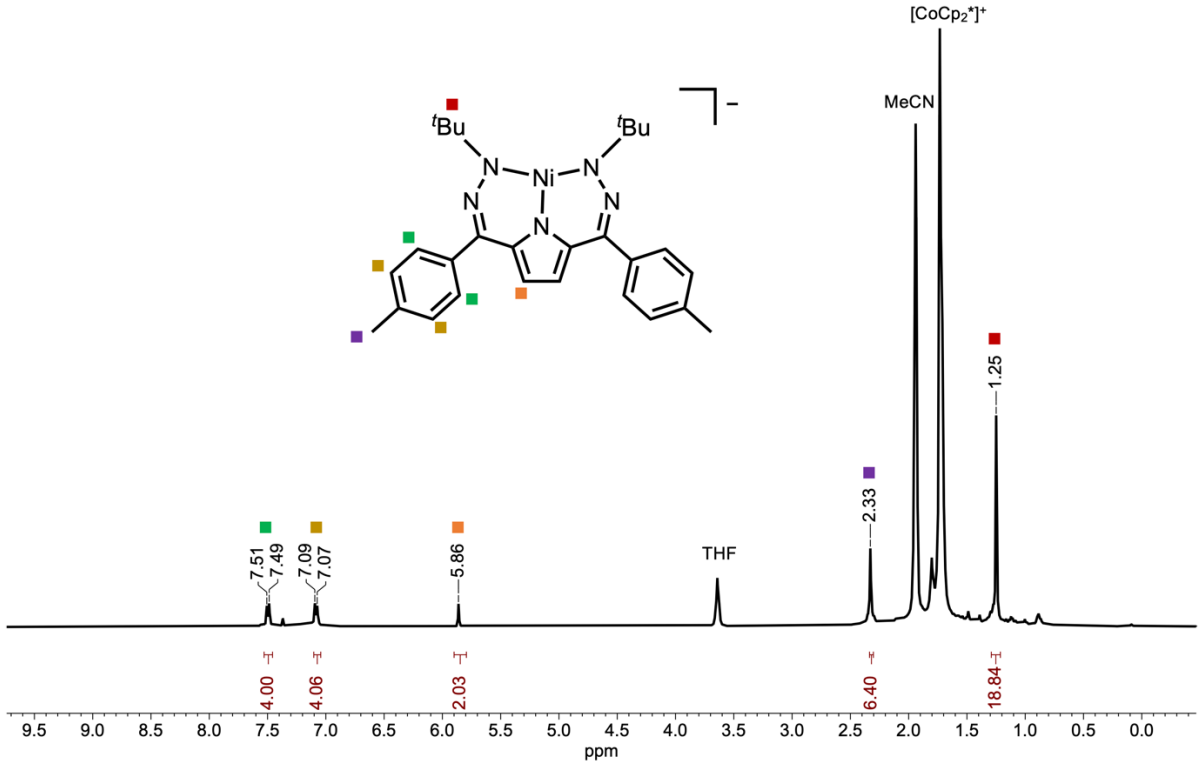

Figure S1. ^{1}H NMR of **2** in CD_3CN.

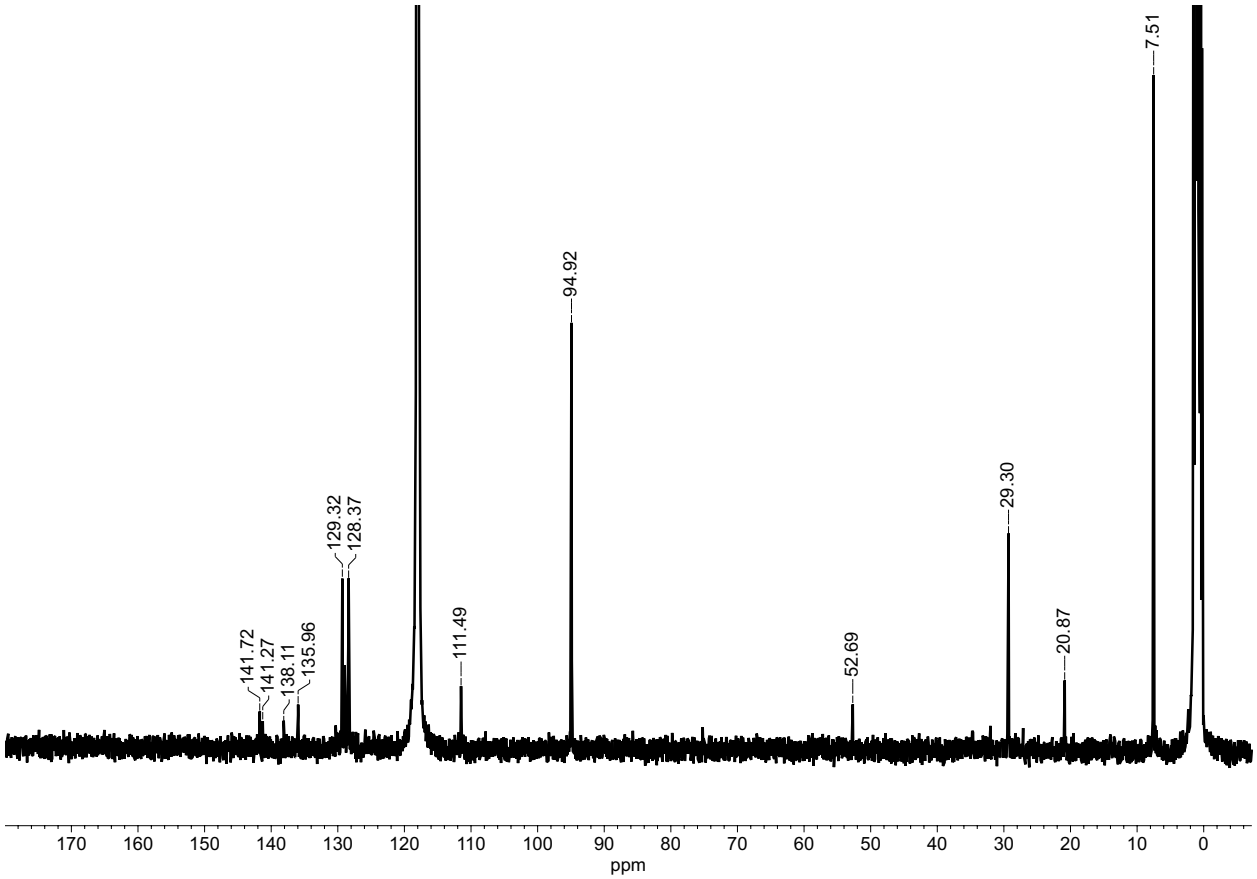

Figure S2. ^{13}C NMR of **2** in CD_3CN.

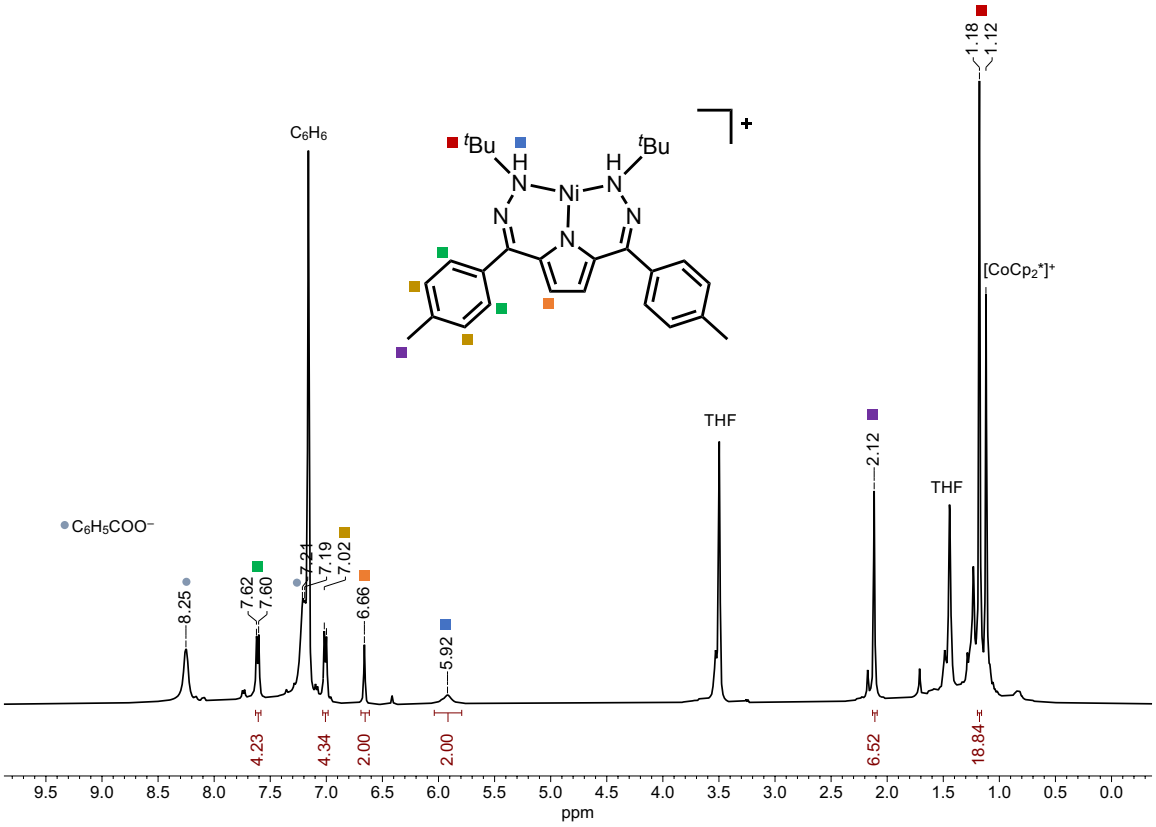

Figure S3. ^{1}H NMR of complex **3**, made in situ from **2** + benzoic acid (2.1 eq) in C_6D_6 + d_8-THF (for solubility). Benzoate peaks (gray) are attributed as counter-anions of complex **3**. Some remaining $[CoCp_2^*]^+$ from complex **2** is also detected.

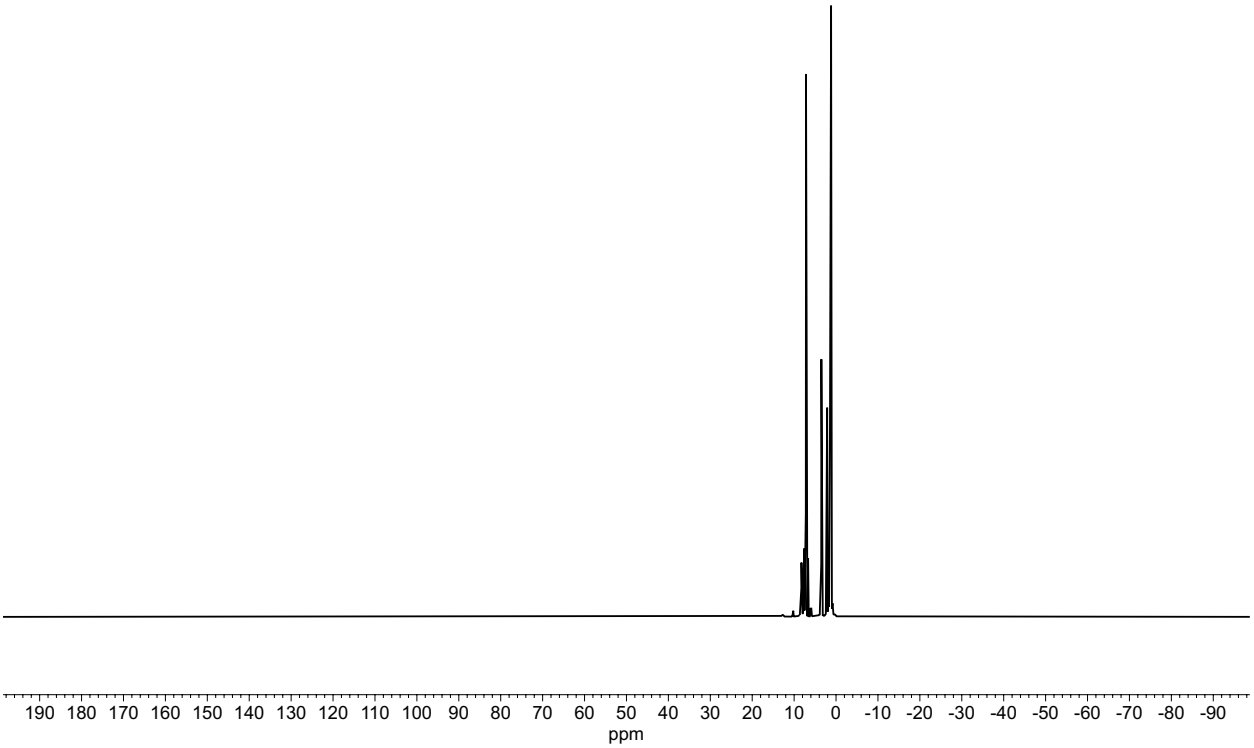

Figure S4. ^{1}H NMR of complex **3** in C_6D_6 + d_8-THF (for solubility) with a widened window to confirm the absence of a Ni hydride resonance.

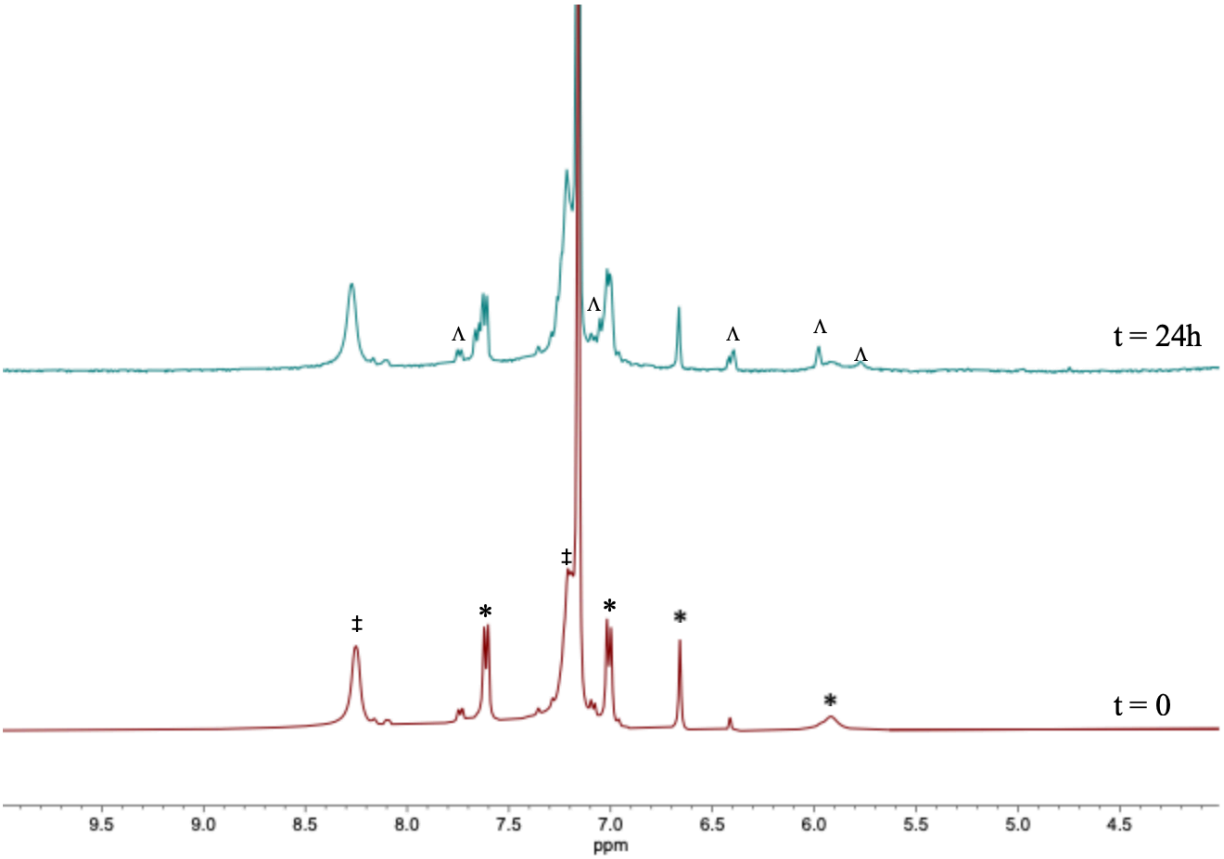

Figure S5. ^{1}H NMR of complex **3** in C_6D_6 + d_8-THF (for solubility) after initial in-situ generation from benzoic acid and complex **2** (bottom spectrum, red) and after 24h at room temperature under N_2 atmosphere (top spectrum, teal). *complex **3,** ‡ benzoate, L decomposition products

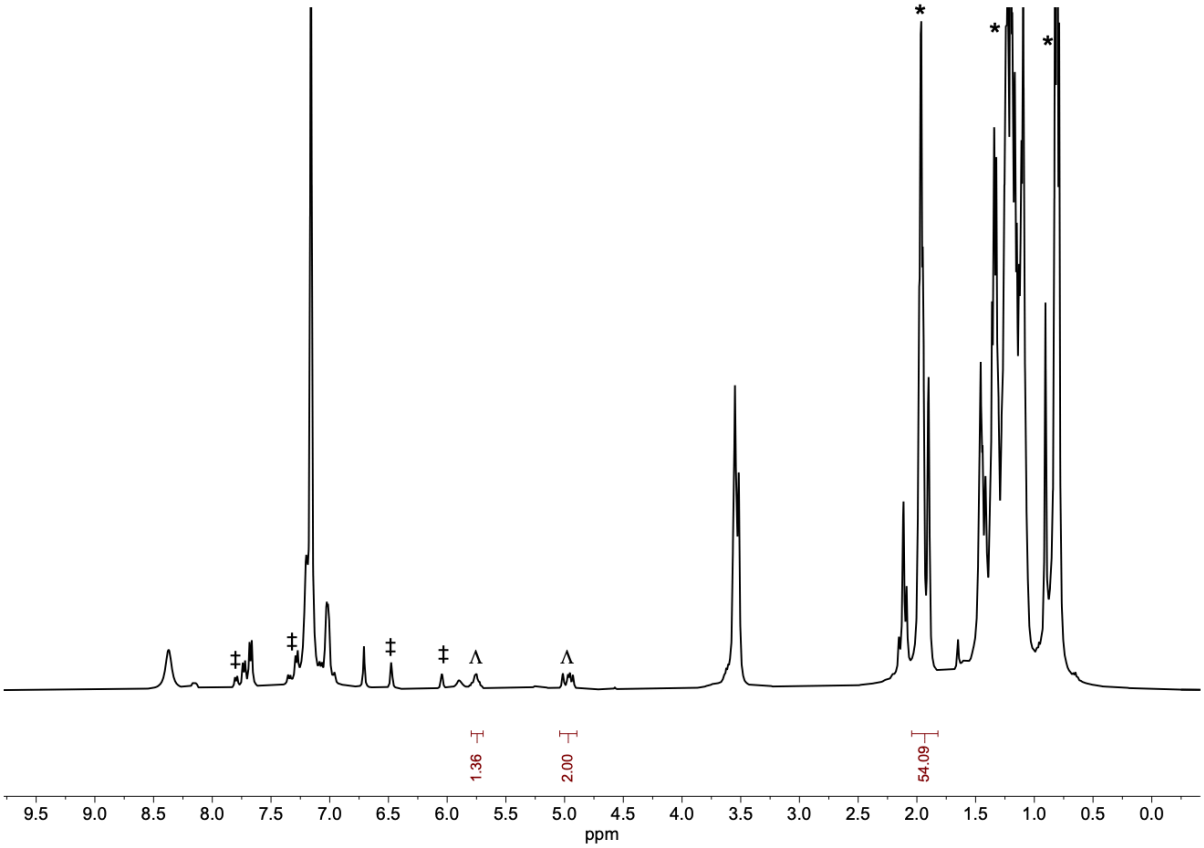

Figure S6. ^{1}H NMR of 1 eq **3** + 10 eq octyne + Na/Hg in C_6D_6 + d_8-THF (for solubility). We note that complex **3** partially decomposes upon reacting with Na/Hg. ^{L}1-octene *1-octyne ‡ligand decomposition products

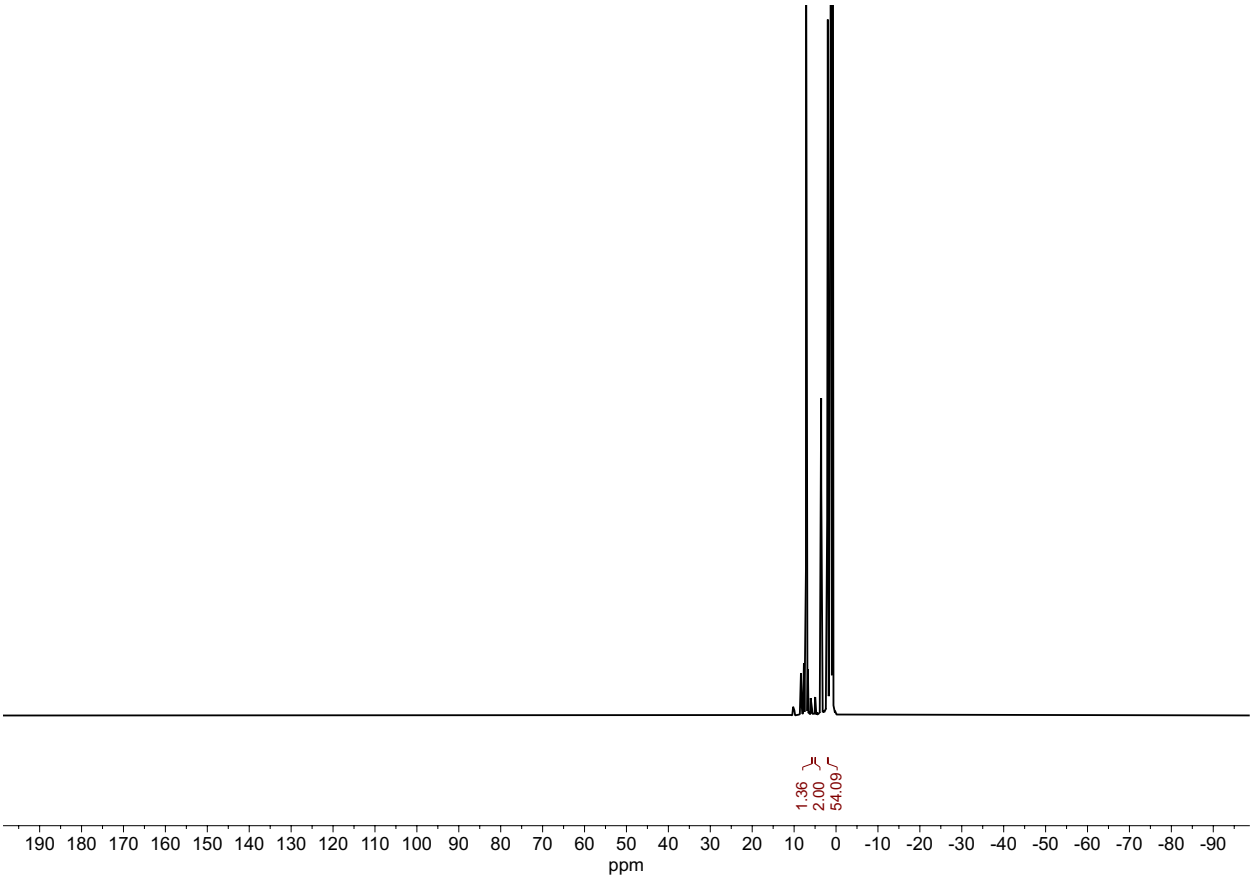

Figure S7. Full spectrum of ^{1}H NMR of 1eq **3** + 10eq octyne + Na/Hg in C_6D_6 + d_8-THF (for solubility) with a widened window to confirm the absence of a Ni hydride resonance.

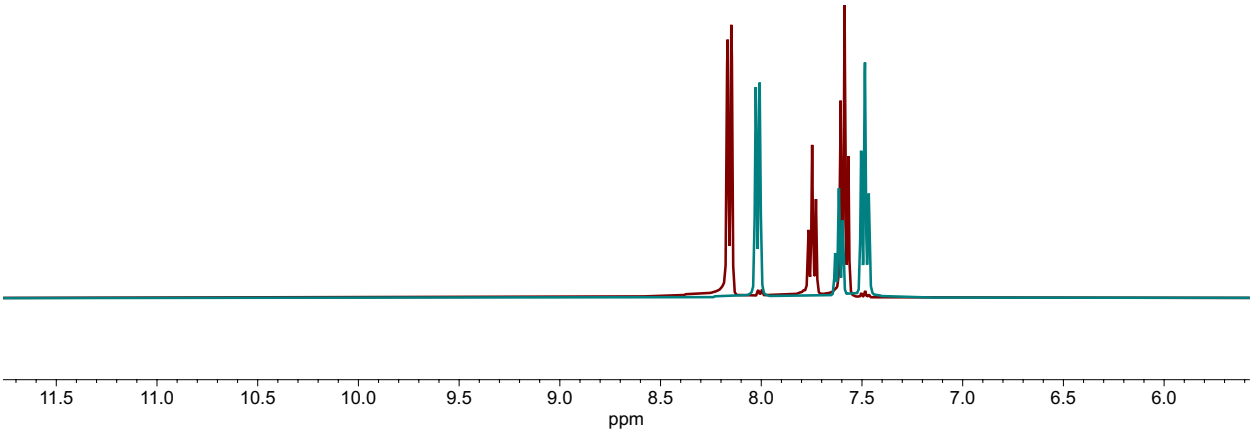

Figure S8. ^{1}H NMR in CD_3CN of benzoic acid anhydride (red) starting material and d_1-benzoic acid (teal) product after refluxing with D_2O and purification. We note the absence of any OH signal.

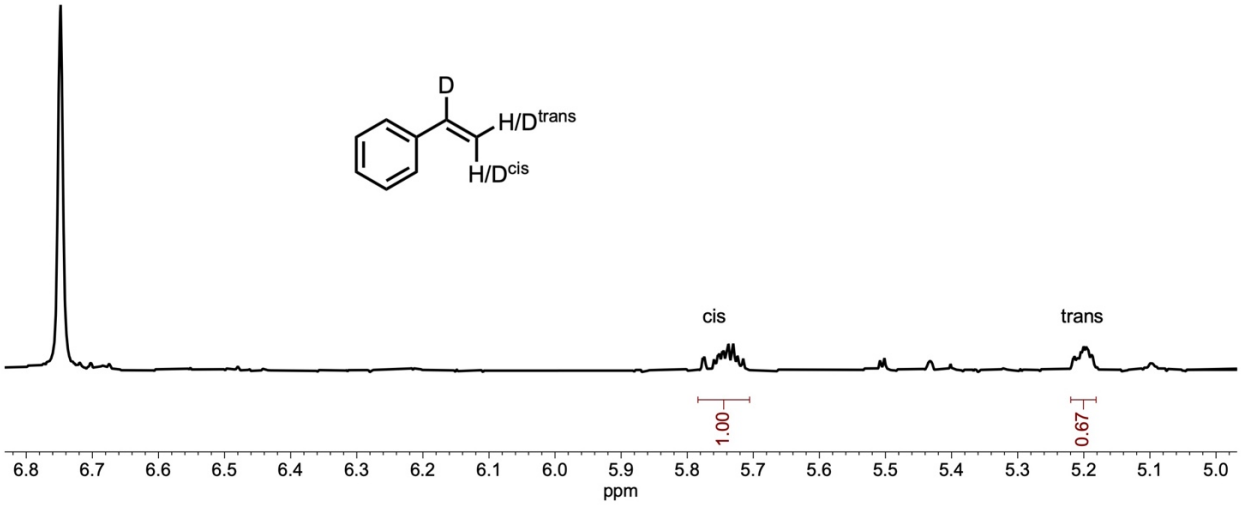

Figure S9. ^{1}H NMR of phenylacetylene after electrolysis with d_1-benzoic acid and **1** in CD_3CN, δ 6.77 is the mesitylene internal standard.

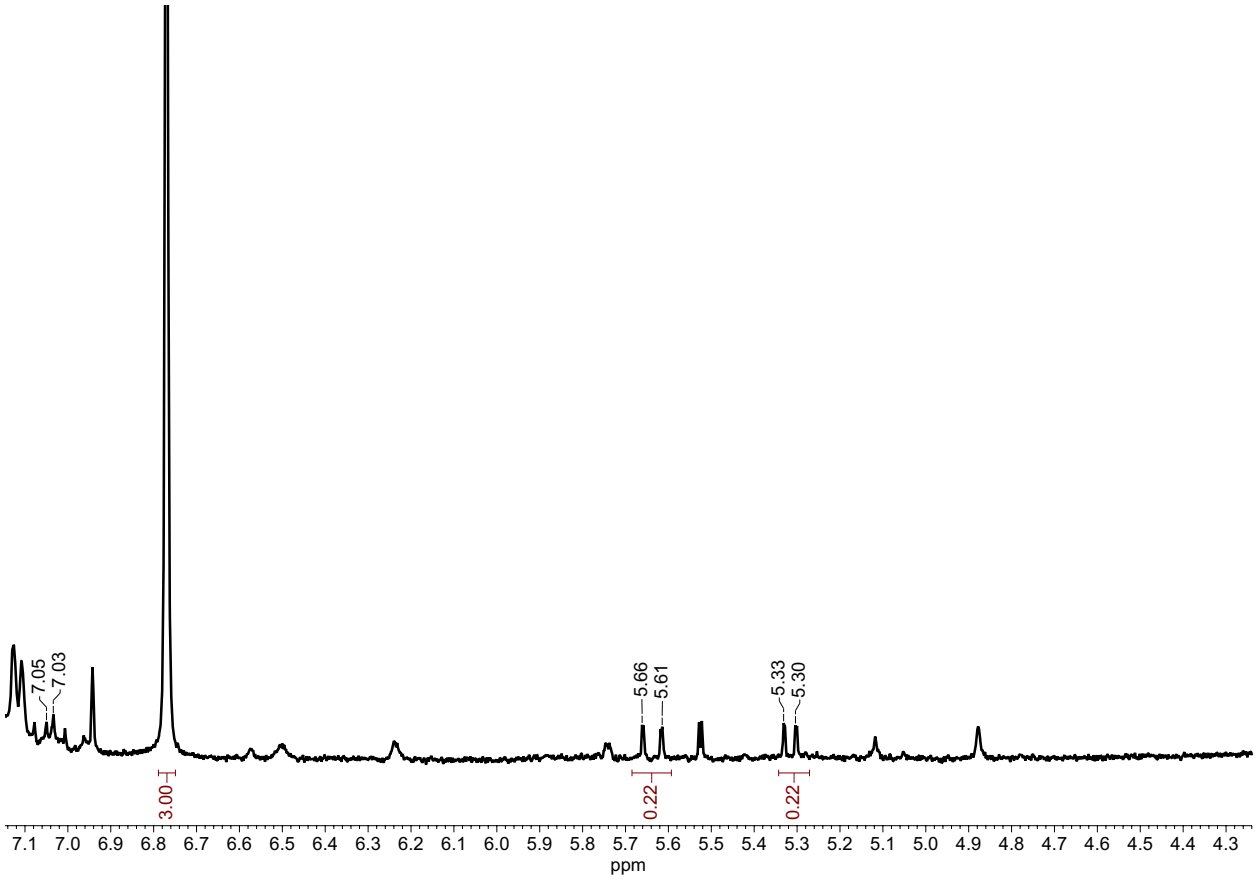

Figure S10. ^{1}H NMR of 1-ethynyl-2-vinylbenzene after electrolysis with **1** and benzoic acid in CD_3CN. The assigned peaks correspond to 1,2-divinylbenzene. No cyclized product is detected.[1] Some non-product peaks correspond to ligand decomposition. Starting material is not indefinitely stable when exposed to MeCN, which resulted in a reduced yield. δ 6.77 is the mesitylene internal standard.

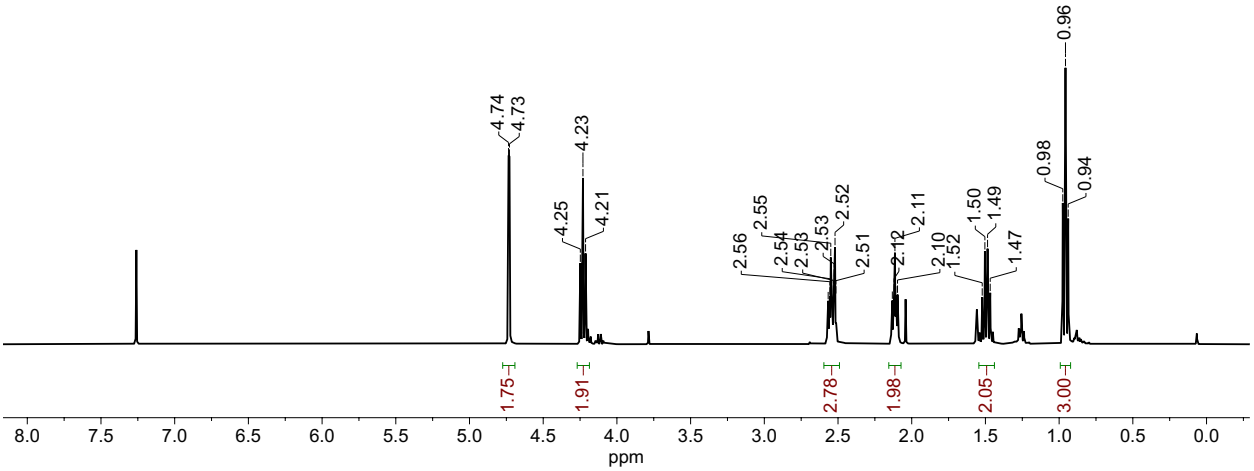

Figure S11. ^{1}H NMR of 1-prop-2-ynyloxy-hept-3-yne in $CDCl_3$.

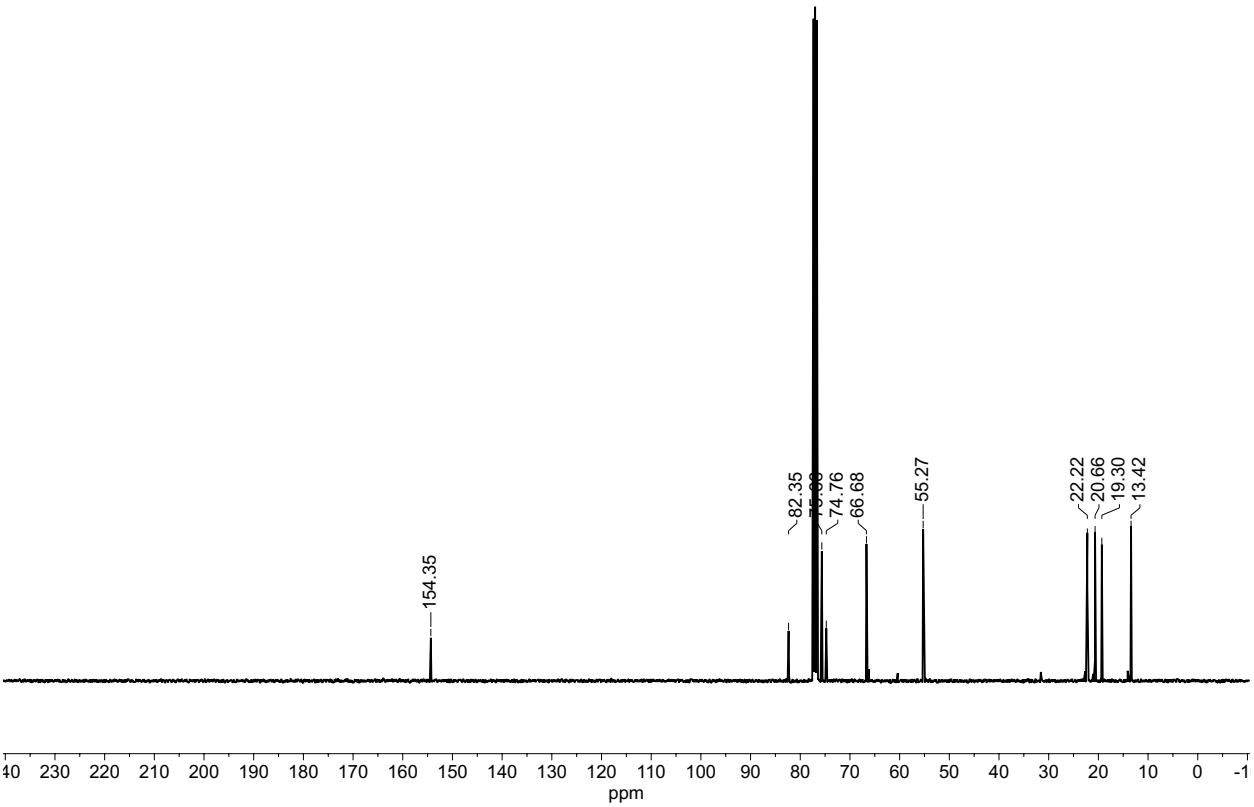

Figure S12. ^{13}C NMR of 1-prop-2-ynyloxy-hept-3-yne in $CDCl_3$.

Electrochemistry

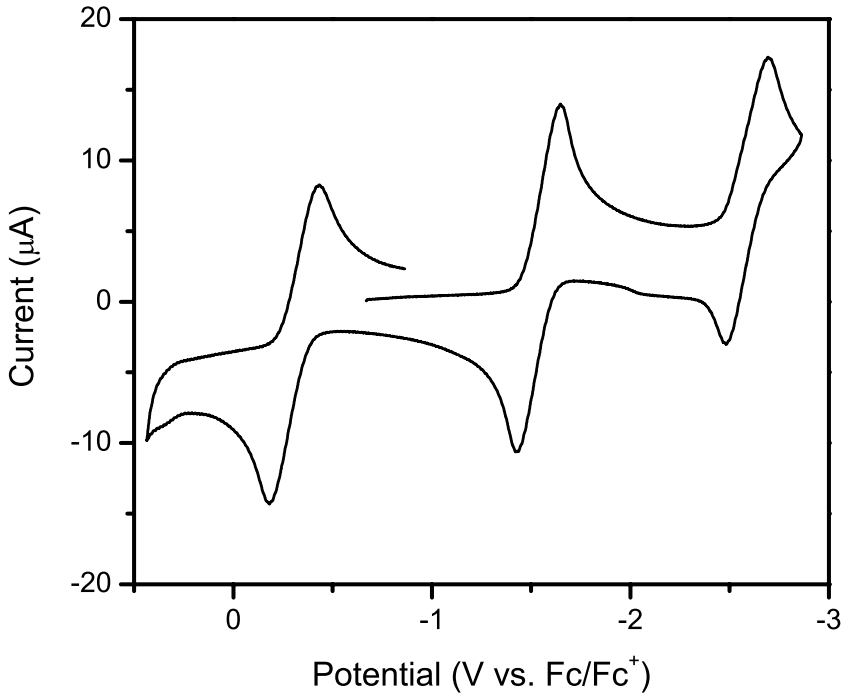

Figure S13. CV of **1** in THF. The Ni(II)/(I) couple is visible at –2.85 V.

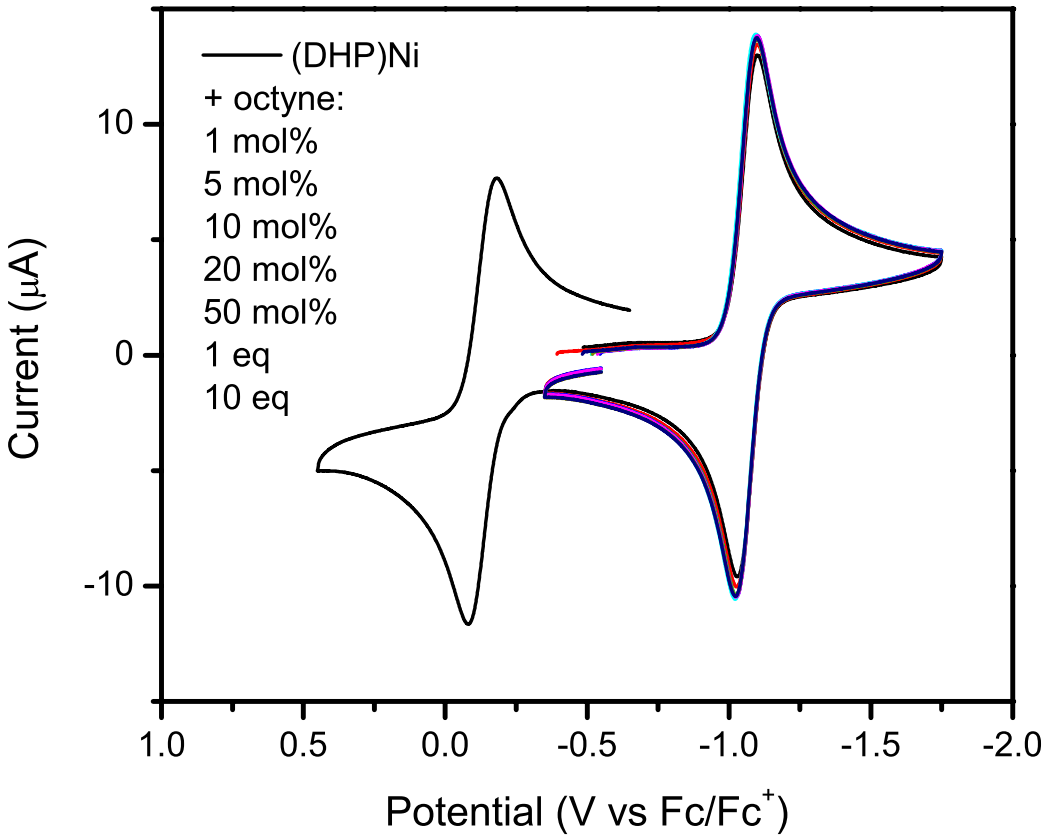

Figure S14. CV of **1** (1 eq) with added 1-octyne in MeCN.

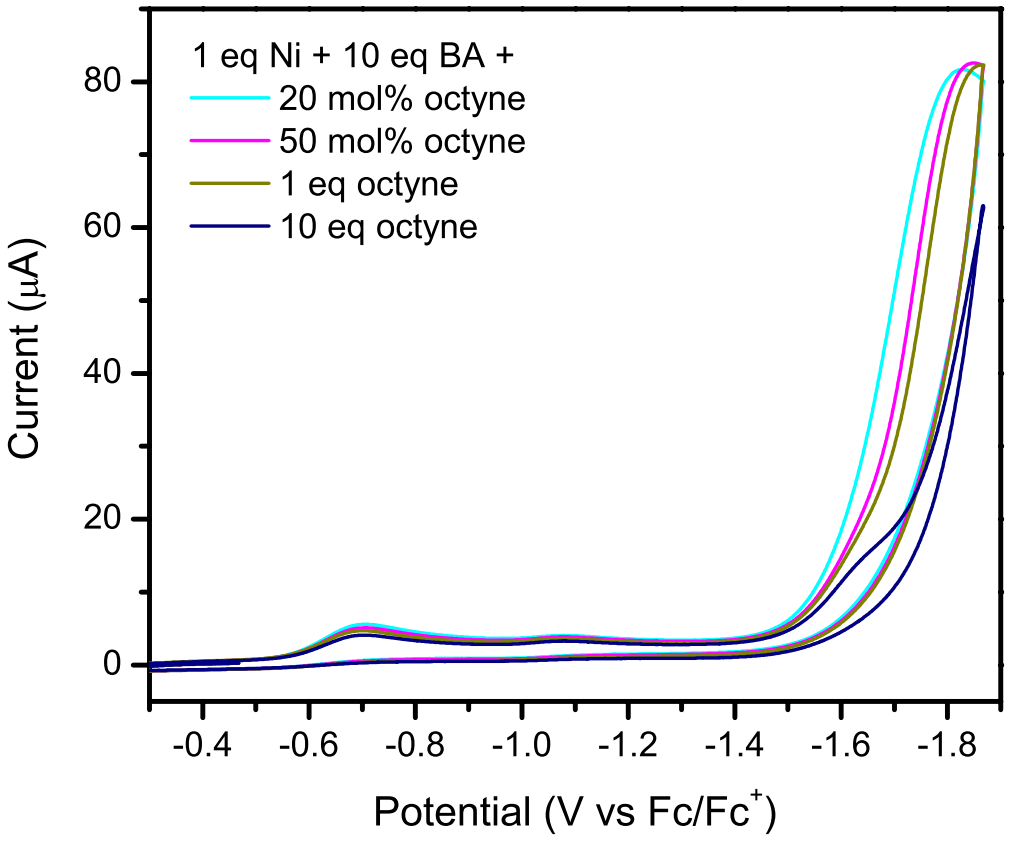

Figure S15. CV of **1** with benzoic acid and added 1-octyne in MeCN.

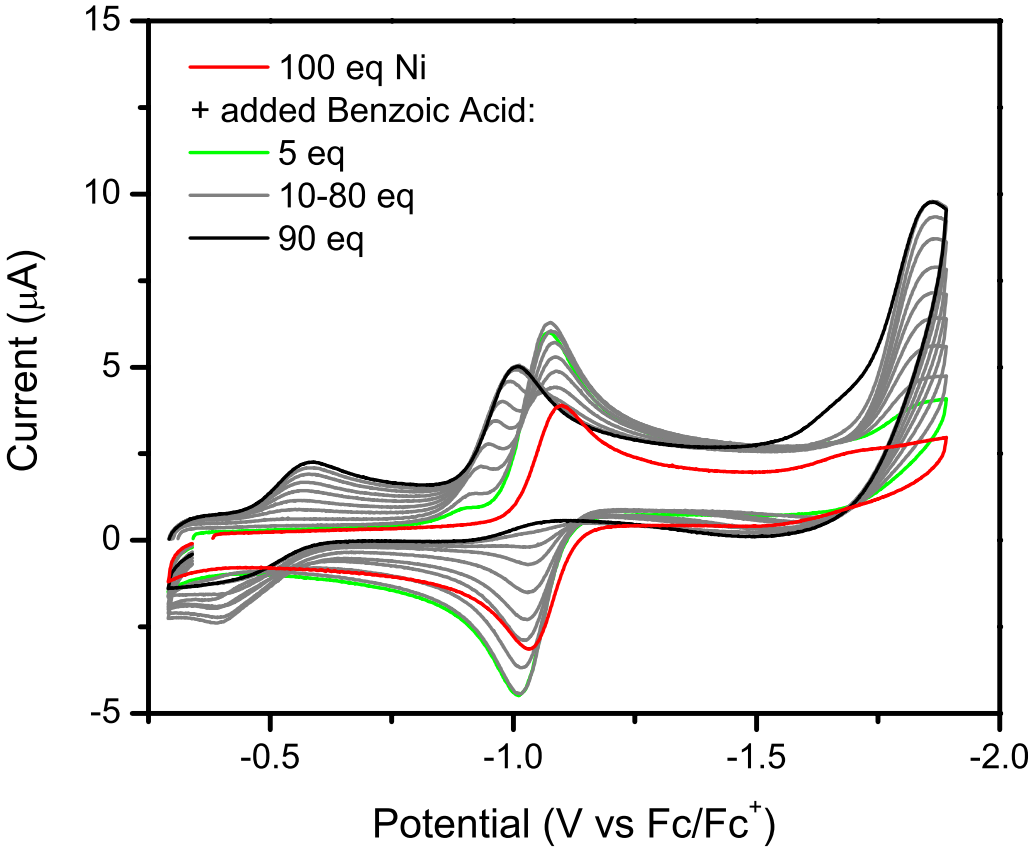

Figure S16. CV of **1** with added benzoic acid in sub-stoichiometric conditions in MeCN.

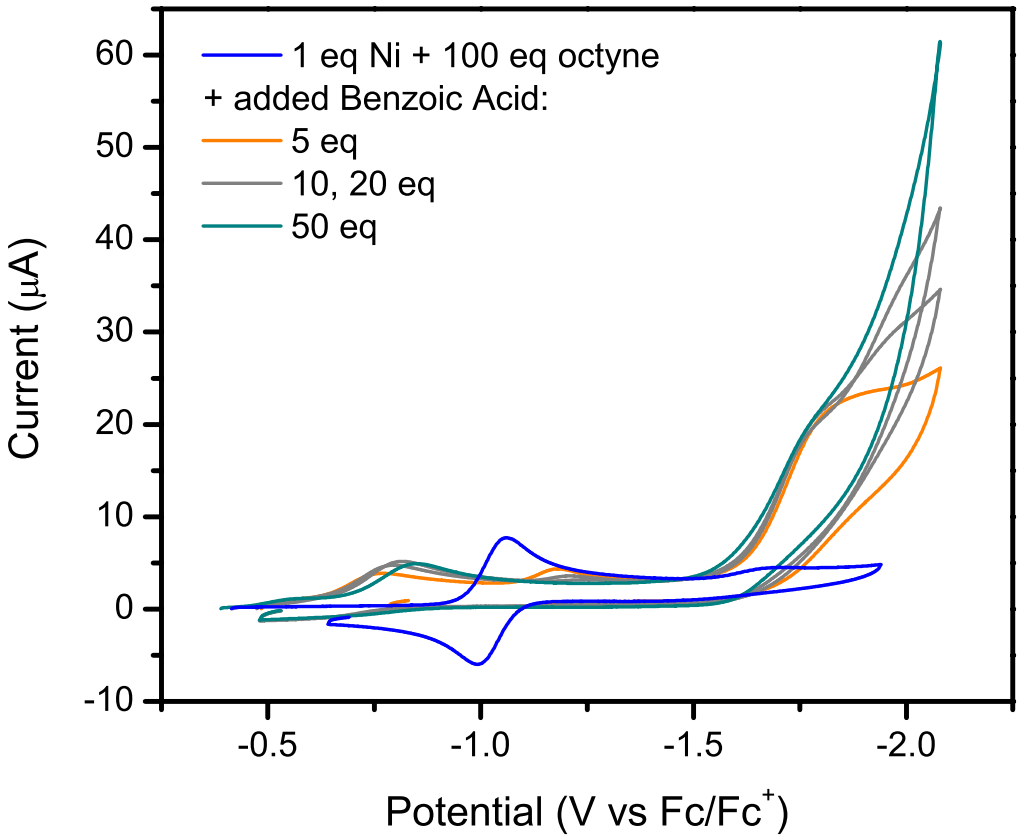

Figure S17. CV of **1** with 1-octyne and added benzoic acid in MeCN. We assign the first inflection point of the catalytic feature to semi-hydrogenation reactivity, and we note that HER is dominant at more negative potentials.

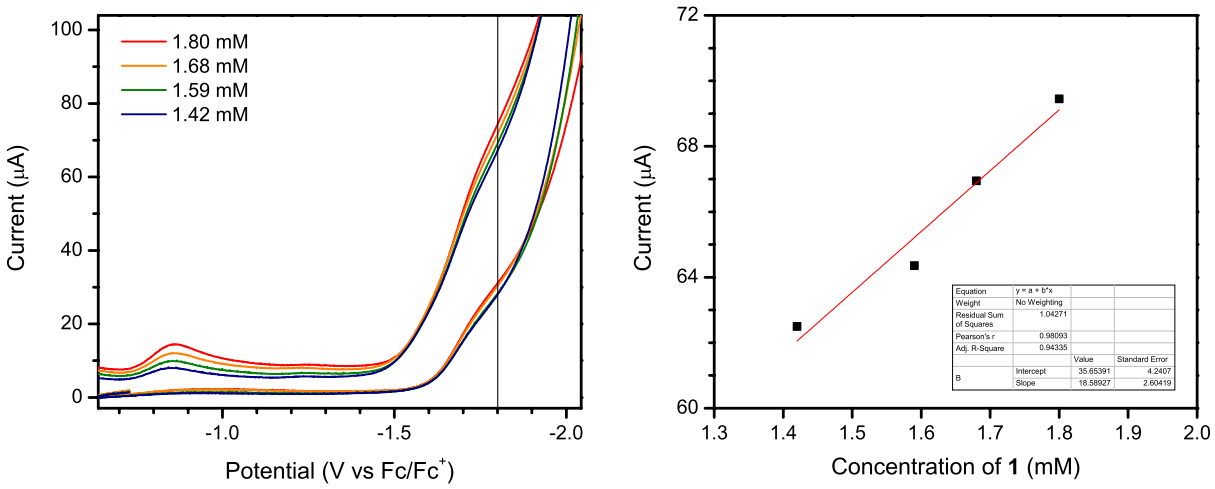

Figure S18. CVs of benzoic acid (71 mM), octyne (71 mM), and varying concentrations of **1** from 1.8-1.42 mM in MeCN. Serial dilutions of 200 μL were done starting from the highest catalyst concentration. The concentration of benzoic acid and octyne was held constant in the starting solution and the diluting solution. A linear relationship between current density and catalyst concentration corresponds to a first order dependence.

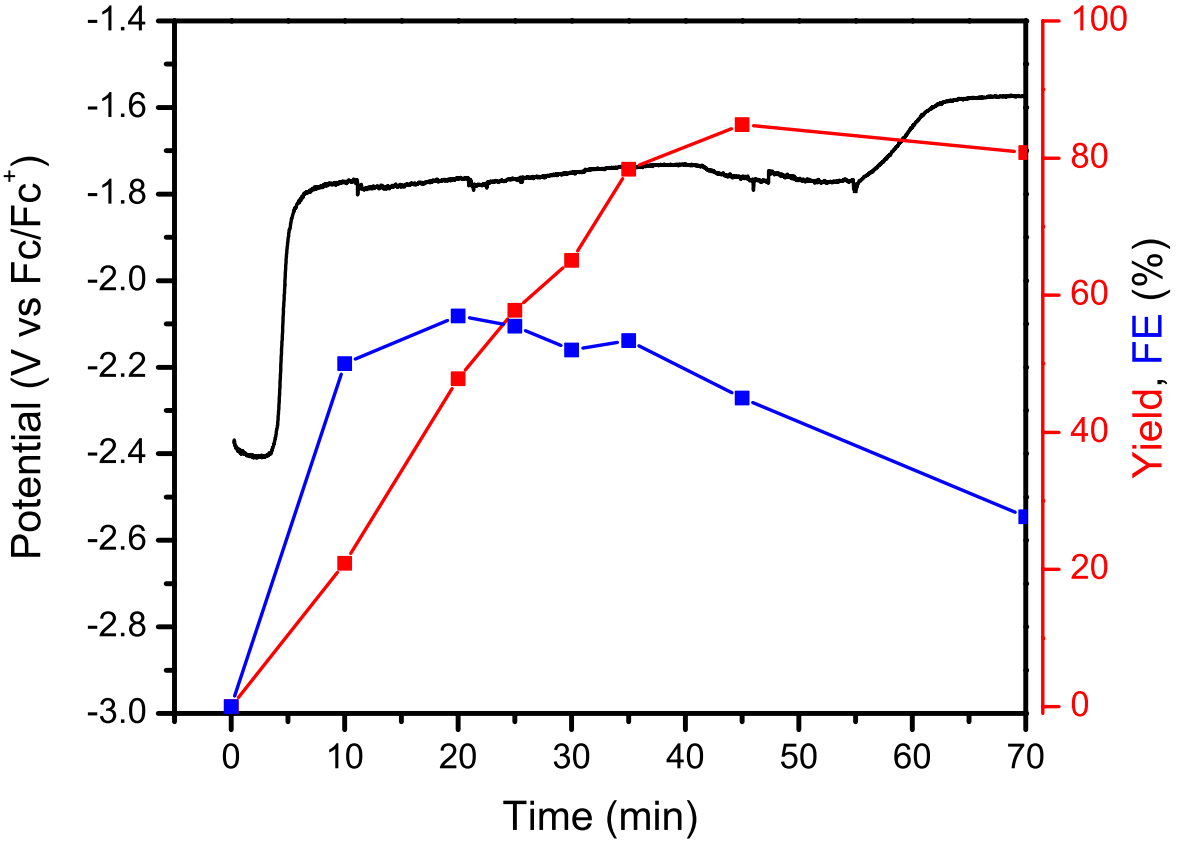

Figure S19. Bulk electrolysis chronopotentiometry of **1** with benzoic acid and 1-octyne in MeCN.

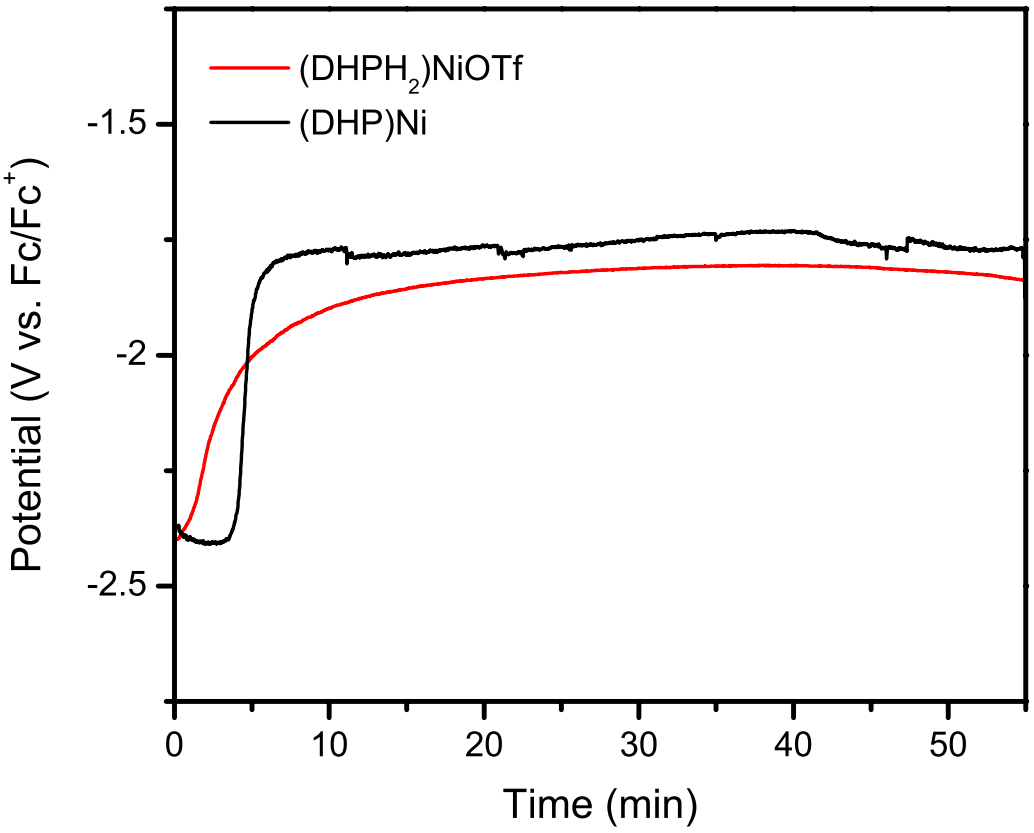

Figure S20. Bulk electrolysis chronopotentiometry of ($^{t\text{Bu, Tol}}$DHPH$_2$)NiOTf with benzoic acid and 1-octyne in MeCN.

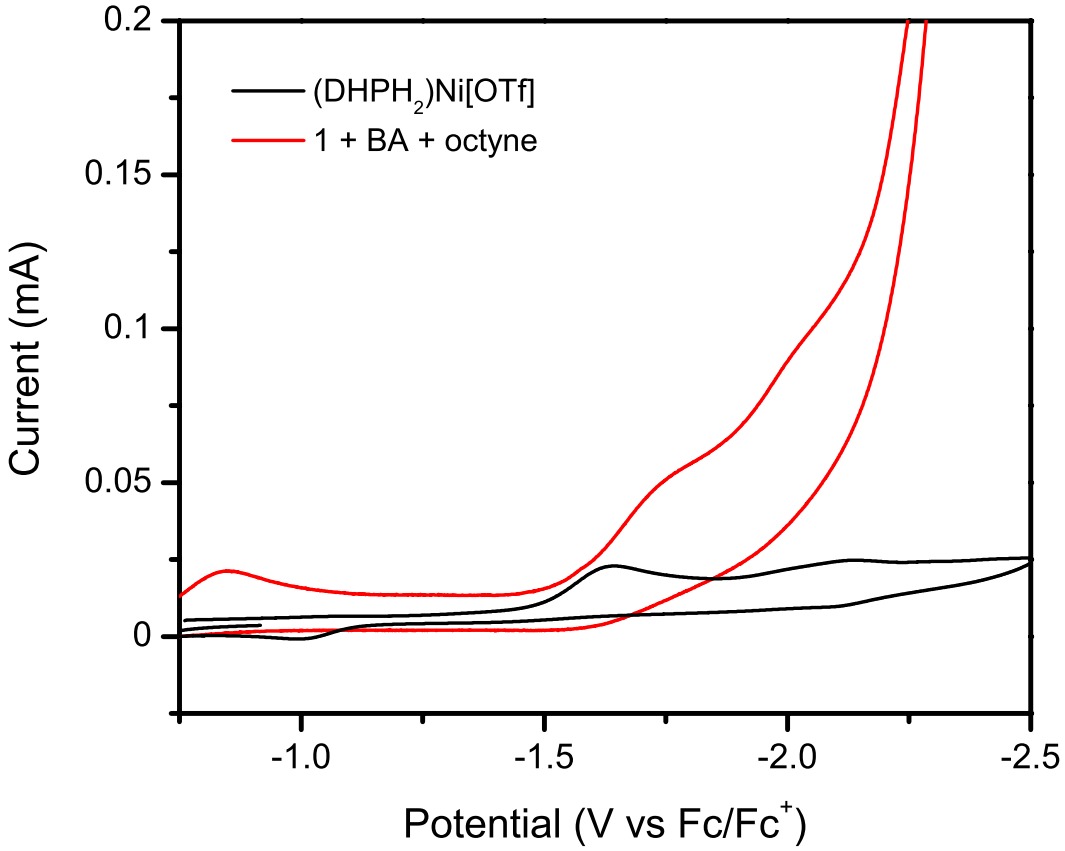

Figure S21. CV of ($^{t\text{Bu, Tol}}$DHPH$_2$)Ni[OTf] overlayed with CV of **1** with benzoic acid (BA) and 1-octyne in MeCN.

Reaction Development

Table S1. Optimization for bulk electrolysis. BA: benzoic acid *Yield of styrene. All reactions performed with 10 mol% catalyst loading of **1** unless otherwise noted.

Substrate (1 eq)	Conditions	Current (mA)	Yield (%)*
Phenylacetylene	BA, 5 eq	6	75
Phenylacetylene	BA, 10eq	6	84
Phenylacetylene	BA, 10 eq	3.9	96
Phenylacetylene	BA, 10 eq	2	37
Phenylacetylene	H_2 atm	3.9	<5
Phenylacetylene	HFIP, 10 eq	3.9	16
Phenylacetylene	10 mol% ligand (no **1**), BA, 10 eq	3.9	<5
Phenylacetylene	THF solvent, BA, 10 eq	3.9	30

Calculation of current passed during electrolysis initiation period

Experimental:

$$0.0039A \times 180\,\text{sec} = 0.702\,C$$

$$0.702C \times \left(6.24 \times 10^{18}\frac{e^-}{C}\right) = 4.38 \times 10^{18}e^-$$

$$4.38 \times 10^{18}e^- = \underline{7.27 \times 10^{-6}\ mol\ e^-\ passed}$$

Theoretical:

$$4 \times 10^{-6}\ mol\ Ni\ added$$

$$\underline{8 \times 10^{-6}\ mol\ e^-\ for\ 2e^-\ reduction\ of\ Ni}$$

Thermodynamic Calculation of Standard Potential

$$S + 2\,HA + 2\,e^- \rightleftharpoons SH_2 + 2\,A^-$$

$$2\,HA + 2\,e^- \rightleftharpoons H_2 + 2\,A^- \quad E^0_{HA/H2,\,MeCN}$$

$$S + H_2 \rightleftharpoons SH_2 \quad \Delta G^0_{Hydrogenation(S),\,MeCN}$$

$$E^0_{S/SH2,\,HA,\,MeCN} = E^0_{HA/H2,\,MECN} - (\Delta G^0_{Hydrogenation(S),\,MeCN})/2F$$

$$E^0_{HA/H2,\,MeCN} = E^0_{H+/H2,\,MeCN} - \ln(10)(RT/F)pK_{a,\,HA,\,MeCN}$$

$$T = 298.15\ K$$

$$E^0_{H+/H2,\ MeCN} = -0.07\ V\ vs\ Fc^{+/0}$$

$$pK_{a,\ BA,\ MeCN} = 20.7$$

$$\text{Thus, } E^0_{BA/H2,\ MeCN} = -1.29\ V\ vs\ Fc^{+/0}$$

$$\Delta G^0_{Hydrogenation(S),\ MeCN} = (\Delta G^0_{f(SH2)} - \Delta G^0_{f(S)} - \Delta G^0_{f(H2)}) + (\Delta G^0_{solv(SH2)} - \Delta G^0_{solv(S)} - \Delta G^0_{solv(H2)})$$

In the case of the hydrogenation of 1-octyne to 1-octene in MeCN:

$$\Delta G^0_{f(H2)} = -39.0\ kJ/mol$$
$$\Delta G^0_{f(S)} = 239.6\ kJ/mol$$
$$\Delta G^0_{f(SH2)} = 104.3\ kJ/mol$$

$$\Delta G^0_{solv(H2)} = 21.4\ kJ/mol$$
$$\Delta G^0_{solv(S)} = 13\ kJ/mol\ *$$
$$\Delta G^0_{solv(SH2)} = 13\ kJ/mol\ *$$

* No published experimental values for ΔG^0_{solv} for octyne or octene in MeCN. Value for n-heptane in MeCN is 13 kJ/mol. Value for 1-octyne and octene in DMF is 15.7 kJ/mol and 20.2 kJ/mol, respectively. Alternative final E^0 using values in DMF will be given below.

$$\Delta G^0_{Hydrogenation(S),\ MeCN} = -96.3 - 21.4 = -117.7\ kJ/mol$$
$$E^0_{S/SH2,\ BA,\ MeCN} = -0.68\ V\ vs\ Fc^{+/0}$$
$$\text{If DMF values for } \Delta G^0_{solv} \text{ are used: } E^0_{S/SH2,\ BA,\ MeCN} = -0.70\ V\ vs\ Fc^{+/0}$$

Overpotential (for base of catalytic wave) = –0.8 V vs $Fc^{+/0}$
Overpotential (at E_{app} –1.8 V vs $Fc^{+/0}$) = –1.1 V vs $Fc^{+/0}$

EPR Spectroscopy

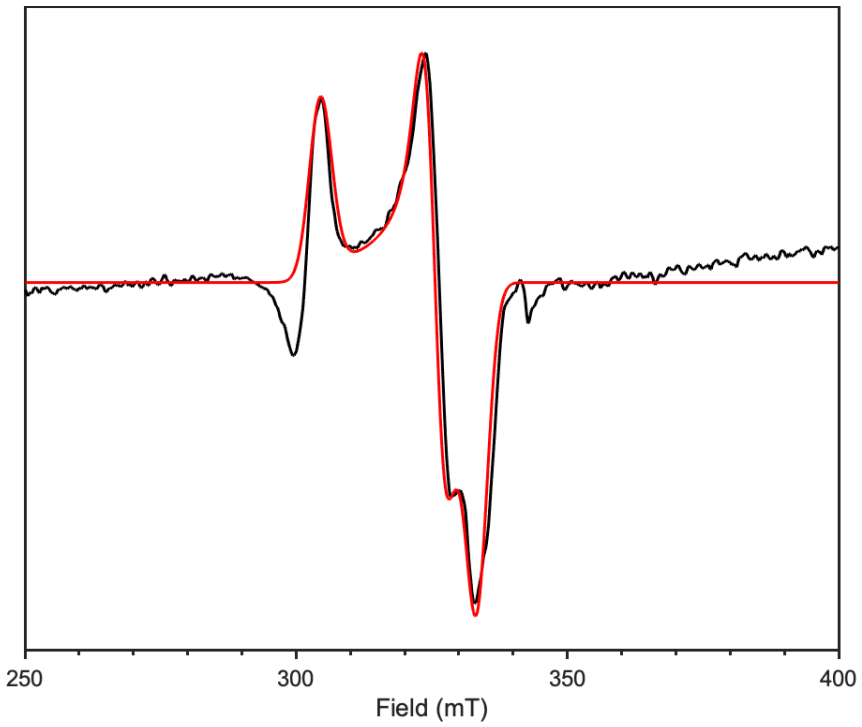

Figure S22. X-band EPR of **4** (the one-electron reduced complex of **3**) in MeCN at 15 K. Fitting parameters: g = 2.073, 2.123, 2.270; A = 8, 8, 5. Note the small paramagnetic impurities at 300 and 345 mT.

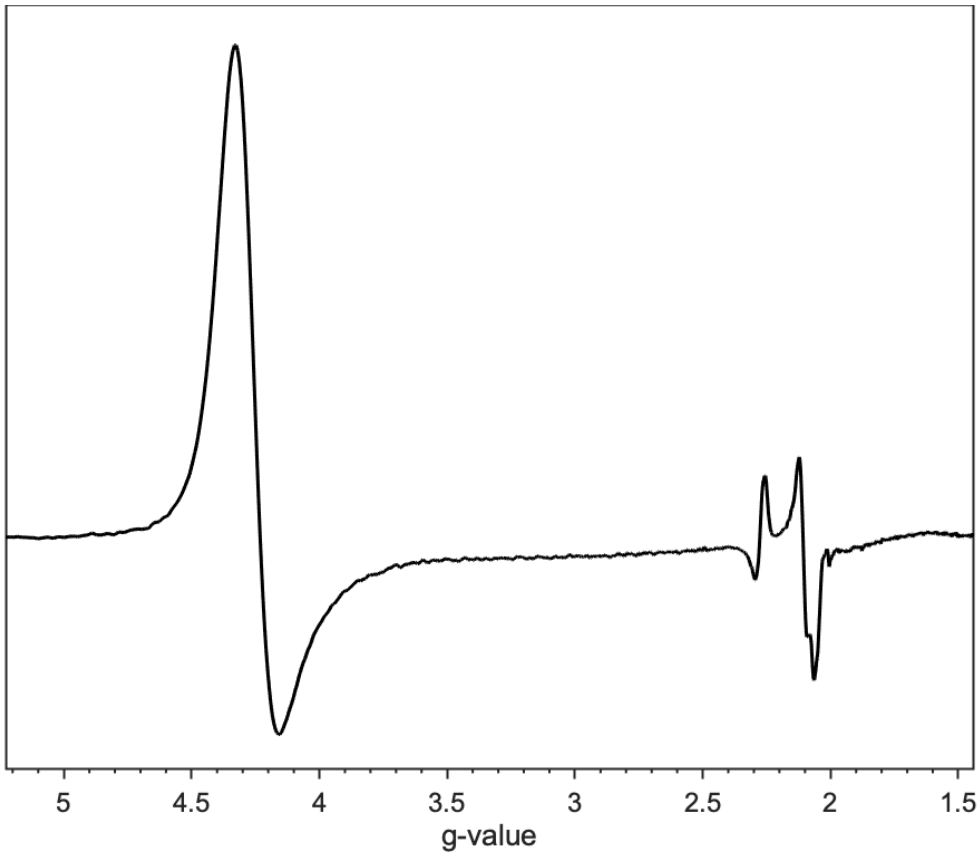

Figure S23. Full EPR of **4** (the one-electron reduced complex of **3**) in MeCN with Co(II) feature at $g = 4.3$ due to the presence of a $CoCp_2^*$ derivative that was not removed after the reaction of complex **2** to form **3**. We note that interpreting differences in intensity is difficult due to different relaxation times for separate metal species.

IR Spectroscopy

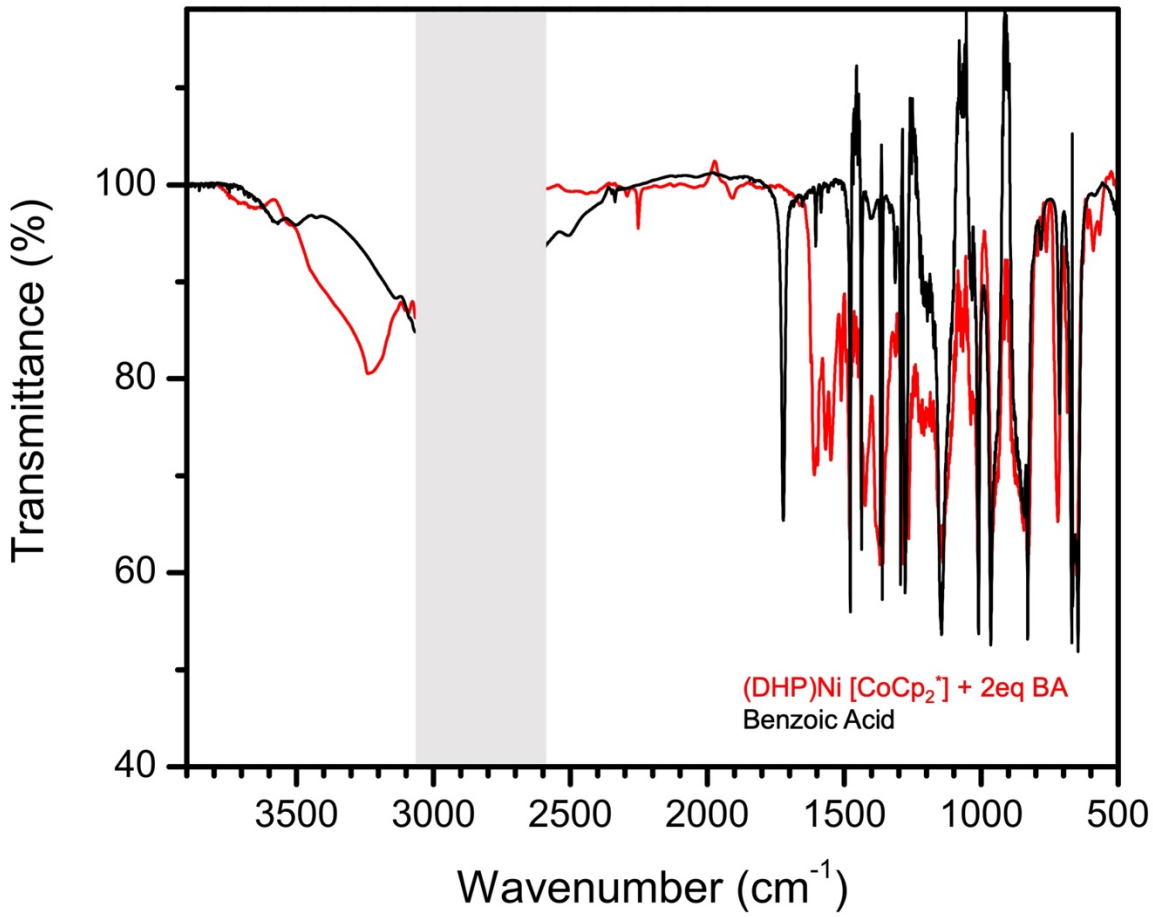

Figure S24. IR of **2** + benzoic acid in THF. Solvent subtraction is removed for clarity.

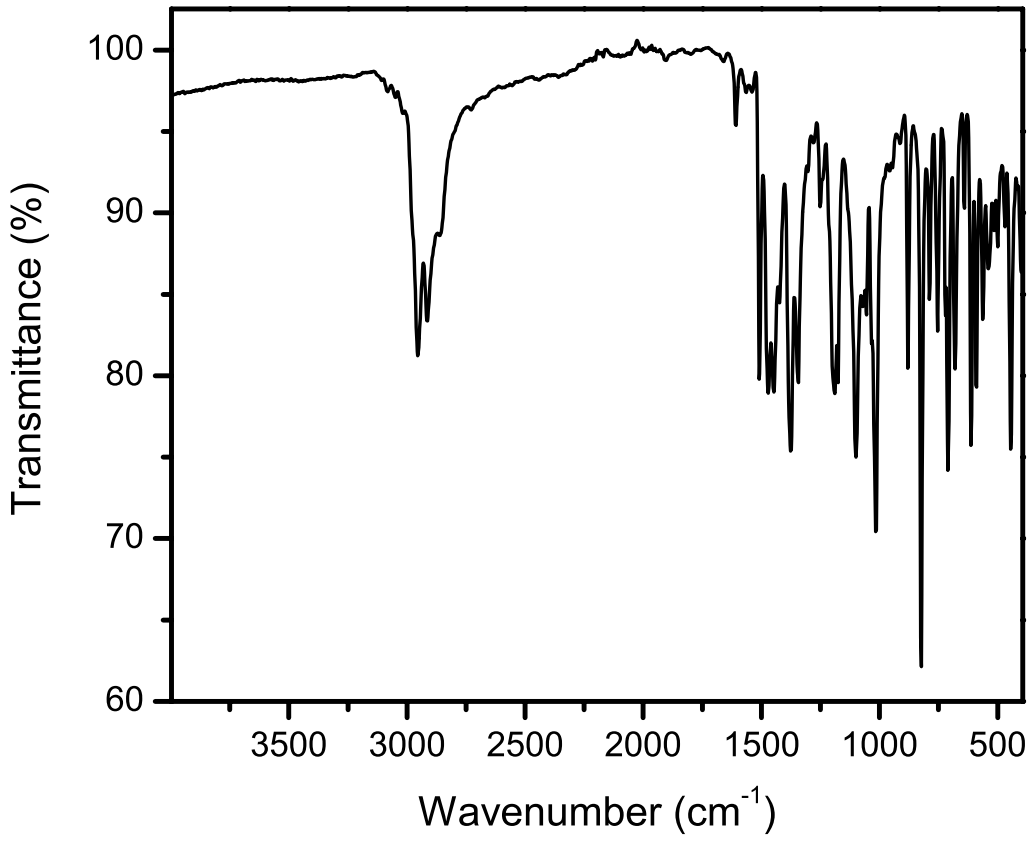

Figure S25. ATR-IR of **2**.

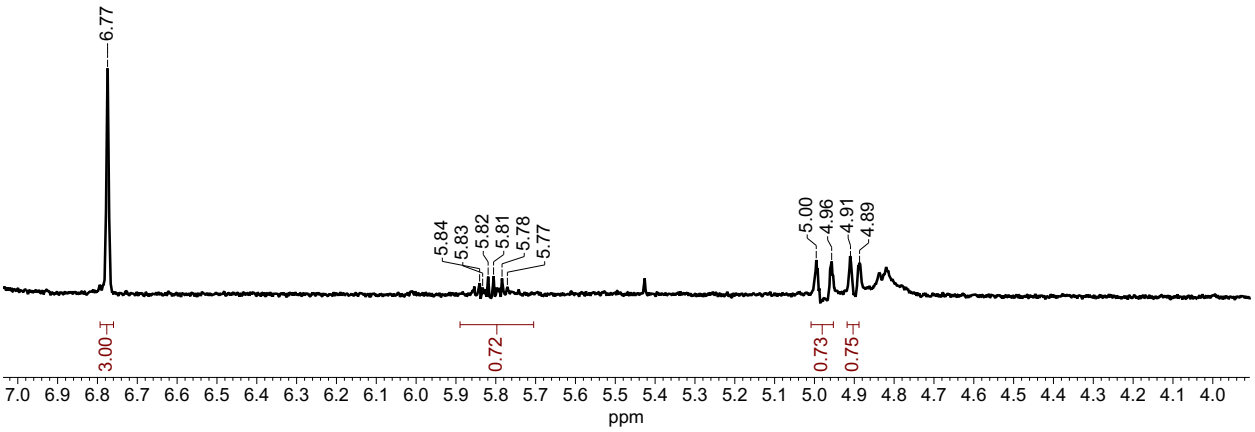

Figure S26. 1-Octyne reaction to form 1-octene in CD_3CN. δ 6.77 is the mesitylene internal standard.

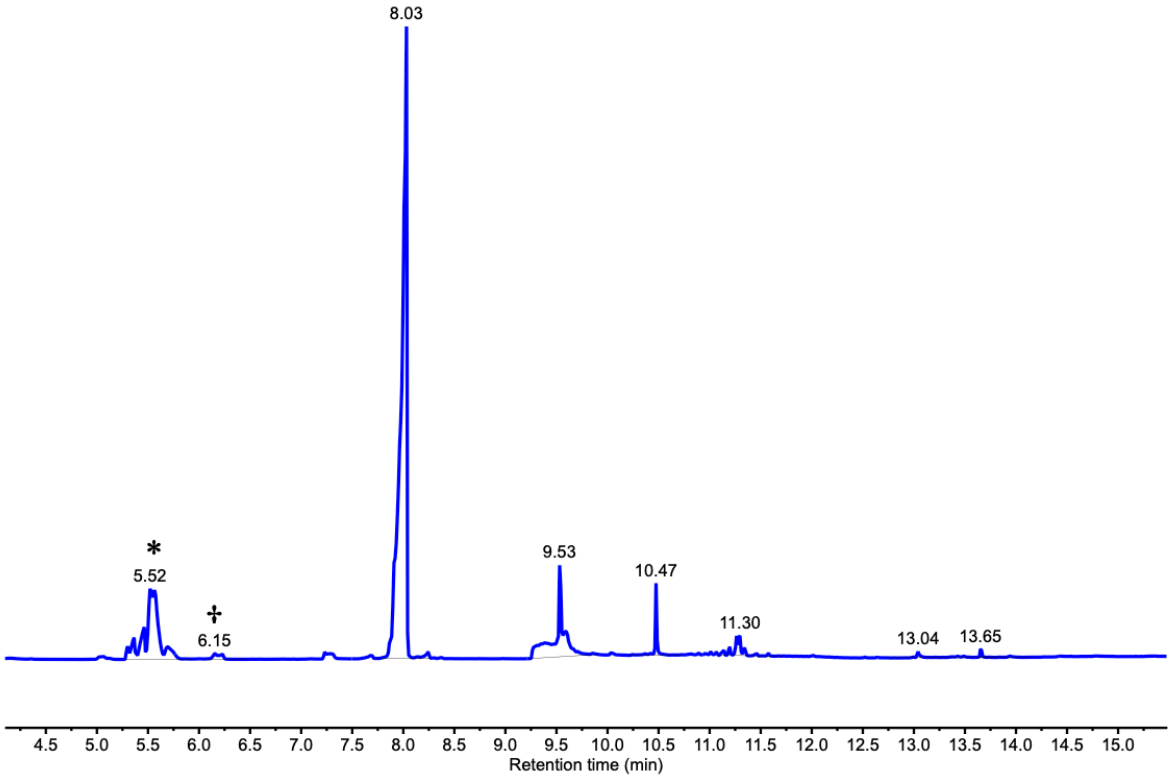

Figure S27. GC-TIC chromatogram of 1-octyne after electrolysis. Due to overlapping retention times with solvents that could not be fully removed, both the peak shape and relative intensity of 1-octene is severely distorted on the instrument used. We therefore relied on NMR integrations which provide a more reliable yield. * = 1-octene, † = 1-octyne, 8.03 min = mesitylene internal standard, 9.53 min = residual nBu$_4$N$^+$, 10.47 min = benzoic acid, 11.30 = residual hexafluorophosphate 13.02, 13.65 = contaminants (see mass spectra below).

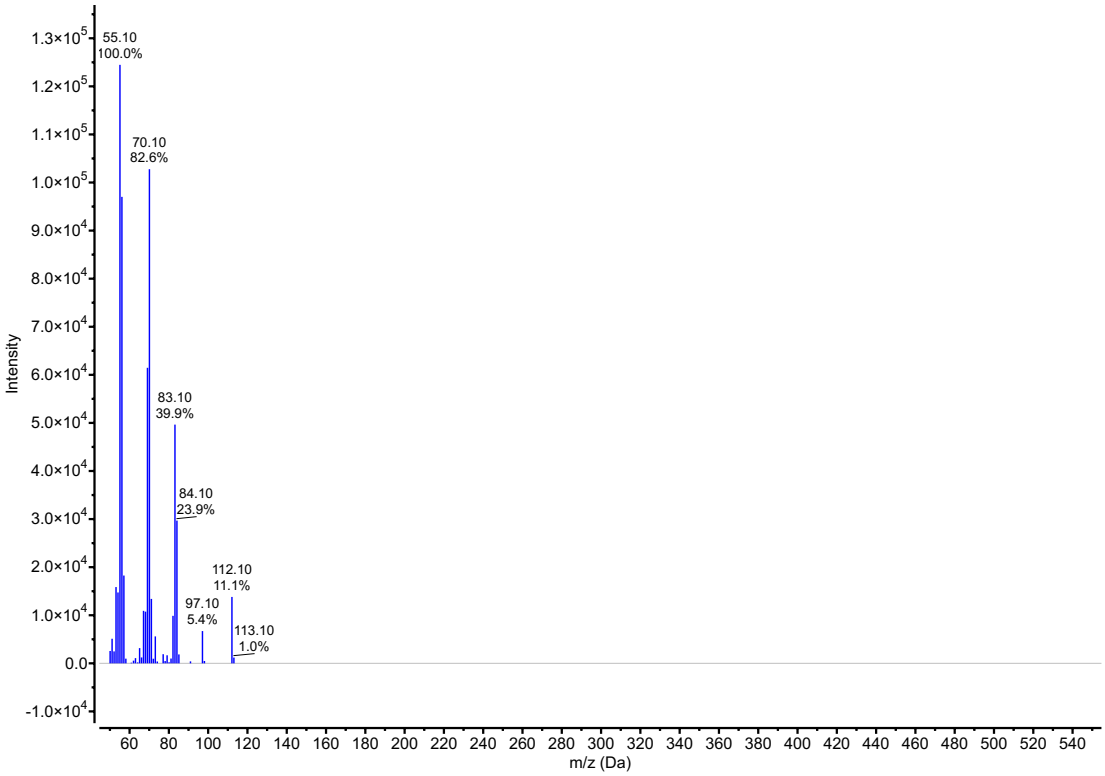

Figure S28. Mass Spectrum at t = 5.52 min of 1-octene (MW 112).

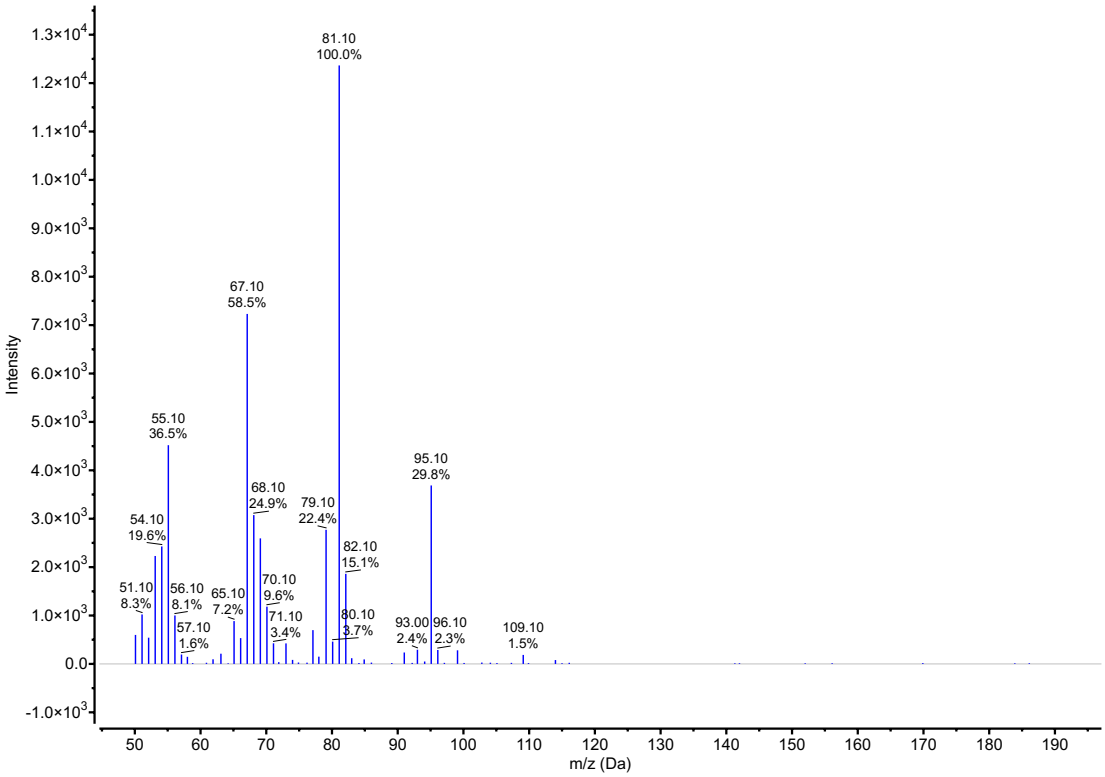

Figure S29. Mass spectrum at t= 6.15 min of 1-octyne (MW 110).

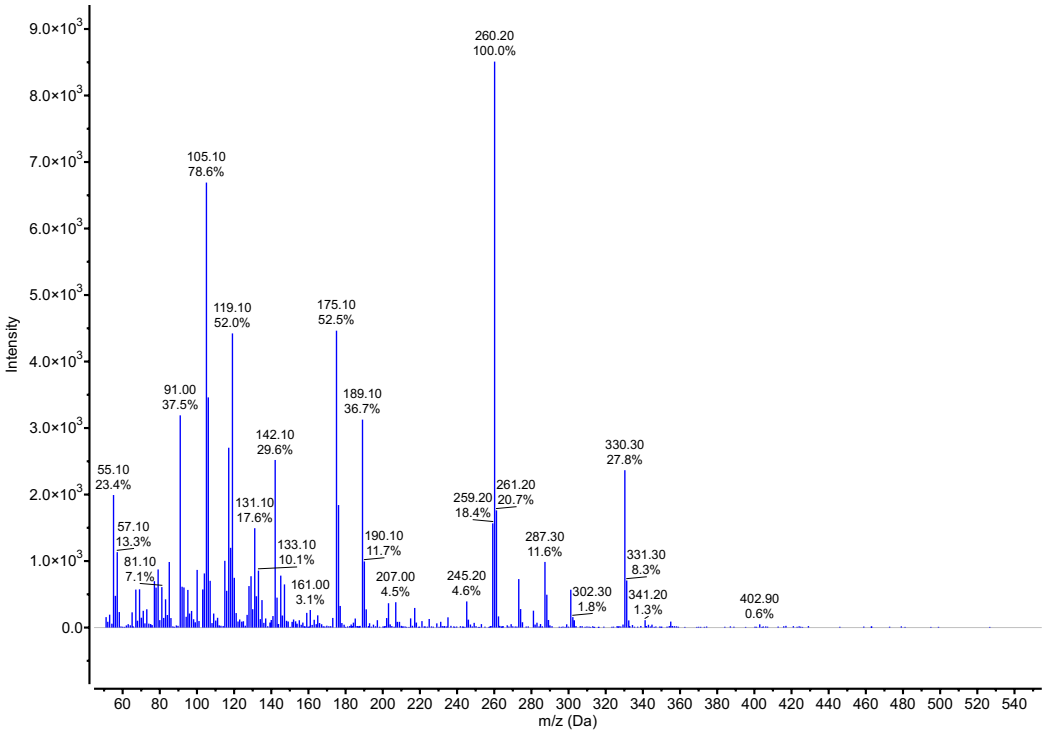

Figure S30. Mass spectrum at t = 13.65 min of column contaminant. Masses do not match product dimer, which has an expected MW = 220.

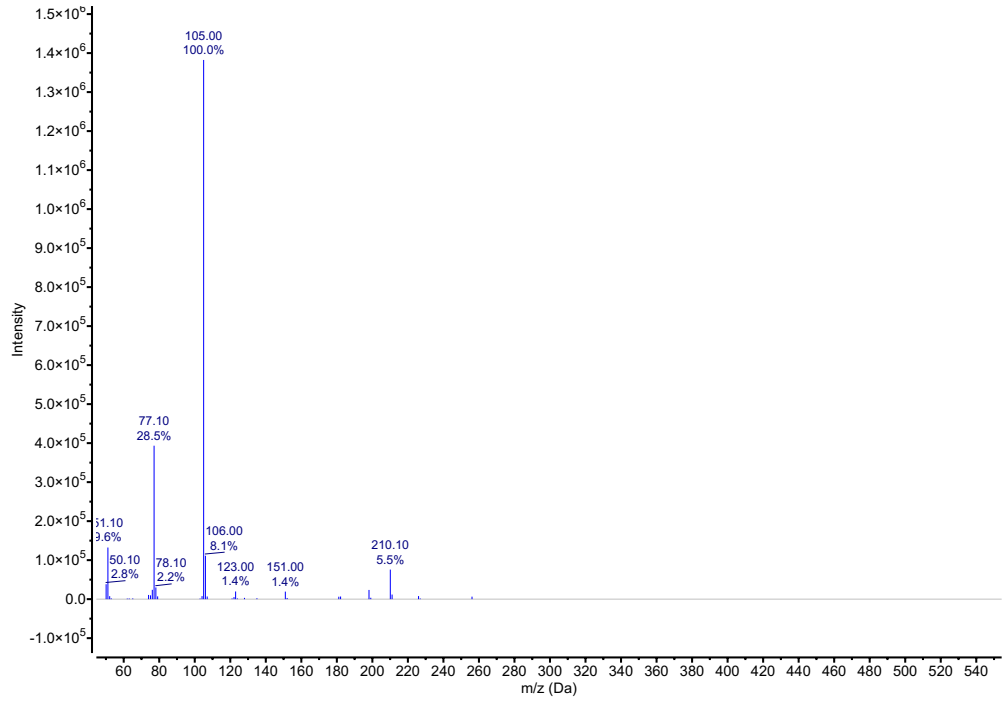

Figure S31. Mass spectrum at 13.04 min of column contaminant. Masses do not match product dimer, which has an expected MW = 220.

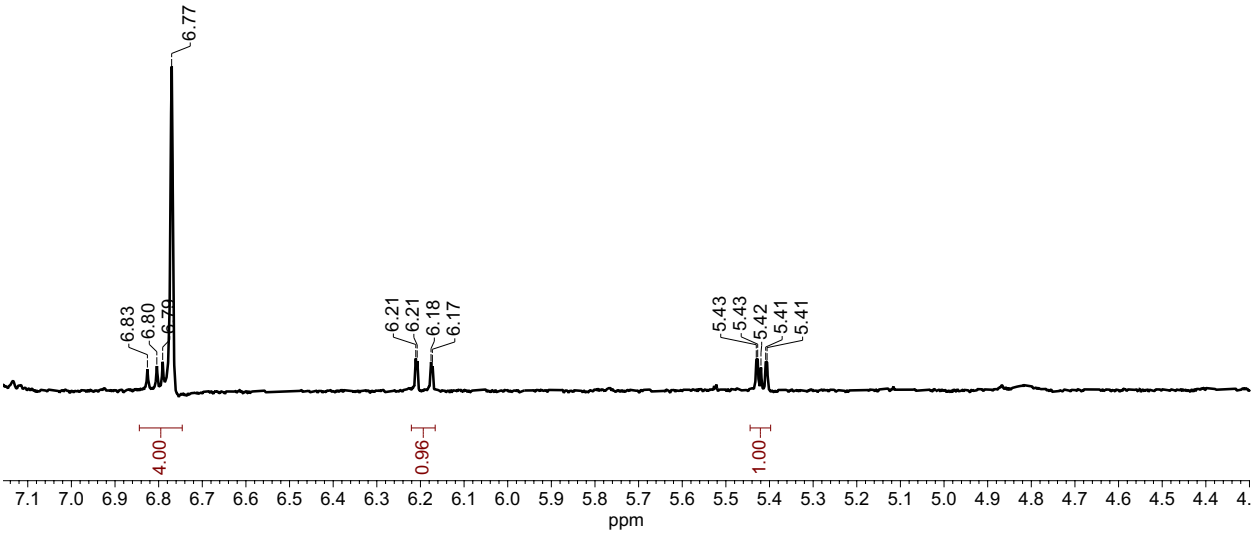

Figure S32. 2-ethynyl-pyridine reaction to form 2-vinyl-pyridine in CD_3CN. δ 6.20 (J = 17.5, 1.5 Hz), 5.42 (J = 11, 1.5 Hz). δ 6.77 is the mesitylene internal standard.

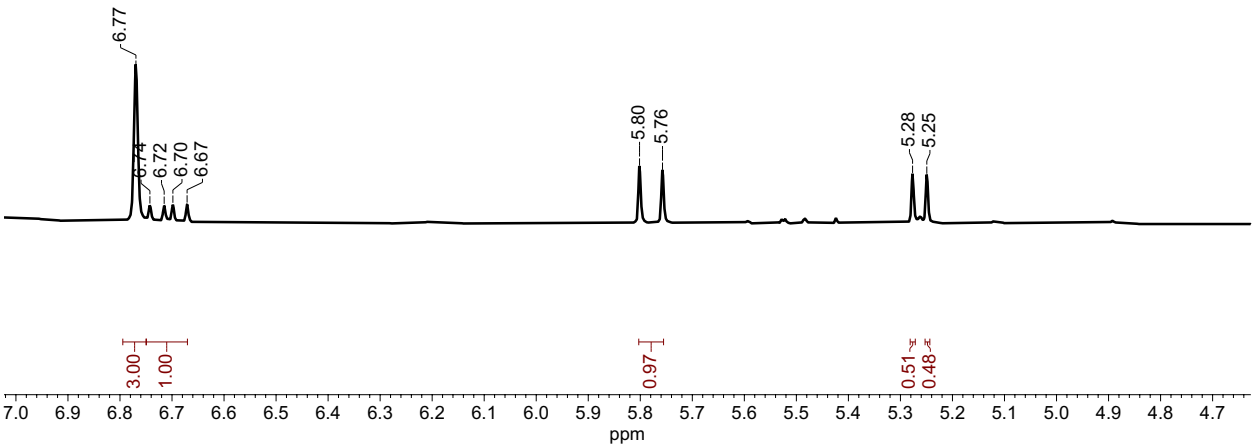

Figure S33. 4-chloro-phenylacetylene reaction to form 4-chloro-styrene in CD_3CN. δ 5.78 (J = 17.7, 0.5 Hz), 5.42 (J = 11, 0.5 Hz). δ 6.77 is the mesitylene internal standard.

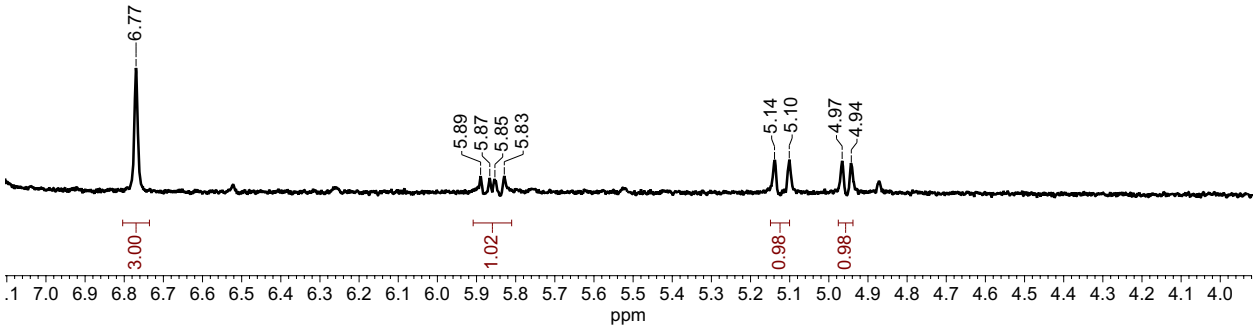

Figure S34. 3-methyl-pentyn-3-ol reaction to form 3-methyl-penten-3-ol in CD_3CN. δ 5.12 (J = 18 Hz), 4.95 (J = 11.5 Hz). δ 6.77 is the mesitylene internal standard.

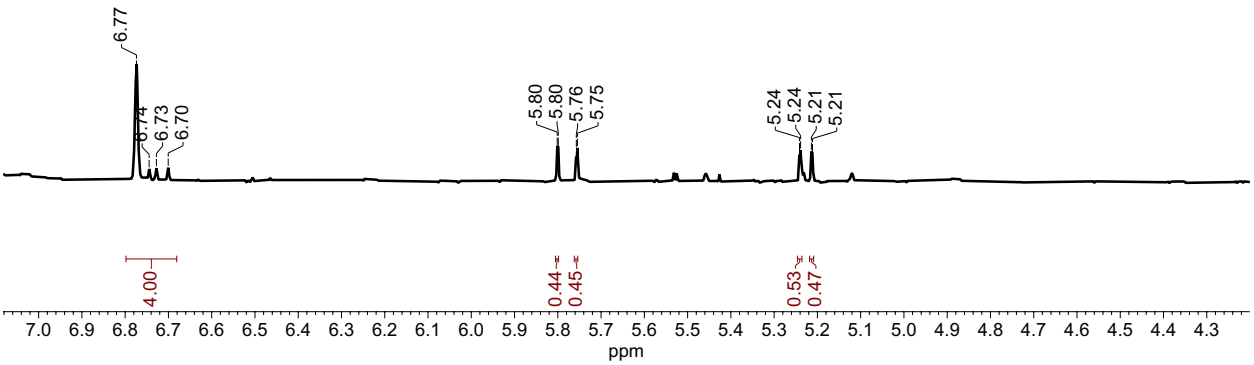

Figure S35. Phenylacetylene reaction to form styrene in CD_3CN. δ 5.78 (*J* = 17.7, 1 Hz), 5.22 (*J* = 11, 1 Hz). δ 6.77 is the mesitylene internal standard.

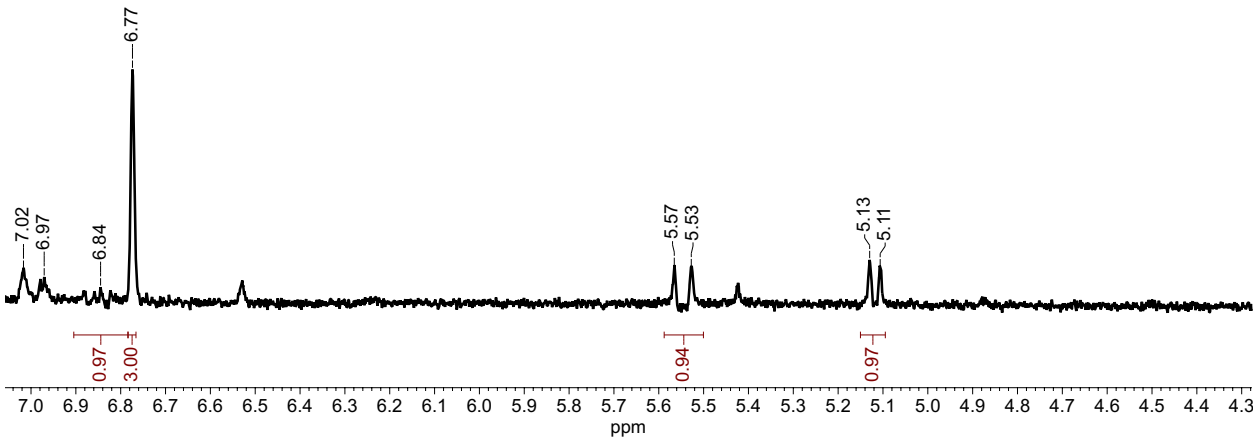

Figure S36. 2-ethynyl-thiophene reaction to form 2-vinyl-thiophene in CD_3CN. δ 5.55 (J = 18.6 Hz), 5.12 (J = 11.7 Hz). δ 6.77 is the mesitylene internal standard.

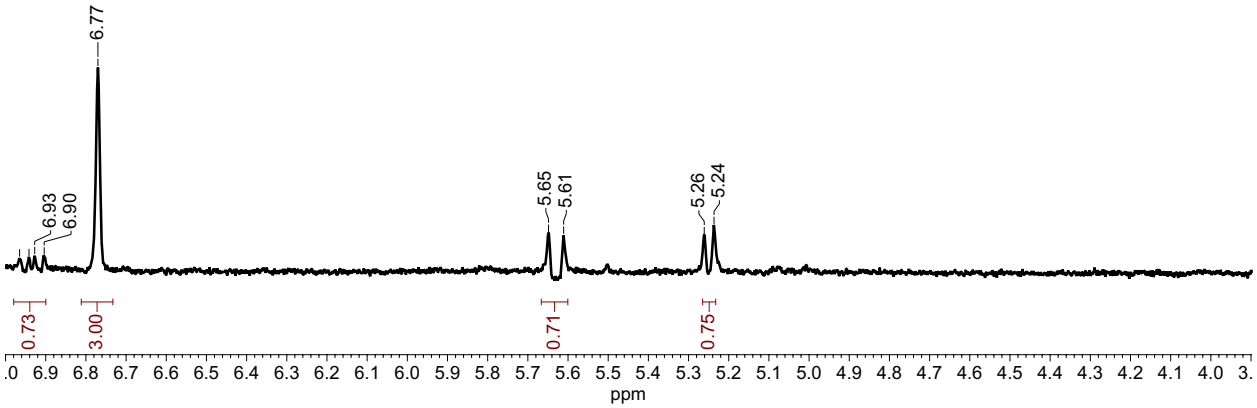

Figure S37. 2-ethynyl-toluene reaction to form 2-methyl-styrene in CD_3CN. δ 5.63 (J = 18.7, 0.9 Hz), 5.24 (J = 12.0, 0.9 Hz). δ 6.77 is the mesitylene internal standard.

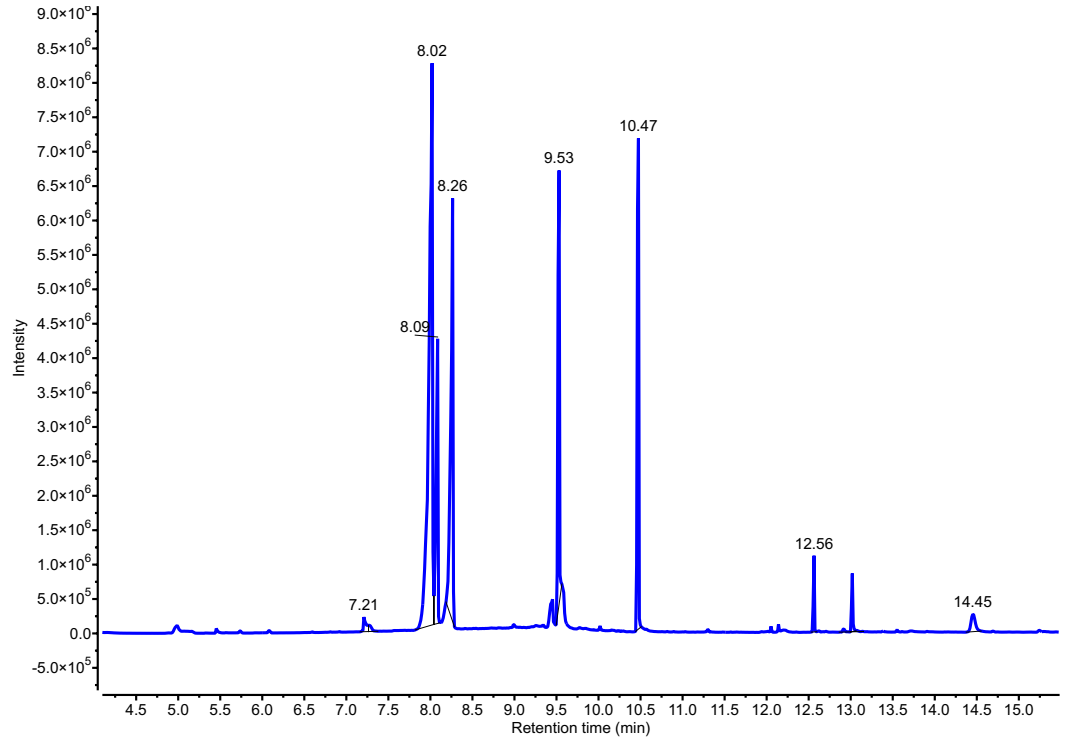

Figure S38. GC-TIC chromatogram of 2-ethynyl-toluene after electrolysis. * = 2-vinyl-toluene, † = 2-ethynyl-toluene, 8.02 min = mesitylene internal standard, 9.53 min = residual $n\text{Bu}_4\text{N}^+$, 10.47 min = benzoic acid, 7.21, 12.56 13.04, 14.45 min = contaminants (see mass spectrum below and Figure S31, S46, and S54).

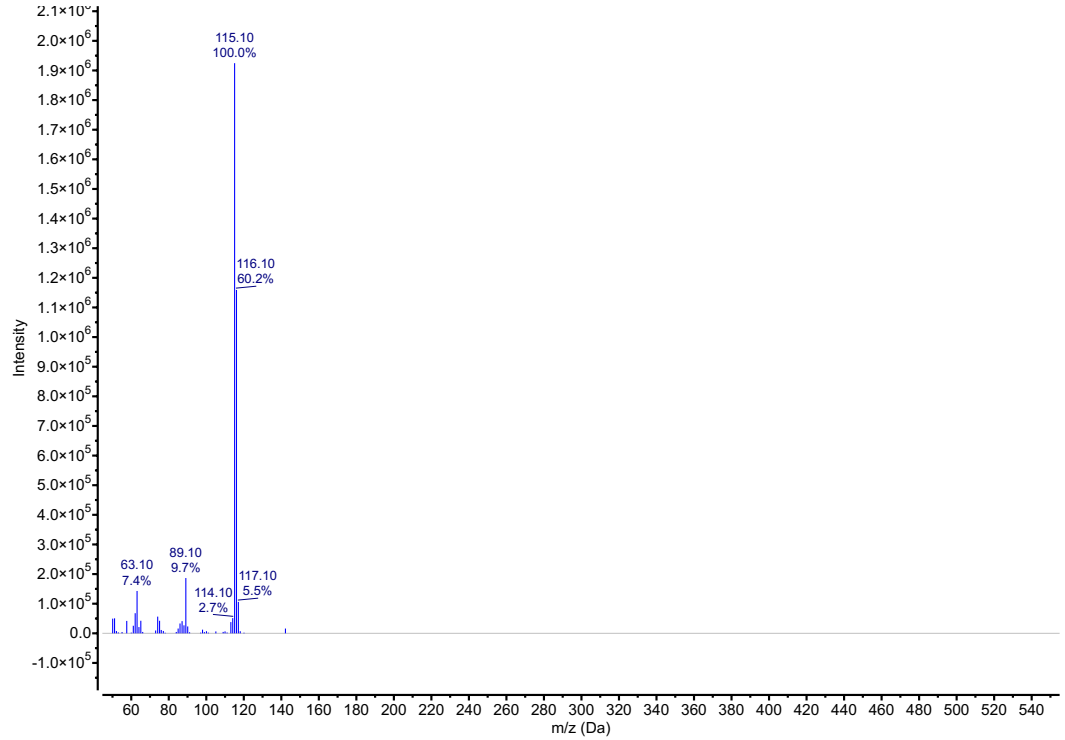

Figure S39. Mass spectrum at t = 8.09 min of 2-ethynyl-toluene (MW 116).

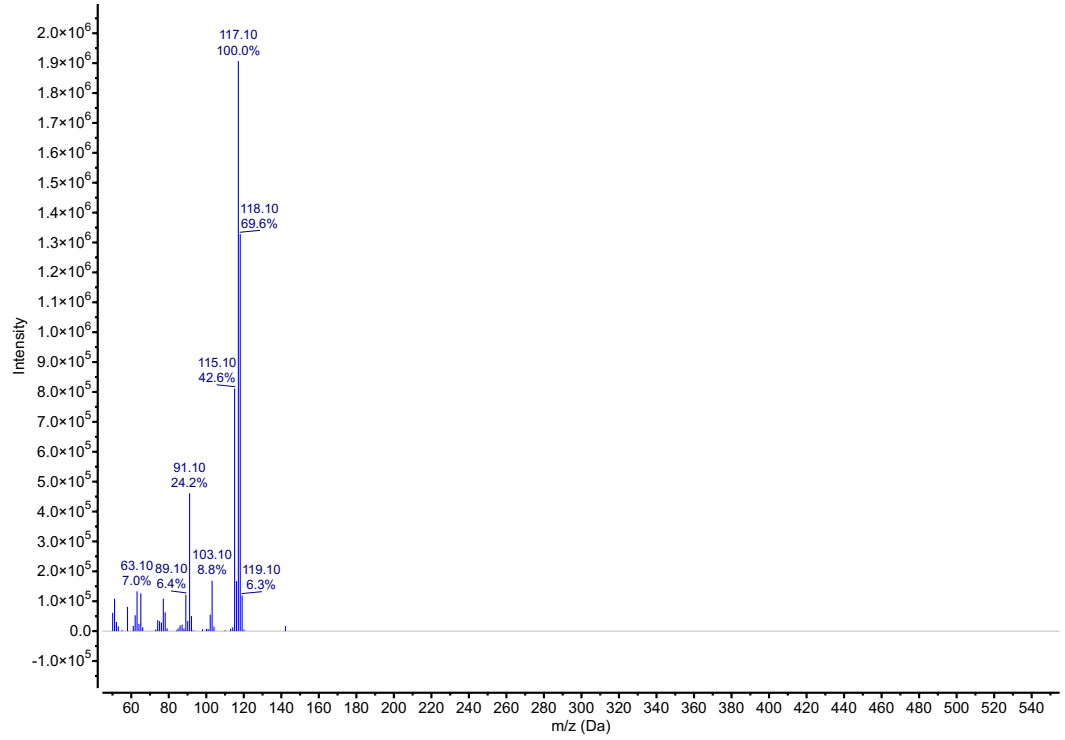

Figure S40. Mass spectrum at t = 8.26 min of 2-vinyl-toluene (MW 118).

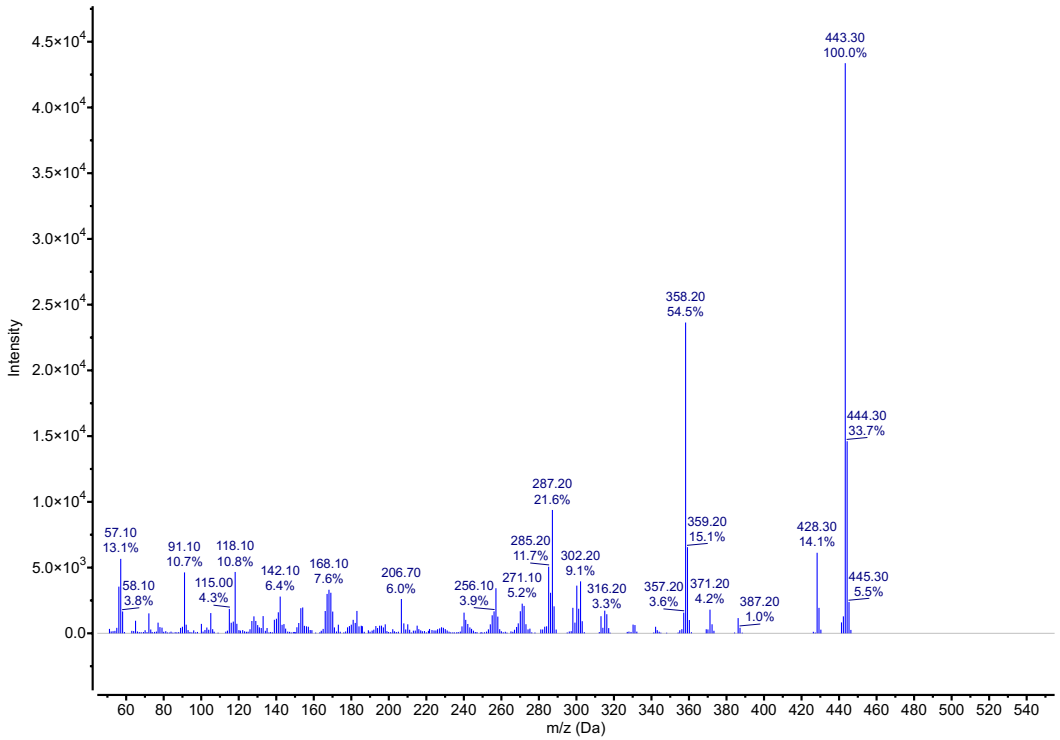

Figure S41. Mass spectrum at t = 14.45 min of ligand. Masses do not match dimerized product, which has an expected MW = 232.

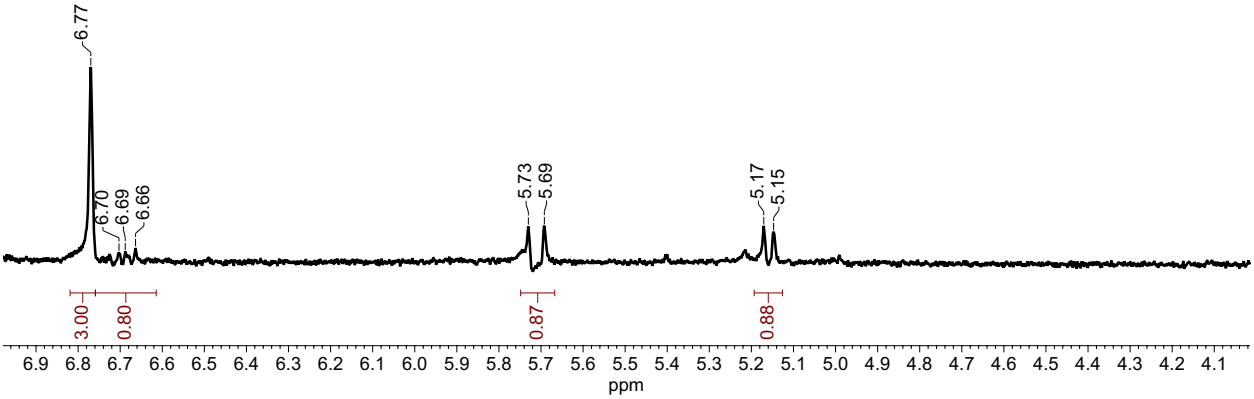

Figure S42. 4-ethynyl-toluene reaction to form 4-methyl-styrene in CD_3CN. δ 5.71 (J = 18.8 Hz), 5.16 (J = 11.7 Hz). δ 6.77 is the mesitylene internal standard.

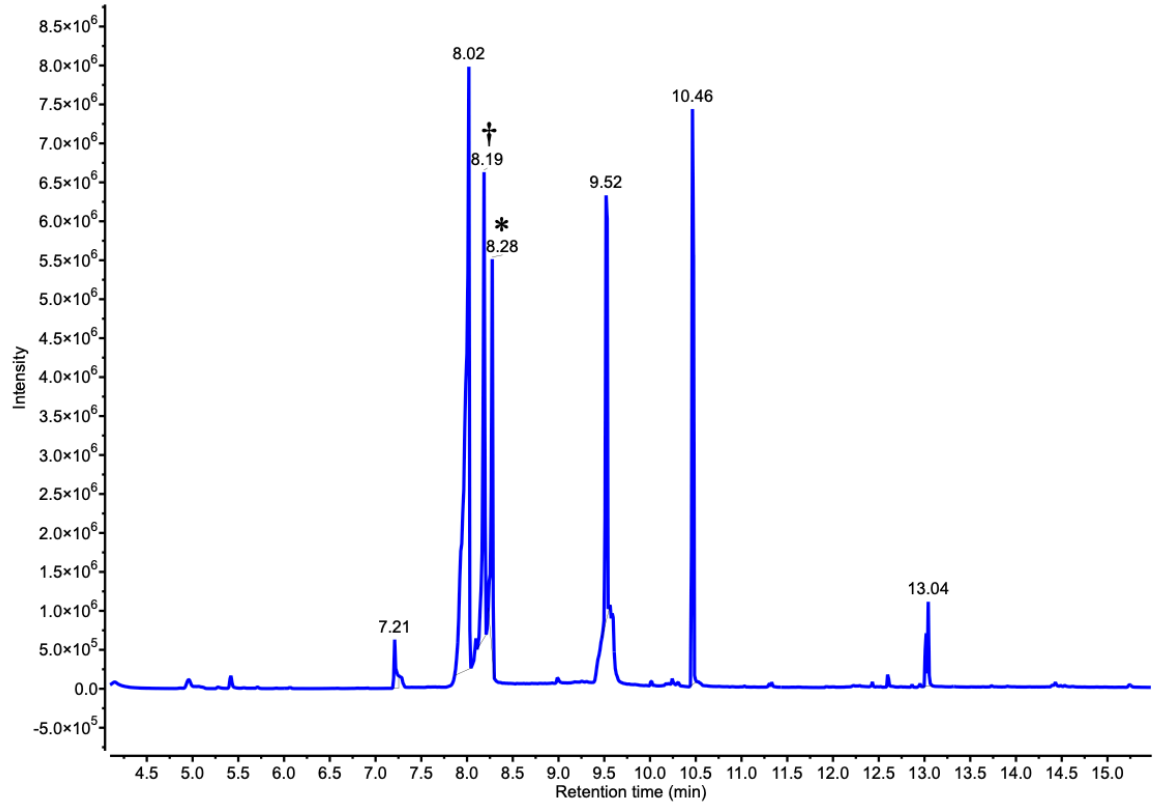

Figure S43. GC-TIC chromatogram of 4-ethynyl-toluene after electrolysis. * = 4-methyl-styrene, † = 4-ethynyl-toluene, 8.02 min = mesitylene internal standard, 9.52 min = residual nBu$_4$N$^+$, 10.46 min = benzoic acid, 7.21 and 13.04 = contaminants (see mass spectrum below and Figure S31).

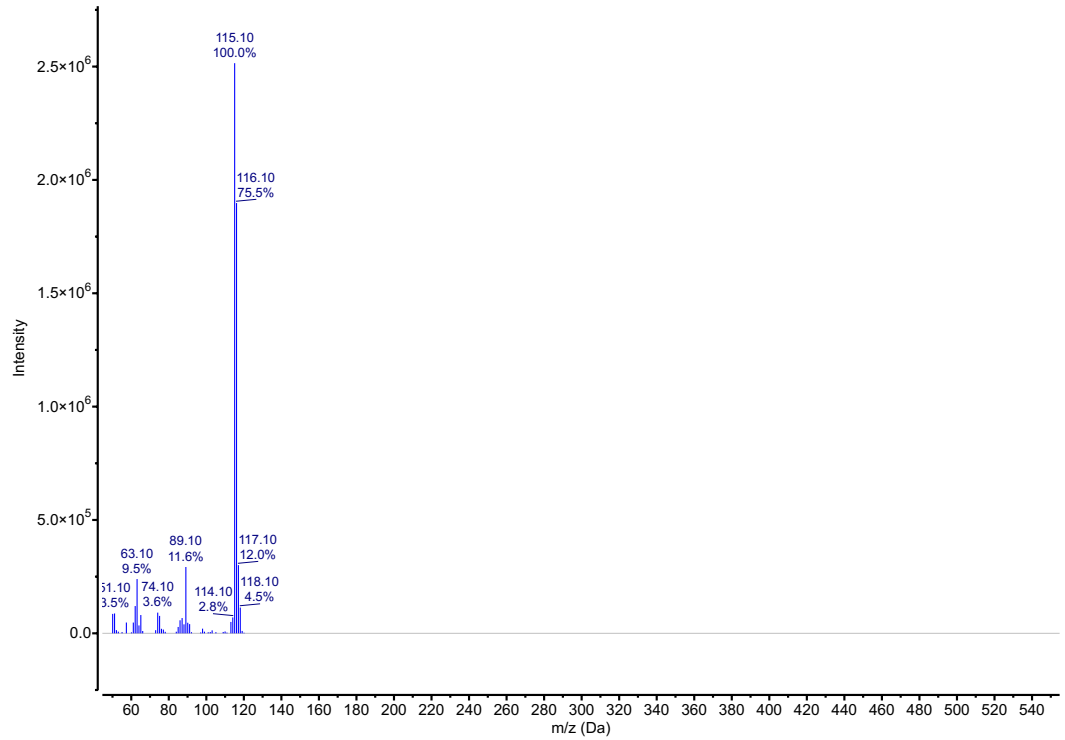

Figure S44. Mass spectrum at t = 8.19 min of 4-ethynyl-toluene (MW 116).

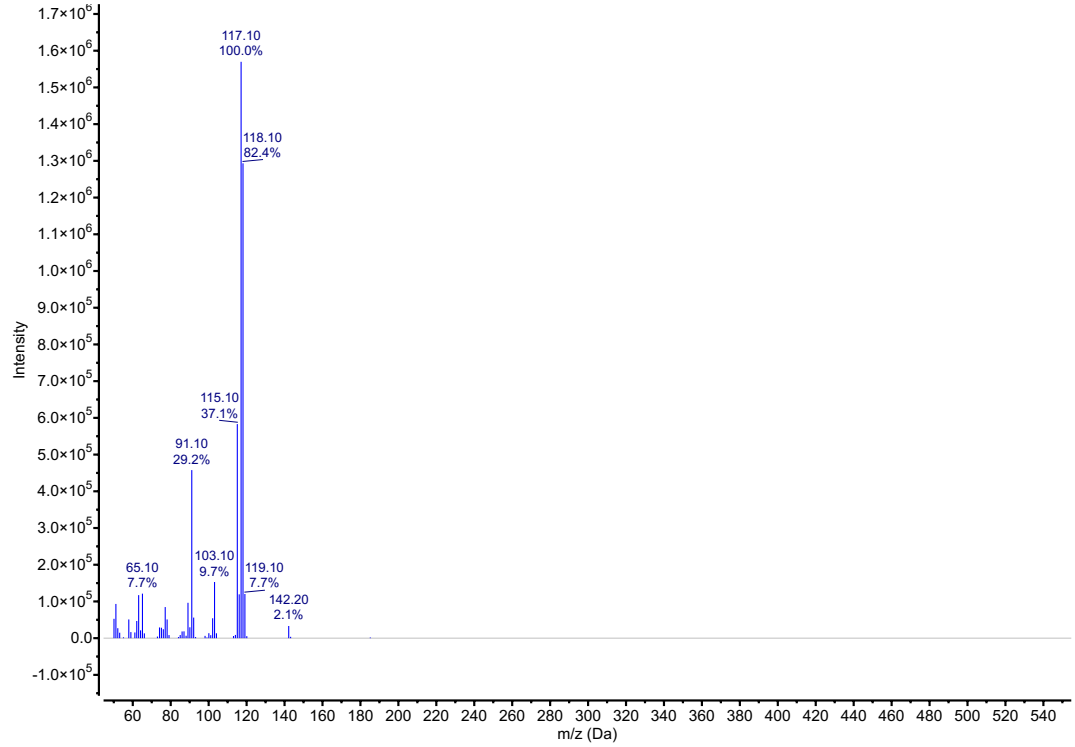

Figure S45. Mass spectrum at t = 8.28 min of 4-methyl-styrene (MW 118).

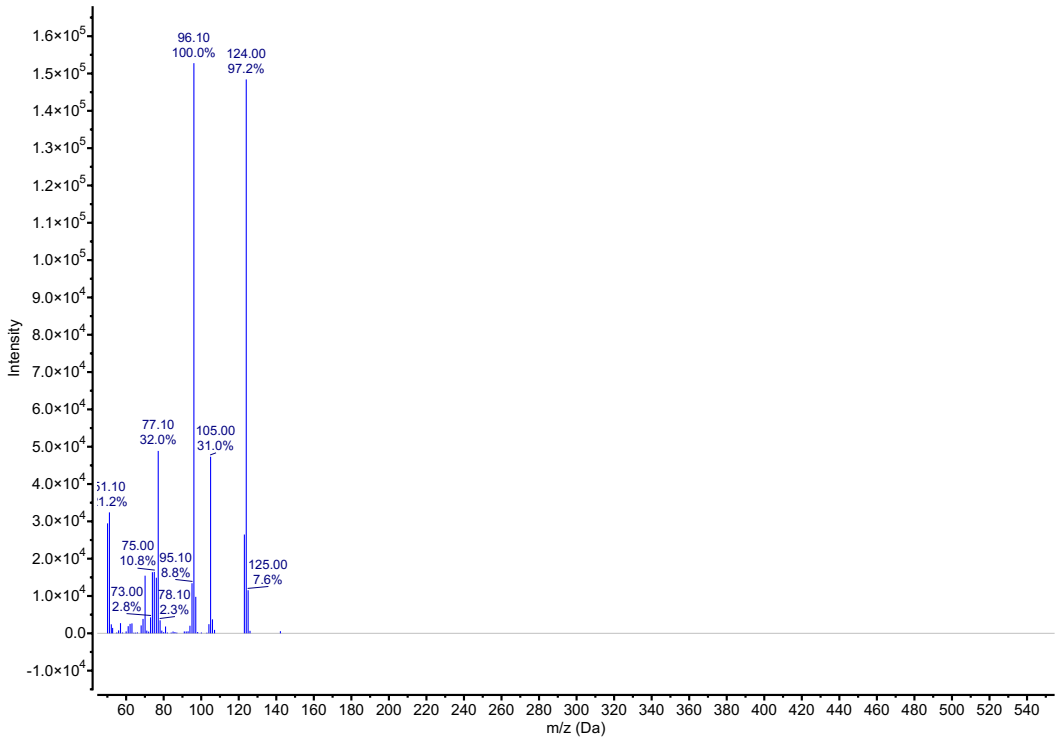

Figure S46. Mass spectrum at t = 7.21 min of column contaminant. Masses do not match fully hydrogenated product (expected MW = 120) or dimerized product (expected MW = 232).

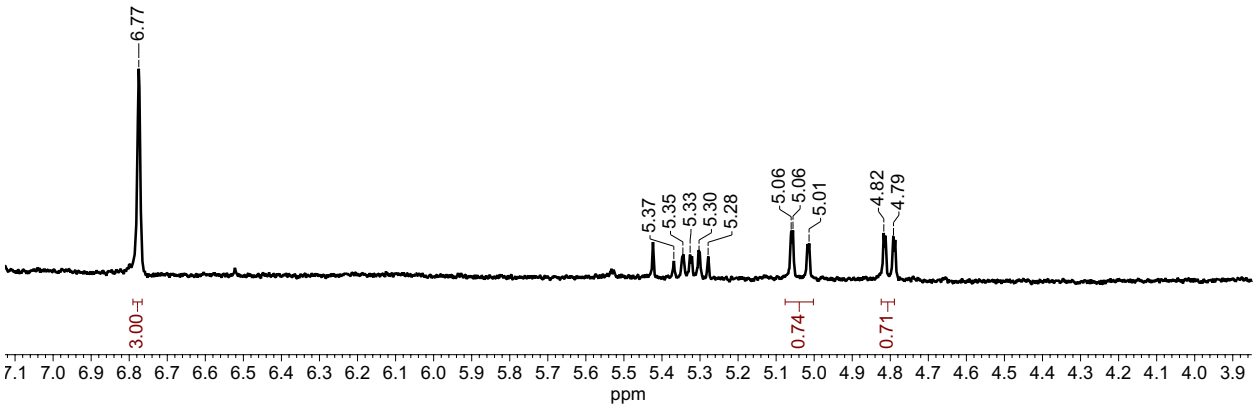

Figure S47. Cyclopropyl acetylene reaction to form ethenyl cyclopropane in CD_3CN. δ 5.03 (J = 17, 1.7 Hz), 4.81 (J = 10.3, 1.7 Hz). δ 6.77 is the mesitylene internal standard.

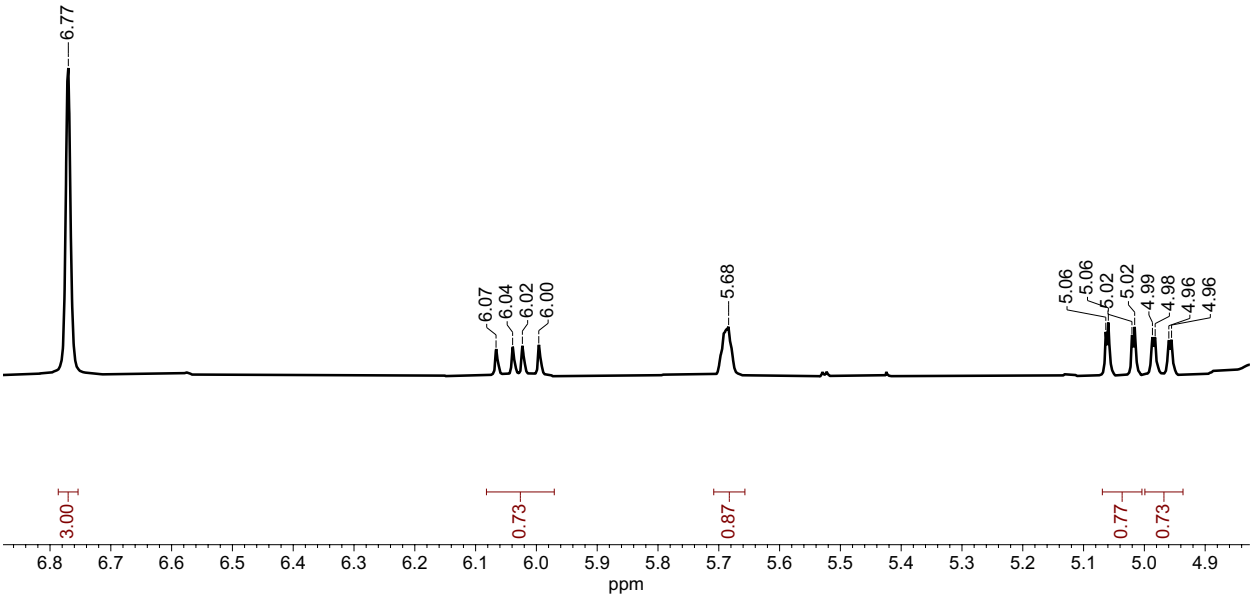

Figure S48. Levonorgestrel reaction to form the semi-hydrogenated analogue in CD_3CN. δ 6.05, 6.01 (J = 10.8 Hz), 5.03 (J = 17.3, 1.6 Hz), 4.97 (J = 10.8, 1.6 Hz). δ 6.77 is the mesitylene internal standard.

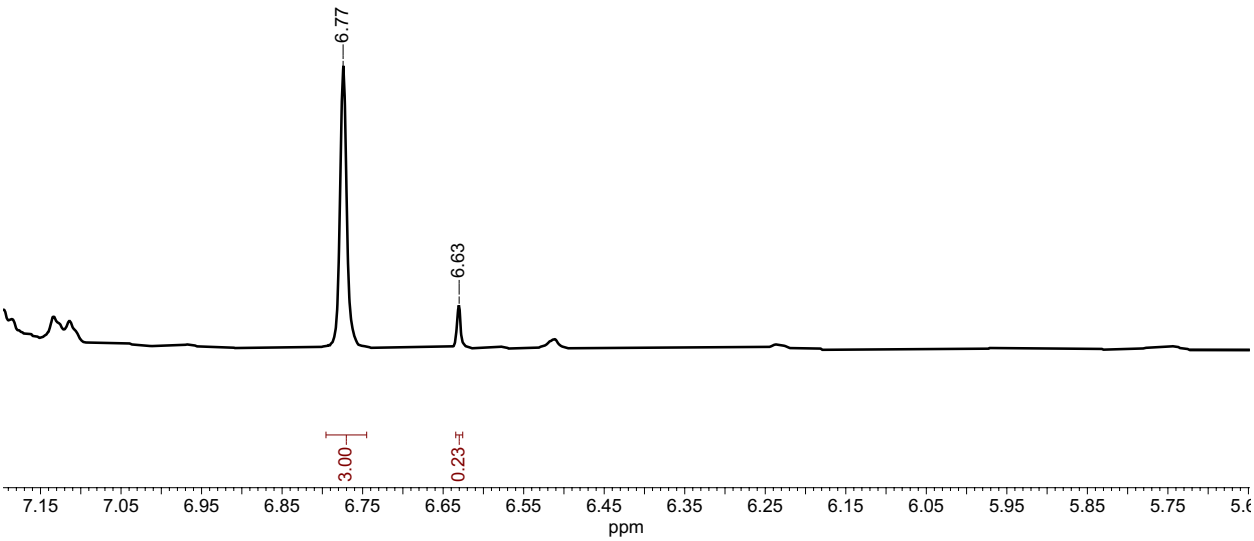

Figure S49. Diphenylacetylene reaction to form *cis*-stilbene in CD_3CN. δ 6.77 is the mesitylene internal standard.

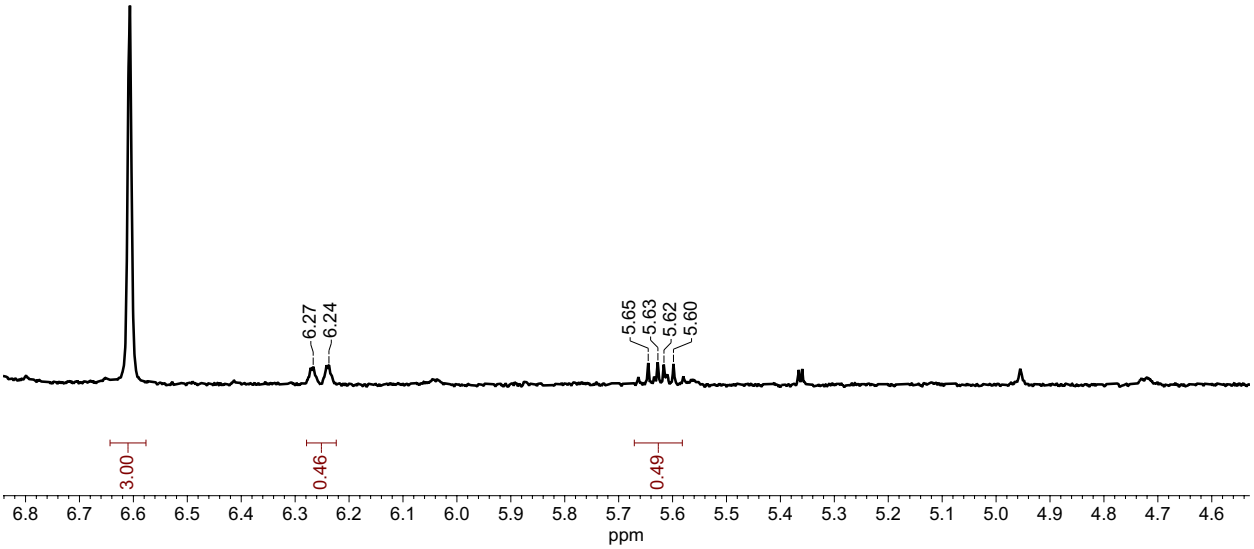

Figure S50. 1-Phenyl-1-propyne reaction to form β-methyl-styrene in CD_3CN. δ 6.25 (J = 11.7, 1.7 Hz). δ 6.77 is the mesitylene internal standard.

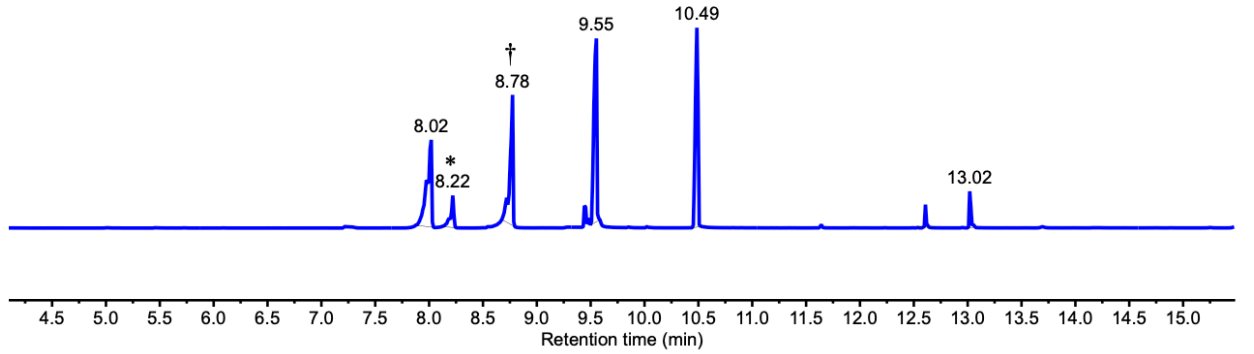

Figure S51. GC-TIC chromatogram of 1-phenyl-1-propyne after electrolysis. * = β-Me-styrene, † = 1-phenyl-1-propyne, 8.02 min = mesitylene internal standard, 9.55 min = residual nBu$_4$N$^+$, 10.49 min = benzoic acid, 12.61 and 13.02 = contaminants (see mass spectrum below and Figure S31).

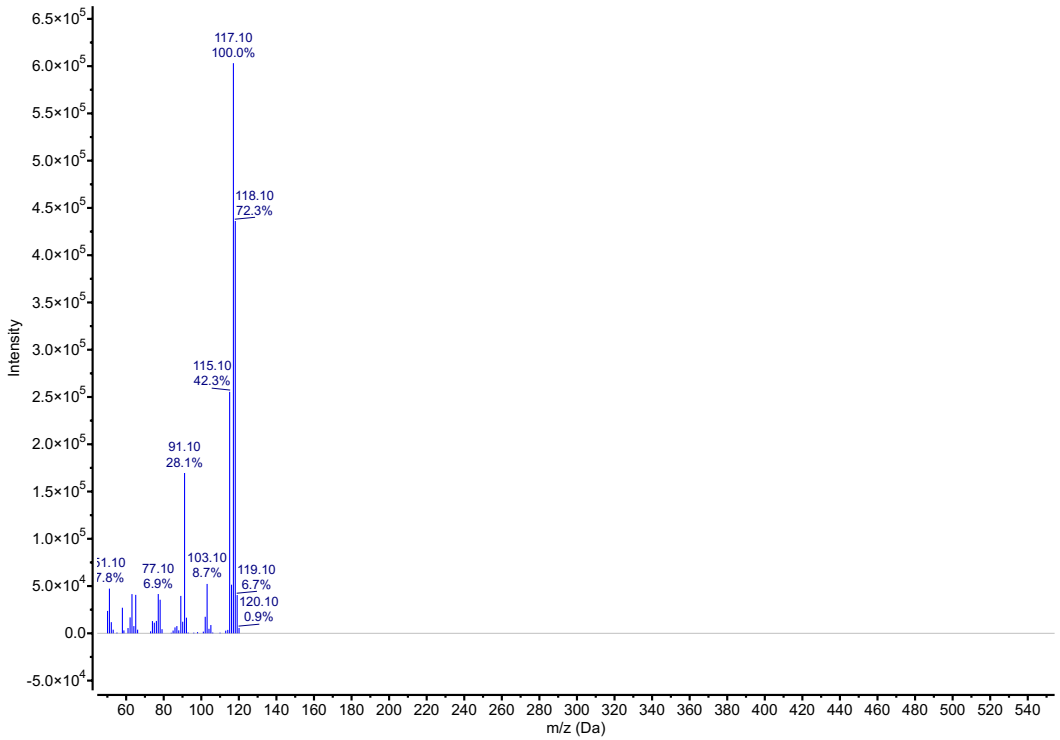

Figure S52. Mass spectrum at t = 8.22 min of β-Me-styrene (MW 118).

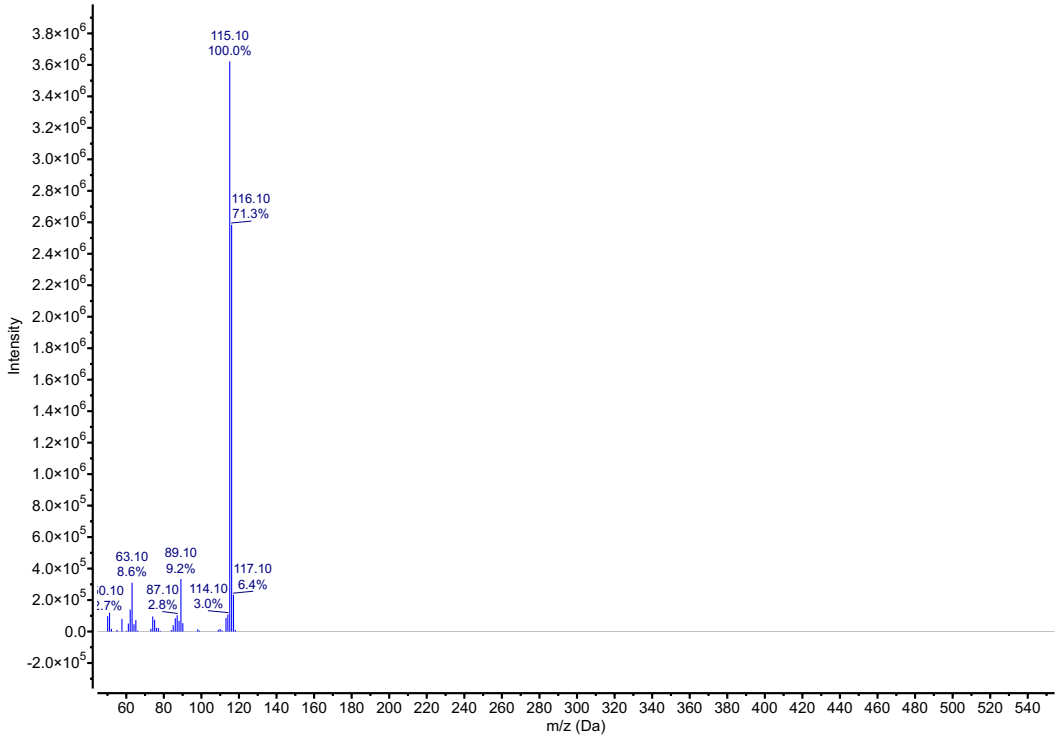

Figure S53. Mass spectrum at t = 8.78 min of 1-Ph-1-propyne (MW 116).

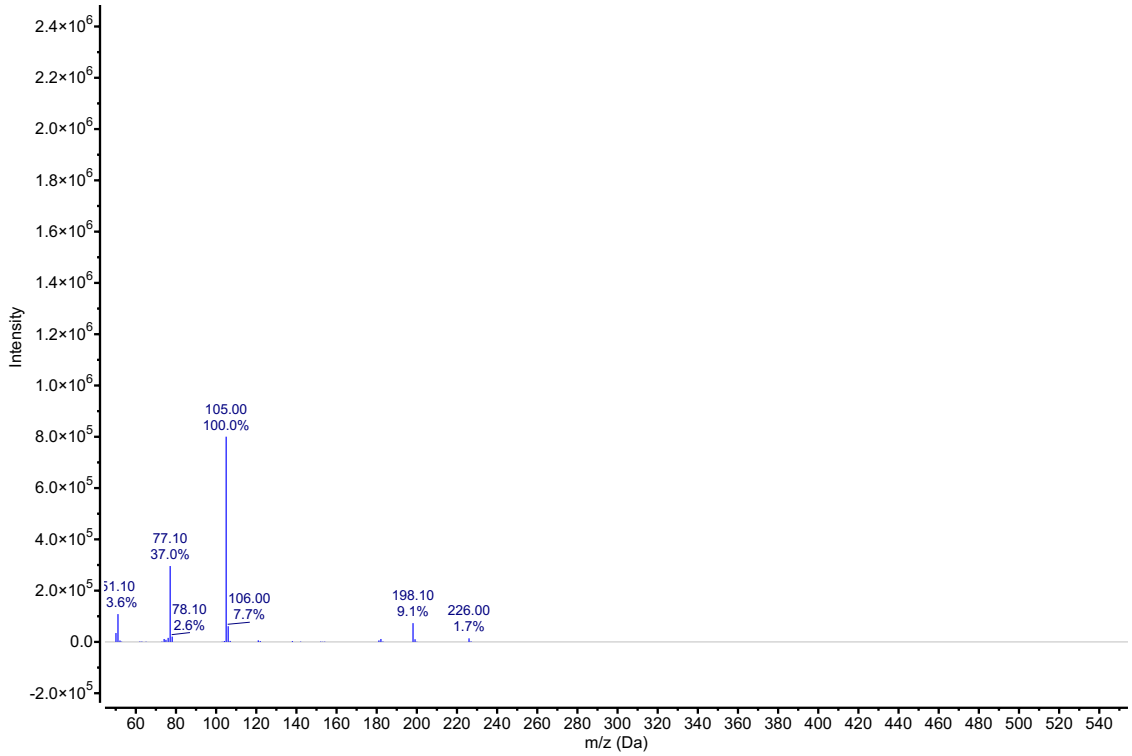

Figure S54. Mass spectrum at t = 12.61 min of column contaminant. Masses do not match a product dimer, which has an expected MW = 232).

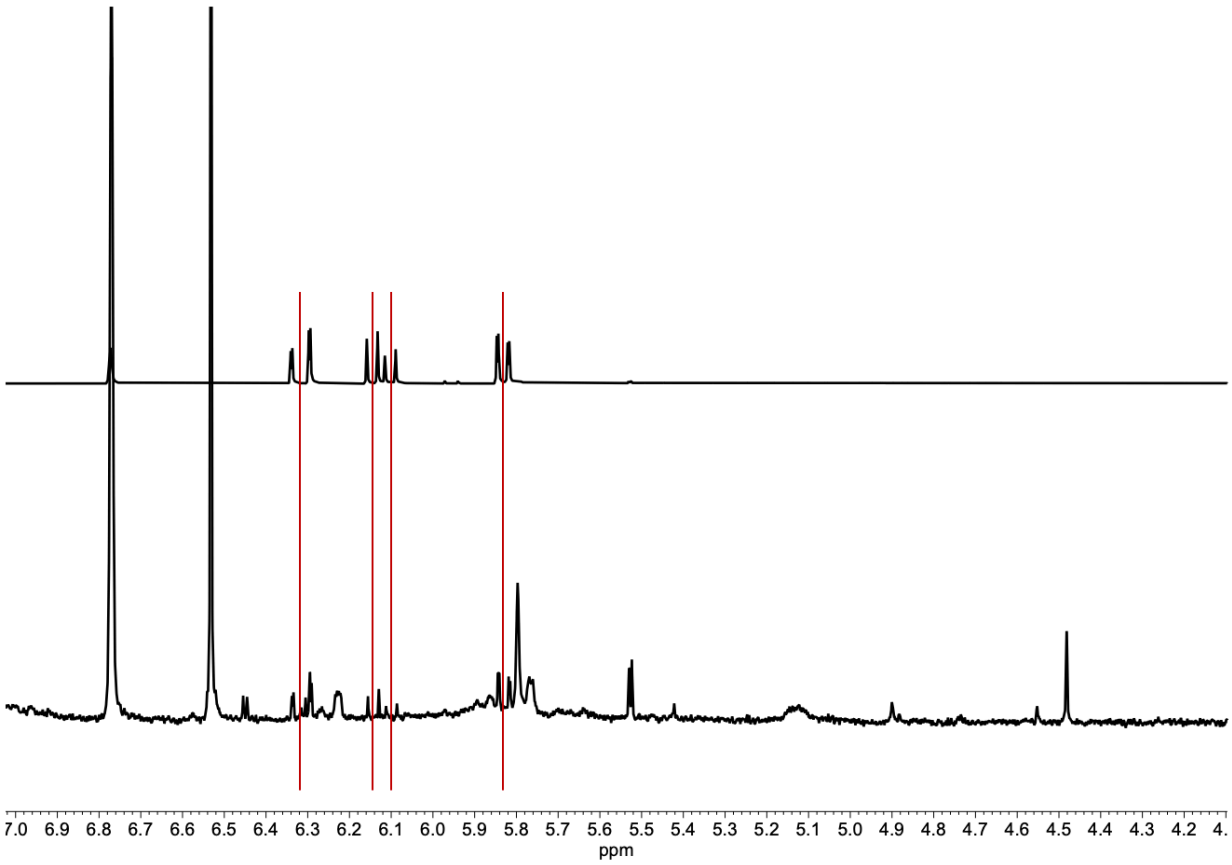

Figure S55. Methyl acrylate (top) and the methyl propiolate post-electrolysis product mixture (bottom) in CD_3CN.

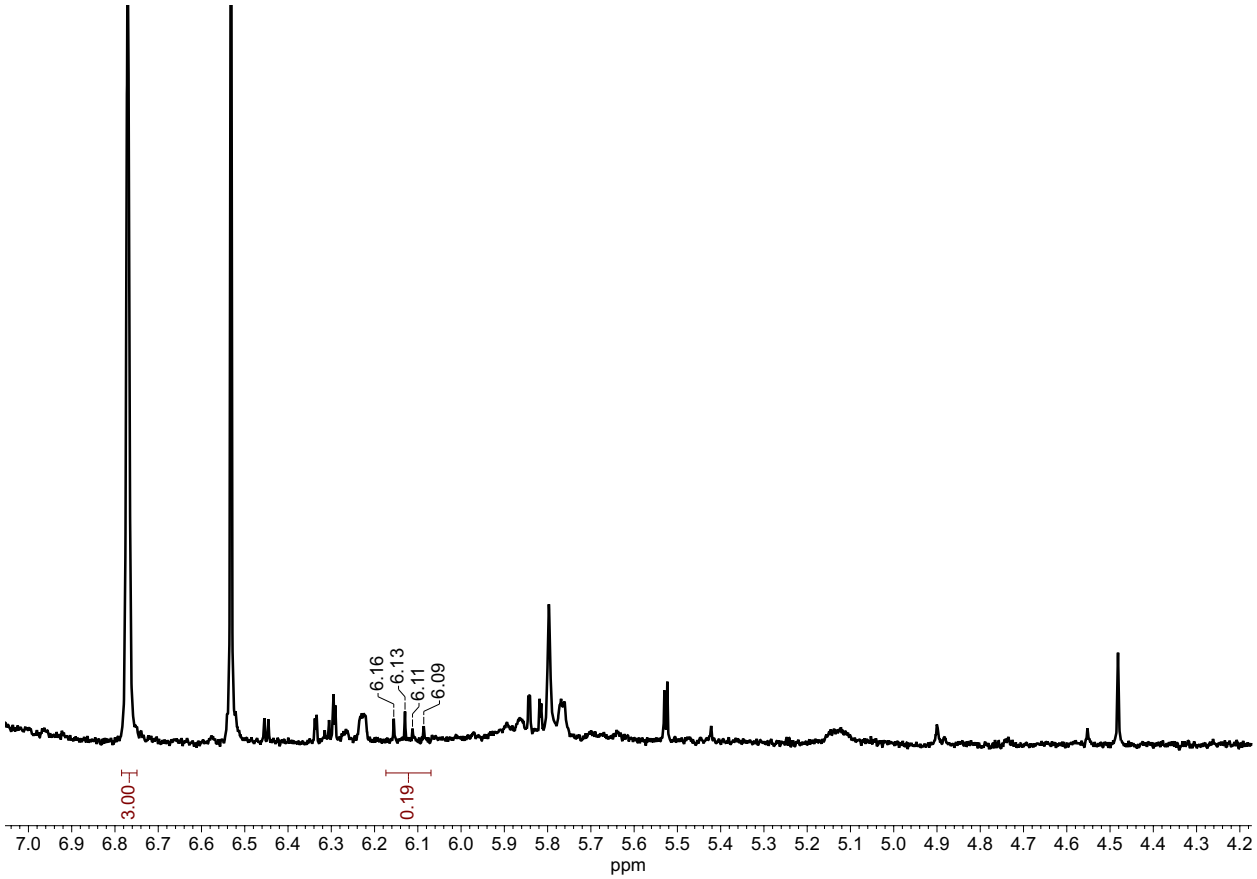

Figure S56. Methyl propiolate reaction to form methyl acrylate in CD_3CN. One alkene peak is integrated for determining yield due to the other signals overlapping with byproducts (*vide supra* for commercial standard methyl acrylate peaks). δ 5.82 (*J* = 10.2, 1.6 Hz). δ 6.77 is the mesitylene internal standard.

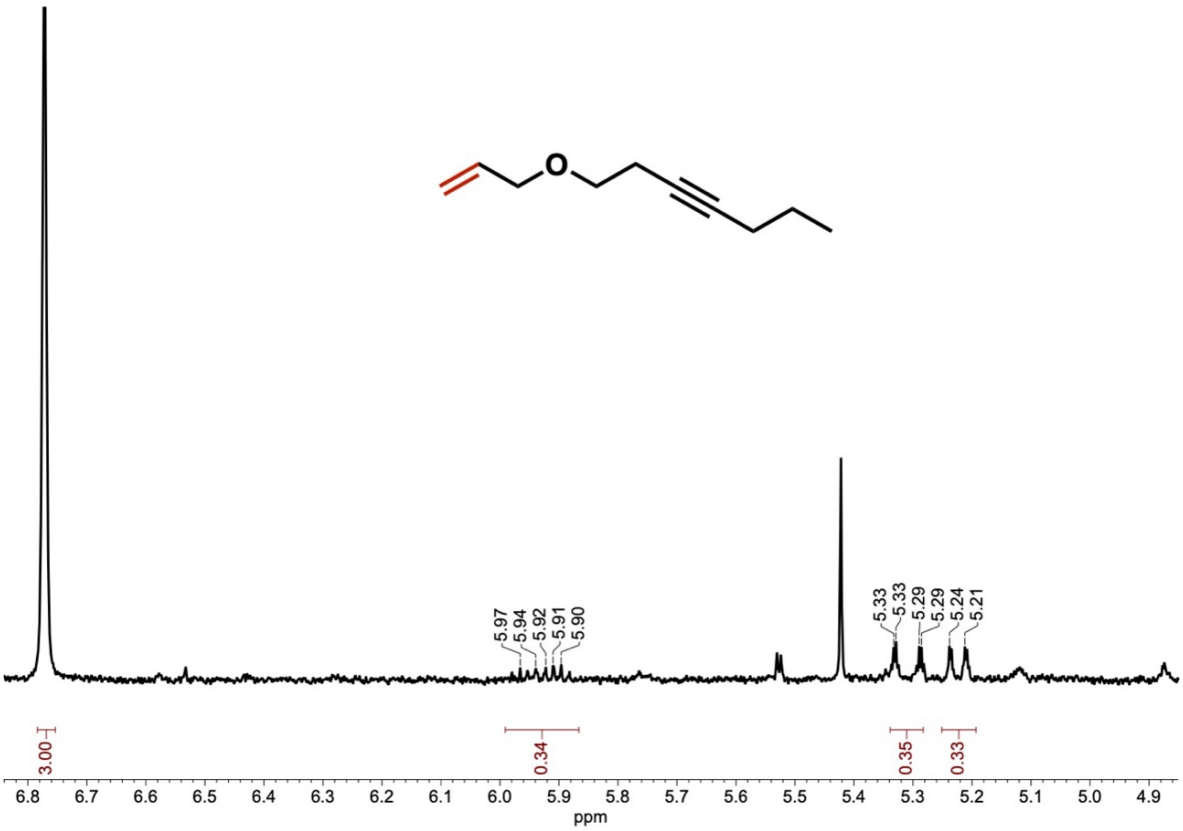

Figure S57. 1-prop-2-ynyloxy-hept-3-yne reaction to form 1-allyloxy-hept-3-yne in CD_3CN, DCM impurity at δ 5.42. δ 6.77 is the mesitylene internal standard.

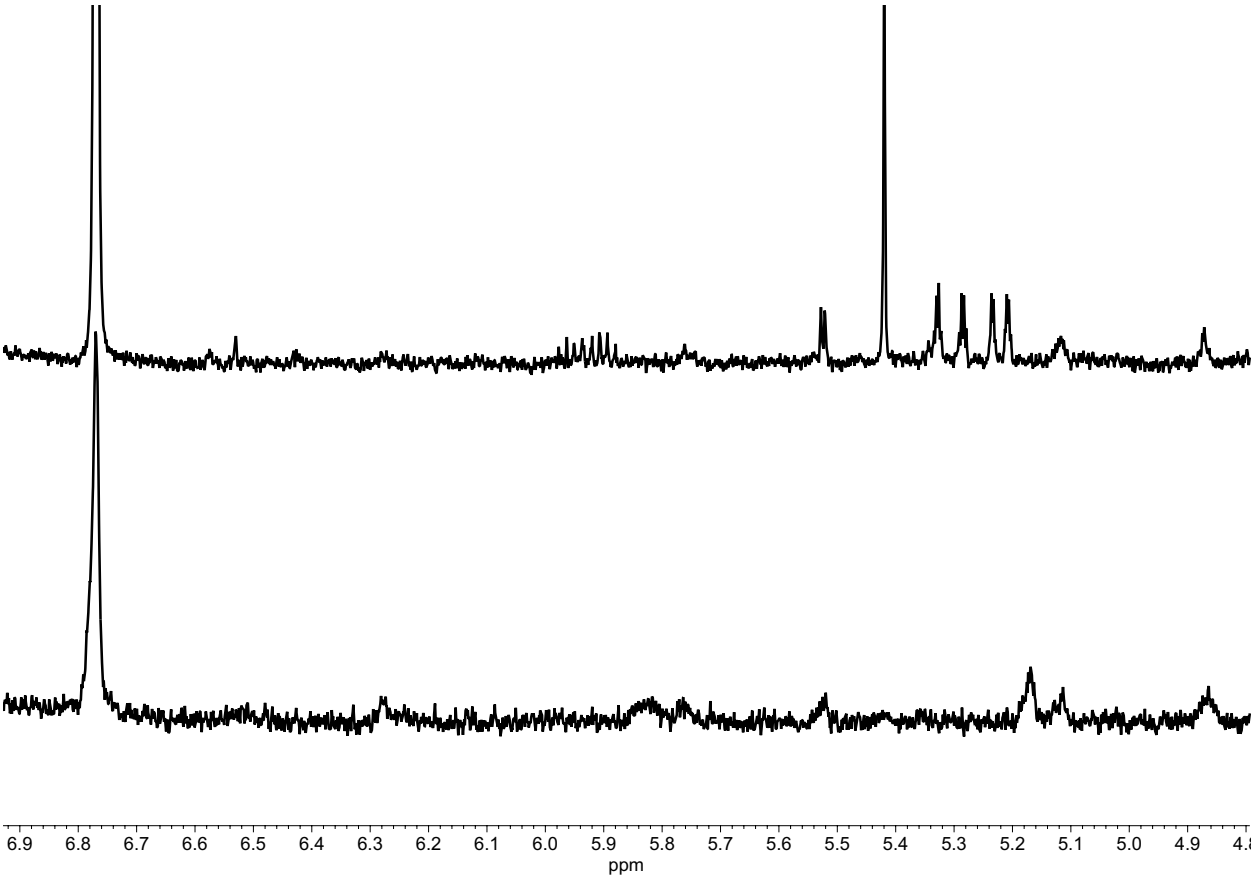

Figure S58. Post-electrolysis reaction mixture in CD_3CN of 1-prop-2-ynyloxy-hept-3-yne showing alkene product (top) and after exposure to silica gel column (bottom) showing instability of the product to attempted isolation. δ 6.77 is the mesitylene internal standard.

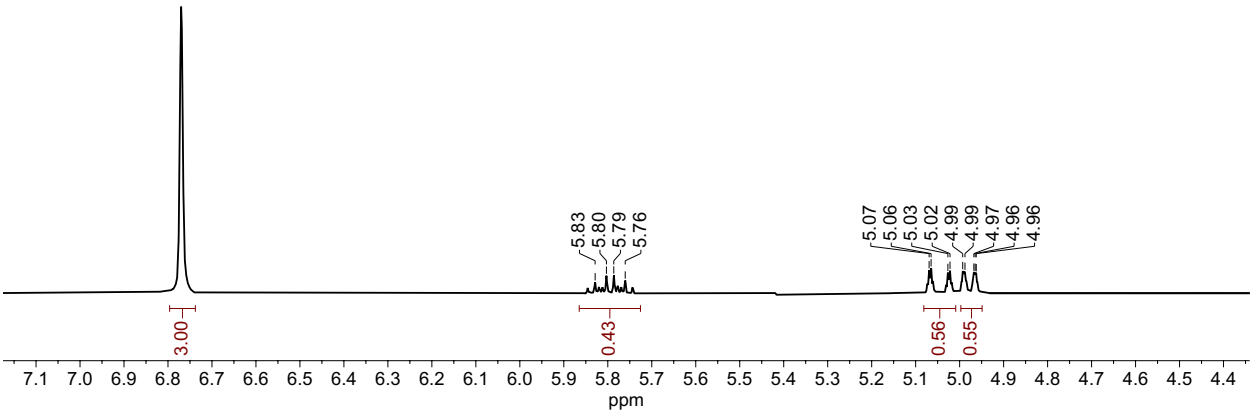

Figure S59. Undeca-5,10-diyne-1-ol reaction to form undeca-10-en-5-yn-1-ol in CD_3CN. Spectrum collected on 500 MHz instrument. δ 6.77 is the mesitylene internal standard.

Table S2. Triplicate yields for all substrates. Electrolysis performed under standard conditions. *yields for semi-hydrogenated products.

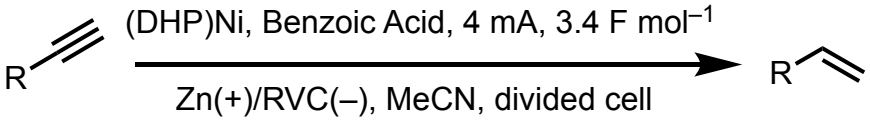

Substrate	Yields* (%)	Average (%)	Faradaic Efficiency (%)
Phenylacetylene	96, 98, 96	97(1)	57
1-Octyne	71, 70, 73	71(2)	42
Diphenylacetylene	11, 10, 14	11(2)	6
2-ethynyl-thiophene	95, 97, 95	95(1)	56
2-ethynyl-pyridine	97, 95, 98	97 (2)	57
4-chloro-phenylacetylene	98, 98, 98	98	57
4-ethynyl-toluene	90, 86, 87	87(2)	51
2-ethynyl-toluene	72, 72, 73	72(1)	42
3-methyl-1-pentyn-3-ol	98, 97, 98	98(1)	57
1-phenyl-1-propyne	46, 40, 41	42(3)	25
Methyl propiolate	18, 15, 16	16(2)	9
Cyclopropyl acetylene	71, 71, 72	71(1)	42
Levonorgestrel	73, 77, 76	75(2)	44
1-prop-2-ynyloxy-hept-3-yne	33, 35, 35	34(1)	20
Undeca-5,10-diyne-1-ol	56, 56, 56	56	33

Control Experiments

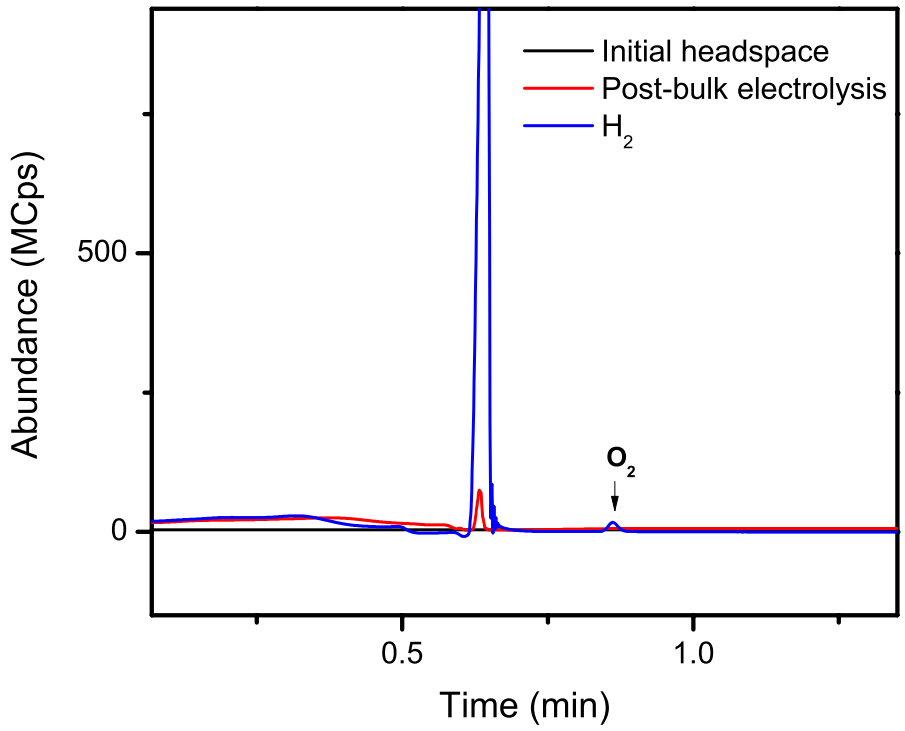

Figure S60. Detection of H_2 by mass spectrometry post-electrolysis.

Table S3. Quantification of H_2 using gas chromatography calibration curve. Comparing the injected volume of H_2 into the H-cell with the calculated volume shows that some gas leakage from the H-cell is occurring. The total H_2 produced was extrapolated from the aliquot to the volume of the H-cell headspace.

		H_2 measured	
H_2 added	**Conditions/considerations**	**Measured**	**Extrapolate to H-cell headspace**
30 µL	From H_2 gas tank, syringed directly into GC (control to test calibration)	28 µL	-
2.6 mL	Injected into to H-cell under N_2 atm, 5 min equilibration before GC injection (50 µL aliquot)	4.6 µL	740 µL
0	Bulk electrolysis (55 min) before injection (50 µL aliquot), 2.6 mL H_2 theoretically generated (assuming 50% FE)	0.94 µL	150 µL

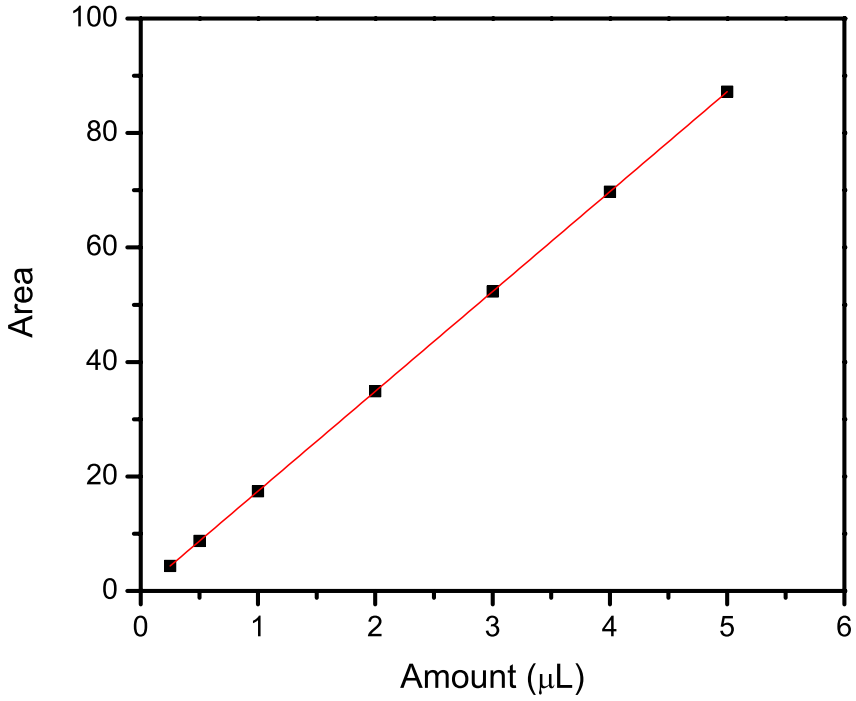

Figure S61. Gas chromatography (TCD detector) calibration curve for H_2 (retention time: 0.630 min).

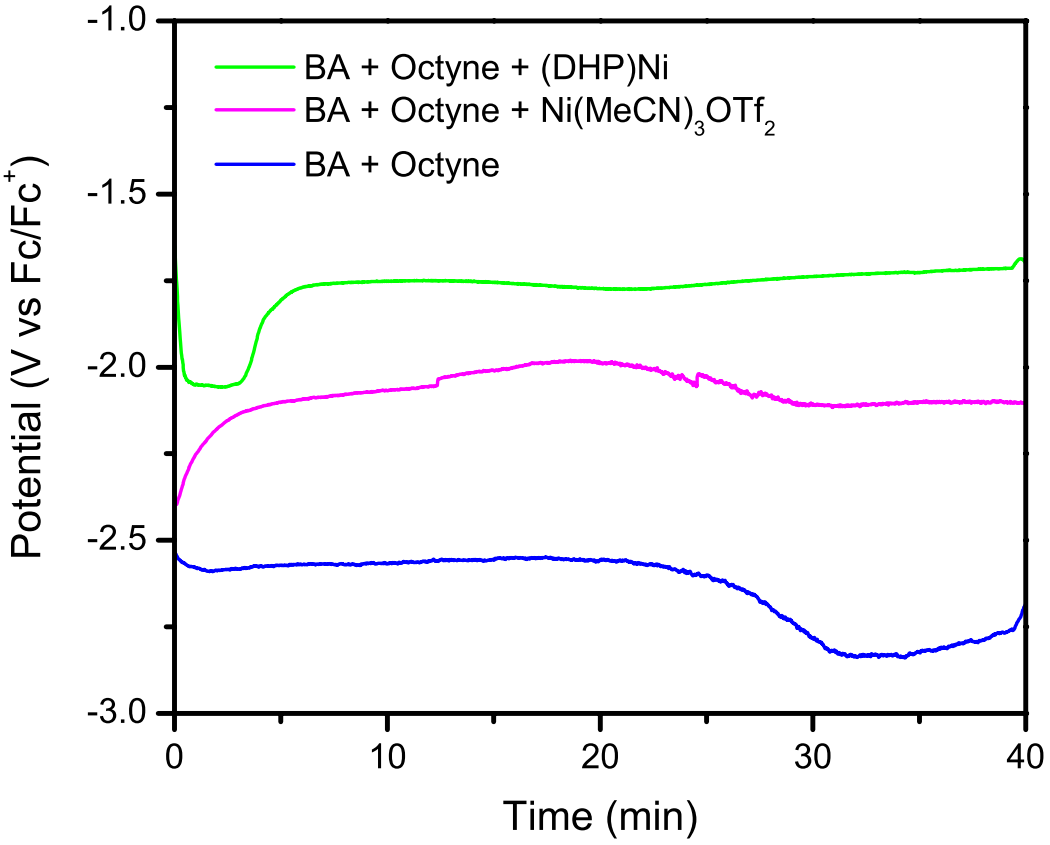

Figure S62. Control bulk electrolysis reactions with $Ni(MeCN)_3OTf_2$ and no catalyst in the presence of benzoic acid (BA) and octyne substrate compared to the standard reaction conditions.

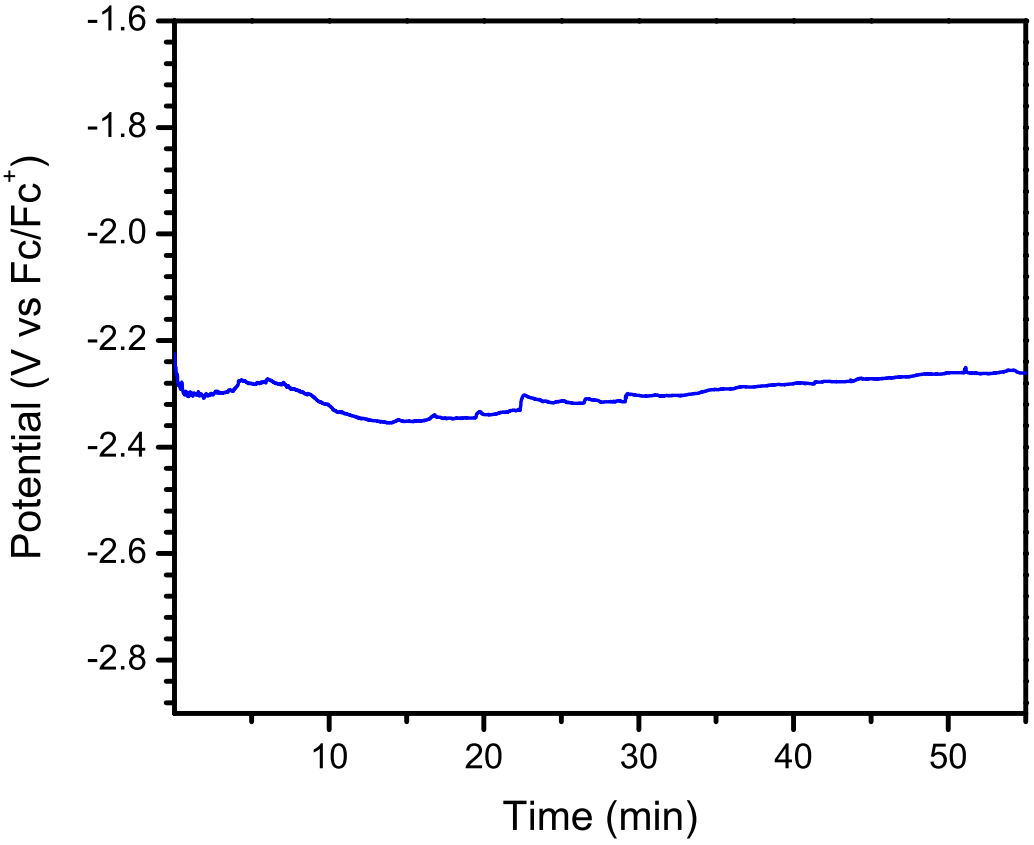

Figure S63. Control bulk electrolysis with ^{tBu,Tol}DHP ligand and no catalyst in the presence of benzoic acid (BA) and octyne substrate.

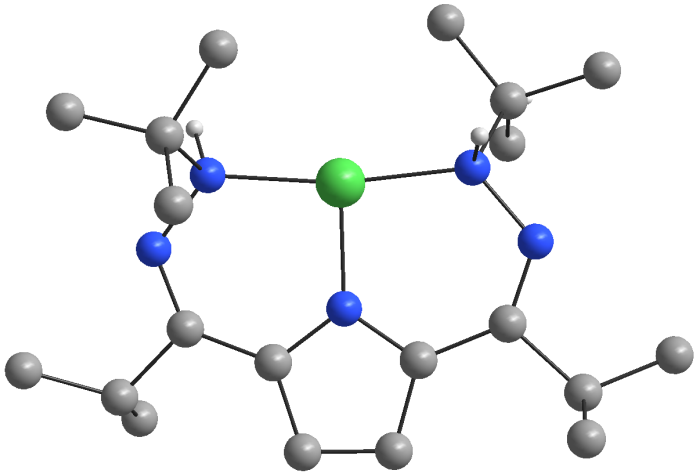

Figure S64. Calculated structure of **4**.

Table S4. Coordinates of calculated structure of **4**.

Ni	14.67901	2.99901	6.46909
N	13.73090	1.96237	7.89802
N	12.30129	2.08754	8.14778
N	13.09716	3.48880	5.55366
N	15.48168	4.51386	3.93604
N	15.91710	3.85385	5.15559
C	13.59918	-0.26844	9.05240
C	15.60158	0.41608	7.73340
H	16.07766	0.92419	8.59207
C	14.08211	0.48083	7.81588
C	11.52569	2.60833	7.24670
C	10.05187	2.61022	7.64592
C	9.68839	1.53848	8.66033
C	9.63880	3.99379	8.14463
C	11.82661	3.23503	5.97173
C	10.91427	3.76236	5.01902
H	9.82318	3.72640	5.06010
C	11.67538	4.35006	4.01666
H	11.28947	4.84764	3.12400
C	13.03812	4.16831	4.37579
C	14.21840	4.61823	3.65784
C	13.95141	5.32614	2.33175
C	13.60166	4.31159	1.24419

C	15.08863	6.22716	1.87663
C	13.45172	-0.09030	6.55690
H	13.75472	-1.14354	6.42472
H	12.34896	-0.06054	6.60752
C	16.95593	4.73183	5.83418
C	17.46874	3.91799	7.01472
H	16.66668	3.73111	7.75818
H	18.28232	4.45574	7.53240
H	17.86589	2.94080	6.68417
C	18.10631	5.05896	4.89005
H	18.56544	4.13556	4.49203
H	18.89205	5.61683	5.42942
H	17.77829	5.67389	4.03635
C	16.25982	5.99465	6.31249
H	15.38271	5.74132	6.93874
H	15.91343	6.60955	5.46367
H	16.94891	6.60962	6.91768
H	14.01646	0.17140	9.97648
H	13.92874	-1.32135	9.00579
H	12.50038	-0.25997	9.13426
H	15.93759	-0.63584	7.73737
H	15.97929	0.88537	6.80271
H	13.77285	0.47780	5.66353
H	14.12501	2.25503	8.80215
H	16.46149	3.05852	4.78872
H	13.34494	4.82715	0.30160
H	12.74462	3.67488	1.52354
H	14.46219	3.64859	1.03743
H	13.06376	5.96732	2.49220
H	15.98333	5.64502	1.59719
H	15.39219	6.93582	2.66657
H	14.78005	6.81178	0.99149
H	9.47591	2.39663	6.72569
H	10.21082	4.26548	9.05113
H	8.56606	4.00964	8.40791
H	9.81021	4.77879	7.38786
H	10.15859	1.72397	9.64099
H	10.00853	0.53565	8.32715
H	8.59418	1.51600	8.81062

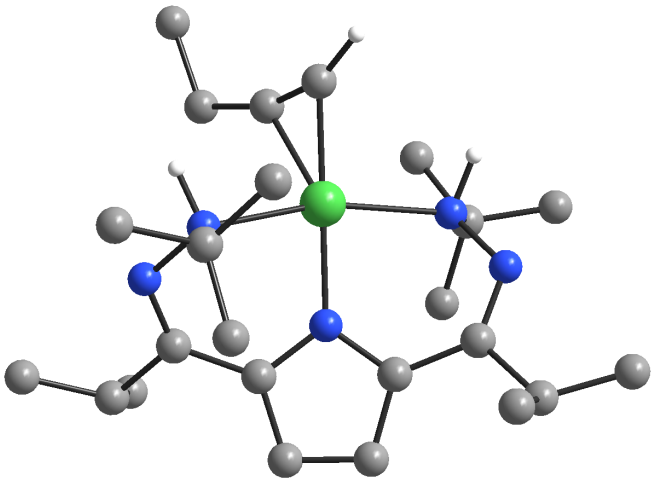

Figure S65. Calculated structure of **I1**.

Table S5. Coordinates of calculated structure of **I1**.

Ni	14.82160	2.52100	6.43348
N	13.46734	1.12280	7.45471
N	12.36221	1.73376	8.15601
N	13.18448	3.26350	5.66104
N	15.47206	4.58519	4.18143
N	15.68382	4.40108	5.59715
C	12.36311	-1.08873	7.79647
C	14.28280	-0.82141	6.22656
H	15.05194	-0.94925	7.00907
C	13.02353	-0.16713	6.77350
C	11.67963	2.63135	7.51931
C	10.50047	3.21182	8.28510
C	10.01241	2.33776	9.42722
C	10.84918	4.61795	8.77338
C	11.93770	3.22066	6.21326
C	11.02864	3.90816	5.37945
H	9.96082	4.05868	5.55574
C	11.75866	4.35697	4.27830
H	11.37602	4.93173	3.43107
C	13.09911	3.97672	4.50574
C	14.27265	4.37832	3.73900
C	14.06432	4.59124	2.25152
C	13.80378	3.24990	1.56432
C	15.19120	5.34706	1.56955
C	12.05861	0.12116	5.63495
H	11.81830	-0.82446	5.11714
H	11.10726	0.54709	5.99724
C	15.58762	5.69332	6.38527

C	15.84091	5.28599	7.83067
H	15.05518	4.59160	8.18880
H	15.84005	6.17365	8.48822
H	16.81766	4.78155	7.94381
C	16.65773	6.67095	5.90562
H	17.66814	6.23195	5.99723
H	16.64102	7.59652	6.50855
H	16.49777	6.94951	4.84945
C	14.21296	6.33078	6.26208
H	13.41245	5.67141	6.63946
H	13.97664	6.60641	5.21960
H	14.19646	7.25840	6.86166
H	13.04746	-1.30769	8.63626
H	12.09401	-2.04986	7.32369
H	11.44242	-0.64541	8.21159
H	14.03993	-1.82137	5.82625
H	14.72148	-0.22628	5.40835
H	12.49100	0.81669	4.89459
H	14.05202	0.78344	8.22728
H	16.68519	4.17741	5.64015
C	18.47665	0.66923	4.68853
H	17.09095	2.20151	4.01915
C	17.08463	1.28675	4.64685
C	16.55661	1.61848	5.97606
C	16.47836	1.80336	7.21970
H	16.80539	1.70848	8.25476
H	16.38041	0.60313	4.13323
H	18.81486	0.40262	3.67271
H	18.48692	-0.24779	5.30238
H	19.21146	1.37081	5.11949
H	9.77513	1.31516	9.08572
H	9.09787	2.76915	9.87188
H	10.76627	2.24728	10.22803
H	9.66790	3.30989	7.56144
H	11.70323	4.58381	9.47614
H	9.99581	5.07855	9.30223
H	11.12818	5.28213	7.93709
H	14.92917	5.55799	0.51742
H	16.12628	4.76048	1.57043
H	15.40321	6.30748	2.07002
H	13.55842	3.39796	0.49779
H	12.96687	2.70310	2.03308
H	14.70022	2.60297	1.61263
H	13.14140	5.19739	2.15450

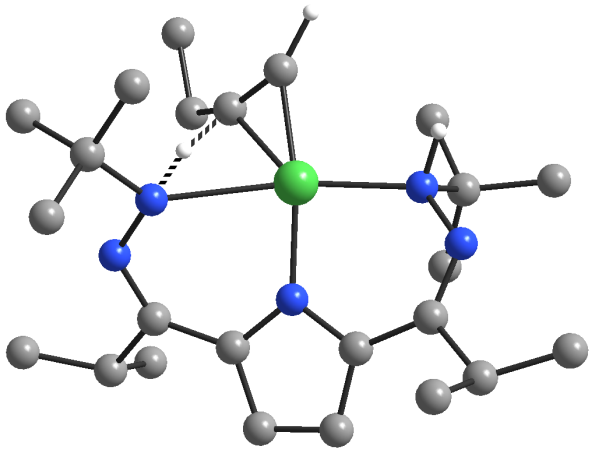

Figure S66. Calculated structure of **TS1**. Note that this is not an optimized TS, but is the closest structure obtained. Both frequency calculations, which show one reasonable imaginary mode, and IRC analysis (Figure S75) supports that this is a reasonable estimate of the true TS geometry.

Table S6. Coordinates of calculated structure of transition state 1 (**TS1**).

Ni	14.43705	2.64912	6.70334
N	13.28020	1.22099	7.66095
N	12.02571	1.67534	8.22430
N	12.86892	3.34075	5.83578
N	15.11725	4.86460	4.40122
N	15.39692	4.64148	5.73728
C	12.37834	-1.08824	7.94652
C	14.48248	-0.68153	6.68207
H	15.12809	-0.67383	7.57889
C	13.09344	-0.14144	6.98585
C	11.28275	2.46121	7.51045
C	9.93143	2.80107	8.11868
C	9.49216	1.85503	9.22245
C	9.92019	4.25173	8.59897
C	11.58873	3.08977	6.23902
C	10.68681	3.56593	5.26489
H	9.59573	3.52442	5.30792
C	11.45561	4.08698	4.22792
H	11.07840	4.53296	3.30501
C	12.81113	3.96791	4.62099
C	13.96444	4.50113	3.91446
C	13.79979	4.71368	2.41801
C	13.78376	3.36275	1.70280
C	14.84695	5.63323	1.81253
C	12.29841	0.01305	5.70091
H	12.24394	-0.96430	5.18970
H	11.26217	0.33962	5.89228
C	16.38729	5.65549	6.23277
C	16.74044	5.27285	7.66489
H	15.82934	5.07889	8.25984

H	17.30033	6.09076	8.15263
H	17.36897	4.36746	7.70454
C	17.64734	5.68973	5.37295
H	18.14803	4.70352	5.36294
H	18.36924	6.42435	5.77432
H	17.41843	5.97051	4.33082
C	15.69435	7.01370	6.21540
H	14.78068	7.00223	6.83698
H	15.40836	7.30200	5.18870
H	16.36813	7.79393	6.61399
H	12.93227	-1.18571	8.89753
H	12.30405	-2.09266	7.49463
H	11.35711	-0.74657	8.17914
H	14.39959	-1.72771	6.34007
H	14.98792	-0.10953	5.88658
H	12.76909	0.73645	5.01018
H	13.82622	0.99762	8.50116
H	15.93594	3.54976	5.78830
C	18.19772	1.33834	4.65702
H	16.82984	2.85605	3.91569
C	16.81514	1.96073	4.56991
C	16.25888	2.31976	5.91030
C	16.18752	2.00085	7.16168
H	16.66371	1.50252	8.01057
H	16.10634	1.26054	4.08362
H	18.55953	1.05030	3.65486
H	18.18985	0.43270	5.28870
H	18.92823	2.04336	5.09079
H	9.50020	0.80318	8.88897
H	8.46551	2.10309	9.54508
H	10.14886	1.92468	10.10644
H	9.19557	2.71898	7.29459
H	10.65690	4.39925	9.41018
H	8.92587	4.52573	8.99321
H	10.16572	4.95605	7.78561
H	14.62121	5.82252	0.74781
H	15.85676	5.19063	1.87149
H	14.88835	6.60544	2.33314
H	13.59579	3.48978	0.62161
H	13.00514	2.69028	2.10486
H	14.75917	2.85272	1.81486
H	12.81020	5.18391	2.25896

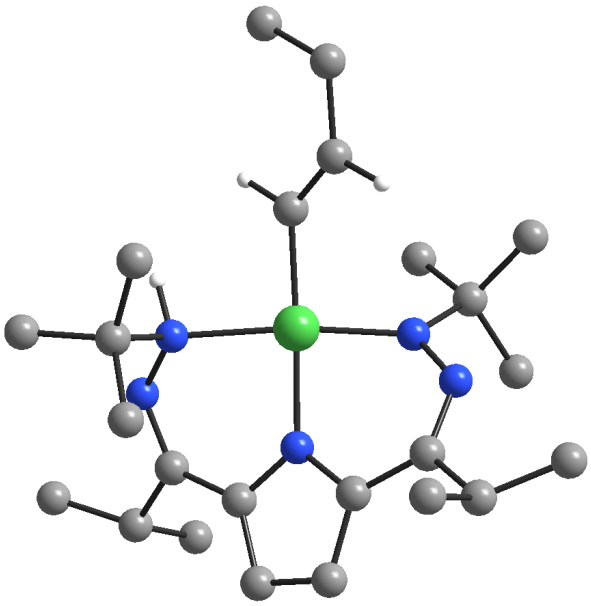

Figure S67. Calculated structure of **I2**.

Table S7. Coordinates of calculated structure of **I2**.

Ni	14.41548	2.84106	6.10451
N	13.45313	1.36980	7.08645
N	12.39549	1.76809	7.99327
N	12.69247	3.53082	5.66010
N	14.72575	4.77757	4.10725
N	15.12039	4.37639	5.29971
C	12.51449	-0.92987	7.33014
C	14.29122	-0.45289	5.65466
H	15.10169	-0.62659	6.38443
C	13.04102	0.09219	6.32473
C	11.50748	2.60978	7.57172
C	10.37018	2.92101	8.52463
C	10.17811	1.88168	9.61548
C	10.55758	4.31757	9.11867
C	11.52576	3.32564	6.31259
C	10.46163	3.87618	5.55725
H	9.40252	3.87141	5.82741
C	11.02622	4.39169	4.39369
H	10.50611	4.89686	3.57572
C	12.42551	4.18249	4.49846
C	13.50095	4.62040	3.65645
C	13.22563	4.97584	2.21707
C	12.93272	3.70299	1.41886
C	14.33873	5.78272	1.57199

C	11.98738	0.39710	5.27450
H	11.75728	-0.53254	4.72460
H	11.04162	0.75701	5.71264
C	16.03258	5.38922	5.93872
C	16.30366	4.98913	7.38095
H	15.36122	4.79630	7.92565
H	16.82975	5.81334	7.89487
H	16.92769	4.08571	7.44759
C	17.33406	5.48117	5.14961
H	17.87940	4.52177	5.17141
H	17.98799	6.25503	5.59025
H	17.13999	5.75342	4.09788
C	15.29830	6.73172	5.92806
H	14.31129	6.64086	6.41826
H	15.13930	7.10459	4.90257
H	15.88380	7.48870	6.47843
H	13.24915	-1.10985	8.13516
H	12.33338	-1.89114	6.81873
H	11.56874	-0.60592	7.79244
H	14.05354	-1.41790	5.17418
H	14.67356	0.23456	4.88204
H	12.34336	1.14438	4.54279
H	14.16636	1.02589	7.73945
C	18.60049	0.54491	7.16037
H	19.25725	1.91919	5.63203
C	18.43596	1.18976	5.79967
C	17.12477	1.88802	5.56816
C	16.10425	2.01349	6.43427
H	16.23531	1.53992	7.43110
H	18.58860	0.42843	5.00598
H	19.59334	0.07412	7.26624
H	17.83978	-0.23840	7.33250
H	18.49556	1.28450	7.97478
H	10.04040	0.86979	9.19797
H	9.28817	2.12777	10.22126
H	11.04750	1.84699	10.29414
H	9.45247	2.94506	7.90349
H	11.45694	4.34712	9.76118
H	9.68920	4.59583	9.74131
H	10.67531	5.08889	8.33783
H	14.06342	6.05850	0.53903
H	15.27576	5.20056	1.52608
H	14.55394	6.71039	2.12950
H	12.67190	3.94624	0.37357
H	12.09497	3.13160	1.85518
H	13.81961	3.04269	1.40144
H	12.30137	5.58836	2.21193
H	17.03123	2.34073	4.56430

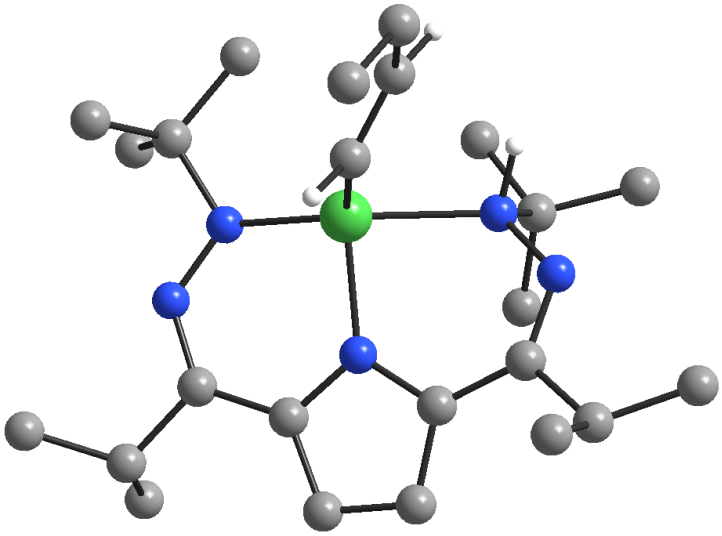

Figure S68. Calculated structure of **I3**.

Table S8. Coordinates of calculated structure of **I3**.

Ni	14.65986	2.79472	5.83054
N	13.78019	0.89367	6.35735
N	12.78156	0.88880	7.40941
N	12.83903	3.49510	5.82710
N	14.51833	5.05792	3.92573
N	15.18303	3.98892	4.36759
C	13.12252	-1.44999	5.78841
C	14.60856	-0.08303	4.31365
H	15.53205	-0.34403	4.86421
C	13.40188	-0.05312	5.24090
C	11.89862	1.84557	7.41544
C	10.86540	1.73490	8.52874
C	10.73312	0.34090	9.12009
C	11.16328	2.76134	9.62230
C	11.79036	3.00764	6.56205
C	10.65928	3.82670	6.33949
H	9.66293	3.69728	6.77215
C	11.04530	4.81946	5.43953
H	10.40918	5.60676	5.02575
C	12.41774	4.59491	5.14345
C	13.28683	5.35463	4.27104
C	12.69813	6.58756	3.59904
C	11.93906	6.21393	2.32565
C	13.73549	7.65986	3.29887
C	12.18780	0.48022	4.49927
H	11.95332	-0.17667	3.64225

H	11.29508	0.51103	5.14813
C	16.57395	3.98677	3.82053
C	17.36125	5.15449	4.41271
H	16.87018	6.11436	4.17123
H	18.39589	5.19046	4.02228
H	17.41733	5.06910	5.51433
C	17.22576	2.67120	4.22943
H	17.17426	2.51510	5.32458
H	18.29284	2.65731	3.94238
H	16.73879	1.81203	3.73676
C	16.56316	4.07962	2.29636
H	16.16654	5.05018	1.95222
H	15.93092	3.28298	1.86157
H	17.58342	3.96483	1.88485
H	13.98307	-1.82592	6.37174
H	12.94009	-2.16130	4.96316
H	12.23537	-1.45760	6.44391
H	14.46837	-0.83094	3.51351
H	14.76186	0.90316	3.83685
H	12.37018	1.49947	4.11387
H	14.57182	0.43211	6.82129
C	16.70292	3.54185	10.35152
H	18.12950	2.19369	9.46571
C	17.02828	2.27190	9.59255
C	16.35617	2.13096	8.24877
C	15.53796	3.00256	7.62026
H	15.35664	3.93848	8.19717
H	16.77026	1.39093	10.21855
H	17.23612	3.58232	11.31760
H	15.62046	3.62056	10.56073
H	16.98788	4.44166	9.77633
H	10.57927	-0.42434	8.33977
H	9.87093	0.30351	9.81026
H	11.63182	0.05148	9.69178
H	9.88699	2.00126	8.08437
H	12.16802	2.59439	10.05591
H	10.42879	2.68208	10.44421
H	11.13020	3.79565	9.23827
H	13.25578	8.57555	2.90677
H	14.46244	7.31442	2.54214
H	14.31247	7.93571	4.19993
H	11.44944	7.09256	1.86468
H	11.15733	5.45674	2.51732
H	12.63575	5.78993	1.57712
H	11.96471	7.02615	4.30498
H	16.59806	1.16745	7.75089

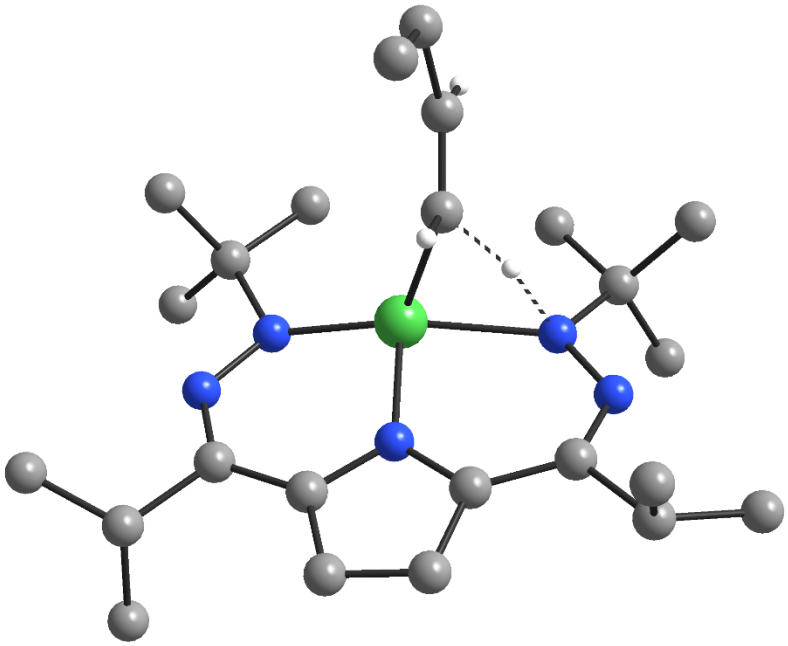

Figure S69. Calculated structure of **TS2–**.

Table S9. Coordinates of calculated structure of anionic transition state 2 (**TS2–**).

Ni	14.33661	2.69164	5.36482
N	13.37002	0.90163	6.13408
N	12.20214	0.88559	6.84970
N	12.69324	3.67085	5.72304
N	14.51960	5.23831	3.93560
N	14.98182	3.98726	4.10430
C	14.11213	-1.22338	7.19486
C	15.11698	-0.39185	5.06946
H	15.89862	0.17840	5.60332
C	13.83526	-0.49175	5.88094
C	11.48873	1.95126	7.07120
C	10.29207	1.75116	7.99427
C	9.88658	0.29836	8.18206
C	10.54711	2.40427	9.35375
C	11.65280	3.29262	6.52806
C	10.74874	4.37422	6.63195
H	9.81420	4.38947	7.19937
C	11.26499	5.42181	5.86469
H	10.81547	6.40871	5.72487
C	12.47842	4.95939	5.30534
C	13.40024	5.67768	4.45235
C	13.01151	7.09917	4.06944

C	11.92167	7.10219	2.99650
C	14.18696	7.95422	3.62225
C	12.78570	-1.24573	5.06893
H	13.13402	-2.26382	4.81346
H	11.84105	-1.34094	5.63175
C	16.33461	3.86567	3.48486
C	17.32887	4.77042	4.21205
H	17.03225	5.83067	4.12664
H	18.34752	4.66572	3.79375
H	17.37498	4.51598	5.28800
C	16.76679	2.41670	3.63583
H	16.82001	2.12445	4.70269
H	17.76906	2.25250	3.20169
H	16.06136	1.73666	3.12633
C	16.28387	4.22604	2.00161
H	15.97365	5.27457	1.85591
H	15.56473	3.58088	1.46414
H	17.27541	4.09482	1.52964
H	14.91427	-0.71725	7.76400
H	14.43344	-2.26542	7.01202
H	13.20877	-1.25155	7.82894
H	15.53019	-1.39612	4.86581
H	14.93625	0.10225	4.09798
H	12.56486	-0.71454	4.12463
H	14.28758	1.58435	6.81818
C	16.63498	3.65360	9.71240
H	18.22738	2.98701	8.41158
C	17.26583	2.60775	8.81739
C	16.41881	2.13567	7.67435
C	15.17454	2.54296	7.34082
H	14.71357	3.29291	8.01380
H	17.56639	1.72529	9.42033
H	17.31329	3.94303	10.53315
H	15.69956	3.28257	10.16847
H	16.37997	4.56929	9.14925
H	9.69622	-0.20676	7.21928
H	8.96530	0.23842	8.79005
H	10.67152	-0.27657	8.70420
H	9.42959	2.27271	7.53263
H	11.36950	1.88591	9.88324
H	9.65113	2.35703	10.00017
H	10.83212	3.46633	9.25599
H	13.86392	8.99742	3.45095
H	14.61968	7.57846	2.67792
H	14.99972	7.96592	4.36963
H	11.56326	8.12739	2.78747
H	11.04826	6.49507	3.29315
H	12.31068	6.68650	2.04739
H	12.57950	7.57356	4.97412
H	16.91129	1.36080	7.05652

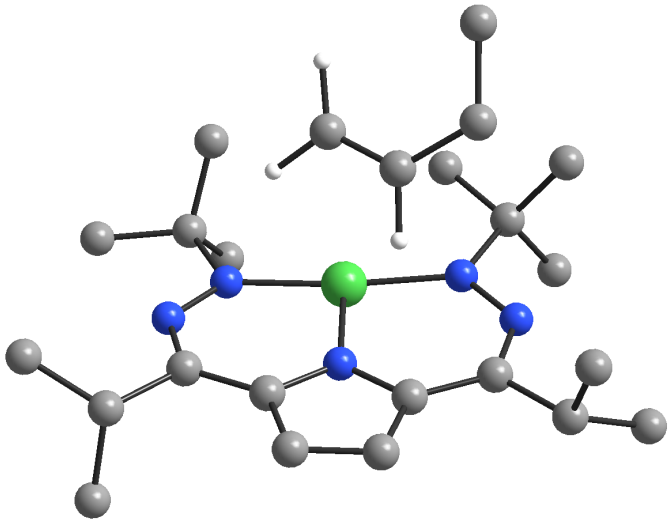

Figure S70. Calculated structure of **2** and butene.

Table S10. Coordinates of calculated structure of **2** and butene.

Ni	14.01828	3.24382	6.93084
N	12.88498	2.05354	7.89581
N	11.69582	1.57984	7.52246
N	12.71687	3.53049	5.54573
N	15.16042	5.11084	5.01135
N	15.31216	4.35897	6.11073
C	13.70613	2.60158	10.13215
C	14.59137	0.61059	8.90152
H	15.37345	1.21078	8.40164
C	13.34896	1.45211	9.19221
C	11.07054	1.93754	6.41777
C	9.69715	1.31643	6.20425
C	9.49946	-0.00810	6.92523
C	8.58563	2.29402	6.58621
C	11.52183	2.88013	5.43221
C	10.89155	3.29713	4.22762
H	9.92173	2.95799	3.85198
C	11.74166	4.22101	3.62183
H	11.57377	4.73526	2.67108
C	12.88230	4.34488	4.46086
C	14.07397	5.12364	4.27036
C	14.14451	6.00885	3.03323
C	14.60462	5.21022	1.81398
C	15.01966	7.23912	3.22060
C	12.30334	0.57523	9.86755
H	12.70709	0.19870	10.82588
H	11.37709	1.13354	10.08479
C	16.68878	4.56134	6.65861
C	16.86876	3.59297	7.81575
H	16.10194	3.75080	8.59732

H	17.85854	3.72096	8.28935
H	16.79325	2.54481	7.47217
C	17.74215	4.25620	5.59477
H	17.62600	3.22512	5.21093
H	18.76077	4.34948	6.01489
H	17.66310	4.94899	4.73993
C	16.84204	5.99520	7.16224
H	16.09615	6.21058	7.94984
H	16.69401	6.72106	6.34313
H	17.84693	6.16372	7.59254
H	14.43741	3.28976	9.66905
H	14.14770	2.22716	11.07440
H	12.80955	3.19484	10.38888
H	15.02604	0.20031	9.83244
H	14.34462	-0.23805	8.23711
H	12.02679	-0.29473	9.24968
C	17.33331	0.55221	2.92244
H	16.55955	2.56543	2.73656
C	16.18938	1.51930	2.70318
C	15.04399	1.39233	3.65299
C	14.91962	0.49290	4.63713
H	15.79719	1.41554	1.67015
H	14.23448	2.12890	3.51758
H	15.68728	-0.26891	4.83427
H	14.03024	0.48064	5.28249
H	10.30810	-0.72604	6.70158
H	8.54044	-0.46983	6.62752
H	9.47851	0.12615	8.02117
H	9.59539	1.11802	5.11794
H	8.62184	2.51893	7.66920
H	7.58495	1.87619	6.36824
H	8.67607	3.25247	6.04464
H	14.96868	7.89623	2.33311
H	16.07841	6.96132	3.36770
H	14.71463	7.83217	4.10142
H	14.61171	5.83403	0.90032
H	13.94959	4.34159	1.61975
H	15.63141	4.82646	1.96789
H	13.11622	6.36507	2.82584
H	18.13626	0.70852	2.18227
H	17.00067	-0.49751	2.83296
H	17.77843	0.66900	3.92707

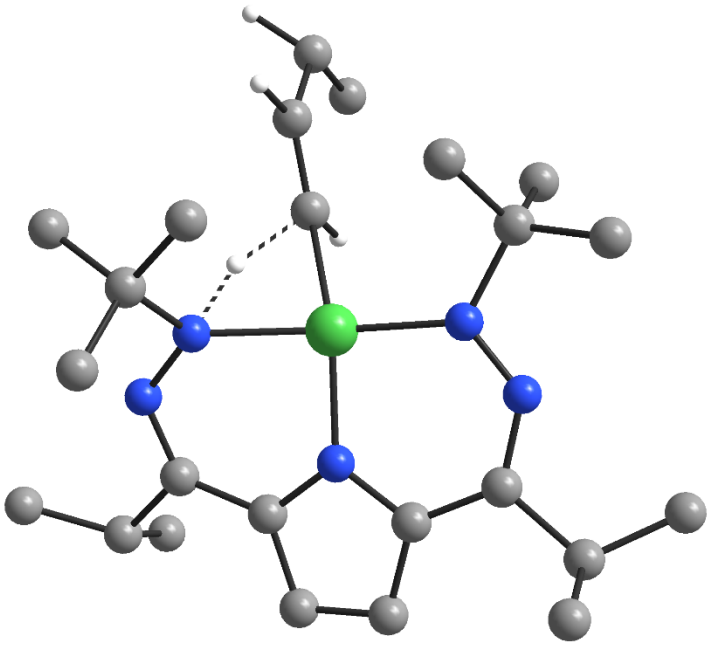

Figure S71. Calculated structure of neutral **TS2**.

Table S11. Coordinates of calculated structure of neutral transition state 2 (**TS2**).

Ni	14.19194	2.86552	5.82260
N	13.38440	1.20369	6.50527
N	12.25453	1.15513	7.26191
N	12.48537	3.60316	5.57532
N	14.40819	5.12448	4.03236
N	15.01864	4.19982	4.71691
C	13.97302	-1.16322	6.96959
C	14.82453	-0.01503	4.91809
H	15.76248	0.24732	5.43001
C	13.65669	-0.14293	5.88158
C	11.37822	2.11856	7.22930
C	10.19912	1.98790	8.17279
C	10.02065	0.58359	8.72423
C	10.31380	3.00784	9.30637
C	11.40647	3.24810	6.33550
C	10.33745	4.14150	6.05116
H	9.33834	4.10511	6.49022
C	10.79594	5.04083	5.10516
H	10.24329	5.86978	4.65778
C	12.15464	4.70260	4.84695
C	13.11665	5.40987	4.08026
C	12.65924	6.57361	3.22377

C	11.92770	6.07701	1.97603
C	13.78414	7.52407	2.84613
C	12.41355	-0.55600	5.09725
H	12.61169	-1.48890	4.53983
H	11.55300	-0.73260	5.76398
C	16.50439	4.18699	4.38322
C	17.24886	4.79626	5.56908
H	16.93976	5.84640	5.71869
H	18.33786	4.78902	5.37960
H	17.06159	4.24601	6.50398
C	16.93138	2.75013	4.12147
H	16.70594	2.09603	4.97330
H	18.01985	2.70746	3.93748
H	16.42041	2.34542	3.22938
C	16.81705	5.00913	3.13660
H	16.62876	6.08407	3.28215
H	16.22405	4.68066	2.26664
H	17.88648	4.87763	2.89275
H	14.88378	-0.88522	7.53023
H	14.14031	-2.15907	6.52129
H	13.13937	-1.24970	7.68662
H	14.98911	-0.98393	4.41474
H	14.62794	0.74190	4.13762
H	12.13199	0.22609	4.36863
H	14.50917	1.59934	7.06621
C	17.48971	3.04243	9.50484
H	18.74559	2.14549	7.98612
C	17.79175	1.93666	8.51654
C	16.75473	1.67796	7.47281
C	15.63158	2.39172	7.24694
H	15.44279	3.21921	7.95881
H	17.99588	0.98695	9.05131
H	18.30746	3.15338	10.23673
H	16.56393	2.83523	10.07068
H	17.35920	4.01946	9.00661
H	9.91556	-0.16630	7.92143
H	9.11446	0.53973	9.35413
H	10.87932	0.28295	9.34916
H	9.29105	2.23844	7.59102
H	11.19205	2.78401	9.93997
H	9.41759	2.98404	9.95159
H	10.42631	4.03751	8.92388
H	13.37186	8.42971	2.36700
H	14.48965	7.06079	2.13458
H	14.36860	7.83925	3.72780
H	11.57880	6.92593	1.36085
H	11.04778	5.46081	2.23230
H	12.59750	5.46108	1.34727
H	11.92629	7.14688	3.82553
H	16.98999	0.81107	6.83145

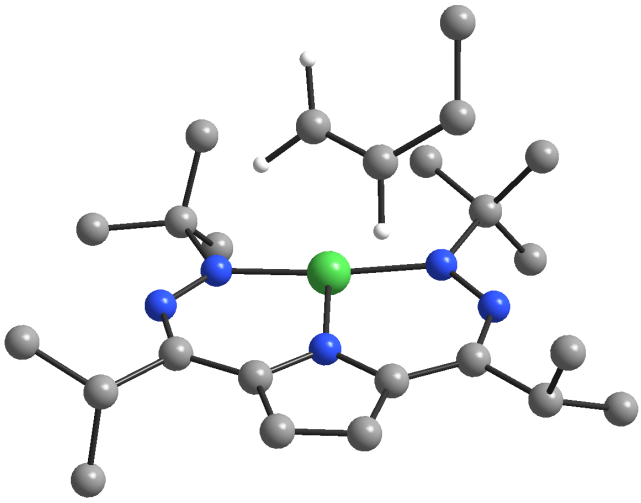

Figure S72. Calculated structure of **1** and butene.

Table S12. Coordinates of calculated structure of **1** and butene.

Ni	13.56489	3.20512	6.31728
N	12.53544	2.01709	7.36983
N	11.23559	1.94525	7.47247
N	12.00342	3.89763	5.43895
N	14.41832	5.11221	4.32549
N	14.71495	4.33176	5.33025
C	12.79894	1.06028	9.64067
C	14.64878	0.95221	7.97900
H	15.05839	1.88775	8.39603
C	13.14716	0.88540	8.16756
C	10.37552	2.69482	6.78038
C	8.91640	2.52603	7.16292
C	8.60499	1.17588	7.78942
C	8.47950	3.66487	8.08471
C	10.71452	3.60159	5.75599
C	9.83658	4.34465	4.88548
H	8.74493	4.32687	4.90480
C	10.63445	5.08418	4.05409
H	10.30893	5.75874	3.25920
C	11.99985	4.78979	4.41351
C	13.18593	5.31021	3.85579
C	13.09330	6.18808	2.62072
C	12.83473	5.33407	1.37856
C	14.30990	7.07643	2.41622
C	12.61642	-0.44327	7.63843
H	13.10762	-1.28222	8.16297
H	11.52804	-0.53190	7.78989
C	16.17512	4.52573	5.67992
C	16.47477	3.67235	6.89462
H	15.82118	3.93861	7.74680
H	17.51956	3.81526	7.22062

H	16.34782	2.60122	6.66889
C	17.03057	4.07353	4.50084
H	16.80071	3.02754	4.22797
H	18.10318	4.12909	4.76093
H	16.85506	4.70747	3.61522
C	16.42189	5.99489	6.00534
H	15.80514	6.31585	6.86447
H	16.18028	6.64089	5.14536
H	17.48216	6.15458	6.27000
H	13.16558	2.02978	10.02369
H	13.27015	0.25943	10.23808
H	11.70863	1.01392	9.80021
H	15.14568	0.11384	8.49695
H	14.92127	0.88904	6.90816
H	12.82545	-0.55026	6.55871
C	20.42083	-0.31347	4.78383
H	18.98417	0.95243	3.77866
C	18.99404	0.08731	4.47314
C	18.15000	0.42941	5.65795
C	18.54595	0.44460	6.93558
H	18.48661	-0.71774	3.90388
H	17.10474	0.69221	5.42795
H	19.57394	0.18875	7.22796
H	17.85795	0.71824	7.74625
H	8.93728	0.33911	7.15101
H	7.51641	1.07274	7.94516
H	9.09587	1.05651	8.77098
H	8.32026	2.60336	6.23374
H	9.06365	3.65140	9.02378
H	7.41099	3.57358	8.34996
H	8.62621	4.65366	7.61458
H	14.12969	7.78182	1.58585
H	15.20699	6.48432	2.16343
H	14.54951	7.66486	3.31840
H	12.77208	5.96403	0.47306
H	11.89335	4.76191	1.45844
H	13.65427	4.60775	1.22418
H	12.21564	6.85039	2.75324
H	20.97924	-0.55089	3.86258
H	20.45753	-1.20683	5.43288
H	20.96630	0.49406	5.30441

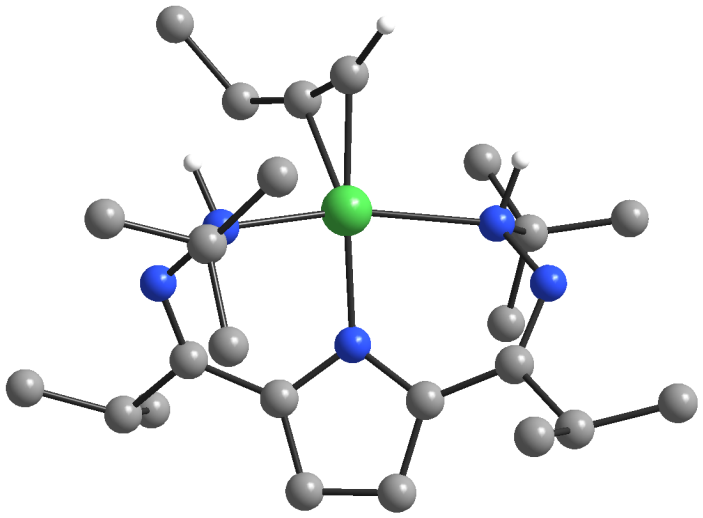

Figure S73. Calculated structure of **TS1** with constrained Ni-N5 distance of 2.0 Å. We note that efforts to constrain the Ni–N bond lengths in the transition state result in increased $H_{hydrazone}$–C_{alkyne} distances, and thus included the unconstrained geometry (Figure S66) in the calculated catalytic cycle.

Table S13. Coordinates of calculated structure of **TS1** with constrained Ni–N5 distance of 2.0 Å.

Ni	14.83636	2.56139	6.38153
N	13.44147	1.13718	7.44485
N	12.35628	1.77151	8.15509
N	13.15077	3.23853	5.63042
N	15.47673	4.45134	4.20883
N	15.66691	4.22025	5.63429
C	12.31497	-1.04941	7.86359
C	14.20422	-0.85040	6.24905
H	14.98511	-0.97629	7.02020
C	12.96767	-0.16155	6.80497
C	11.66410	2.65637	7.51100
C	10.49858	3.25566	8.28229
C	10.00284	2.38979	9.42728
C	10.87039	4.65646	8.76834
C	11.91020	3.22190	6.19137
C	11.00983	3.92891	5.36071
H	9.94574	4.10046	5.54166
C	11.74345	4.36672	4.25684
H	11.36978	4.95121	3.41208
C	13.07588	3.95526	4.47945
C	14.27387	4.32688	3.74281
C	14.10185	4.59790	2.26061
C	13.85388	3.28182	1.52176
C	15.24586	5.37166	1.63050
C	11.98432	0.10939	5.67769
H	11.72578	-0.84603	5.18713

H	11.04352	0.55305	6.04623
C	15.61834	5.52690	6.42840
C	15.87279	5.12017	7.87364
H	15.07383	4.44876	8.24438
H	15.89558	6.01308	8.52341
H	16.83860	4.59513	7.98320
C	16.71752	6.46388	5.93705
H	17.71429	5.99473	6.02837
H	16.72909	7.39055	6.53795
H	16.56314	6.74515	4.88137
C	14.26564	6.20867	6.31232
H	13.44422	5.57415	6.68663
H	14.03648	6.49953	5.27263
H	14.27931	7.13248	6.91785
H	13.01646	-1.25858	8.69175
H	12.01598	-2.01756	7.42394
H	11.41347	-0.57896	8.29085
H	13.93265	-1.85450	5.87790
H	14.63959	-0.28343	5.40916
H	12.40995	0.78302	4.91372
H	14.03840	0.80753	8.21238
H	16.66840	3.98757	5.66553
C	18.52545	1.26765	4.47208
H	16.51718	1.78891	3.85285
C	17.01288	1.14972	4.61061
C	16.53005	1.50009	5.95251
C	16.46287	1.75753	7.18141
H	16.78129	1.69927	8.22183
H	16.68842	0.11860	4.36735
H	18.84785	0.97255	3.45889
H	19.04658	0.62103	5.19849
H	18.85927	2.30537	4.64603
H	9.74303	1.37204	9.08739
H	9.10111	2.83763	9.88182
H	10.76241	2.28496	10.22094
H	9.66583	3.36768	7.56111
H	11.72376	4.61094	9.47112
H	10.02449	5.13227	9.29605
H	11.15838	5.31480	7.93054
H	15.00579	5.61901	0.58105
H	16.17839	4.78132	1.62924
H	15.45152	6.31424	2.16676
H	13.62787	3.46823	0.45680
H	13.00757	2.72032	1.95456
H	14.74896	2.63306	1.56506
H	13.18091	5.20640	2.16412

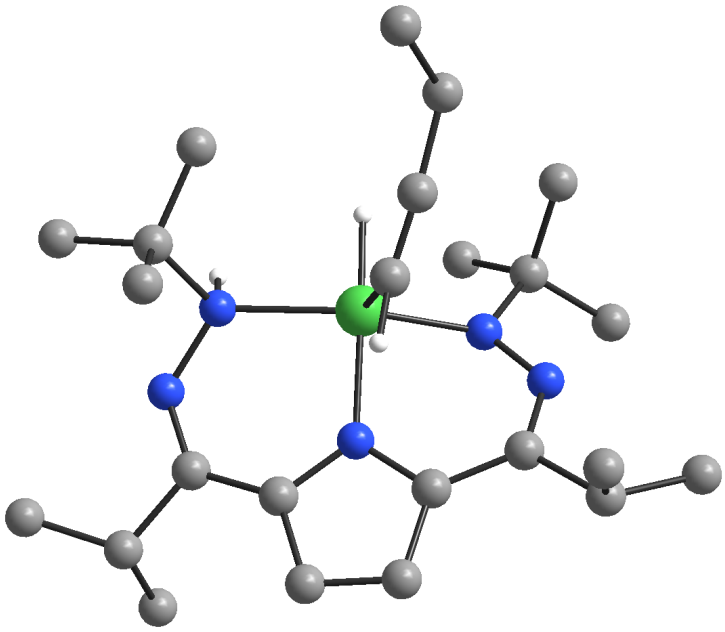

Figure S74. Calculated structure of a Ni-hydride complex bound to butyne (Ni-C_{alkyne}: 2.0 Å). Bond constraints were implemented in order to optimize an alkyne-bound structure.

Table S14. Coordinates of calculated structure of (DHPH)Ni–H bound to butyne.

Ni	14.04080	3.28285	6.59565
N	12.95326	2.13692	7.95094
N	11.58735	2.46579	8.29573
N	12.40734	3.92416	5.81622
N	14.69077	5.39850	4.82193
N	14.88800	4.91281	6.03090
C	14.53987	0.24561	7.97079
C	12.32738	0.02461	6.79942
H	12.74058	0.39436	5.84579
C	13.06295	0.60163	7.99487
C	10.79989	2.99372	7.41542
C	9.34783	3.11736	7.85686
C	8.94908	2.11789	8.92930
C	9.03914	4.54725	8.29553
C	11.13129	3.58678	6.14067
C	10.25536	4.09770	5.14763
H	9.16616	4.01372	5.13668
C	11.04469	4.73885	4.20179
H	10.70528	5.26500	3.30660
C	12.38565	4.63342	4.65701
C	13.57995	5.22484	4.13169
C	13.56669	5.75259	2.71395
C	13.63842	4.58978	1.72178
C	14.65924	6.77021	2.43229
C	12.45891	0.07567	9.29656

H	12.65796	-1.00742	9.37475
H	12.91768	0.56437	10.17503
C	16.12820	5.49774	6.65701
C	15.95212	5.48249	8.16963
H	15.06368	6.06785	8.46866
H	16.83535	5.93373	8.65584
H	15.83563	4.45923	8.56319
C	17.33864	4.66909	6.24315
H	17.25553	3.63260	6.61338
H	18.26788	5.10085	6.65800
H	17.43630	4.63938	5.14244
C	16.31305	6.94784	6.21262
H	15.40396	7.54245	6.41322
H	16.54452	7.03196	5.13957
H	17.14558	7.40234	6.77851
H	15.01929	0.53530	7.02635
H	14.65347	-0.84586	8.09235
H	15.08180	0.73544	8.80003
H	12.41705	-1.07575	6.80359
H	11.25103	0.27004	6.82989
H	11.37026	0.22836	9.34798
H	15.27693	2.89267	7.35241
H	13.45987	2.42406	8.79682
H	9.25807	5.28114	7.50070
H	9.63686	4.82000	9.18491
H	7.97295	4.65036	8.56406
H	8.73718	2.90210	6.95871
H	9.46474	2.31572	9.88464
H	9.18969	1.08240	8.63269
H	7.86219	2.17507	9.11632
H	13.55433	4.95205	0.68130
H	12.83337	3.85219	1.88932
H	14.60392	4.05834	1.81681
H	12.58864	6.25177	2.56186
H	15.66301	6.31985	2.52597
H	14.61769	7.62372	3.13075
H	14.55983	7.16540	1.40573
H	17.56484	1.86044	4.57766
C	14.35118	2.15204	4.97548
C	15.51011	1.70108	4.95744
H	16.84806	-0.44992	3.77860
H	13.42641	2.20190	4.40495
C	16.86572	1.23566	5.16693
C	17.07075	-0.23984	4.83799
H	18.11714	-0.52878	5.03016
H	17.13341	1.42571	6.22775
H	16.42025	-0.88249	5.45553

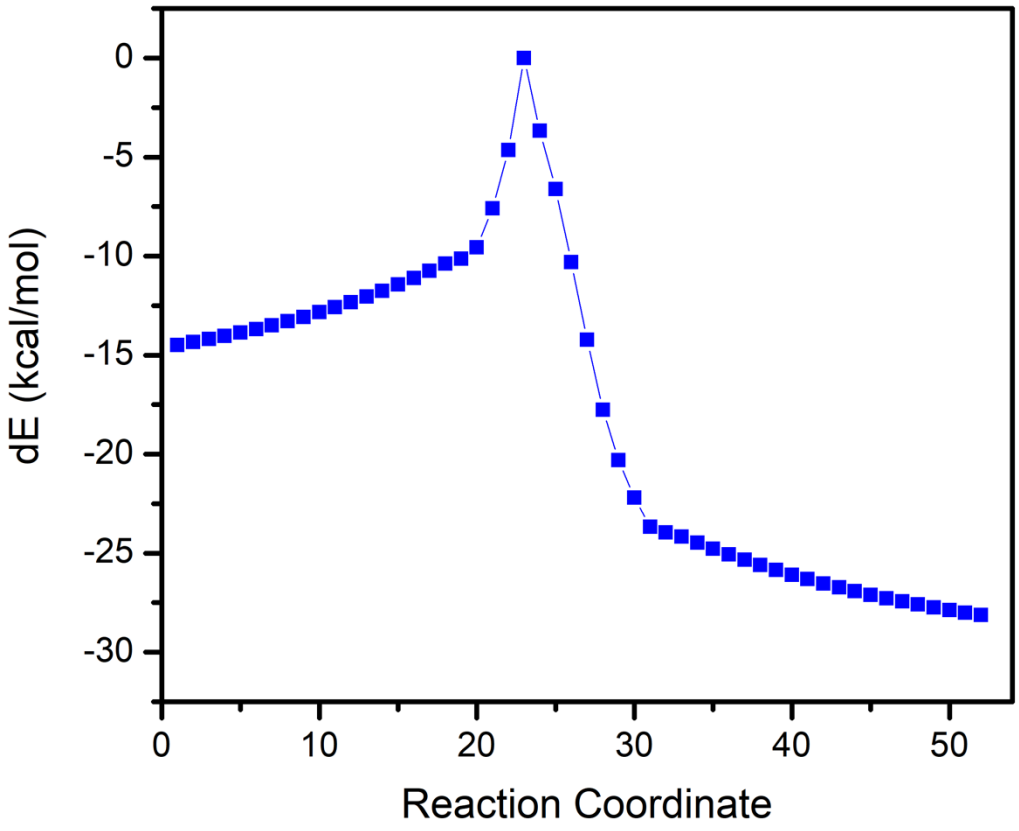

Figure S75. Intrinsic Reaction Coordinate pathway for **TS1**. The transition state geometry determined from a surface scan maximum is calculated to lie on same reaction coordinate as the proposed mechanistic cycle (Figure 5A).

Table S15. Tabulated energies for calculation of N–H BDE.

	(DHPH)Ni	Phenol	→	($DHPH_2$)Ni	PhO•	Reaction Energy	N–H BDE (kcal/mol)
Energy (kcal/mol)	-1800736.75	-193006.45		-1801106.3	-192604.85	-32.0025	55.9975

Table S16. Mulliken charges for H's involved in the semi-hydrogenation of butyne by 1 for the first H-atom transfer event (H47) and the second H-atom transfer event (H46).

	Mulliken Charge	
Complex	**H46**	**H47**
$(DHPH_2)$Ni-alkyne	0.200799	0.188343
TS1	0.21224	0.171320
(DHPH)Ni-vinyl (–)	0.203133	0.093693
TS2 (–)	0.217193	0.147006
(DHP)Ni alkene (–)	0.158664	0.142618

Table S17. Tabulated Gibbs free energies for the formation of a Ni hydride from a ligand protonated Ni species.

Reaction and Gibbs Free Energy (Eh)			$\Delta G_{reaction}$ (kcal/mol)
$(DHPH_2)$Ni	→	(DHPH)Ni–H	
–2564.7004		–2564.6937	+ 4.26

Table S18. Tabulated Gibbs free energies for alkyne substrate binding to a Ni hydride species (See Figure S73). Constraints on the Ni-C_{alkyne} bond length were employed in order to optimize a bound structure. The Ni-C_{alkyne} bond length of 2.0 Å was selected because it is the calculated bond length of the comparable complex **I1**.

Reaction and Gibbs Free Energy (Eh)			$\Delta G_{reaction}$ (kcal/mol)
(DHPH)Ni-H + butyne (free)	→	(DHPH)NiH(butyne)	
–2720.4352		–2720.4105	+ 15.4438

Table S19. Data from computational studies used in catalytic cycle. *constrained Ni–N5 bond (Figure S73)

Complex	Electronic Energy (Eh)	Gibbs free energy (Eh)	Imaginary mode (cm^{-1})
I1	–2721.0277	–2720.4574	-
TS1	–2720.9744	–2720.4120	–73.47
I2	–2721.0503	–2720.4761	-
TS2	–2721.0026	–2720.4385	–1277.11
1	–2721.0747	–2720.5069	-
I3	–2721.1631	–2720.5954	-
TS2–	–2721.1360	–2720.5759	–1266.11
2	–2721.1990	–2720.6324	-
TS1*	–2721.0225	–2720.4532	–117.24

Calculation of reduction potential of I2 in MeCN

Gibbs Free Energy of reduced species – Gibbs Free Energy of oxidized species = –0.119 eH

$$\frac{-\Delta G°(\mathrm{eH})\times 2625.50(\mathrm{kJ}\ mol^{-1})/\mathrm{eH}}{n\times 96.485\ kJ/(V\ mol)} = 3.24\ \mathrm{V}$$

$$3.24\ V - 4.988\ V\ \left(Fc\ ref^{1}\right) = -1.74\ V\ vs\ Fc^{0/+}$$

X-ray Crystallography

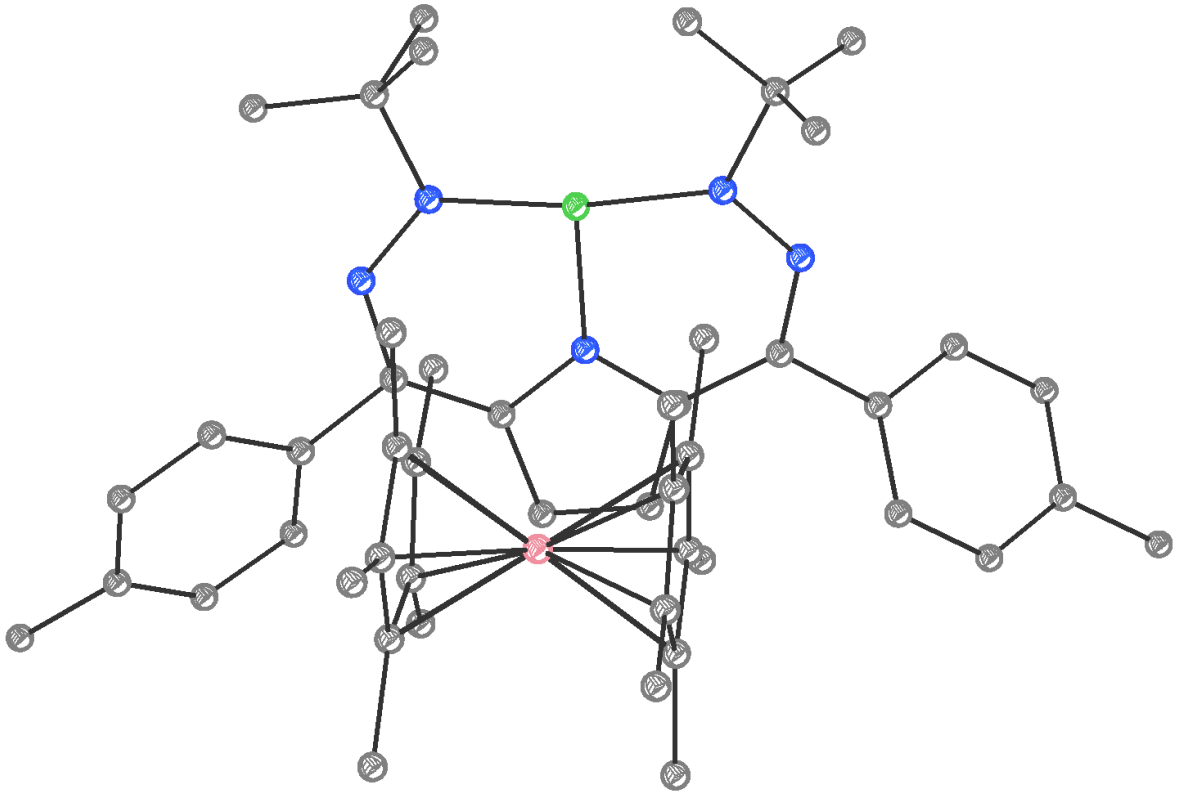

Figure S76. SXRD of **2**. Ellipsoids are set to 50% probability. H's omitted for clarity.

Table S20. Details for crystal structure of **2**

Identification code	(**2**)
Empirical formula	$C_{48}H_{64}N_5CoNi$
Formula weight	828.43
Temperature/K	100(2)
Crystal system	triclinic
Space group	P-1
a/Å	13.8834(10)
b/Å	15.5603(11)
c/Å	21.2620(17)
α/°	85.705(2)
β/°	80.052(2)
γ/°	71.455(2)
Volume/Å3	4288.3(6)
Z	4
ρcalcg/cm3	1.283
μ/mm-1	0.205
F(000)	1767.0
Crystal size/mm3	0.09 × 0.04 × 0.02
Radiation	MoKα (λ = 0.41328)
2Θ range for data collection/°	1.822 to 30.616
Index ranges	$-17 \leq h \leq 17$, $-19 \leq k \leq 19$, $-27 \leq l \leq 26$
Reflections collected	166684
Independent reflections	17681 [R_{int} = 0.0729, R_{sigma} = 0.4268]
Data/restraints/parameters	17681/2/1242
Goodness-of-fit on F2	1.104
Final R indexes [I>=2σ (I)]	R_1 = 0.0753, wR_2 = 0.1268
Final R indexes [all data]	R_1 = 0.1326, wR_2 = 0.1336
Largest diff. peak/hole / e Å-3	0.84/-0.91

Appendix III: Chapter III Supplementary Information

Product Characterization

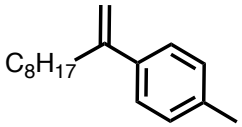

1-(dec-1-en-2-yl)-4-methylbenzene. Yield: 70%. Eluent: 100% hexane. ^{1}H NMR (400 MHz, Chloroform-*d*) δ 7.32 (d, *J* = 8.2 Hz, 2H), 7.15 (d, *J* = 8.2 Hz, 2H), 5.23 (m, 1H), 5.01 (m, 1H), 2.32 (s, 3H), 1.97 (m, 2H), 1.27 (m, 8H), 0.88 (m, 6H). ^{13}C NMR (101 MHz, Chloroform-*d*) δ 149.3, 138.8, 137.8, 129.5, 126.5, 111.4, 35.4, 33.9, 32.2, 29.9, 29.6, 28.7, 22.9, 20.6, 13.9. GCMS (EI, 70 eV, m/z) 230 [M^+].

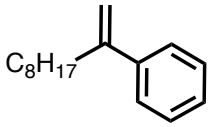

dec-1-en-2-ylbenzene. Yield: 73%. Eluent: 100% hexane. ^{1}H NMR (400 MHz, Chloroform-*d*) δ 7.43 (d, *J* = 7.3 Hz, 2H), 7.36 (m, 2H), 7.30 (m, 1H), 5.29 (s, 1H), 5.08 (s, 1H), 2.52 (t, *J* = 7.1 Hz, 2H), 1.29 (m, 12H), 0.91 (m, 3H). ^{13}C NMR (101 MHz, Chloroform-*d*) δ 148.8, 141.5, 131.3, 129.7, 128.1, 127.2, 126.1, 111.9, 35.4, 33.1, 31.9, 29.7, 29.3, 28.3, 22.7, 14.1. GC-MS (EI, 70 eV, m/z) 216 [M^+].

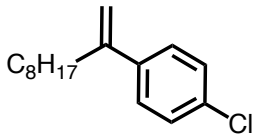

1-chloro-4-(dec-1-en-2-yl)benzene. Yield: 71%. Eluent: 100% hexane. ^{1}H NMR (400 MHz, Chloroform-*d*) δ 7.33 (d, *J* = 13.6 Hz, 2H), 7.27 (d, *J* = 4.1 Hz, 2H), 5.26 (s, 1H), 5.08 (s, 1H), 2.48 (t, *J* = 7.7 Hz, 2H), 1.28 (m, 12H), 0.91 (m, 3H). ^{13}C NMR (101 MHz, Chloroform-*d*) δ 147.7, 141.9, 139.9, 128.4, 127.4, 112.5, 35.3, 31.9, 29.7, 29.4, 29.3, 28.2, 22.7, 14.1. GCMS (EI, 70 eV, m/z) 250 [M^+].

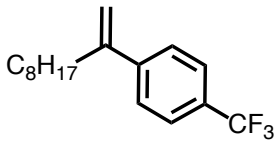

1-(dec-1-en-2-yl)-4-(trifluoromethyl)benzene. Yield: 66%. Eluent: 100% hexane. ^{1}H NMR (400 MHz, Chloroform-*d*) δ 7.60 (d, *J* = 8.1 Hz, 2H), 7.52 (d, *J* = 8.1 Hz, 2H), 5.37 (s, 1H), 5.20 (s, 1H), 2.57 (t, *J* = 7.7 Hz, 2H), 1.29 (m, 12H), 1.14 (m, 3H). ^{19}F NMR (377 MHz, Chloroform-*d*) δ –62.5. GCMS (EI, 70 eV, m/z) 284 [M^+].

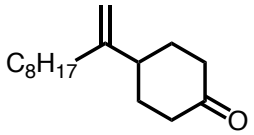

4-(dec-1-en-2-yl)cyclohexan-1-one. Yield: 62%. Eluent: 5:1 hexane/ethyl acetate. ^{1}H NMR (400 MHz, Chloroform-*d*) δ 4.81 (m, 2H), 2.42 (m, 5H), 2.07 (m, 2H), 1.62 (m, 2H), 1.46 (m, 2H), 1.30 (m, 12H), 0.90 (m, 3H). ^{13}C NMR (101 MHz, Chloroform-*d*) δ 211.8, 152.5, 108.1, 42.2, 41.2, 40.6, 39.1, 38.7, 35.2, 32.8, 39.1, 29.5, 29.3, 28.2, 22.7, 14.1. GCMS (EI, 70 eV, m/z) 236 [M^+].

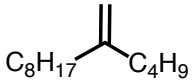

5-methylenetridecane. Yield: 44%. Eluent: 100% hexane. ^{1}H NMR (400 MHz, Chloroform-*d*) δ 4.62 (s, 2H), 1.92 (t, *J* = 7.2 Hz, 4H), 1.37-1.19 (m, 16H), 0.83 (m, 6H). GCMS (EI, 70 eV, m/z) 196 [M^+].

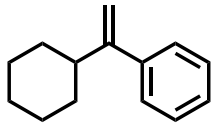

(1-cyclohexylvinyl)benzene. Yield: 48%. Eluent: 100% hexane. ^{1}H NMR (400 MHz, Chloroform-*d*) δ 7.44 (m, 3H), 7.35 (m, 2H), 5.30 (s, 1H), 5.08 (s, 1H), 2.54 (q, *J* = 7.3 Hz, 1H), 1.30 (m, 6H), 1.13 (m, 2H), 0.91 (m, 2H). GCMS (EI, 70 eV, m/z) 186 [M^+].

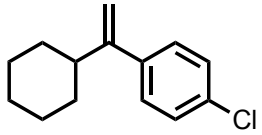

1-chloro-4-(1-cyclohexylvinyl)benzene. Yield: 45%. Eluent: 100% hexane. ^{1}H NMR (400 MHz, Chloroform-*d*) δ 7.31-7.34 (m, 4H), 5.27 (s, 1H), 5.09 (s, 1H), 2.51 (q, *J* = 7.3 Hz, 1H), 1.81-1.72 (m, 5H), 1.30 (m, 5H). ^{13}C NMR (101 MHz, Chloroform-*d*) δ 153.9, 137.6, 129.9, 129.7, 128.3, 127.2, 126.1, 110.9, 42.5, 33.2, 32.7, 26.8, 26.1, 26.0. GCMS (EI, 70 eV, m/z) 220 [M^+].

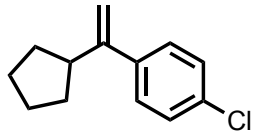

1-chloro-4-(1-cyclopentylvinyl)benzene. Yield: 51%. Eluent: 100% hexane. ^{1}H NMR (400 MHz, Chloroform-*d*) δ 7.42 (m, 2H), 7.35 (m, 2H), 5.22 (s, 1H), 5.14 (s, 1H), 2.13 (m, 1H), 1.97 (m, 8H). ^{13}C NMR (101 MHz, Chloroform-*d*) δ 130.7, 129.1, 128.8, 128.7, 127.9, 126.9, 126.5, 110.8, 44.6, 34.3, 32.3, 25.8, 25.0. GCMS (EI, 70 eV, m/z) 206 [M^+].

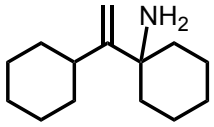

1-(1-cyclohexylvinyl)cyclohexan-1-amine. Yield: 40%. Eluent: 5:1 hexane/ethyl acetate. ^{1}H NMR (400 MHz, Chloroform-*d*) δ 8.33 (bs, 2H), 4.98 (s, 1H), 4.78 (s, 1H), 2.01 (m, 1H), 1.68-1.45 (m, 12H), 1.25-1.13 (m, 8H). GCMS (EI, 70 eV, m/z) 207 [M^{+}].

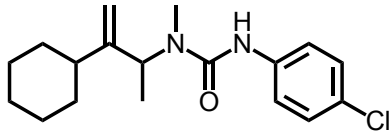

3-(4-chlorophenyl)-1-(3-cyclohexylbut-3-en-2-yl)-1-methylurea. Yield: 49%. Eluent 5:1 hexane/ethyl acetate. ^{1}H NMR (400 MHz, Chloroform-*d*) δ 7.27 (d, *J* = 8.6 Hz, 2H), 7.16 (d, *J* = 8.6 Hz, 2H), 6.39 (s, 1H), 5.03 (s, 1H), 4.97 (s, 1H), 4.79 (m, 1H), 2.73, (s, 3H), 1.80-1.58 (m, 7H), 1.22 (m, 4H). ^{13}C NMR (101 MHz, Chloroform-*d*) δ 155.5, 145.6, 138.5, 128.7, 128.0, 120.5, 109.5, 51.7, 41.4, 34.0, 32.2, 28.0, 26.9, 26.7, 26.3, 15.3. HR-MS Calcd. For $C_{18}H_{25}ClN_2O$: 320.1655 Found: 320.1661.

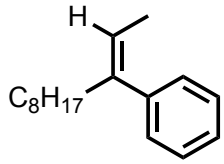

(Z)-undec-2-en-3-ylbenzene (14). Yield: 26%. Eluent 100% hexane. ^{1}H NMR (400 MHz, Chloroform-*d*) δ 7.33 (m, 2H), 7.23 (m, 1H), 7.15 (m, 2H), 5.53 (m, 1H), 2.32 (m, 2H), 1.54 (m, 5H), 1.22 (m, 10H), 0.85 (t, 3H). ^{13}C NMR (101 MHz, Chloroform-*d*) δ 142.0, 141.3, 128.5, 127.9, 126.2, 120.8, 39.2, 31.9, 29.4, 29.3, 29.2, 28.2, 22.6, 14.6, 14.1.

Reaction Optimization

Table S21. Screening conditions for acid sources

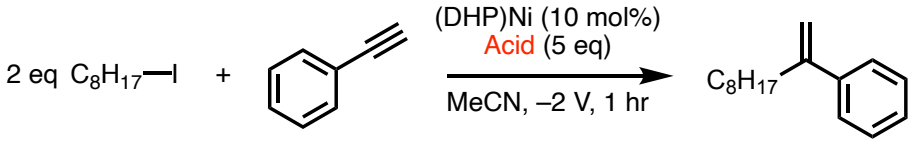

Deviation from standard conditions	pK_a (MeCN)	Yield (%)
Phenol	29.2[a]	73
2,4,6-*t*Bu$_3$-phenol	not reported	8
2,4-*t*Bu$_2$-phenol	not reported	28
Benzoic acid	21.5[a]	8
4-OMe-benzoic acid	20 (predicted)[b]	21
HFIP	22.5 (predicted)[b]	24

[a] *Eur. J. Org. Chem.* **2021,** *2021*, 1407-1419.
[b] *ACS Omega* **2018,** *3*, 1653-1662.

Table S22. Screening conditions for alkyl radical sources. *Phth = phthalimide*

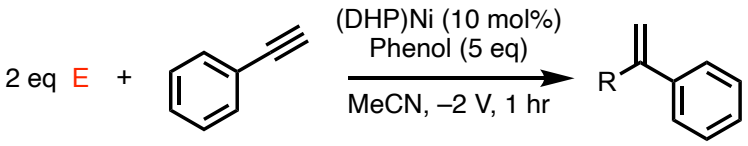

Deviation from standard conditions	Yield (%)
I-octane	73
I-cyclohexane	48
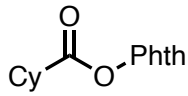	16
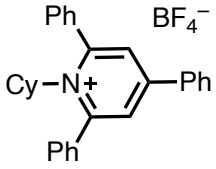	8
Br-cyclohexane	0
Br-cyclohexane + $(SiEt_3)_3Si$-O-Phth	0
Br-cyclohexane + (TPMA)Cu (10 mol%)	22
Br-octane + NaI (4 eq)	20
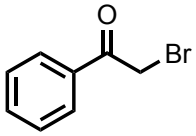	0
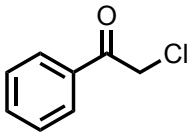	0
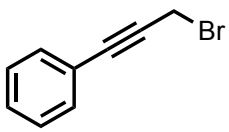	0

Table S23. Optimization of reagent equivalents and potential.

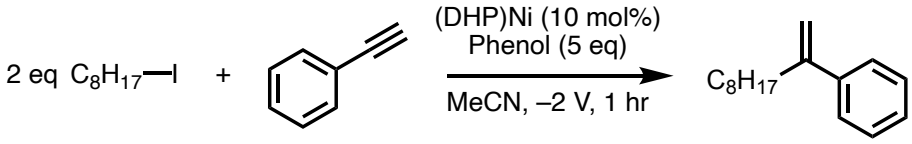

Deviation from standard conditions	**Yield (%)**
None	73
0.5 eq I-octane	10
1.0 eq I-octane	22
1.5 eq I-octane	46
2.5 eq I-octane	66
3.0 eq I-octane	41
Constant current (5 mA)	65
–1.80 V (vs $Fc^{0/+}$)	9
–1.9 V	54
–2.1 V	51
–2.2 V	28
2.5 eq phenol	38
8 eq phenol	68
10 eq phenol	67
0 eq phenol	0[a]

[a] Other products: $C_{16}H_{34}$ 42%, coupled product dec-1-ynylbenzene putatively formed from addition of the alkyl radical followed by elimination. This product is not observed under acidic conditions.

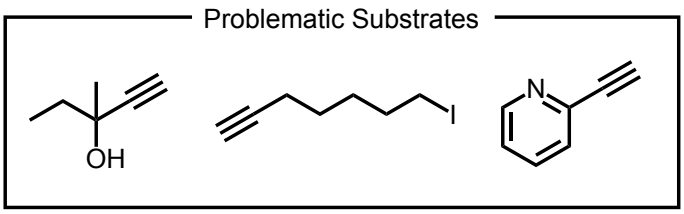

Figure S1. Substrates found to be incompatible or low yielding with standard electrolysis conditions using (DHP)Ni and iodo-octane for hydroalkylation

Table S24. Control reactions

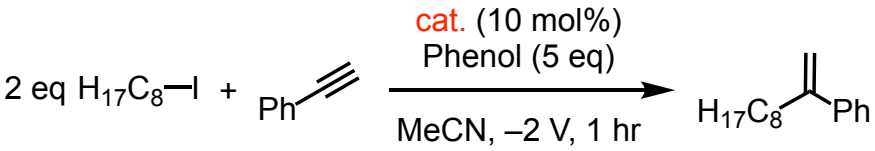

Deviation from standard conditions	Yield (%)
None [(DHP)Ni cat.]	73
No cat.	0
DHP ligand (no Ni)	0
(DHP)Cu instead of Ni	0
$Ni(OTf)_2$	0
$Ni(bpy)_3[BF_4]_2$	8[a]

[a] plus 6% (*Z*)-1,2-disubsituted and 10% (E)-1,2-disubstituted product

Cyclic Voltammetry

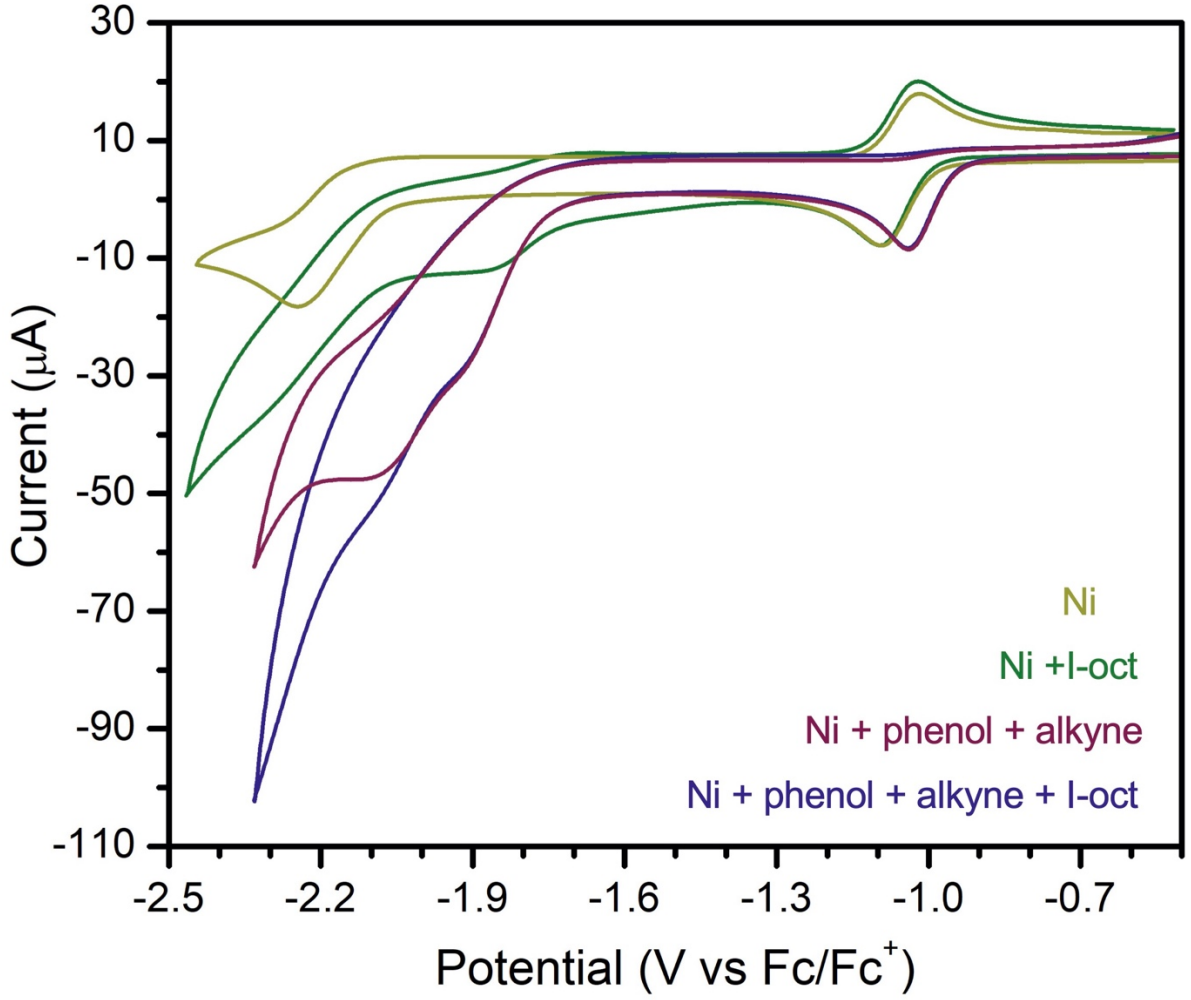

Figure S2. Cyclic voltammogram overlay of 0.1 eq (DHP)Ni (abbreviated **Ni**) with reaction components including 2 eq iodo-octane (abbreviated **I-oct**, green), 5 eq phenol and 1 eq phenylacetylene (abbreviated **alkyne**, purple), and with all reaction components (blue). 0.1 M $TBAPF_6$ in MeCN, glassy carbon working electrode, platinum wire counter, and silver wire reference.

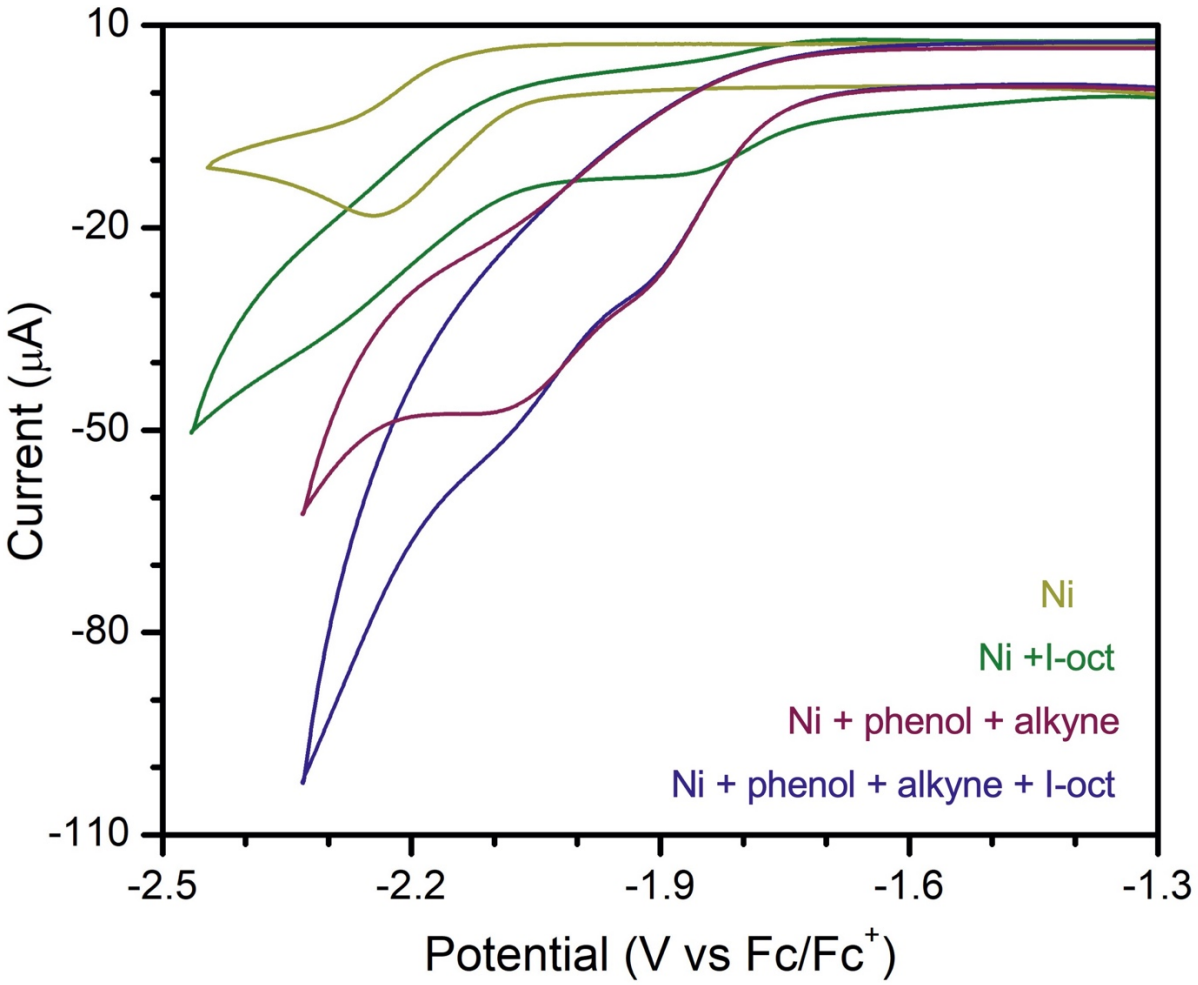

Figure S3. Zoomed in cyclic voltammogram overlay *of* 0.1 eq (DHP)Ni (abbreviated **Ni**) with reaction components including 2 eq iodo-octane (abbreviated **I-oct**, green), 5 eq phenol and 1 eq phenylacetylene (abbreviated **alkyne**, purple), and with all reaction components (blue). X-axis chosen to focus on catalytic features. 0.1 M $TBAPF_6$ in MeCN, glassy carbon working electrode, platinum wire counter, and silver wire reference.

NMR Spectroscopy

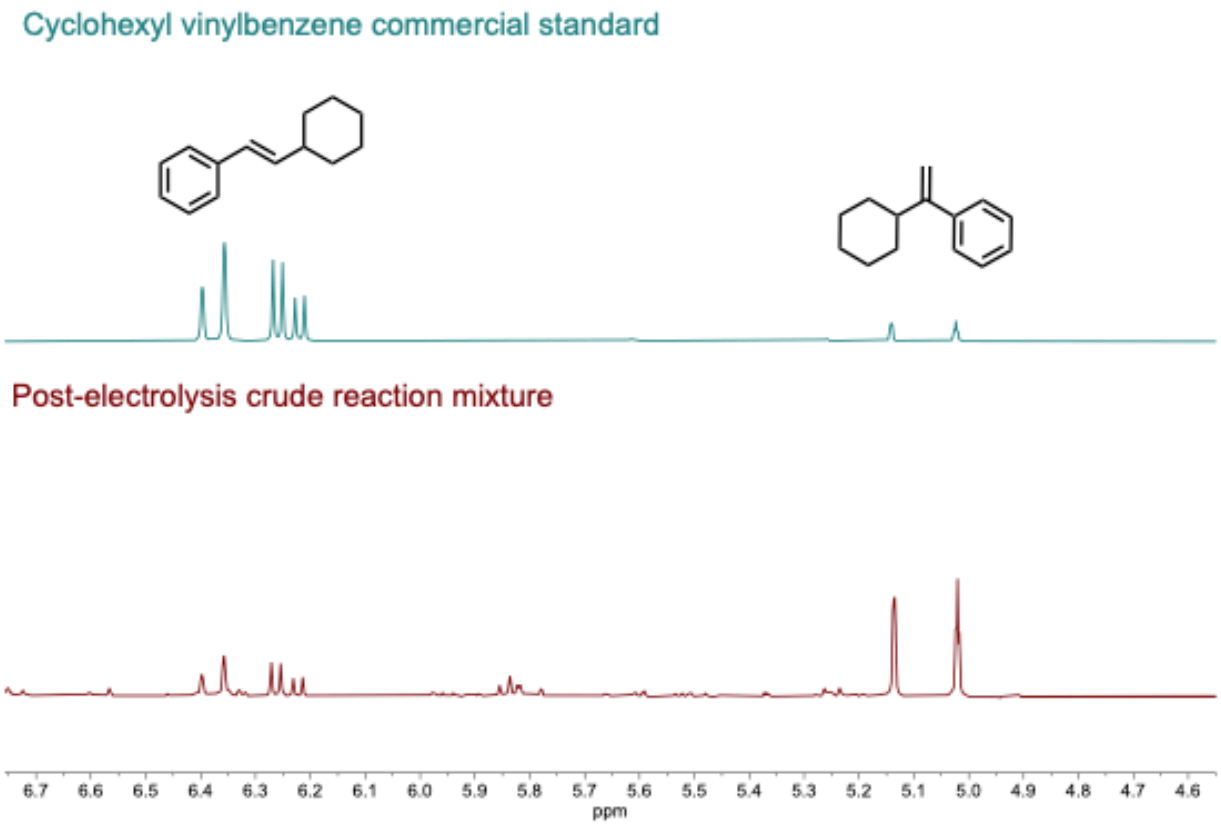

Figure S4. ^{1}H NMR of the initial hit crude reaction mixture in CD_3CN from the bulk electrolysis of cyclohexyl-iodide and phenylacetylene before the optimization of reaction conditions (bottom, red) showing a greater amount of 1,1-disubsituted alkene product compared to the (*Z*)-1,2-disubstituted product. Commercial standards (top, teal) confirm the assignment of the product alkene peaks.

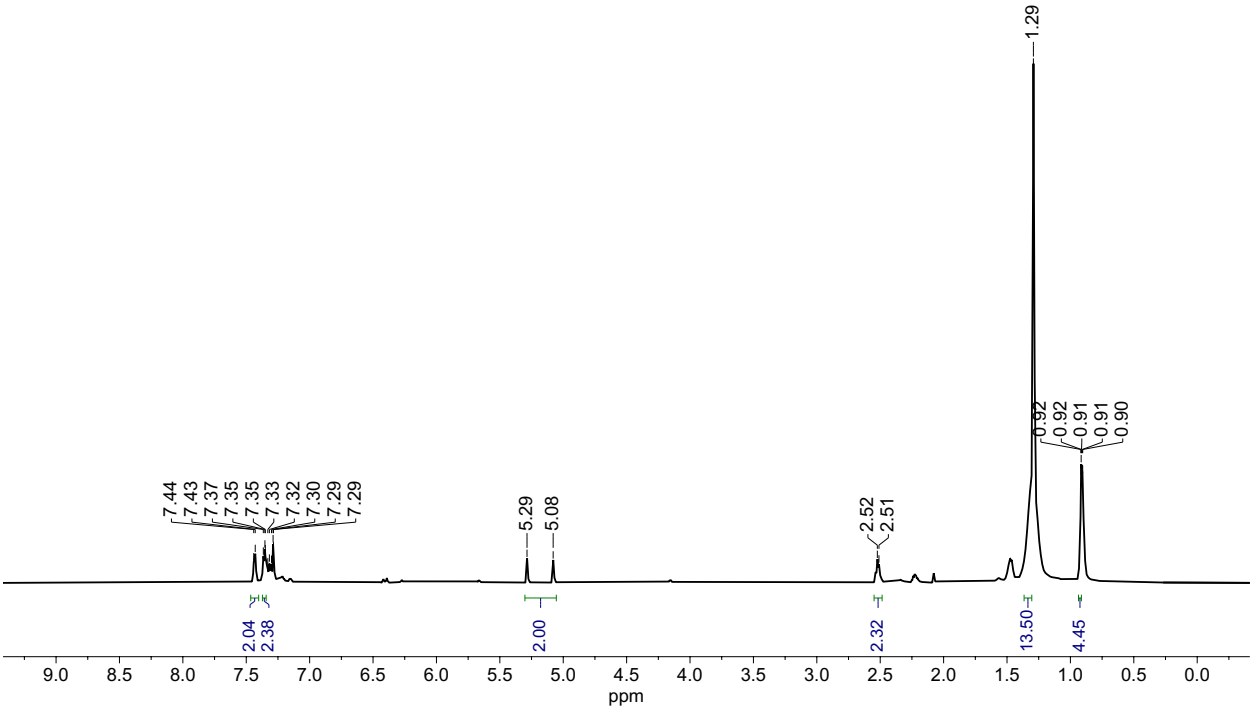

Figure S5. ^{1}H NMR of dec-1-en-2-ylbenzene (**2**) in $CDCl_3$, product of phenylacetylene and iodo-octane. Hexanes (δ = 0.88 and 1.26) overlaps with some aliphatic signals.

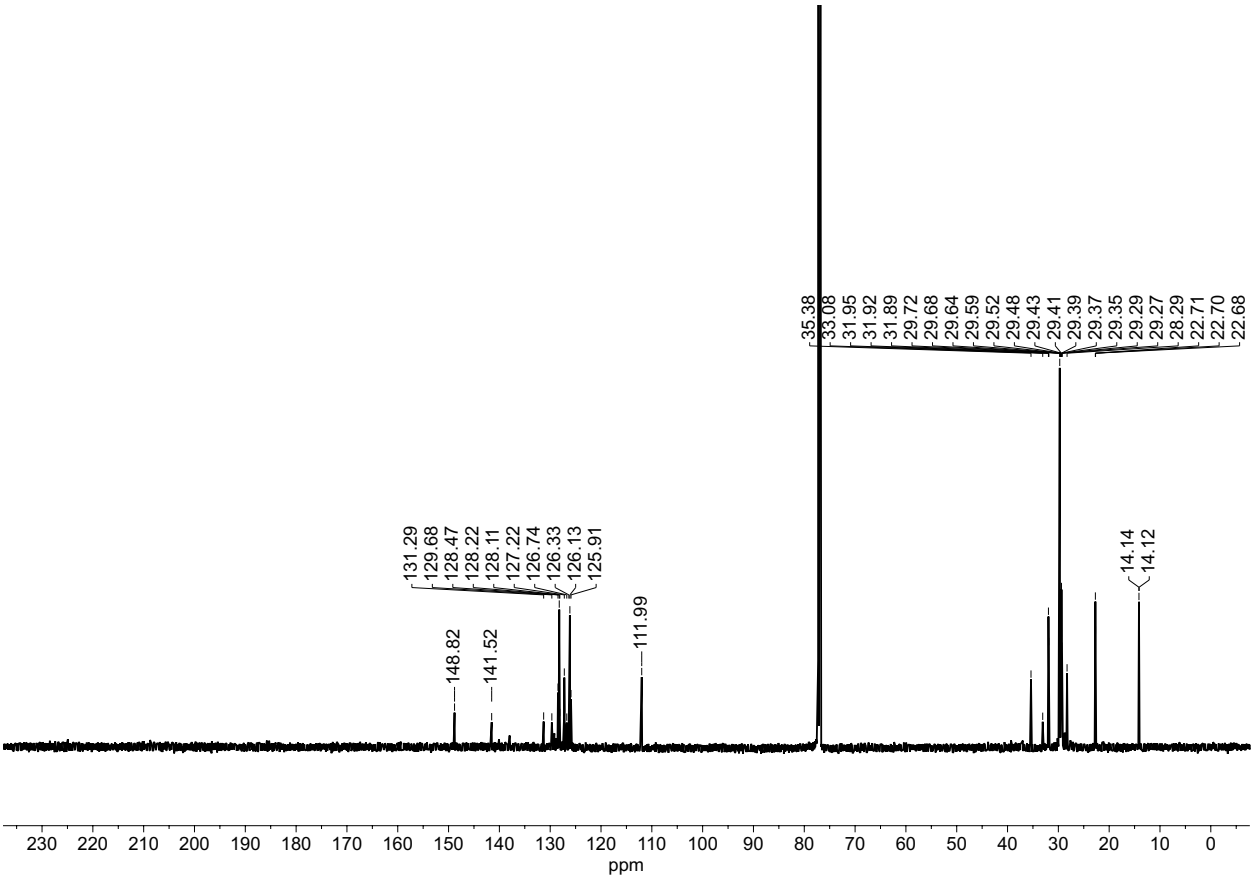

Figure S6. ^{13}C NMR of dec-1-en-2-ylbenzene (**2**) in $CDCl_3$, product of phenylacetylene and iodo-octane

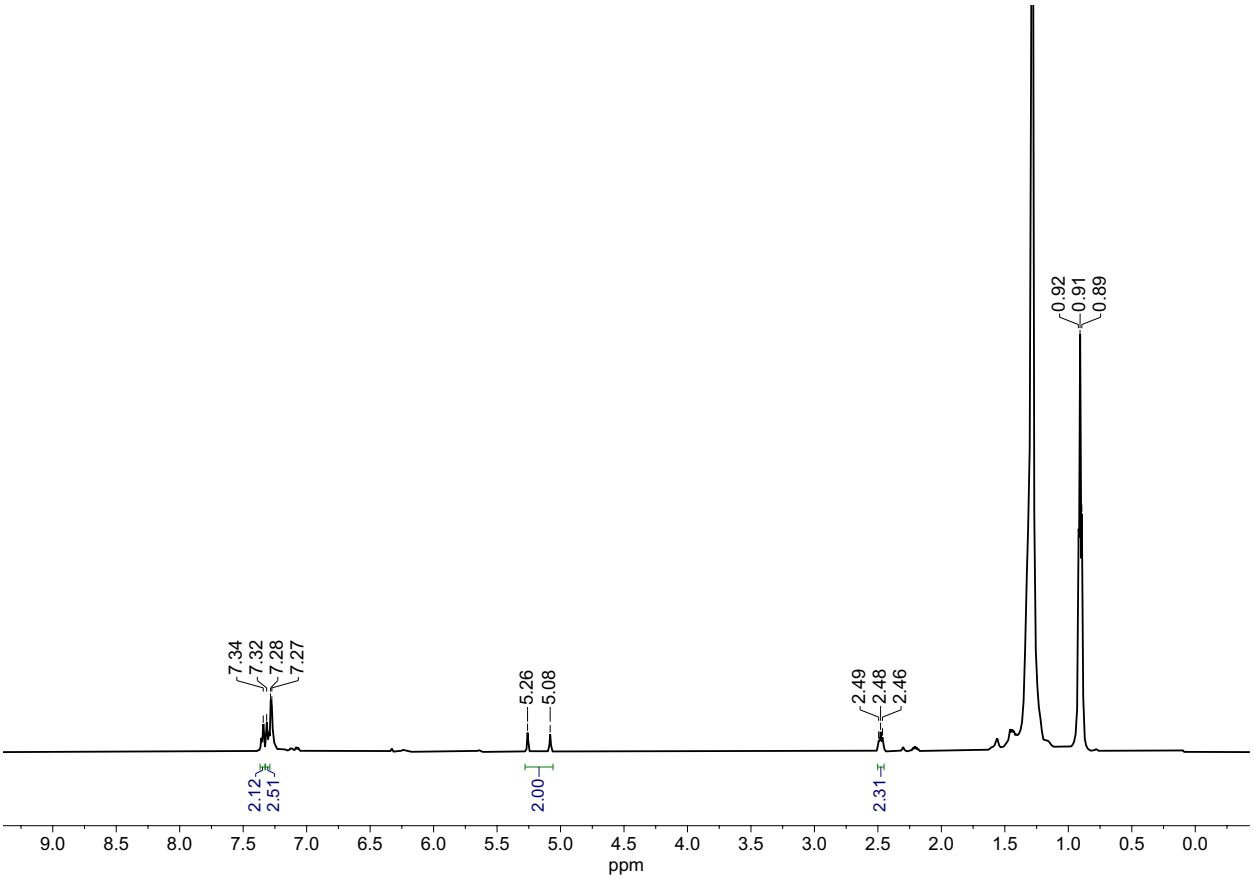

Figure S7. ^{1}H NMR of 1-chloro-4(dec-1-en-2-yl)benzene (**3**) in $CDCl_3$, product of 4-Cl-phenylacetylene and iodo-octane. Hexanes (δ = 0.88 and 1.26) overlaps with some aliphatic signals.

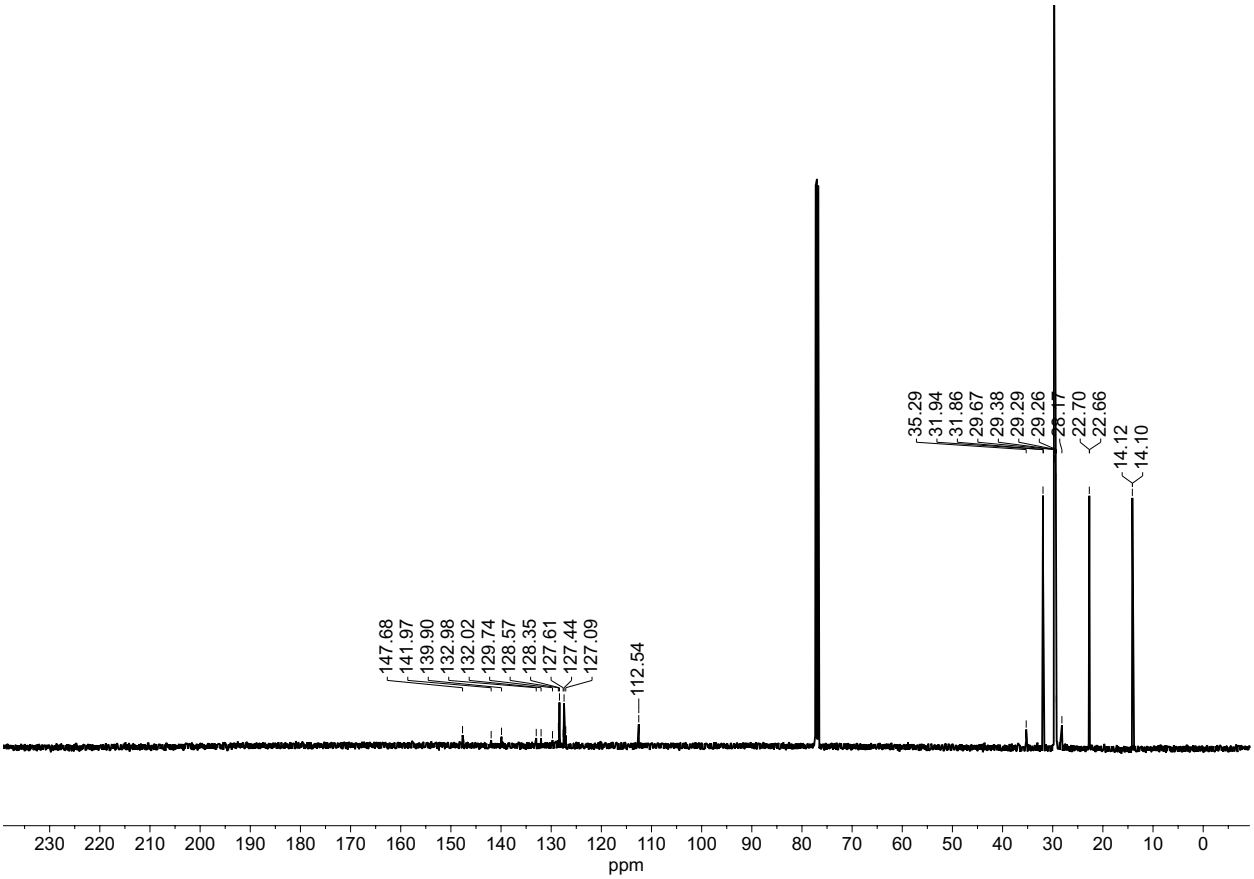

Figure S8. ^{13}C NMR of 1-chloro-4(dec-1-en-2-yl)benzene (**3**) in $CDCl_3$, product of 4-Cl-phenylacetylene and iodo-octane.

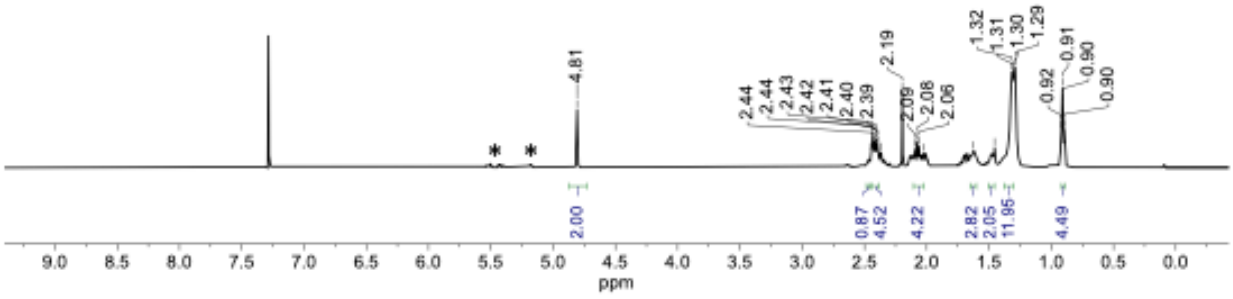

Figure S9. ^{1}H NMR of 4-(dec-1-en-2-yl)cyclohexan-1-one (**6**) in $CDCl_3$, product of 4-ethynylcyclohexan-1-one and iodo-octane. Alkene **6** was isolated as a mixture of regioisomers (ratio 6:1). The signals of the minor *E*-isomer are marked with an asterisk. Hexanes (δ = 0.88 and 1.26) overlaps with some aliphatic signals. Residual acetone (δ = 2.19) and acetonitrile (δ = 2.09) are also present.

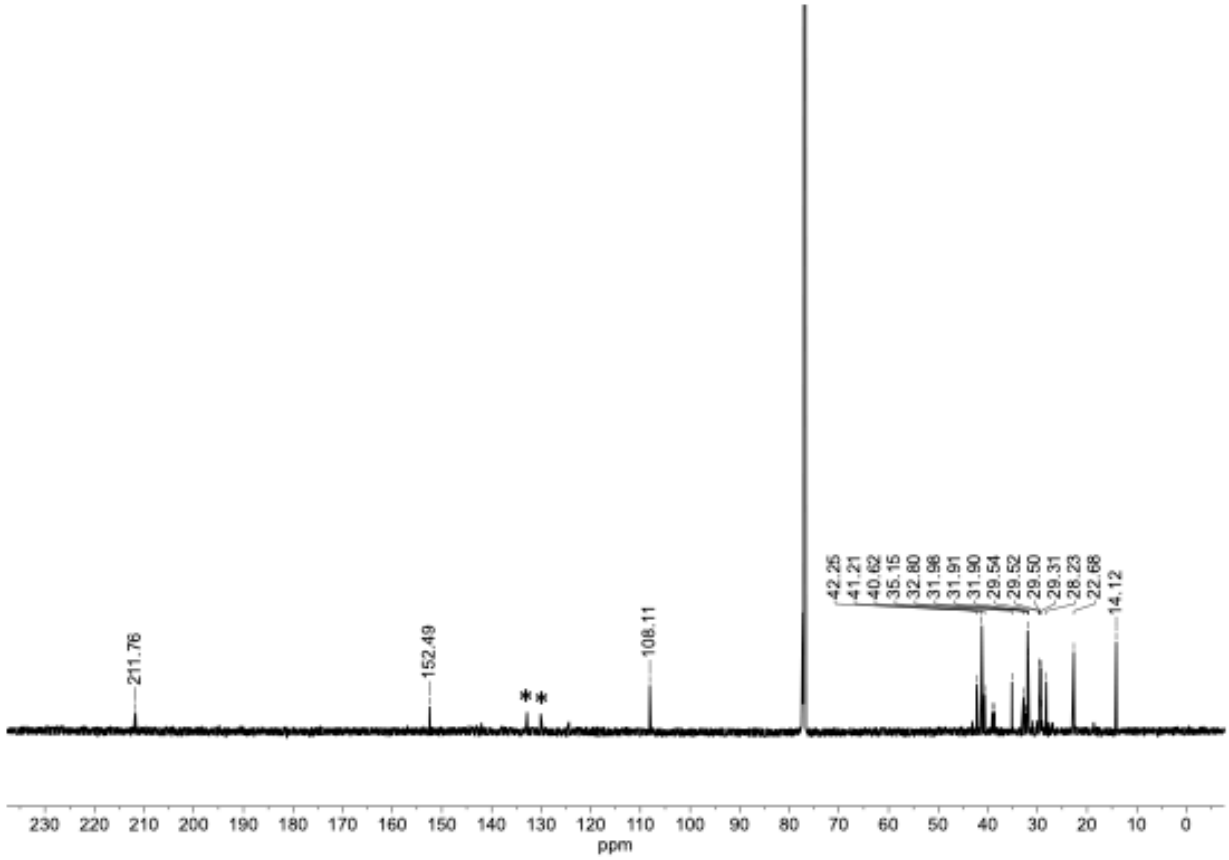

Figure S10. ^{13}C NMR of 4-(dec-1-en-2-yl)cyclohexan-1-one (**6**) in $CDCl_3$, product of 4-ethynylcyclohexan-1-one and iodo-octane. Alkene **6** was isolated as a mixture of regioisomers (ratio 6:1). The signals of the minor *E*-isomer are marked with an asterisk.

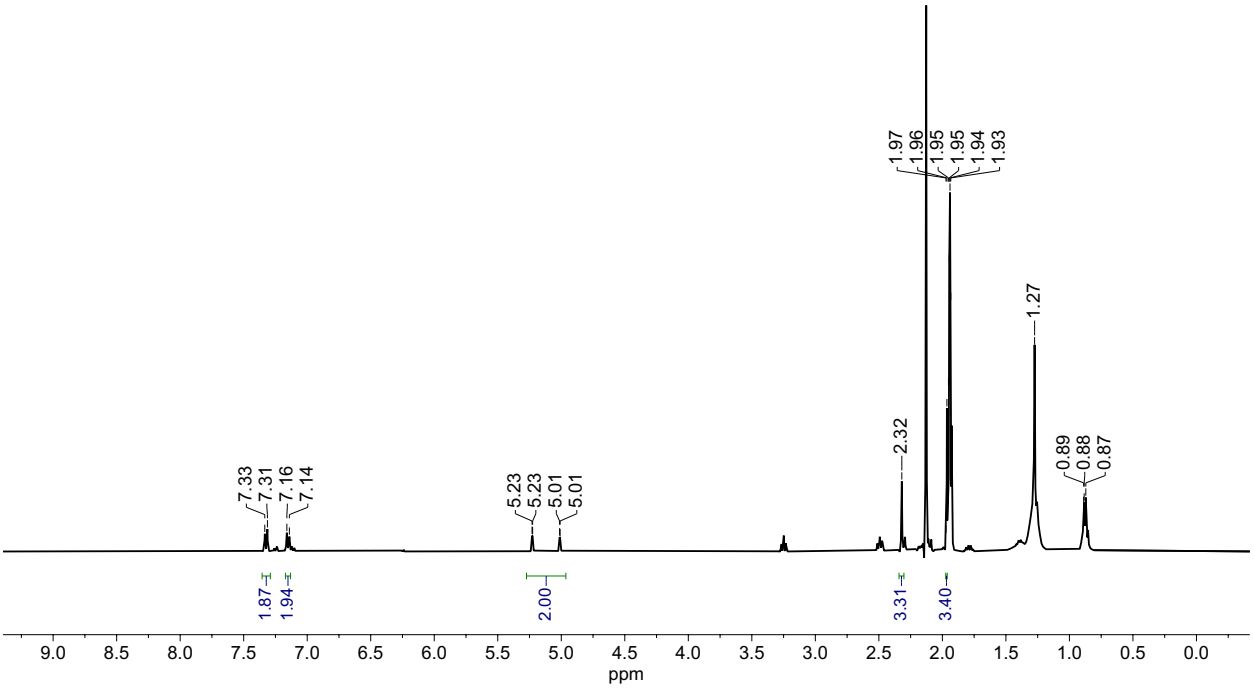

Figure S11. ^{1}H NMR of 1-(dec-1-en-2-yl)-4-methylbenzene (**1**) in $CDCl_3$, product of 4-Me-phenylacetylene and iodo-octane. Hexanes (δ = 0.88 and 1.26) overlaps with some aliphatic signals.

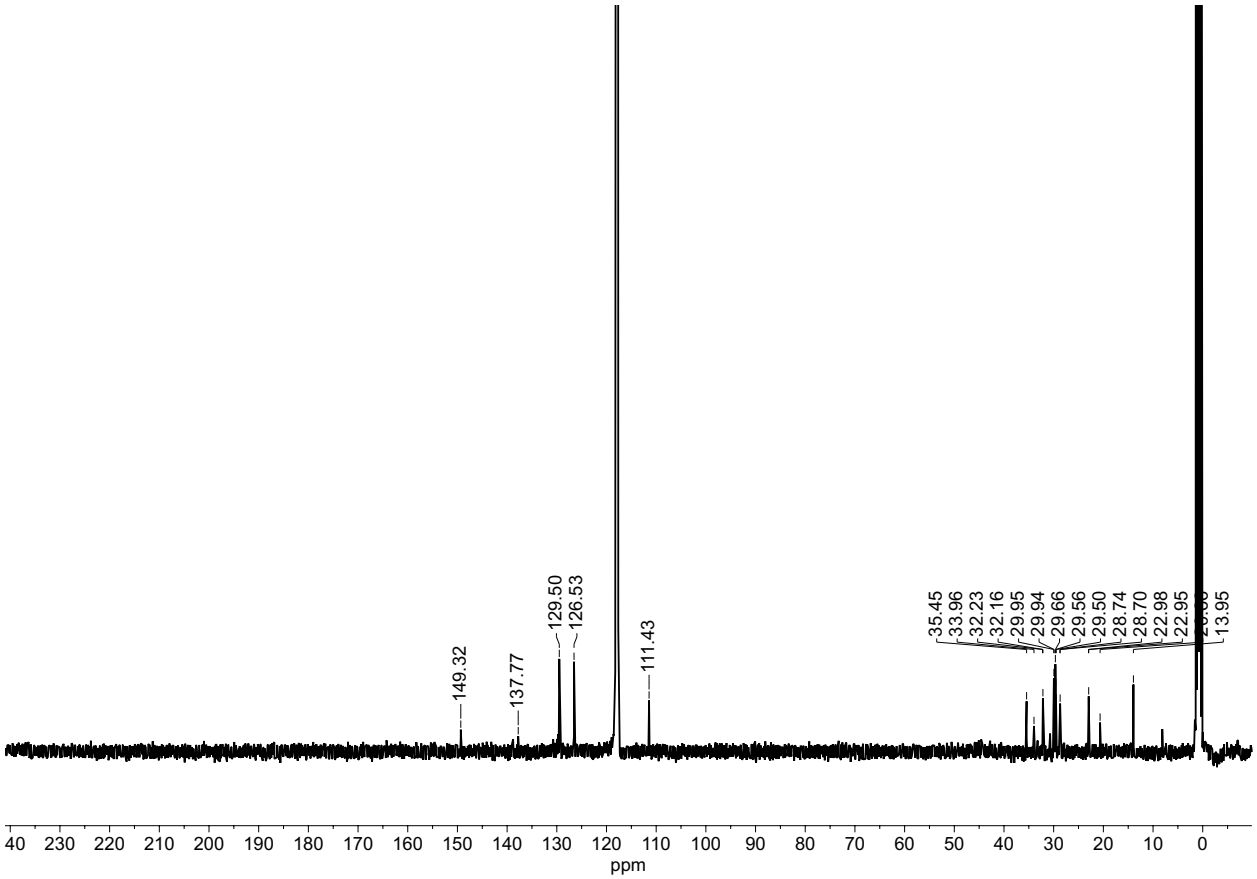

Figure S12. ^{13}C NMR of 1-(dec-1-en-2-yl)-4-methylbenzene (**1**) in $CDCl_3$, product of 4-Me-phenylacetylene and iodo-octane.

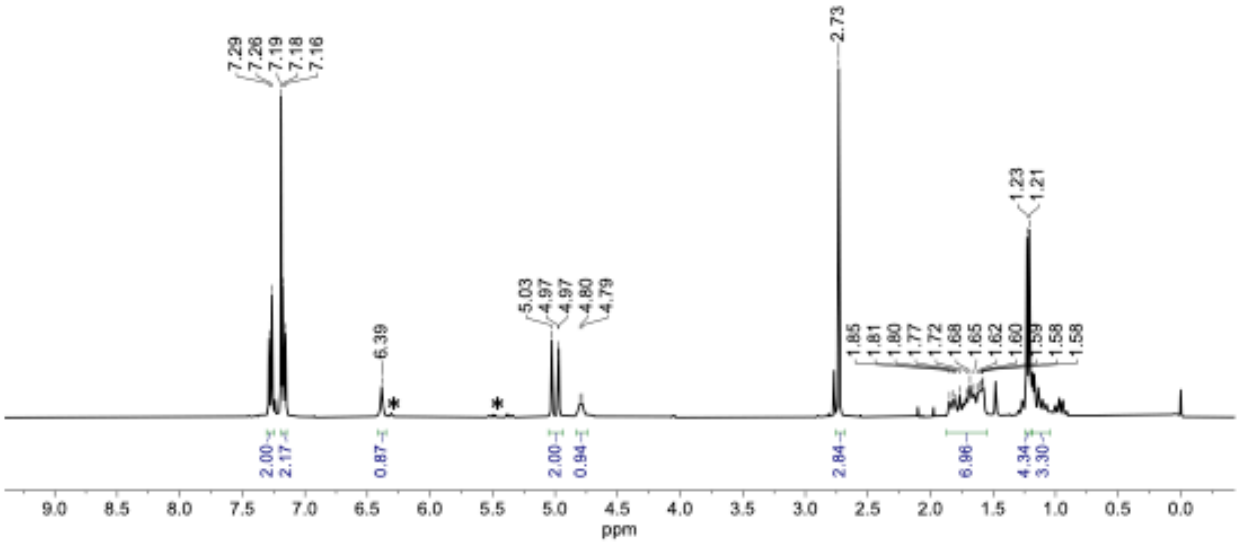

Figure S13. ^{1}H NMR of 3-(4-chlorophenyl)-1-(3-cyclohexylbut-3-en-2-yl)-1-methylurea (**13**) in $CDCl_3$, product of buturon and iodo-cyclohexane. Alkene **13** was isolated as a mixture of regioisomers (ratio 8:1). The signals of the minor *E*-isomer are marked with an asterisk.

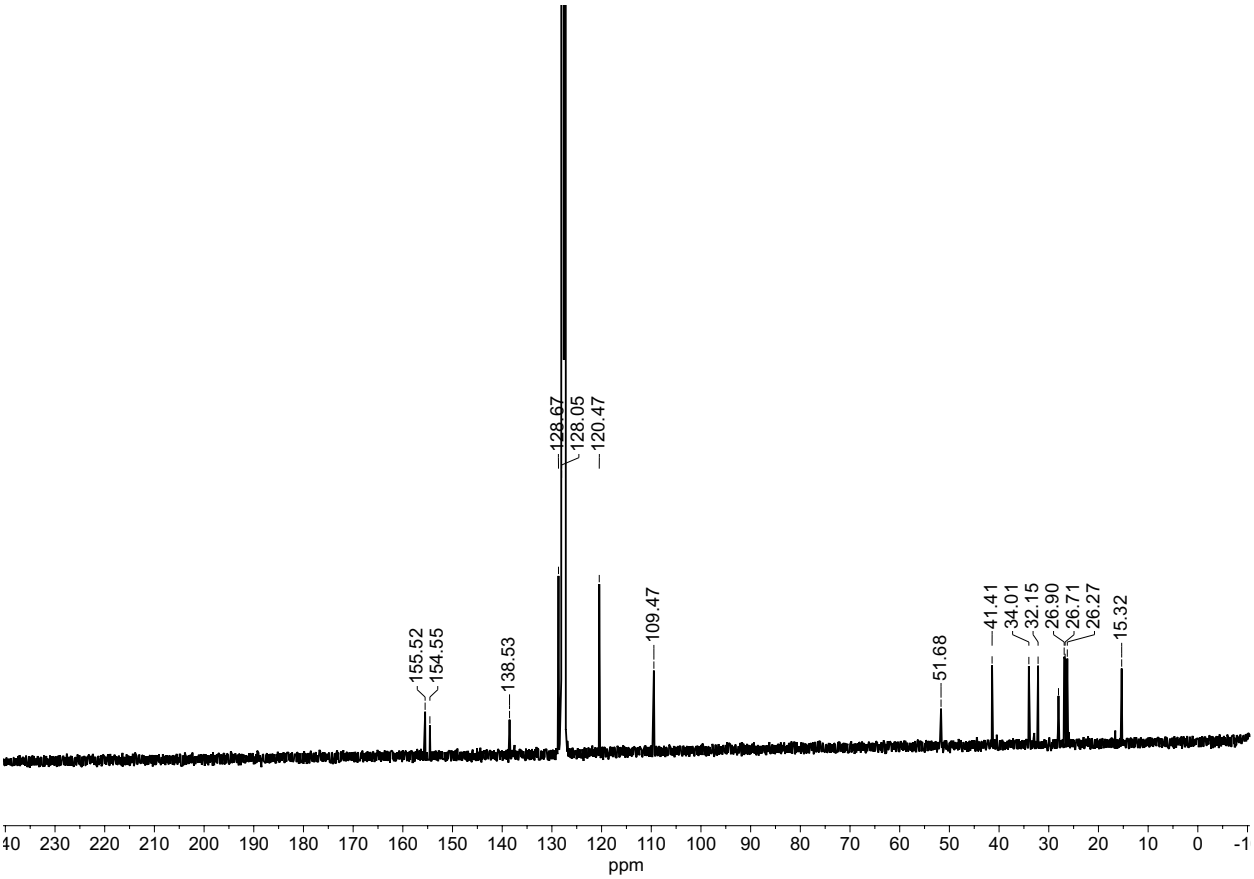

Figure S14. ^{13}C NMR of 3-(4-chlorophenyl)-1-(3-cyclohexylbut-3-en-2-yl)-1-methylurea (**13**) in $CDCl_3$, product of buturon and iodo-cyclohexane

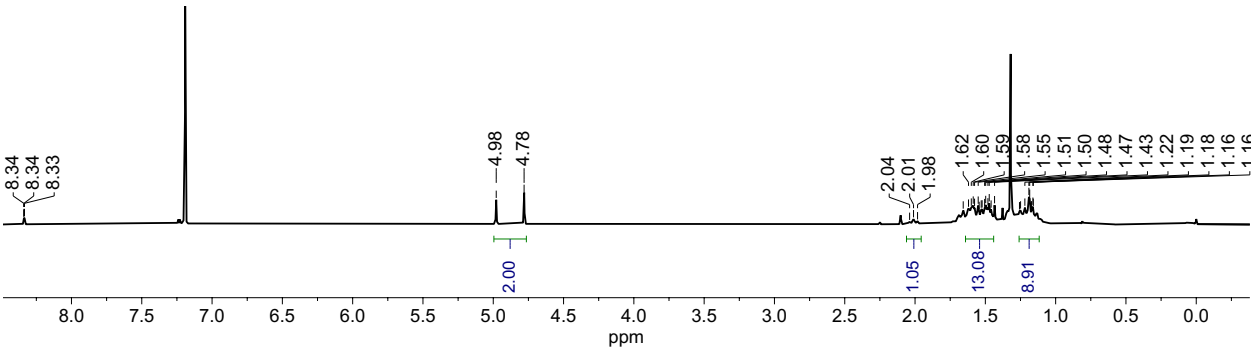

Figure S15. ^{1}H NMR of 1-(1-cyclohexylvinyl)cyclohexan-1-amine (**12**) in $CDCl_3$, product of 1-ethynylcyclohexan-1-amine and iodo-cyclohexane

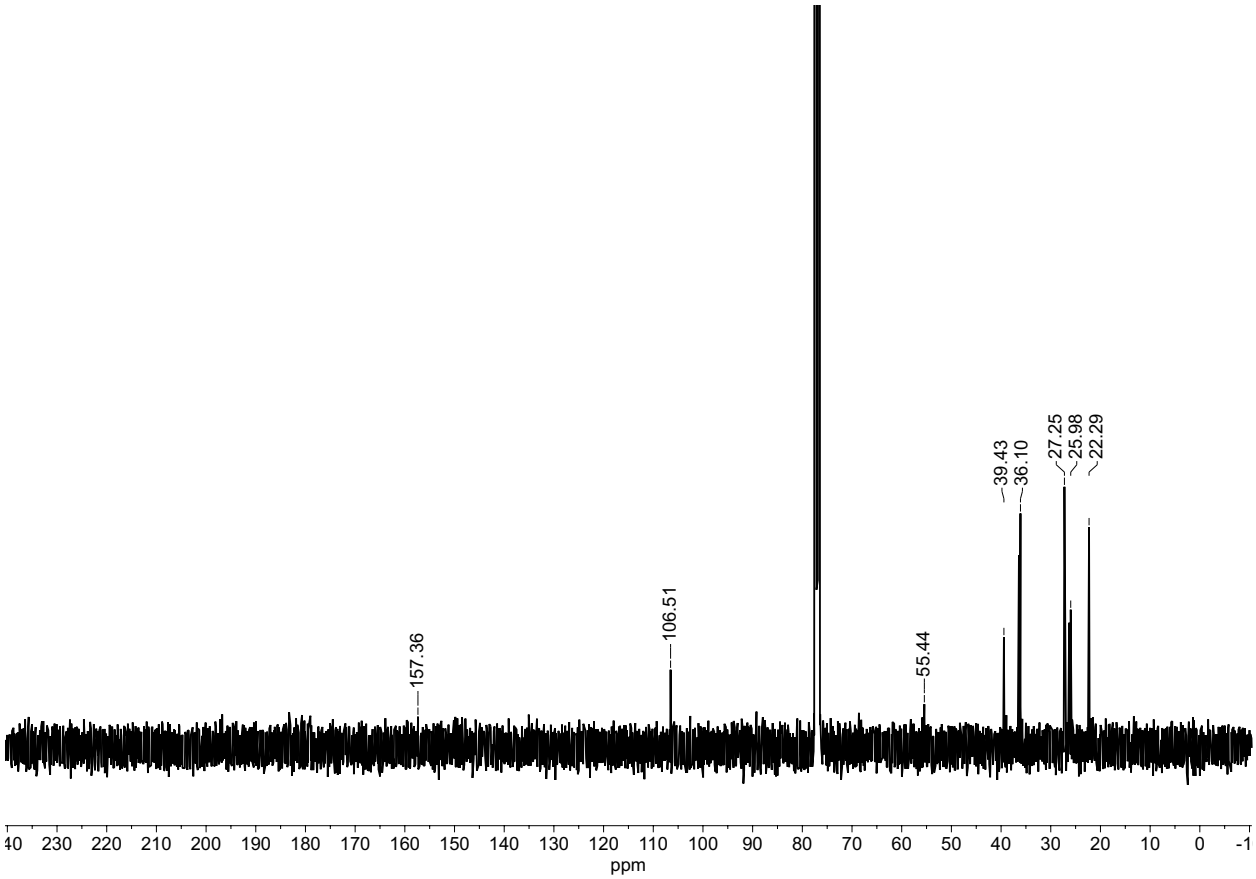

Figure S16. ^{13}C NMR of 1-(1-cyclohexylvinyl)cyclohexan-1-amine (**12**) in $CDCl_3$, product of 1-ethynylcyclohexan-1-amine and iodo-cyclohexane

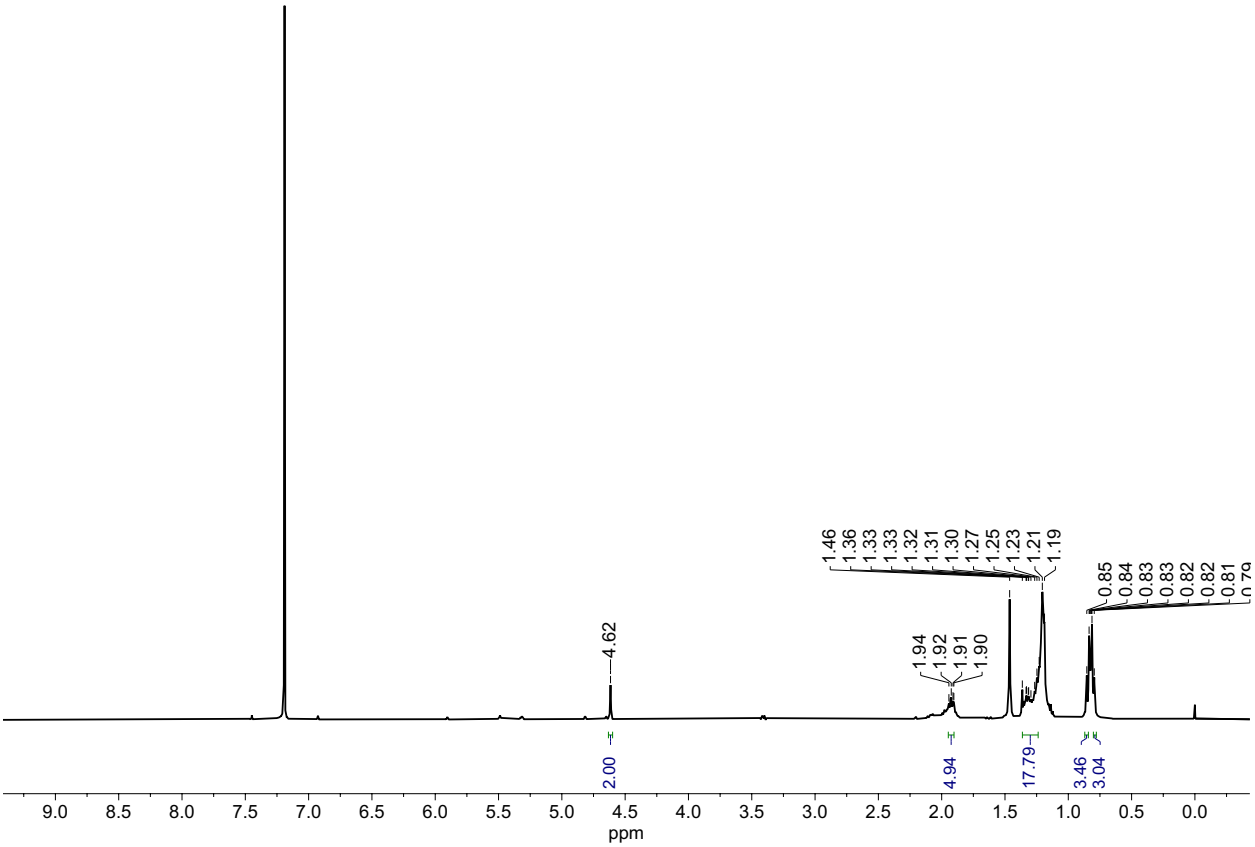

Figure S17. ^{1}H NMR of 5-methylenetridecane (**7**), product of 1-hexyne and iodo-octane in $CDCl_3$. Hexanes (δ = 0.88 and 1.26) overlaps with some aliphatic signals. Residual cyclohexane (δ = 1.46) is also present.

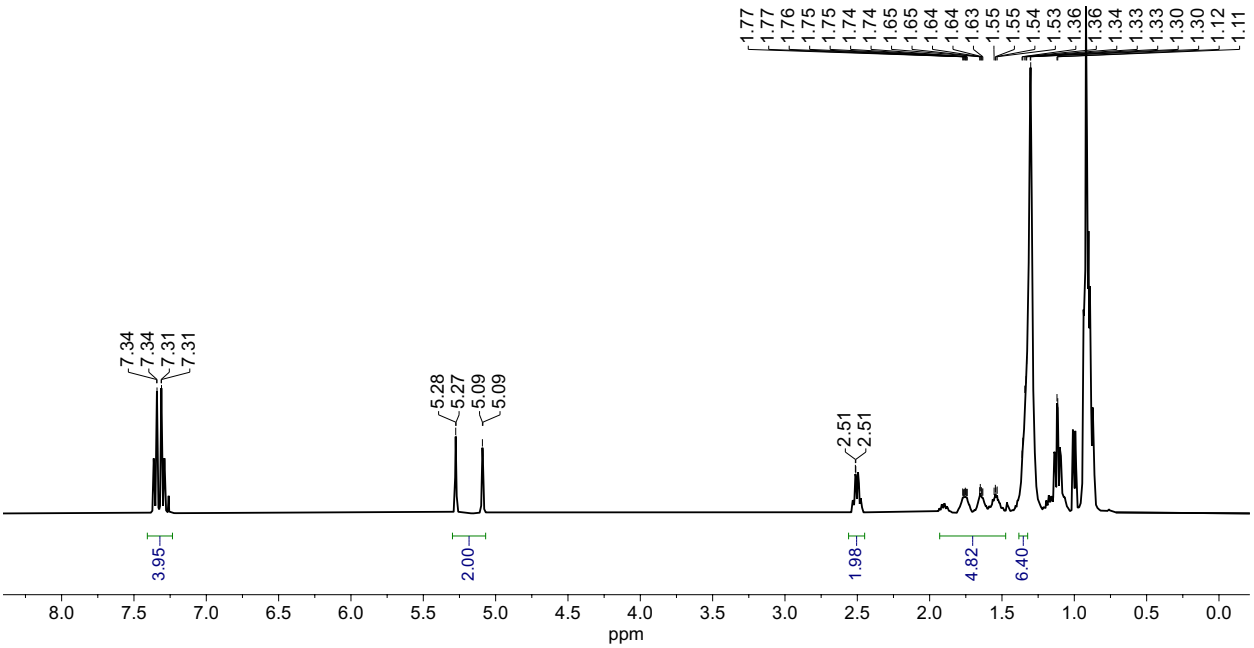

Figure S18. ^{1}H NMR of 1-chloro-4-(1-cyclohexylvinyl)benzene (**9**) in $CDCl_3$, product of 4-chloro-phenylacetylene and iodo-cyclohexane. Hexanes (δ = 0.88 and 1.26) overlaps with some aliphatic signals.

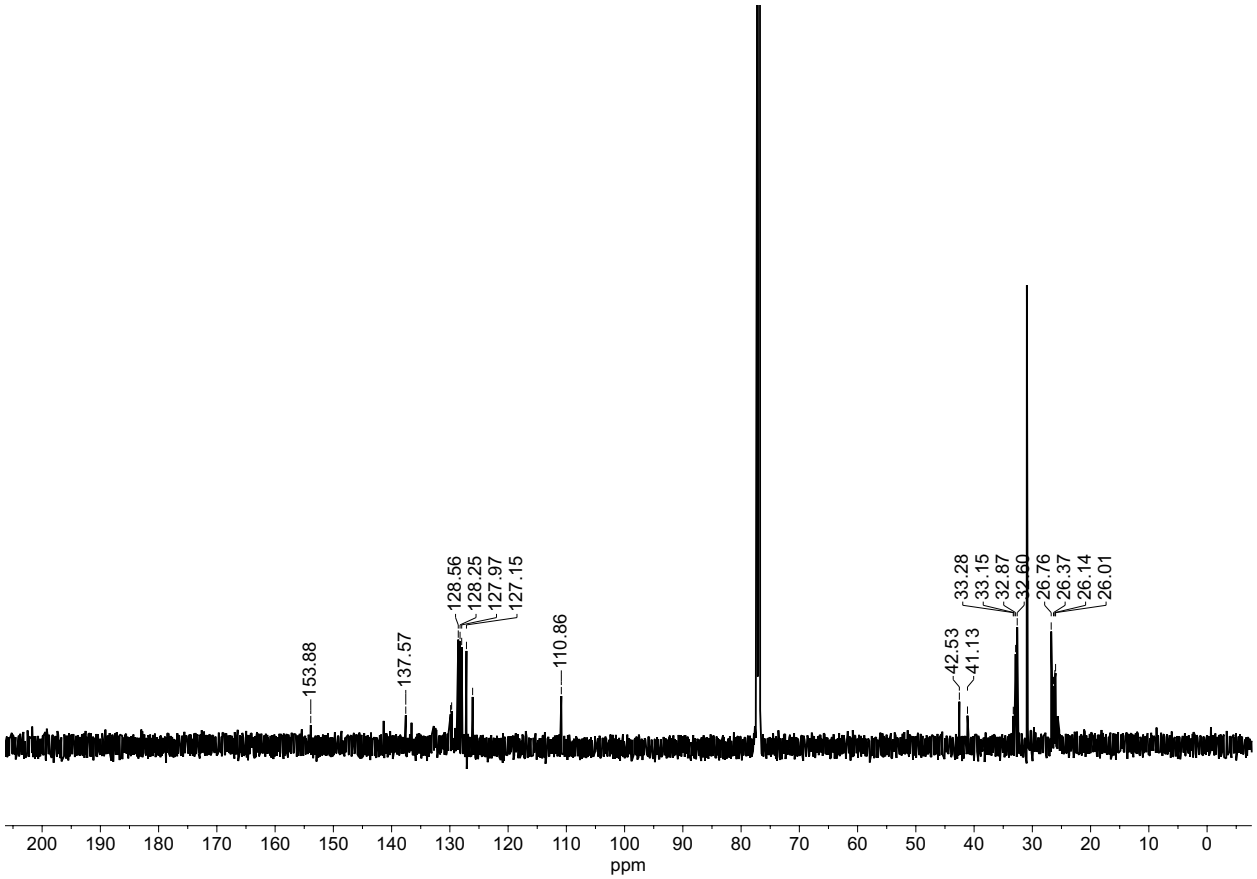

Figure S19. ^{13}C NMR of 1-chloro-4-(1-cyclohexylvinyl)benzene (**9**) in $CDCl_3$, product of 4-chloro-phenylacetylene and iodo-cyclohexane.

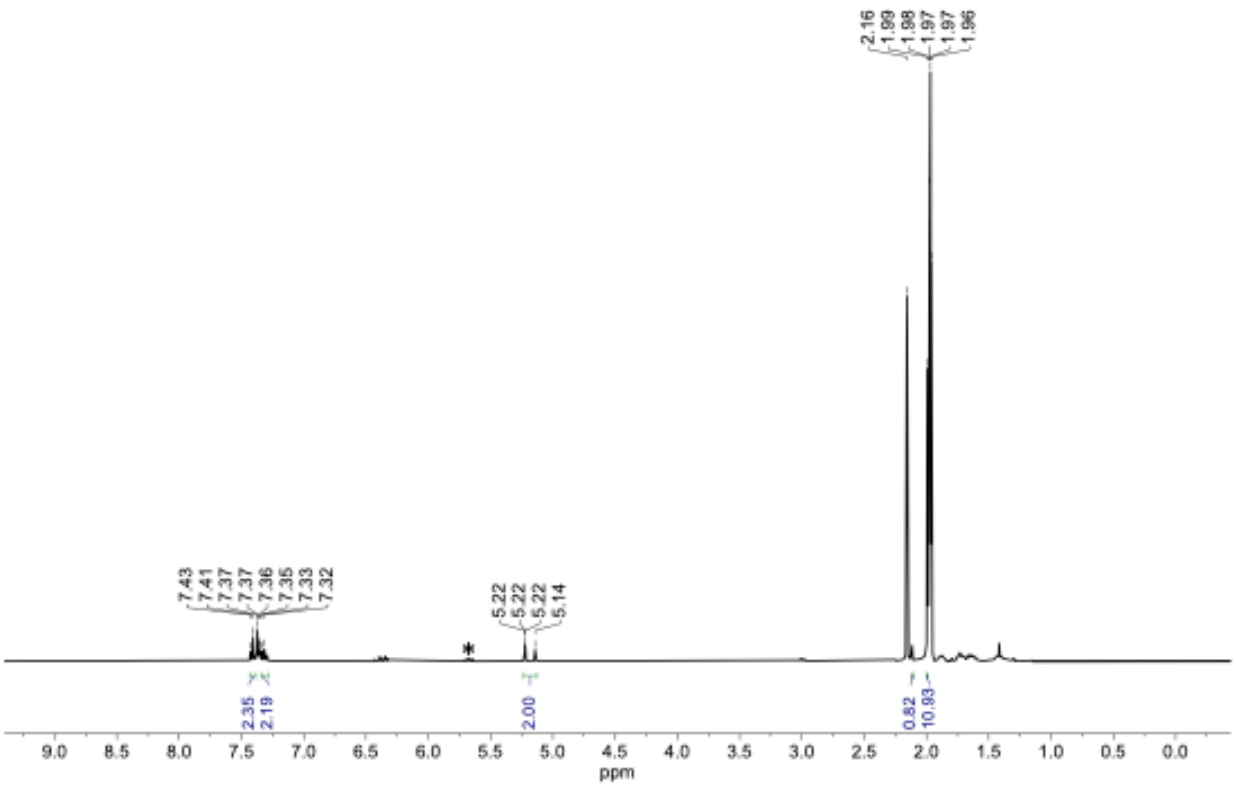

Figure S20. ^{1}H NMR of 1-chloro-4-(1-cyclopentylvinyl)benzene (**10**) in $CDCl_3$, product of 4-chloro-phenylacetylene and iodo-cyclopentane. Alkene **10** was isolated as a mixture of regioisomers (ratio 4:1). The signals of the minor *E*-isomer are marked with an asterisk. Residual acetone (δ = 2.16) present.

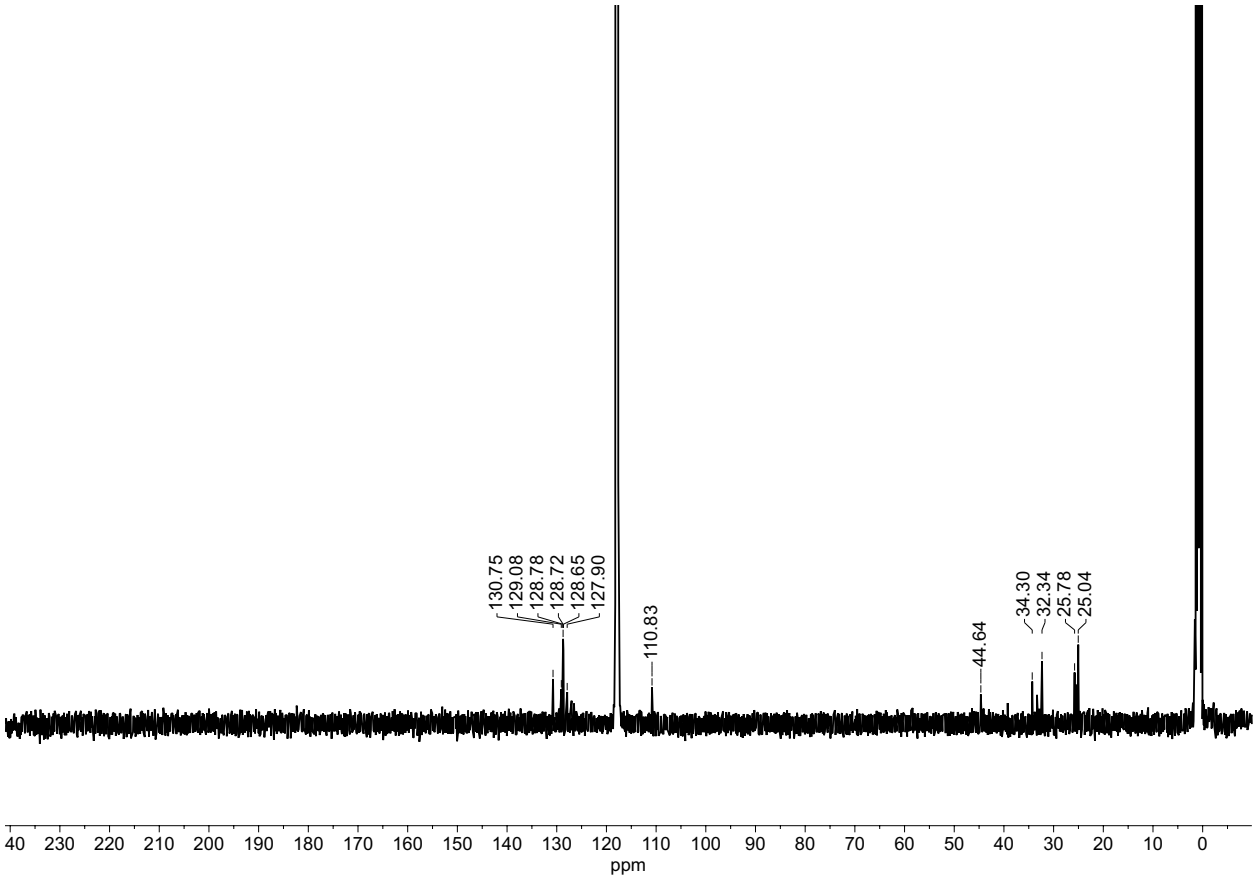

Figure S21. ^{13}C NMR of 1-chloro-4-(1-cyclopentylvinyl)benzene (**10**) in $CDCl_3$, product of 4-chloro-phenylacetylene and iodo-cyclopentane

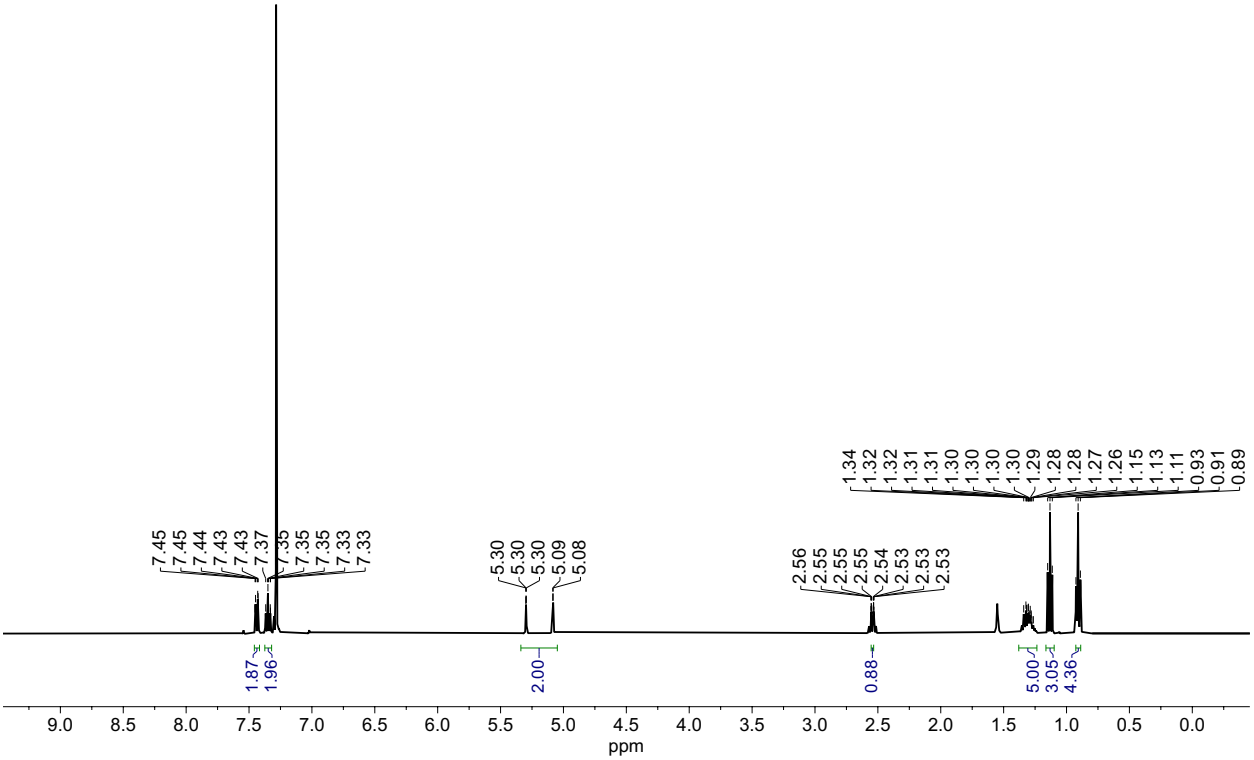

Figure S22. ^{1}H NMR of (1-cyclohexylvinyl)benzene (**8**) in $CDCl_3$, product of phenylacetylene and iodo-cyclohexane. Residual water (δ = 1.56) present. Residual hexanes (δ = 0.88 and 1.26) overlaps with some peaks in the aliphatic region.

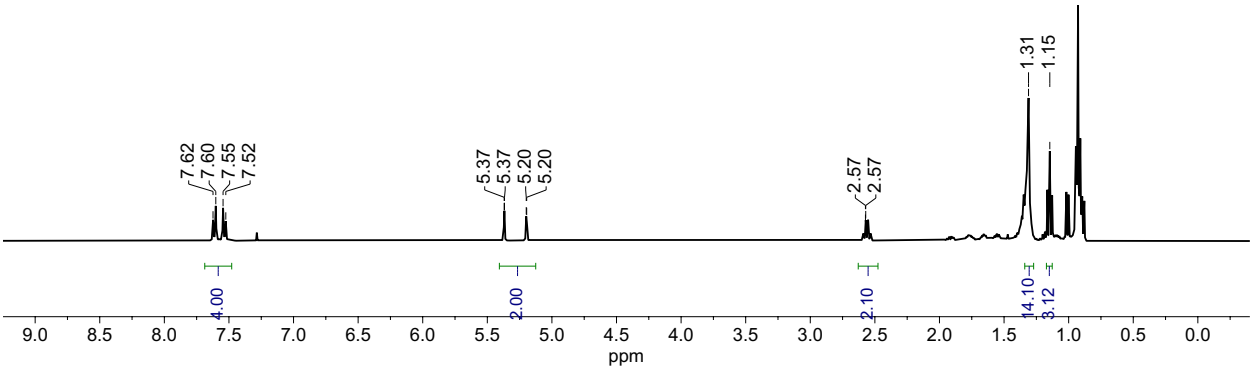

Figure S23. ^{1}H NMR of 1-(dec-1-en-2-yl)-4-trifluoromethylbenzene (**4**) in $CDCl_3$, product of 4-CF_3-phenylacetylene and iodo-octane. Residual hexanes (δ = 0.88 and 1.26) is also present.

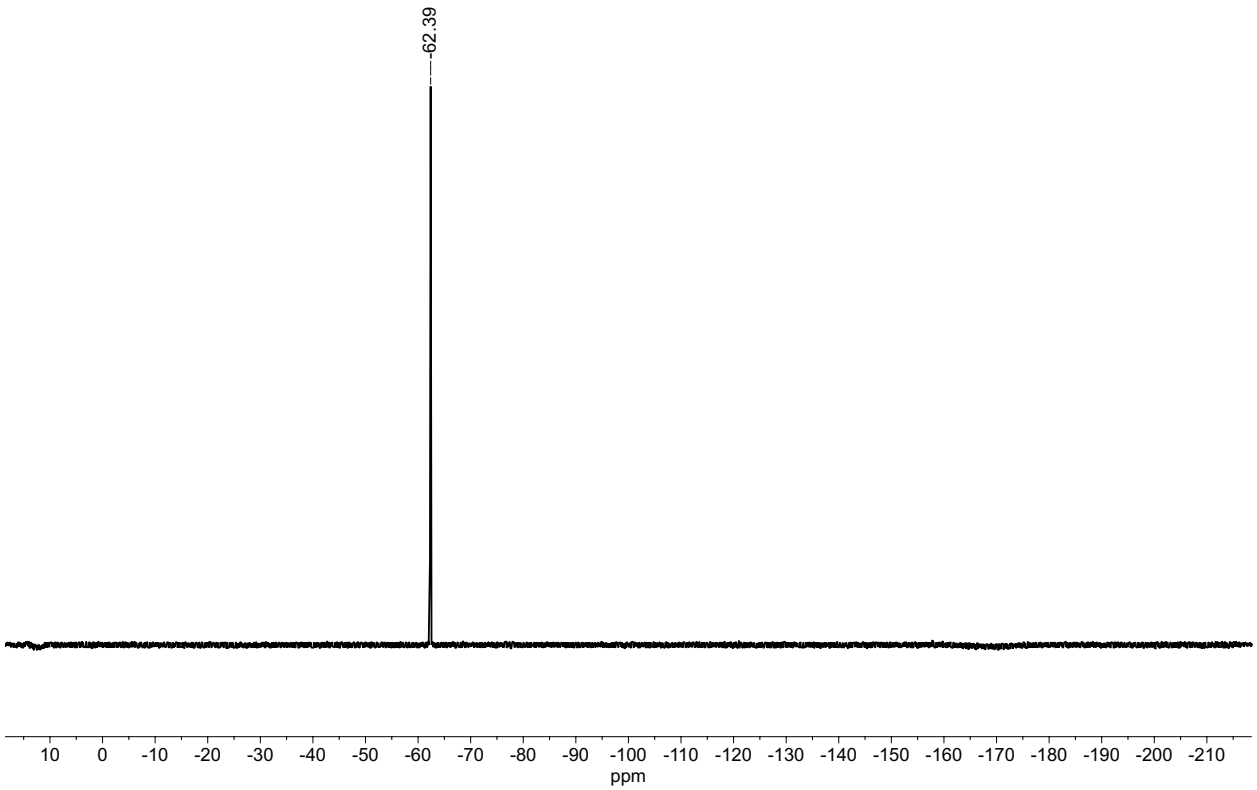

Figure S24. ^{19}F NMR of 1-(dec-1-en-2-yl)-4-trifluoromethylbenzene (**4**) in $CDCl_3$, product of 4-CF_3-phenylacetylene and iodo-octane

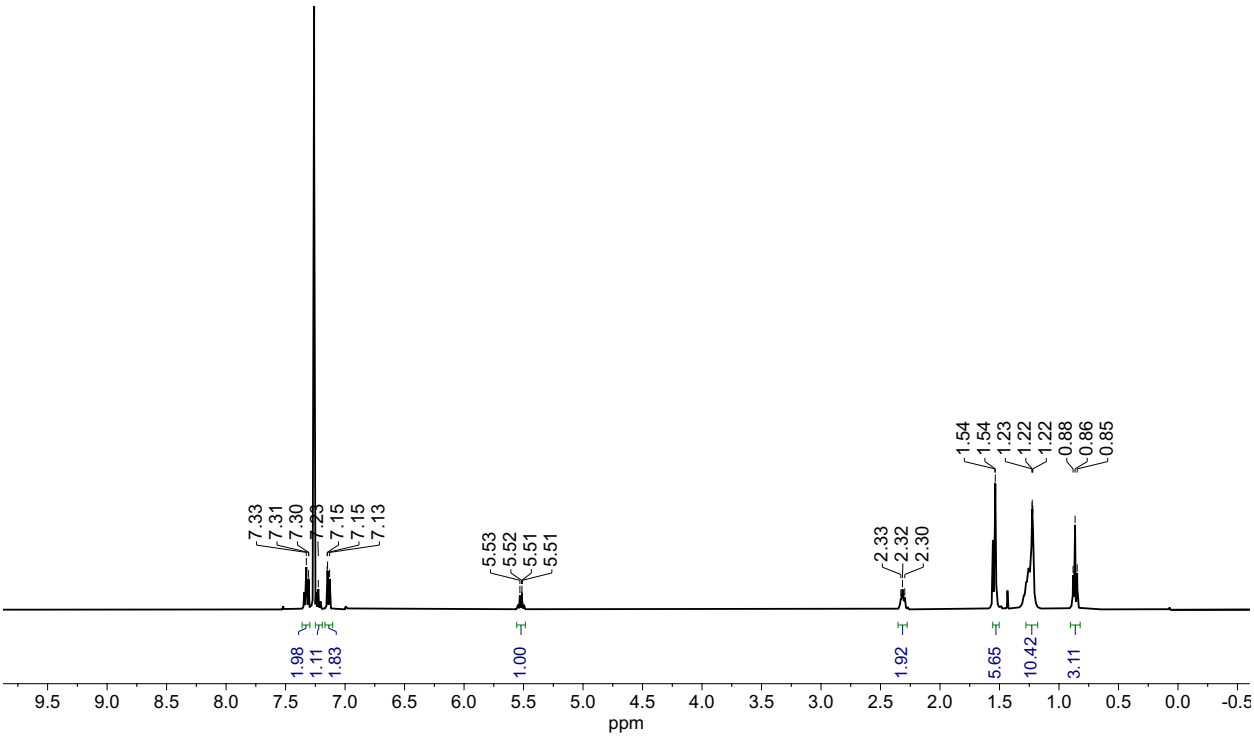

Figure S25. ^{1}H NMR of (*Z*)-undec-2-en-3-ylbenzene (**14**) in $CDCl_3$, *product* of 1-phenyl-1-propyne and iodo-octane. Residual cyclohexane (δ = 1.43) and water (δ = 1.55) is also present.

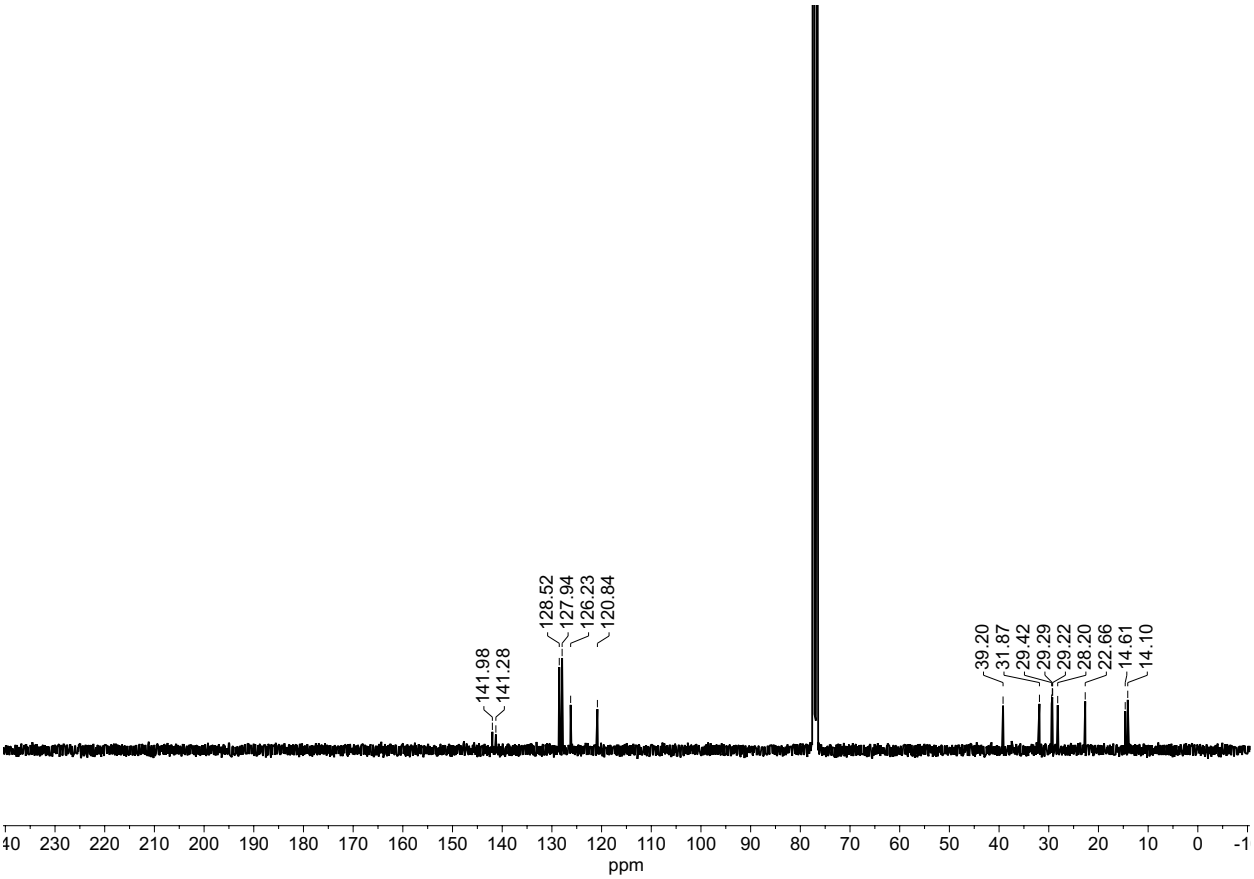

Figure S26. ^{13}C NMR of (*Z*)-undec-2-en-3-ylbenzene (**14**) in $CDCl_3$, product of 1-phenyl-1-propyne and iodo-octane.

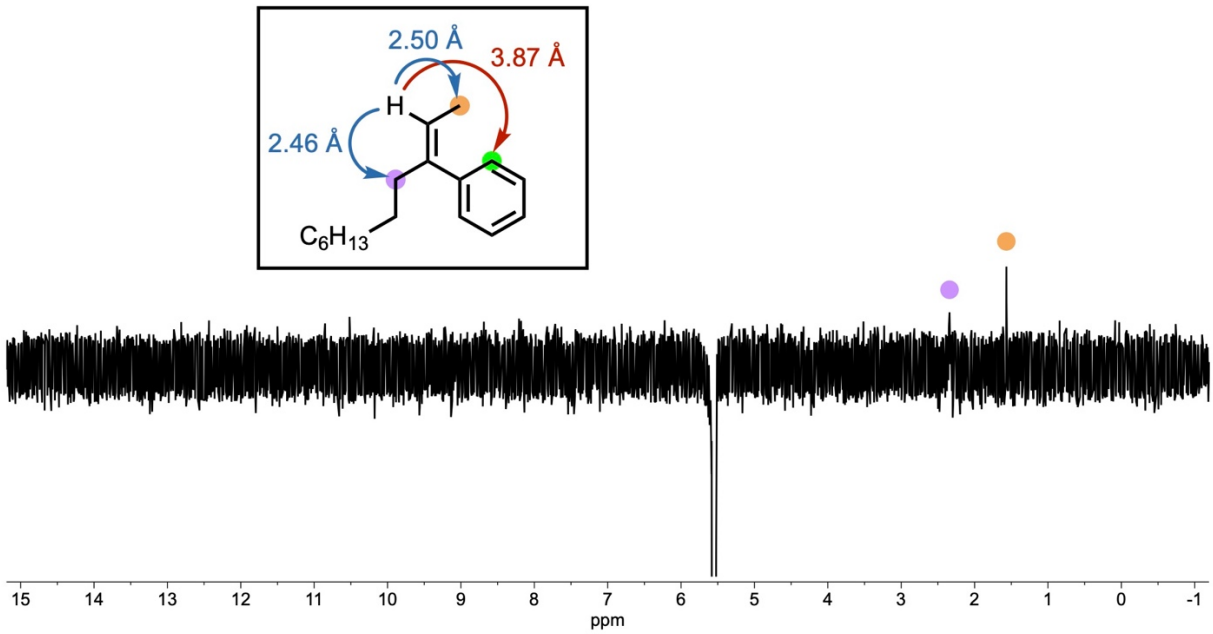

Figure S27. 1D NOESY excitation of the alkenyl proton (δ = 5.52) in product **14** confirming (*Z*)-configuration.

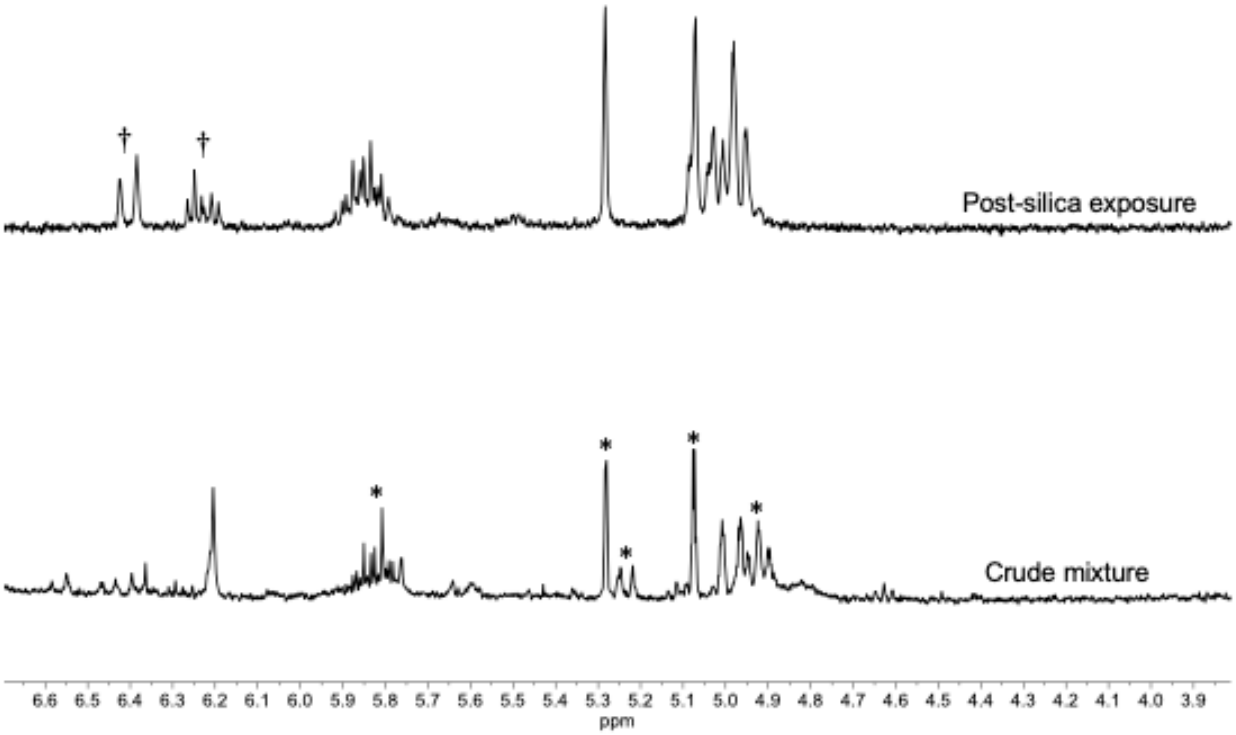

Figure S28. ^{1}H NMR of the reaction mixture from phenylacetylene and cyclopropyl methyl iodide in CD_3CN. Bottom spectrum is crude reaction mixture, with product peaks indicated by *. Top spectrum shows that product decomposes upon separation on silica gel TLC plates. Decomposition generates a new species containing an internal alkene product indicated by †.

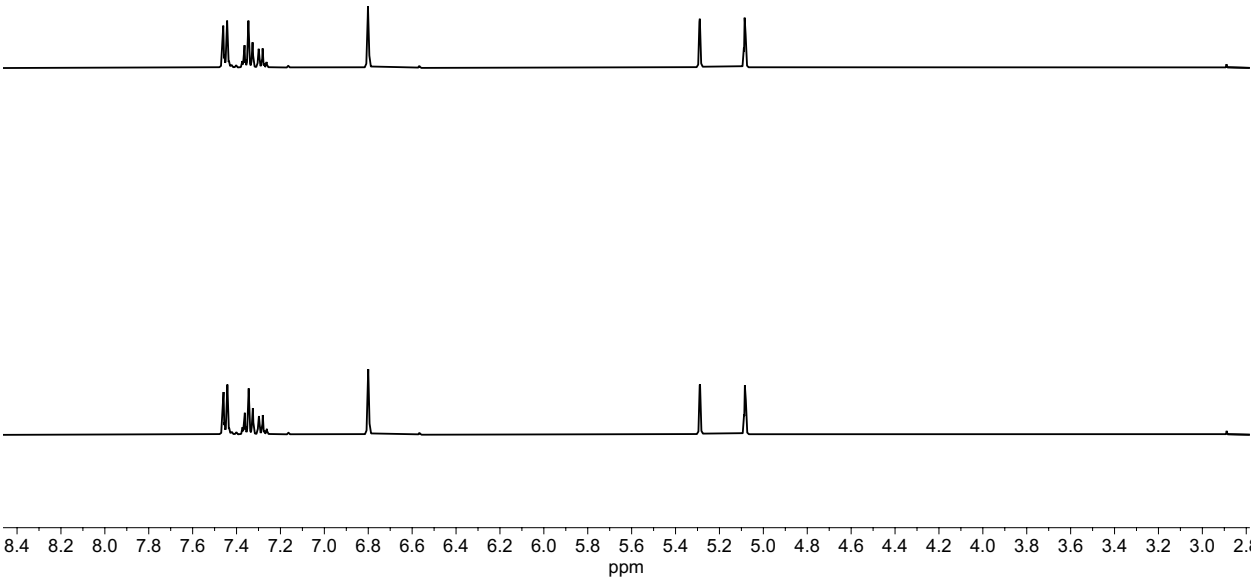

Figure S29. ^{1}H NMR of but-1-en-2-ylbenzene reversibility experiment before (bottom) and after (top) standard electrolysis with 10 mol% (DHP)Ni and no added phenol in CD_3CN.

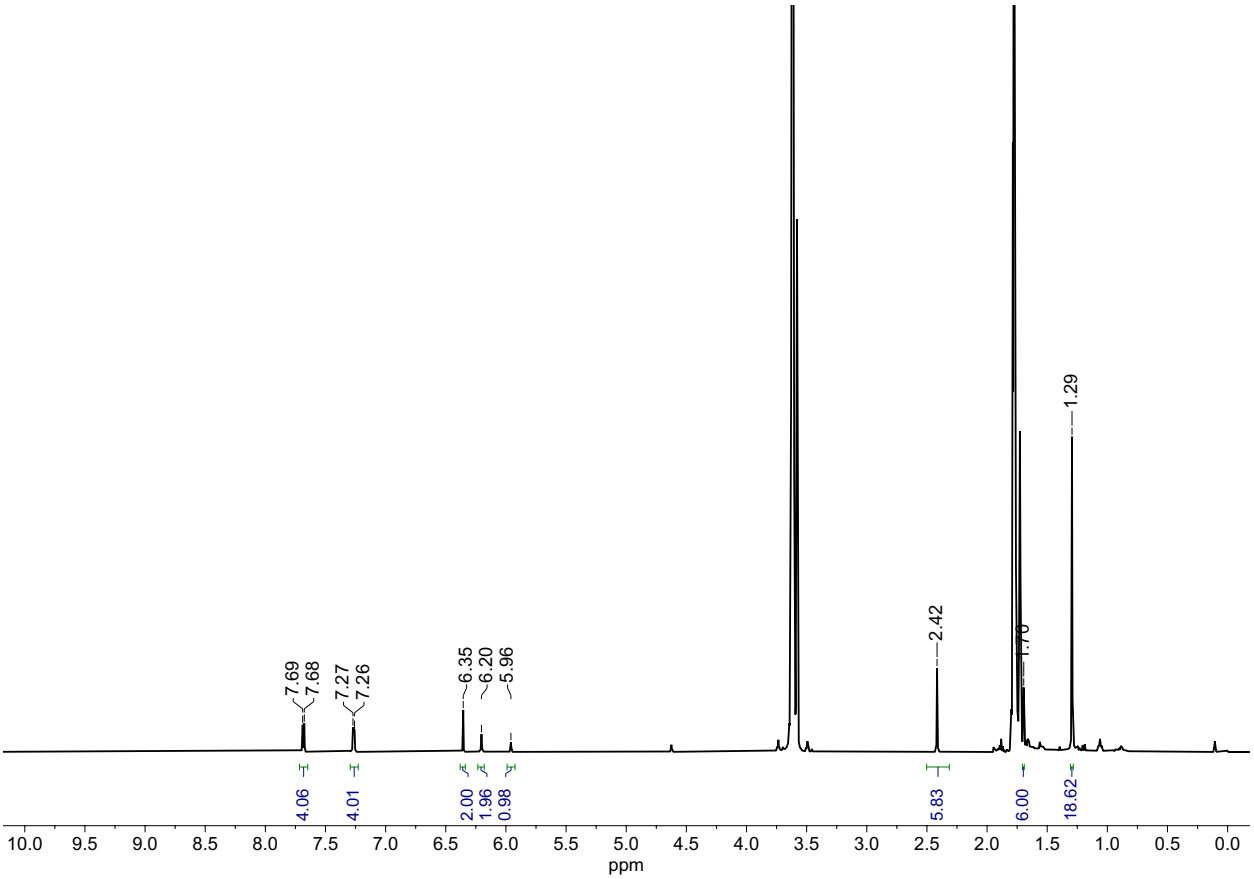

Figure S30. ^{1}H NMR of (DHP·H_2)Ni-isobutene in d_8-THF, the product of (DHP·H_2)Ni[OTf] and isobutenylmagnesium bromide. Proteo-THF solvent peaks from the Grignard solution (0.5 M in THF): δ 3.62 and 1.77; residual d_n-THF from the d_8-THF solvent: δ 3.58 and 1.72. Residual isobutene: δ 4.62 and 1.66.

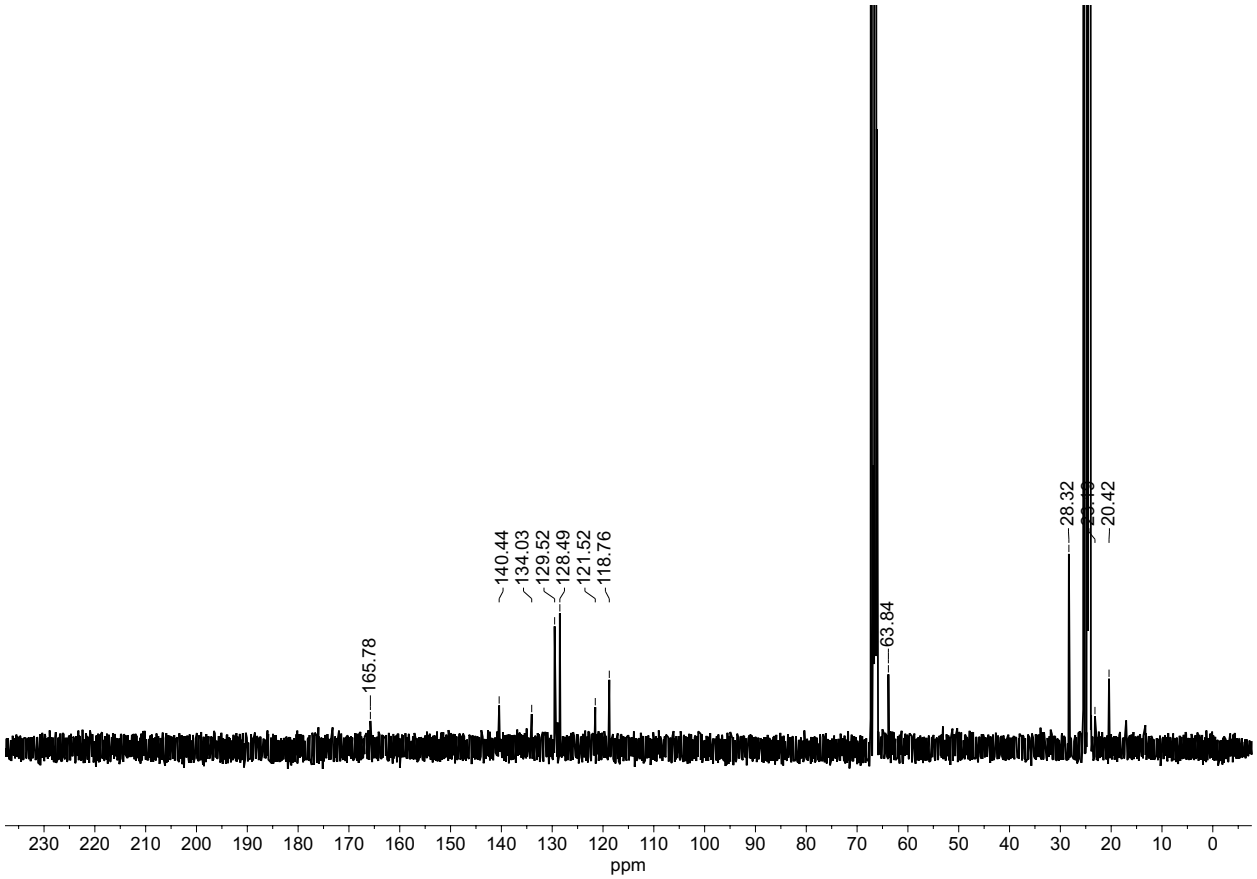

Figure S31. ^{13}C NMR of (DHP·H2)Ni-isobutene in d_8-THF, the product of (DHP·H_2)Ni[OTf] and isobutenylmagnesium bromide.

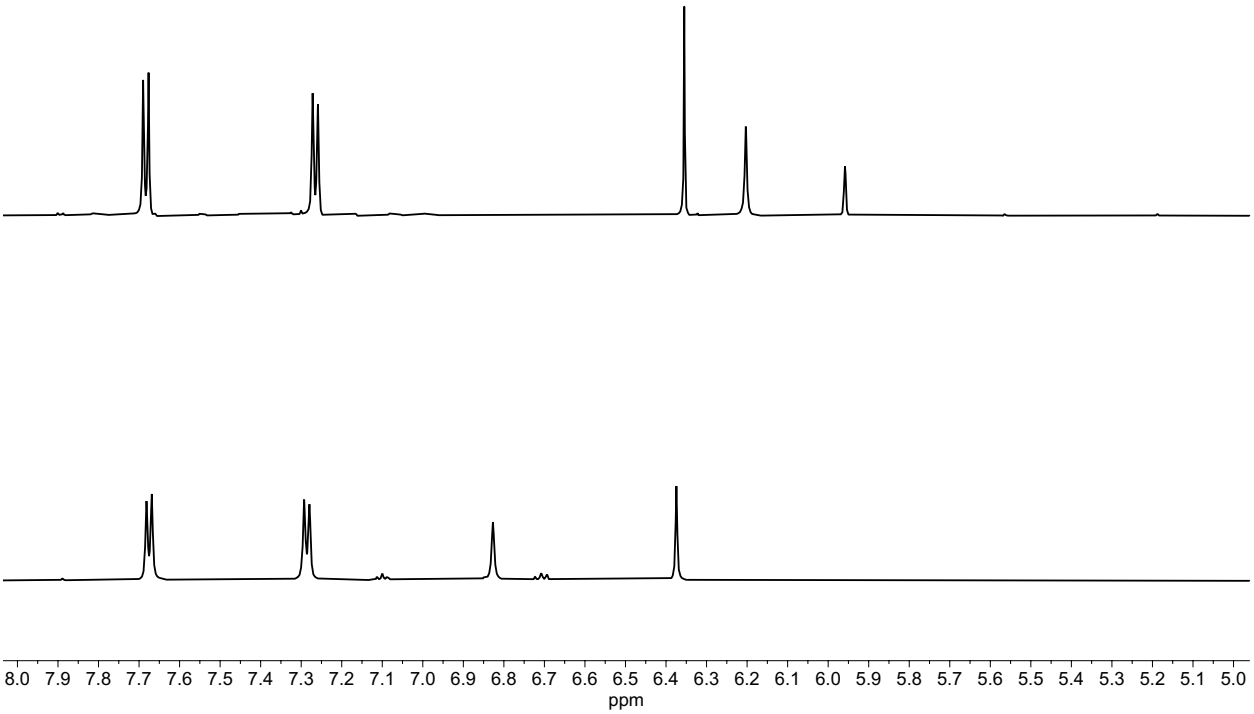

Figure S32. Stacked ^{1}H NMR downfield spectra of (DHP·H_2)Ni[OTf] (bottom) and (DHP·H_2)Ni-isobutene (top) in d_8-THF. Ligand arm N-H peak shifts from 6.83 to 6.20 ppm, and the alkenyl C-H shift for the bound isobutene appears at 5.96 ppm.

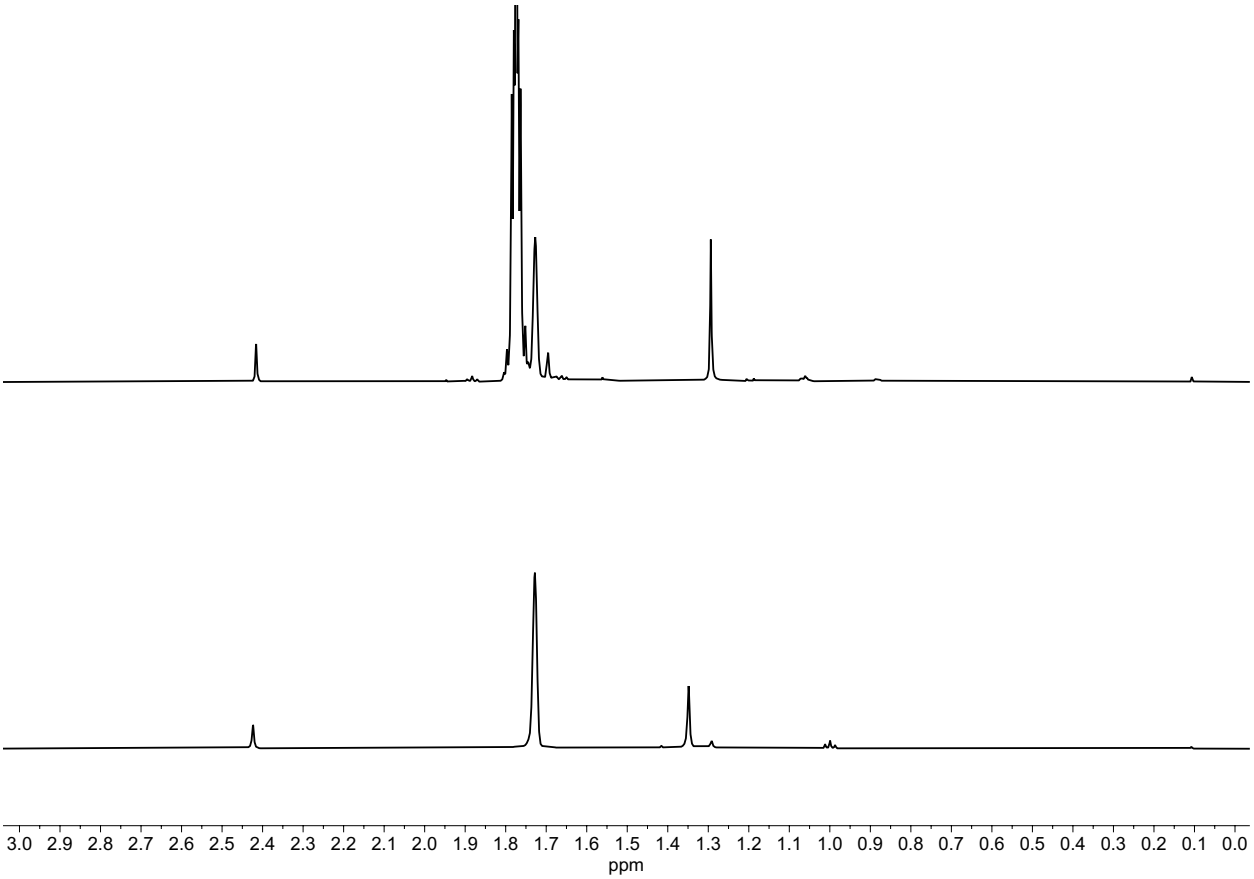

Figure S33. Stacked ^{1}H NMR upfield spectra of (DHP·H_2)Ni[OTf] (bottom) and (DHP·H_2)Ni-isobutene (top) in d_8-THF. Ligand ^{t}Bu C-H peak shifts from 1.35 to 1.29 ppm, and the methyl shift for the bound isobutene appears at 1.70 ppm. THF solvent from the Grignard reagent solution appears at 1.77 ppm while residual d_n-THF appears at 3.58 ppm.

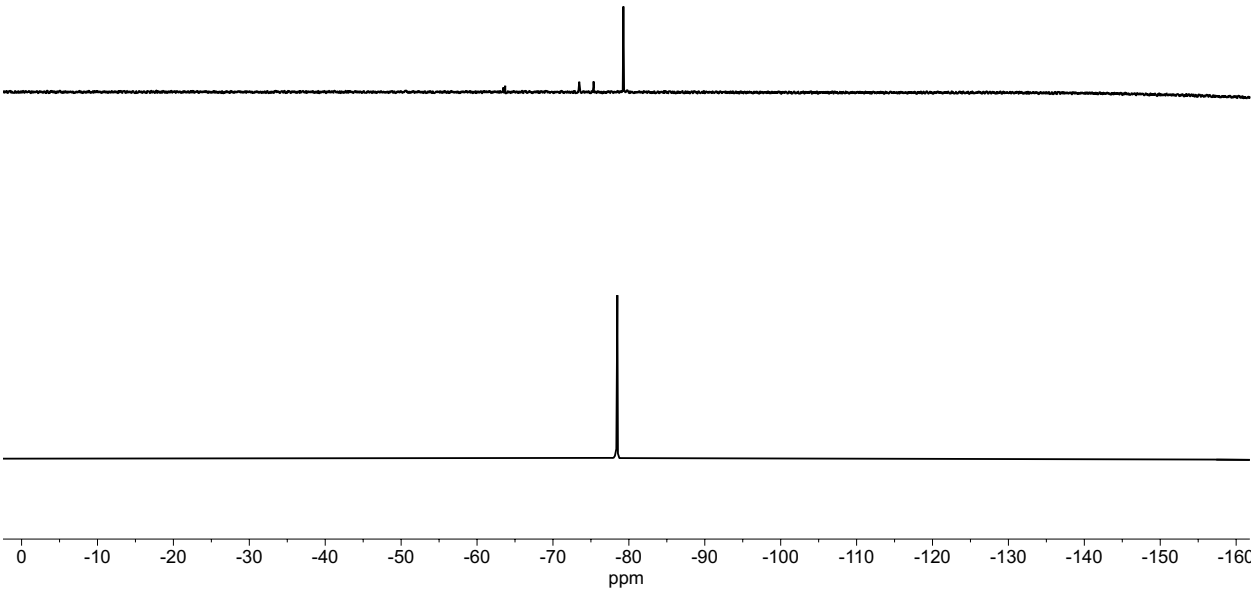

Figure S34. Stacked ^{19}F NMR spectra of (DHP·H_2)Ni[OTf] (bottom) and (DHP·H_2)Ni-isobutene (top) in d_8-THF. Major peak shifts from –78 to –79 ppm and small F-containing byproducts appear at –63, –73, and –75 ppm.

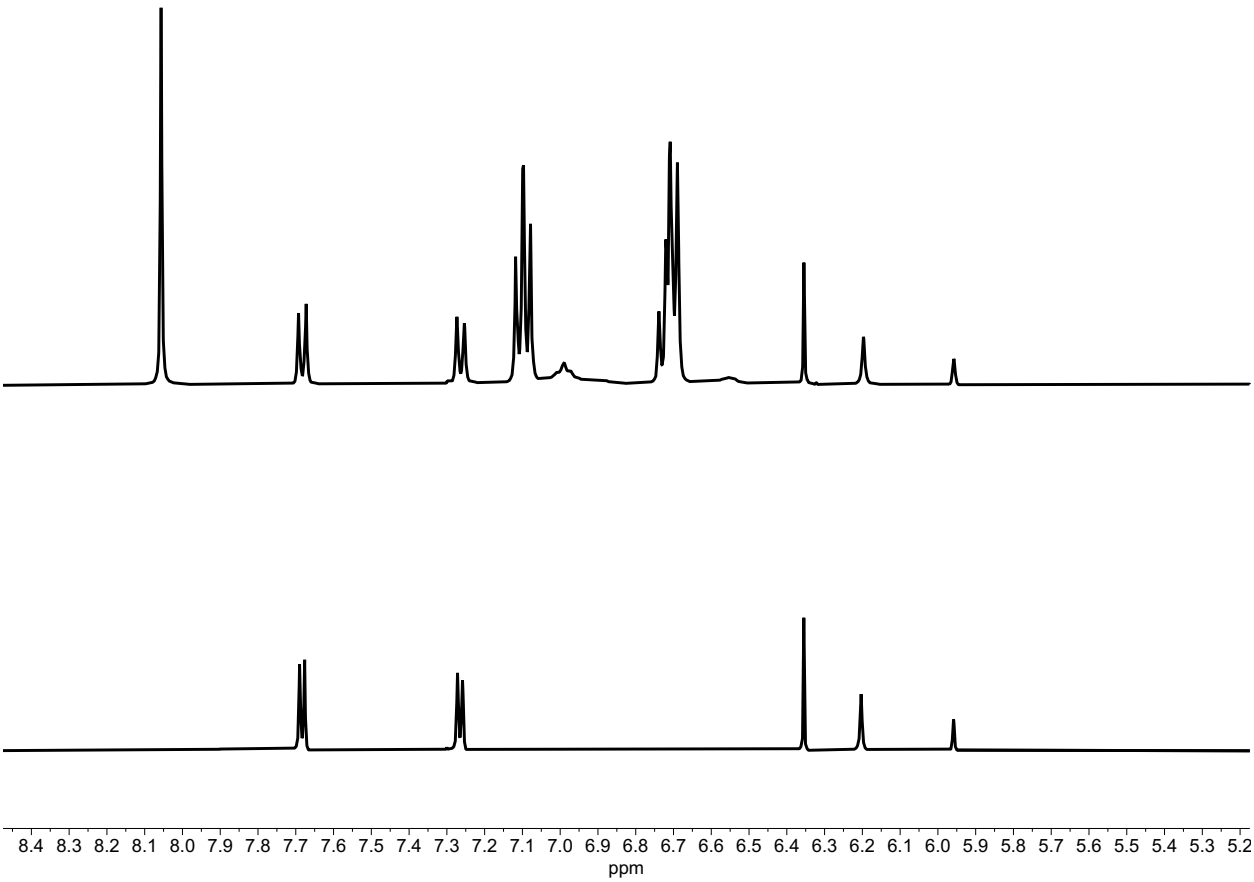

Figure S35. Stacked ^{1}H NMR spectra of (DHP·H_2)Ni-isobutene alone (bottom) and in the presence of 3 eq phenol (top) in d_8-THF. Phenol peaks: 8.05, 7.1, and 6.7 ppm.

Mass Spectra

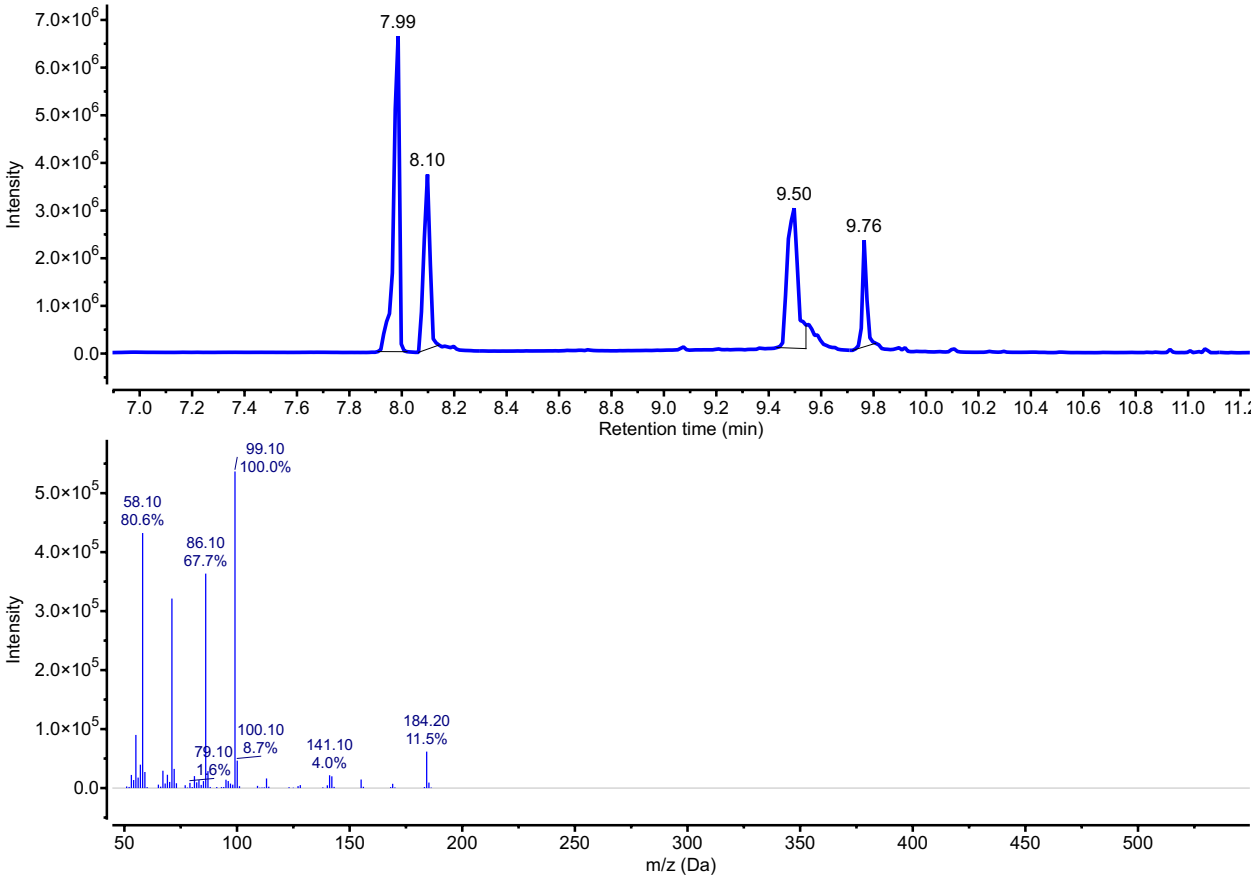

Figure S36. GC-MS (EI, 70 eV, m/z) of 2-ethoxydec-1-ene (11) (9.76 min, MS bottom), product of ethoxyethyne and iodo-octane. Other chromatogram peaks (min): 7.99 = mesitylene internal standard, 8.10 = phenol, 9.50 = tributylamine from electrolyte.

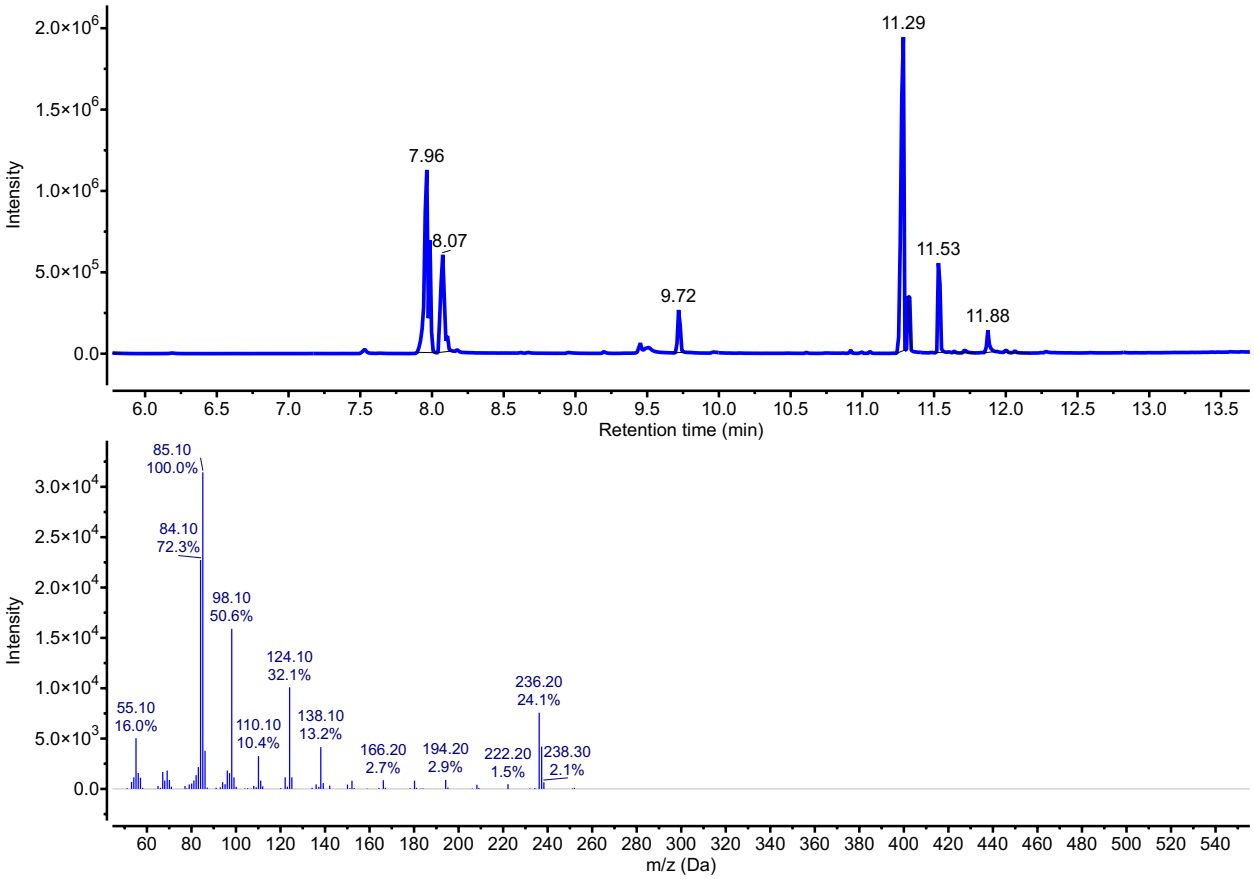

Figure S37. GC-MS (EI, 70 eV, m/z) of 1-(2-methylenedecyl)piperidine (5) (11.29 min, MS bottom), product of 1-(prop-2-yn-1-yl)piperidine and iodo-octane. Other chromatogram peaks (min): 7.96 = mesitylene internal standard, 8.07 = phenol, 9.72 = iodo-octane, 11.33 = (E)-1-(undec-2-en-1-yl)piperidine minor product, 11.53 = hexadecane, 11.88 = column contamination.

	$(DHPH_2)Ni$	I-octane	→	$(DHPH_2)Ni$-octyl	I$^{\bullet}$	Reaction Energy	Ni-C_{octyl} BDE
Energy (kcal/mol)	-2564.70	-612.47		-2879.26	-192548.38	-297.87	31.9

Table S25. Tabulated energies for calculation of Ni-C_{octyl} BDE. [a] For $(DHPH_2)Ni$ structure see **Error! Reference source not found.**. [b] For $(DHPH_2)Ni$-octyl structure see **Error! Reference source not found.**. [c] Ni-C_{octyl} BDE = Reaction energy – 55.8 kcal/mol (I-Octane BDE)[1]

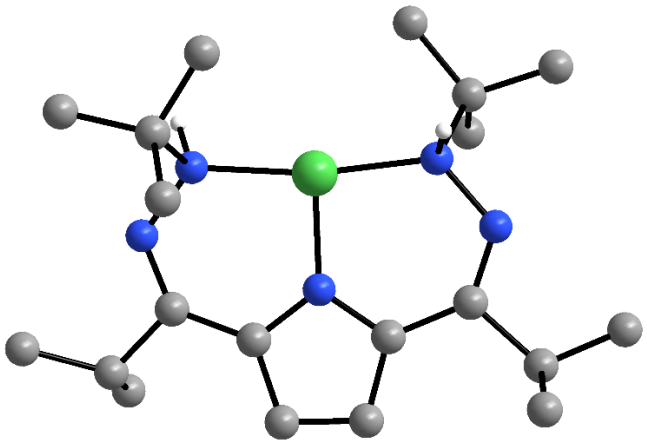

Figure S38. Calculated structure of $(DHPH_2)Ni$. Some H atoms removed for clarity.

Table S26. Coordinates for the calculated structure of $(DHPH_2)Ni$

Ni	14.67901	2.99901	6.46909
N	13.73090	1.96237	7.89802
N	12.30129	2.08754	8.14778
N	13.09716	3.48880	5.55366
N	15.48168	4.51386	3.93604
N	15.91710	3.85385	5.15559
C	13.59918	-0.26844	9.05240
C	15.60158	0.41608	7.73340
H	16.07766	0.92419	8.59207
C	14.08211	0.48083	7.81588
C	11.52569	2.60833	7.24670
C	10.05187	2.61022	7.64592
C	9.68839	1.53848	8.66033
C	9.63880	3.99379	8.14463
C	11.82661	3.23503	5.97173
C	10.91427	3.76236	5.01902
H	9.82318	3.72640	5.06010
C	11.67538	4.35006	4.01666
H	11.28947	4.84764	3.12400
C	13.03812	4.16831	4.37579

C	14.21840	4.61823	3.65784
C	13.95141	5.32614	2.33175
C	13.60166	4.31159	1.24419
C	15.08863	6.22716	1.87663
C	13.45172	-0.09030	6.55690
H	13.75472	-1.14354	6.42472
H	12.34896	-0.06054	6.60752
C	16.95593	4.73183	5.83418
C	17.46874	3.91799	7.01472
H	16.66668	3.73111	7.75818
H	18.28232	4.45574	7.53240
H	17.86589	2.94080	6.68417
C	18.10631	5.05896	4.89005
H	18.56544	4.13556	4.49203
H	18.89205	5.61683	5.42942
H	17.77829	5.67389	4.03635
C	16.25982	5.99465	6.31249
H	15.38271	5.74132	6.93874
H	15.91343	6.60955	5.46367
H	16.94891	6.60962	6.91768
H	14.01646	0.17140	9.97648
H	13.92874	-1.32135	9.00579
H	12.50038	-0.25997	9.13426
H	15.93759	-0.63584	7.73737
H	15.97929	0.88537	6.80271
H	13.77285	0.47780	5.66353
H	14.12501	2.25503	8.80215
H	16.46149	3.05852	4.78872
H	13.34494	4.82715	0.30160
H	12.74462	3.67488	1.52354
H	14.46219	3.64859	1.03743
H	13.06376	5.96732	2.49220
H	15.98333	5.64502	1.59719
H	15.39219	6.93582	2.66657
H	14.78005	6.81178	0.99149
H	9.47591	2.39663	6.72569
H	10.21082	4.26548	9.05113
H	8.56606	4.00964	8.40791
H	9.81021	4.77879	7.38786
H	10.15859	1.72397	9.64099
H	10.00853	0.53565	8.32715
H	8.59418	1.51600	8.81062

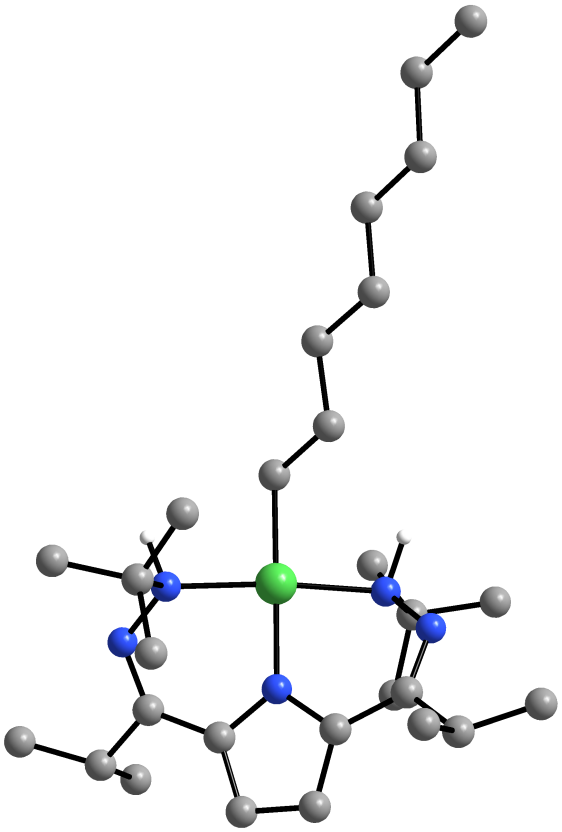

Figure S39. Calculated structure of ($DHPH_2$)Ni-octyl. Some H atoms removed for clarity.

Table S27. Coordinates for the calculated structure of ($DHPH_2$)Ni-octyl

Ni 13.83907 3.12437 5.04280
N 13.07521 1.65268 6.13776
N 12.83473 1.92080 7.54126
N 12.45660 4.22444 5.73564
N 13.45165 5.37928 3.20851
N 14.45579 4.70668 4.01213
C 11.76896 -0.45418 6.35330
C 12.32792 0.49491 4.10813
H 13.26214 -0.09135 4.06525
C 11.92457 0.82484 5.53677
C 12.25846 3.03717 7.85653
C 12.00042 3.25511 9.33401
C 12.00058 1.97716 10.15493
C 13.00655 4.26872 9.88144
C 11.88282 4.11039 6.95756
C 10.90250 5.11974 7.11221
H 10.26853 5.28805 7.98634
C 10.87492 5.82895 5.91208
H 10.23488 6.68033 5.66645
C 11.87194 5.25877 5.08674
C 12.31174 5.64717 3.76149

C 11.31359 6.39868 2.90190
C 10.20861 5.44776 2.44281
C 11.93841 7.12485 1.72335
C 10.61659 1.59797 5.53407
H 9.83027 0.94753 5.11217
H 10.29521 1.87818 6.55146
C 15.38175 5.73208 4.68991
C 16.52805 4.94320 5.30054
H 16.16897 4.24591 6.07871
H 17.24864 5.64051 5.76259
H 17.07096 4.35859 4.53682
C 15.91632 6.68378 3.62323
H 16.42454 6.13364 2.81056
H 16.65238 7.37428 4.07064
H 15.11231 7.29019 3.17533
C 14.65920 6.51678 5.77192
H 14.28217 5.86648 6.58023
H 13.81612 7.10213 5.36888
H 15.37116 7.23469 6.21644
H 12.71227 -1.02866 6.38612
H 11.00087 -1.10179 5.89591
H 11.46023 -0.23812 7.38964
H 11.53188 -0.09978 3.62668
H 12.47458 1.41771 3.51751
H 10.66613 2.51080 4.91567
H 13.84185 0.97255 6.18364
H 11.29069 1.23293 9.75391
H 11.71505 2.19711 11.19884
H 12.99852 1.50703 10.17357
H 10.99472 3.71282 9.41390
H 14.03330 3.86053 9.83484
H 12.78643 4.50879 10.93664
H 12.99376 5.21158 9.30674
H 11.17587 7.72933 1.20140
H 12.36231 6.41592 0.99131
H 12.75311 7.79782 2.04099
H 9.42304 5.99683 1.89413
H 9.72711 4.93043 3.29124
H 10.61658 4.67732 1.76230
H 10.84724 7.15440 3.56451
C 15.25144 1.96310 4.31790
C 15.36000 1.88034 2.79993
C 16.32593 0.81548 2.28825
H 15.69401 2.85390 2.37800
H 14.36644 1.69886 2.33819
C 16.44118 0.76477 0.77297
H 16.00251 -0.17715 2.66562
H 17.32816 0.98696 2.73359
C 17.48848 -0.20996 0.25982
H 16.67310 1.77952 0.38856
H 15.45192 0.50946 0.34014
C 17.53299 -0.32191 -1.25512
H 17.31185 -1.21370 0.69842
H 18.48588 0.10079 0.63364

C 18.62858 -1.23910 -1.77600
H 17.66276 0.68850 -1.69558
H 16.55022 -0.67900 -1.62667
C 18.65279 -1.34931 -3.28801
H 17.69827 -1.74830 -3.67817
H 19.45858 -2.01566 -3.64242
H 18.80805 -0.36173 -3.76030
H 18.50408 -2.24593 -1.32921
H 19.61029 -0.87548 -1.41179
H 15.06140 4.30333 3.28979
H 16.23053 2.29816 4.72298
H 15.12110 0.93270 4.71560

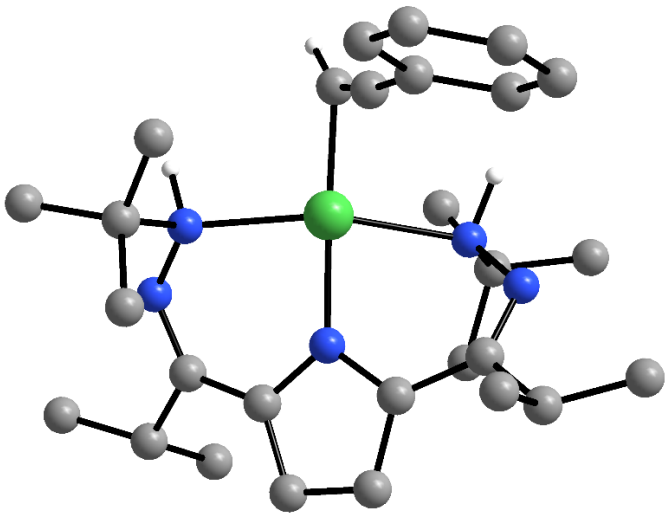

Figure S40. Calculated structure of **2a**. Some H atoms removed for clarity.

Table S28. Coordinates for the calculated structure of **2a**
Ni 14.69032 2.30913 6.27260
N 13.40031 1.09788 7.49594
N 12.36777 1.80767 8.21541
N 13.05231 3.08618 5.56215
N 15.32936 4.31798 4.02858
N 15.58969 4.10480 5.43453
C 12.30945 -1.04381 8.16857
C 14.02923 -0.96538 6.36053
H 14.88210 -1.05407 7.05656
C 12.85555 -0.24014 6.99236
C 11.65129 2.65542 7.54734
C 10.51981 3.30445 8.33035
C 10.14143 2.55544 9.59620
C 10.86256 4.76161 8.64262
C 11.84116 3.13618 6.18858
C 10.92985 3.86130 5.38949
H 9.88550 4.08276 5.62362
C 11.62384 4.25023 4.24352
H 11.23446 4.84087 3.41054
C 12.94908 3.79077 4.40712

C 14.11555 4.15057 3.61131
C 13.88234 4.37001 2.12878
C 13.57780 3.03148 1.45388
C 15.01300 5.09804 1.42354
C 11.76957 -0.02690 5.95099
H 11.44341 -1.00963 5.56682
H 10.87822 0.46789 6.37293
C 15.58610 5.38999 6.24340
C 16.03361 4.97481 7.63934
H 15.32684 4.24786 8.08481
H 16.08043 5.85602 8.30283
H 17.03479 4.50772 7.62077
C 16.57219 6.38765 5.64195
H 17.58885 5.95955 5.57365
H 16.62682 7.29515 6.26911
H 16.26241 6.69621 4.62852
C 14.19732 6.00270 6.29918
H 13.46109 5.31492 6.74966
H 13.83713 6.29395 5.29741
H 14.22757 6.91832 6.91641
H 13.08602 -1.20178 8.93891
H 11.97229 -2.03712 7.82346
H 11.45154 -0.54231 8.64674
H 13.72675 -1.98354 6.05855
H 14.37030 -0.42650 5.46115
H 12.13155 0.57194 5.09725
H 14.03493 0.81732 8.25231
H 16.58373 3.84297 5.43028
C 16.65210 -0.50005 3.94964
C 16.81254 0.84328 4.36306
C 16.45252 1.25550 5.67992
C 16.36114 1.55030 6.90415
H 16.79806 1.50147 7.90471
H 9.91515 1.49434 9.39381
H 9.24923 3.01458 10.05788
H 10.95624 2.58453 10.33964
H 9.63692 3.30602 7.66070
H 11.75957 4.81672 9.28811
H 10.03221 5.25644 9.17724
H 11.07130 5.34212 7.72777
H 14.73912 5.30658 0.37409
H 15.93870 4.49653 1.41523
H 15.24830 6.05834 1.91354
H 13.32044 3.18147 0.39049
H 12.73302 2.50947 1.93677
H 14.45696 2.36070 1.49272
H 12.96933 4.99274 2.04692
C 16.99185 -0.89245 2.65866
C 17.50414 0.03359 1.74580
C 17.68708 1.36032 2.14549
C 17.34814 1.76494 3.43230
H 16.86238 -1.94017 2.36406
H 16.27470 -1.24090 4.66220
H 17.77101 -0.27885 0.73022

H 18.10271 2.09216 1.44250
H 17.50031 2.80755 3.72977

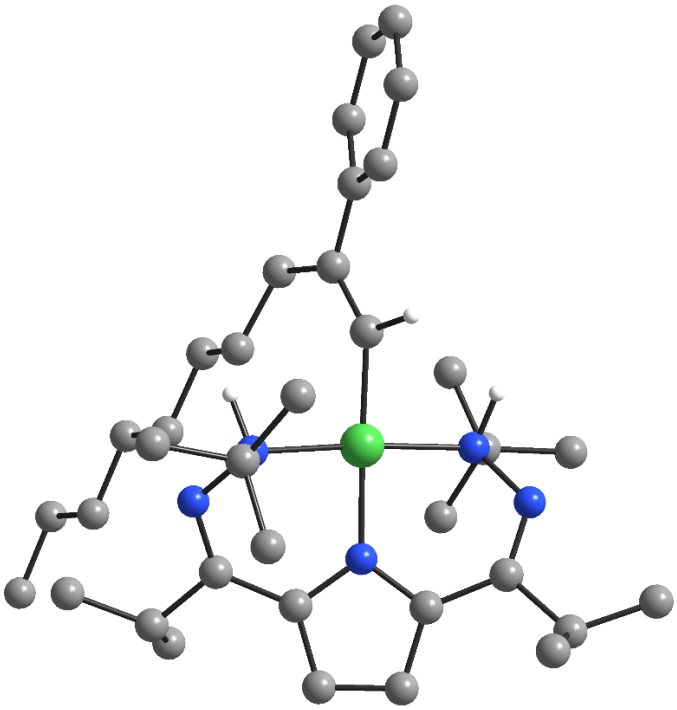

Figure S41. Calculated structure of **2b**. Some H atoms removed for clarity.

Table S29. Coordinates for the calculated structure of **2b**

Ni 15.17447 2.79674 5.10423
N 14.07423 1.20776 5.61114
N 12.89715 1.45521 6.41869
N 13.58109 3.67536 4.58013
N 15.88846 5.10871 3.39448
N 16.14012 4.48119 4.67580
C 12.90435 -0.95033 5.10034
C 15.12351 -0.42232 4.11510
H 15.64241 -0.89680 4.96792
C 13.77976 0.15806 4.52464
C 12.12185 2.44084 6.10105
C 10.86842 2.59689 6.94236
C 10.50927 1.36071 7.74846
C 10.98798 3.82524 7.84554
C 12.34368 3.44434 5.08206
C 11.41754 4.32530 4.47733
H 10.34424 4.37729 4.67576
C 12.13827 5.08628 3.56056
H 11.74831 5.86913 2.90561
C 13.48631 4.67275 3.66684
C 14.65657 5.21596 3.00690

C 14.41155 6.01864 1.74150
C 13.82236 5.15085 0.63073
C 15.62868 6.77708 1.24408
C 13.10743 0.80630 3.32705
H 12.93197 0.03694 2.55419
H 12.12979 1.25028 3.58100
C 16.24985 5.55433 5.77450
C 16.72204 4.85207 7.03751
H 15.97691 4.12549 7.40706
H 16.88702 5.60363 7.82957
H 17.67371 4.31690 6.87353
C 17.28974 6.58457 5.34414
H 18.26416 6.10584 5.13789
H 17.44339 7.32013 6.15286
H 16.97830 7.13528 4.44190
C 14.91240 6.22947 6.02576
H 14.14293 5.51368 6.36490
H 14.53628 6.75939 5.13442
H 15.04480 6.98543 6.81991
H 13.35287 -1.38797 6.00984
H 12.80083 -1.75585 4.35233
H 11.89278 -0.59639 5.35536
H 14.97227 -1.19466 3.34087
H 15.78701 0.35381 3.70542
H 13.74567 1.59416 2.88689
H 14.67122 0.69660 6.26995
C 19.05621 1.23871 7.51737
C 18.92390 0.83234 6.17312
C 17.90592 1.43403 5.26921
C 16.75025 1.95015 5.76566
H 10.45854 0.45807 7.11656
H 9.52798 1.49723 8.23612
H 11.25453 1.16965 8.53963
H 10.04640 2.79206 6.22518
H 11.78317 3.67993 8.60021
H 10.04176 4.00339 8.38621
H 11.22843 4.73834 7.27336
H 15.35210 7.40471 0.37830
H 16.42627 6.08911 0.91320
H 16.05514 7.43434 2.02024
H 13.53241 5.77386 -0.23424
H 12.92879 4.59263 0.95835
H 14.56617 4.41836 0.27220
H 13.63795 6.76378 2.01942
C 20.00585 0.67420 8.36378
C 20.86921 -0.32131 7.89769
C 20.76582 -0.73416 6.56976
C 19.81618 -0.16260 5.72167
H 19.76145 -0.51693 4.68661
H 21.61956 -0.76200 8.56415
H 21.43673 -1.51035 6.18177
H 18.40786 2.03365 7.90351
H 20.08239 1.02632 9.39964
C 18.22076 1.31171 3.79247

C 17.46671 2.21638 2.83679
H 18.05175 0.25581 3.48584
H 19.30780 1.46094 3.63260
C 17.59934 1.81393 1.37841
H 17.82388 3.25941 2.94608
H 16.38830 2.24975 3.10940
C 16.75388 2.67439 0.45616
H 17.30869 0.74968 1.25901
H 18.66497 1.86430 1.07348
C 16.95882 2.40688 -1.02504
H 16.95842 3.74451 0.66868
H 15.68479 2.52543 0.71621
C 16.08531 3.26271 -1.92753
H 16.76873 1.33472 -1.23777
H 18.02521 2.57394 -1.28123
C 16.31757 3.03539 -3.41311
H 16.25139 4.33492 -1.69005
H 15.01760 3.07191 -1.69355
C 15.43279 3.89289 -4.29719
H 14.36186 3.69592 -4.10596
H 15.61713 3.70735 -5.36987
H 15.60395 4.96952 -4.11325
H 16.15360 1.96451 -3.64727
H 17.38276 3.22942 -3.65015
H 16.65720 1.85108 6.86748
H 17.10847 4.15364 4.57609

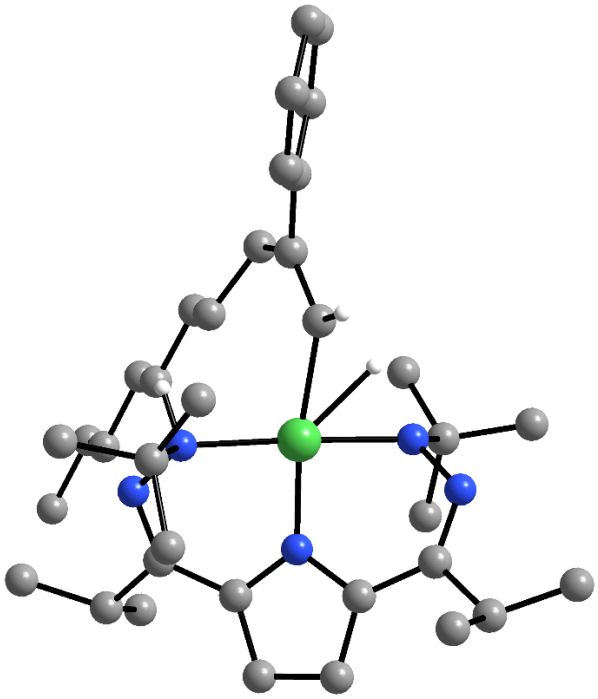

Figure S42. Calculated structure of **TS2**. Some H atoms removed for clarity.

Table S30. Coordinates for the calculated structure of **TS2**

Ni 15.04210 2.80509 4.95427
N 14.00186 1.18478 5.28305
N 12.94871 1.34824 6.20675
N 13.50577 3.73127 4.55521
N 15.75553 5.19638 3.37071
N 16.04086 4.52402 4.62578
C 13.02139 -1.03468 4.82822
C 14.86516 -0.14737 3.43027
H 15.61540 -0.61728 4.09049
C 13.61317 0.23180 4.20366
C 12.19014 2.39996 6.13271
C 11.06126 2.51534 7.13591
C 10.73957 1.20874 7.84036
C 11.36418 3.62509 8.14260
C 12.32984 3.48637 5.17389
C 11.37266 4.40988 4.69434
H 10.32258 4.46658 4.99230
C 12.01662 5.20295 3.74028
H 11.57836 6.02590 3.16988
C 13.36131 4.77243 3.70118
C 14.51361 5.32405 3.01822
C 14.24777 6.12753 1.76035
C 13.78484 5.20845 0.63048
C 15.41514 6.99398 1.32128
C 12.59509 0.86177 3.25193
H 12.29549 0.14243 2.46696
H 11.67897 1.16635 3.78866
C 16.19546 5.54934 5.75738
C 16.66642 4.77290 6.97543
H 15.89893 4.05877 7.32441
H 16.87868 5.47442 7.80096
H 17.59229 4.21046 6.76034
C 17.25188 6.57237 5.35275
H 18.21671 6.08293 5.12744
H 17.42208 7.28318 6.18005
H 16.94449 7.15198 4.46677
C 14.87852 6.24482 6.05627
H 14.09338 5.53498 6.37004
H 14.50990 6.82456 5.19325
H 15.03552 6.96080 6.88211
H 13.71241 -1.46177 5.57667
H 12.85444 -1.79579 4.04469
H 12.05682 -0.84103 5.32563
H 14.61765 -0.86921 2.63226
H 15.31958 0.73325 2.94764
H 13.01680 1.75702 2.75796
H 15.40497 1.20102 5.56469
C 19.05198 1.50384 7.50847
C 18.85439 0.87210 6.26558
C 17.76613 1.26806 5.33869
C 16.57027 1.71825 5.82934
H 10.54724 0.39489 7.12094
H 9.84544 1.32526 8.47794
H 11.57412 0.88601 8.48657

H 10.16567 2.82469 6.55997
H 12.27117 3.38117 8.72725
H 10.53088 3.74789 8.85724
H 11.53114 4.59864 7.64930
H 15.12202 7.61953 0.45973
H 16.28149 6.38449 1.01050
H 15.75619 7.66258 2.13024
H 13.50468 5.79874 -0.26019
H 12.91049 4.59949 0.92006
H 14.59653 4.52056 0.33366
H 13.39829 6.79480 2.00910
C 20.05699 1.08594 8.37751
C 20.88184 0.01104 8.03826
C 20.69698 -0.63313 6.81436
C 19.70742 -0.19919 5.93498
H 19.57445 -0.72850 4.98516
H 21.66668 -0.32381 8.72594
H 21.32825 -1.48616 6.53956
H 18.42144 2.35469 7.79098
H 20.19840 1.60481 9.33268
C 18.05137 1.06180 3.86914
C 17.51686 2.11448 2.91121
H 17.66534 0.06633 3.56534
H 19.14335 0.99081 3.71561
C 17.63516 1.70077 1.45407
H 18.05983 3.06862 3.07029
H 16.45469 2.34469 3.14304
C 16.91945 2.63945 0.49953
H 17.22480 0.67732 1.33059
H 18.70598 1.62265 1.17651
C 17.06194 2.25746 -0.96410
H 17.28981 3.67514 0.64719
H 15.84223 2.66662 0.76928
C 16.32270 3.18290 -1.91520
H 16.70084 1.21865 -1.10897
H 18.13782 2.23599 -1.23394
C 16.48246 2.81487 -3.38171
H 16.66836 4.22606 -1.75728
H 15.24366 3.19012 -1.65678
C 15.75090 3.75355 -4.32079
H 14.66615 3.77085 -4.10842
H 15.87585 3.46111 -5.37800
H 16.11965 4.79074 -4.21934
H 16.12452 1.77751 -3.53652
H 17.56051 2.79556 -3.63863
H 16.53417 1.78107 6.93277
H 17.00328 4.19605 4.47834

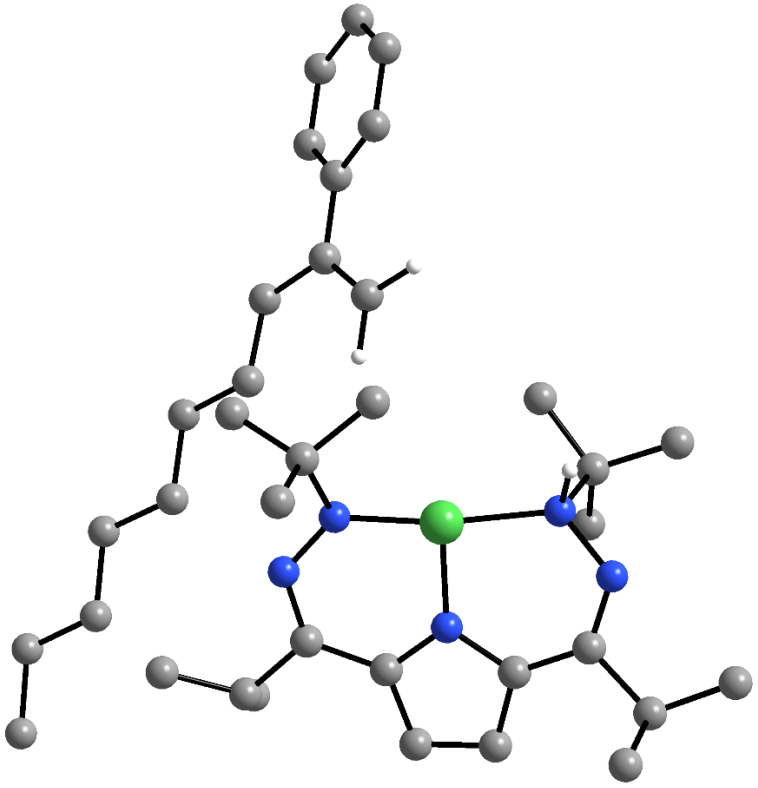

Figure S43. Calculated structure of **2c**. Some H atoms removed for clarity.

Table S31. Coordinates for the calculated structure of **2c**

Ni 15.34560 2.76336 5.07291
N 14.32859 1.64421 6.37864
N 12.91385 1.83422 6.61832
N 13.89324 3.04114 4.01070
N 16.28546 4.12798 2.72985
N 16.50043 3.57097 3.90882
C 14.12738 -0.60218 7.46616
C 16.13896 0.03971 6.13185
H 16.64418 0.52368 6.98817
C 14.62544 0.14916 6.23844
C 12.18486 2.23834 5.62212
C 10.69165 2.29746 5.90715
C 10.26114 1.44595 7.08986
C 10.23529 3.74558 6.07512
C 12.60504 2.66337 4.31032
C 11.80687 2.89657 3.17080
H 10.73158 2.72058 3.09168
C 12.63544 3.41032 2.17729
H 12.34544 3.68837 1.16157
C 13.93813 3.49630 2.72410
C 15.13276 4.03168 2.11820
C 15.05078 4.54053 0.69406
C 15.02770 3.38309 -0.30410

C 16.15867 5.52360 0.35045
C 13.96349 -0.37502 4.97560
H 14.24718 -1.43039 4.82027
H 12.86223 -0.33423 5.04215
C 17.52999 4.26078 4.73316
C 17.57804 3.42170 6.01080
H 16.56374 3.32059 6.48952
H 18.16373 3.91500 6.80520
H 18.00777 2.42050 5.84013
C 18.88488 4.25136 4.04136
H 19.19431 3.22195 3.78974
H 19.65366 4.68496 4.70659
H 18.86347 4.84442 3.11081
C 17.09557 5.68961 5.04450
H 16.14887 5.70235 5.61587
H 16.93889 6.25484 4.10887
H 17.86133 6.21908 5.63957
H 14.56486 -0.18978 8.39334
H 14.42265 -1.66382 7.39977
H 13.02964 -0.56000 7.55544
H 16.44520 -1.02060 6.11533
H 16.51146 0.50415 5.19863
H 14.28069 0.19828 4.08531
H 14.73837 1.88702 7.29038
C 21.74160 -1.10253 5.77798
C 21.53800 -1.12192 4.38412
C 20.46659 -0.31983 3.74209
C 19.42185 0.15570 4.44856
H 10.61165 0.40391 6.99255
H 9.15943 1.43190 7.16534
H 10.65673 1.84036 8.04160
H 10.19055 1.89298 5.00670
H 10.70789 4.20463 6.96312
H 9.14096 3.79629 6.21498
H 10.49310 4.36282 5.19722
H 16.02216 5.91857 -0.67258
H 17.15210 5.04342 0.39382
H 16.17809 6.38086 1.04621
H 14.90170 3.75377 -1.33816
H 14.20691 2.67365 -0.09761
H 15.97763 2.81904 -0.26639
H 14.08397 5.07476 0.59773
C 22.74171 -1.86228 6.37630
C 23.57919 -2.66711 5.59899
C 23.40391 -2.69214 4.21642
C 22.40247 -1.92714 3.61839
H 22.29077 -1.97174 2.53030
H 24.36911 -3.26198 6.07137
H 24.05258 -3.31573 3.58982
H 21.11617 -0.46242 6.41005
H 22.87596 -1.81944 7.46343
C 20.59769 -0.07084 2.26180
C 19.57111 0.85251 1.63284
H 20.57117 -1.04329 1.72999

H 21.61596 0.32082 2.05980
C 19.83790 1.13352 0.16397
H 19.55044 1.81202 2.18473
H 18.55574 0.42183 1.74725
C 18.73843 1.94667 -0.49735
H 19.96427 0.17642 -0.38200
H 20.80784 1.66143 0.06133
C 19.05109 2.37724 -1.92046
H 18.51797 2.84538 0.11803
H 17.80083 1.35382 -0.49132
C 17.90836 3.12055 -2.58910
H 19.31843 1.48629 -2.52571
H 19.95941 3.01433 -1.92029
C 18.20384 3.60076 -3.99996
H 17.61909 3.98912 -1.96202
H 17.01126 2.46812 -2.60860
C 17.04078 4.34796 -4.62338
H 16.13495 3.71494 -4.66549
H 17.26185 4.67956 -5.65296
H 16.77764 5.24620 -4.03360
H 18.47552 2.73185 -4.63245
H 19.10367 4.24788 -3.98852
H 18.63284 0.75637 3.98189
H 19.29379 -0.04708 5.51834

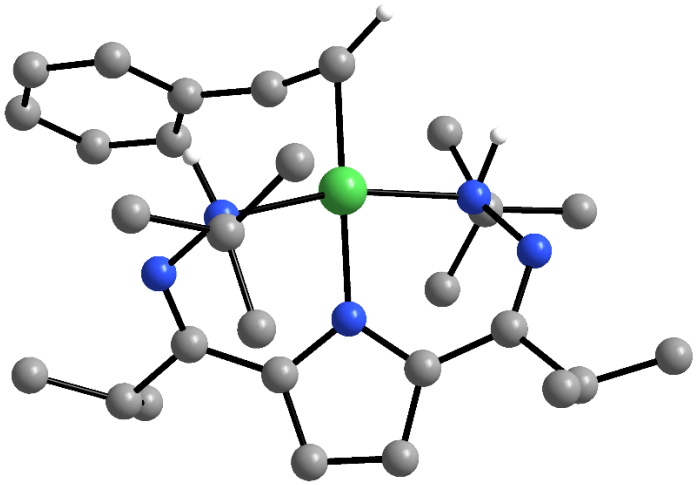

Figure S44. Calculated structure of **TS1**. Some H atoms removed for clarity.

Table S32. Coordinates for the calculated structure of **TS1**
Ni 14.65119 2.16485 6.35133
N 13.33753 1.00881 7.59240
N 12.33614 1.75217 8.32405
N 13.02038 3.01288 5.66787
N 15.25589 4.01709 3.91359
N 15.55778 3.93826 5.32213
C 11.85729 -0.96168 8.04082
C 13.93982 -1.18224 6.69675

H 14.53813 -1.40430 7.60106
C 12.75446 -0.28029 7.01108
C 11.65433 2.65127 7.68816
C 10.58551 3.35204 8.51160
C 10.10966 2.55525 9.71445
C 11.07676 4.73822 8.92778
C 11.83638 3.13885 6.33239
C 10.91755 3.85517 5.53202
H 9.88940 4.12300 5.78953
C 11.57375 4.14303 4.33559
H 11.16861 4.68818 3.47881
C 12.88658 3.64086 4.47032
C 14.01477 3.87240 3.57712
C 13.70747 3.97032 2.09502
C 13.18369 2.63002 1.57416
C 14.87569 4.46251 1.25864
C 11.97540 0.00724 5.73739
H 11.58144 -0.94194 5.33238
H 11.11398 0.67238 5.91520
C 15.63238 5.29514 5.99318
C 16.01098 4.98895 7.43673
H 15.20380 4.43094 7.94872
H 16.19160 5.92384 7.99716
H 16.93248 4.37981 7.48659
C 16.71914 6.13157 5.32248
H 17.69604 5.61435 5.35784
H 16.83634 7.10475 5.83143
H 16.47613 6.33050 4.26423
C 14.30302 6.02858 5.94124
H 13.49536 5.46962 6.44559
H 13.98967 6.23501 4.90297
H 14.41256 7.00263 6.45077
H 12.38616 -1.10747 8.99930
H 11.55207 -1.95562 7.67072
H 10.94277 -0.38235 8.24343
H 13.57634 -2.14402 6.29400
H 14.61026 -0.73096 5.94665
H 12.61731 0.47126 4.96710
H 13.93729 0.66795 8.35163
H 16.54173 3.64783 5.30984
C 16.26360 0.46935 3.43653
C 16.92624 1.18885 4.45217
C 16.41144 1.25512 5.78140
C 16.26328 1.33205 7.03654
H 16.55842 1.02344 8.04221
H 9.76159 1.54836 9.42526
H 9.27132 3.07630 10.21197
H 10.91088 2.42611 10.46202
H 9.71683 3.49857 7.84168
H 11.93480 4.65708 9.62009
H 10.27764 5.29507 9.44850
H 11.39686 5.34009 8.05978
H 14.56932 4.56852 0.20318
H 15.72537 3.75784 1.29528

H 15.24814 5.44084 1.60918
H 12.87824 2.71198 0.51610
H 12.31068 2.27792 2.15068
H 13.96728 1.85187 1.63893
H 12.88344 4.70631 1.99459
C 16.77248 0.44663 2.14206
C 17.93273 1.15639 1.82137
C 18.58771 1.88699 2.81241
C 18.10152 1.89731 4.11617
H 16.25151 -0.12616 1.36743
H 15.33936 -0.06940 3.67765
H 18.32232 1.14111 0.79732
H 19.49283 2.45466 2.56861
H 18.62361 2.46403 4.89562

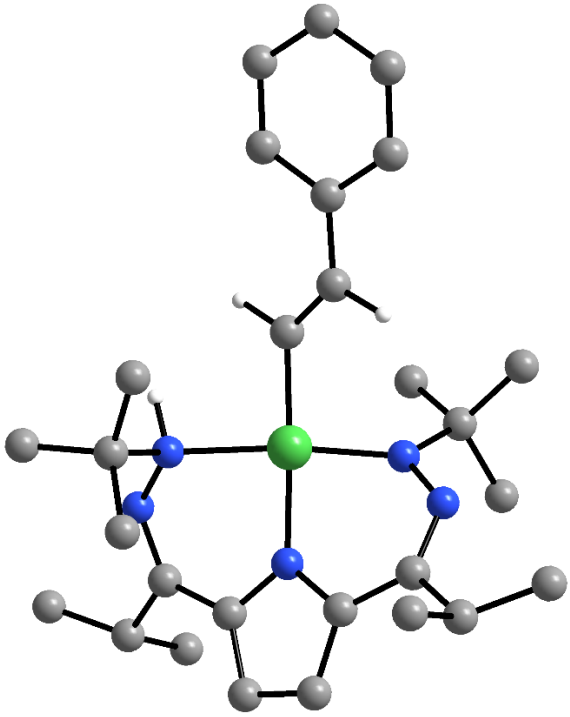

Figure S45. Calculated structure of **3a**. Some H atoms removed for clarity.

Table S33. Coordinates for the calculated structure of **3a**
Ni 14.42238 2.82510 6.13732
N 13.44525 1.37498 7.13525
N 12.38574 1.79364 8.02991
N 12.71163 3.52839 5.68078
N 14.76044 4.72775 4.10817
N 15.14969 4.34061 5.30361
C 12.46981 -0.90858 7.39769
C 14.28003 -0.48379 5.74395
H 15.07757 -0.65953 6.48765
C 13.02730 0.09048 6.38617
C 11.50692 2.63691 7.59398

C 10.36674 2.96979 8.53536
C 10.16454 1.94879 9.64150
C 10.55843 4.37494 9.10714
C 11.53888 3.33549 6.32485
C 10.48217 3.87029 5.54846
H 9.42068 3.87047 5.80878
C 11.05761 4.36079 4.37974
H 10.54527 4.84963 3.54725
C 12.45590 4.15364 4.50128
C 13.53611 4.56716 3.65465
C 13.26920 4.89268 2.20715
C 12.97953 3.60332 1.43432
C 14.38709 5.68519 1.55249
C 11.99624 0.39748 5.31477
H 11.76334 -0.53468 4.77047
H 11.04804 0.77394 5.73356
C 16.06063 5.35669 5.93989
C 16.33843 4.95322 7.37944
H 15.39864 4.76042 7.92852
H 16.86800 5.77540 7.89285
H 16.96305 4.04975 7.44259
C 17.35791 5.46125 5.14497
H 17.91881 4.51077 5.16459
H 18.00259 6.24436 5.58252
H 17.15637 5.73035 4.09385
C 15.31660 6.69385 5.93288
H 14.33308 6.59709 6.42870
H 15.14974 7.06327 4.90732
H 15.90029 7.45565 6.47837
H 13.18858 -1.08745 8.21703
H 12.28437 -1.87418 6.89616
H 11.52094 -0.56505 7.83901
H 14.03529 -1.45366 5.27736
H 14.68023 0.18313 4.96279
H 12.37411 1.13248 4.58142
H 14.15044 1.03367 7.79838
C 18.57959 0.15701 6.67387
C 18.34071 1.09736 5.65022
C 17.10113 1.87307 5.53961
C 16.08936 1.96374 6.43249
H 10.02419 0.93155 9.23837
H 9.27332 2.20737 10.24000
H 11.03122 1.91997 10.32386
H 9.45236 2.98847 7.90903
H 11.45780 4.41153 9.74920
H 9.69067 4.66384 9.72570
H 10.67759 5.13436 8.31491
H 14.11769 5.94144 0.51297
H 15.32330 5.10069 1.52231
H 14.60000 6.62314 2.09333
H 12.71902 3.82667 0.38461
H 12.14252 3.03907 1.88135
H 13.86767 2.94456 1.42940
H 12.34543 5.50527 2.18487

C 19.76668 -0.56774 6.72315
C 20.75577 -0.37951 5.75171
C 20.53985 0.54788 4.73050
C 19.35016 1.27180 4.68154
H 19.18770 2.00031 3.87606
H 21.68487 -0.95979 5.78669
H 21.30537 0.70471 3.96105
H 17.81276 -0.01467 7.43917
H 19.92072 -1.30101 7.52401
H 17.02058 2.43241 4.59189
H 16.21129 1.40649 7.38539

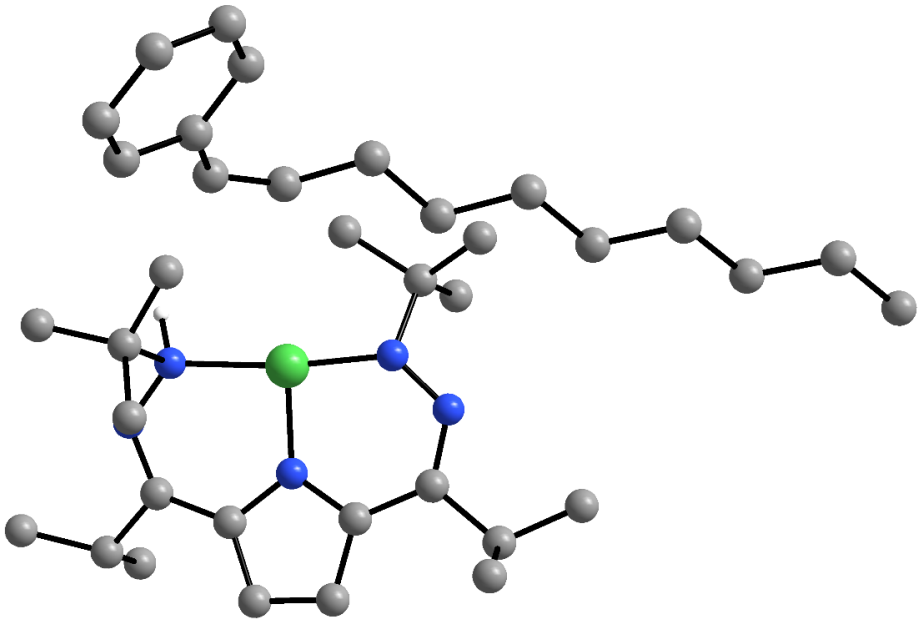

Figure S46. Calculated structure of **3b**. Some H atoms removed for clarity.

Table S34. Coordinates for the calculated structure of **3b**

Ni 14.62019 3.60258 6.51355
N 13.82216 2.24596 7.73684
N 12.39183 2.10001 7.89574
N 13.20171 3.57096 5.37247
N 15.37181 5.17173 4.23577
N 15.62786 4.66734 5.42625
C 14.03373 -0.02361 8.76768
C 15.96401 1.09887 7.64328
H 16.26913 1.62477 8.56616
C 14.46241 0.86162 7.60470
C 11.63779 2.36289 6.87082
C 10.15810 2.08809 7.09511
C 9.89179 1.01838 8.14278
C 9.43132 3.38776 7.43308
C 12.01156 2.91544 5.59372
C 11.24509 2.99673 4.41129
H 10.24238 2.58873 4.26440

C 11.99561 3.70008 3.47362
H 11.70936 3.93209 2.44528
C 13.21740 4.05298 4.09525
C 14.30286 4.83700 3.55758
C 14.20590 5.31760 2.12488
C 14.48043 4.17849 1.14125
C 15.10984 6.50520 1.83421
C 14.05369 0.24839 6.27707
H 14.55268 -0.72837 6.15026
H 12.96500 0.07239 6.22672
C 16.48729 5.52191 6.28954
C 16.57463 4.72128 7.58927
H 15.55459 4.51715 8.01751
H 17.07504 5.28195 8.39660
H 17.12074 3.77329 7.45070
C 17.86816 5.68672 5.67120
H 18.32857 4.70384 5.46937
H 18.53174 6.24748 6.35425
H 17.81267 6.24196 4.71949
C 15.83302 6.87743 6.52937
H 14.84067 6.75984 7.00276
H 15.69255 7.40883 5.57159
H 16.45563 7.51200 7.18584
H 14.24996 0.45859 9.73814
H 14.58985 -0.97671 8.73598
H 12.95673 -0.25395 8.73186
H 16.50465 0.13775 7.60382
H 16.29360 1.69920 6.77316
H 14.34323 0.89197 5.42605
H 14.11327 2.55857 8.67305
C 22.02827 -1.66590 5.41348
C 20.66163 -1.99743 5.50266
C 19.60302 -1.00943 5.72688
C 19.58117 0.29979 5.40441
H 10.44283 0.08774 7.92076
H 8.81417 0.77882 8.17539
H 10.19407 1.34838 9.15128
H 9.75452 1.71766 6.13436
H 9.80241 3.79996 8.38971
H 8.34599 3.21385 7.54068
H 9.57510 4.15651 6.65370
H 14.92303 6.89406 0.81750
H 16.17632 6.22379 1.89222
H 14.94931 7.32790 2.55241
H 14.37087 4.52163 0.09651
H 13.78939 3.33007 1.28840
H 15.51104 3.79587 1.26250
H 13.15869 5.64468 1.96351
C 20.60043 1.11136 4.67230
C 19.97583 2.26007 3.89176
C 20.98338 3.10247 3.13030
H 19.40466 2.90264 4.59170
H 19.22317 1.85656 3.18415
C 20.36975 4.30333 2.42959

H 21.50551 2.46658 2.38658
H 21.77418 3.45060 3.82625
C 21.35754 5.08920 1.58411
H 19.91596 4.97554 3.18618
H 19.52656 3.96885 1.79059
C 20.76125 6.31877 0.92065
H 21.78189 4.42079 0.80691
H 22.22114 5.39152 2.21196
C 21.74351 7.08592 0.05019
H 20.35412 6.99807 1.69808
H 19.88536 6.02008 0.30789
C 21.13766 8.30989 -0.60765
H 20.75379 9.02394 0.14433
H 20.28586 8.03687 -1.25746
H 21.87021 8.85078 -1.23172
H 22.14818 6.40533 -0.72554
H 22.61838 7.38346 0.66258
C 20.31261 -3.35944 5.40703
C 22.99365 -2.65061 5.20814
C 22.62404 -3.99137 5.08973
C 21.27628 -4.34222 5.19551
H 24.05116 -2.36674 5.15371
H 22.34907 -0.62810 5.54670
H 20.97398 -5.39324 5.12002
H 23.38638 -4.76295 4.93235
H 19.25636 -3.64316 5.49551
H 21.34029 1.52972 5.38858
H 21.19539 0.47069 3.99153
H 18.67322 0.85572 5.68558
H 18.69500 -1.41663 6.19580

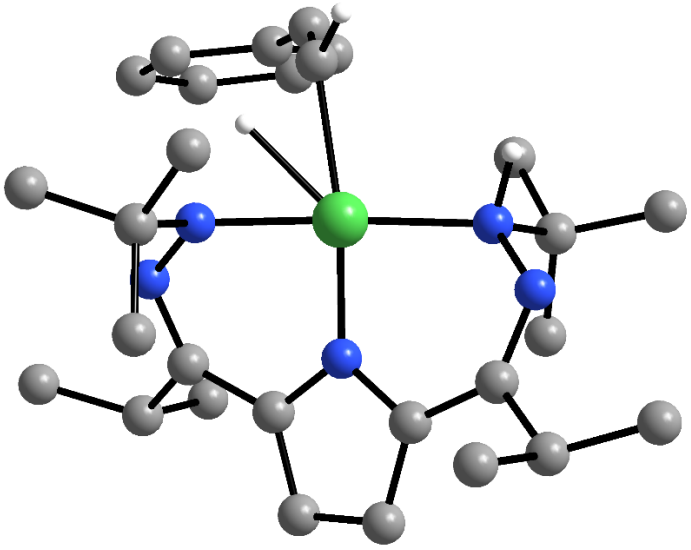

Figure S47. Calculated structure of **TS1′**. Some H atoms removed for clarity.

Table S35. Coordinates for the calculated structure of **TS1′**

Ni 13.84897 3.32059 5.43001
N 13.35777 1.50211 6.21120
N 12.68302 1.42019 7.48723
N 12.16705 4.01682 6.03434
N 13.33634 5.74528 3.97619
N 14.04810 4.63644 4.10267
C 12.65310 -0.84759 5.77839
C 13.65802 0.58945 3.99060
H 14.69223 0.31168 4.26678
C 12.72835 0.55738 5.19478
C 11.82043 2.33604 7.80137
C 11.19856 2.17001 9.17703
C 11.29128 0.75936 9.73256
C 11.83820 3.17888 10.13310
C 11.42928 3.51638 7.06064
C 10.34399 4.39124 7.30938
H 9.56999 4.26602 8.07046
C 10.45098 5.44408 6.40732
H 9.77161 6.29379 6.31133
C 11.61034 5.19326 5.63015
C 12.20871 5.99548 4.60188
C 11.46483 7.24088 4.15791
C 10.29500 6.86526 3.24630
C 12.35558 8.27345 3.48698
C 11.34670 1.06292 4.81644
H 10.90417 0.38663 4.06468
H 10.66788 1.08498 5.68655
C 15.37167 4.79333 3.40099
C 16.06670 3.44067 3.42134
H 16.16891 3.03784 4.44661
H 17.08692 3.52722 3.00892
H 15.52108 2.69906 2.81360
C 15.11723 5.19222 1.94846
H 14.42153 4.48377 1.46427
H 16.06565 5.17693 1.38236
H 14.68688 6.20359 1.87049
C 16.21077 5.85224 4.10469
H 16.42257 5.56125 5.14878
H 15.67626 6.81870 4.12173
H 17.17396 6.00103 3.58386
H 13.65028 -1.20118 6.09763
H 12.27020 -1.55129 5.01898
H 11.97995 -0.88737 6.65072
H 13.30775 -0.11726 3.21934
H 13.68293 1.59536 3.52815
H 11.39025 2.07770 4.38169
H 14.26821 1.06859 6.42365
C 15.91783 1.73464 8.04740
C 16.16768 2.84809 7.21869
C 15.09392 3.79591 6.88966
H 10.89333 0.01235 9.02417
H 10.71347 0.68763 10.67084
H 12.33483 0.48115 9.95968
H 10.12686 2.42811 9.08081

H 12.92454 2.98958 10.22382
H 11.39561 3.09584 11.14161
H 11.70624 4.21843 9.78581
H 11.77966 9.18919 3.26397
H 12.76112 7.89429 2.53275
H 13.21518 8.55405 4.12039
H 9.69904 7.75709 2.98113
H 9.61587 6.13521 3.72036
H 10.66498 6.41924 2.30432
H 11.03713 7.70073 5.07052
C 16.92853 0.82611 8.35627
C 18.21494 1.00025 7.84211
C 18.48341 2.10418 7.02943
C 17.47549 3.01506 6.72034
H 17.70601 3.88182 6.08928
H 19.00740 0.27968 8.07328
H 19.49240 2.25812 6.62933
H 14.91327 1.59863 8.47093
H 16.70556 -0.02696 9.00794
C 14.84235 4.91981 7.57231
H 15.44589 5.20854 8.45117
H 14.02791 5.60779 7.29965

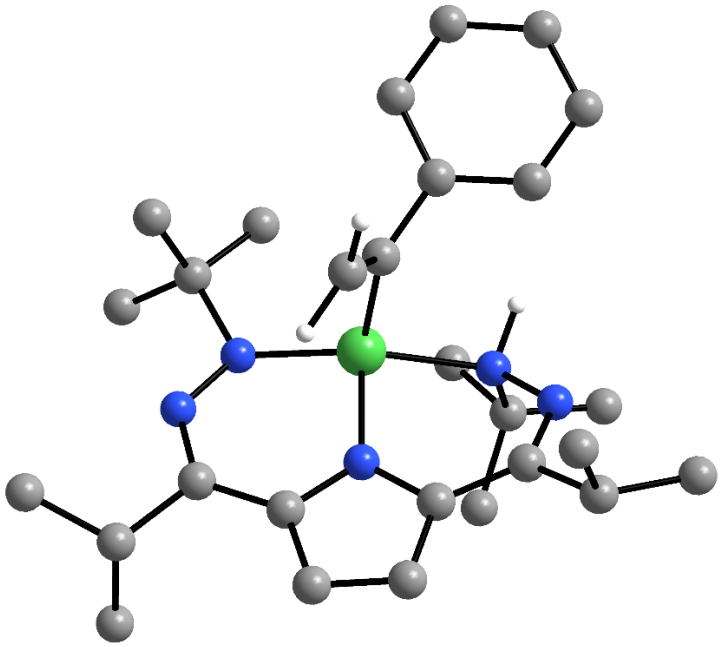

Figure S48. Calculated structure of **4a**. Some H atoms removed for clarity.

Table S36. Coordinates for the calculated structure of **4a**
Ni 13.84897 3.32059 5.43001
N 13.35777 1.50211 6.21120
N 12.68302 1.42019 7.48723
N 12.16705 4.01682 6.03434
N 13.33634 5.74528 3.97619

N 14.04810 4.63644 4.10267
C 12.65310 -0.84759 5.77839
C 13.65802 0.58945 3.99060
H 14.69223 0.31168 4.26678
C 12.72835 0.55738 5.19478
C 11.82043 2.33604 7.80137
C 11.19856 2.17001 9.17703
C 11.29128 0.75936 9.73256
C 11.83820 3.17888 10.13310
C 11.42928 3.51638 7.06064
C 10.34399 4.39124 7.30938
H 9.56999 4.26602 8.07046
C 10.45098 5.44408 6.40732
H 9.77161 6.29379 6.31133
C 11.61034 5.19326 5.63015
C 12.20871 5.99548 4.60188
C 11.46483 7.24088 4.15791
C 10.29500 6.86526 3.24630
C 12.35558 8.27345 3.48698
C 11.34670 1.06292 4.81644
H 10.90417 0.38663 4.06468
H 10.66788 1.08498 5.68655
C 15.37167 4.79333 3.40099
C 16.06670 3.44067 3.42134
H 16.16891 3.03784 4.44661
H 17.08692 3.52722 3.00892
H 15.52108 2.69906 2.81360
C 15.11723 5.19222 1.94846
H 14.42153 4.48377 1.46427
H 16.06565 5.17693 1.38236
H 14.68688 6.20359 1.87049
C 16.21077 5.85224 4.10469
H 16.42257 5.56125 5.14878
H 15.67626 6.81870 4.12173
H 17.17396 6.00103 3.58386
H 13.65028 -1.20118 6.09763
H 12.27020 -1.55129 5.01898
H 11.97995 -0.88737 6.65072
H 13.30775 -0.11726 3.21934
H 13.68293 1.59536 3.52815
H 11.39025 2.07770 4.38169
H 14.26821 1.06859 6.42365
C 15.91783 1.73464 8.04740
C 16.16768 2.84809 7.21869
C 15.09392 3.79591 6.88966
H 10.89333 0.01235 9.02417
H 10.71347 0.68763 10.67084
H 12.33483 0.48115 9.95968
H 10.12686 2.42811 9.08081
H 12.92454 2.98958 10.22382
H 11.39561 3.09584 11.14161
H 11.70624 4.21843 9.78581
H 11.77966 9.18919 3.26397
H 12.76112 7.89429 2.53275

H 13.21518 8.55405 4.12039
H 9.69904 7.75709 2.98113
H 9.61587 6.13521 3.72036
H 10.66498 6.41924 2.30432
H 11.03713 7.70073 5.07052
C 16.92853 0.82611 8.35627
C 18.21494 1.00025 7.84211
C 18.48341 2.10418 7.02943
C 17.47549 3.01506 6.72034
H 17.70601 3.88182 6.08928
H 19.00740 0.27968 8.07328
H 19.49240 2.25812 6.62933
H 14.91327 1.59863 8.47093
H 16.70556 -0.02696 9.00794
C 14.84235 4.91981 7.57231
H 15.44589 5.20854 8.45117
H 14.02791 5.60779 7.29965

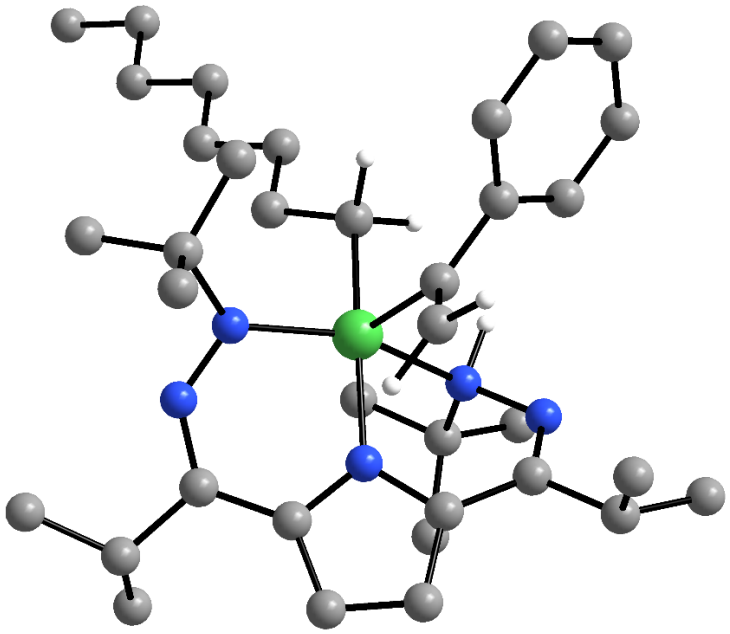

Figure S49. Calculated structure of **4b**. Some H atoms removed for clarity.

Table S37. Coordinates for the calculated structure of **4b**

Ni 14.20503 3.12495 5.26998
N 13.11599 1.37480 5.87108
N 12.75048 1.34658 7.26440
N 12.54221 3.96255 5.88289
N 13.61254 5.41551 3.69890
N 14.59438 4.68182 4.15362
C 11.90130 -0.72433 5.35934
C 12.50159 0.90928 3.55986
H 13.47969 0.42311 3.39948
C 12.02112 0.75217 4.99088

C 12.17159 2.40175 7.74335
C 11.75230 2.32788 9.19653
C 11.71796 0.91510 9.75218
C 12.64772 3.23097 10.04427
C 11.86698 3.61112 7.00892
C 10.76128 4.47335 7.17938
H 10.02505 4.42612 7.98628
C 10.75422 5.34157 6.08804
H 10.03426 6.13630 5.87868
C 11.88557 5.00165 5.31030
C 12.38253 5.56532 4.08697
C 11.45628 6.37682 3.20972
C 10.36643 5.48229 2.61759
C 12.18750 7.14595 2.12347
C 10.67246 1.43430 5.15415
H 9.94232 0.90740 4.51491
H 10.29702 1.37894 6.18967
C 15.86630 5.52886 4.05548
C 17.09294 4.77695 4.53203
H 16.94368 4.35031 5.53441
H 17.93684 5.48622 4.59220
H 17.39624 3.97155 3.84593
C 16.05715 5.93803 2.59438
H 16.07295 5.05704 1.92906
H 17.02283 6.46242 2.48298
H 15.25499 6.61156 2.25211
C 15.68106 6.77065 4.92533
H 15.57964 6.49544 5.98978
H 14.79026 7.35056 4.62744
H 16.55993 7.43298 4.83157
H 12.86785 -1.24669 5.23864
H 11.16699 -1.22229 4.70242
H 11.56607 -0.85306 6.40271
H 11.77879 0.44899 2.86377
H 12.58947 1.97909 3.28788
H 10.68934 2.49084 4.83712
H 13.85832 0.66839 5.82905
C 16.01872 1.08924 7.64527
C 16.25686 2.46180 7.44064
C 15.20878 3.38874 6.98409
H 11.09393 0.24647 9.13407
H 11.30633 0.92075 10.77691
H 12.72952 0.47580 9.80172
H 10.72509 2.74075 9.24714
H 13.69338 2.87038 10.02633
H 12.30945 3.23718 11.09595
H 12.64802 4.27256 9.67767
H 11.47757 7.75951 1.54159
H 12.69282 6.46090 1.41990
H 12.95716 7.81739 2.54132
H 9.64087 6.07879 2.03664
H 9.80916 4.94194 3.40278
H 10.80384 4.72954 1.93510
H 10.95562 7.10946 3.87566

C 17.02381 0.24144 8.10568
C 18.30514 0.73524 8.36075
C 18.56257 2.09333 8.16835
C 17.55259 2.94300 7.71855
H 17.76251 4.01066 7.58190
H 19.09701 0.06452 8.71339
H 19.56083 2.49972 8.36978
H 15.01307 0.68800 7.48070
H 16.80304 -0.81960 8.27173
C 15.63675 2.00342 4.49206
C 15.66371 2.06794 2.97802
C 16.34186 0.86249 2.33032
C 16.28227 0.89223 0.81185
H 15.86949 -0.07120 2.69969
H 17.39816 0.81075 2.66513
C 16.99363 -0.26777 0.13504
H 16.70771 1.84885 0.44453
H 15.21885 0.90551 0.49432
C 16.89110 -0.24034 -1.38065
H 16.58313 -1.22570 0.51567
H 18.06256 -0.26851 0.43238
C 17.60649 -1.38871 -2.07496
H 17.29298 0.72263 -1.75848
H 15.82123 -0.24477 -1.67553
C 17.48674 -1.34051 -3.58559
H 16.42968 -1.38579 -3.90658
H 18.01565 -2.17787 -4.07380
H 17.90757 -0.40213 -3.99155
H 17.20636 -2.35087 -1.69693
H 18.67605 -1.38186 -1.78379
C 14.91337 4.48638 7.69734
H 15.40239 4.67206 8.67105
H 16.18118 2.98753 2.65022
H 16.62694 2.22468 4.92280
H 15.38377 0.97723 4.82890
H 14.64724 2.16415 2.55167
H 14.16659 5.23001 7.39164

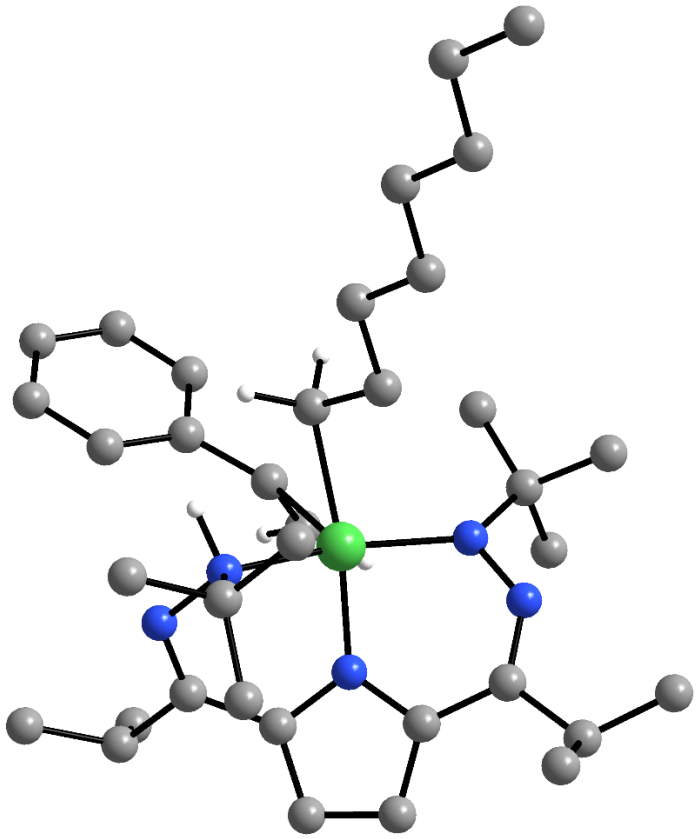

Figure S50. Calculated structure of **TS3′**. Some H atoms removed for clarity.

Table S38. Coordinates for the calculated structure of **TS3′**

Ni 14.15914 3.24774 5.19964
N 13.21619 1.47835 5.76474
N 12.87168 1.43009 7.16716
N 12.54188 4.03570 5.78773
N 13.50683 5.50270 3.55566
N 14.52975 4.85274 4.08607
C 12.07861 -0.68190 5.34132
C 12.57046 0.89496 3.46850
H 13.56895 0.45173 3.30680
C 12.13333 0.78393 4.91804
C 12.26395 2.46515 7.66009
C 11.90469 2.38350 9.12829
C 11.87223 0.96607 9.67250
C 12.86879 3.26058 9.92781
C 11.89572 3.65208 6.93216
C 10.72259 4.42203 7.06593
H 9.98781 4.33895 7.87153
C 10.64598 5.24565 5.94000
H 9.85287 5.95582 5.69292
C 11.80357 4.98192 5.17183
C 12.26961 5.56730 3.93878

C 11.28277 6.30283 3.05833
C 10.24508 5.33700 2.48380
C 11.94990 7.10734 1.95649
C 10.76651 1.42584 5.08794
H 10.04501 0.86892 4.46443
H 10.40641 1.37491 6.12887
C 15.73877 5.78013 3.92097
C 17.06226 5.17641 4.37403
H 17.06084 4.84313 5.42129
H 17.83476 5.96064 4.28571
H 17.39902 4.34252 3.73940
C 15.87763 6.12099 2.43247
H 15.92002 5.20371 1.81762
H 16.81301 6.68441 2.26393
H 15.03481 6.73218 2.07292
C 15.48993 7.06598 4.71152
H 15.43370 6.87815 5.79866
H 14.54588 7.54432 4.39878
H 16.30576 7.79283 4.54524
H 13.06384 -1.17007 5.22561
H 11.35830 -1.23232 4.71155
H 11.76120 -0.78874 6.39209
H 11.85940 0.34846 2.82488
H 12.58484 1.94972 3.13477
H 10.75042 2.47920 4.75802
H 13.99459 0.80953 5.70996
C 15.85200 0.63384 7.76530
C 16.40926 1.84660 7.32952
C 15.69996 2.90127 6.54444
H 11.21206 0.31393 9.07429
H 11.50699 0.96429 10.71468
H 12.87810 0.51098 9.66889
H 10.89270 2.82135 9.23602
H 13.90216 2.87278 9.85148
H 12.59217 3.27216 10.99714
H 12.87240 4.30380 9.56537
H 11.19528 7.67497 1.38321
H 12.48708 6.45073 1.24919
H 12.68671 7.82364 2.36022
H 9.47434 5.87691 1.90435
H 9.72942 4.77352 3.28186
H 10.72126 4.60219 1.80742
H 10.73404 7.01206 3.71331
C 16.60511 -0.26811 8.51812
C 17.93463 0.00818 8.84028
C 18.50806 1.20230 8.40245
C 17.75382 2.10541 7.65598
H 18.20815 3.04019 7.30318
H 18.52214 -0.70466 9.42997
H 19.55240 1.43494 8.64186
H 14.80166 0.40388 7.55785
H 16.14151 -1.19982 8.86286
C 16.00618 2.21659 4.82299
C 15.72316 2.28873 3.30503

C 16.38485 1.09607 2.62088
C 16.22345 1.11362 1.10990
H 15.96782 0.15242 3.02762
H 17.46308 1.07931 2.88031
C 16.90021 -0.05601 0.41307
H 16.62695 2.06574 0.70878
H 15.14345 1.12134 0.85528
C 16.75486 -0.03538 -1.09882
H 16.49245 -1.00840 0.80982
H 17.97739 -0.06567 0.67830
C 17.44368 -1.19535 -1.80134
H 17.15574 0.92144 -1.49264
H 15.67780 -0.03277 -1.36584
C 17.29612 -1.15527 -3.30965
H 16.23326 -1.19502 -3.61157
H 17.81095 -1.99950 -3.80111
H 17.71688 -0.22262 -3.72850
H 17.04138 -2.15136 -1.41024
H 18.51863 -1.19782 -1.53085
C 15.62857 4.11668 7.13211
H 15.97017 4.22439 8.17429
H 16.11475 3.22357 2.87977
H 17.07514 2.45845 4.94973
H 15.90135 1.15776 5.11341
H 14.65091 2.30054 3.05377
H 15.21667 5.01652 6.66699

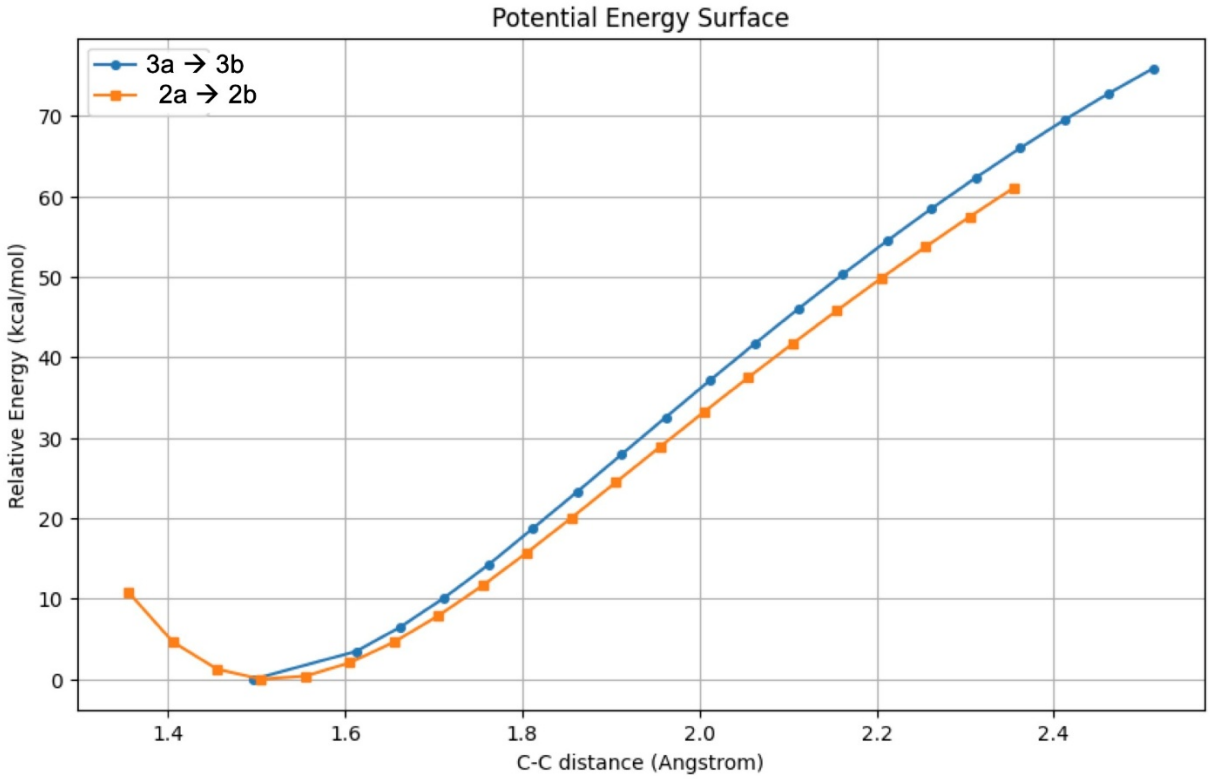

Figure S51. Constrained reaction coordinate scans over the C-C bond forming alkyl radical addition to intermediates **3a** (blue) and **2a** (orange). No local maximum was detected, supporting a computed barrierless addition. Other reorganization energies not well accounted for using DFT likely means there is a very small transition state barrier experimentally.

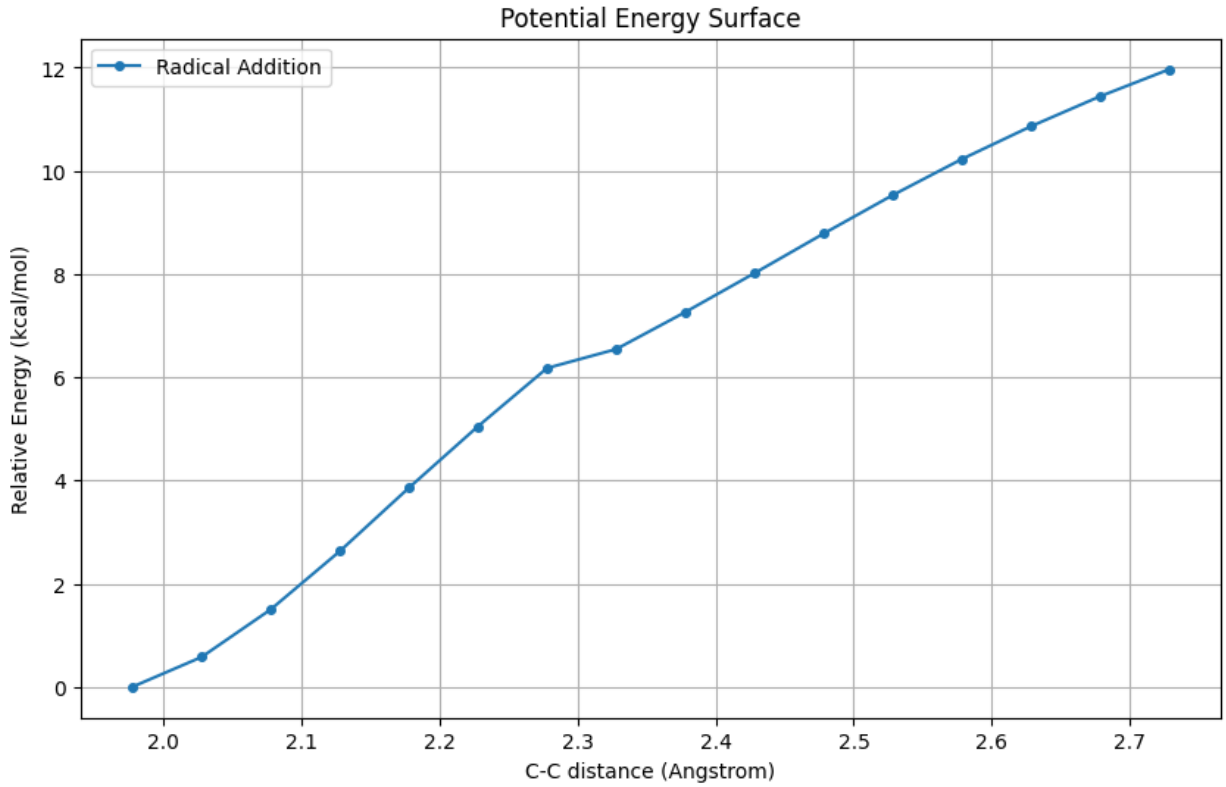

Figure S52. Constrained reaction coordinate scans over the C-C bond forming alkyl radical addition to intermediate **4a** to form the Ni-octyl adduct. No *significant* local maximum was detected, supporting a computed barrierless addition. Other reorganization energies not well accounted for using DFT likely means there is a very small transition state barrier experimentally.

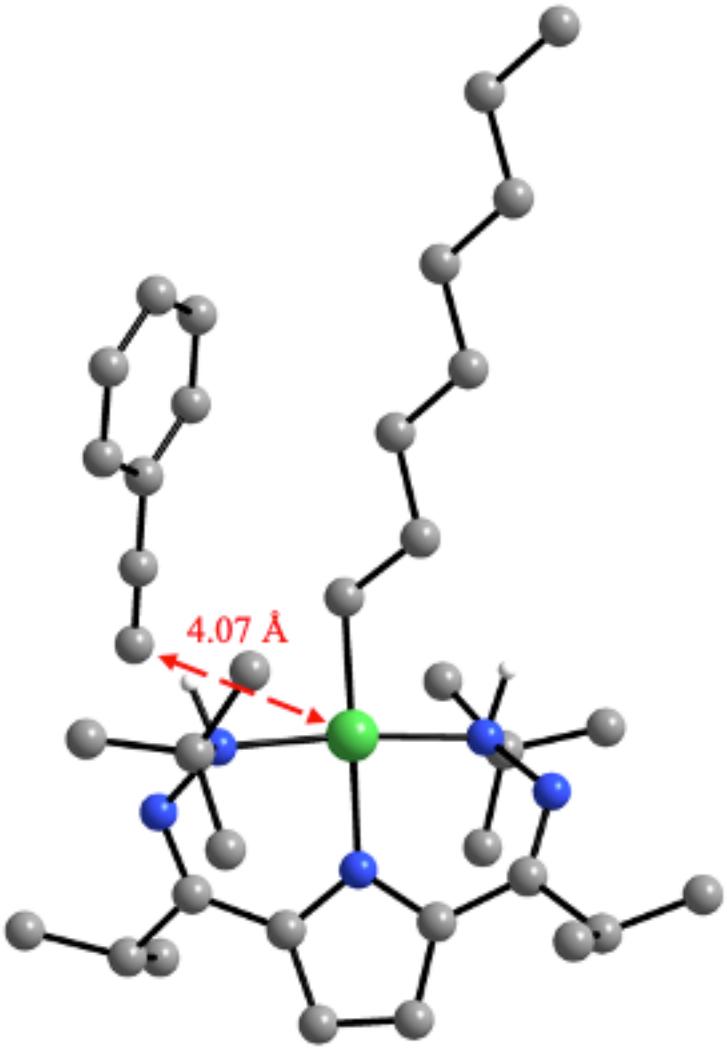

Figure S53. Calculated structure of ($DHPH_2$)Ni-octyl phenylacetylene adduct (phenylacetylene disassociates from Ni center). Some H atoms removed for clarity.

Table S39. Coordinates for the calculated structure of ($DHPH_2$)Ni-octyl phenylacetylene adduct

Ni 13.79618 3.17478 4.98022
N 13.08767 1.66102 6.06031
N 12.85881 1.89642 7.47009
N 12.41553 4.24201 5.73281
N 13.35555 5.48533 3.22596
N 14.37580 4.78524 3.98400
C 11.79375 -0.45008 6.32017
C 12.36199 0.43721 4.05503
H 13.26669 -0.19671 4.03510
C 11.95257 0.80865 5.47240
C 12.28152 2.99887 7.82477
C 12.07412 3.18196 9.31499

C 12.10927 1.88378 10.10255
C 13.10641 4.17925 9.84427
C 11.87212 4.09050 6.96350
C 10.88956 5.08801 7.17023
H 10.27538 5.22319 8.06400
C 10.83021 5.83257 5.99233
H 10.17736 6.68431 5.78504
C 11.81175 5.29308 5.12838
C 12.22505 5.72831 3.80931
C 11.20947 6.50600 2.99417
C 10.09515 5.56842 2.53008
C 11.81119 7.26466 1.82443
C 10.64471 1.58193 5.44245
H 9.85882 0.92506 5.02971
H 10.31828 1.88597 6.45131
C 15.32051 5.78256 4.67591
C 16.46080 4.96426 5.25969
H 16.09839 4.25690 6.02833
H 17.19661 5.64206 5.72694
H 16.98548 4.38525 4.47912
C 15.85903 6.74958 3.62516
H 16.35679 6.20960 2.79916
H 16.60549 7.42266 4.08165
H 15.05941 7.37455 3.19502
C 14.61753 6.55148 5.78169
H 14.23898 5.88698 6.57769
H 13.77861 7.15803 5.40132
H 15.34224 7.24954 6.23694
H 12.75040 -0.99519 6.41186
H 11.06291 -1.13159 5.85069
H 11.43642 -0.21495 7.33631
H 11.54588 -0.12768 3.57154
H 12.56219 1.34106 3.45059
H 10.70310 2.48183 4.80547
H 13.88635 1.01221 6.08807
C 16.11245 -1.53406 5.60287
C 16.90014 -0.44307 6.01996
C 16.40618 0.46878 6.99937
C 15.97672 1.25198 7.82760
H 11.38438 1.14895 9.71103
H 11.86936 2.07432 11.16350
H 13.10805 1.41574 10.06051
H 11.07296 3.63855 9.44409
H 14.12874 3.76865 9.74155
H 12.93377 4.39175 10.91411
H 13.07184 5.13753 9.29653
H 11.03939 7.88231 1.33246
H 12.22317 6.57534 1.06733
H 12.63161 7.92958 2.14455
H 9.30808 6.12959 1.99595
H 9.61780 5.04068 3.37436
H 10.49354 4.80642 1.83447
H 10.75781 7.24261 3.68801
C 16.58696 -2.41589 4.63627

C 17.85036 -2.22622 4.07024
C 18.63746 -1.14610 4.47476
C 18.17121 -0.26013 5.44244
H 18.78547 0.59237 5.75294
H 18.22497 -2.92452 3.31302
H 19.62690 -0.99196 4.02905
H 15.11962 -1.67731 6.04460
H 15.96603 -3.26345 4.32497
C 15.21092 2.05179 4.20863
C 15.40238 2.03488 2.69777
C 16.35118 0.93548 2.23027
H 15.79702 3.00601 2.32399
H 14.42765 1.90206 2.18105
C 16.53994 0.84536 0.72542
H 15.97790 -0.03835 2.61513
H 17.33806 1.07741 2.71849
C 17.47117 -0.27582 0.29321
H 16.92576 1.81270 0.34193
H 15.55167 0.70986 0.23919
C 17.66031 -0.37522 -1.21134
H 17.08338 -1.24202 0.67826
H 18.45976 -0.14280 0.78075
C 18.58595 -1.50043 -1.64604
H 18.04905 0.58936 -1.59875
H 16.67074 -0.50769 -1.69573
C 18.75586 -1.59328 -3.15002
H 17.78455 -1.75330 -3.65338
H 19.41904 -2.42658 -3.44115
H 19.18713 -0.66380 -3.56511
H 18.19861 -2.46253 -1.25467
H 19.57612 -1.36566 -1.16621
H 14.96333 4.40490 3.23532
H 15.58835 1.94254 8.55929
H 16.17728 2.30826 4.69504
H 15.02399 1.00396 4.52132